CONTROLLING LIGHT-MATTER INTERACTIONS USING LOCAL-ASSEMBLIES AND LARGE-SCALE ARRANGEMENTS OF PLASMONIC AND QUANTUM-CONFINED NANOSTRUCTURES

A Dissertation
Presented to
The Academic Faculty

by

Sidney T. Malak

In Partial Fulfillment
Of the Requirements for the Degree
Doctor of Philosophy in the
School of Materials Science and Engineering

Georgia Institute of Technology
May 2017

CONTROLLING LIGHT-MATTER INTERACTIONS USING LOCAL-ASSEMBLIES AND LARGE-SCALE ARRANGEMENTS OF PLASMONIC AND QUANTUM-CONFINED NANOSTRUCTURES

Dissertation committee:

Dr. Vladimir V. Tsukruk, Advisor
School of Materials Science and Engineering
Georgia Institute of Technology

Dr. Zhiqun Lin
School of Materials Science and Engineering
Georgia Institute of Technology

Dr. Dong Qin
School of Materials Science and Engineering
Georgia Institute of Technology

Dr. Wenshan Cai
School of Electrical and Computer Engineering,
School of Materials Science and Engineering
Georgia Institute of Technology

Dr. Mostafa El-Sayed
School of Chemistry and Biochemistry
Georgia Institute of Technology

Date of Final Approval: **December 20, 2016**

Dedicated to my friends and family for their love and support, in particular my parents who have always encouraged me to keep learning and pushing forward toward new and more challenging pursuits.

ACKNOWLEDGEMENTS

I really want to thank my advisor Prof. V.V. Tsukruk for his motivation and guidance. From the onset he encouraged me to develop strong technical skills, to critically examine data (especially my own), and to tackle challenging projects. I also appreciate his patience because I took a bit longer to finish than initially planned. Prof. Tsukruk has developed a research group that provides the tools and materials needed for quality research. He has also pushed for a lab environment that encourages collaboration between group members, which made it a fun place to perform research and mature as a scientist and engineer. I also sincerely appreciate the recommendations and direction provides by my PhD dissertation committee members, Prof. M.A. El-Sayed, Prof. Z. Lin, Prof. W. Cai, and Prof. D. Qin. Their thoughts and recommendations have served as an additional valuable critical perspective on the research I've performed.

I also want to thank my collaborators from the Georgia Institute of Technology. These include Dr. M.A. Mahmoud and Dr. R. Near from Prof. El-Sayed's group for providing plasmonic colloidal nanoparticles and EBL structures, respectively. In addition, thanks to Dr. J. Jung and Y.J. Yoon from Prof. Lin's group for providing colloidal quantum dots. Further thanks go to my collaborators from other institutions on the Synthetic Photonics Multidisciplinary University Research Initiative (MURI) for their practical suggestions, measurement assistance, and theoretical insights regarding lasing and parity-time system design. These collaborators include Dr. E. Lafalce/Prof. V. Vardeny (University of Utah), Dr. G. Liang/Dr. T. Ramathasan/Prof. E. Thomas (Rice University), Prof. T. Kottos (Wesleyan University), and A.K. Jahromi/Prof. A. Abouraddy/ Prof. D. Christodoulides (University of Central Florida).

Finally, I want to thank all the SEMA group members who provided technical assistance and discussion, in particular Dr. T. König, Dr. D. Kulkarni, Dr. P.A. Ledin, Dr. C. Ye, Dr. I. Choi, Dr. S. Young, Dr. W. Xu, and Dr. K. Hu. Special thanks to Dr. Z.A. Combs and Dr. R. Kodiyath who mentored me and helped me develop my technical skills when I first joined the group. Final thanks to C.H. Lin and M.J. Smith who are my current teammates on the Synthetic Photonics MURI project and played a large part in helping me complete much of the work outlined in this dissertation.

TABLE OF CONTENTS

LIST OF TABLES

LIST OF EQUATIONS

LIST OF FIGURES

SUMMARY

Plasmonic nanostructures and quantum dots have great potential in the area of photonics due to their tunable optical absorption, scattering, and emission, as well as their compatibility with many nano/microscale deposition and patterning techniques. However, a large variety of internal and external factors influence confined plasmonic nanostructures and quantum dots, and their characteristics of optical scattering and photoluminescence emission. Accordingly, an in-depth knowledge of these factors is required to effectively utilize these tunable plasmonic nanostructures and quantum dots in scientific and technological applications. This dissertation develops an understanding of how the confinement mechanisms/conditions and resulting light-matter interactions of plasmonic and quantum dot nanostructures depend on three levels of system hierarchy. These levels of hierarchy include individual nanostructure, nanostructure-nanostructure local-assembly, and large-scale nanostructure arrangement. The surface confinement of plasmons (collective electron oscillations) and their localized-surface plasmon resonances are the focus for plasmonic nanostructures. The quantum confinement of excitons (electron-hole pair quasiparticles) and their electronic radiative relaxation pathways are examined for quantum dots (QDs).

Both plasmonic (Au and Ag) and quantum confined (CdSe and CdSe/ZnS) nanostructures are utilized as the active optical component in these systems since they exhibit tunable optical properties (via changes to shape, size, and material), can be surface functionalized (capping agent), and are compatible with various deposition and nano/microscale patterning techniques. Since the optical properties of plasmonic nanostructures and quantum dots arise from fundamentally different confinement phenomena (surface confinement of plasmons and quantum confinement of exciton wavefunctions, respectively), a wide breadth of optical phenomena can be studied, including enhanced localized scattering, electric-field enhancement/localization, tunable emission, optical gain/loss, and spatial emission patterning. The general approaches and results of these studies are summarized below:

- As a first step, non-traditional local-assemblies of plasmonic nanostructures (vertically stacked) are identified and developed, and structure-optical scattering correlations for specific individual plasmonic nanostructures and their local-assemblies are made via direct SEM-AFM-hyperspectral comparisons. In conjunction with finite-difference time-domain (FDTD) electromagnetic modeling, we show that higher-order plasmonic resonances exist in these novel stacked nanostructure assemblies. Utilizing a stacked design reduces the lateral footprint and provides new ways to tailor plasmonic coupling and overall electromagnetic enhancement (compared to traditional lateral coupled assemblies).

- Next, a more complex hierarchal system is developed from individual and locally-assembled plasmonic Ag nanocubes (AgNCs) and nanospheres (AgNSs) within a 3D porous waveguide. In this system, the local assembly of AgNCs is controlled using a polyelectrolyte layering method, allowing for the deposition of either individual (dispersed) or locally-assembled (aggregated) AgNCs, while the arrangement of the nanostructures is controlled by the 3D porous waveguide. FDTD modeling shows that assembled nanocubes exhibit the highest electric fields due to the presence of edges/corners and strong plasmonic coupling. These hierarchal

plasmonic systems are shown to exhibit exceptional limits-of-detection for vapor phase benzene thiol and n-methyl-4-nitroaniline (500 ppb and 3 ppb, respectively).

- Focus is then shifted to optically emitting quantum dot and how the QD architecture (core, core/shell, core/graded shell) of individual quantum dots affects the evolution of its optical characteristics while in darkness or under light exposure in a thin film. Distinct shifts are shown to occur for different QD architectures due to the exposure of the QD core to the surrounding environment. For example, changes of emission intensity (decreases and increases) and spectral position (blue shifts and red shifts) are all observed, which can be reversible or irreversible (depending on QD architecture and exposure conditions). Additionally, it is revealed that competition between the reversible and irreversible mechanisms underlying these emission changes leads to unique and important behavior, including: decay-to-recovery intensity trends, meta-stable bright states that can be activated/deactivated numerous times, and decoupled optical changes (reversible intensity changes with irreversible spectral shifts).

- The next step examined how the average QD-QD spacing in thin films affects light-matter interactions over larger scales (microns-millimeters). Specific attention is placed on characteristics like light propagation, optical amplification, and optical attenuation. It is shown that the molecular dimensions of the QD ligand affects important physical properties (film morphology, QD-packing density) and optical characteristics of the QD films (optical density, refractive index). These changes directly influence the light-matter interactions over larger spatial scales, specifically waveguiding efficiency/losses and optical amplification/attenuation within the film. More specifically, we show that increasing QD-packing density increases both optical gain (via increased stimulated emission and improved waveguiding) and optical attenuation (via increased optical density and reabsorption).

- Finally, we use knowledge of QD architecture to develop new and unique patterning strategies that vastly expand the ability to spatially modulate QD emission via non-physical photopatterning. A variety of novel positive, negative, negative-to-positive, edge-profile, face-profile, and multicolor photopatterns are developed that have exceptional contrast, uniformity, and spatial-spectral complexity. Furthermore, novel interference-based exposure strategies are implemented to reach exceptional sub-micron feature resolution while increasing throughput by orders of magnitude.

The fundamental principles identified in this work will help guide the development of miniaturized, tunable, efficient photonic systems that exceed or exhibit properties that cannot be achieved by bulk materials. By understanding the relationship between the nanostructure confinement mechanisms/conditions and the system hierarchy, light-matter interactions (like localized-scattering, localized electric field enhancements, spectral emission evolution, spatial light propagation, optical attenuation/enhancement, and spatially modulated light emission) can be measured, controlled, and potentially implemented in new technologies like extremely sensitive chemical sensors, miniaturized lasers, advanced anti-counterfeiting labels, and parity-time optical isolators.

CHAPTER 1

INTRODUCTION

The increasing demand for advanced photonic systems that exhibit well-controlled scattering/absorption/reflection/transparency/emission, electric field enhancement and localization, and gain/loss has driven the investigation of new materials and the development of novel system designs that function and have results different from conventional practices. Nanoscale systems, including planar films, patterned surfaces, and nanostructures are a promising candidate for these next-generation photonic systems due to advances in the control and manipulation of their synthesis, deposition, and patterning.[1] In addition, the development of improved characterization methods has ushered in an unprecedented understanding of the interesting physical, thermal, electronic, and optical properties of these nanomaterial systems.

The discovery and subsequent development of plasmonic nanostructures and quantum confined particles (quantum dots) shows particular promise for new optical systems, including those involved with detection, imaging, intensity/spectral/phase modulation of light, and communication.[2,3,4] The great advantage of these nanomaterials over conventional bulk materials (for photonic systems) is that these nanostructures exhibit optical properties that can be tuned by simply changing their size, shape, and proximity to adjacent nanoparticles. This tunability is due to confinement of plasmons (for plasmonic particles) or quantum confinement of excitons (for quantum dots) which results from the small dimensions of the nanostructures. By combining these nanoparticles with micro and nanoscale patterning techniques, optical systems can be created that exceed or exhibit properties that cannot be achieved using bulk materials for the development of photonic technologies with highly tunable characteristics.

1.1 Plasmonic nanostructures and systems

1.1.1 Introduction to plasmonic nanoparticles

Plasmonic nanostructures are generally composed of Au, Ag, or Cu and have sizes ranging from 5-100 nm.[5,6] A number of well-established synthesis protocols make it possible to obtain plasmonic nanostructures with a wide variety of shapes including spherical/spheroidal,[5,7,8] cubic, [9,10] rods,[11] rhombic,[10] and triangular prism (as well as others) (**Figure 1.1**).[12,13] These approaches include both bottom-up seed-growth reduction methods and top-down lithographies and template assisted growth, with both offering relatively shape and size polydispersity below ~15%.[3,5,10,14]

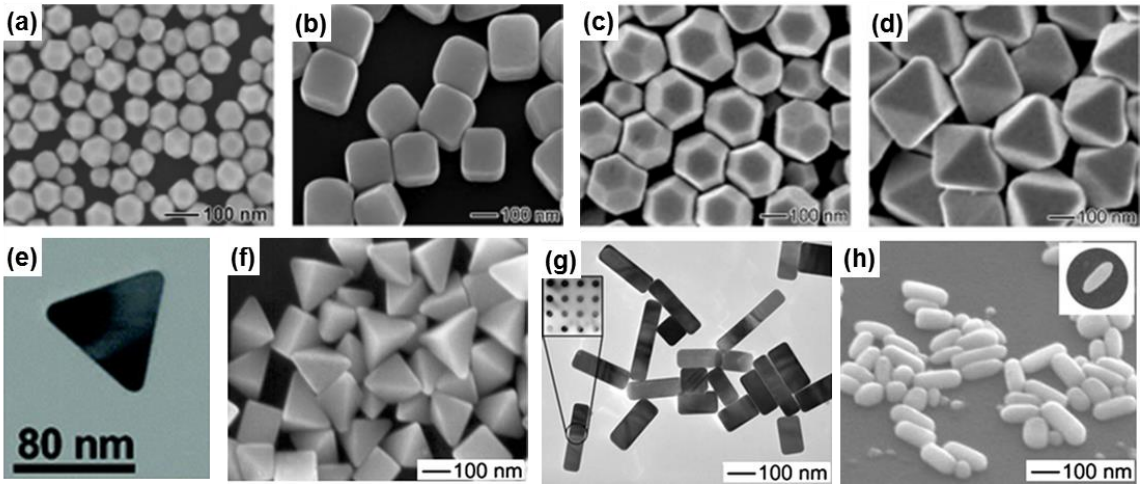

Figure 1.1: Various crystalline Ag nanostructures created via a seed-growth method, displaying the large variety of nanostructures that are available. **(Frames (a-d) adapted from ref.9, frame (e) from ref.12, and frames (f-h) ref.11)**

The study of plasmonic nanostructures has been driven in large part by the ability to tune the optical absorption and scattering of these structures across the visible spectrum and intro the near infrared region (**Figure 1.2**).[6,11,15,16] Furthermore, the optical

absorption and scattering from these nanostructures is often very intense due to the very strong light-matter interactions between incident photons and free electrons.[3,11] These two behaviors result from the presence of localized surface plasmons, which emerge within these plasmonic nanostructures under incident electromagnetic radiation (discussed in more detail later).

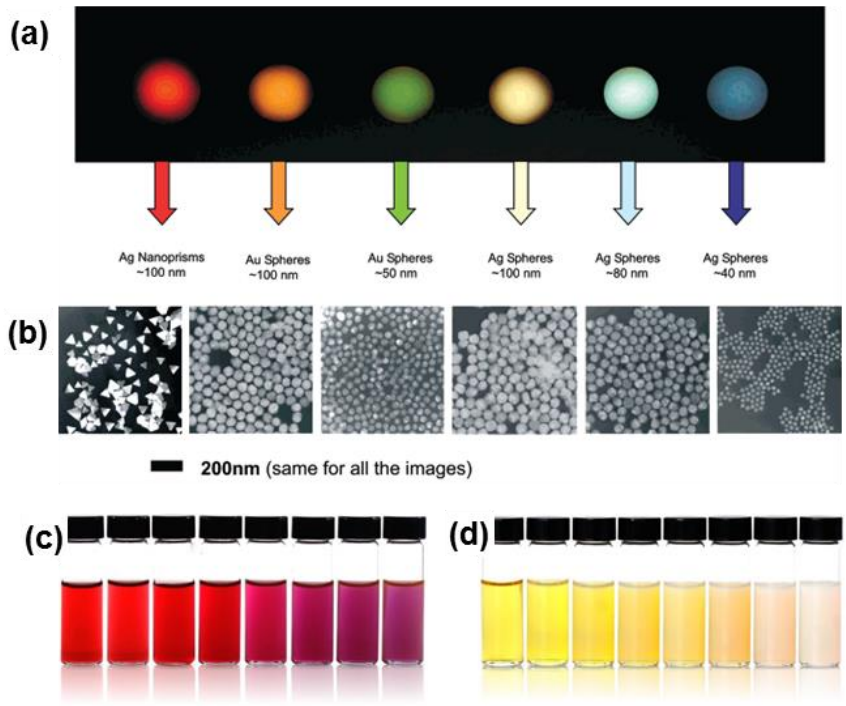

Figure 1.2: (a) Light scattering from plasmonic nanostructures of various size, shape, and material, and (b) SEM of the corresponding structures. Images of solutions of (c) Au nanoparticles (5-100 nm) and (d) Ag nanoparticles (5-100 nm). **(Frames (a,b) adapted from ref.15, frames (c,d) adapted from ref.16)**

1.1.2 Localized surface plasmons

The electric field of incident electromagnetic radiation can strongly interact with the free electrons in materials like Au, Ag, and Cu, and can lead to collective electron displacement. The collective electron displacement can be either oscillations or a propagating wave depending upon the degree of confinement the electrons experience

(**Figure 1.3**).[3] In the case of plasmonic nanostructures, the electrons are restricted by the sub-wavelength physical dimensions of the structure. The driving electrostatic force from the incident radiation collectively displaces the free electrons from the positive lattice. However, the displaced free electrons become localized at the surface of the nanostructure due to a difference in sign of the real component of the complex permittivity between the metal nanoparticle and the ambient dielectric.[3,11] The combination of an oscillatory driving force, an electrostatic restoring force between the electrons and lattice, and confinement to the nanostructure leads to the formation of localized surface plasmon resonances (LSPR). This situation is often approximated using the Mie solution to Maxwell's equations.[3,11,17] On the other hand, plasmons can propagate when the collective electron displacement is not confined to a small volume (**Figure 1.3**).

As with acoustic resonances in pipes, the strength of a LSPR will depend on the specific conditions of the confinement, in this case the size, shape, material, and surrounding environment of the nanostructure.[6,18,19,20] Furthermore, the collective and coherent nature of the LSPR generates very intense localized electric fields at the surface of the nanostructures, which lead to very strong light-matter interactions. The combination of specific LSPR energies and strong-light matter interactions leads to the pronounced optical scattering and absorption observed from these nanostructures (**Figure 1.2**).[15,17,16]

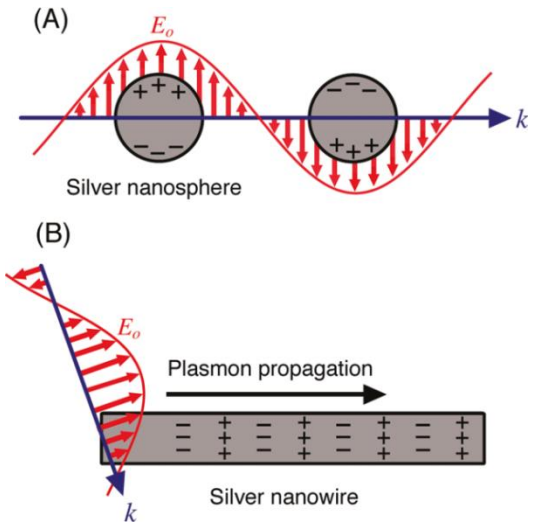

Figure 1.3: Schematic outlining the light-matter interaction in a plasmonic material. When electromagnetic radiation is incident on a plasmonic material is can produce either localized or propagating surface plasmons. (a) When the free electrons are confined to a small space ($d << \lambda$), such as in a nanostructure, they collectively oscillate within the structure to form localized surface plasmons (LSPR). (b) In the absence of confinement the plasmons can propagate. **(Figure from ref.3)**

1.1.3 Plasmonic nanostructure scientific studies

The unique properties of localized surface plasmons and the readily observed light-matter interactions have led to a large amount of theoretical and experimental fundamental research on these plasmonic nanostructures. Much of it has focused on Ag and Au nanoparticles because the real component of their complex permittivity is negative across much of the optical range, allowing them to satisfy the LSPR requirement mentioned earlier, and the internal losses are small.[21,22] For instance, it is well known from light scattering and absorption measurements that the plasmonic properties of noble metal nanostructures are sensitive to a combination of factors including material, shape, size, aspect ratio, dielectric ambient, distance between and orientation with respect to other nanostructures, and interactions with the excitation light source.[18,19,20,23,24]

Furthermore, due to the coherent nature of plasmons and their localization on the surface of the plasmonic nanostructure, very intense localized electric fields emerge when the nanostructure is excited with electromagnetic waves.[3,25] In turn, these localized electric fields are heavily impacted by the size, shape, and curvature of the corners/edges of the nanostructure (since these factors affect the surface plasmons). For example, it has been reported that nanostructures with sharp edges show higher E-field intensity than that of spherical nanoparticles due to charge concentration at the edges and corners.[26,27,28]

A number of general trends occur across nanostructures of different physical design and chemical composition. These trends were identified from experimental data and finite-differen time-domain (FDTD) theoretical modeling of optical scattering and absorption spectra. Furthermore, theoretical modeling of spatial charge distributions and electric field distributions of excited plasmonic nanostructures has been performed to understand the underlying plasmonic resonances leading to this optical behavior.

Size

First, smaller nanostrucures experience greater confinement of the LSPR and therefore will have higher energy LSPRs that leads to more pronounced optical scattering and absorption for blue frequencies (**Figure 1.4**).[11,15,29] Conversely, larger nanostructures have been observed to have red-shifted optical scattering and absorption resonances. In addition, smaller nanoparticles exhibit a greater absorption-to-scattering ratio (and larger nanoparticles greater scattering-to-absorption) since optical scattering scales according to R^6 and optical absorption to R^3.[3] Therefore, tuning the size of the nanoparticle has been shown to can change both the spectral position of the exctinction and the relative strength of each component (scattering versus absorption).

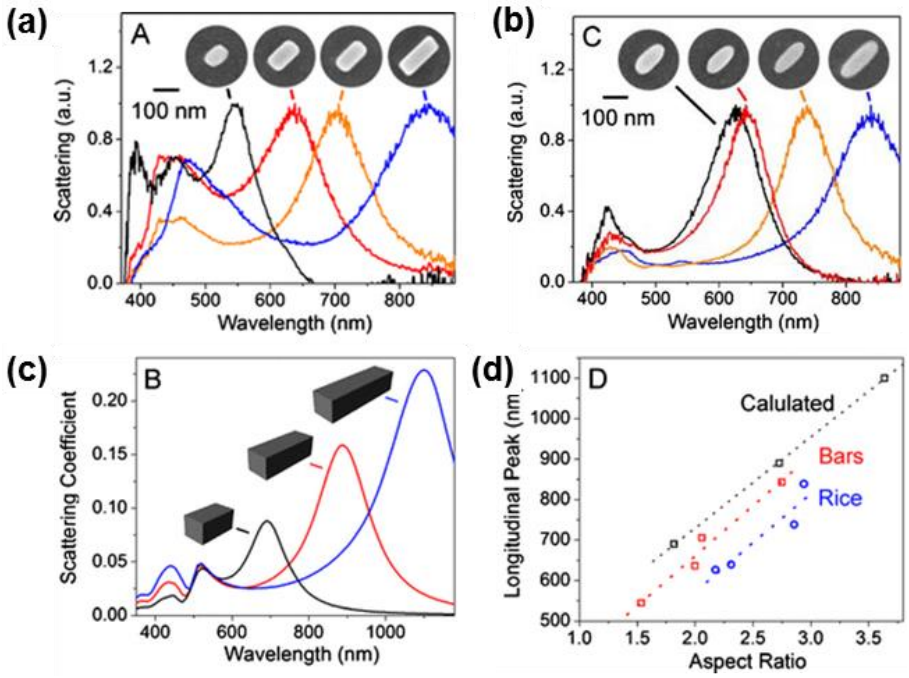

Figure 1.4: (a,b) Experimental and (c) theoretical scattering spectra from plasmonic Ag nanobars and nanrice of different size (volume and length). (d) Relationship of the primary resonance peak with aspect ratio (and length) showing the spectral tunability. **(Figure from ref.29)**

Shape

Second, the shape of the nanostructure has been shown to dictate the spatial complexity of the LSPR charge distribution. For example, smaller spherical nanostructures will have a simple dipole charge distribution while cubic nanostructures can exhibit higher order multipoles due to symmetry lowering (**Figure 1.5a-d**).[11,30] High aspect ratio nanostructures can also exhibit multiple plasmon resonances, one for the transverse and longitundinal directions (**Figure 1.4a,b**).[11,29] In fact, the transverse and longitudinal resonances can be selectively activated by controlling the polarization of the incident light.[29,31]

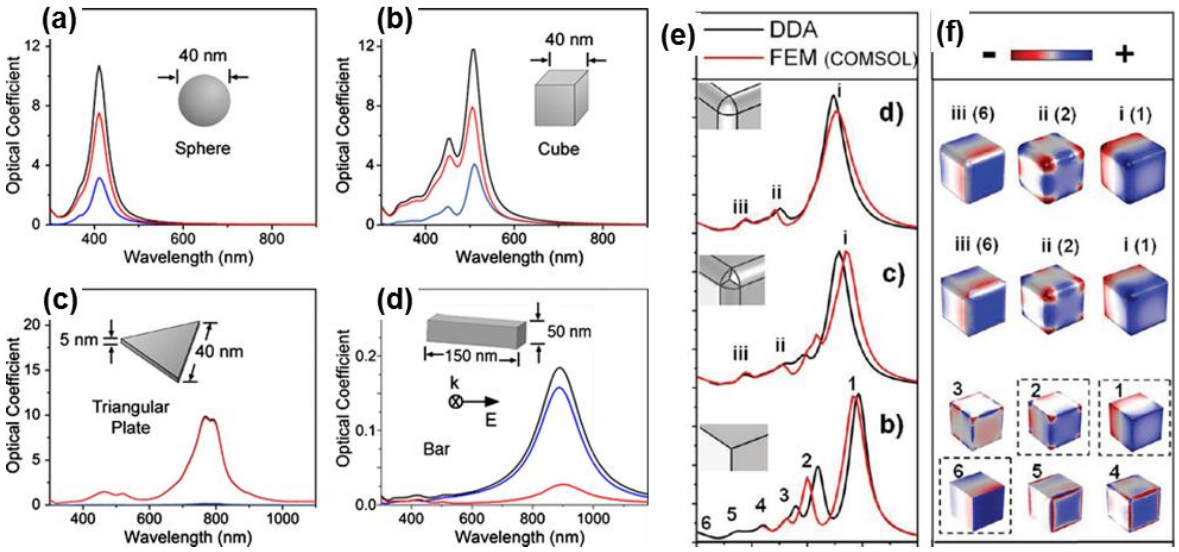

Figure 1.5: (a-d) Theoretical discrete dipole approximation modeling of the scattering, absorption, and total extinction of different Ag nanostructures. The number of resonance peaks depends on the shape of the nanostructure and its symmetries. (e,f) DDA modeling of be (e) extinction and (f) charge distributions for Ag nanocubes with different edge/corner rounding. **(Frames (a-d) reproduced from ref.11 and frames (e,f) acquired from ref.30)**

The rounding of sharp edges and corners has also been shown to alter the charge distributions and shift the plasmonc resonances, with rounding leading to a red-shift of the resonances since it effectively removes regions of high charge density (**Figure 1.5e,f**).[30] Sharp edges can lead to higher charge densities which increase the intensity of the localized electric fields (termed the lighting rod effect).[32] In fact, the electric field at sharp edges and corners can experience enhancements of orders of magnitude (**Figure 1.6**).

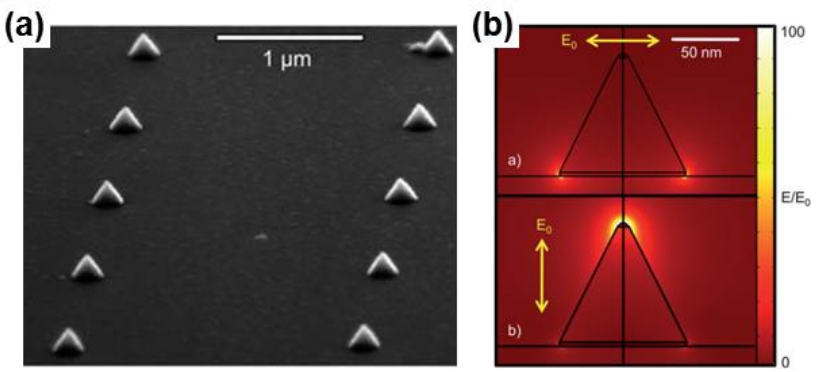

Figure 1.6: (a) SEM images of plasmonic conical nanoantennas and (b) finite element method modeling of the electric field enhancement that occurs at the sharp tip of the nanostructure under different incident light polarization. **(Figure acquired from ref.32)**

Surrounding environment

Third, the confinement conditions and resulting charge distributions, electric fields, and plasmon resonances of a nanostructure depend on the surrounding environment. For example, increasing the refractive index of the material surrounding a nanostructure can red-shift its plasmonic resonances.[33,34] Furthermore, putting a nanostructure on, or in close proximity to, a substrate can lead to bonding and antibonding modes that affect the optical extinction spectral position and localized electric fields (and enhancement) (**Figure 1.7**).[34]

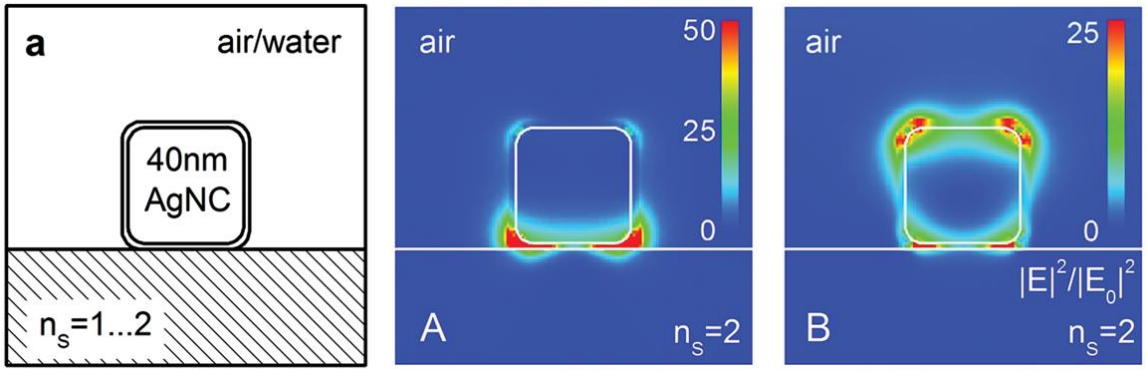

Figure 1.7: (a) Simple schematic of a Ag nanocube on a substrate, and FDTD modeling of the resulting electric field enhancement of the (b) bonding and (c) anti-bonding modes that result from optical excitation. **(Figure acquired from ref.34)**

In fact, depositing Ag nanocubes on concave surfaces was shown to make their primary plasmon peak more sensitive to the refractive index of the surrounding environment (compared to flat surfaces), presumably due to the presence of more complex and pronounced anti-bonding charge distributions.

Local-assembly (coupled nanostructures)

Lastly, the local-assembly of plasmonic particles plays a significant role on the confinement of the localized surface plasmons, resulting in significant changes to the resonance position, charge distribution, and intensity/location of the electric fields.[3,35,36,37] In fact, the local-assembly of plasmonic nanostructures is one of the most powerful, and most popular, strategies to modify the LSPR and to obtain exceptionally intense localized electric fields. When plasmonic particles are brought in close proximity, their surface plasmons begin to interact with each other which leads to the emergence of new red-shifted coupling resonances (**Figure 1.8**).

The spectral shift can be quite large (up to 75 nm) and is therefore easily observed.[37] However, the activation of the coupling resonance has been shown to be highly dependent upon the polarization of the incident light with respect to the local-assembly axis, with a longitudinal polarization providing the greatest red-shift (**Figure 1.8d,e**).[2] In fact, the strength of the plasmonic coupling behavior has been shown to follow a universal scaling law (exponential decay with separation distance) termed the plasmon ruler equation (**Figure 1.8f**)(**Equation 1.1**).[36,37]

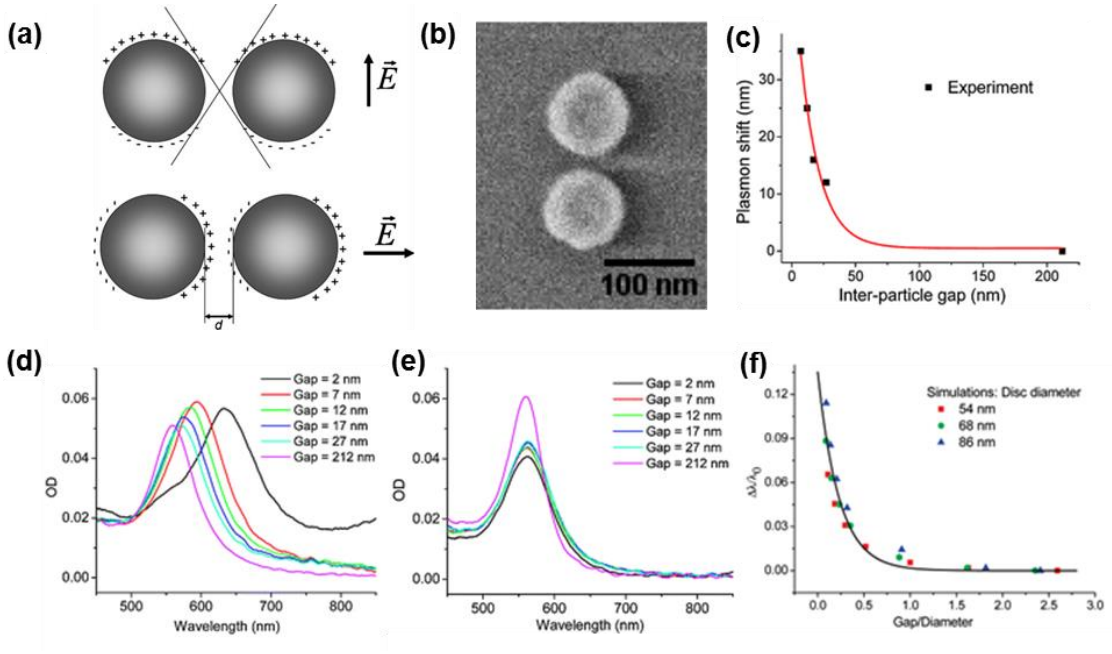

Figure 1.8: (a) Schematic of an electromagnetically coupled local-assembly of plasmonic nanostructures under different polarization. (b) SEM of a local-assembly of nano disks. (c) Shift of the plasmonic coupling resonance with gap distance. (d,e) Extinction spectra of the local-assembly under (d) longitudinal and (e) transverse polarization. (e) The universal scaling behavior for coupled plasmonic nanostructures. **(Frame (a) adapted from ref.2 and frame (b-f) from ref.36)**

Equation 1.1: Universal plasmon ruler equation for the spectral shift of the coupling resonance for coupled plasmonic nanostructures. **(Equation obtained from ref.36)**

$$\frac{\Delta\lambda}{\lambda_0} = A\, e^{\left[\frac{-\left(\frac{s}{D}\right)}{B}\right]}$$

Where, "$\Delta\lambda/\lambda_0$" is the fractional plasmon shift, "s" is the edge-edge separation, "D" is the nanostructure diameter, and "A" and "B" are fitted constants.

In addition, the electric field intensity present on the surface of the excited plasmonic nanostructure (and coupled assemblies) depends on the presence of adjacent plasmonic nanostructures (i.e. the local-assembly).[38,39] Typically, the greatest electric field enhancement occurs within the coupling region of these locally-assembled

plasmonic nanostructures, and as with the plasmon resonances, is heavily influenced by the inter-particle spacing and orientation of the individual structures with respect to each other. The EM enhancement factor for these coupled EM has been estimated, often via finite-difference time-domain (FDTD) electromagnetic modeling, in the hot spot formed between dimers of spherical nanoparticles as well as nanostructures with sharp edges.[40,41,42,43] These theoretical estimations predict that EM enhancements spanning orders of magnitude can occur in these hot spot regions.

1.1.4 Plasmonic nanostructure films and assemblies

Colloidal plasmonic nanostructures have been despoited into films and assembled into large-scale patterned arrangements using a variety of strategies. For example, infiltration techniques have been shown to yield simple free-standing close-packed Au nanoparticle (AuNP) films (**Figure 1.9a**).[44] Colloidal nanostructures can be assembled in solution using various binding strategies including molecular cross-linkers (**Figure 1.9b**),[45] controlled colloidal instability (**Figure 1.9c**),[46] DNA-origami (**Figure 1.9d**),[47] template-assisted layer-by-layer electrostatic assembly (**Figure 1.9e**),[48] and electron beam lithography (**Figure 1.9f-i**).[49] Many other strategies to assemble plasmonic nanoparticles exist as well due to the ability to easily functionalize the nanoparticles surface chemistry.[50,51,52,53,54,55]

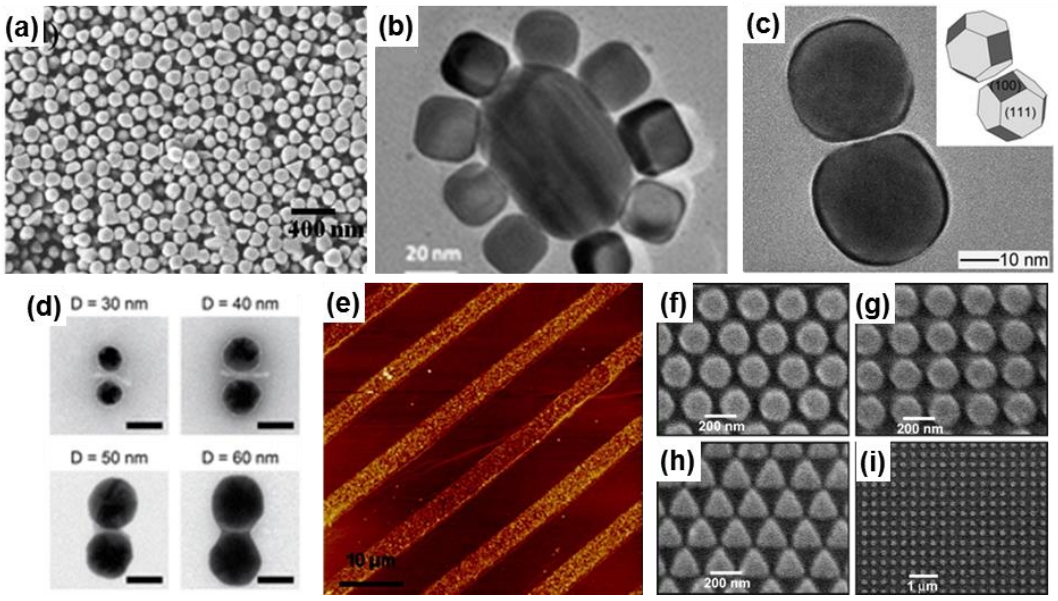

Figure 1.9: (a) SEM of a free-standing close-packed AuNP film, TEM of (b) a AuNP core-satellite assembly, (c) AgNS dimers, and (d) AuNP dimers assembled via DNA-origami. (e) AFM of AgNP patterned via capillary transfer lithography and (f-i) SEM of Ag nanostructures fabricated using EBL. **(Frame (a) adapted from ref.44, frame (b) from ref.45, frame (c) from ref.46, frame (d) from ref.47, frame (e) from ref.48, frame (f-i) from ref.49)**

However, as mentioned, the localized plasmonic resonances (and therefore optical characteristics) of plasmonic nanostructures are highly dependent on the characteristics of both the individual structures and their local-assembly. Therefore, a critical obstacle facing the investigation of fundamental plasmonic structure-property relationships is the design and control of well-defined nanostructures, their local-assembly, and their large-scale arrangement.

Top-down nanofabrication techniques like electron beam lithography (EBL) have often been employed to fabricate plasmonic nanostructures to address these obstacles. EBL can produce nanostructures of almost any shape with exceptional spatial resolution (~5-10 nm), making it possible to create well-controlled local-assemblies and large-scale arrangements (**Figure 1.10**).[56,57]

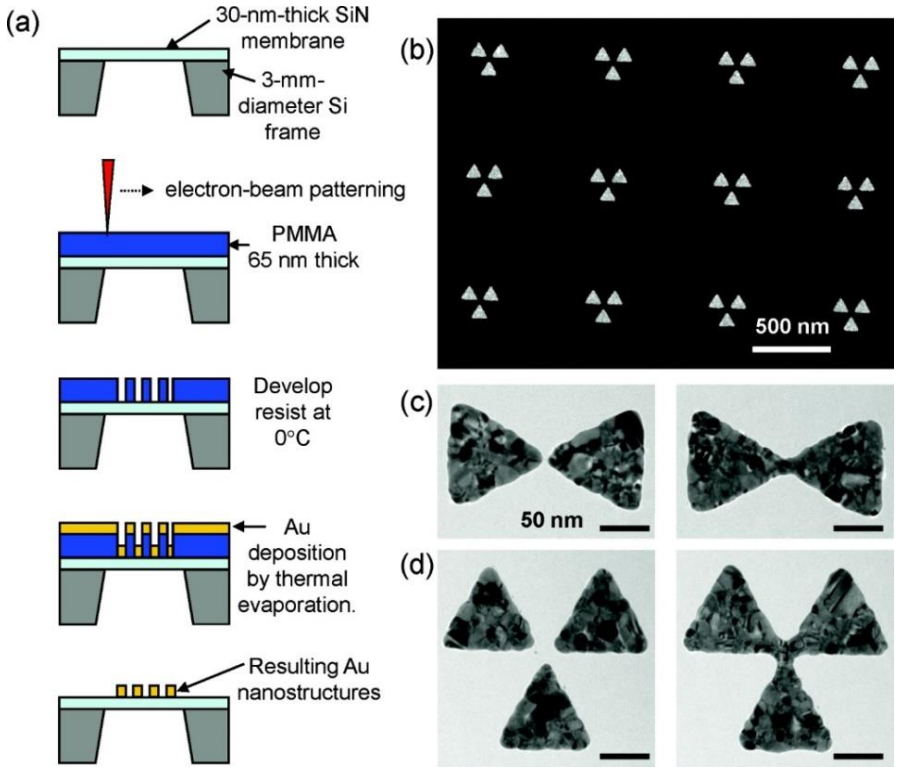

Figure 1.10: Schematic of the EBL approach and SEM micrographs of the resulting arrayed Au nanostructures. The high resolution and tight control of size, shape, and position of the nanostructures make this a powerful technique for investigating fundamental plasmonic properties. **(Adapted from ref.58)**

EBL provides a unique avenue for systematically varying specific geometric parameters like the size and shape of the nanostructures and their local assembly to understand how these factors independently affect the localized plasmon resonances. In addition, this technique can fabricate grid-like arrays of nanostructures, making it possible to locate and systematically characterize individual nanostructures with specific structural defects using a variety of techniques.[58]

As mentioned in the previous section, the plasmonic properties of EBL nanostructure arrays have been studied to determine how the size, shape, and spacing of the

nanostructures affect their plasmon resonance and coupling.[38,49] However, two important limitations remain: *First,* most of these plasmonic assemblies are limited to simple, 2D side-adjacent plasmonic local-assemblies (dimers of discs, rings, triangles) that do not take advantage of the third dimension to manipulate resonances and electric field distributions.[49] The fabrication and characterization of 3D EBL nanostructures is extremely rare due to the complexity of creating these nanoscale features and the difficulty of investigating optical properties that are highly-dependent upon specific structural "defects." *Second,* these studies often rely on simultaneous measurement of hundreds or thousands of nanostructures in order to reach practical signal-to-noise ratios.[59] However, small physical variations can result in dramatic changes in the plasmon resonances, so investigating the optical properties of specific nanostructures to develop clear structure-properties trends is particularly important.

In short, the control of plasmonic resonances through the manipulation of the local-assembly and large-scale arrangement of nanostructures is still a key objective in the development of sophisticated plasmonic sensing systems. This provides a motivation to investigate systems that utilize unique local coupling assemblies and large-scale arrangements. For instance, new ways to manipulate resonances and electromagnetic enhancement may be possible through the introduction of "stacked" dimer coupling schemes or by utilizing large-scale 3D assemblies.

1.1.5 Current plasmonic nanostructure systems and prospective applications

Plasmonic nanostructures have been utilized in a variety of applications due to their widely-tunable optical absorption and scattering, the emergence of new plasmonic resonances upon coupling, and the greatly enhanced and localized electric fields that

can surround these nanostructures. These include complex systems that can manipulate light for use in energy transport,[60,61] optical circuits,[62] light concentration and manipulation,[63,64] biodiagnostics,[65] and sensing.[66,67,68] For example, Au nanoparticles have been incorporated into multilayered thin films to produce broadband super absorbers (**Figure 1.11**).[69] The broadband behavior results from the individual Au nanoparticle resonances and the coupling resonances that emerge with the Au film.

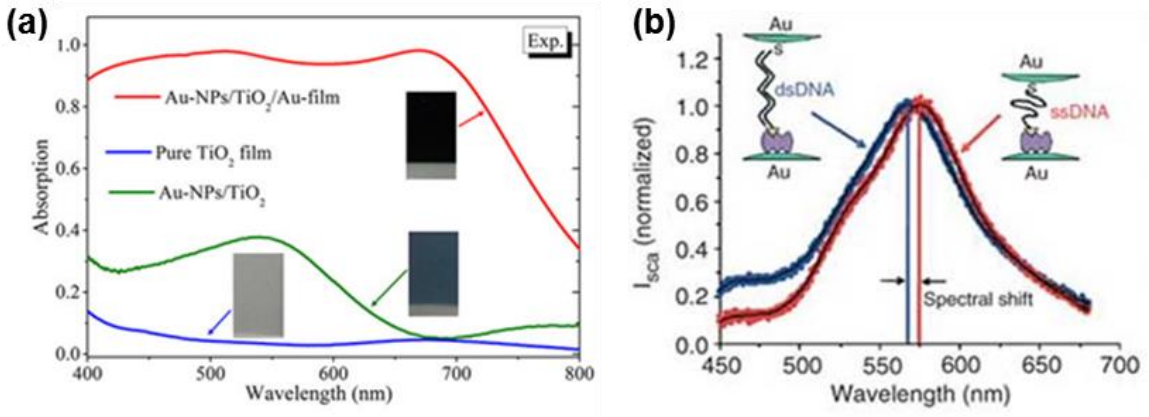

Figure 1.11: (a) Exceptionally high and spectrally broad optical absorption from a layered system utilizing Au nanoparticles. (b) LSPR DNA hybridization biological sensor. **(Figure (a) adapted from ref.69 and figure (b) adapted from ref.67)**

Sensing platforms utilizing plasmonic nanostructures, in particular surface enhanced Raman scattering (SERS) and localized surface plasmon resonance (LSPR), have been the focus of many detection schemes because of their high sensitivity, non-destructive behavior, and fast response time.[66,67,70,71] Biological sensors have been developed using Au nanoparticles functionalized with ssDNA.[67] Upon exposure to a specific ssDNA, DNA hybridization occurs, causing the spacing between the Au nanoparticle assembly to change which leads to a shift in the LSPR position.

Surface-enhanced Raman scattering (SERS) is another detection technique that utilizes plasmonic nanostructures. SERS enhancement is largely due to the huge electromagnetic field that exists in the small gaps between plasmonic metal nanostructures, termed SERS hot spots.[66,70,71,72] It was discovered that local-assemblies of closely-spaced plasmonic nanostructures provide very high SERS enhancement of the target analyte due to the exceptionally enhanced electric fields within the SERS hot spot region of the local-assembly (**Figure1.12**).[73]

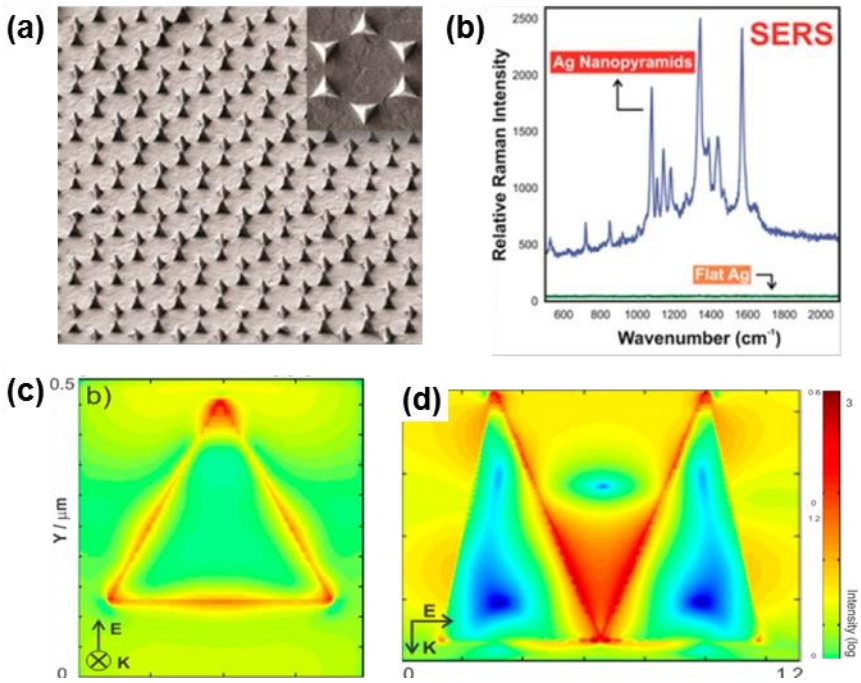

Figure 1.12: (a) SEM of plasmonic Au tetrahedral nanopyramids fabricated using nanosphere lithography. (b) SERS enhancement of 4-nitrothiophenol. FDTD modeling of the electric field enhancement at the (c) tip/edges of a nanopyramid and (d) between adjacent coupled nanopyramids. **(Figure adapted from ref.73)**

The various fundamental discoveries in nanoscale plasmonic science has led to great advancements in SERS detection, including exceptional trace-level detection of hazardous chemicals and biomolecules,[48] with levels of detection down to a single

molecule.[74,75,76,77,78] Furthermore, SERS works at typical environmental temperatures and pressures.

1.2 Quantum-confined nanostructures & systems (quantum dots)

The highly-localized and intense electric fields of localized plasmons (of plasmonic structures) allows for greatly enhanced light-matter interactions. Strong light-matter interactions in turn make it possible to leverage the tunable properties of these nanostructures to create photonic systems with enhanced optical scattering and absorption, and to generate exceptionally intense and localized electromagnetic fields. For example, strong optical scattering and absorption could be particularly useful when trying to develop very thin film optical filters and light absorbers that require specific spectral profiles (i.e. targeted low-pass, high-pass, or band-pass filtering). However, a drawback of plasmonic nanostructures is that they do not emit light and thus have limited application in emission-based systems like lasers and display technologies. Therefore, we shift attention to quantum dots, another confinement-based photonic nanostructure that can emit light when excited.

1.2.3 Introduction to quantum dots

Quantum dots (QDs) are zero-dimensional spheroidal nanostructures with sizes ranging from 1-10 nm composed of semiconducting material combinations like CdSe, CdS, InP, PbS, and PbSe (**Figure 1.13**).[79] As with plasmonic nanoparticles, QDs have well-known synthesis approaches, which generally involve the pyrolysis of organometallic precursors in a coordinating solvent like trioctylphosphine oxide (TOPO).[80,81,82,83,84] In addition, promising greener synthesis of QDs has also been developed using an enzyme

controlled biomineralization process which could also significantly reduce costs.[85] These synthesis procedures have been refined to the point where exceptionally low polydispersity can be achieved (<10%), which leads to highly uniform optical properties within a single batch of QDs.[86]

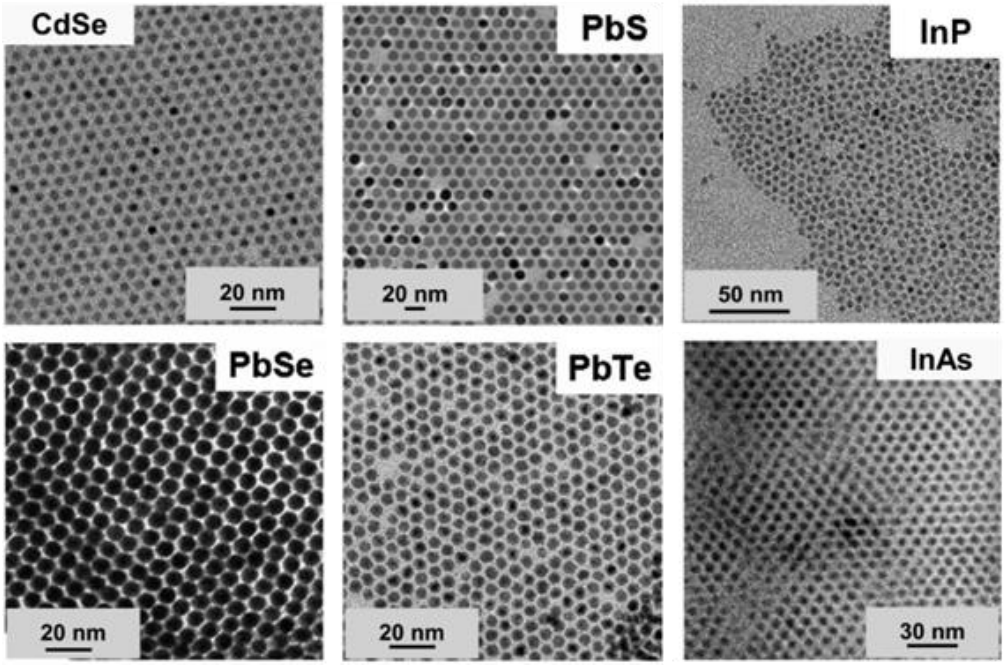

Figure 1.13: TEM micrographs of core QDs of different material composition. **(Images adapted from ref.79)**

The synthesis of more complex QD architectures like core/shell, core/shell/shell, and core/grade shell has also been well-established (**Figure 1.14a**).[87,88,89,90] These layered QDs are typically designated according to where the excited electron and hole wavefunctions are localized within the QD (**Figure 1.14b**).[90,91,92] Type-I core/shell QDs (like CdSe/ZnS) have electron and hole energy levels that cause the exciton to be confined to the same region within the QD (either the core or the shell). Type-II core/shell QDs (like CdTe/CdSe & InP/CdS) have the excited electron and hole wavefunctions confined to separate regions of the QD (one in the core and one in the shell).[88,92] Quasi type-2 QDs (like CdSe/CdS) have either the hole or electron

wavefunction delocalized across the QD, leading to a partial reduction in wavefunction overlap.[90,91]

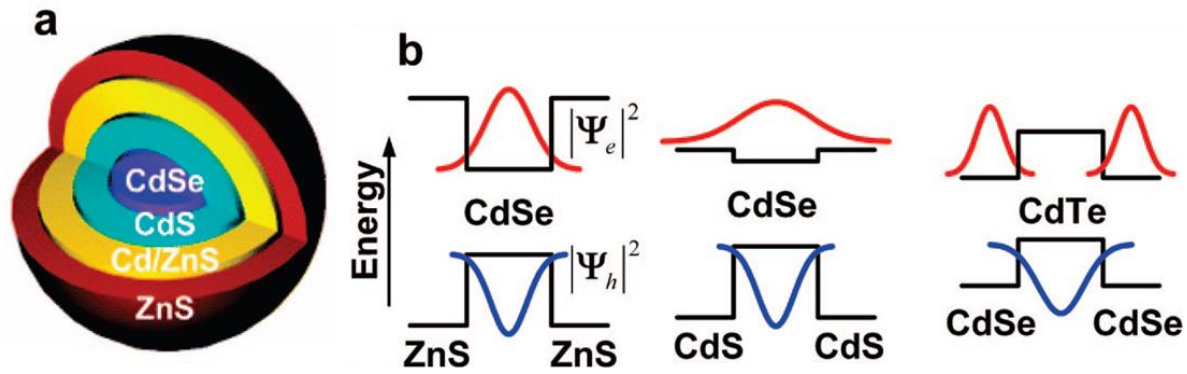

Figure 1.14: QDs can be synthesized to have simple (core) or complex core/shell architectures. (a) Schematic of a core/multishell QD. (b) Schematics of the localization of the electron and hole wavefunctions in type-I (left), quasi type-II (center), and type-II (right) core/shell QDs. **(Figure adapted from ref.91)**

There are a variety of selection criteria to consider when determining which type of QD (type-I, type-II, quasi type-II) is appropriate for a specific application, since the localization and overlap of the electron and hole wavefunctions affects the available exciton relaxation pathways and the rates of these pathways (which affects a number of important QD properties (discussed later)). For example, type-I core/shell QDs with core-localized electrons and holes are often used as optical emitters, since the inorganic shell can isolate the exciton from the environment which can stabilize the QD optical characteristics against environmental factors. In addition, the protective shell tends to passivate non-radiative surface traps on the surface of the QD core, which makes the QDs much more efficient optical emitters (discussed later).[79,93]

Quantum dots (QDs) are an ideal nanostructure for studying confinement mechanisms and conditions for two reasons: First, the wavefunction of the exciton (quantified via the Bohr radius) spans approximately 5-7 nm for many common QD materials. This means

QDs with size from 2-10 nm, which can be reliably synthesized using well-known protocols, can exhibit quantum confinement of the exciton.[94] Second, quantum confinement of the QD exciton leads to a number of unique and easy-to-observe optical phenomena, the most important being the emergence of size-dependent optical absorption (Abs) and photoluminescence (PL). In this case, smaller QDs display bluer absorption/emission due to greater exciton confinement, while larger QDs exhibit redder emission due to less pronounced exciton confinement.[95,96,97] In fact, QD photoluminescence emission can be tuned from the ultraviolet (UV) across the visible range to the near-infrared (NIR) by controlling the material and size of the quantum dot during synthesis (**Figure 1.15**).[79,98,99]

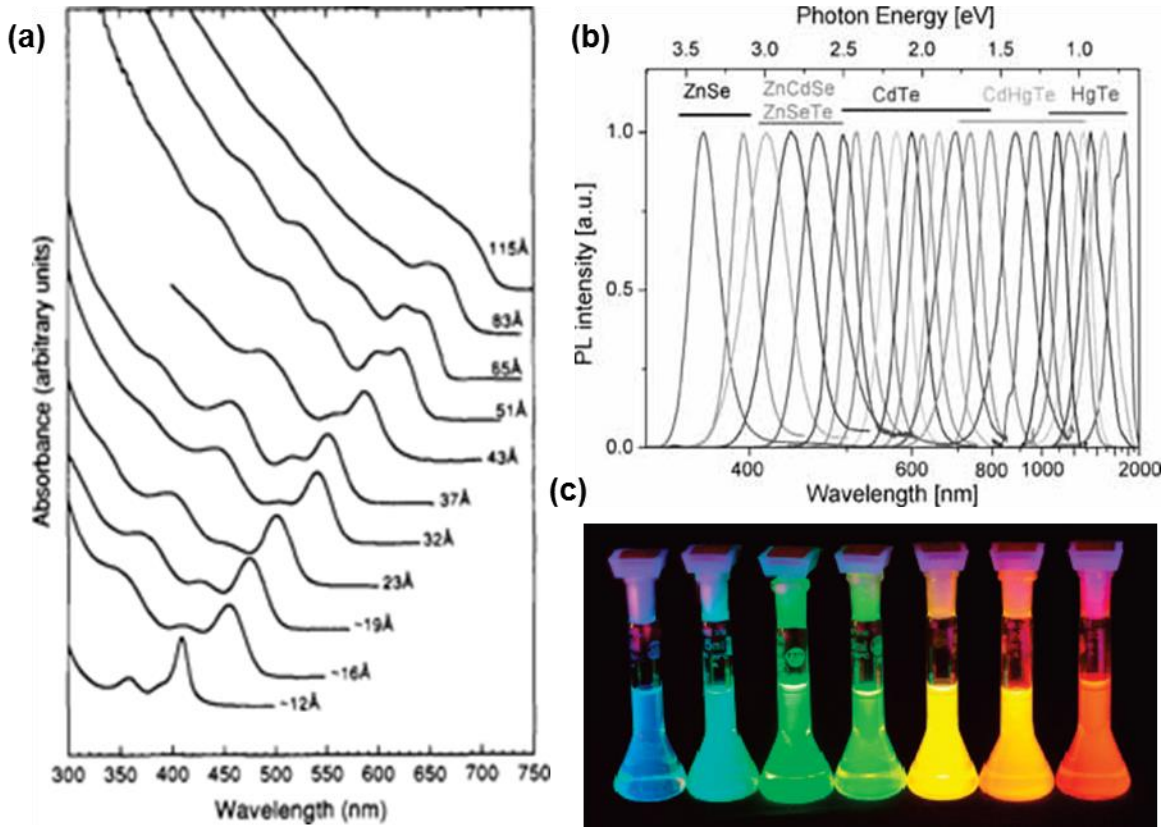

Figure 1.15: (a) Optical absorbance and (b) photoluminescence emission spectra of core QDs of different size and material combination. (c) Image of the photoluminescence from QD solutions under UV excitation. **(Plots (a,b) adapted from ref.98 and image (c) from ref.99)**

The optical absorption and photoluminescence of QDs of different size and composition do have a number of common characteristics, which include broad-band absorption (down to the UV), narrow-band emission (full-width half-max < 40 nm),[98] tunable Stokes shifts (10 nm to >100 nm),[100] and strong emission (quantum yields up to 90%).[93] Furthermore, QDs can be synthesized with low polydispersity (<10%),[86] are compatible with ligand exchange processes (polar to non-polar solvent compatibility),[86] and can be integrated with film deposition processes and various nanoscale and microscale patterning techniques. These characteristics have opened QDs up to a variety of applications including imaging/labelling/sensing in biological investigations,4 LEDs,[101] solar cells,[102,103] and optical gain media.[104,105]

1.2.4 Exciton quantum confinement

The wide-range of absorption and emission options that can be achieved using QDs could have profound ramifications for scientific experimentation and technological development. For example, a report discussing global market growth and future commercial prospects of QD technology has suggested that QD revenue could reach $3 billion by 2018, where a large portion of this revenue will likely be due to integration with LED technologies.[106] Therefore, understanding how quantum dots interact with light is very important for scientific understanding and technological development.

To understand quantum confinement of the QD exciton, a number of things need to be considered: *First,* the exciton is a neutral quasi-particle composed of an electron-hole pair bound to each other via the Coulomb interaction that emerges upon absorption of electromagnetic radiation.[107] *Second,* quantum confinement of this QD exciton

essentially follows the particle-in-a-box example commonly examined in quantum mechanics.[97,108] In short, the quantum confinement of a particle's wave function within a quantum potential well restricts the available energy levels, leading to discrete energy bands and in the case of semiconducting QD, a tunable band gap. The band gap energy becomes dependent upon the degree of quantum confinement, which depends on the size of the quantum well (QD) and the unconfined band gap of the bulk material (**Equation 1.2**).[97]

Equation 1.2: Relationship between the band gap energy of a QD and the bulk material using the approximation of a spherical quantum well with an infinite barrier. **(Equation obtained from ref.97)**

$$E_g(QD) = E_g(bulk) + \frac{\pi^2 \hbar^2}{2m_r R^2}$$

$$m_r = \frac{1}{\left(\frac{1}{m_e} + \frac{1}{m_h}\right)}$$

Where "m_r" is the reduced electron-hole mass and "R" is the radius of the QD. In the case of a semiconducting nanoparticle, discrete widely-separated energy levels form around the bandgap, the bandgap will depend on the degree of quantum confinement, and the higher energy levels will have minimal energetic separation (**Figure 1.16a,b**).[109,110] This combination of discrete energy levels and a band of closely spaced higher energy levels makes QDs an intermediate form of matter between discrete molecules and bulk-scale materials (**Figure 1.16**).[109]

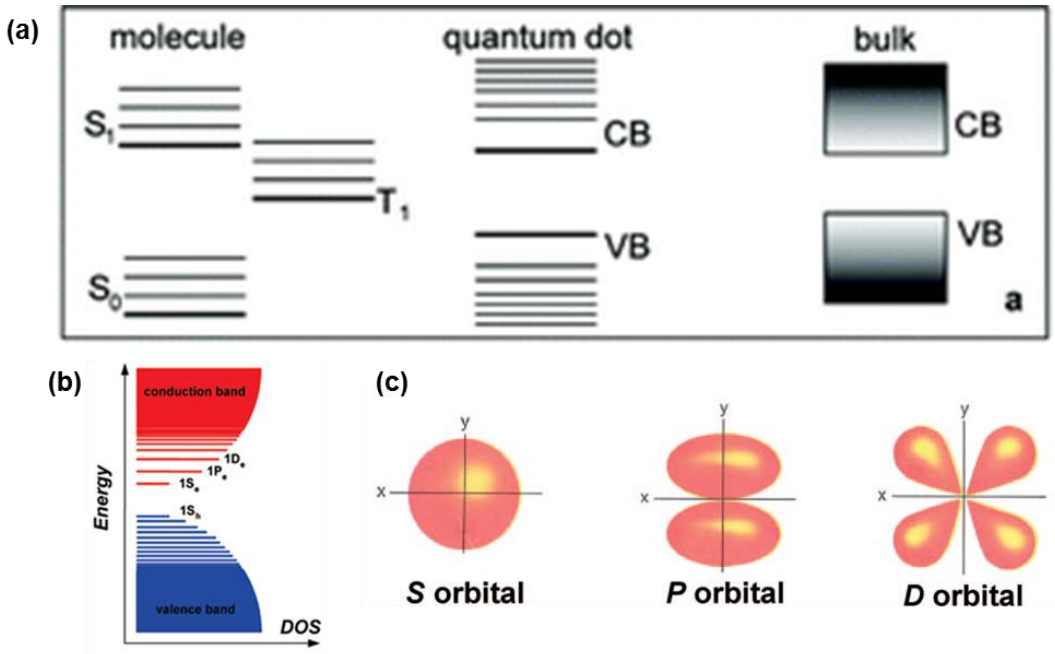

Figure 1.16: (a) General energy level schematic for a generic molecule, quantum dot, and bulk semiconductor material. The molecule has the most pronounced spacing between energy levels while bulk semiconductor materials have a continuous energy level continuum (around the band gap). (b) Energy diagram of QDs showing the discrete (molecule-like) energy level spacing around the band gap and the more continuous (bulk-like) energy level continuum at much higher energy levels. (c) The atomic orbitals corresponding to the discrete energy states around the band gap. **(Panel (a) reproduced from ref.109 and panels (b,c) from ref.110)**

In fact, the degree of quantum confinement experienced by an exciton depends on the Bohr radius of the exciton and the space available for that exciton,[111] where the exciton Bohr radius is the most probable exciton radius in its lowest energy state. Higher quantum confinement occurs if the size of the potential well is reduced or the exciton Bohr radius is increased.[108] Higher quantum confinement causes greater energy level spacing, which in the case of QDs increases the band gap and leads to bluer PL emission. The exciton Bohr radius depends on the dielectric constant of the material and the effective mass of the electron and hole that make up the exciton (which also depends on material), and the energy levels being considered.[112] A table detailing the exciton Bohr radius for various materials is shown below (**Table 1.1**).[111,112] Cadmium

and lead chalcogenides are often used as the QD material due to the large exciton Bohr radii, which makes it possible to achieve quantum confinement with particle sizes ranging from 2-10 nm.[113]

Table 1.1: The Bohr exciton radius (nm) for various common QD materials. **(values obtained from ref.111 & 112)**

Material	Bohr Exciton Radius (nm)	Reference
CdSe	6.1, 5.4	Grahn, Fox
CdS	3.1, 2.7	Grahn, Fox
CdTe	6.5, 6.7	Grahn, Fox
ZnSe	2.8, 4.5	Grahn, Fox
ZnS	1.7	Grahn
ZnTe	4.6	Grahn

Third, the strength of the interaction between the QD exciton and incident electromagnetic radiation (technically called the exciton-polariton[107]) is dictated primarily by the QD absorption cross-section (cm^2). A simple relationship for predicting the absorption cross-section has been identified which depends on the size and material of the QD. Essentially, the absorption cross-section is related to the physical cross-section with corrective factors to account for local field effects and size-scaling (**Equation 1.3**).[113,114,115]

Equation 1.3: Relationship between the absorption cross-section of a spherical nanostructure and its physical and electromagnetic characteristics. **(Equation obtained from refs.113,114,115)**

$$\sigma_{NC} = \frac{4\pi}{3} |f|^2 \alpha_b R^3$$

Where "f" is the coefficient for local field effects, "α_b" is the absorption coefficient (bulk material), and "R" is the radius of the QD (cm). Absorption cross-section values of 10^{-15} for PbS, 10^{-15} for PbSe, and 10^{-14} - 10^{-16} for CdSe are common.[116,117,118,119] It is important to note that the values for absorption cross-section are nearly 10-1000 times smaller than the physical cross-section (10^{-13} cm^2) due to weak light-matter interactions.[113]

Fourth, the relaxation of the exciton can follow both radiative and non-radiative paths, which often follows the expectations from the Jablonski energy description developed for more traditional fluorescent dyes (**Figure 1.17**). Results indicate that there are a number of steps involved in the excitation and emission process, including: photoexcitation ($\tau = 10^{-15}$ sec), intra-system conversion and vibrational relaxation ($\tau = 10^{-12}$ sec),[116] non-radiative Auger relaxation ($\tau = 10^{-11}$ to 10^{-10} sec),[120,] solvent relaxation ($\tau = 10^{-10}$ sec), radiative relaxation via PL emission ($\tau = 10^{-9}$ sec), and relaxation from a triplet state ($\tau = 10^{-3}$ to 10^{2} sec). Although the excitation-emission process is relatively complex, the large difference in magnitude of life-time of each step combined with the myriad relaxation mechanisms provides many ways to control and manipulate the PL of these particles.[97,121]

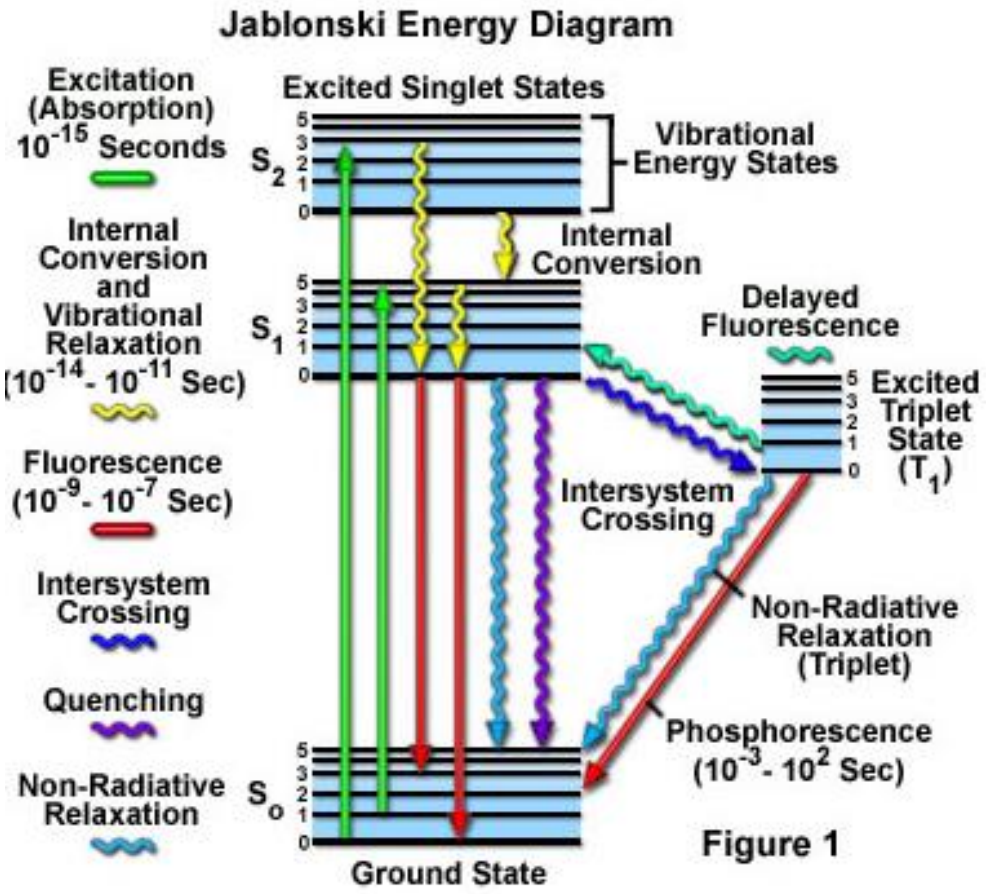

Figure 1.17: Jablonski energy diagram outlining the various radiative and non-radiative relaxation pathways and their typical lifetime for excited state electrons. **(Figure adapted from ref.121)**

1.2.3 Quantum dot scientific studies

A significant amount of theoretical and experimental work has focused on understanding exciton dynamics in quantum dots, which can be quite complex due to the variety of quantum dot architectures (core, core/shell, core/grade shell), different sizes, and many material combinations. However, much of the complexity involved in QD exciton dynamics stems from two additional (and very important) factors. First, the unique intermediate status of quantum dots (between molecules and bulk-scale materials) allows for many different electronic transitions. Second, under specific conditions a QD can sustain more than one exciton (X) at a time, including biexcitons (XX) and multi-

excitons (MX). These higher order excitons can experience different relaxation pathways than single excitons and can lead to different light-matter interactions. Understanding these various exciton dynamics is important for the successful utilization of QDs in new emission technologies.

1.2.3.1 Single exciton (X) relaxation

As mentioned, an exciton (X) is a bound electron-hole pair that emerges in semiconducting materials upon the absorption of either electromagnetic waves or change injection.[122] Although this quasiparticle is composed of charged particles, it has the interesting property of being able to transmit energy while being net neutral (no net charge is transmitted). The dynamics of excitons (X), including the rate and state pathways of their generation and recombination are important to understand when utilizing quantum dots for in gain media, LEDs, solar cells, etc.[105,123,124]

Single excitons can relax via non-radiative pathways and radiative pathways (**Figure 1.17**). Although the primary type of radiative relaxation (PL emission) in QDs is due to band-edge exciton recombination, which has a Stokes shift of 10-20 nm and full-width half-maximum (FWHM) of ~30-40 nm, there are other relaxation pathways as well. For example, emission can occur from trap states arising from unpassivated surface states (electron orbitals) at the surface of the QD. Emission from trap states often follows a low-energy deep-trap radiative pathway with a Stokes shift greater than 100 nm and a FWHM greater than 100 nm,[125] and is typically exhibited by small QD (< 2nm) due to their molecular-like HOMO-LUMO electronic structure (as opposed to the band-like structure observed in larger QD).[94,125] Trap states can also act as a non-radiative pathway that reduces quantum yield (QY), so reducing their presence has garnered much attention. Often non-radiative surface trap states are removed by

incorporating an inorganic shell into the QD architecture during synthesis or by passivating the QD surface with specific ligands or coatings, both of which have been shown to increase the quantum yield of QDs..[126,127,128] Quantum yield is a particularly important parameter to consider when utilizing QDs for emission applications since QY indicates the efficiency of the emission pathways (photons emitted versus photons absorbed), which determines how strong the excitation source has to be for the QDs. Common core/shell combinations include CdSe/ZnS,[131] CdSe/ZnSe,[129] and CdSe/CdS, with QY approaching 95%.[93,130] In addition, a shell with a larger band-gap than the core (traditional type-I QD) can localize the exciton to the interior of the QD which helps maintain the optical properties of the QD against the environment.[131]

The lifetime of exciton and surface states is also often different. For example, QDs often display a bi-exponential distribution for the radiative lifetime due to there being two recombination mechanisms: intrinsic exciton recombination at core states (several nanoseconds) and surface related emission (tens of nanoseconds) caused by surface states interacting with charge carriers.[132] The longer lifetime of the surface-related emission is attributed to poor overlap between the electron and hole wavefunctions due to differences in their localization (caused by their difference in effective mass).

The relative contribution of emission from trap states compared to emission from excitons has also been shown to increase when the excitation energy is increased.[94] Surface-trap emission can be reduced by filling the carrier surface states, such as through the introduction of an amine (hole acceptor) which occupies surface hole sites, which effectively blocks their radiative recombination.[95,133]

The size of the QD can also affect these trends, due to the difference in the energy difference between the excited and ground state, and the relative importance of surface trap emission between large (> 2nm) and small (< 2nm) QDs. For example, when high concentrations of a hole acceptor (butylamine) are added to a QD solution, the small QDs experience a decrease in QY and PL lifetime (70 ns to 18 ns) whereas larger QDs exhibit only a decrease in QY with no change in PL lifetime. The different response of large and small QDs is attributed to the larger band-gap of the small QD and the dominance of trap-state emission, which allows an energetically preferred nonradiative pathway via electron-transfer with adsorbed molecules to become accessible.[125]

Finally, exciton relaxation includes both the study of hot electrons (much higher energy state than band edge state) and cold electrons (very near the band edge state). State-resolved pump/probe measurements on colloidal QDs have been performed to examine how hot electrons and holes relax under different amounts of quantum confinement.[134] It was expected that QDs would exhibit less efficient phonon relaxation than bulk semiconductors (with a continuous energy spectrum) since QD energy level spacing (50-200 meV) is significantly higher than either acoustic (2 meV) or optical (20 meV) phonons energies. Intraband relaxation of electrons/holes would therefore require multiphonon emission (**Figure 1.18**).[109]

This multiphonon emission requirement was expected to cause a phonon-bottleneck that would hinder relaxation, particularly in smaller (more confined) QDs with the larger energy spacing. However, for electrons, Auger recombination prevented this bottleneck from occurring, in this case allowing for a unidirectional energy transfer from an electron to a hole.[134] Surprisingly, holes also exhibited a trend totally opposite to the expected

bottleneck behavior, with the state-to-state transition rate being independent of QD size and the hole energy loss rate increasing for smaller more confined QDs (**Figure 1.18**).[134]

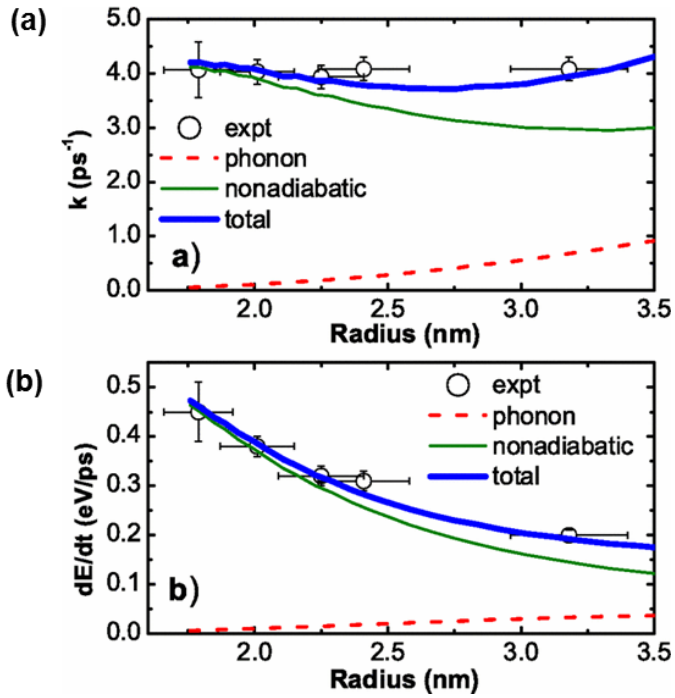

Figure 1.18: Hole relaxation dynamics in CdSe QDs. The (a) state-to-state transition rate and (b) energy loss rate for holes in different sized QDs (under different quantum confinement). **(Reproduced from ref.134)**

The hole behavior was attributed to a non-adiabatic process (process involving the addition or removal of heat from the system) mediated by the QD ligand. Furthermore, this ligand-mediated non-radiative hole relaxation was shown to occur in QDs with an inorganic ZnS shell as well, albeit reduced due to a reduction of electronic coupling between the core and ligand states.[109,134]

1.2.3.2 Biexciton (XX) and multi-exciton (MX) relaxation

As mentioned, quantum dots have the interesting property of being able to support more than one exciton at the same time under relatively common pumping conditions (typically

pulsed high fluence optical pumping).[120,122,134,135] This can lead to the formation of biexcitons (XX) and higher order multi-excitons (MX).[136] A biexciton can form multiple ways. One way involves multiple exciton generation (MEG) where a high energy exciton splits into multiple lower energy excitons (to form a multiexciton), with minimal thermal energy losses (**Figure 1.19a**).[97,122] A second way multiexcitons are produced (biexcitons in particular) is when the presence of a single exciton perturbs the electronic energy states (the electronic structure) so that a XX state is lower in energy than two single X states, which means the XX is more energetically favorable than two X.[122] The preference for a biexciton to form in place of two single excitons is related to the energy difference between these two states (Δ_{XX}), as shown in **Figure 1.19b.** As would be expected, a biexciton is more likely to form as Δ_{XX} increases.

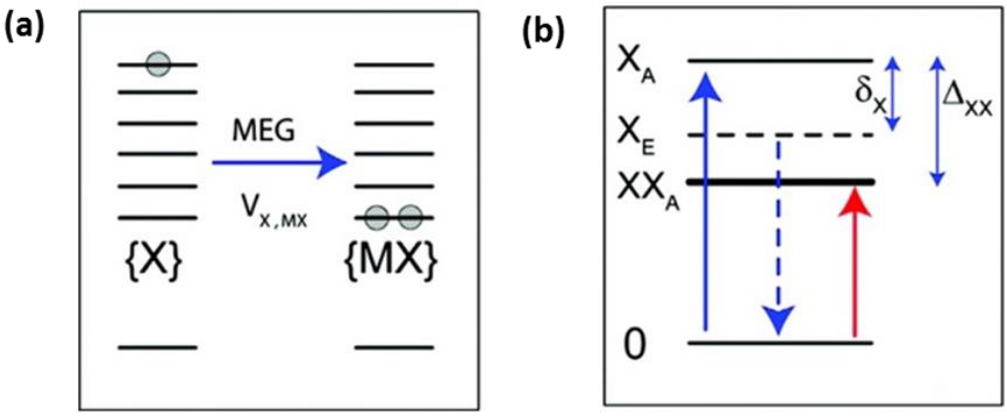

Figure 1.19: A number of electronic transitions are available within an excited quantum dot. (a) Multi-exciton generation occurs when a high energy exciton decays into a lower energy multiexciton. (b) The electronic transitions that lead to the formation of single excitons and biexcitons. (**Reproduced (cropped and modified) from ref.122)**

The formation and dynamics of XX formation and relaxation can be examined with state-resolved pump-probe techniques, which use a pump to obtain a specific electronic state and then a probe to investigate the availability of remaining specific electronic

states.[109,135] In this scenario, the availability of an electronic state is determined by whether a probe photon is absorbed or not by the excited QD and is measured by the change in optical density (ΔOD). If a probe photon is absorbed then that electronic state (or transition) was available and will show up as photo-induced absorption (positive ΔOD). A reduction of absorption (negative ΔOD) indicates photobleaching since the probed electronic state is already occupied. These results led to the development of a preliminary modified Jablonski diagram that incorporates a XX state which is offset from the X state by Δ_{XX}, as well as Stokes shift for both X and XX (δ_X and δ_{XX}, respectively) (**Figure 1.20**).

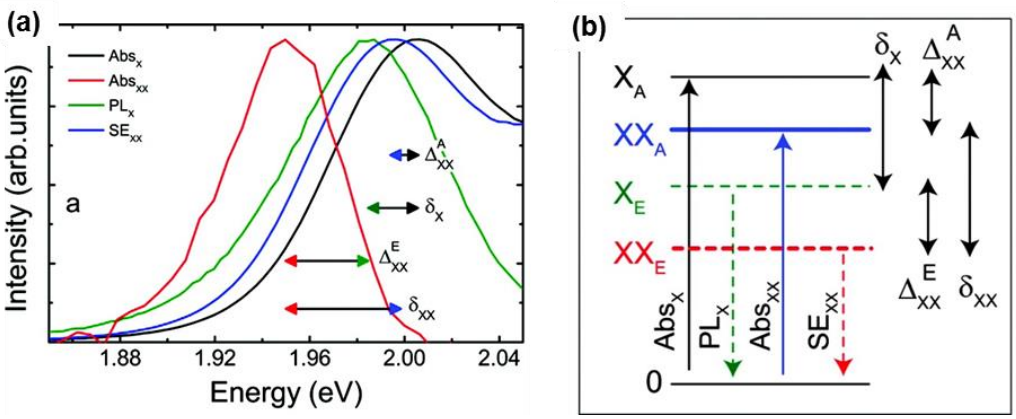

Figure 1.20: (a) The absorption and photoluminescence spectra of single excitons (X) and biexcitons (XX). (b) A modified Jablonski diagram outlining the energy levels (and transitions) of excitons and biexcitons within a QD. **(Reproduced from ref.122)**

The great advantage of the state-resolved optical pumping (pump-probe) technique is that the formation and dynamics of excitons, biexcitons, and multiexcitons in specific electronic states (and transitions) can be examined. This is particularly interesting since QD absorption profiles exhibit multiple available excitonic states (X1, X2, X3, ….Xi) that have different degeneracies and therefore can support different types of multiexcitons (**Figure 1.21**). For example, the X1 state has a double degeneracy and therefore can

support at most a biexciton, while the X3 state has a six-fold degeneracy that can support multiexcitons.[136]

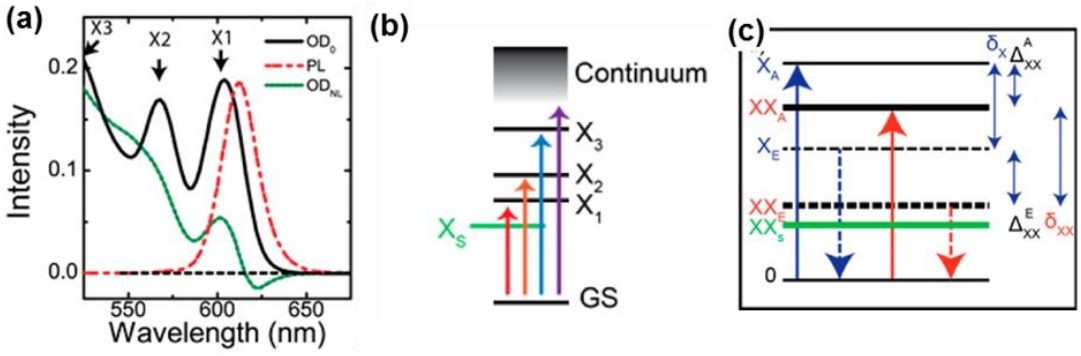

Figure 1.21: There are many electronic states available to excitons, biexcitons, and multiexcitons in quantum dots. (a) The absorption profile of a QD can sometimes show clear exciton transitions that correspond to (b) various electronic transitions corresponding to different exciton symmetries, degeneracy, and order (single, bi-, multi-). (c) The formation of higher order excitons allows for multiple electronic transitions beyond those of single excitons. **(Image reproduced (cropped and modified) from ref.136)**

The formation and dynamics of single excitons and multiexcitons have also been shown to depend on the presence (and type) of inorganic shell. Core/graded shell quantum dots were shown to exhibit lower optical gain thresholds (average of 1 exciton, $N_{th} \approx 1$) compared to core and core/shell QDs ($N_{th} \approx 1.5$). The reduction of threshold for the core/graded shell QDs is attributed to a reduction of coupling between surface trap states and the core exciton/biexciton.[136] These phenomena can be examined in greater detail by examining the temperature dependence of optical phonons, which are the primary mechanism of non-radiative relaxation for surface trap states.

1.2.3.3 Auger recombination

An important consequence of biexcitons and multiexcitons is that they lead to the emergence of Auger recombination, a non-radiative process where the energy released

by a relaxing exciton is non-radiatively transferred to another charge carrier, moving this other carrier to a higher electronic or kinetic state.[90,97,137] This non-radiative relaxation method reduces the quantum yield of a QD and alters the PL lifetime.[90,138] Smaller QDs often exhibit faster Auger recombination (AR) rates than radiative relaxation rates because Coulomb electron-electron coupling is stronger than electron-photon coupling. For example, the AR rate increases approximately 50 times when reducing the QD diameter from 4 to 1.2 nm[120,139]

Auger recombination is believed to be thermally mediated, being totally suppressed at temperature at/below 30 K, leading to an observed quantum yield of 100%.[137] Increasing the temperature above 30 K causes the quantum yield to steadily drop due to the emergence of AR. This behavior stems from the charged behavior (negative in this case) of CdSe/CdS QDs. During excitation at 30 K the QD has an exciton as well as an extra excited state electron (forming a trion). Increasing the temperature above 30 K causes the conduction band offset between CdSe and CdS to diminish to such an extent that one of the excited electrons can delocalize from the core, which allows the excited electron to participate in surface-assisted Auger recombination (**Figure 1.22**).[137]

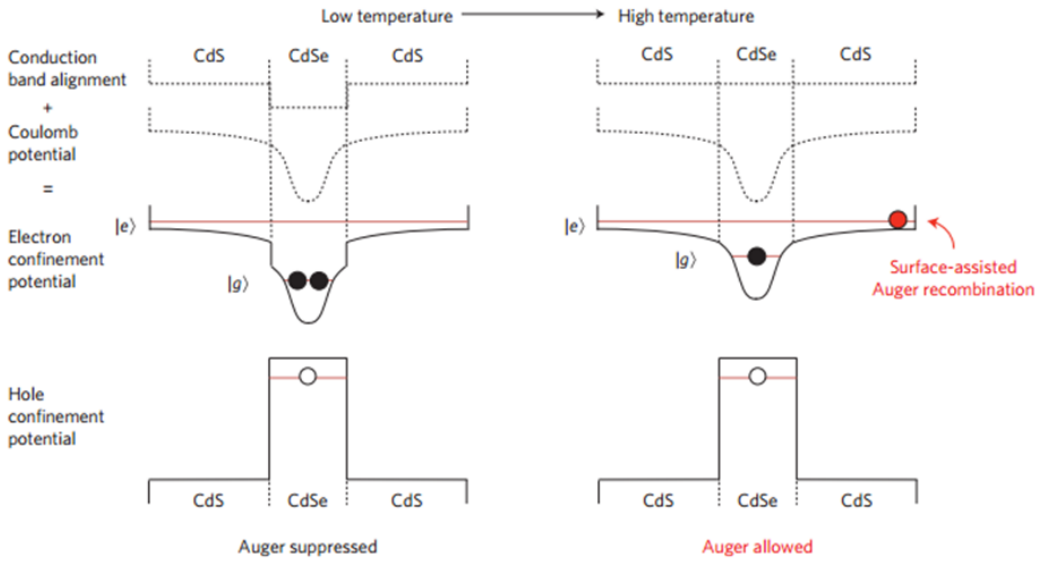

Figure 1.22: The band structure of CdSe/CdS QDs changes with temperature. As the temperature increases above 30 K, the conductor band offset decreases, allowing for delocalization of one of the excited state electrons from the core, and in term, its participation in surface-assisted Auger recombination. **(Image reproduced from ref.137)**

Suppressing AR at room temperatures can be achieved via three routes. First, interfacial alloying of the core-shell interface, which smooths the confinement potential, has been shown through theoretical modeling and experimental studies to reduce the Auger recombination rate.[138,140] Second, the efficiency of AR is inversely related to the QD volume, with larger QDs exhibiting lower AR rates.[120] Third, the utilization of type-II or quasi type-II electronic QD structures has been shown to reduce the AR rate by smearing (spatially delocalizing) either the electron or hole wavefunction across the QD volume, which reduces the overlap of the electron-hole wavefunctions (**Figure 1.23**).[141,142,143,144,145]

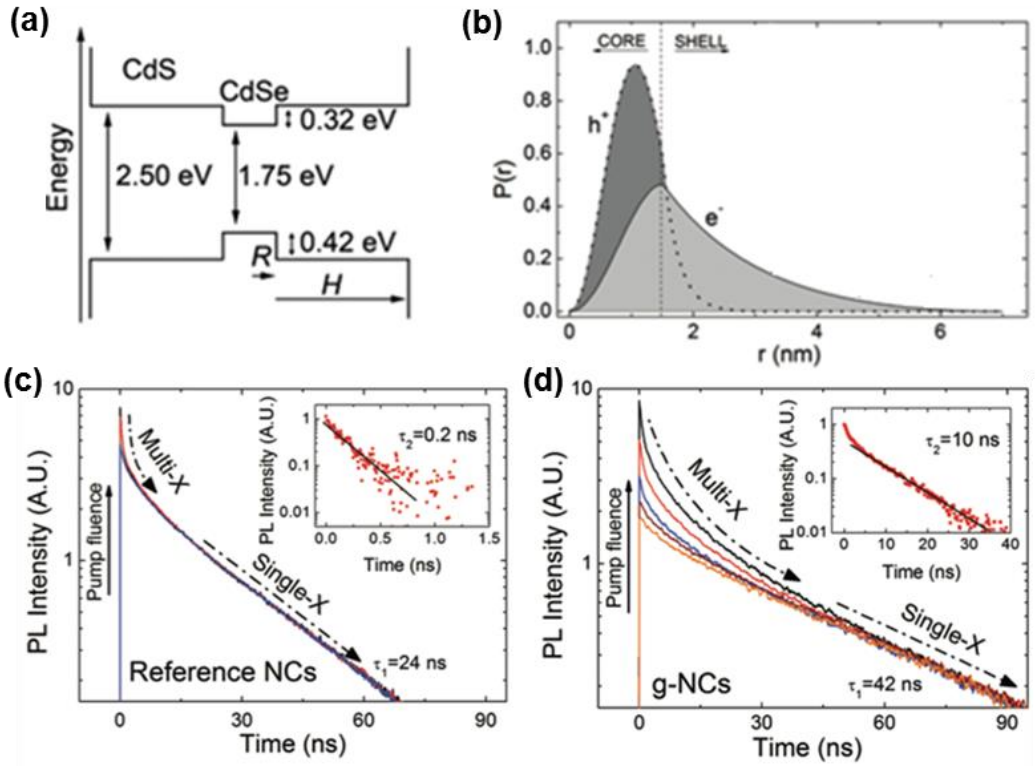

Figure 1.23: (a) Energy level diagram of quasi type-II QD. (b) Radial probability distributions of the confined wave-functions for the electron and hole within a QD. Transient absorption spectra for (c) a traditional CdSe/ZnS QD and (d) a giant CdSe/CdS QD. **(Figure adapted from ref.90)**

Suppressing Auger relaxation becomes particularly important in lasing QD systems since the high intensity pulsed optical pumping can lead to the generation of multi-excitons. Overall, suppressing the AR rate has been a common theme in QD optical gain studies (discussed later).

1.2.3.4 Physical and optical stability of QDs

The utilization of QDs for their PL emission into photonic systems like lasing disks, LEDs, and displays will require that the QDs have a well-understood optical response (stable or unstable PL color and PL intensity) when exposed to various external stimuli, including: light, gases, moisture, different polymers matrices, and chemicals.

Typically, an inorganic shell is deposited on the QD core during synthesis to isolate the core form the environment. Isolating the QD core from the environment hinders surface reactions from modifying the QD core and the core exciton (and its radiative relaxation pathways). As mentioned previously, it has been experimentally verified that the presence of an inorganic shell can increase quantum yield.[87,89,93] On the other hand, it is often assumed that long-term physical and optical stability also occurs when an inorganic shell is deposited on the QD core. However, this assumption is often not necessarily reasonable when considering the thermodynamic conditions of many core/shell QDs. For example, lattice strain between the inorganic core and shell for core/shell QDs can affect QY, absorption position, and PL relaxation of QDs.[146,147,148,149] Lattice strain is caused by a mismatch of the core and shell material lattice parameters and can lead to cracking of the shell which reduces QY and can shift the absorption position (**Table 1.2**). Furthermore, cracks in the shell could allow environmental factors (oxygen, moisture, ligands) to directly interact with the QD core.

Table 1.2: Lattice constants for a number of common QD semiconductor materials. **(values obtained from ref.107)**

Semiconductor	Lattice Constant (A)
CdSe	4.3,7.01
ZnS	5.41
CdS	4.14, 6.7
CdTe	6.48

However, the formation of cracks in the shell generally does not occur until a critical shell thickness is reached.[146] Once this thickness is exceeded, the accumulated lattice strain energy is sufficiently high to allow the system to move toward its thermodynamic equilibrium position by releasing the strain energy in the form of cracks and defects in the shell.[146] The size of the core also affects the maximum shell thickness that can be

deposited before strain relaxation. Smaller cores can typically accommodate a thicker shell since the core material can undergo compression, essentially undergoing a strain as well as the shell. This compression alters the electronic structure, typically causing a blue shift of the 1s absorption peak.[146,148]

Clearly, the breakdown of the protective inorganic shell will affect how exposed the QD core is to the environment, which can lead to physical changes that manifest as changes to the PL emission. A number of preliminary disparate studies have examined the stability of QD PL emission upon light exposure. These studies have shown that the PL emission from both core and core/shell QDs can evolve upon light exposure..[150,151,152,153,154,155] The most common phenomenon is an increase in PL intensity (termed photo-enhancement) with a corresponding spectral blue shift (**Figure 1.24**). The enhancement phenomenon is time-dependent; with longer light exposure leading to larger increases in the PL intensity (an order of magnitude or more has been observed).[150]

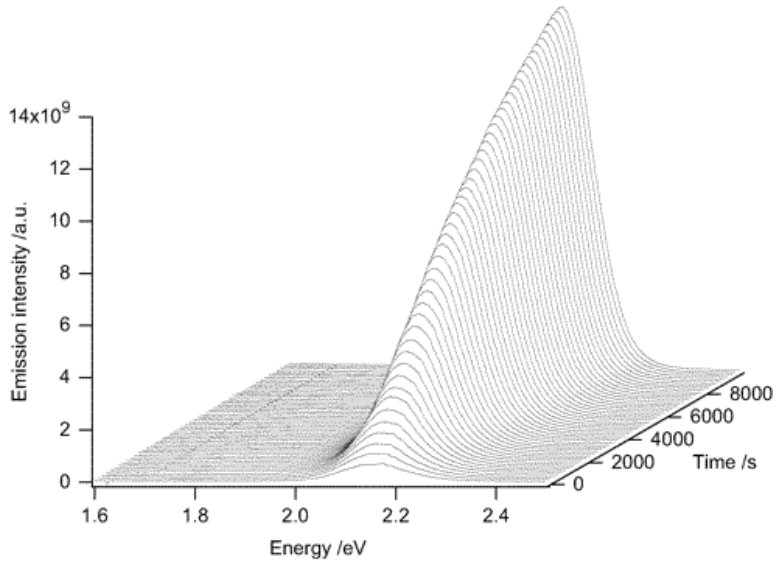

Figure 1.24: Increase in PL of CdSe/ZnS QD upon continuous exposure to light with an energy above the QD band-gap. **(Figure adapted from ref.150)**

A variety of mechanisms have been considered to explain changes to QD PL intensity and spectral position upon exposure to external factors like light, oxygen, and moisture:

1. *Photoactivation:* the passivation of QD surface traps via H_2O adsorption or smoothing via photooxidation.[152,153]
2. *Photoelectrification*: a mechanism where photoionized QDs (which are dark and have charge carriers trapped near the QD surface) act to block the non-radiative pathways of QDs in close proximity due to the electrostatic blockade effect. This effect is more dominant in close-packed QD films.[154,155]
3. *Photoneutralization:* the neutralization by photo-generated excitons of charged centers in the QD that act as traps for non-radiative recombination.[156] This mechanism likely dominates when QDs are not in close proximity such that photoelectrification cannot occur. Charged centers can be due to photoionization and have been shown (through modeling) to be due primarily to an interfacial fast ionization process (10^{-5}-10^{-8} sec).[154]
4. *Photoinduced rearrangement of ligands:* a process where the rearrangement of ligands may increase the lifetime of the non-radiative states, increasing the probability that excitons thermalize back to states that allow radiative relaxation.[150]
5. *Photoinduced transformation of ligands:* occurs when UV light curing causes cross-linking and polymerization of the capping molecule, increasing its ability to passivate the non-radiative surface states.[157]
6. *Chemical etching:* an increase of PL intensity caused by the removal of non-radiative surface states caused by surface roughness. However, etching can also reduce the size of the QD which can cause a blue-shift in absorption and PL.[158,159,160]

7. *Polyelectrolyte matrices:* Encapsulating QDs into polyelectrolyte films like poly(diallyldimethylammonium chloride) or poly(allylamine hydrochloride) can increase in PL (up to 30x) due to passivation of surface states.[128]
8. *Fluorescence resonance energy transfer (FRET):* non-radiative energy transfer between QDs and an acceptor that can reduce QY. This is a short-range mechanism (< 10nm) that inversely scales with spacing (d^{-6}) between the donor and acceptor, and can occur with metal surfaces,[161,162] semi-conductor surfaces,[163] and proteins[164] acting as acceptors.

Although these studies have provided a preliminary idea on how the optical properties of QDs shift in response to various external factors, they have often focused on QD solutions, continuous light exposure, and have not explicitly examined the role of the QD architecture (core, core/shell, core/graded shell).

1.2.4 Quantum dot films and patterns

1.2.4.1 QD thin films

A great deal of research has been done to integrate QDs into films and patterns to utilize their optical properties. For example, QDs have been deposited into planar films via spin-casting,[165,166] spin-assisted layer-by-layer assembly (SA-LBL),[162,167,168] phase-separation (via aromatic-aliphatic capping groups),[169] Langmuir-Blodgett,[170] and Langmuir-Schaefer.[171] For example, some impressive demonstrations of nanoparticle film super-lattices have been achieved via film deposition of binary mixtures of nanostructure of different size and shape (**Figure 1.25**).[172,173,174] SA-LBL has been used to encapsulate QDs in polyelectrolytes,[128,162,175] and more traditional polymer films like poly(methyl methacrylate), poly(lauryl methacrylate), or polystyrene.[176,177,178,179] The

ability to incorporate QDs into polymer matrices makes it possible to combine the merits of QDs with those of polymers. Polymers are an ideal material for hosting QDs for a number of reasons, which include: physical robustness, high optical transparency, well-known refractive indices, deposition into flexible films, micro/nanoscale patterning compatibilities, tunable loading of QDs, responsive behavior, low cost, and accessibility.

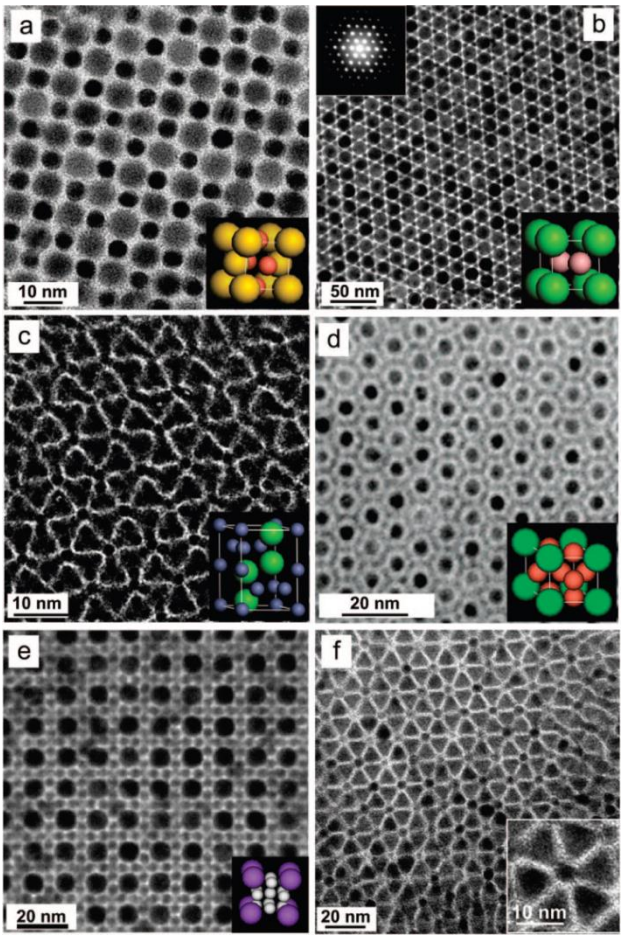

Figure 1.25: TEM micrographs of nanoparticle super-lattices composed of binary mixtures of various types of nanostructures (QDs, plasmonic nanoparticles, or magnetic nanoparticles). **(Figure adapted from refs.172,173,174)**

Typically the system-wide film properties that are considered pertain to current densities and electroluminescence in LEDs,[169,171,185] energy conversion and photocurrent in solar cells,[102,103] and PL position and intensity for labelling, imaging and sensing.[4,180,181,182]

1.2.4.2 QD patterns (physical and non-physical)

Physical microscale and nanoscale patterning

In addition to films, patterns of QDs and polymers can be fabricated using the wide-variety of microscale and nanoscale techniques that have been developed over the past decade. These include capillary transfer lithography,[183] capillary force lithography,[184] μContact printing and solvent-assisted μContact molding,[185,186,187] inkjet printing,[188] pattern replication,[189] and photo- and electron-beam lithographies.[190,191] These techniques have produced patterns composed of pure polymers, pure QDs, and QD-polymer composites (**Figure 1.26**).

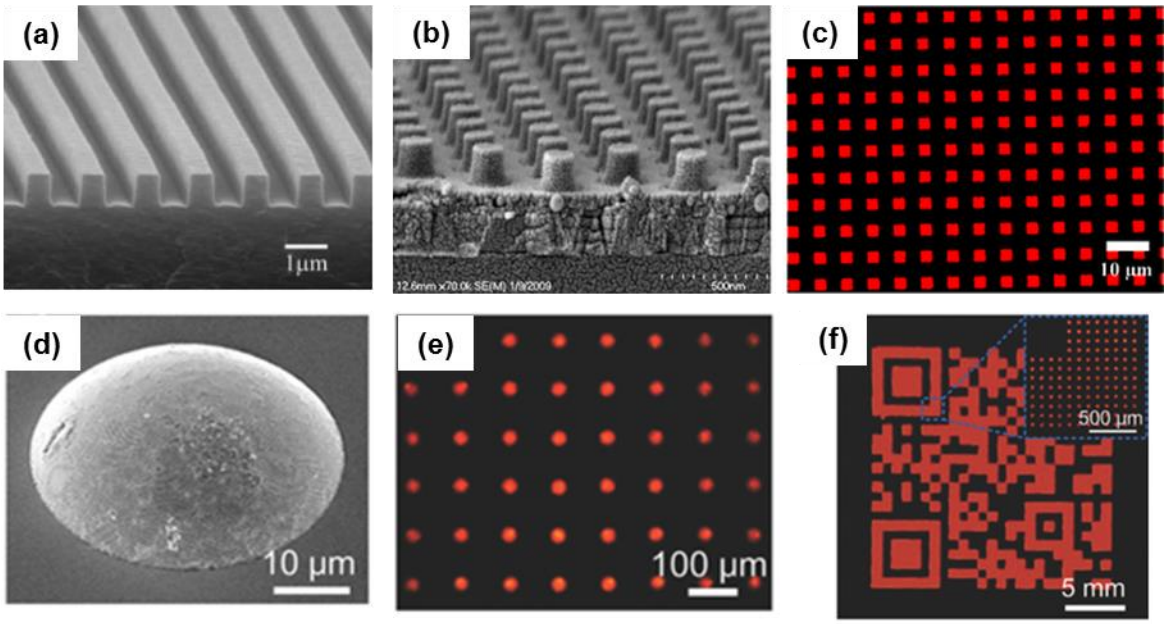

Figure 1.26: (a) SEM micrograph of well-defined polymer channels fabricated using the capillary force lithography technique. (b) SEM and (d) PL microscopy of QD structures fabricated using a pattern replication process. (a) SEM micrograph, (b) bright field microscopy, and (c) photoluminescence microscopy of circular QD-polymer dots made using reactive inkjet printing. (d) Photoluminescence microscopy of a large-scale pattern of the QD-polymer dots. **(Frame (a) adapted from ref.184, frames (b,c) from ref.189, and frames (d-f) from ref.188)**

Physical patterns of QDs and QD-polymer composites are typically employed to guide emitted light (waveguides) (**Figure 1.26a**), provide control over the spectral emission (optical cavities) (**Figure 1.26b**), produce coupling phenomena (coupled disk), assist in the investigation of structure-property relationships (well-ordered arrays) (**Figure 1.26c,e**), or provide patterns required for various technologies (QR codes)(**Figure 1.26f**).

Nonphysical photopatterning using QDs

The previous examples of microscale and nanoscale patterning fall under the field of physical patterning (the pattern is formed from the physical deposition, rearrangement, or removal of material). However, light-responsive QDs can be used to create unique non-physical emissive patterns as well (**Figure 1.27**).[192,193,194,195] These emissive patterns derive their contrast from spatially selective light exposure of a light-responsive QD-polymer. The resulting photopattern has an emissive pattern but appears totally featureless if examined with techniques like SEM or AFM since the emission contrast arises from intrinsic modification of QDs in the areas of the film exposed to light (**Figure 1.27**).[192]

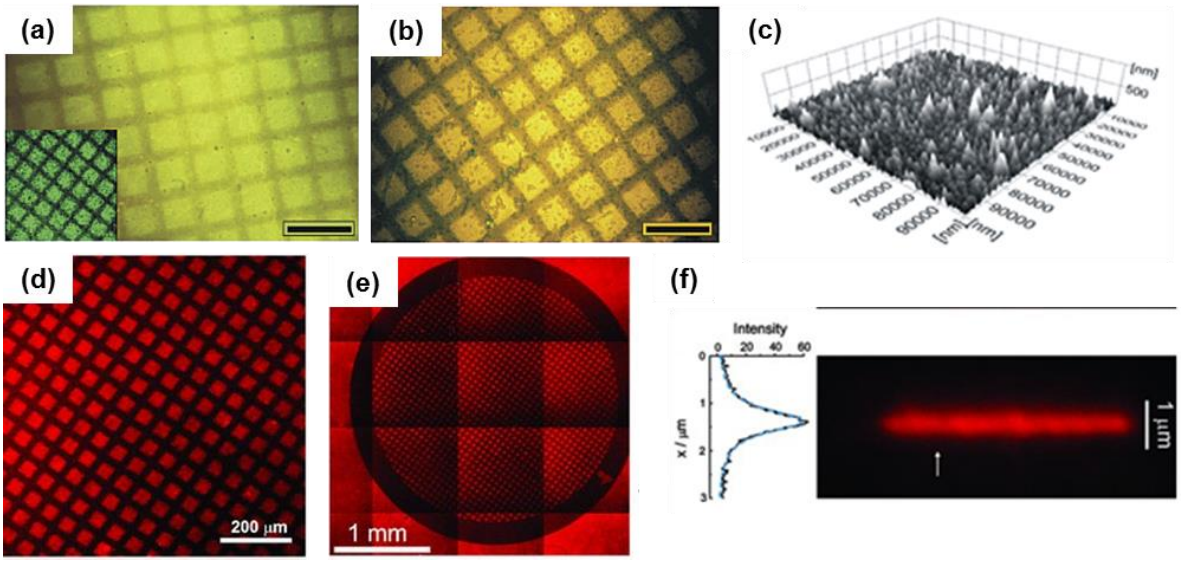

Figure 1.27: (a,b,d,e) Photoluminescence images of photopatterned QD films (TEM grid photomask). (c) AFM surface topography of photopatterned QD films. (f) PL image of a photopatterned lines of sub-micron width patterned using a scanning laser beam. **(Frame (a-c) adapted from ref.192, frames (d-f) from ref.194)**

Common exposure approaches involve shadow masks (using TEM grids), which provide regions with microscale features.[192,195] Higher resolution (but lower throughput) exposure techniques employ direct laser writing which yields sub-microscale features.[193,194] Photopatterns with moderate intensity contrast have been created using both core and core/shell architectures of different colors.[192,194,195] However, current photopattern strategies, in particular the methods employed for light exposure, cannot simultaneously provide high-resolution (sub-micron features) and high throughput since either low-resolution photomasks or direct-write laser scanning are used to create the photopattern.[192-195] Furthermore, almost all demonstrations of photopatterning have been monochromatic (single color) which limits their application in display technologies and anticounterfeiting labels (important potential areas of application).

1.2.5 Current QD systems and applications

1.2.5.1 QD-LEDs, labels, and photodetectors

The characteristics of QD emission, in particular their spectral color tunability, narrow emission peak, and PL stability have led to their incorporation into QD light emitting diodes (QD-LEDs) (**Figure 1.28a,b**).[79,196] The utilization of QDs as the active optical components in LEDs has the potential to increase efficiency while providing greater color options. These advances in QD-LEDs have also been driven by the compatibility of QDs with the many common film deposition approaches and microscale/nanoscale patterning techniques mentioned earlier. In addition, because the surface of QDs can be functionalized to be soluble in water, they can be readily employed as cellular trackers (**Figure 1.28c**).[4]

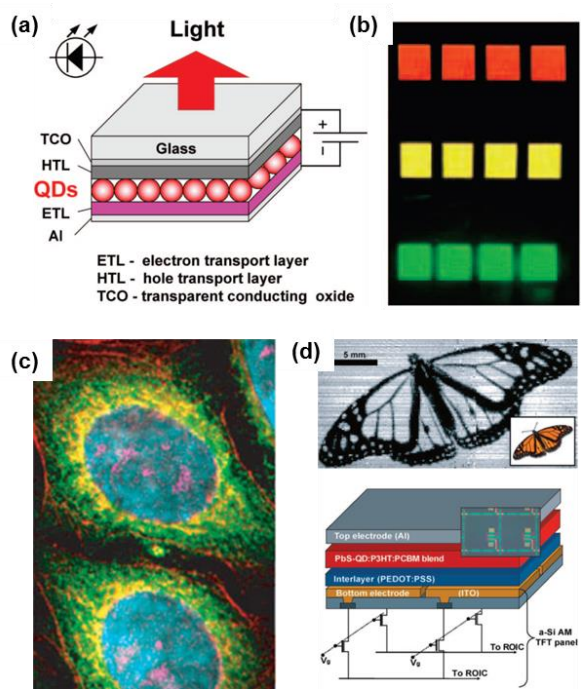

Figure 1.28: (a) Schematic of a QD LED, (b) PL images of red, yellow, and green QD LEDs. (c) PL image of cells stained with five different colored QDs. (d) False color NIR image (top) and schematic (bottom) of a NIR QD photodetector. **(Frame (a) adapted from ref.79, frame (b) from ref.196, frame (c) from ref.4, frame (d) from ref.197)**

Furthermore, combinations of QDs of different color and surface functionalization can be utilized to target specific biomolecules and monitor the efficacy of this targeting via PL imaging. QDs therefore offer many advantages over traditional organic fluorophores whose solubility and emission color cannot be modified easily. Finally, light-sensitive QDs (as discussed previously) can be integrated into photodiodes to act as near-infrared (NIR) photodetectors (**Figure 1.28d**).[197] The tunable nature of QD optical absorption and emission with QD size also potentially makes it possible to target specific wavelength ranges for detection without having to employ new materials or film deposition practices. In addition, these photodiodes can exhibit lifetimes up to more than a year with high quantum efficiencies.

1.2.5.2 QD optical gain systems

Another very promising application for QD films is in the area of optical gain (amplification) materials because optical gain depends on QD properties that can be measured, controlled, and tuned (optical density, quantum yield, and PL lifetime of the QDs). Gain is simply the amplification of light (cm^{-1}) as it passes through a material, and occurs when there is a population inversion in the medium (as in a laser cavity). Population inversion occurs when there are more electrons in an excited state than in the ground state, and can be obtained by continuously pumping energy into a gain medium. Typically the gain medium is an organic dye. However, the utilization of QDs as the active component in gain materials has seen promising initial results.[104,105,198] For example, gain from the blue to NIR has been demonstrated using many types of QDs including CdTe,[199] PbS,[200] CdSe,[139,201] CdSe/ZnS,[202] and CdSe/CdS/ZnS.[203] Typical gain values range from 60-200 cm^{-1} depending on the pumping conditions, system design, and type of QD.[199-203]

Optical gain is often measured using the variable strip length (VSL) method.[202,204] Briefly, a QD film is pumped with a pulsed pump laser (fs, ps, or ns) to excite the QD film. The pump light is focused into a strip of variable length that can be changed (**Figure 1.29a**). As the length of the pump strip increases the emission from the QD film will increase.[205] If optical gain occurs then the increase of intensity will be exponential after a threshold is reached and spectral narrowing will occur (**Figure 1.29b-d**).

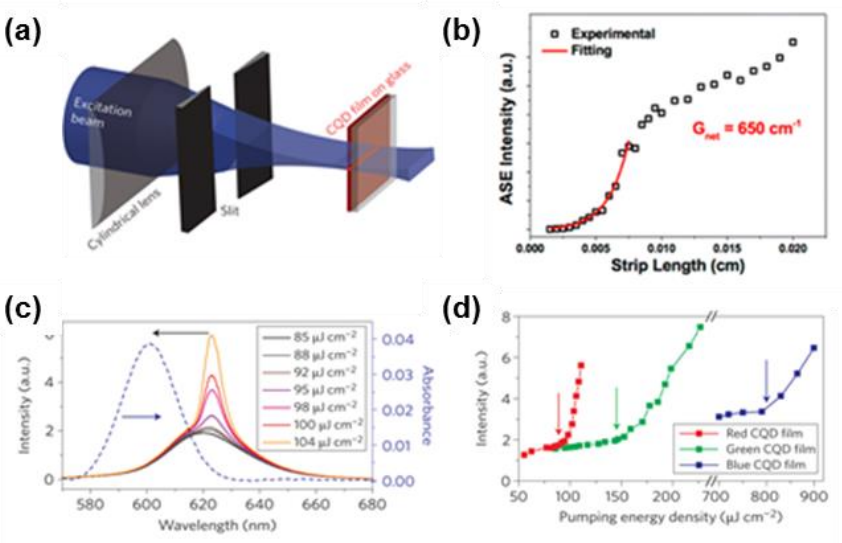

Figure 1.29: Overview of the VSL method and resulting data. (a) Schematic of the VSL excitation scheme. (b) Gain fitting to QD film intensity, (c) emission spectra at different pump power, and (d) optical gain threshold behavior. **(Frames (a,c,d) adapted from ref.104 and frame (b) from ref.205)**

The relationship between QD emission intensity and pump strip length can be used to fit the data and calculate the gain value (**Equation 1.4**).[204]

Equation 1.4: The Malko method equation relating emission intensity and pump strip length that is used in the VSL method. (**Equation obtained from ref.204)**

$$I = (A_x)(L) + (A_{bx})\frac{(e^{g_{bx}L} - 1)}{g_{bx}}$$

Where, "I" is the QD film emission intensity, "A_x" is the spontaneous emission constant, "A_{bx}" is the biexciton emission constant, "L" is the pump strip length, and "g_{bx}" is the biexciton optical gain value.

Impressive increases in optical gain from QD films have been made recently by reducing Auger recombination rates, typically via the mechanisms mentioned earlier.[90,105] However, the stimulated emission lifetime and optical gain also depend on a variety of other factors like QD size, QD packing density, and film refractive index (**Equation 1.5).**[113] However, the modification of these system characteristics in QD films to enhance QD gain has not been thoroughly investigated.

Equation 1.5: Equation relating stimulated emission, optical gain, and various physical characteristics of a QD film. **(Equation obtained from ref.113)**

$$\tau_{SE} = \frac{n_r}{cG} = \frac{n_r V_{dot}}{c\sigma_g \xi}$$

Where "τ_{SE}" is the stimulated emission build up time, "c" is the speed of light, "G" is the gain value, "n_r" is the effective refractive index, "V_{dot}" is the volume of QD, "ξ" is the QD packing fraction, and "σ_g" is the gain cross-section.

The utilization of QDs as a lasing medium could have important practical considerations since their emission wavelength can be tuned in a variety of ways and they can be combined within both hard and soft materials and subsequently patterned. The combination of these capabilities could lead to miniaturized lasers with high efficiency, directional emission, and highly tunable emission wavelength. In addition, by using soft

materials like polymers as the host material, flexible gain systems could be developed, a clear limitation of gain systems that use hard materials as the encapsulation material.

1.2.5.3 Gain-loss systems (parity-time systems)

Finally, QDs could be implemented in parity-time (PT) systems, which are optical films and patterns with periodically modulated optical gain and loss that exhibit unique directional optical properties and have been the focus of much work recently.[206] [207] [208] Various types of symmetry principles can present themselves in systems/processes. Two common and important symmetry principles are parity and time reversal. If a systems/process satisfies parity symmetry (P invariant) then it acts the same (is indistinguishable) even if all coordinates are inverted. If a system satisfies time symmetry (T invariant) then it acts the same even if the direction of time is inverted.[209] Not all systems/processes satisfy these symmetries. Radioactive beta decay is an example of a system with broken parity symmetry.[209] Systems that violate an individual symmetry may still satisfy a combined symmetry.[210] For example a PT symmetric system may violate parity symmetry and time symmetry but may be symmetric (invariant) after a combined PT operation.

Optical systems that have both gain and loss have been shown to display unique optical properties if their optical gain and loss satisfy parity-time symmetry. In order to satisfy the parity-time requirement, systems need to have the real component “n” of the complex refractive index be an even function “$n(x, \lambda) = n(-x, \lambda)$” and the imaginary component “k” be an odd function “$k(x, \lambda) = -k(-x, \lambda)$.” In this case, optical gain is denoted by negative k and optical loss by positive k.

Although satisfying these requirements is difficult, modeling and some experiments have shown that these systems exhibit novel photonic properties, including: unidirectional invisibility,[206] transitions from ballistic to diffusive transport,[208] and unidirectional reflection/directional optical manipulation (**Figure 1.30a**).[207]

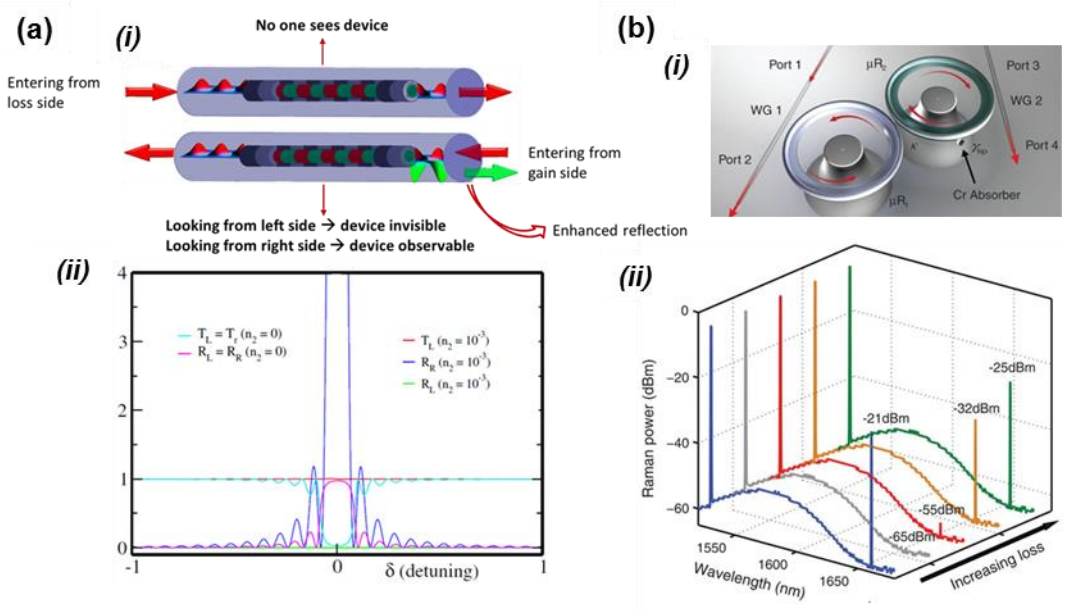

Figure 1.30: (a) (i) Bragg mirror with gain-loss components incorporated into its design that satisfy the parity-time requirements, (ii) leading to unidirectional invisibility. (b) (i) Diagram of coupled optical PT resonators that (ii) exhibit a PT loss-induced revival of Raman lasing. **(Frame (a) from ref.206 and (b) from ref.211)**

Typically these systems are composed of periodic structures[206,207,208] that can be produced using the microscale and nanoscale patterning techniques previously mentioned. In addition to the interesting fundamental principles associated with these systems, their realization could eventually lead to miniaturized optical isolators, PT Bragg mirrors that manipulate beamshape and intensity, and nanostructured paints with specified reflection characteristics (for stealth capabilities). In fact, a number of PT systems have been experimentally developed and shown to exhibit parity time

phenomenon. For example, coupled gain-loss microresonator pairs were shown to undergo a PT induced loss-induced revival of lasing when the loss exceeds a critical value (**Figure 1.30b**).[211] This result is unexpected since an increase in loss generally suppresses lasing.

QDs are very promising candidates for PT systems because their emission efficiency (QY) can be tuned without significantly changing their real index component (by using the CdSe/ZnS QD architecture). In other words, the various approaches for altering the PL intensity of QDs using light or chemicals make it possible to control whether the QDs act as a gain or loss component. In addition, by changing the loading density of QDs in the polymer matrix, the magnitude of the n,k components can be altered, which becomes important in PT systems that are sensitive to the gain-loss contrast between regions. In addition, QD-polymer composites could address current PT challenges, including: properties in the optical regime, phenomenona over wider bandwidths, and reconfigurable/responsive systems.

1.3 Summary of critical issues and motivation

Clearly a significant amount of theoretical and experimental work has been conducted in the fields of photonic nanostructures (plasmonic nanostructures and quantum dots) and their confinement phenomena/conditions. However, a comprehensive study on how the underlying confinement phenomenona of these optical nanostructures are affected by each level of system design (individual nanostructure, nanostructure-nanostructure local-assembly, and large-scale nanostructure arrangement) has not been performed. We propose that this type of study could help provide a scientific and engineering framework

that could be referenced when designing and fabricating photonic systems composed of nanostructures that need to display specific optical characteristics.

For example, work still needs to be done to measure, examine, and understand the mechanisms affecting the confinement phenomena/conditions of plasmons and excitons in individual photonic nanostructures (under various environmental conditions) and their local-assemblies (using unique coupling schemes), in order to expand upon the versatility/tunability offered by these nanostructures. Furthermore, more work should be done to examine how the large-scale arrangement (of individual and coupled nanostructures) affects the overall light propagation, absorption, and emission resulting from the confined nanostructures, and show how the large-scale arrangement can be utilized to develop novel photonic systems.

In addition, a large amount of research in the field of plasmonics has focused on the optical characteristics of individual particles and their coupling behavior. However, most studies develop structure-photonic relationships by averaging physical/optical data over hundreds of nanostructures. Although this approach does provide useful information on general trends, it cannot easily identify how specific physical variations/defects (and unique coupling schemes) specifically affect optical scattering (since this data tends to get washed out in the statistics). Therefore, direct correlation should be made between specific nanostructures using multiple techniques like AFM, SEM, and hyperspectral scanning so that specific structure-scattering relationships can be identified. Moreover, most plasmonic coupling studies have focused on lateral planar assemblies (side-side local-assemblies). However this focus on planar assemblies is a significant limitation since vertically stacked assemblies could offer unique plasmonic resonances because the substrate is only directly influencing the base nanostructure.

Furthermore, few studies have examined how each level of design in a complex hierarchal plasmonic system could influence its properties. For example, a study examining how the individual nanostructure design (sphere versus cube), local-assembly options (coupled versus dispersed), and overall novel large-scale arrangement affect a specific electromagnetic characteristic would provide valuable insight into the importance of these factors, particularly in applications like chemical sensing that heavily rely on enhanced electromagnetic fields.

A number of important issues remain in the field of quantum dots. For example, although the complex internal relaxation dynamics of QD excitons and biexcitons has received much attention, little work has been done to examine how the quantum confinement conditions and PL emission of the exciton evolve upon light exposure over time scale relevant to most experimental studies and QD applications (seconds-minutes-hours). Many studies using QDs assume that the QD is not physically changed as it interacts with light. However, preliminary studies have shown that QDs can undergo physical and chemical changes upon light exposure and environmental exposure (even when a protective shell is incorporated into the QD architecture). Therefore, a comprehensive understanding of how the evolution of QD PL emission relates to the compositional architecture of the quantum dot is needed (core, core/shell, core/graded shell). Without an understanding of long-term QD physical/optical stability, the important fundamental discoveries pertaining to exciton dynamics cannot truly be utilized in new technologies. This suggests that an overview of the experimental tests and procedures that should be employed when examining the emission stability of isolated quantum dots of specific compositional design should be developed so that new QD architectures can

be examined to determine their applicability to specific scientific experiments and engineering applications.

Furthermore, little research has examined how the ligand capping a QD can be utilized to affect its optical gain behavior in QD thin films. Almost all QD gain studies focus on how the QD architecture affects optical gain. Although this work has yielded important discoveries, particularly in the area of Auger recombination, QD architecture is only one of the important characteristics that can be altered to control these light-matter interactions. Work should be done to determine how the ligand affects the physical and thermal properties of the QD thin film, and how the ligand can control the average QD-QD spacing. All these factors will likely result in changes to the optical gain and loss, providing an additional strategy for tuning gain and loss and potentially leading to the development of QD gain systems with enhanced optical gain.

Finally, the majority of patterning studies in the field of micro and nanoscience have focused on physical patterning (i.e. patterns fabricated by the addition, removal, or rearrangement of material). Although advances in physical patterning approaches have led to the development of novel nanostructures and arrangements, it has limited application in certain exciting areas of photonics. These limitations are particularly apparent in the area of photonic parity-time systems where changes to the refractive index need to be minimized. Therefore, more investigations should focus on the use of non-physical photopatterning since it allows for the modulation of emission intensity (dark regions and bright regions) but has minimal modulation of the refractive index, and therefore could satisfy the parity-time requirements. Currently, only rudimentary developments have been made in the area of photopatterning, and it could benefit enormously from an understanding of QD architecture and various exposure strategies.

Specific emphasis should be placed on improving pattern contrasts, spectral color variations, feature resolution, large-scale uniformity, and throughput.

1.4 References (Chapter 1)

1 Biswas, A.; Bayer, I.S.; Biris, A.S.; Wang, T.; Dervishi, E.; Faupel, F., Advances in top-down and bottom-up surface nanofabrication: Techniques, applications & future prospects. *Adv. Colloid and Interface Sci.* **2012,** *170,* 2-27.

2 Moskovits, M., Surface-enhanced Raman spectroscopy: a brief retrospective. *J. Raman Spec.* **2005,** *36,* 485-496.

3 Rycenga, M.; Cobley, C M.; Zeng, J.; Li, W.Y.; Moran, C.H.; Zhang, Q.; Qin, D.; Xia, Y.N., Controlling the synthesis and assembly of silver nanostructures for plasmonic applications. *Chem. Rev.* **2011,** *111,* 3669-3712.

4 Medintz, I. L.; Uyeda, H. T.; Goldman, E. R.; Mattoussi, H., Quantum dot bioconjugates for imaging, labelling and sensing. *Nat. Mater.* **2005,** *4,* 435-446.

5 Jana, N.R.; Gearheart, L.; Murphy, C.J., Seeding growth for size control of 5-40 nm diameter gold nanoparticles. *Langmuir* **2001,** *17,* 6782-6786.

6 Stewart, M.E.; Anderton, C.R.; Thompson, L.B.; Maria, J.; Gray, S.K.; Rogers, J.A.; Nuzzo, R.G., Nanostructured plasmonic sensors. *Chem. Rev.* **2008,** *108,* 494-521.

7 Pyatenko, A.; Yamaguchi, M.; Suzuki, M., Synthesis of spherical silver nanoparticles with controllable sizes in aqueous solutions. *J. Phys. Chem. C* **2007,** *111,* 7910-7917.

8 Li, H.; Xia, H.; Ding, W.; Li, Y.; Shi, Q.; Wang, D.; Tao, X., Synthesis of monodisperse, quasi-spherical silver nanoparticles with sizes defined by the nature of silver precursors. *Langmuir* **2014,** *30,* 2498-2504.

9 Xia, Y.N.; Xiong, Y.J.; Lim, B.; Skrabalak, S.E., Shape-controlled synthesis of metal nanocrystals: simple chemistry meets complex physics? *Angewandte Chemie-Inter. Ed.* **2009,** *48,* 60-103.

10 Wu, H.-L.; Kuo, C.-H.; Huang, M.H., Seed-mediated synthesis of gold nanocrystals with systematic shape evolution from cubic to trisoctahedral and rhombic dodecahedral structures. *Langmuir* **2010,** *26,* 12307-12313.

11 Cobley, C.M.; Skrabalak, S.E.; Campbell, D.J.; Xia, Y.N., Shape-controlled synthesis of silver nanoparticles for plasmonic and sensing applications. *Plasmonics* **2009,** *4,* 171-179.

12 Blaber, M.G.; Henry, A.-I.; Bingham, J.M.; Schatz, G.C.; Van Duyne, R.P., LSPR imaging of silver triangular nanoprisms: Correlating scattering with structure using electrodynamics for plasmon lifetime analysis. *J. Phys. Chem. C* **2012,** *116,* 393-403.

13 Zhang, M.; Zhao, A.; Sun, H.; Guo, H.; Wang, D.; Li, D.; Gan, Z.; Tao, W., Rapid, large-scale, sonochemical synthesis of 3D nanotextured silver microflowers as highly efficient SERS substrates. *J. Mater. Chem.* **2011,** *21,* 18817-18824.

14 Mahmoud, M.A.; El-Sayed, M.A., Comparative study of the assemblies and the resulting plasmon fields of Langmuir−Blodgett assembled monolayers of silver nanocubes and gold nanocages. *J. Phys. Chem. C* **2008**, *112*, 14618-14625.

15 Rosi, N.L.; Mirkin, C.A., Nanostructures in biodiagnostics. *Chem. Rev.* **2005,** *105,* 1547-1562.

16 nanoComposix Inc., **2016,** San Diego, CA. http://nanocomposix.com/collections/gold-spheres & http://nanocomposix.com/collections/silver-spheres

17 Mulvaney, P., Surface plasmon spectroscopy of nanosized metal particles. *Langmuir* **1996,** *12,* 788-800.

18 Xu, H.; Aizpurua, J.; Kall, M.; Apell, P., Electromagnetic contributions to single-molecule sensitivity in surface-enhanced Raman scattering. *Phys. Rev. E.* **2000**, *62*, 4318-4324.

19 Xu, H.; Kall, M., Polarization-dependent surface-enhanced Raman spectroscopy of isolated silver nanoaggregates. *ChemPhysChem.* **2003**, *4*, 1001-1005.

20 Sundaramurthy, A.; Crozier, K.B.; Kino, G.S.; Fromm, D.P.; Schuck, P.J.; Moerner, W.E., Field enhancement and gap-dependent resonance in a system of two opposing tip-to-tip Au nanotriangles. *Phys. Rev. B* **2005**, *72*, 165409-6.

21 Lee, K.S.; El-Sayed, M.A., Gold and silver nanoparticles in sensing and imaging: Sensitivity of plasmon response to size, shape, and metal composition. *J. Phys. Chem. B* **2006,** *110*, 19220-19225.

22 Rakic, A.D.; Djurisic, A.B.; Elazar, J.M.; Majewski, M.L., Optical properties of metallic films for vertical-cavity optoelectronic devices. *Appl. Opt.* **1998,** *37*, 5271-5283.

23 Sweatlock, L.A.; Maier, S.A.; Atwater, H.A.; Penninkhof, J.J.; Polman, A., Highly confined electromagnetic fields in arrays of strongly coupled Ag nanoparticles. *Phys. Rev. B* **2005**, *71*, 235408-7.

24 Sun, Y.G.; Xia, Y.N., Gold and silver nanoparticles: A class of chromophores with colors tunable in the range from 400 to 750 nm. *Analyst* **2003,** *128*, 686-691.

25 Lee, S.Y.; Hung, L.; Lang, G.S.; Cornett, J.E.; Mayergoyz, I.D.; Rabin, O., Dispersion in the SERS enhancement with silver nanocube dimers. *ACS Nano* **2010,** *4,* 5763-5772.

26 McLellan, J.M.; Seikkinen, A.; Chen, J.; Xia, Y., Comparison of the surface-enhanced Raman scattering on sharp and truncated silver Nanocubes. *Chem. Phys. Lett*., **2006,** *427,* 122-126.

27 Yang, Y.; Matsubara, S.; Xiong, L.; Hayakawa, T.; Nogami, M., Solvothermal synthesis of multiple shapes of silver nanoparticles and their SERS properties. *J. Phys. Chem. C,* **2007,** *111,* 9095-9104.

28 Rycenga, M.; Kim, M.H.; Camargo, P.H.C.; Cobley, C.; Li, Z.Y.; Xia, Y., Surface-enhanced Raman scattering: Comparison of three different molecules on single-crystal nanocubes and nanospheres of silver. *J. Phys. Chem. A,* **2009,** *113,* 3932-3939.

29 Wiley, B.J.; Chen, Y.; McLellan, J.M.; Xiong, Y.; Li, Z.-Y.; Ginger, D.; Xia, Y., Synthesis and optical properties of silver nanobars and nanorice. *Nano Lett.* **2007,** *7*, 1032-1036.

30 Grillet, N.; Manchon, D.; Bertorelle, F.; Bonnet, C.; Broyer, M.; Cottancin, E.; Lerme, J.; Hillenkamp, M.; Pellarin, M., Plasmon coupling in silver nanocube dimers: Resonance splitting induced by edge rounding. *ACS Nano* **2011,** *5*, 9450-9462.

31 Schubert, O.; Becker, J.; Carbone, L.; Khalavka, Y.; Provalska, T.; Zins, I.; Sönnichsen, C., Mapping the polarization pattern of plasmon modes reveals nanoparticle symmetry. *Nano Lett.* **2008,** *8*, 2345-2350.

32 Schafer, C.; Gollmer, D.A.; Horrer, A.; Fulmes, J.; Weber-Bargioni, A.; Cabrini, S.; Schuck, P. J.; Kern, D.P.; Fleischer, M., A single particle plasmon resonance study of 3D conical nanoantennas. *Nanoscale* **2013,** *5*, 7861-7866.

33 Willets, K.A.; Van Duyne, R.P., Localized surface plasmon resonance spectroscopy and sensing. *Ann. Rev. Phys. Chem.* **2007,** *58*, 267-297.

34 Konig, T.; Kodiyath, R.; Combs, Z.A.; Mahmoud, M.A.; El-Sayed, M.A.; Tsukruk, V.V., Silver nanocube aggregates in cylindrical pores for higher refractive index plasmonic sensing. *Particle & Particle Sys. Charac.* **2014,** *31*, 274-283.

35 Thaxton, C.S.; Elghanian, R.; Thomas, A.D.; Stoeva, S.I.; Lee, J-S.; Smith, N.D.; Schaeffer, A.J.; Horninger, W.; Bartsch, G.; Mirkin, C., Nanoparticle-based bio-barcode assay redefines

"undetectable" PSA and biochemical recurrence after radical prostatectomy. *Proc. Natl. Acad. Sci. U.S.A.,* **2009,** *106,* 18437-18442.

36 Jain, P.K.; Huang, W.; El-Sayed, M.A., On the universal scaling behavior of the distance decay of plasmon coupling in metal nanoparticle pairs: A plasmon ruler equation. *Nano Lett.* **2007,** *7*, 2080-2088.

37 Reinhard, B.M.; Siu, M.; Agarwal, H.; Alivisatos, A.P.; Liphardt, J., Calibration of dynamic molecular rulers based on plasmon coupling between gold nanoparticles. *Nano Lett.* **2005,** *5*, 2246-2252.

38 Gunnarsson, L.; Bjerneld, E.J.; Xu, H.; Petronis, S.; Kasemo, B.; Kall, M., Interparticle coupling effects in nanofabricated substrates for surface-enhanced Raman scattering. *Appl. Phys. Lett.,* **2001,** *78,* 802-804.

39 Mulvihill, M.; Tao, A.; Benjauthrit, K; Arnold, J.; Yang, P., Surface-enhanced Raman spectroscopy for trace arsenic detection in contaminated water. *Angew. Chem., Int. Ed*., **2008,** *47,* 6456-6460.

40 Li, W.; Camargo, P.H.C.; Au, L.; Zhang, Q.; Rycenga, M.; Xia, Y., Etching and dimerization: A simple and versatile route to dimers of silver nanospheres with a range of sizes. *Angew. Chem., Int. Ed.,* **2010,** *49,* 164-168.

41 Talley, C.E.; Jackson, J.B.; Oubre, C.; Grady, N.K.; Hollars, C.W.; Lane, S.M.; Huser, T.R.; Nordlander, P.; Halas, N.J., Surface-enhanced Raman scattering from individual Au nanoparticles and nanoparticle dimer substrates. *Nano Lett*., **2005,** *5,* 1569-1574.

42 Camargo, P.H.C.; Rycenga, M.; Au, L.; Xia, Y., Isolating and probing the hot spot formed between two silver nanocubes. *Angew. Chem., Int. Ed*., **2009,** *48,* 2180-2184.

43 Yang, S.-C.; Kobori, H.; He, C.L.; Lin, M.H.; Chen, H.Y.; Li, C.C.; Kanehara, M.; Teranishi, T.; Gwo, S., Plasmon hybridization in individual gold nanocrystal dimers: direct observation of bright and dark modes. *Nano Lett*., **2010,** *10,* 632-637.

44 Yu, Q.; Huang, H.W.; Peng, X.S.; Ye, Z.Z., Ultrathin free-standing close-packed gold nanoparticle films: Conductivity and Raman scattering enhancement. *Nanoscale* **2011,** *3*, 3868-3875.

45 Gandra, N.; Abbas, A.; Tian, L.M.; Singamaneni, S., Plasmonic planet-satellite analogues: Hierarchical self-assembly of gold nanostructures. *Nano Lett*. **2012**, *12*, 2645-2651.

46 Li, W.Y.; Camargo, P.H.C.; Lu, X.M.; Xia, Y.N., Dimers of silver nanospheres: Facile synthesis and their use as hot spots for surface-enhanced Raman scattering. *Nano Lett.* **2009,** *9*, 485-490.

47 Roller, E.M.; Argyropoulos, C.; Hogele, A.; Liedl, T.; Pilo-Pais, M., Plasmon-exciton coupling using DNA templates. *Nano Lett.* **2016,** *16*, 5962-5966.

48 Combs, Z.A.; Chang, S.H.; Clark, T.; Singamaneni, S.; Anderson, K.D.; Tsukruk, V.V., Label-free Raman mapping of surface distribution of protein A and IgG biomolecules. *Langmuir* **2011,** *27*, 3198-3205.

49 Haynes, C.L.; McFarland, A.D.; Zhao, L.L.; Van Duyne, R.P.; Schatz, G.C.; Gunnarsson, L.; Prikulis, J.; Kasemo, B.; Kall, M., Nanoparticle optics: The importance of radiative dipole coupling in two-dimensional nanoparticle arrays. *J. Phys. Chem. B* **2003,** *107*, 7337-7342.

50 Alvarez-Puebla, R.; Cui, B.; Bravo-Vasquez, J.P.; Veres, T.; Fenniri, H., Nanoimprinted SERS-active substrates with tunable surface plasmon resonances. *J. Phys. Chem. C* **2007,** *111*, 6720-6723.

51 Chen, L.M.; Liu, Y.N., Ag-nanoparticle-modified single Ag nanowire for detection of melamine by surface-enhanced Raman spectroscopy. *J. Raman Spectrosc.* **2012,** *43*, 986-991.

52 Ko, H.; Tsukruk, V.V., Nanoparticle-decorated nanocanals with enhanced Raman scattering. *Small* **2008**, *4,* 1980-1984.

53 Braun, G.; Lee, S.J.; Dante, M.; Nguyen, T.Q.; Moskovits, M.; Reich, N., Surface-enhanced Raman spectroscopy for DNA detection by nanoparticle assembly onto smooth metal films. *J. Amer. Chem. Soc.* **2007,** *129*, 6378-6379.

54 Freeman, R.G.; Grabar, K.C.; Allison, K.J.; Bright, R.M.; Davis, J.A.; Guthrie, A.P.; Hommer, M.B.; Jackson, M.A.; Smith, P.C.; Walter, D.G.; Natan, M.J., Self-assembled metal colloid monolayers – An approach to SERS substrates. *Science* **1995,** *267*, 1629-1632.

55 Hu, X.G.; Cheng, W.L.; Wang, T.; Wang, Y.L.; Wang, E.K.; Dong, S.J., Fabrication, characterization, and application in SERS of self-assembled polyelectrolyte-gold nanorod multilayered films. *J. Phys. Chem. B* **2005,** *109*, 19385-19389.

56 Near, R.; Tabor, C.; Duan, J.S.; Pachter, R.; El-Sayed, M., Pronounced effects of anisotropy on plasmonic properties of nanorings fabricated by electron beam lithography. *Nano Lett.* **2012,** *12*, 2158-2164.

57 Duan, H.G.; Fernandez-Dominguez, A.I.; Bosman, M.; Maier, S.A.; Yang, J.K.W., Nanoplasmonics: Classical down to the nanometer scale. *Nano Lett.* **2012,** *12*, 1683-1689.

58 Koh, A.L.; Fernández-Domínguez, A.I.; McComb, D.W.; Maier, S.A.; Yang, J.K. W., High-resolution mapping of electron-beam-excited plasmon modes in lithographically defined gold nanostructures. *Nano Lett.* **2011,** *11,* 1323-1330.

59 Tsai, C.-Y.; Lin, J.-W.; Wu, C.-Y.; Lin, P.-T.; Lu, T.-W.; Lee, P.-T., Plasmonic coupling in gold nanoring dimers: Observation of coupled bonding mode. *Nano Lett.* **2012,** *12*, 1648-1654.

60 Solis, D.; Willingham, B.; Nauert, S.L.; Slaughter, L.S.; Olson, J.; Swanglap, P.; Paul, A.; Chang, W.S.; Link, S., Electromagnetic energy transport in nanoparticle chains via dark plasmon modes. *Nano Lett.* **2012,** *12,* 1349-1353.

61 Willingham, B.; Link, S., Energy transport in metal nanoparticle chains via sub-radiant plasmon modes. *Opt. Express* **2011,** *19,* 6450-6461.

62 Bozhevolnyi, S.I.; Volkov, V.S.; Devaux, E.; Laluet, J.Y.; Ebbesen, T.W., Channel plasmon subwavelength waveguide components including interferometers and ring resonators. *Nature* **2006,** *440,* 508-511.

63 Schuller, J.A.; Barnard, E.S.; Cai, W.S.; Jun, Y.C.; White, J.S.; Brongersma, M.L., Plasmonics for extreme light concentration and manipulation. *Nat. Mater.* **2010,** *9,* 193-204.

64 Alu, A.; Engheta, N., Achieving transparency with plasmonic and metamaterial coatings. *Phys. Rev. E* **2005,** *72,* 016623-9.

65 Jain, P.K.; Huang, X.H.; El-Sayed, I.H.; El-Sayed, M.A., Noble metals on the nanoscale: Optical and photothermal properties and some applications in imaging, sensing, biology, and medicine. *Acc. Chem. Res.* **2008,** *41,* 1578-1586.

66 Anker, J.N.; Hall, W.P.; Lyandres, O.; Shah, N.C.; Zhao, J.; Van Duyne, R.P., Biosensing with plasmonic nanosensors. *Nat. Mater.* **2008,** *7,* 442-453.

67 Sonnichsen, C.; Reinhard, B.M.; Liphardt, J.; Alivisatos, A.P., A molecular ruler based on plasmon coupling of single gold and silver nanoparticles. *Nat. Biotechnol.* **2005,** *23,* 741-745.

68 Xie, W.; Qiu, P.H.; Mao, C.B., Bio-imaging, detection and analysis by using nanostructures as SERS substrates. *J. Mater. Chem.* **2011,** *21,* 5190-5202.

69 Lu, Y.H.; Dong, W.; Chen, Z.; Pors, A.; Wang, Z.L.; Bozhevolnyi, S.I., Gap-plasmon based broadband absorbers for enhanced hot-electron and photocurrent generation. *Scientific Reports* **2016,** *6*.

70 Ko, H.; Singamaneni, S.; Tsukruk, V.V., Nanostructured surfaces and assemblies as SERS media. *Small* **2008,** *4,* 1576-1599.

71 Kim, N.H.; Lee, S.J.; Moskovits, M., Reversible tuning of SERS hot spots with aptamers. *Adv. Mater.* **2011,** *23,* 4152-4156.

72 Thaxton, C.S.; Elghanian, R.; Thomas, A.D.; Stoeva, S.I.; Lee, J.S.; Smith, N.D.; Schaeffer, A. J.; Klocker, H.; Horninger, W.; Bartsch, G.; Mirkin, C.A., Nanoparticle-based bio-barcode assay redefines "undetectable" PSA and biochemical recurrence after radical prostatectomy. *Proc. Nat. Acad. Sci. United States of America* **2009,** *106*, 18437-18442.

73 Tabatabaei, M.; Sangar, A.; Kazemi-Zanjani, N.; Torchio, P.; Merlen, A.; Lagugne-Labarthet, F., Optical properties of silver and gold tetrahedral nanopyramid arrays prepared by nanosphere lithography. *J. Phys. Chem. C* **2013,** *117*, 14778-14786.

74 Nie, S.M.; Emery, S.R., Probing single molecules and single nanoparticles by surface-enhanced Raman scattering. *Science* **1997,** *275*, 1102-1106.

75 Kneipp, K.; Wang, Y.; Kneipp, H.; Perelman, L.T.; Itzkan, I.; Dasari, R.; Feld, M.S., Single molecule detection using surface-enhanced Raman scattering (SERS). *Phys. Rev. Lett.* **1997,** *78*, 1667-1670.

76 Camden, J.P.; Dieringer, J.A.; Wang, Y.M.; Masiello, D.J.; Marks, L.D.; Schatz, G.C.; Van Duyne, R.P., Probing the structure of single-molecule surface-enhanced Raman scattering hot spots. *J. Amer. Chem. Soc.* **2008,** *130*, 12616.

77 Kneipp, K.; Kneipp, H.; Deinum, G.; Itzkan, I.; Dasari, R.R.; Feld, M.S., Single-molecule detection of a cyanine dye in silver colloidal solution using near-infrared surface-enhanced Raman scattering. *Appl. Spec.* **1998,** *52*, 175-178.

78 Kleinman, S.L.; Ringe, E.; Valley, N.; Wustholz, K.L.; Phillips, E.; Scheidt, K.A.; Schatz, G.C.; Van Duyne, R.P., Single-molecule surface-enhanced Raman spectroscopy of crystal violet isotopologues: Theory and experiment. *J. Amer. Chem. Soc.* **2011,** *133*, 4115-4122.

79 Talapin, D.V.; Lee, J.S.; Kovalenko, M.V.; Shevchenko, E.V., Prospects of colloidal nanocrystals for electronic and optoelectronic applications. *Chem. Rev.* **2010,** *110,* 389-458.

80 Murray, C.B.; Norris, D.J.; Bawendi, M.G., Synthesis and characterization of nearly monodisperse CdE (E = S, Se, Te) Semiconductor nanocrystallites. *J. Amer. Chem. Soc.* **1993,** *115,* 8706-8715.

81 Qu, L.; Peng, Z.A.; Peng, X., Alternative routes toward high quality CdSe nanocrystals. *Nano Lett.* **2001,** *1,* 333-337.

82 Gaponik, N.; Talapin, D.V.; Rogach, A.L.; Hoppe, K.; Shevchenko, E.V.; Kornowski, A.; Eychmüller, A.; Weller, H., Thiol-capping of CdTe nanocrystals: An alternative to organometallic synthetic routes. *J. Phys. Chem. B* **2002,** *106*, 7177-7185.

83 Talapin, D.V.; Rogach, A.L.; Kornowski, A.; Haase, M.; Weller, H., Highly luminescent monodisperse CdSe and CdSe/ZnS nanocrystals synthesized in a hexadecylamine-trioctylphosphine oxide-trioctylphospine mixture. *Nano Lett.* **2001,** *1*, 207-2.

84 Morello, G.; De Giorgi, M.; Kudera, S.; Manna, L.; Cingolani, R.; Anni, M., Temperature and size dependence of nonradiative relaxation and exciton-phonon coupling in colloidal CdTe quantum dots. *J. Phys. Chem. C* **2007,** *111*, 5846-5849.

85 Dunleavy, R.; Lu, L.; Kiely, C.J.; McIntosh, S.; Berger, B.W., Single-enzyme biomineralization of cadmium sulfide nanocrystals with controlled optical properties. *Proc. Nat. Acad. Sci.* **2016,** *113,* 5275-5280.

86 Bailey, R.E.; Smith, A.M.; Nie, S.M., Quantum dots in biology and medicine. *Physica E-Low-Dimensional Sys. & Nanostructures* **2004,** *25,* 1-12.

87 Jung, J.; Lin, C.H.; Yoon, Y.J.; Malak, S.T.; Zhai, Y.X.; Thomas, E.L.; Vardeny, V.; Tsukruk, V.V.; Lin, Z.Q., Crafting core/graded shell-shell quantum dots with suppressed re-absorption and tunable Stokes shift as high optical gain materials. *Angewandte Chemie-International Edition* **2016,** *55*, 5071-5075.

88 Blackman, B.; Battaglia, D.M.; Mishima, T.D.; Johnson, M.B.; Peng, X.G., Control of the morphology of complex semiconductor nanocrystals with a type II heterojunction, dots vs peanuts, by thermal cycling. *Chem. Mater.* **2007,** *19*, 3815-3821.

89 Chen, Y.; Vela, J.; Htoon, H.; Casson, J.L.; Werder, D.J.; Bussian, D.A.; Klimov, V.I.; Hollingsworth, J.A., "Giant" multishell CdSe nanocrystal quantum dots with suppressed blinking. *J. Amer. Chem. Soc.* **2008,** *130,* 5026.

90 Garcia-Santamaria, F.; Chen, Y.F.; Vela, J.; Schaller, R.D.; Hollingsworth, J.A.; Klimov, V.I., Suppressed Auger recombination in "giant" nanocrystals boosts optical gain performance. *Nano Lett.* **2009,** *9,* 3482-3488.

91 Xie, R.G.; Kolb, U.; Li, J.X.; Basche, T.; Mews, A., Synthesis and characterization of highly luminescent CdSe-Core CdS/Zn0.5Cd0.5S/ZnS multishell nanocrystals. *J. Amer. Chem. Soc.* **2005,** *127*, 7480-7488.

92 Dennis, A.M.; Mangum, B.D.; Piryatinski, A.; Park, Y.S.; Hannah, D.C.; Casson, J.L.; Williams, D.J.; Schaller, R.D.; Htoon, H.; Hollingsworth, J.A., Suppressed blinking and Auger recombination in near-infrared type-II InP/CdS nanocrystal quantum dots. *Nano Lett.* **2012,** *12,* 5545-5551.

93 Greytak, A.B.; Allen, P.M.; Liu, W.; Zhao, J.; Young, E.R.; Popovic, Z.; Walker, B.J.; Nocera, D.G.; Bawendi, M.G., Alternating layer addition approach to CdSe/CdS core/shell quantum dots with near-unity quantum yield and high on-time fractions. *Chem. Sci.* **2012,** *3,* 2028-2034.

94 Kapitonov, A.M.; Stupak, A.P.; Gaponenko, S.V.; Petrov, E.P.; Rogach, A.L.; Eychmuller, A., Luminescence properties of thiol-stabilized CdTe nanocrystals. *J. Phys. Chem. B* **1999,** *103,* 10109-10113.

95 Lin, K.F.; Cheng, H.M.; Hsu, H.C.; Lin, L.J.; Hsieh, W.F., Band gap variation of size-controlled ZnO quantum dots synthesized by sol-gel method. *Chem. Phys. Lett.* **2005,** *409,* 208-211.

96 Bagaa, A.; Chattopadhyay, P.K.; Ghosh, S., Stokes shift in quantum dots: Origin of dark exciton. **2007;** 876-879.

97 Klimov, V.I., Spectral and dynamical properties of multilexcitons in semiconductor nanocrystals. In *Ann, Rev. Phys. Chem.*, Annual Reviews: Palo Alto, **2007;** *58,* 635-673.

98 Gaponik, N.; Hickey, S.G.; Dorfs, D.; Rogach, A.L.; Eychmüller, A., Progress in the light emission of colloidal semiconductor nanocrystals. *Small* **2010,** *6,* 1364-1378.

99 Rogach, A.L.; Talapin, D.V.; Shevchenko, E.V.; Kornowski, A.; Haase, M.; Weller, H., Organization of matter on different size scales: Monodisperse nanocrystals and their superstructures. *Adv. Func. Mater.* **2002,** *12*, 653-664.

100 Kundu, J.; Ghosh, Y.; Dennis, A.M.; Htoon, H.; Hollingsworth, J.A., Giant nanocrystal quantum dots: stable down-conversion phosphors that exploit a large Stokes shift and efficient shell-to-core energy relaxation. *Nano Lett.* **2012,** *12,* 3031-3037.

101 Mashford, B.S.; Stevenson, M.; Popovic, Z.; Hamilton, C.; Zhou, Z.Q.; Breen, C.; Steckel, J.; Bulovic, V.; Bawendi, M.; Coe-Sullivan, S.; Kazlas, P.T., High-efficiency quantum-dot light-emitting devices with enhanced charge injection. *Nat. Photonics* **2013,** *7,* 407-412.

102 Gratzel, M., Solar energy conversion by dye-sensitized photovoltaic cells. *Inorganic Chem.* **2005,** *44,* 6841-6851.

103 Kamat, P.V., Quantum Dot Solar Cells. Semiconductor nanocrystals as light harvesters. *J. Phys. Chem. C* **2008,** *112,* 18737-18753.

104 Dang, C.; Lee, J.; Breen, C.; Steckel, J.S.; Coe-Sullivan, S.; Nurmikko, A., Red, green and blue lasing enabled by single-exciton gain in colloidal quantum dot films. *Nat. Nanotech.* **2012,** *7,* 335-339.

105 Klimov, V.I.; Ivanov, S.A.; Nanda, J.; Achermann, M.; Bezel, I.; McGuire, J.A.; Piryatinski, A., Single-exciton optical gain in semiconductor nanocrystals. *Nature* **2007,** *447,* 441-446.

106 BCC Research. Quantum dots: Global market growth and future commercial prospects. BCC Research *Nanotechnology Report Nano27D,* **April 2014.**

107 Yu, P.T.; Cardona, M., Fundamentals of semiconductors, physics and materials properties, 4th ed. *Springer* **2010,** *chapter 7 emission spectroscopies.*

108 Thornton, S.T.; Rex, A., Modern physics for scientists and engineers, 3rd ed. *Thomson Brooks/Colse* **2006,** *chapter 6: quantum mechanics.*

109 Kambhampati, P., Unraveling the structure and dynamics of excitons in semiconductor quantum dots. *Acc. Chem. Res.* **2011,** *44,* 1-13.

110 Vanmaekelbergh, D.; Liljeroth, P., Electron-conducting quantum dot solids: novel materials based on colloidal semiconductor nanocrystals. *Chem. Soc. Rev.* **2005,** *34*, 299-312.

111 Fox, A.M., Optical properties of solids (Section: Free Excitons, pg.78), *Oxford Univ. Press,* **2001.**

112 Grahn, H.T., Introduction to semiconductor physics (Section: Exciton binding energies, pg.119), *World Scientific,* **1999.**

113 Hoogland, S., Optical gain and lasing in colloidal quantum dots, colloidal quantum dot optoelectronics and photovoltaics. Cambridge University Press: **2013.**

114 Ricard, D.; Ghanassi, M.; Schanneklein, M.C., Dielectric confinement and the linear and nonlinear-optical properties of semiconductor r-doped glasses. *Opt. Comm.* **1994,** *108,* 311-318.

115 Yu, P.R.; Beard, M.C.; Ellingson, R.J.; Ferrere, S.; Curtis, C.; Drexler, J.; Luiszer, F.; Nozik, A.J., Absorption cross-section and related optical properties of colloidal InAs quantum dots. *J. Phys. Chem. B* **2005,** *109,* 7084-7087.

116 Istrate, E.; Hoogland, S.; Sukhovatkin, V.; Levina, L.; Myrskog, S.; Smith, P.W.E.; Sargent, E.H., Carrier relaxation dynamics in lead sulfide colloidal quantum dots. *J. Phys. Chem. B* **2008,** *112,* 2757-2760.

117 Luther, J.M.; Beard, M.C.; Song, Q.; Law, M.; Ellingson, R.J.; Nozik, A.J., Multiple exciton generation in films of electronically coupled PbSe quantum dots. *Nano Lett.* **2007,** *7,* 1779-1784.

118 Klimov, V.I.; Schwarz, C.J.; McBranch, D.W.; Leatherdale, C.A.; Bawendi, M.G., Ultrafast dynamics of inter- and intraband transitions in semiconductor nanocrystals: Implications for quantum-dot lasers. *Phys. Rev. B* **1999,** *60,* R2177-R2180.

119 Leatherdale, C.A.; Woo, W.K.; Mikulec, F.V.; Bawendi, M.G., On the absorption cross section of CdSe nanocrystal quantum dots. *J. Phys. Chem. B* **2002,** *106,* 7619-7622.

120 Klimov, V.I.; Mikhailovsky, A.A.; McBranch, D.W.; Leatherdale, C.A.; Bawendi, M.G., Quantization of multiparticle Auger rates in semiconductor quantum dots. *Science* **2000,** *287,* 1011-1013.

121 Herman, B.; Frohlich, V.E.; Lakowicz, J.R.; Murphy, D.B.; Spring, K.R.; Davidson, M.W., Fluorescence microscopy: Basic concepts in fluorescence microscopy. *National High Magnetic Field Laboratory, Florida State University,* **2013.**

122 Kambhampati, P., Multiexcitons in semiconductor nanocrystals: A platform for optoelectronics at high carrier concentration. *J. Phys. Chem. Lett.* **2012,** *3,* 1182-1190.

123 Nozik, A.J.; Beard, M.C.; Luther, J.M.; Law, M.; Ellingson, R.J.; Johnson, J.C., Semiconductor quantum dots and quantum dot arrays and applications of multiple exciton generation to third-generation photovoltaic solar cells. *Chem. Rev.* **2010,** *110,* 6873-6890.

124 Nair, G.; Chang, L. Y.; Geyer, S.M.; Bawendi, M.G., Perspective on the prospects of a carrier multiplication nanocrystal solar cell. *Nano Lett.* **2011,** *11,* 2145-2151.

125 Landes, C.F.; Braun, M.; El-Sayed, M.A., On the nanoparticle to molecular size transition: Fluorescence quenching studies. *J. Phys. Chem. B* **2001,** *105,* 10554-10558.

126 Dabbousi, B.O.; RodriguezViejo, J.; Mikulec, F.V.; Heine, J.R.; Mattoussi, H.; Ober, R.; Jensen, K.F.; Bawendi, M.G., (CdSe)ZnS core-shell quantum dots: Synthesis and characterization of a size series of highly luminescent nanocrystallites. *J. Phys. Chem. B* **1997,** *101,* 9463-9475.

127 Zhang, H.; Zhou, Z.; Yang, B.; Gao, M.Y., The influence of carboxyl groups on the photoluminescence of mercaptocarboxylic acid-stabilized CdTe nanoparticles. *J. Phys. Chem. B* **2003,** *107,* 8-13.

128 Shicheng, Z.; Jianhua, Y.; Xingguo, L.; Wenhuai, T., Photoluminescence properties of mercaptocarboxylic acid-stabilized CdSe nanoparticles covered with polyelectrolyte. *Nanotechnology* **2004,** *15,* 1108.

129 Danek, M.; Jensen, K.F.; Murray, C.B.; Bawendi, M.G., Synthesis of luminescent thin-film CdSe/ZnSe quantum dot composites using CdSe quantum dots passivated with an overlayer of ZnSe. *Chem. Mater.* **1996,** *8*, 173-180.

130 Qin, H.Y.; Niu, Y.; Meng, R.Y.; Lin, X.; Lai, R.C.; Fang, W.; Peng, X.G., Single-dot spectroscopy of zinc-blende CdSe/CdS Core/Shell nanocrystals: Nonblinking and correlation with ensemble measurements. *J. Amer. Chem. Soc.* **2014,** *136,* 179-187.

131 Dabbousi, B.O.; Rodriguez-Viejo, J.; Mikulec, F.V.; Heine, J.R.; Mattoussi, H.; Ober, R.; Jensen, K.F.; Bawendi, M.G., (CdSe)ZnS core-shell quantum dots: Synthesis and characterization of a size series of highly luminescent nanocrystallites. *J. Phys. Chem. B* **1997,** *101*, 9463-9475.

132 Wang, X.Y.; Qu, L.H.; Zhang, J.Y.; Peng, X.G.; Xiao, M., Surface-related emission in highly luminescent CdSe quantum dots. *Nano Lett.* **2003,** *3,* 1103-1106.

133 Landes, C.; Burda, C.; Braun, M.; El-Sayed, M.A., Photoluminescence of CdSe nanoparticles in the presence of a hole acceptor: n-butylamine. *J. Phys. Chem. B* **2001,** *105,* 2981-2986.

134 Cooney, R.R.; Sewall, S.L.; Anderson, K.E.H.; Dias, E.A.; Kambhampati, P., Breaking the phonon bottleneck for holes in semiconductor quantum dots. *Phys. Rev. Lett.* **2007,** *98,* 177403.

135 Cooney, R.R.; Sewall, S.L.; Sagar, D.M.; Kambhampati, P., Gain control in semiconductor quantum dots via state-resolved optical pumping. *Phys. Rev. Lett.* **2009,** *102.*

136 Walsh, B.R.; Saari, J.I.; Krause, M.M.; Nick, R.; Coe-Sullivan, S.; Kambhampati, P., Controlling the surface of semiconductor nanocrystals for efficient light emission from single excitons to multiexcitons. *J. Phys. Chem. C* **2015,** *119,* 16383-16389.

137 Javaux, C.; Mahler, B.; Dubertret, B.; Shabaev, A.; Rodina, A.V.; EfrosAl, L.; Yakovlev, D.R.; Liu, F.; Bayer, M.; Camps, G.; Biadala, L.; Buil, S.; Quelin, X.; Hermier, J.P., Thermal activation of non-radiative Auger recombination in charged colloidal nanocrystals. *Nat. Nano* **2013,** *8,* 206-212.

138 García-Santamaría, F.; Brovelli, S.; Viswanatha, R.; Hollingsworth, J.A.; Htoon, H.; Crooker, S.A.; Klimov, V.I., Breakdown of volume scaling in Auger recombination in CdSe/CdS heteronanocrystals: The role of the core−shell interface. *Nano Lett.* **2011**, *11,* 687-693.

139 Klimov, V.I.; Mikhailovsky, A.A.; Xu, S.; Malko, A.; Hollingsworth, J.A.; Leatherdale, C.A.; Eisler, H.J.; Bawendi, M.G., Optical gain and stimulated emission in nanocrystal quantum dots. *Science* **2000,** *290,* 314-317.

140 Cragg, G.E.; Efros, A.L., Suppression of Auger processes in confined structures. *Nano Lett.* **2010,** *10,* 313-317.

141 Hollingsworth, J.A., Heterostructuring nanocrystal quantum dots toward intentional suppression of blinking and Auger recombination. *Chem. Mater.* **2013,** *25,* 1318-1331.

142 Nanda, J.; Ivanov, S.A.; Achermann, M.; Bezel, I.; Piryatinski, A.; Klimov, V.I., Light amplification in the single-exciton regime using exciton-exciton repulsion in type-II nanocrystal quantum dots. *J. Phys. Chem. C* **2007,** *111,* 15382-15390.

143 Nanda, J.; Ivanov, S.A.; Htoon, H.; Bezel, I.; Piryatinski, A.; Tretiak, S.; Klimov, V.I., Absorption cross sections and Auger recombination lifetimes in inverted core-shell nanocrystals: Implications for lasing performance. *J. Appl. Phys.* **2006,** *99.*

144 Chepic, D.I.; Efros, A.L.; Ekimov, A.I.; Vanov, M.G.; Kharchenko, V.A.; Kudriavtsev, I.A.; Yazeva, T.V., Auger ionization of semiconductor quantum drops in a glass matrix. *J. Luminescence* **1990,** *47,* 113-127.

145 Klimov, V.I.; McGuire, J.A.; Schaller, R.D.; Rupasov, V.I., Scaling of multiexciton lifetimes in semiconductor nanocrystals. *Phys. Rev. B* **2008,** *77,* 195324.

146 Smith, A.M.; Nie, S., Semiconductor nanocrystals: Structure, properties, and band gap engineering. *Acc. Chem. Res.* **2010,** *43,* 190-200.

147 Gong, K.; Kelley, D.F., Lattice strain limit for uniform shell deposition in zincblende CdSe/CdS quantum dots. *J. Phys. Chem. Lett.* **2015,** *6,* 1559-1562.

148 Smith, A.M.; Mohs, A.M.; Nie, S., Tuning the optical and electronic properties of colloidal nanocrystals by lattice strain. *Nat. Nanotech.* **2009,** *4,* 56-63.

149 Sadhu, S.; Patra, A., Lattice strain controls the carrier relaxation dynamics in CdxZn1-xS alloy quantum dots. *J. Phys. Chem. C* **2012,** *116,* 15167-15173.

150 Jones, M.; Nedeljkovic, J.; Ellingson, R.J.; Nozik, A.J.; Rumbles, G., Photoenhancement of luminescence in colloidal CdSe quantum dot solutions. *J. Phys. Chem. B* **2003,** *107,* 11346-11352.

151 Hess, B.C.; Okhrimenko, I.G.; Davis, R.C.; Stevens, B.C.; Schulzke, Q.A.; Wright, K.C.; Bass, C.D.; Evans, C.D.; Summers, S.L., Surface transformation and photoinduced recovery in CdSe nanocrystals. *Phys. Rev. Lett.* **2001,** *86,* 3132-3135.

152 Cordero, S.R.; Carson, P.J.; Estabrook, R.A.; Strouse, G.F.; Buratto, S.K., Photo-Activated Luminescence of CdSe Quantum Dot Monolayers. *J. Phys. Chem. B* **2000,** *104,* 12137-12142.

153 Wang, Y.; Tang, Z.; Correa-Duarte, M.A.; Pastoriza-Santos, I.; Giersig, M.; Kotov, N.A.; Liz-Marzán, L.M., Mechanism of strong luminescence photoactivation of citrate-stabilized water-soluble nanoparticles with CdSe cores. *J. Phys. Chem. B* **2004,** *108,* 15461-15469.

154 Maenosono, S., Modeling photoinduced fluorescence enhancement in semiconductor nanocrystal arrays. *Chem. Phys. Lett.* **2003,** *376,* 666-670.

155 Shinya, M.; Ceco Danov, D.; Soichiro, S.; Yukio, Y., Optical memory media based on excitation-time dependent luminescence from a thin film of semiconductor nanocrystals. *Jap. J. Appl. Phys.* **2000,** *39,* 4006.

156 Oda, M.; Shen, M.Y.; Saito, M.; Goto, T., Photobrightening of CuBr nanocrystals in PMMA. *J. Luminescence* **2000,** *87–89,* 469-471.

157 Bol, A.A.; Meijerink, A., Luminescence quantum efficiency of nanocrystalline ZnS:Mn2+. 2. enhancement by UV irradiation. *J. Phys. Chem. B* **2001,** *105,* 10203-10209.

158 Li, R.F.; Lee, J.; Yang, B.C.; Horspool, D.N.; Aindow, M.; Papadimitrakopoulos, F., Amine-assisted facetted etching of CdSe nanocrystals. *J. Amer. Chem. Soc.* **2005,** *127*, 2524-2532.

159 Lim, S.J.; Kim, W.; Jung, S.; Seo, J.; Shin, S.K., Anisotropic etching of semiconductor nanocrystals. *Chem. Mater.* **2011,** *23*, 5029-5036.

160 Lee, W.; Kim, H.; Jung, D.-R.; Kim, J.; Nahm, C.; Lee, J.; Kang, S.; Lee, B.; Park, B., An effective oxidation approach for luminescence enhancement in CdS quantum dots by H2O2. *Nanoscale Res.Lett.* **2012,** *7*.

161 Borges, C.A.M.; Rodrigues, C.A.; Faria, R.M.; Guimaraes, F.E.G., Strong luminescence intensity modulation near a metal-organic interface. *Synthetic Metals* **2005,** *154,* 133-136.

162 Zimnitsky, D.; Jiang, C.; Xu, J.; Lin, Z.; Tsukruk, V.V., Substrate- and time-dependent photoluminescence of quantum dots inside the ultrathin polymer LbL film. *Langmuir* **2007,** *23,* 4509-4515.

163 Wang, C.F.; Badolato, A.; Wilson-Rae, I.; Petroff, P.M.; Hu, E.; Urayama, J.; Imamoğlu, A., Optical properties of single InAs quantum dots in close proximity to surfaces. *Appl. Phys. Lett.* **2004,** *85,* 3423-3425.

164 Clapp, A.R.; Medintz, I.L.; Mauro, J.M.; Fisher, B.R.; Bawendi, M.G.; Mattoussi, H., Fluorescence resonance energy transfer between quantum dot donors and dye-labeled protein acceptors. *J. Amer. Chem. Soc.* **2004,** *126,* 301-310.

165 Menon, V.M.; Husaini, S.; Valappil, N.; Luberto, M., Photonic emitters and circuits based on colloidal quantum dot composites. In *Quantum Dots, Particles, and Nanoclusters Vi*, Eyink, K. G.; Szmulowicz, F.; Huffaker, D. L., Eds. **2009,** *7224.*

166 Song, H.; Lee, S., Photoluminescent (CdSe) ZnS quantum dot-polymethylmethacrylate polymer composite thin films in the visible spectral range. *Nanotechnology* **2007,** *18.*

167 Zimnitsky, D.; Jiang, C.Y.; Xu, J.; Lin, Z.Q.; Zhang, L.; Tsukruk, V.V., Photoluminescence of a freely suspended monolayer of quantum dots encapsulated into layer-by-layer films. *Langmuir* **2007,** *23*, 10176-10183.

168 Kharlampieva, E.; Kozlovskaya, V.; Zavgorodnya, O.; Lilly, G.D.; Kotov, N.A.; Tsukruk, V.V., pH-responsive photoluminescent LbL hydrogels with confined quantum dots. *Soft Matter* **2010,** *6*, 800-807.

169 Coe-Sullivan, S.; Steckel, J.S.; Woo, W.K.; Bawendi, M.G.; Bulovic, V., Large-area ordered quantum-dot monolayers via phase separation during spin-casting. *Adv. Funct. Mater.* **2005,** *15*, 1117-1124.

170 Gole, A.; Jana, N.R.; Selvan, S.T.; Ying, J.Y., Langmuir−Blodgett thin films of quantum dots: Synthesis, surface modification, and fluorescence resonance energy transfer (FRET) studies. *Langmuir* **2008,** *24,* 8181-8186.

171 Bourvon, H.; Le Calvez, S.; Kanaan, H.; Meunier-Della-Gatta, S.; Philippot, C.; Reiss, P., Langmuir-Schaeffer monolayers of colloidal nanocrystals for cost-efficient quantum dot light-emitting diodes. *Adv. Mater.* **2012,** *24,* 4414-4418.

172 Shevchenko, E.V.; Talapin, D.V.; Kotov, N.A.; O'Brien, S.; Murray, C.B., Structural diversity in binary nanoparticle superlattices. *Nature* **2006,** *439,* 55-59.

173 Chen, Z.Y.; Moore, J.; Radtke, G.; Sirringhaus, H.; O'Brien, S., Binary nanoparticle superlattices in the semiconductor-semiconductor system: CdTe and CdSe. *J. Amer. Chem. Soc.* **2007,** *129,* 15702-15709.

174 Overgaag, K.; Evers, W.; de Nijs, B.; Koole, R.; Meeldijk, J.; Vanmaekelbergh, D., Binary superlattices of PbSe and CdSe nanocrystals. *J. Amer. Chem. Soc.* **2008,** *130,* 7833.

175 Komarala, V.K.; Rakovich, Y.P.; Bradley, A.L.; Byrne, S.J.; Corr, S.A.; Gun'ko, Y.K., Emission properties of colloidal quantum dots on polyelectrolyte multilayers. *Nanotechnology* **2006,** *17,* 4117-4122.

176 Tamborra, M.; Striccoli, M.; Comparelli, R.; Curri, M.L.; Petrella, A.; Agostiano, A., Optical properties of hybrid composites based on highly luminescent CdS nanocrystals in polymer. *Nanotechnology* **2004,** *15,* S240-S244.

177 Suarez, I.; Gordillo, H.; Abargues, R.; Albert, S.; Martinez-Pastor, J., Photoluminescence waveguiding in CdSe and CdTe QDs-PMMA nanocomposite films. *Nanotechnology* **2011,** *22.*

178 Khanna, P.K.; Singh, N., Light emitting CdS quantum dots in PMMA: Synthesis and optical studies. *J. Luminescence* **2007,** *127,* 474-482.

179 Lee, J.; Sundar, V.C.; Heine, J.R.; Bawendi, M.G.; Jensen, K.F., Full color emission from II-VI semiconductor quantum dot-polymer composites. *Adv. Mater.* **2000,** *12,* 1102.

180 Wu, X.Y.; Liu, H.J.; Liu, J.Q.; Haley, K.N.; Treadway, J.A.; Larson, J.P.; Ge, N.F.; Peale, F.; Bruchez, M.P., Immunofluorescent labeling of cancer marker Her2 and other cellular targets with semiconductor quantum dots. *Nat. Biotech.* **2003,** *21,* 41-46.

181 Hanaki, K.; Momo, A.; Oku, T.; Komoto, A.; Maenosono, S.; Yamaguchi, Y.; Yamamoto, K., Semiconductor quantum dot/albumin complex is a long-life and highly photostable endosome marker. *Biochem. & Biophys. Res. Comm.* **2003,** *302,* 496-501.

182 Kim, S.; Lim, Y.T.; Soltesz, E.G.; De Grand, A.M.; Lee, J.; Nakayama, A.; Parker, J.A.; Mihaljevic, T.; Laurence, R.G.; Dor, D.M.; Cohn, L.H.; Bawendi, M.G.; Frangioni, J.V., Near-infrared fluorescent type II quantum dots for sentinel lymph node mapping. *Nat. Biotech.* **2004,** *22,* 93-97.

183 Ko, H.H.; Jiang, C.Y.; Tsukruk, V.V., Encapsulating nanoparticle arrays into layer-by-layer multilayers by capillary transfer lithography. *Chem. Mater.* **2005,** *17,* 5489-5497.

184 Suh, K.Y.; Lee, H.H., Capillary force lithography: Large-area patterning, self-organization, and anisotropic dewetting. *Adv. Funct. Mater.* **2002,** *12,* 405-413.

185 Kim, L.; Anikeeva, P.O.; Coe-Sullivan, S.A.; Steckel, J.S.; Bawendi, M.G.; Bulovic, V., Contact printing of quantum dot light-emitting devices. *Nano Lett.* **2008,** *8,* 4513-4517.

186 Rizzo, A.; Mazzeo, M.; Palumbo, M.; Lerario, G.; D'Amone, S.; Cingolani, R.; Gigli, G., Hybrid light-emitting diodes from microcontact-printing double-transfer of colloidal semiconductor CdSe/ZnS quantum dots onto organic layers. *Adv. Mater.* **2008,** *20,* 1886.

187 Qin, D.; Xia, Y.N.; Whitesides, G.M., Soft lithography for micro- and nanoscale patterning. *Nat. Protocols* **2010,** *5,* 491-502.

188 Bao, B.; Li, M.; Li, Y.; Jiang, J.; Gu, Z.; Zhang, X.; Jiang, L.; Song, Y., Patterning fluorescent quantum dot nanocomposites by reactive inkjet printing. *Small* **2015,** *11,* 1649-1654.

189 Hampton, M.J.; Templeton, J.L.; DeSimone, J.M., Direct patterning of CdSe quantum dots into sub-100 nm structures. *Langmuir* **2010,** *26,* 3012-3015.

190 Gates, B.D.; Xu, Q.B.; Stewart, M.; Ryan, D.; Willson, C.G.; Whitesides, G.M., New approaches to nanofabrication: Molding, printing, and other techniques. *Chem. Rev.* **2005,** *105,* 1171-1196.

191 Biswas, A.; Bayer, I.S.; Biris, A.S.; Wang, T.; Dervishi, E.; Faupel, F., Advances in top–down and bottom–up surface nanofabrication: Techniques, applications & future prospects. *Adv. Colloid and Interfac Sci.* **2012,** *170,* 2-27.

192 Wang, Y.; Tang, Z.Y.; Correa-Duarte, M.A.; Liz-Marzan, L.M.; Kotov, N.A., Multicolor luminescence patterning by photoactivation of semiconductor nanoparticle films. *J. Amer. Chem. Soc.* **2003,** *125,* 2830-2831.

193 Chen, J.; Chan, Y.-H.; Yang, T.; Wark, S.E.; Son, D.H.; Batteas, J.D., Spatially selective optical tuning of quantum dot thin film luminescence. *J. Amer. Chem. Soc.* **2009,** *131,* 18204.

194 Tagliazucchi, M.; Amin, V.A.; Schneebeli, S.T.; Stoddart, J.F.; Weiss, E.A., High-contrast photopatterning of photoluminescence within quantum dot films through degradation of a charge-transfer quencher. *Adv. Mater.* **2012,** *24,* 3617-3621.

195 Park, Y.; Felipe, M.J.; Advincula, R.C., Facile patterning of hybrid CdSe nanoparticle films by photoinduced surface defects. *ACS Appl. Mater. & Interfaces* **2011,** *3,* 4363-4369.

196 Sun, Q.; Wang, Y.A.; Li, L.S.; Wang, D.Y.; Zhu, T.; Xu, J.; Yang, C.H.; Li, Y.F., Bright, multicoloured light-emitting diodes based on quantum dots. *Nat. Photonics* **2007,** *1*, 717-722.

197 Rauch, T.; Boberl, M.; Tedde, S.F.; Furst, J.; Kovalenko, M.V.; Hesser, G.N.; Lemmer, U.; Heiss, W.; Hayden, O., Near-infrared imaging with quantum-dot-sensitized organic photodiodes. *Nat. Photonics* **2009,** *3*, 332-336.

198 Chan, Y.; Caruge, J.M.; Snee, P.T.; Bawendi, M.G., Multiexcitonic two-state lasing in a CdSe nanocrystal laser. *Appl. Phys. Lett.* **2004,** *85*, 2460-2462.

199 Roither, J.; Pichler, S.; Kovalenko, M.V.; Heiss, W.; Feychuk, P.; Panchuk, O.; Allam, J.; Murdin, B.N., Two- and one-dimensional light propagations and gain in layer-by-layer-deposited colloidal nanocrystal waveguides. *Appl. Phys. Lett.* **2006,** *89*.

200 Sukhovatkin, V.; Musikhin, S.; Gorelikov, I.; Cauchi, S.; Bakueva, L.; Kumacheva, E.; Sargent, E.H., Room-temperature amplified spontaneous emission at 1300 nm in solution-processed PbS quantum-dot films. *Opt. Lett.* **2005,** *30*, 171-173.

201 Petruska, M.A.; Malko, A.V.; Voyles, P.M.; Klimov, V.I., High-performance, quantum dot nanocomposites for nonlinear optical and optical gain applications. *Adv. Mater.* **2003,** *15*, 610-613.

202 Chan, Y.; Steckel, J.S.; Snee, P.T.; Caruge, J.M.; Hodgkiss, J.M.; Nocera, D.G.; Bawendi, M.G., Blue semiconductor nanocrystal laser. *Appl. Phys. Lett.* **2005,** *86*.

203 Jasieniak, J.J.; Fortunati, I.; Gardin, S.; Signorini, R.; Bozio, R.; Martucci, A.; Mulvaney, P., Highly efficient amplified stimulated emission from CdSe-CdS-ZnS quantum dot doped waveguides with two-photon infrared optical pumping. *Adv. Mater.* **2008,** *20*, 69.

204 Malko, A.V.; Mikhailovsky, A.A.; Petruska, M.A.; Hollingsworth, J.A.; Htoon, H.; Bawendi, M. G.; Klimov, V.I., From amplified spontaneous emission to microring lasing using nanocrystal quantum dot solids. *Appl. Phys. Lett.* **2002,** *81,* 1303-1305.

205 Lin, C.H.; Lafalce, E.; Jung, J.; Smith, M.J.; Malak, S.T.; Aryal, S.; Yoon, Y.J.; Zhai, Y.; Lin, Z.; Vardeny, Z.V.; Tsukruk, V.V., Core/alloyed-shell quantum dot robust solid films with high optical gains. *ACS Photonics* **2016,** *3,* 647-658.

206 Lin, Z.; Ramezani, H.; Eichelkraut, T.; Kottos, T.; Cao, H.; Christodoulides, D.N., Unidirectional invisibility induced by PT-symmetric periodic structures, *Phys. Rev. Lett.* **2011,** *106,* 213901.

207 Feng, L.; Xu, Y.L.; Fegadolli, S.; Lu, M.H.; Oliveira, J.E.B.; Almeida, V.R.; Chen, Y-F.; Scherer, A., Experimental demonstration of a unidirectional reflectionless parity-time metamaterial at optical frequencies, *Nat. Mater.,* **2012,** *online advance publication.*

208 Eichelkraut, T.; Heilmann, R.; Weimann, S.; Stuetzer, S.; Dreisow, F.; Christodoulides, D.N.; Nolte, S.; Szameit, A., Mobility transition from ballistic to diffusive transport in non-Hermitian lattices. *Nat. Communications* **2013,** *4,* online.

209 Charge, parity, and time reversal (CPT) symmetry (Guide to Nuclear Wallchart). **August 2000.** http://www2.lbl.gov/abc/wallchart/chapters/05/2.html

210 CPT Invariance (Hyperphysics), <http://hyperphysics.phy-astr.gsu.edu/hbase/particles/cpt.html>. Das, Ashok and Ferbel, Thomas, Introduction to Nuclear and Particle Physics (Ch.11), Wiley, **1994.**

211 Peng, B.; Oezdemir, S.K.; Rotter, S.; Yilmaz, H.; Liertzer, M.; Monifi, F.; Bender, C.M.; Nori, F.; Yang, L., Loss-induced suppression and revival of lasing. *Science* **2014,** *346,* 328-332.

CHAPTER 2

RESEARCH GOALS, TECHNICAL OBJECTIVES, AND DISSERTATION OVERVIEW

2.1 Research goals

The primary goal of this research is to develop an understanding of how the confinement conditions and resulting light-matter interactions of plasmonic and quantum dot nanostructures depend on three levels of system hierarchy. These levels of hierarchy include: individual nanostructure, nanostructure-nanostructure local-assembly, and large-scale nanostructure arrangement (**Figure 2.1**). The surface confinement of plasmons (collective electron oscillations) and their localized-surface plasmon resonances are focused on for plasmonic nanostructures. The quantum confinement of excitons (electron-hole pair quasiparticles) and their electronic radiative relaxation pathways are examined for quantum dots (QDs). By understanding the relationship between the nanostructure confinement mechanisms and the system hierarchy, light-matter interactions like localized-scattering, localized electric field enhancements, spectral emission evolution, spatial light propagation, optical attenuation/enhancement, and spatially modulated light emission can be measured and controlled.

Novel experimental fabrication and characterization approaches are developed to facilitate the fundamental investigations of these hierarchical nanostructure systems. These approaches include strategies for controlled nanoparticle encapsulation into polymer films, schemes for fabricating coupled local-assemblies, and strategies to control the emission and propagation of light over larger-scales (via pre-determined long-range particle arrangements and long-range modulation of particle properties).

These discoveries yield a general set of guidelines that can be referenced when designing and fabricating nanostructure-based photonic systems that need to exhibit specific optical characteristics. This scientific and engineering framework could accelerate the development of novel nanostructured photonic systems that exhibit properties like electric field enhancement, localized scattering/absorption, controlled optical amplification, and spatially modulated photoluminescence.

Since the optical properties and general behavior of plasmonic nanostructures and quantum dots arise from fundamentally different confinement phenomena, this research has two general tasks (**Figure 2.1**):

Task 1 *focuses on the measurement and understanding of structure-property relationships of individual plasmonic nanostructures that exhibit optical extinction. Following this, emphasis is placed on how to introduce and control electromagnetic (EM) coupling between 2D and 3D assemblies of plasmonic nanostructures in order to investigate how EM coupling leads to various advantageous enhanced EM phenomenona. The final focus is on how the long-range arrangement of plasmonic nanoparticles can be utilized to modulate the light-matter interactions over larger spatial scales;*

Task 2 *concentrates on how the optical emission properties of individual quantum dots depend on the QD compositional design (core, core/shell, core/graded shell), and how these properties can be altered via external factors like oxygen, material matrix, and light exposure. This knowledge is then utilized in conjunction with long-range QD arrangements to understand and control light-matter interactions over larger-scales (light confinement/amplification in films and PL emission patterns).*

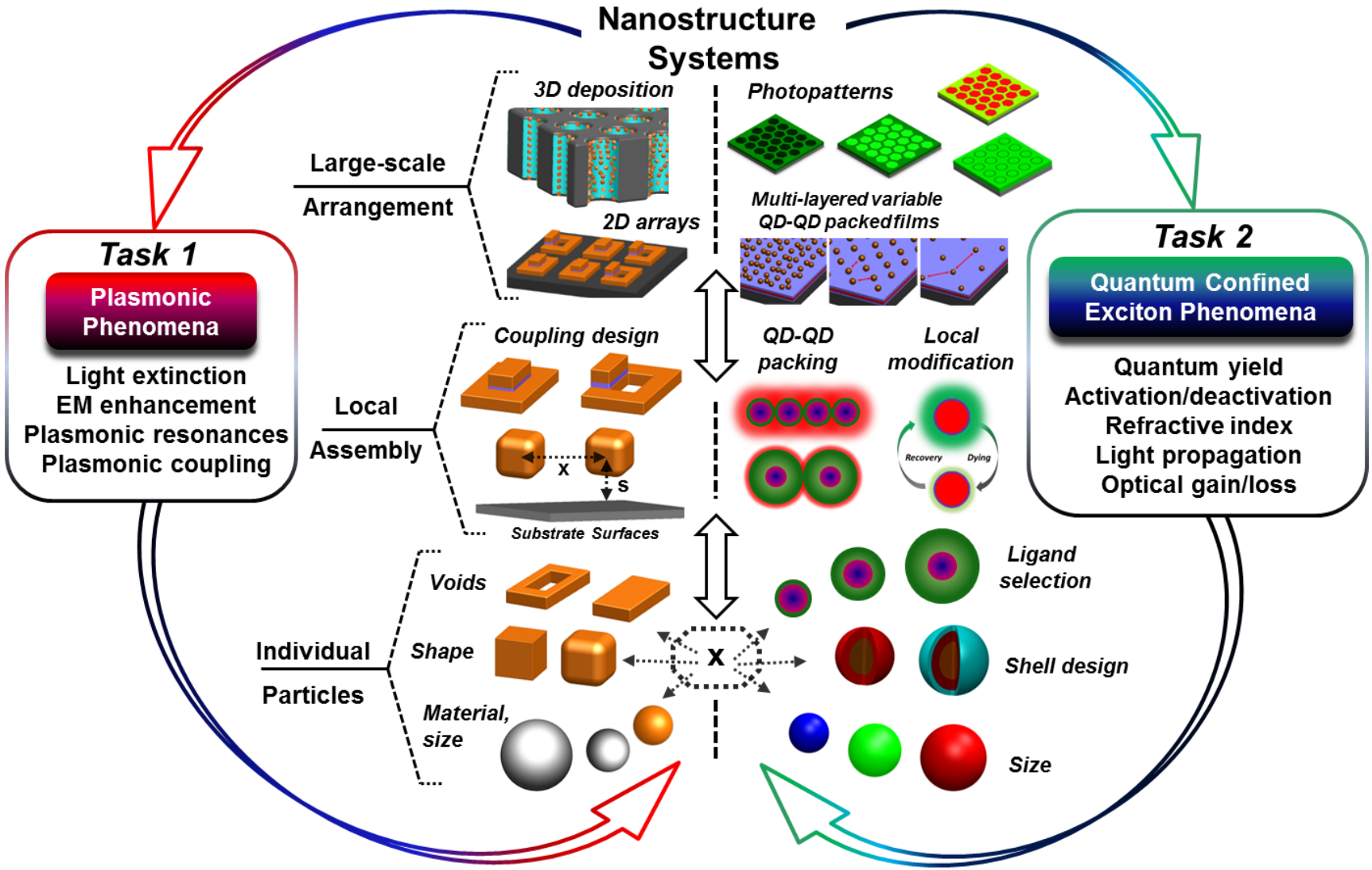

Figure 2.1. Global schematic of the hierarchical approach that will be implemented to understand the fundamental light-matter interaction occurring at each level of the photonic system, from individual particles, to local-assemblies, up to large-scale arrangements.

2.2 Technical objectives

The global focus is on how to control the local-assembly and large-scale arrangement of these highly tunable optical nanostructures in order to develop powerful approaches to alter specific light-matter characteristics (**Figure 2.1**). The aim is to achieve controlled light scattering, absorption, transmission, or amplification/attenuation that cannot be attained using current knowledge and approaches. Specific emphasis is put toward implementing non-traditional local-assemblies (particle stacking) or large-scale arrangements (3D substrates) of plasmonic nanostructures to introduce new ways for tailoring plasmonic coupling and overall electromagnetic enhancement. In addition, substantial effort focuses on how the emission characteristics of quantum dots (spectral position, full-width half-maximum, and quantum yield) can be tuned via nanoparticle design and external factors so that the large-scale spatial arrangements yield well-controlled light amplification/attenuation and spatial emission patterns.

Task 1: Plasmonic nanostructures

- Examine the light extinction of individual nanostructures in solution of different size, shape, and edge-rounding in order to develop an understanding of how the extinction depends on the geometry of individual “non-interacting” nanoparticles;
- Corroborate the optical characteristics of non-interacting nanostructures with electromagnetic modeling with the aim to understand the plasmonic resonances and surface charge distributions leading to this extinction behavior;
- Identify and introduce novel plasmonic nanostructure-nanostructure local-assemblies in well-ordered arrangements so that unique coupling mechanisms can be investigated via direct structure-property comparisons across multiple characterization techniques like AFM-SEM-hyperspectral;

- Experimentally investigate how the optical scattering of novel stacked local-assemblies like stacked dimers depends on their assembly via direct structure-property comparison (AFM-SEM-hyperspectral) and investigate the underlying plasmonic resonances and electric fields using electromagnetic modeling;
- Assemble nanostructures in ordered 2D & 3D arrangements to investigate how the electric field enhancement depends on the shape (spherical or cubic) and proximity (isolated or assembled) of the nanostructures, and explain the results by modeling the coupled nanostructures and examining the magnitude of their electromagnetic hot spot;
- Examine how the extinction, electric field enhancement, and surface-enhanced Raman scattering (SERS) saturation point depend on the surface density of the nanostructures (degree of coupling) in the 3D arrangements and develop an understanding of the interplay between these factors;
- Monitor the SERS enhancement along the depth of the 3D arrangements in order to gain an understanding of how the light propagates within the 3D waveguiding substrate and therefore interacts with individual and assembled nanostructures located at different depths within the 3D substrate.

Task 2: Quantum dot nanostructures

- Measure the optical absorbance, photoluminescence, and quantum yield of core, core/shell, and core/graded shell QDs, before and after ligand exchange procedures to determine how the properties of non-interacting QDs can be manipulated;

- Develop experimental procedures for measuring the photoluminescence evolution of QD films over short (seconds) and long (minutes-to-hours) time scales when in darkness or under continuous light exposure;
- Measure the evolution of photoluminescence (PL) from QD films upon light exposure for QDs of different compositional design (core, core/shell, core/graded shell) and identify the potential mechanisms underlying this behavior;
- Identify the characteristics (rate, reversibility/irreversibility, required environmental factors) and interplay of the various physical and chemical mechanisms in a QD exposed to light which lead to the decay and recovery of QD emission;
- Establish a general set of guidelines to consult when trying to identify the appropriate QD design for a specific application. These guidelines should also outline the specific experimental procedures that can be employed to confirm the selection;
- Examine how the nature of the ligand capping the QD affects the average QD-QD spacing (QD-loading), surface roughness, and uniformity of QD films;
- Determine how the average QD-QD loading in QD films affects long-range characteristics like refractive index and refractive index contrast, and examine how this affects the optical gain (threshold and magnitude) and optical attenuation;
- Demonstrate control of QD optical gain and loss in QD thin films, and match or exceed the highest reported QD thin film gain values of ~500 cm^{-1};
- Develop a list of ligand selection rules that can be consulted (in a general manner) to identify an appropriate ligand for obtaining a specific system characteristic like low gain threshold, high optical gain, low optical loss, or stable amplified spontaneous emission;

- Develop photopatterning approaches that allow for controlled and predetermined changes in QD PL intensity with reliable spatial pattern control and arrangement, emission contrast, and pattern evolution (i.e. positive/negative photopatterning);
- Identify and implement strategies (unique photomasks or exposure setups) that increase the feature resolution, patternable area, and throughput of photopatterning (without compromising pattern contrast, uniformity, or reliability);
- Develop photopatterning approaches to reliably control the emission intensity of specific QD colors in multicolor mixed QD-polymer films and use these strategies to modify the overall spectral profile to fabricate multicolor QD photopatterns.

2.3 Organization and composition of dissertation

Chapter 1 provides a critical review of the literature dealing with plasmonic structures and quantum dots. Initial emphasis is on the fundamental confinement phenomena (confined plasmons and quantum confined excitons) and how these depend on the characteristics of the individual particle (size, shape, composition) and the particle-particle local-assembly. Following this, the role the large-scale arrangement plays in controlling the resulting incoming or outgoing light from the system is examined (typically via patterned systems or substrate templates). To conclude, a brief outline of the motivation for this dissertation is provided.

Chapter 2 outlines the research goals and technical objectives of this body of work. A summary of its organization and brief descriptions of each chapter are also provided.

Chapter 3 outlines the materials used in this work, the experimental procedures employed for synthesizing the plasmonic and semi-conducting nanostructures, and the

film deposition approaches. Finally, the various characterization techniques that are used to examine the physical, optical, and material properties of the particles, films, and patterns are outlined. Techniques for physical characterization include atomic force microscopy (AFM), scanning electron microscopy (SEM), transmission electron microscopy (TEM), and optical microscopies (bright field and dark field). The optical properties were measured using optical spectroscopies (bright field, dark field, photoluminescence) and spectroscopic ellipsometry. Material properties were examined using Raman spectroscopy, spectroscopic ellipsometry, zeta-potential, dynamic light scattering, proton nuclear magnetic resonance (HNMR), and thermal gravimetric analysis (TGA). The modeling techniques (FDTD: finite-difference time-domain and DFT: density functional theory) are also covered. Some of the outlined techniques were explicitly utilized by collaborators (mentioned in the text). More detailed information is provided for specific techniques in relevant chapters.

Chapter 4 is an investigation of well-ordered arrays of stacked plasmonic structures via AFM, SEM, and hyperspectral scanning characterization. Direct correlations between the structural characteristics of specific plasmonic structures (and their stacked assemblies) and their unique optical scattering spectrum are made. The position of the Au cap on the hollow rectangular Au nanostructures is shown to dramatically affect the primary plasmon resonances and the local electrical field within the electromagnetic "hotspots." Electromagnetic modeling of the plasmonic modes in these assemblies, compared to the conventional solid nanorectangles, indicates that the electric field from the higher energy dipole and quadrupolar modes is increased manifold through the interaction of the cap with the underlying hollow nanostructure.

Chapter 5 examines approaches for creating hierarchal systems of individual and local-assemblies of Ag nanocubes (AgNCs) within a microscale three-dimension porous alumina membrane (PAM). The local assembly of AgNCs is controlled using a polyelectrolyte layering method, allowing for either dispersed (individual) AgNCs or aggregated (locally-assembled) AgNCs. The 3D arrangement of the AgNCs is controlled by the 3D PAM substrate. The electric fields and electric hot-spot volume of the plasmons associated with the local nanocube-nanocube contacts are examined with finite-different time-domain (FDTD) modeling and show greatly enhanced electric fields compared to individual nanocubes. Furthermore, FDTD modeling showed that the coupled AgNCs exhibited larger integrated electric field intensities than nanosphere-nanosphere contacts. The FDTD predictions on EM field strength are tested (and confirmed) by comparing the limits of chemical detection from each substrate via surface-enhanced Raman scattering (SERS). These substrates are shown to exhibit exceptionally low limits-of-detection for vapor phase benzene thiol and n-methyl-4-nitroaniline (500 ppb and 3 ppb, respectively).

Chapter 6 is an in-depth examination of how the QD compositional design (CdSe core, CdSe/ZnS core/shell, and CdSe/CdSe/$Cd_{1-x}Zn_xSe_{1-y}S_y$ core/graded shell) affects the photoluminescence (exciton) evolution under various light exposure conditions. The results show that the compositional design of the quantum dot significantly affects how its optical characteristics evolve in darkness and under light exposure, with distinct shifts occurring, including intensity decreases, intensity increases, and spectral shifts. The results (and the strategies to obtain them) are relevant to a wide range of quantum dot based material studies and applications.

Chapter 7 focuses on how QD-QD spacing in thin films affects light-matter interactions (light propagation, optical amplification, and optical attenuation) over larger scales (hundreds of microns). The molecular dimensions and functionality of the QD ligand are shown to affect important physical properties (film morphology, QD-packing density) and optical characteristics (optical density, refractive index, refractive index contrast). These changes directly influence the light-matter interactions over larger scales, specifically waveguiding efficiency/losses and optical amplification/attenuation.

Chapter 8 outlines how the two-step decay-to-recovery of PL intensity can be utilized for novel and facile photopatterning strategies. It is shown that careful control of the duration of light exposure makes it possible to develop photopatterns of either negative or positive intensity contrast. These photopatterns are analogous to traditional positive and negative patterning in electron/photolithography but have no physical topographical modulation. In addition, negative-to-positive contrast switching is successfully demonstrated using an understanding of the overall evolution of the emission intensity curve under continuous light exposure.

Chapter 9 explores how interference-based exposure strategies can be implemented to fabricate photopatterns with exceptional feature resolution, throughput, and uniformity. The utilization of interference-based exposure represents a strong departure from traditional photopatterning strategies. A near-field interference approach using PDMS photomasks is shown to yield both edge-profile and face-profile photopatterns depending on how the exposure light is incident on the photomask. Far-field (maskless) laser interference lithography is also employed to obtain photopatterns with sinusoidal intensity contrast modulation. Both interference approaches represent a departure from traditional photopatterning exposure strategies (based on transmission-based exposure).

Chapter 10 examines approaches for creating multicolor QD photopatterns, which is a first in the field of photopatterning. QD-polymer films composed of two quantum dot colors are fabricated and then exposed to specific light wavelengths to develop a multicolored photopattern. By judicious consideration and implementation of the development wavelength, specific QD colors within the film can be selectively or collectively modified to alter chromaticity. These strategies allow for unprecedented control over the development of multicolor photopatterns, representing a significant departure from previous single-component (monochromatic) photopatterning studies.

Chapter 11 is a summary of the results and conclusions resulting from the earlier chapters, as well as the significance of these results in the context of the current scientific literature. A brief discussion of the potential applications and future prospects of this work is provided, with particular focus on how the QD optical gain/loss work and QD photopatterning strategies could be combined to develop photonic parity-time systems. A brief discussion of the potential uses of photopatterning in the areas of QD display technologies and anti-counterfeiting labels is also provided.

CHAPTER 3

EXPERIMENTAL TECHNIQUES AND MATERIALS

3.1 Ag & Au nanostructures

3.1.1 Chemicals and materials

Porous alumina membranes (PAMs) with a diameter of 47 mm, cylindrical pore diameter of 243±20 nm, wall thickness of 40 nm, and total thickness (depth) of 60 μm were purchased from Anodisc 47, Whatman. Poly(allylamine hydrochloride) (PAH)(M_w = 55,000) and Poly(sodium 4-styrenesulfonate) (PSS)(M_W = 70,000) were purchased from Sigma-Aldrich. Polyethylenimine (PEI)(*M*W = 70,000) was purchased from Polysciences.

3.1.2 Synthesis of Ag nanocubes (AgNC)

Ag nanocubes (AgNCs) of 40 nm edge-length with polyvinylpyrrolidone (PVP) as the stabilizing capping agent were synthesized by our collaborators (Dr. M.A. Mahmoud from Prof. El-Sayed group, School of Chemistry and Biochemistry, Georgia Institute of Technology) using a polyol method as described elsewhere.[1,2] Briefly, in a 100 mL round bottom glass flask, 70 mL of ethylene glycol (EG) was heated to 150°C for 1 h. Then a solution of 0.85 g polyvinylpyrrolidone (PVP) dissolved in 10 mL EG was added to the hot EG. 0.4 mL of Na_2S (3 mM) dissolved in EG and 6 mL of 282 mM silver nitrate dissolved in EG were injected, respectively, into the reaction mixture. The reaction mixture was stirred at 200 rpm and refluxed at 150°C for 10 minutes until the solution became opaque. In order to purify the AgNCs, 5 mL of the prepared AgNCs solution was diluted with water and centrifuged at 10,000 rpm for 5 minutes. The precipitated AgNCs were re-dispersed in water.

3.1.3 3D PAM-AgNC substrate via vacuum infiltration method

Porous alumina membranes (PAMs) were decorated with Ag Nanocubes (AgNCs) by infiltrating AgNCs suspended in water (AgNC solution) through surface-modified PAMs with a diameter of 47 mm, cylindrical pore diameter of 24±20 nm, wall thickness of 40 nm, and total thickness (depth) of 60 μm. The immobilization of nanocubes on porous alumina membranes was done using a modified literature procedure.[3,4] Briefly, the inner surface of the pore walls was modified with a polyelectrolyte to electrostatically assemble the AgNCs onto the pore walls (detailed in Chapter 4).[5] The inner surface of the porous membranes was modified with poly(allylamine hydrochloride), polyethylenimine, or poly(sodium 4-styrenesulfonate) by spin-coating (3,000 rpm, ~45 s) 0.2% aqueous solution followed by rinsing with Nanopure water (18.2 MΩ cm). The pressure was maintained at 600-700 mmHg during the vacuum infiltration process to ensure widespread, dense deposition of AgNCs onto the pore walls. Substrates were sonicated and washed after vacuum infiltration to remove excess polymer and AgNCs adsorbed on the PAM surface.

3.1.4 Colloidal Ag nanospheres (AgNS) grown in-situ

AgNS were grown on the pore walls following a two-step electroless deposition process involving the deposition of silver seeds through the replacement of Sn2+ by Ag and growth of the silver seeds by immersion in $AgNO_3$ and ascorbic acid.[6,7] A detailed growth mechanism and time dependence of particle size and distribution using this method have been reported elsewhere.[6,8]

3.1.5 Au nanorectangles from electron beam lithography

The gold nanorectangle arrays were fabricated using electron beam lithography (EBL) by Dr. Rachel Near (Prof. El-Sayed group, School of Chemistry and Biochemistry, Georgia Institute of Technology) using a JEOL JBX-9300FS 100 kV EBL system and were supported on a Si wafer in distributed in arrays with dimensions of 200 x 200 μm^2. The specific procedure is described in Chapter 5 and the publication this chapter is based on.[9]

3.2 Quantum dots (QDs)

3.2.1 Chemicals and materials

The following chemicals were obtained and used by our by our collaborators (typically Dr. Jaehan Jung or Young Jun Yoon from Prof. Z. Lin's group, School of Materials Science and Engineering, Georgia Institute of Technology) to synthesis quantum dots. Cadmium oxide (CdO), zinc acetate (99.99%), zinc acetylacetonate, tri-n-octylphosphine (TOP, 90%), selenium powder, and 1-dodecanethiol (98%) were obtained from Sigma Aldrich. Hexanes, heptane, and octylamine (OctA, 98%), 1-tetradecylphosphonic acid (TDPA, 98%), tri-n-octylphosphine oxide (TOPO, 90%), diethylzinc (15 weight% in hexane), were obtained from Alfa Aesar. 1-octadecene (ODE, 90%), hexadecylamine (HDA, 90%), butylamine (BA, 98%), are oleic acid (97%) were obtained from TCI. Toluene was obtained from BDH Chemicals. The fluorinated polymer CYTOP was obtained from AGC Chemicals. All chemicals were used as received.

3.2.2 Synthesis of CdSe core QDs

All quantum dots (CdSe core, CdSe/ZnS core/shell, and CdSe/$Cd_{1-x}Zn_xSe_{1-y}S_y$ core/graded shell QDs where synthesized by our collaborators (typically Dr. Jaehan Jung or Young Jun Yoon from Prof. Z. Lin's group, School of Materials Science and Engineering, Georgia Institute of Technology) through the pyrolysis of organometallic precursors in the coordinating solvent trioctylphosphine oxide (TOPO). The QD were capped with various ligands to make them soluble in either non-polar organic solvents or polar solvents H_2O.

Green and yellow emitting CdSe QDs were synthesized following a literature procedure.[10,11] Initially, 50 mg of CdO, 300 mg of TDPA, and 4 g of TOPO were inserted into a three neck flask. The mixture was heated to 120°C and degassed for 1 hour. Subsequently, the temperature was increased to 290°C under Argon. After the solution became clear and transparent, 1 ml of 1 M Se/TBP solution was quickly injected in order to initiate nucleation and growth. Green CdSe QDs were obtained by allowing the reaction to proceed at 290°C for 10 sec, while yellow CdSe QDs were obtained by allowing it to proceed at 290°C for 30 sec. The heating mantle was then removed to stop the reaction. Afterwards, once the temperature reached 70°C, 5 ml of hexane was added to the solution.

Red emitting CdSe core QDs were synthesized using a slightly modified reported procedure.[12,13] Specifically, 1 mmol of CdO and 5 ml of oleic acid (OA) were placed in a three neck flask. The mixture was heated to 150°C and degassed for 1 hr. Subsequently, 15 ml of octadecylamine (ODE) was added to the solution and the temperature was increased to 300°C under Ar. When the solution became transparent

and clear, 0.2 ml of 1 M Se/TOP solution was injected to initiate nucleation and growth. CdSe QDs were allowed to grow at 300°C for 5 mins and the heating mantle was removed to stop the reaction. 5 ml of hexane was added to the solution once the temperature reached 70°C.

3.2.3 Synthesis of CdSe/ZnS core/shell QDs

The ZnS shell for the unstable CdSe/ZnS core/shell QDs was synthesized following a procedure reported in literature.[10,14] Initially, 2 g of TOPO and 1 g of hexadecylamine (HDA) were inserted into a three-neck flask and degassed at 120°C for 1 hour. Afterwards, 5 ml of CdSe core QDs were added and the temperature was increased to 220°C under Argon. Following this, precursor solution (0.15 ml of diethylzinc and 0.05 ml of bis(trimethylsilyl) sulfide in 1 ml of trioctylphosphine) was injected dropwise to the vigorously stirring reaction mixture. The reaction proceeded for 30 min to grow the ZnS shell. The heating mantel was then removed to stop reaction. 5 ml of hexane was added to the solution once the temperature reached 70°C.

3.2.4 Synthesis of CdSe/$Cd_{1-x}Zn_xSe_{1-y}S_y$ core/graded shell QDs

Green core/graded shell CdSe/$Cd_{1-x}Zn_xSe_{1-y}S_y$ QDs were synthesized by modifying a reported method.[15,16] Briefly, 0.2 mmol of CdO, 4 mmol of $Zn(acetate)_2$, 5 ml of oleic acid, and 15 ml of 1-octadecene were inserted into a three-neck flask and degassed at 150°C for 1 hour. The reaction was heated to 300°C under Argon. At the elevated temperature (300°C), 1 mmol of Se and 4 mmol of S in 2 ml of TOP were rapidly injected into the reaction vessel. The reaction was allowed to proceed at 300°C for 10 min and then the reaction was stopped by removing the heating mantle. 5 ml of hexane was added to the solution once the temperature reached 70°C.

Oleic acid-capped red emitting core/graded shell CdSe/$Cd_{1-x}Zn_xSe_{1-y}S_y$ QDs were prepared by slightly modifying the reported method.[15,16,17,18] 1 mmol of CdO, 2 mmol of zinc acetylacetonate, 5 ml of oleic, and 25 ml of ODE were placed in a 150 ml three neck flask. The mixture was degassed at 150 °C for 1 hr. The temperature was then increased to 300°C under Ar. Subsequently, 0.2 ml of 1 M Se/TOP solution was rapidly injected to initiate nucleation and growth. After 5 min elapsed, 0.3 ml of dodecanethiol was added drop-wise. The reaction was kept at 300 °C for 10 min (for green QDs) and 20 min (for red QDs). Then, 1 ml of 2 M S/TOP was injected. The heating mantle was removed to stop the reaction after 10 min. 10 ml of hexanes was added when the temperature becomes 70°C.

3.2.5 Ligand exchange: preparation & characterization

The ligand capping the QDs was exchanged from oleic acid (the original ligand used during QD synthesis) to one of the other ligands used in this study by a multistep ligand exchange. The prepared CdSe/$Cd_{1-x}Zn_xSe_{1-y}S_y$ QDs were purified with acetone three times to remove excess oleic acid and ODE. Subsequently, oleic acid-capped CdSe/$Cd_{1-x}Zn_xSe_{1-y}S_y$ QDs were re-dispersed in hexane, and then an excess amount of the new ligand (butylamine, octylamine, or hexadecylamine) was added. The ligand exchange reaction was allowed to proceed at 45℃ for 4 hours. The solution was then precipitated using methanol and re-dispersed in a mixture of hexane and the new ligand. This procedure was repeated three times. It is worth noting that a residual amount of the original ligand is typically present after a ligand exchange so a mixture of oleic acid and the new ligand (butylamine, octylamine, or hexadecylamine) likely exists.[19] However,

the three rounds of ligand exchange should minimize this possibility. The resulting product was finally precipitated using methanol and dispersed in the desired solvent.

3.3 Matrix materials (polymers)

Poly(methyl methacrylate) (PMMA), Poly(lauryl methacrylate) (PLMA), PMMA-copolymer, and polystyrene (PS) were used as matrix materials (purchased commercially and diluted to desired concentration). These polymers were selected due to their ease of use and availability, and their near-transparency over the optical region which minimizes attenuation of the excitation and emission light. A variety of polyelectrolytes will be used for spin-assisted layer-by-layer assembly (SA-LbL) depending on the strength of the electrostatic interaction that is required, the thickness that is required, and the polymer's influence on the FL intensity of the QD. The polyelectrolytes include poly(allylamine hydrochloride) (PAH, M_w = 58,000), branched polyethylenimine (PEI, M_w = 70,000), poly(diallyldimethylammonium chloride) (PDDA, M_w = 100,000-200,000), and poly(sodium 4-styrenesulfonate) (PSS).

3.4 Film deposition & patterning methods

Spin-assisted layer-by-layer assembly (SA-LbL), Langmuir-Blodgett (LB), and Langmuir-Schaefer (LS) deposition were used for film deposition. The choice of deposition technique will depend on the film thickness that is required, the number of layers, and the type of capping agent on the QD.

3.4.1 Preparation of pure QD-ligand films

QD films were fabricated via spin-casting (2000 rpm, 1.5 minutes) a QD solution (heptane or toluene). Film thickness ranged from 150-250 nm in order to support only the first waveguide mode. QD films were deposited on a CYTOP film (1400-1600 nm thick) which has a sufficiently low refractive index ($n_{650} = 1.34$) to cause light confinement and waveguiding within the QD film.[20] The CYTOP was exposed to air or Ar plasma for 5 seconds in order to improve wetting of the CYTOP by the QDs. Silicon with a 290-295 nm thick SiO_2 surface layer was used as a substrate to minimize leakage (and attenuation) of light from the QD film. However, the attenuation of light that does leak from the QD film into the Si substrate helps ensure that the light detected at the edge is the light that has propagated through the QD film (and not the substrate). The substrates were cleaved to obtain sharper, cleaner edges which improve the intensity of the output light and to help ensure that the area of the film exposed to the pump light was uniform over the length of the pump strip length.

3.4.2 Preparation of QD-polymer composite films

QD-polymer films of thickness 250-600 nm (as evaluated by ellipsometry) were prepared by spin-casting a QD-polymer mixture at 2000-3000 rpm for 1 min, as outlined previously.[10] Films had a QD-loading of approximately 1% (volume fraction) which was estimated via fitting of refractive indices derived from ellipsometry data with the Bruggeman model.[21] The QD-polymer mixture was made by mixing equal volumes of QD (toluene) solution with a 10-12% PMMA (toluene) solution, which was then vortexed. Films were typically deposited on silicon with either a ≈2 nm or ≈290 nm surface layer of SiO_2.

3.4.3 Near-field photopatterning using a PDMS stamp

The patterned PDMS photomask (used for near-field photopatterning) was fabricated using the typical procedure for a PDMS soft-lithography stamp.[22] Patterns of various size, shape, and spacing were dictated by a chrome master pattern on a quartz substrate. Photopatterning using the near-field patterned PDMS stamp used a 10x objective (NA: 0.30) with excitation light of either UV or 450-490 nm (over a range of powers), as outlined in previous work.[10,23] The light source was a 120 W Hg vapor short arc lamp (X-cite series, 120Q, Lumen Dynamics) with controllable power output.

3.4.4 Laser interference lithography (LIL)

Laser interference lithography patterning was performed by our collaborators (typically Dr. Thevamaran Ramathasan and Guanquan Liang from Dr. Prof. Ned Thomas' research group, Rice University). Far-field photopatterning via laser interference lithography was conducted by creating an interference pattern using two (interfering) laser beams.[24,25,26] Specifically, a 532 nm laser beam was output from a Coherent Verdi 5 system and then passed through a beam splitter cube to create two laser beams. The two beams traveled the same optical path length after the beam-splitting point. Each beam was expanded to have a diameter of approximately 18 mm. The power density of each beam was measured to be near 955 mW/cm^2. The two beams were symmetrically incident on the same side of the polymer film at an incident angle "θ" with respect to the normal of the film. An angle of 3.05° was used to obtain a sinusoidal periodicity "a" of approximately 5 μm (predicted via $a = \lambda/2\sin\theta$). A high interference contrast of the two beams was obtained by utilizing parallel linear polarization. The interference pattern manifested itself as a 1D grating on the polymer-quantum dot film. The cross-hatched array was fabricated by a two-step exposure of the

1D grating. More specifically, QD-polymer film was mounted on a rotational stage and rotated 90° after the first exposure for the consequent exposure. Short light exposure times during pattern development were used to minimize the effects of spatial drift on the photopattern contrast.

3.5 Thermal gravimetric analysis (TGA)

The mass fraction of the QDs in solution was determined by analyzing the amount of mass present versus temperature using a thermal gravimetric analysis (TGA) instrument (TA Instruments TGA Q50) with a 100 uL open platinum pan. Samples were analyzed by first equilibrating at 30°C followed by ramping of the temperature to 600°C using a 10°C/min temperature profile under a constant flow of nitrogen. Volume fractions of the organic and inorganic components were calculated using the bulk density of each component. TGA measurements were typically made by Marcus Smith (Prof. Vladimir V. Tsukruk's group, Georgia Institute of Technology).

3.6 Proton nuclear magnetic resonance (HNMR)

Proton nuclear magnetic resonance (HNMR) was used to examine how effectively the new QD ligand displaced the original QD ligand by examining changes in peak intensity, shifts in peak position, and the emergence of new peaks. Measurements were made using a Varian Mercury 400 NMR instrument with samples in deuterated chloroform. All HNMR measurements were performed by our collaborators (Dr. Jaehan Jung in Prof. Lin's research group, Georgia Institute of Technology).

3.7 Zeta-potential and dynamic light scattering

Zeta-potential and dynamic light scattering measurements were made at 25°C using a Malvern Nano S Zetasizer with a 633 nm laser which can probe a particle size range of 0.0003-10 μm and has a sensitivity of 0.1 mg/mL.

3.8 SEM / EDX / TEM

SEM micrographs of the Au nanorectangles fabricated via electron beam lithography were examined using a Zeiss Ultra60 scanning electron microscope (SEM) with an In-Lens secondary electron detector. An operating voltage of 5–10 kV under high vacuum was used to collect images down to 250,000x magnification with a working distance of 4-8 mm. Additional SEM micrographs were collected with a Hitachi SU8010 cold field emission SEM with an ultra-clean vacuum system with a turbo pump and an oil free dry-scroll pump. SEM images were collected using a secondary electron detector with 1.0 nm resolution at an operating voltage of 3 kV.

Energy dispersive X-ray spectroscopy (EDX) of the Au nanorectangles was also performed using the Hitachi SU8010 cold field emission SEM with an accelerating voltage of 5-10 kV and working distance of 8 mm.

Transmission electron microscope image of silver nanostructures were recorded by Dr. Z.A. Combs (Prof. Vladimir V. Tsukruk's group, Georgia Institute of Technology) using a FEI Tecnai F30 TEM with an operating voltage of 300 kV and a JEOL 100CX operated at 100 kV. The TEM samples for Ag nanospheres were prepared by dissolving the SERS substrate in 0.1 M NaOH solution and then subjected to dialysis. The resulting solution was drop cast onto a formvar carbon coated TEM grid.

The morphology of the core/graded shell CdSe/$Cd_{1-x}Zn_xSe_{1-y}S_y$ QDs was studied by transmission electron microscopes (JEOL 100cx (100 kV) and Tecnai F30 (300 kV)) by Dr. Jaehan Jung (Prof. Zhiqun Lin's group, Georgia Institute of Technology).

3.9 Atomic force microscopy (AFM)

Atomic force microscopy (AFM) images were collected using an Icon microscope (Bruker) in tapping mode according to usual procedure.[27] MikroMasch pyramidal silicon tips were used with a height of 15 µm and a cantilever length of 150 µm. Scan sizes ranged from 800 nm to 60 µm (on a side) with a scan rate in the range of 0.3-0.8 Hz.

3.10 Optical microscopies (bright field, dark field, photoluminescence)

Dark field, bright field, and photoluminescence images were collected using a Dagexcel-M Digital Firewire camera (cooled) and a 50x objective (NA: 0.80). Photoluminescence imaging was performed using excitation from a blue bandpass filter (450-490 nm) with a dichroic mirror that reflects optical wavelengths below 495 nm and with a longpass emission filter that passes optical wavelengths above 500 nm. All filters and dichroic mirror are from Chroma Technology Corp. The light source was a quartz halogen lamp with an aluminum reflector providing an emission range of 420-850 nm and a maximum power of 150 Watts.

3.11 Spectroscopic ellipsometry

The QD films were examined using a spectroscopic ellipsometer from Woollam (model M2000) with a wavelength range of 245-1000 nm and a rotating compensator

configuration. Film thickness was determined by applying a Cauchy model to the transparent region of the optical spectrum. The refractive index at 650 nm (also in the transparent region) was estimated with the Cauchy model. QD-loading (volume fraction) was calculated using the Bruggeman model, the effective refractive index of the film (at 650 nm), and the refractive index of the appropriate ligand. The refractive index of the CdSe/$Cd_{1-x}Zn_xSe_{1-y}S_y$ QD material was approximated using CdSe while the refractive index value of the ligands was determined from literature or supplier.

3.12 UV-vis spectroscopy

The UV-vis extinction spectra of nanostructures in solution (plasmonic and QD) were collected using a Shimadzu UV-vis-2450 spectrometer with D2 and tungsten lamps offering a wavelength range of 300-1100 nm. The UV-vis extinction spectra of the 3D PAM-AgNC substrates from 400-800 nm were collected using a Craic QDI 202 microspectrophotometer attached to a Leica DM 4000M microscope. The extinction spectra were corrected against the pure solvent background and the same (quartz or polymer) cuvette. QD molar concentration was approximated using the Beer-Lambert law and extinction cross-sections of core CdSe QDs.[28]

3.13 Photoluminescence spectroscopies

Photoluminescence of the quantum dots in solution and film were obtained using a Shimadzu RF-5301 spectrofluorometer with a 150 W xenon lamp light source and a R928 photomultiplier offering a wavelength range of 220-900 nm and an accuracy of 1.5 nm. Photoluminescence from QD-polymer films were also collected from a CytoViva hyperspectral imaging system utilizing a diffraction grating spectrophotometer with a spectral range of 400-1000 nm and a spectral resolution of 2.8 nm. Typically, a 10x

objective (NA: 0.30) was used to scan the surface with scans of 696 x 59 lines with an automated stage (10 nm step size scan resolution). An exposure time ranging from 0.1-5.0 second (per line) was often used. PL hyperspectral scans were performed using either the blue bandpass filter (450-490 nm) excitation setup or UV light (325-375 nm) excitation setup already mentioned. The light source was the 120 W Hg vapor short arc lamp, X-cite series, 120Q, Lumen Dynamics.

3.14 Hyperspectral scanning and imaging

Hyperspectral images were collected using a CytoViva Hyperspectral imaging system utilizing a diffraction grating spectrophotometer with a spectral range of 420-1000 nm and a spectral resolution of 2.8 nm.

For scanning the Au nanorectangle plasmonic arrays, a 100x dark field objective (NA: 0.90) in reflectance mode was used to scan the surface with scans of 1392 x 75-200 lines with an automated stage with a 10 nm step size scan resolution. A 15 second exposure time (per line) was used when using non-polarized light and 60 seconds when using polarized light for the 100x objective. The light source is a Quartz halogen lamp with an aluminum reflector providing a wavelength range of 420-850 nm and a power of 150 Watts. Non-polarized light was used to excite the nanostructures. Polarized measurements for the transverse and longitudinal directions were also performed; however, establishing clear trends was often difficult due to the complexity of the plasmonic response and the low signal-to-noise ratio. Hyperspectral maps of the EBL substrates were corrected by dark current intensity subtraction and a normalized average lamp spectrum (more than 700 spectra) to take into account the sensitivity of the lamp to different wavelengths. Color images are constructed from the scattering

curves using the intensity at three wavelengths (blue: 460.5 nm, green: 550.5 nm, and red: 640.5 nm). Average scattering spectra were obtained from hundreds of pixels over multiple nanostructures.

For scanning the quantum dot-polymer photopatterns, a 10x objective (NA: 0.30) was typically employed. Photoluminescence scanning was typically performed using either UV or blue excitation setups. The UV setup has a UV bandpass excitation filter (325-375 nm) with an emission filter that passes wavelengths above UV. The blue setup has a blue bandpass excitation filter (450-490 nm) with a dichroic mirror that reflects optical wavelengths below 495 nm and a longpass emission filter that passes optical wavelengths above 500 nm. The light source was a 120 W Hg vapor short arc lamp (X-cite series, 120Q, Lumen Dynamics). 120-250 spectra were collected and averaged from the exposed and protected regions of the photopatterns from the hyperspectral maps to provide data on the development of the photopattern under the various development conditions over the period of development. Hyperspectral images were constructed from the data cube by the tracking three wavelength bands (red, green, and blue). The red and green emission bands were centered at the position of the red and green emission peaks, while the blue emission was centered at a default position with 400-460 nm. Hyperspectral images were smoothed with a Savitzky-Golay filter to reduce noise. Noise from the blue region was also reduced during filtering.

3.15 Confocal Raman spectroscopy and mapping

All Raman spectroscopy and mapping measurements were made using a WiTec confocal Raman microscope (Alpha 300R) with an Ar+ ion laser of wavelength 514 nm.

Raman measurements for the AgNC-PAM studies were performed using a laser of wavelength 514 nm and power 50 µW according to usual procedure adapted in our laboratory.[29] At least 5 spectra, each with a 10 s exposure time, were collected and averaged to ensure accurate results. Mapping images were acquired with a lateral resolution of about 300 nm and a vertical resolution of about 1 µm with a 50x objective lens (spot size diameter ≈ 830 nm).

Au nanorectangles fabricated via EBL were examined with Raman using the following procedure. The substrate was exposed to 20 µL of 10^{-5} M R6G, a common Raman marker (Sigma-Aldrich) solution through a simple drop cast procedure. Raman mapping measurements were performed using a power of 1.3 mW. The area of the 520 cm^{-1} peak for Si and the area of the 1374 cm^{-1} and 1658 cm^{-1} peaks for R6G[30,31] were monitored and mapped after background subtraction. Maps were acquired with a 100x objective lens (NA: 0.90)(WD: 0.26) providing a theoretical diffraction limited spatial resolution of approximately 350 nm. The scan size (typically 10 x 10 μm^2) was adjusted in order to map multiple nanostructure pairs with 100 points per line and 100 lines per image with a pixel size of 100 nm. The integration time for each point of 1.0 sec provided adequate signal strength and minimized collection time, helping avoid spatial drift.

3.16 Quantum yield (QY) determination

The quantum yield of the QDs was approximated using the relative method according to outlined procedures.[32] Rhodamine 101 was typically used as the reference dye due to its appropriate absorption and emission overlap with the QDs used in this work.

3.17 Optical gain and loss measurements (and fitting)

Optical gain measurements (threshold and magnitude) were performed according to the standard variable stripe length (VSL) measurement procedure by our collaborators (typically Dr. Evan Lafalce, Prof. Vardeny's research group, University of Utah).[33] The third harmonic (355 nm) of a Spectra Physics Quanta-Ray INDI-series Pulsed Nd:YAG laser (pulse width of 5-8 ns, repetition rate of 10 Hz) was used as a seed for a GWU-Lasertechnik basiScan Beta-Barium Borate Optical Parametric Oscillator, producing a pulse of wavelength 440 nm. 440 nm was used for all ASE threshold, gain, and loss measurements.

Optical gain threshold values were obtained by determining the intersection of the linear fits to the low intensity (linear) region and the high intensity (superlinear) region of the pump fluence versus emission plot (on a log-log scale).

Optical gain magnitude was determined using the VSL measurement. The excitation beam was shaped into a stripe of 125 μm width using a cylindrical lens (15 cm focus length), and the stripe length was controlled by a pair of blades mounted on mechanically controlled stages that provided an adjustable slit. Only the central 10% of the beam was used to minimize pump inhomogeneity due the Gaussian intensity profile. The pump beam intensity, I_{pump}, was varied by means of a pair of polarizers or neutral density filters. One end of the stripe excitation was placed on the cleaved edge of the film while the length of the excitation stripe was progressively increased. The emission from the edge was collected with a 5 mm fiber and recorded using a commercial spectrometer (Ocean Optics USB4000; resolution 2 nm). Gain values were extracted according to the model proposed by Malko et al.,[34] that, in addition to the exponential

gain term, incorporates a linear exciton term to account for photoluminescence. This has been a common approach for fitting QD gain.[18,35,36,37]

Loss measurements were conducted in the same experimental geometry. However, in this case, the length of the excitation stripe was held constant, while the distance of the stripe from the edge of the film, d, was varied by simultaneously varying the position of both blades.[38] As the emission propagates towards the collecting fiber, it experiences attenuation by scattering and re-absorption in the unexcited region of the film. The decay of the collected emission signal with increasing distance, d, from the edge was fit to an exponential law: $I(d) = I(0) \exp(-\alpha d)$ to extract the loss coefficient α.

3.18 Finite-difference time-domain (FDTD) modeling

Simulations of scattering spectra and surface charge distributions were done using Lumerical Solutions software (FDTD Solutions, Version 8.0.2) by Dr. Tobias Konig (Prof. Vladimir V. Tsukruk's group, Georgia Institute of Technology). More details are provided in Chapter4 and 5 and the publications these chapters are based on.[9]

3.19 Density functional theory (DFT) simulation

Molecular simulations were done using the quantum chemistry package Gaussian 03 by Dr. Rajesh Kodiath (Prof. Vladimir V. Tsukruk's group, Georgia Institute of Technology). More details are provided in Chapter4 and the publication this chapter is based on.[39]

3.20 Collaborative efforts

Much of the work outlined in this thesis was done in collaboration with other research groups at the Georgia Institute of Technology and universities around the United States. Many plasmonic nanoparticles (colloidal and EBL patterned) were obtained from Professor El-Sayed's research group (Georgia Institute of Technology). All the quantum dots were obtained from Professor Z. Lin's research group (Georgia Institute of Technology). The pulsed laser optical gain measurements were typically done by Professor Vardeny's research group (University of Utah). The laser interference lithography photopatterning was conducted in Professor Thomas' group (Rice University).

3.21 References (Chapter 3)

1 Mahmoud, M.A.; Tabor, C.E.; El-Sayed, M.A., Surface-enhanced Raman scattering enhancement by aggregated silver nanocube monolayers assembled by the Langmuir-Blodgett technique at different surface pressures. *J. Phys. Chem. C* **2009,** *113,* 5493-5501.

2 Mahmoud, M.A.; El-Sayed, M.A., Comparative study of the assemblies and the resulting plasmon fields of Langmuir−Blodgett assembled monolayers of silver nanocubes and gold nanocages. *Phys. Chem. C* **2008,** *112,* 14618-14625.

3 Lahav, M.; Sehayek, T.; Vaskevich, A.; Rubinstein, I., Nanoparticle nanotubes. *Angew. Chem. Int. Ed.* **2003,** *42,* 5575-5579.

4 Bruening, M.L.; Dotzauer, D.M.; Jain, R.; Baker, G.L., Creation of functional membranes using polyelectrolyte multilayers and polymer brushes. *Langmuir* **2008,** *24,* 7663-7673.

5 Jiang, C.; Tsukruk, V.V., Freestanding nanostructures via layer-by-layer assembly. *Adv. Mater*. **2006,** *18,* 829-840.

6 Chang, S.; Combs, Z.A.; Gupta, M.K.; Davis, R.; Tsukruk, V.V., In situ growth of silver nanoparticles in porous membranes for surface-enhanced Raman scattering. *ACS Appl. Mater. & Interf.* **2010,** *2,* 3333-3339.

7 Kodiyath, R.; Wang, J.; Combs, Z.A.; Chang, S.; Gupta, M.K.; Anderson, K.D.; Brown, R.J.C.; Tsukruk, V.V., SERS effects in silver-decorated cylindrical nanopores. *Small* **2011,** *7*, 3452-3457.

8 Lee, W.; Scholz, R.; Nielsch, K.; Gosele, U., A template-based electrochemical method for the synthesis of multisegmented metallic nanotubes*. Angew. Chem. Int. Ed*., **2005,** *44,* 6050-6054.

9 Malak, S.T.; König, T.; Near, R.; Combs, Z.A.; El-Sayed, M.A.; Tsukruk, V.V., Stacked gold nanorectangles with higher order plasmonic modes and top-down plasmonic coupling. *J. Phys. Chem. C* **2014,** *118,* 5453-5462.

10 Malak, S.T.; Jung, J.; Yoon, Y.J.; Smith, M.J.; Lin, C.H.; Lin, Z.; Tsukruk, V.V., Large-area multicolor emissive patterns of quantum dot–polymer films via targeted recovery of emission signature. *Adv. Opt. Mater.* **2016,** *4,* 608-619.

11 Peng, Z.A.; Peng, X.G., Formation of high-quality CdTe, CdSe, and CdS nanocrystals using CdO as precursor. *J. Amer. Chem. Soc.* **2001,** *123,* 183-184.

12 Qu, L.H.; Peng, Z.A.; Peng, X.G., Alternative routes toward high quality CdSe nanocrystals. *Nano Let.* **2001,** *1*, 333-337.

13 Qu, L.H.; Peng, X.G., Control of photoluminescence properties of CdSe nanocrystals in growth. *J. Amer. Chem. Soc.* **2002,** *124*, 2049-2055.

14 Dabbousi, B.O.; RodriguezViejo, J.; Mikulec, F.V.; Heine, J.R.; Mattoussi, H.; Ober, R.; Jensen, K.F.; Bawendi, M.G., (CdSe)ZnS core-shell quantum dots: Synthesis and characterization of a size series of highly luminescent nanocrystallites. *J. Phys. Chem. B* **1997,** *101,* 9463-9475.

15 Bae, W.K.; Char, K.; Hur, H.; Lee, S., Single-step synthesis of quantum dots with chemical composition gradients. *Chem. Mater.* **2008,** *20*, 531-539.

16 Bae, W.K.; Nam, M.K.; Char, K.; Lee, S., Gram-scale one-pot synthesis of highly luminescent blue emitting Cd1−xZnxS/ZnS nanocrystals. *Chem. Mater.* **2008,** *20*, 5307-5313.

17 Jung, J.; Lin, C.H.; Yoon, Y.J.; Malak, S.T.; Zhai, Y.; Thomas, E.L.; Vardeny, V.; Tsukruk, V.V.; Lin, Z., Crafting core/graded shell–shell quantum dots with suppressed re-absorption and tunable Stokes shift as high optical gain materials. *Angewandte Chemie International Edition* **2016,** *55,* 5071-5075.

18 Lin, C.H.; Lafalce, E.; Jung, J.; Smith, M.J.; Malak, S.T.; Aryal, S.; Yoon, Y.J.; Zhai, Y.X.; Lin, Z.Q.; Vardeny, Z.V.; Tsukruk, V.V., Core/alloyed-shell quantum dot robust solid films with high optical gains. *Amer. Chem. Soc. Photonics* **2016,** *3*, 647-658.

19 Kuo, C.Y.; Su, M.S.; Ku, C.S.; Wang, S.M.; Lee, H.Y.; Wei, K.H., Ligands affect the crystal structure and photovoltaic performance of thin films of PbSe quantum dots. *J. Mater. Chem.* **2011,** *21*, 11605-11612.

20 Bellex International Coportation, Wilmington DE, USA. CYTOP chemical and physical properties. http://www.bellexinternational.com/products/cytop/

21 J.A. Woollam Co. Inc. “Guide to using WVase32.” Ch.2, A short course in ellipsometry. **2010.**

22 Qin, D.; Xia, Y.N.; Whitesides, G.M., Soft lithography for micro- and nanoscale patterning. *Nat. Protocols* **2010,** *5,* 491-502.

23 Malak, S.T.; Smith, M.J.; Yoon, Y.J.; Lin, C.H.; Jung, J.; Lin, Z.; Tsukruk, V.V., Programmed emission transformations: Negative-to-positive patterning using the decay-to-recovery behavior of quantum dots. *Adv. Opt. Mater.* **2016**.

24 Maldovan, M.; Thomas, E.L., Periodic materials and interference lithography: for photonics, phononics, and mechanics. *Wiley-VCH* **November 2008.**

25 Jia, L.; Bita, I.; Thomas, E.L., Level set photonic quasicrystals with phase parameters. *Adv. Func. Mater.* **2012,** *22,* 1150-1157.

26 Liang, G.Q.; Zhu, X.L.; Xu, Y. G.; Li, J.; Yang, S., Holographic design and fabrication of diamond symmetry photonic crystals via dual-beam quadruple exposure. *Adv. Mater.* **2010,** *22,* 4524-4529.

27 McConney, M.E.; Singamaneni, S.; Tsukruk, V.V., Probing soft matter with the atomic force microscopies: Imaging and force spectroscopy. *Polym. Rev.* **2010,** *50*, 235-286.

28 Jasieniak, J.; Smith, L.; van Embden, J.; Mulvaney, P.; Califano, M., Re-examination of the size-dependent absorption properties of CdSe quantum dots. *J. Phys. Chem. C* **2009,** *113*, 19468-19474.

29 Singamaneni, S.; Gupta, M.; Yang, R.S.; Tomczak, M.M.; Naik, R.R.; Wang, Z.L.; Tsukruk, V.V., Nondestructive in situ identification of crystal orientation of anisotropic ZnO nanostructures. *Amer. Chem. Soc. Nano* **2009,** *3*, 2593-2600.

30 Dieringer, J.A.; Wustholz, K.L.; Masiello, D.J.; Camden, J.P.; Kleinman, S L.; Schatz, G.C.; Van Duyne, R P., Surface-enhanced Raman excitation spectroscopy of a single rhodamine 6G molecule. *J. Amer. Chem. Soc.* **2009,** *131*, 849-854.

31 Michaels, A.M.; Jiang, J.; Brus, L., Ag nanocrystal junctions as the site for surface-enhanced Raman scattering of single rhodamine 6G molecules. *J. Phys. Chem. B* **2000,** *104*, 11965-11971.

32 Wurth, C.; Grabolle, M.; Pauli, J.; Spieles, M.; Resch-Genger, U., Comparison of methods and achievable uncertainties for the relative and absolute measurement of photoluminescence quantum yields. *Anal. Chem.* **2011,** *83*, 3431-3439.

33 Cragg, G.E.; Efros, A.L., Suppression of Auger processes in confined structures. *Nano Lett.* **2010,** *10*, 313-317.

34 Malko, A.V.; Mikhailovsky, A.A.; Petruska, M.A.; Hollingsworth, J.A.; Htoon, H.; Bawendi, M.G.; Klimov, V.I., From amplified spontaneous emission to microring lasing using nanocrystal quantum dot solids. *Appl. Phys. Lett.* **2002,** *81*, 1303-1305.

35 Dang, C.; Lee, J.; Breen, C.; Steckel, J.S.; Coe-Sullivan, S.; Nurmikko, A., Red, green and blue lasing enabled by single-exciton gain in colloidal quantum dot films. *Nat. Nanotechnology* **2012,** *7*, 335-339.

36 Roither, J.; Pichler, S.; Kovalenko, M.V.; Heiss, W.; Feychuk, P.; Panchuk, O.; Allam, J.; Murdin, B.N., Two- and one-dimensional light propagations and gain in layer-by-layer-deposited colloidal nanocrystal waveguides. *Appl. Phys. Lett.* **2006,** *89*.

37 Petruska, M.A.; Malko, A.V.; Voyles, P.M.; Klimov, V.I., High-performance, quantum dot nanocomposites for nonlinear optical and optical gain applications. *Adv. Mater.* **2003,** *15*, 610-613.

38 McGehee, M.D.; Gupta, R.; Veenstra, S.; Miller, E.K.; Diaz-Garcia, M.A.; Heeger, A.J., Amplified spontaneous emission from photopumped films of a conjugated polymer. *Phys. Rev. B* **1998,** *58*, 7035-7039.

39 Kodiyath, R.; Malak, S.T.; Combs, Z.A.; Koenig, T.; Mahmoud, M.A.; El-Sayed, M.A.; Tsukruk, V.V., Assemblies of silver nanocubes for highly sensitive SERS chemical vapor detection. *J. Mater. Chem. A* **2013,** *1,* 2777-2788.

CHAPTER 4

STACKED GOLD NANORECTANGLES WITH HIGHER ORDER PLASMONIC MODES AND TOP-DOWN PLASMONIC COUPLING

Chapter Based On:
Malak, S.T.; König, T.; Near, R.; Combs, Z.A.; El-Sayed, M.A.; Tsukruk, V.V., Stacked gold nanorectangles with higher order plasmonic modes and top-down plasmonic coupling. *J. Phys. Chem. C* **2014,** *118,* 5453-5462.

Chapter Overview

A large amount of research in the field of plasmonics has focused on the optical characteristics of individual particles and their coupling behavior. However, most studies develop structure-photonic relationships by averaging physical/optical data over hundreds of nanostructures, which makes it difficult to identify how specific physical variations/defects (and unique coupling schemes) specifically affect optical scattering (since this data tends to get washed out in the statistics). This chapter examines the optical scattering from single layer and stacked solid and hollow nanostructures created using electron beam lithography (EBL), with direct physical structure-optical property characterization and comparison (**Figure 4.1**). An understanding of the complex optical scattering is gained by examining the complex combination of local surface plasmon resonances and top-down electromagnetic hotspots that occur due to the incorporation of the third dimension into the structure design. These hollow rectangular gold nanostructures with gold caps show a significant red-shift in their main scattering peak as compared to the solid structures. Finite-difference time-domain modeling shows that the plasmonic response of these structures is dominated by higher order plasmonic modes, and that the strength of these modes is shown to vary according to whether a cap is present. The higher order dipolar mode caused by the capped nanostructure

results in manifold increase in the intensity of the electric field compared to the quadrupolar mode from a solid rectangle. This analysis provides important information on how complex plasmonic resonances respond to structural changes which will be useful in future studies that utilize these coupled resonances for detection or light manipulation. In addition, the stacking scheme presents a new route for modifying the optical response of plasmonic nanostructures through top-down plasmonic coupling which may yield plasmon resonance modes not observed in common 2D nanostructures along with significant increases in the local electric fields of these open “hot spots”.

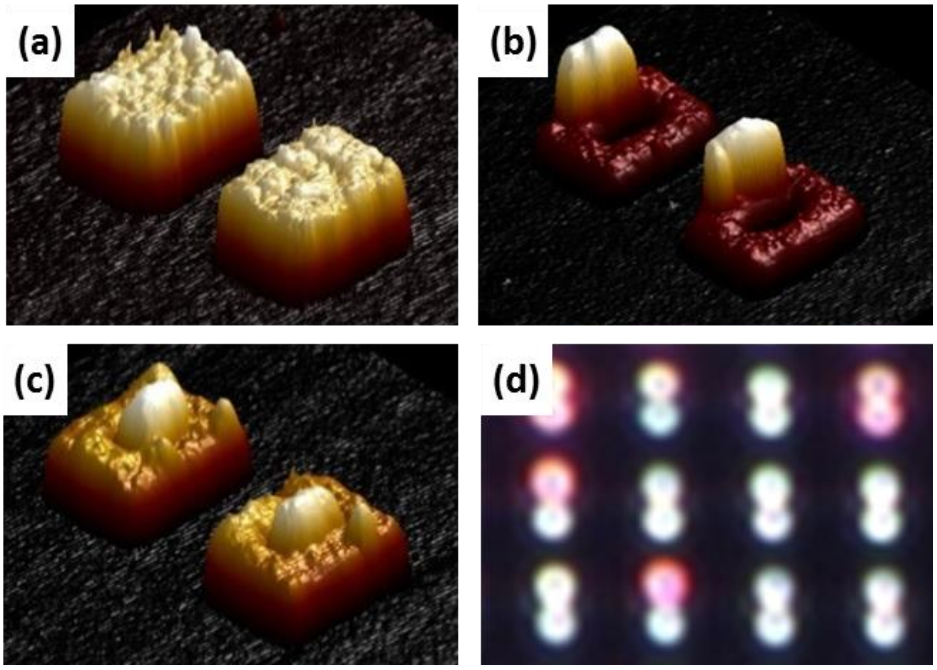

Figure 4.1: 3D atomic force microscopy height projections of (a) solid rectangles, (b) offset-capped hollow rectangles, and (c) central-capped hollow rectangles. (d) Hyperspectral optical scattering map of an Au nanorectangle array composed of offset-capped and central-capped Au nanorectangles.

4.1 Introduction

4.1.1 Controlling plasmonic resonances

The development of nano-systems utilizing plasmonics has led to the emergence of a variety of complex systems that can manipulate light in various ways for use in energy transport,[1,2] optical circuits,[3] light concentration and manipulation,[4,5] biodiagnostics,[6] and sensing.[7,8,9] Sensing platforms utilizing plasmonic nanostructures, in particular surface enhanced Raman scattering (SERS) and localized surface plasmon resonance (LSPR), have been the focus of many detection schemes because of their high sensitivity, non-destructive behavior, and response time.[7,8,10,11] Due to the ease of fabrication and diversity of colloidal particles a variety of detection platforms using these structures have been developed, including colloidal deposition,[7,8] assemblies and films,[12,13] decorated nanowires, [14,15,16] patterned two-dimensional surfaces, [17] and three-dimensional substrates.[18,19,20] However, the control of the plasmonic resonances through the manipulation of the shape and arrangement of these elements is still a critical obstacle facing the development of sophisticated plasmonic sensing systems. In addition, many plasmonic systems are limited to simple, planar side-adjacent coupling arrangements which could benefit from the introduction of a new means for manipulating resonances, for instance, through the use of a more complex, non-planar plasmonic coupling scheme.

4.1.2 Challenges of structure-optical tuning

It is well known that the plasmonic properties of noble metal nanostructures are sensitive to a combination of factors including shape, size, dielectric ambient, distance between and orientation with respect to other nanostructures, and interactions with the excitation light source.[21,22,23,24,25] These plasmonic aggregates are typically fabricated from

colloidal nanostructures that are synthesized in solution through seed-growth reduction methods[26,27,28] and which are assembled on substrates using patterning,[17,29] electrostatic binding,[14,19] and self-assembly approaches.[30,31,32] However, the large number of parameters that determine the plasmonic response of these nanostructures can make it difficult to design systems that provide a consistent response and to systematically determine fundamental structure-property relationships. For example, the surface roughness of colloidal particles with diameters on the order of 100-250 nm has been shown to shift the plasmon wavelength by 50-250 nm,[33,34] demonstrating the importance of having nanostructures with well-controlled shape, size, and roughness.

4.1.3 Plasmonic structures fabricated via EBL

Top-down nanofabrication techniques like electron beam lithography (EBL) address the issues associated with the formation and control of plasmonic properties (and their characterization using multiple techniques) through strict control (5-10 nm resolution) of the parameters that determine these properties[35,36] EBL can produce nanostructures that have almost any shape,[37,38] along with holes[39] and channels[40] on materials like silicon, silicon nitride,[37,38] and quartz.[41] The control offered by this technique has made it useful in a variety of studies, including single-electron transistors,[42] nanoelectromechanical systems,[43] photonic-bandgap materials,[44] and metamaterials.[45] This well-known technique provides a unique avenue for systematically varying specific geometric parameters like the size, shape, and spacing of the nanostructures to study how these factors independently affect the plasmonic response. More importantly, this technique can be used to fabricate grid-like arrays of nanostructures[40] making it possible to locate and characterize individual nanostructures with specific structural defects using a variety of techniques.

The plasmonic properties of EBL nanostructures arrays have been experimentally studied to determine how the size, shape, and spacing of the nanostructures affect their plasmon resonance and coupling.[40,46,47] However, most of these plasmonic systems are limited to simple, 2D side-adjacent plasmonic coupling arrangements which do not take advantage of the third dimension to manipulate resonances and electric field distributions (discs, rings, triangles).[46] Moreover, these studies rely on simultaneous measurements of hundreds or thousands of nanostructures in order to reach practical signal-to-noise ratio.[48] The fabrication and characterization of 3D EBL nanostructures are extremely rare due to the complexity of creating these structures with nanoscale features and the difficulty of investigating optical properties that are highly-dependent upon specific structural "defects". The investigation of individual nanostructures is particularly important when fine tuning can result in dramatic changes in the plasmon resonance signature.

In this study, we demonstrate that 3D EBL hollow rectangular nanostructures act as intriguing optical nanostructures with a complex combination of surface plasmon resonance modes and electromagnetic hotspots due to their stacked morphology. The peculiar light scattering properties are investigated using high-resolution hyperspectral imaging to probe the underlying plasmonic properties of the individual plasmonic features, an analysis that is not possible with typical bulk light scattering techniques. FDTD modeling is utilized to determine the reasons for the coupled out-of-plane plasmonic response, and in particular, the electromagnetic field enhancement for each complex nanostructure. We suggest that this 3D stacking scheme presents a new route for modifying the response of plasmonic nanostructures that yields coupled plasmonic resonances not observed in typical 2D nanostructures and increases manifold the local

enhancement of the electrical fields in these open “hotspots” as compared to planar nanostructures.

4.2 Experimental details

Substrate fabrication by electron-beam lithography. The gold nanorectangle arrays were fabricated using a JEOL JBX-9300FS 100 kV EBL system by our collaborators in Prof. El-Sayed’s research group (Georgia Institute of Technology). The nanorectangles were supported on a Si wafer and were distributed in arrays with array dimensions of 200 x 200 μm^2. An 80 nm thick layer of poly(methyl methacrylate) (PMMA), a positive electron resist, was spin coated onto the Si wafer. The pattern was written using a base dose of 1000 $\mu C/cm^2$ and a beam current of 1.98 nA. A solution of 1:3 methyl isobutyl ketone:isopropyl alcohol (MIBK:IPA) was used to develop the exposed sample for 10 s, after which it was rinsed in IPA and gently dried with N_2. A CVC electron beam evaporator was then used to deposit an adhesion layer of chrome (0.5 Å at 0.1 Å/s), followed by a layer of gold (270 Å at 0.5 Å/s). Finally, the sample was placed in 1165 remover (MicroChem) to achieve lift-off, wherein the remaining PMMA was removed, including the metal film deposited on top of the PMMA, leaving the metal nanostructures on the substrate. In order to minimize any far-field coupling, the hollow rectangle arrays were designed so that, within an array, the center-to-center distance between each neighboring pair in any direction was at least 2000 nm. Additionally, the interparticle spacing never exceeded five particle dimensions to ensure that any coupling was dominated by the near field.[49]

Stacked nanostructures with different orientation and separation distances were formed by incorporating a hollow core region in the EBL design pattern. The stacked structures

resulted from incomplete removal during the lift-off step of the EBL procedure of the hollow core region of the nanorectangles (**Figure 4.1**). This occurs when the height of the polymer resist (PMMA) in the core region is reduced due to proximity exposure during the e-beam writing step, allowing this material to become surrounded and protected from the solvent by the gold cap and surrounding nanostructure during the lift-off step. The offset caps result from central-caps being pulled from the center to the edge of the nanorectangle during lift-off. This technique can be used to fabricate consistently both individual and dimer nanostructures with central, offset, and mixed cores with relatively high yield (>85% of total nanostructures).

Additional substrate cleaning. Substrates were put through an additional cleaning procedure to help ensure any residual resist and other contaminates were removed. The sample was soaked in acetone for 2 minutes, sonicated in Nanopure water (18.2 MΩ cm) for 1 minute, and then rinsed with acetone and subsequently Nanopure water and blown dry with a dry air stream. Minor damage and removal of some nanostructures was observed with dark field optical imaging but not to areas relevant to this study. No change to or removal of the caps of the stacked structures was detected.

FDTD simulations. Simulations of scattering spectra and surface charge distributions were done using Lumerical Solutions software (FDTD Solutions, Version 8.0.2) by Dr. Tobias Konig (Prof. Vladimir V. Tsukruk's group, Georgia Institute of Technology). For all nanorectangle structures, the base has outside lateral dimensions of 265 x 198 nm with a height of 28 nm. The edges and corners of the rectangle are rounded using cylinders and spheres with a radius of 30 nm, respectively. The hollow rectangle had a core region with dimensions of 100 x 50 nm. In the case of the stacked rectangle setup the rectangular residual cap was placed on a 28 nm height pillow (n = 1.5). This pillow is

located inside the core region of the hollow rectangle as was observed in SEM and AFM. The simulation assumed that the polymer-resist filled the entire core region of the rectangular base of the stacked structure since this region was likely protected from washing and sonication. The residual cap stacked on top of the pillow has the same lateral dimensions as the core region of the hollow rectangle, a height of 28 nm, and an edge/corner rounding of 14 nm. All dimensions here are taken from high-resolution SEM and AFM measurements.

All structures were placed (except for the simulation of the solid nanorectangle in air) on a silicon substrate with a 2 nm silicon oxide layer (as derived from ellipsometry measurements). The gold refractive index data was from Johnson and Christy.[50] The simulation software fitted this material data with eight coefficients and a RMS error of 0.206 (400-1000 nm wavelength). The refractive index of silicon and silicon oxide were obtained from Palik,[51] which was fitted with ten and three coefficients and a RMS error of 0.055 and 0.005, respectively. The scattering response was calculated using plane wave excitation with an incident angle of 74 degrees with respect to the normal to represent the excitation light from the dark field objective. The surface charge distributions were obtained using plane wave excitation at normal incidence to represent illumination during Raman spectroscopy. A simulation mesh size of 2 nm was chosen to balance between accuracy and simulation time. For the best simulation stability, the mesh area was chosen to be 80 nm larger than the existing structure in all three principal directions. The integrated electric field enhancement was calculated using a volume integration over the hot spot region, where the hot spot region was equivalent to the simulation area. All simulations reached the auto shut off level of 10^{-4} a.u. before reaching 150 fs simulation time. The perfect match layer (PML) method was use for boundary conditions. The second conformal variant mesh refinement was used.

4.3 Results and discussion

4.3.1 Structural dimensions and characteristics of EBL nanorectangles

Stacked nanostructures with caps at different positions and orientations resulted from incomplete removal of the hollow core region of the hollow nanorectangles during the lift-off step of the EBL procedure (**Figure 4.2**).

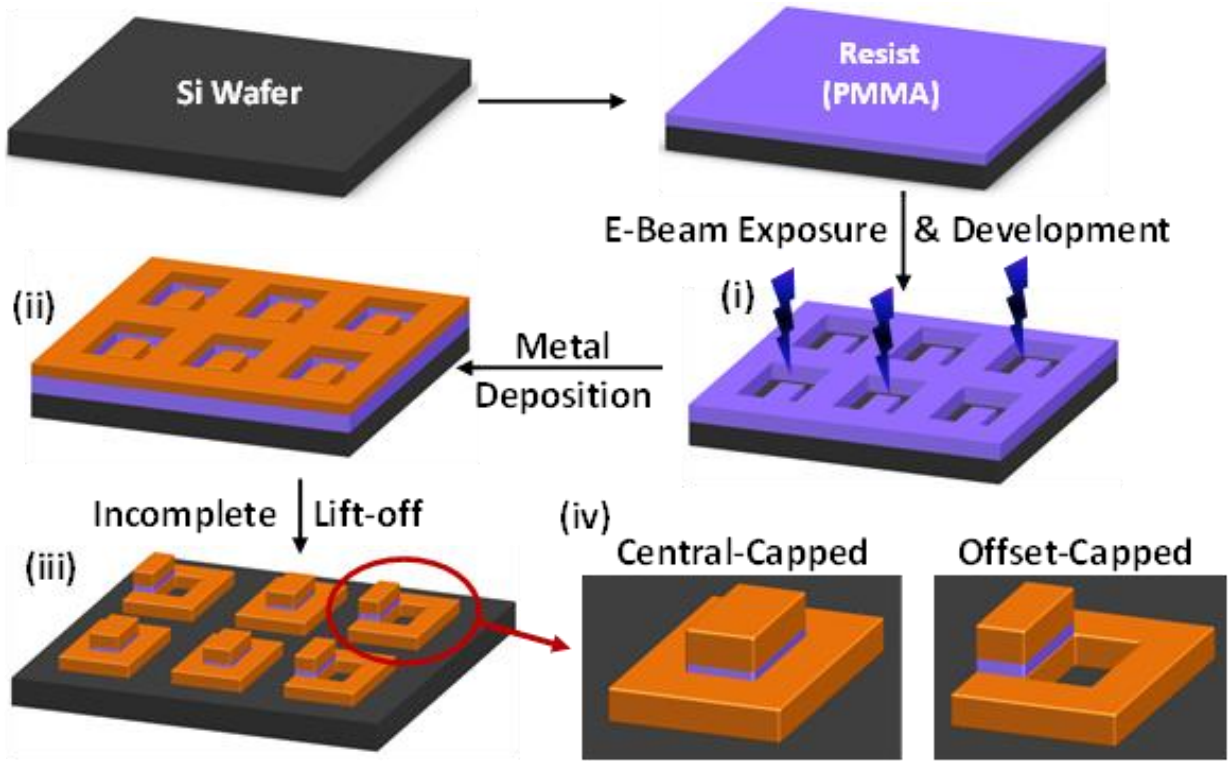

Figure 4.2: Schematic of the EBL fabrication of the stacked nanostructures. The critical step is the incorporation of a "hollow" core region in the pattern which is not removed during the final lift-off step. During e-beam exposure and development the height of the resist in the core region is reduced due to proximity exposure during rectangle patterning (i), allowing the core material to become surrounded by the gold cap and surrounding nanorectangle during metal deposition (ii). Since the surrounded core is protected from the remover solvent during the lift-off step, it is not removed (incomplete lift-off) (iii), leading to a cap (iv). The probability of incomplete lift-off increases when the nanostructure is less than a few hundred nanometers. The offset caps result from central-caps being pulled from the center of the nanorectangle during lift-off.

SEM and AFM images show that the caps are typically at a central or offset position and have lateral dimensions close to those of the hollow regions, which means the shape and size of the cap can be EBL-constructed by adjusting the “hollow” region (**Figure 4.3, Appendix A Figure A.1,A2**). Although the placement and lateral dimensions of the base structure can be tightly stipulated using EBL, controlling the placement of the cap on the nanostructure is difficult due to complex stresses on the cap during the lift-off step of the EBL procedure.

This led to a seemingly random distribution of central- and offset-capped structures throughout the arrays (**Figure 4.3, Appendix A Figure A.3b,c, A.4**). However, the occurrence of stacking increases (up to 85% yield observed) when the sizes of the nanostructure and core region are decreased (**Appendix A Figure A.4**). Increasing the size of the nanostructures decreased the chance of stacking (capping), and led to a variety of randomized structures being present in the same arrays (**Figure 4.3, Appendix A Figure A.3**).

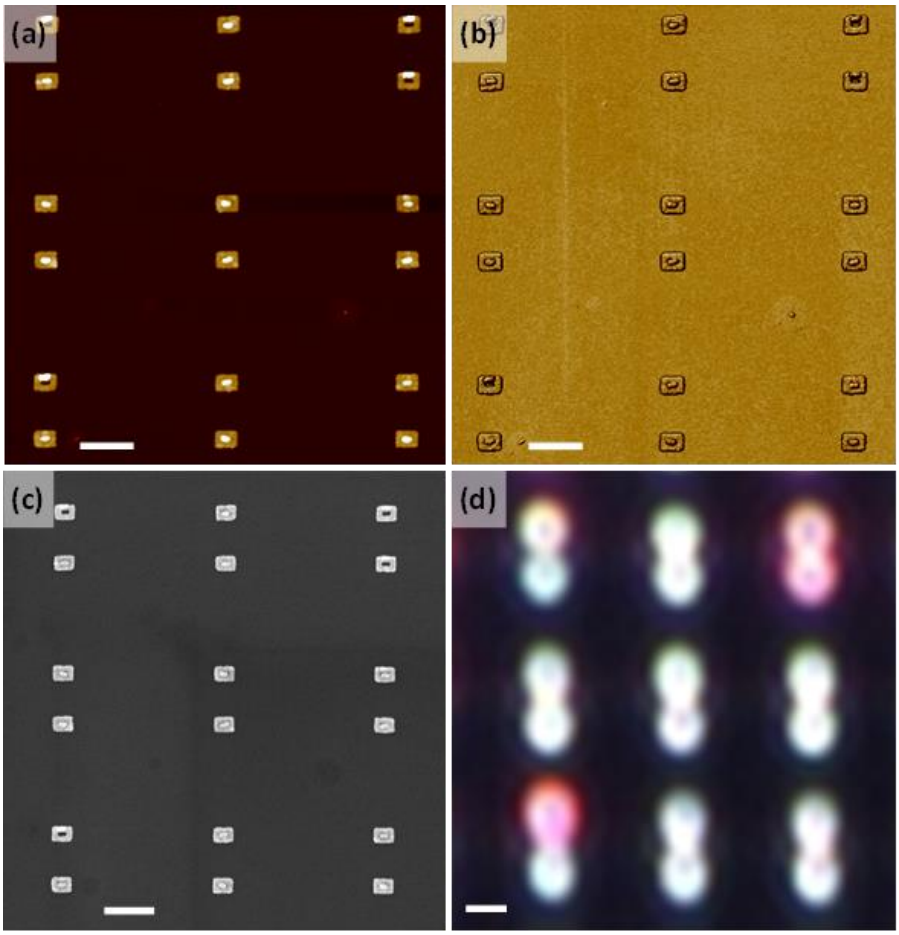

Figure 4.3: AFM topography (a) and phase (b) images; SEM (c), and hyperspectral imaging using unpolarized light (d) of an EBL array (all scale bars are 600 nm). Hyperspectral imaging shows that the presence of central cores and offset cores lead to different light scattering properties, with the offset-capped structures scattering red wavelengths more strongly (red color) than the central-capped structures (which appear white). The nanostructures have a separation of 433 ±7 nm. The AFM z-scale and phase is 65 nm and 30°, respectively.

AFM cross-sections show that the central cap has a thickness of 33 nm which is slightly larger than the nanorectangle base (**Figure 4.4**). This difference indicates that the Au layer of the cap is suspended on PMMA approximately 5-6 nm above the top of the Au nanorectangle base. The offset cap has a thickness closer to 50 nm which means there is residual PMMA layer of about 23 nm is attached to the Au layer since 27 nm of Au was deposited (**Figure 4.4**). This is additionally supported by EDX data of an isolated residual cap that shows the presence of both Au and carbon (**Appendix A Figure A.5**).

All gold nanorectangles fabricated and studied here have outside length 260±6 nm, width 198±5 nm, and height 27 nm with an edge rounding of 29±5 nm (Figure. 3). Edge rounding was determined by fitting a circle to the rounded edge and measuring its radius. The hollow nanorectangles have a rectangular core with a length of 102±9 nm and a width of 53±6 nm (**Appendix A Figure A.6,A.7**). In this study, the outer and inner dimensions of the nanorectangles were selected because they fell within a transition region where solid, hollow, and capped nanostructures (approximately 50%) could be fabricated (**Figure 4.4, Appendix A Figure A.1,A.2**), making it possible to determine how the various structural parameters affect their plasmonic properties.

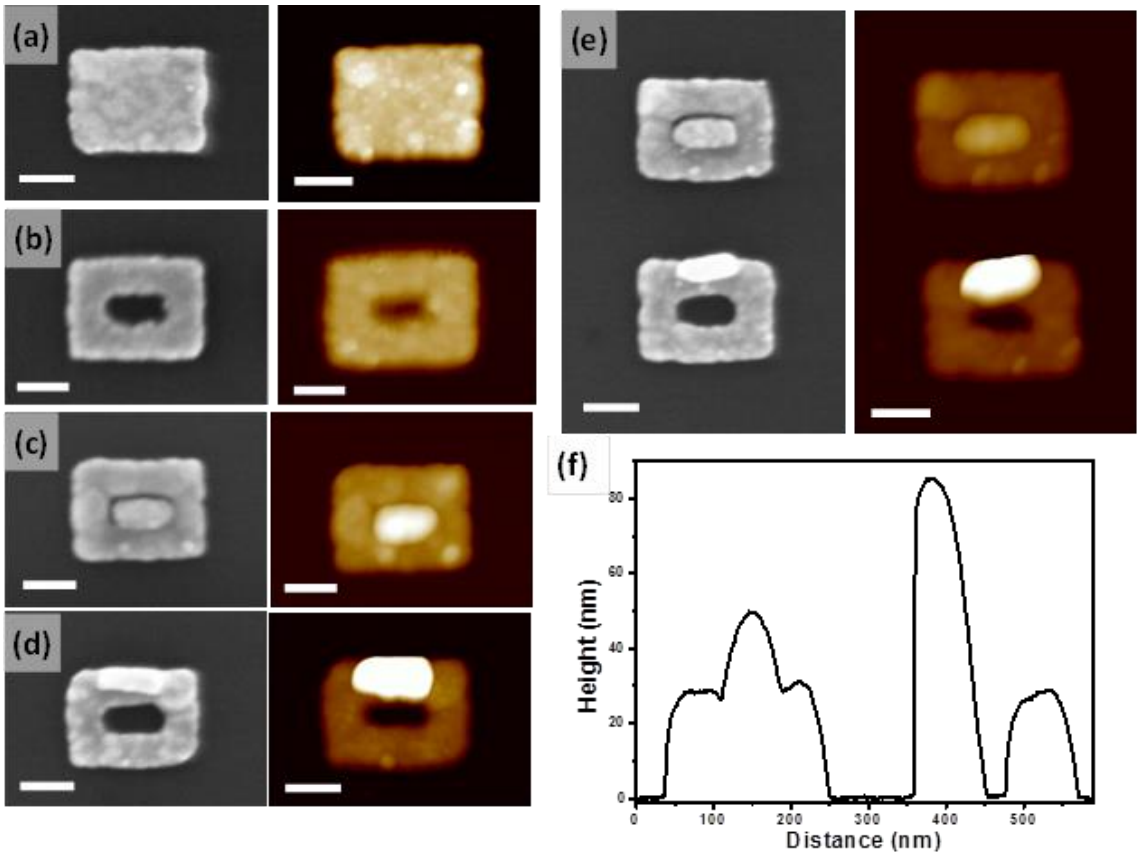

Figure 4.4: SEM and AFM images of the different EBL nanostructures: (a) solid (height scale, 40 nm), (b) hollow (height scale, 50 nm), (c) central-capped (height scale, 60 nm), and (d) offset-capped (height scale, 65 nm) nanorectangles. (e) A dimer (separation distance 141±4 nm) composed of a central and offset-capped nanorectangle and (f) its AFM cross section. The scale bar is 100 nm for all images.

The EBL nanostructures were arranged in arrays so that nanostructures with specific structural characteristics (hollow cores, central- or offset-caps) could be exactly located and examined with different characterization tools in order to determine how the structural characteristics of these individual nanostructures affect their spectral properties which can be dramatically different for different morphologies (**Figure 4.3**).

4.3.2 Light scattering of simple and complex nanostructures

In this study, we exploited the mapping capabilities of hyperspectral imaging to determine how specific structural characteristics of individual EBL nanostructures, like hollow regions, central caps, or offset caps, affect the light scattering compared to well-known solid nanorectangles/rods.[52,53,54,55] An example of the light scattering of the individual nanostructures with central and offset caps is shown in **Figure 4.3**. Each pair of nanostructures can be directly linked to their light scattering response in **Figure 4.3d**. Overall, such a comparison clearly demonstrates that the central and offset caps lead to dramatic differences in light scattering, with the offset caps scattering more red light and the central caps scattering red, green, and blue light more evenly.

Further analysis of spectral characteristics of specific selected nanostructures allows for unique quantitative comparison of different individual nanostructures (**Figure 4.5a**). The similar overall scattering shape for all the nanostructures suggests that the outer dimensions, thickness, and interaction of the structure with the substrate strongly influence the type of plasmonic modes.

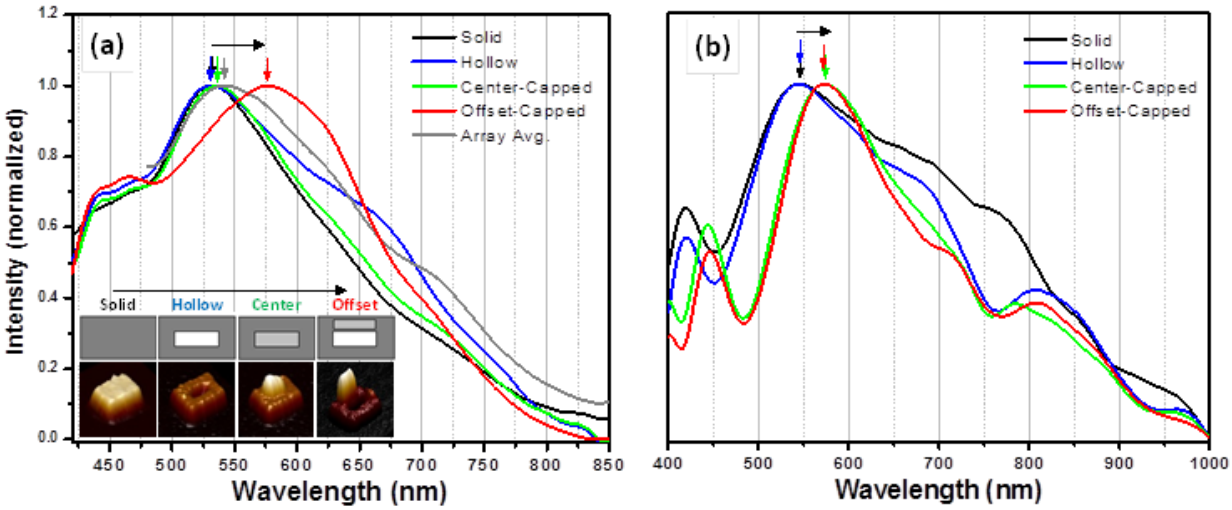

Figure 4.5: Light scattering of different nanostructures using unpolarized incident light from (a) hyperspectral measurements and (b) FDTD modeling. Inset in (a) shows different types of nanostructures. Both the data and modeling show that an offset cap causes a red-shift in the main scattering peak. The bulk response is included to demonstrate how the scattering response from different types of nanostructures can be difficult to interpret when many types of structures are included in the measurement.

The position of the main extinction peak does show a critical dependence on whether a cap is present, with the offset-capped structures displaying the most significant red-shift of approximately 45 nm (up to 80 nm in some cases) (**Figure 4.5a**). The red-shift is caused by an increase in the strength of the lower energy modes toward the red-end of the spectrum caused by interaction of the cap with the underlying structure, as suggested by FDTD calculations (see below). The central-capped nanostructures display a considerably less pronounced red-shift (around 5 nm). The hollow structure has a similar primary scattering peak compared to the solid rectangle but has a more pronounced shoulder near 650 nm due to the emergence of a new mode from the hollow core.

FDTD modeling of the scattering response shows the same general shape for the scattering response as the experimental data and corroborates the red-shift exhibited by

the capped structures (**Figure 4.5b**). However, the modeling predicts the same red-shift (approximately 30 nm) for both the central and offset-capped structures which was not observed in the hyperspectral measurements. The reason for this difference could be caused by surface roughness, the presence of residual polymer, and differences in the refractive index of the ideal (in modeling) and actual grainy (in experiment) materials.

Closer examination of nanostructures with offset-caps showed that the magnitude of the red-shift of their main resonance peak varied between 30 to 80 nm compared to the solid and hollow rectangles. This behavior likely occurs due to subtle variations in the orientation and spacing of the cap with respect to the underlying nanostructure, causing selective enhancements of different resonances. In order to investigate the red-shifts of the main scattering peak of these offset-capped nanostructures, the scattering from five regions along the axis of a pair composed of an offset-capped and central-capped nanostructure was collected (each curve is an average of 9 pixels from the dots shown in insets) (**Figure 4.6**).

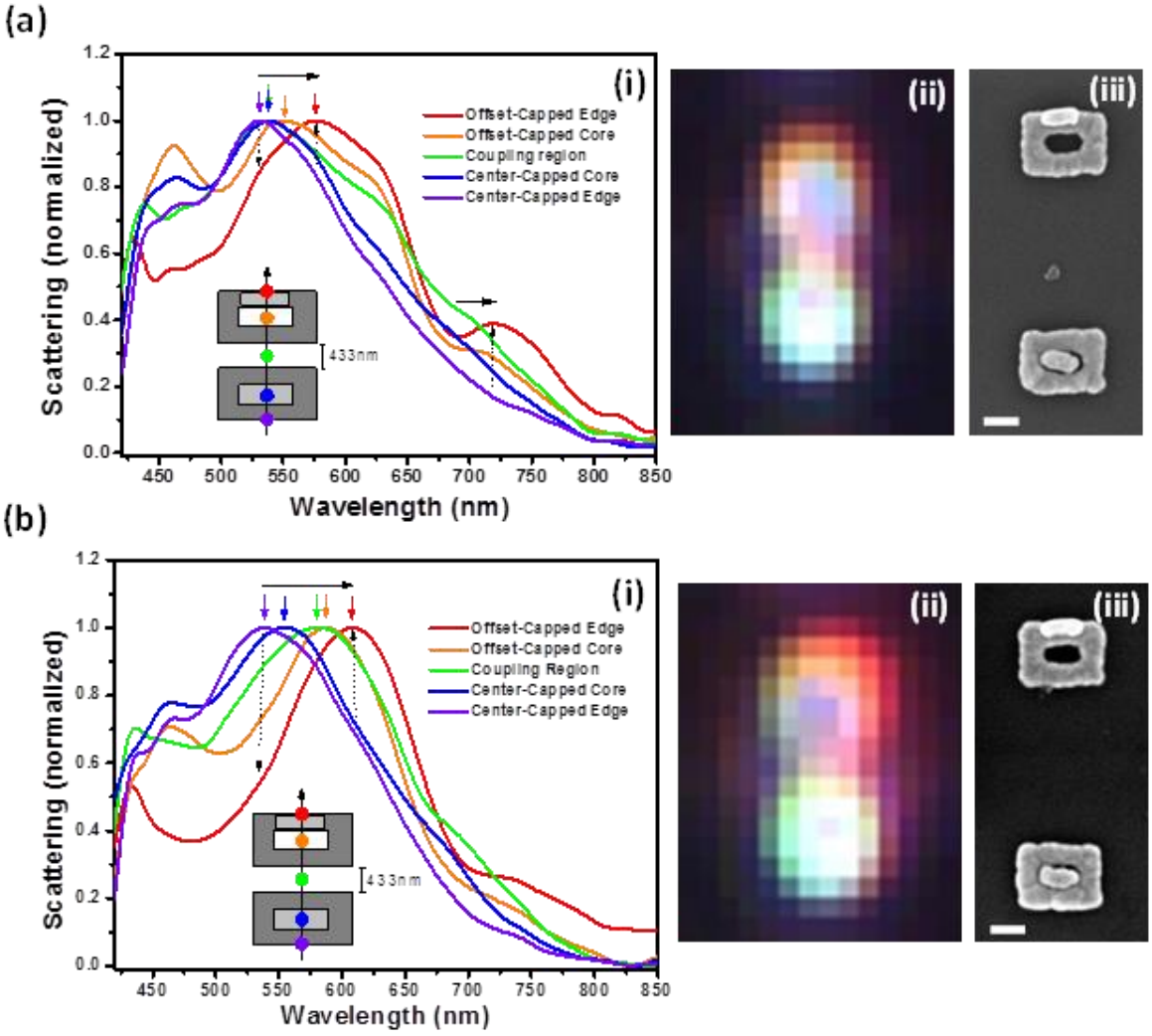

Figure 4.6: (i) Scattering (along the dimer axis) obtained from (ii) hyperspectral mapping of an offset-closed dimer (separation of 433 ±7nm), and (iii) its SEM image for (a) offset-type-1 and (b) offset-type-2 nanostructures. Type-1 and type-2 nanostructures appear similar in SEM but subtle differences in the orientation of the cap with respect to the underlying structure cause different scattering to occur. The dashed arrows show the vertical changes in the resonances while the solid arrow shows how the main resonance evolves at different positions along the dimer axis. There is a red-shift in the main resonance peak due to the interaction of the cap with the underlying structure. Scale bars are 100 nm and 500 nm for the SEM and hyperspectral images, respectively.

In all cases, the light scattering from the central-capped nanorectangle has its primary peak centered near 530 nm (**Figure 4.6**, purple curves). In addition, pixels which are located further from the central-capped structure and closer to the nanostructure with the offset cap demonstrates a clear red-shift in the main scattering peak, with the maximum red-shift observed at the outer edge of the offset cap (**Figure 4.6**, red curves). The dashed arrows show the vertical changes in the resonances while the solid arrow shows how the main resonance evolves at different positions along the pair axis. The green curve shows a convolution of the scattering from the offset and central-capped nanorectangles, again confirming that plasmonic coupling does not occur in this wavelength range.

However, two general scattering profiles for the offset-capped nanostructures were observed, termed type-1 and type-2 nanostructures, which show clear differences in the magnitude of the red-shift of the main peak and in the strength of a secondary peak (**Figure 4.6**). These two types look very similar under SEM (**Figure 4.6iii**) so they are identified by their scattering properties. A comparison between the two cases shows that offset-type-2 nanostructures display a red-shift of the main peak that is nearly 30 nm larger than offset-type-1 nanostructures which display a stronger resonance near 730 nm. These differences typically cause type-1 nanostructures to appear less red in the hyperspectral images. As mentioned previously, distinct scattering for the offset-capped nanorectangles is caused by changes in the interaction of the offset-cap with the underlying rectangle due to variations in the position and orientation of the offset-cap.

4.3.3 Plasmonic modes of solid, hollow, and capped gold nanorectangles

The differences in the overall plasmonic response of the various nanostructures are attributed to changes in the relative strength of the plasmonic modes, which are caused by the interaction of the cap with different parts of the underlying nanorectangular structures. Surface charge distributions of the nanostructures used in this study were calculated to gain an understanding of the underlying plasmonic responses (**Figure 4.7**).

The modeling shows that these nanostructures exhibit complex higher order plasmonic modes and that the silicon substrate has a significant effect on the plasmonic modes that are excited, likely because of their large size and low height/weight aspect ratio. When a solid rectangle is placed in air (no contact with a substrate) it shows two simple dipole distributions, dubbed primitive dipolar plasmonic modes. The two primitive dipolar modes are termed the longitudinal and transverse modes and are caused by the geometric difference between the length and width, respectively. The longitudinal mode (D_L^0) has a lower energy associated with it than the transverse mode (D_T^0).

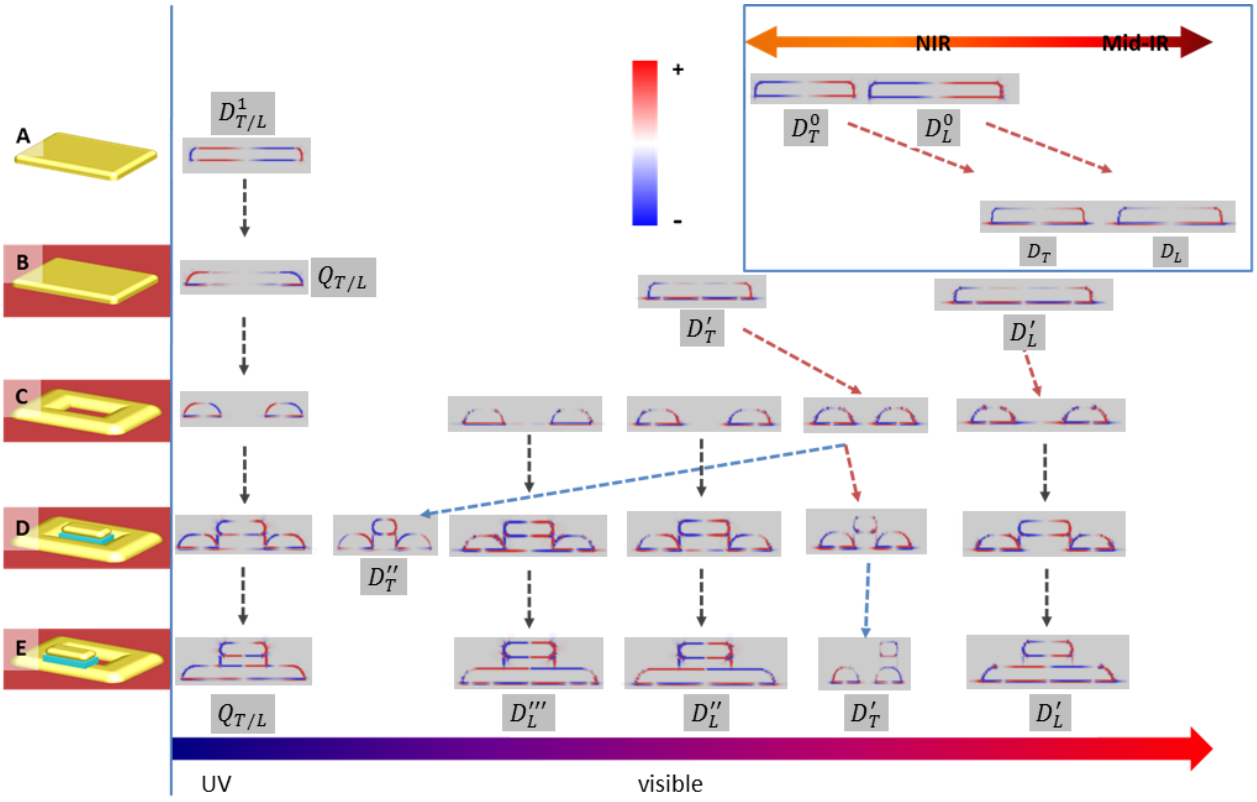

Figure 4.7: Surface charge distributions for the EBL nanostructures from FDTD modeling. Row A: The gold rectangle in air shows primitive dipolar modes $\boldsymbol{D^0}$ and higher primitive dipolar mode $\boldsymbol{D^1}$ for longitudinal (index L) and transversal (index T) axes. Row B: When the gold rectangle is placed in contact with a silicon substrate the plasmonic modes hybridize into a dipolar mode (bonding) $\boldsymbol{D}$, a higher energy dipolar mode (bonding) $\boldsymbol{D'}$, and a quadrupolar modes (anti-bonding) $\boldsymbol{Q}$. Further modification to the rectangle (hollow (row C), central-capped (row D), and offset-capped (row E)) causes additional higher dipolar modes (**D**'' and **D**''')) to emerge.

When the solid gold nanorectangle is brought into contact with the silicon substrate the primitive modes hybridize into dipolar modes D and quadrupolar modes Q. These hybridized modes are a result of the primitive dipolar mode and primitive quadrupolar mode coupling and interfering.[56] Furthermore, we observe that the ultrathin sandwich layer (silicon oxide) acts as a dielectric waveguide.[57] At 265 x 200 nm^2 dimensions we observe this dipolar mode in the mid-infrared, as shown in **Figure 4.7**. The number of plasmonic modes typically increases as the symmetry of structure decreases.[58] Higher order dipolar modes are clearly identified in the ultraviolet and visible range by their dipole-like symmetry and additional charge separations (compared to the primitive modes). These modes are labeled D, D', D'', and D''' in order of increasing complexity where more energy is required to excite the higher order modes than the lower order modes.

An increase in the energy required to excite a mode (the order of the mode) is often accompanied by a decrease in its scattering cross-section.[54] For instance, the scattering cross-section of the zero dipolar mode of the solid gold nanorectangle is about 3.5 times higher compared to the first order mode. It is also important to mention that the hybridized dipolar mode has a concentrated electric field at the interface between the nanostructure and substrate called the plasmonic bonding mode.[56] The counterpart to the bonding mode is the anti-bonding mode, which was present for all our nanorectangles as a quadrupolar mode in the UV. This quadrupolar mode ($Q_{T/L}$) appears independent from the axial excitation of the nanostructure.

The incorporation of a hollow region into the solid rectangle causes a spectral red shift of the first order dipolar modes (red arrow in **Figure 4.7**). This is attributed to an easier separation of surface charges that occurs with hollow nanostructures.[59] As we

systematically modify the structure with caps, we observe that both the number of higher order dipolar modes and their resonance positions does not change significantly (the centrally-capped structure exhibits an additional resonance that is associated with the symmetry of the cap). Although the positions of the resonances do not change appreciably with different capping schemes, there can still be differences in the overall scattering profiles due to changes in the relative strengths (peak heights) between modes.

The consequences of structural changes, like central and offset capping, on the electric field intensity is presented in **Figure 4.8a**. These simulations show that the solid and hollow nanorectangles exhibit their largest electric field enhancement at the interface with the Si substrate. In contrast, the capped nanostructures, with their elevated element, both exhibit a strong field between the cap and the hollow rectangular base whose intensity distribution depends upon the position of the cap with respect to the underlying nanostructure. The fundamental result from lifting a single element in z-direction is that the hotspot (the region of strongest electrical field enhancement) can be moved further from the solid substrate (**Figure 4.8a**). Moreover, such a modification of the nanostructure composition results in significant enhancement of the local electrical field compared to planar gold nanostructures with identical dimensions.

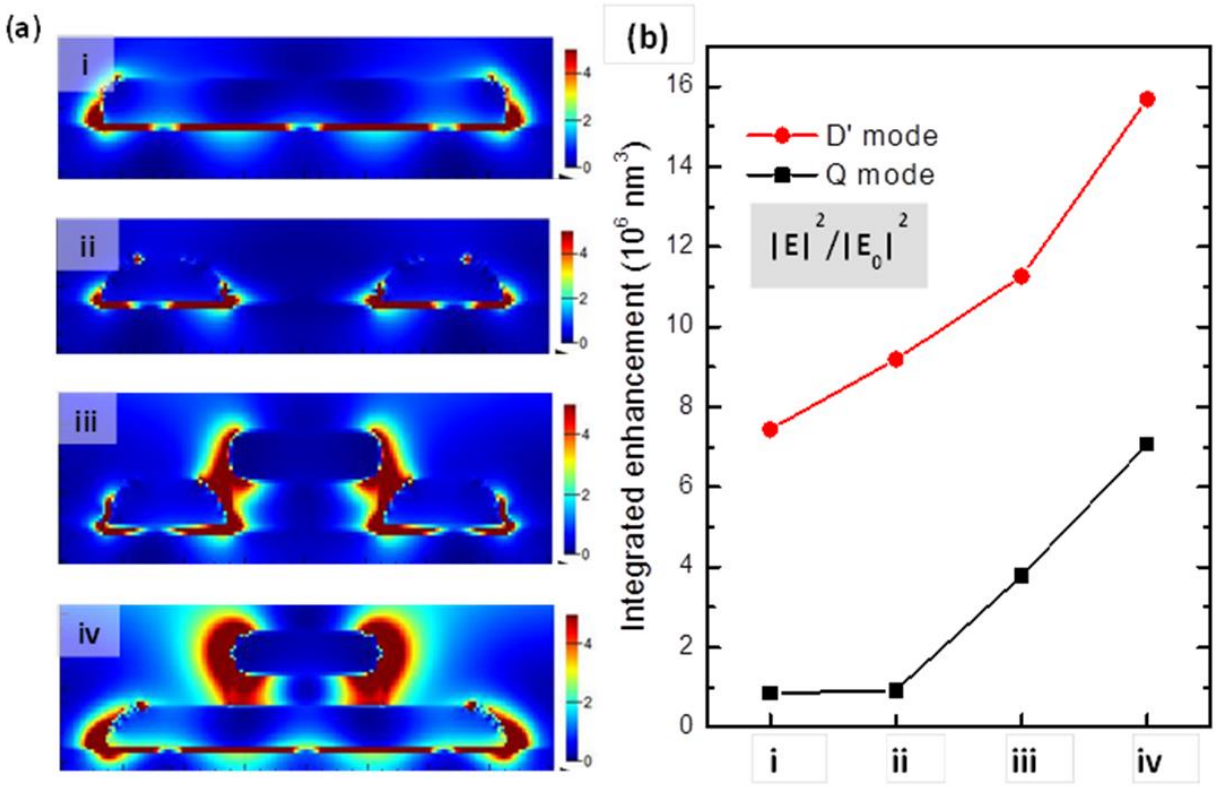

Figure 4.8: FDTD modeling of the (a) intensity of the electric field for the (i) solid, (ii) hollow, (iii) central-capped, and (iv) offset-capped nanorectangles. The presence of a cap shifts the hot spot from the base of the nanorectangle to an upper region due to coupling between the cap and base. (b) The integrated enhancement over a simulation volume for the quadrupolar mode Q and the first higher energy dipolar mode D' for each nanostructure. The integrated enhancement for both the D' and Q mode for the capped structures is manifold larger than for the solid or hollow structures (b).

The relative strengths of these electric field hotspots was evaluated using a volume integration of the electric field in the hotspot regions and is presented in **Figure 4.8b**. This comparison shows that the offset-capped rectangular nanostructures possess electrical field enhancement that are much higher than those for solid nanostructures with the same volume and lateral footprint. The enhancement for two different nanostructures with a lifted element is manifold (three to seven times for different cases and modes) higher those for the solid rectangle. The D' plasmonic mode provides a larger contribution to the electromagnetic enhancement than does the Q mode, with the

D' mode of the capped nanostructure exhibiting an electric field intensity that is 18 times higher than that of the quadrupolar mode from a solid rectangular nanostructure.

Such a dramatic increase of the local electrical field is a basis for potential significant increase in local Raman enhancement (SERS), the basis for surface enhanced Raman scattering sensing.[10] Therefore, in initial testing, the Raman response of the central-capped nanorectangles was investigated using surface mapping to determine prospective SERS properties (**Appendix A Figure A.8,A9**). These preliminary results demonstrate that these structures do exhibit a promising SERS response that with additional modifications to boost their enhancement could be practical for applications in trace detection.

4.4 Conclusions

In conclusion, this study revealed that the introduction of lifted caps in hollow EBL gold nanostructures can dramatically change their plasmonic properties with significantly shifted primary plasmon resonances and manifold increased local electrical field within open "hotspots". The intensity of the electric field from the higher energy dipole and quadrupolar modes is increased manifold compared to the conventional solid nanorectangles through the interaction of the cap with the underlying hollow nanostructure. These initial results open up an avenue for investigating the interplay between resonances from stacked structures and traditional 2D coupled adjacent structures that will be interesting from a fundamental, as well as, a practical point of view, particularly for LSPR systems that utilize higher order modes. Future studies should concentrate on improving the reliability of whether stacking occurs and on controlling the placement of the cap on the nanostructure.

4.5 Chapter acknowledgements

Dr. Rachel Near (Prof. Mostafa El-Sayed's research group, Georgia Institute of Technology): the Au nanorectangle arrays fabricated using electron beam lithography. Dr. Tobias König (Prof. Vladimir V. Tsukruk's research group, Georgia Institute of Technology): the FDTD simulations.

4.6 References (Chapter 4)

1 Solis, D.; Willingham, B.; Nauert, S.L.; Slaughter, L.S.; Olson, J.; Swanglap, P.; Paul, A.; Chang, W.S.; Link, S., Electromagnetic energy transport in nanoparticle chains via dark plasmon modes. *Nano Lett.* **2012,** *12,* 1349-1353.

2 Willingham, B.; Link, S., Energy transport in metal nanoparticle chains via sub-radiant plasmon modes. *Opt. Exp.* **2011,** *19,* 6450-6461.

3 Bozhevolnyi, S.I.; Volkov, V.S.; Devaux, E.; Laluet, J.Y.; Ebbesen, T.W., Channel plasmon subwavelength waveguide components including interferometers and ring resonators. *Nature* **2006,** *440,* 508-511.

4 Schuller, J.A.; Barnard, E.S.; Cai, W.S.; Jun, Y.C.; White, J.S.; Brongersma, M.L., Plasmonics for extreme light concentration and manipulation. *Nat. Mater.* **2010,** *9,* 193-204.

5 Alu, A.; Engheta, N., Achieving transparency with plasmonic and metamaterial coatings. *Phys. Rev. E* **2005,** *72,* 016623.

6 Jain, P.K.; Huang, X.H.; El-Sayed, I.H.; El-Sayed, M.A., Noble metals on the nanoscale: Optical and photothermal properties and some applications in imaging, sensing, biology, and medicine. *Acc. Chem. Res.* **2008,** *41,* 1578-1586.

7 Anker, J.N.; Hall, W.P.; Lyandres, O.; Shah, N.C.; Zhao, J.; Van Duyne, R.P., Biosensing with plasmonic nanosensors. *Nat. Mater.* **2008,** *7,* 442-453.

8 Sonnichsen, C.; Reinhard, B.M.; Liphardt, J.; Alivisatos, A.P., A molecular ruler based on plasmon coupling of single gold and silver nanoparticles. *Nat. Biotechnol.* **2005,** *23,* 741-745.

9 Xie, W.; Qiu, P.H.; Mao, C.B., Bio-imaging, detection and analysis by using nanostructures as SERS substrates. *J. Mater. Chem.* **2011,** *21,* 5190-5202.

10 Ko, H.; Singamaneni, S.; Tsukruk, V.V., Nanostructured surfaces and assemblies as SERS media. *Small* **2008,** *4,* 1576-1599.

11 Kim, N.H.; Lee, S.J.; Moskovits, M., Reversible tuning of SERS hot spots with aptamers. *Adv. Mater.* **2011,** *23,* 4152-4156.

12 Yu, Q.; Huang, H.W.; Peng, X.S.; Ye, Z.Z., Ultrathin free-standing close-packed gold nanoparticle films: Conductivity and Raman scattering enhancement. *Nanoscale* **2011,** *3*, 3868-3875.

13 Gandra, N.; Abbas, A.; Tian, L.M.; Singamaneni, S., Plasmonic planet-satellite analogues: Hierarchical self-assembly of gold nanostructures. *Nano Lett*. **2012**, *12*, 2645-2651.

14 Chen, L.M.; Liu, Y.N., Ag-nanoparticle-modified single Ag nanowire for detection of melamine by surface-enhanced Raman spectroscopy. *J. Raman Spec.* **2012,** *43*, 986-991.

15 Gunawidjaja, R.; Peleshanko, S.; Ko, H.; Tsukruk, V.V., Bimetallic nanocobs: Decorating silver nanowires with gold nanoparticles. *Adv. Mater.* **2008,** *20,* 1544-1549.

16 Gupta, M.K.; Chang, S.; Singamaneni, S.; Drummy, L.F.; Gunawidjaja, R.; Naik, R.R.; Tsukruk, V.V., pH triggered SERS via modulated plasmonic coupling in individual bimetallic nanocobs. *Small* **2011,** *7,* 1192-1198.

17 Combs, Z.A.; Chang, S.H.; Clark, T.; Singamaneni, S.; Anderson, K.D.; Tsukruk, V.V., Label-free Raman mapping of surface distribution of protein A and IgG biomolecules. *Langmuir* **2011,** *27*, 3198-3205.

18 Chang, S.; Combs, Z.A.; Gupta, M.K.; Davis, R.; Tsukruk, V.V., In situ growth of silver nanoparticles in porous membranes for surface-enhanced Raman scattering. *ACS Appl. Mater. & Interfaces* **2010,** *2*, 3333-3339.

19 Ko, H.; Tsukruk, V.V., Nanoparticle-decorated nanocanals with enhanced Raman scattering. *Small* **2008**, *4,* 1980-1984.

20 Kodiyath, R.; Malak, S.T.; Combs, Z.A.; Koenig, T.; Mahmoud, M.A.; El-Sayed, M.A.; Tsukruk, V.V., Assemblies of silver nanocubes for highly sensitive SERS chemical vapor detection. *J. Mater. Chem. A* **2013,** *1*, 2777-2788.

21 Stewart, M.E.; Anderton, C.R.; Thompson, L.B.; Maria, J.; Gray, S.K.; Rogers, J.A.; Nuzzo, R.G., Nanostructured plasmonic sensors. *Chem. Rev.* **2008**, *108*, 494-521.

22 Xu, H.; Aizpurua, J.; Kall, M.; Apell, P., Electromagnetic contributions to single-molecule sensitivity in surface-enhanced Raman scattering. *Phys. Rev. E.* **2000**, *62*, 4318-4324.

23 Xu, H.; Kall, M., Polarization-dependent surface-enhanced Raman spectroscopy of isolated silver nanoaggregates. *ChemPhysChem.* **2003**, *4*, 1001-1005.

24 Sundaramurthy, A.; Crozier, K.B.; Kino, G.S.; Fromm, D.P.; Schuck, P.J.; Moerner, W.E., Field enhancement and gap-dependent resonance in a system of two opposing tip-to-tip Au nanotriangles. *Phys. Rev. B* **2005**, *72*, 165409.

25 Sweatlock, L.A.; Maier, S.A.; Atwater, H.A.; Penninkhof, J.J.; Polman, A., Highly confined electromagnetic fields in arrays of strongly coupled Ag nanoparticles. *Phys. Rev. B* **2005**, *71*, 235408.

26 Jana, N.R.; Gearheart, L.; Murphy, C.J., Seeding growth for size control of 5-40 nm diameter gold nanoparticles. *Langmuir* **2001**, *17*, 6782-6786.

27 Mahmoud, M.A.; El-Sayed, M.A., Comparative study of the assemblies and the resulting plasmon fields of Langmuir−Blodgett assembled monolayers of silver nanocubes and gold nanocages. *J. Phys. Chem. C* **2008**, *112*, 14618-14625.

28 Wu, H.-L.; Kuo, C.-H.; Huang, M.H., Seed-mediated synthesis of gold nanocrystals with systematic shape evolution from cubic to trisoctahedral and rhombic dodecahedral structures. *Langmuir* **2010**, *26*, 12307-12313.

29 Alvarez-Puebla, R.; Cui, B.; Bravo-Vasquez, J.P.; Veres, T.; Fenniri, H., Nanoimprinted SERS-active substrates with tunable surface plasmon resonances. *J. Phys. Chem. C* **2007,** *111*, 6720-6723.

30 Braun, G.; Lee, S.J.; Dante, M.; Nguyen, T.Q.; Moskovits, M.; Reich, N., Surface-enhanced Raman spectroscopy for DNA detection by nanoparticle assembly onto smooth metal films. *J. Amer. Chem. Soc.* **2007,** *129*, 6378-6379.

31 Freeman, R.G.; Grabar, K.C.; Allison, K.J.; Bright, R.M.; Davis, J.A.; Guthrie, A.P.; Hommer, M.B.; Jackson, M.A.; Smith, P.C.; Walter, D.G.; Natan, M.J., Self-assembled metal colloid monolayers - An approach to SERS substrates. *Science* **1995,** *267*, 1629-1632.

32 Hu, X.G.; Cheng, W.L.; Wang, T.; Wang, Y.L.; Wang, E.K.; Dong, S.J., Fabrication, characterization, and application in SERS of self-assembled polyelectrolyte-gold nanorod multilayered films. *J. Phys. Chem. B* **2005,** *109*, 19385-19389.

33 Rodriguez-Fernandez, J.; Funston, A.M.; Perez-Juste, J.; Alvarez-Puebla, R.A.; Liz-Marzan, L.M.; Mulvaney, P., The effect of surface roughness on the plasmonic response of individual sub-micron gold spheres. *Phys. Chem. Chem. Phys.* **2009,** *11*, 5909-5914.

34 Wang, H.; Goodrich, G.P.; Tam, F.; Oubre, C.; Nordlander, P.; Halas, N.J., Controlled texturing modifies the surface topography and plasmonic properties of Au nanoshells. *J. Phys. Chem B* **2005,** *109*, 11083-11087.

35 Tseng, A.A.; Chen, K.; Chen, C.D.; Ma, K.J., Electron beam lithography in nanoscale fabrication: Recent development. *IEEE Trans. Electron. Packag. Manuf.* **2003**, *26*, 141-149.

36 Khoury, M.; Ferry, D.K., Effect of molecular weight on poly(methyl methacrylate) resolution. *J. Vac. Sci. Technol. B* **1996**, *14*, 75-79.

37 Near, R.; Tabor, C.; Duan, J.S.; Pachter, R.; El-Sayed, M., Pronounced effects of anisotropy on plasmonic properties of nanorings fabricated by electron beam lithography. *Nano Lett.* **2012,** *12*, 2158-2164.

38 Duan, H.G.; Fernandez-Dominguez, A.I.; Bosman, M.; Maier, S.A.; Yang, J.K.W., Nanoplasmonics: Classical down to the nanometer scale. *Nano Lett.* **2012,** *12*, 1683-1689.

39 Yue, W.S.; Wang, Z.H.; Yang, Y.; Chen, L.Q.; Syed, A.; Wong, K.; Wang, X.B., Electron-beam lithography of gold nanostructures for surface-enhanced Raman scattering. *J. Micromechanics and Microengineering* **2012,** *22*, 125007.

40 Jain, P.K.; Huang, W.Y.; El-Sayed, M.A., On the universal scaling behavior of the distance decay of plasmon coupling in metal nanoparticle pairs: A plasmon ruler equation. *Nano Lett.* **2007,** *7*, 2080-2088.

41 Gopinath, A.; Boriskina, S.V.; Premasiri, W.R.; Ziegler, L.; Reinhard, B.M.; Dal Negro, L., Plasmonic nanogalaxies: Multiscale aperiodic arrays for surface-enhanced Raman sensing. *Nano Lett.* **2009,** *9,* 3922-3929.

42 Guo, L.J.; Leobandung, E.; Chou, S.Y., A silicon single-electron transistor memory operating at room temperature. *Science* **1997,** *275*, 649-651.

43 Craighead, H.G., Nanoelectromechanical systems. *Science* **2000,** *290*, 1532-1535.

44 Foresi, J.S.; Villeneuve, P.R.; Ferrera, J.; Thoen, E.R.; Steinmeyer, G.; Fan, S.; Joannopoulos, J.D.; Kimerling, L.C.; Smith, H.I.; Ippen, E.P., Photonic-bandgap microcavities in optical waveguides. *Nature* **1997,** *390*, 143-145.

45 Jiang, Z.H.; Yun, S.; Lin, L.; Bossard, J.A.; Werner, D.H.; Mayer, T.S., Tailoring dispersion for broadband low-loss optical metamaterials using deep-subwavelength inclusions. *Sci. Rep.* **2013,** *3,* 1571.

46 Haynes, C.L.; McFarland, A.D.; Zhao, L.L.; Van Duyne, R.P.; Schatz, G.C.; Gunnarsson, L.; Prikulis, J.; Kasemo, B.; Kall, M., Nanoparticle optics: The importance of radiative dipole coupling in two-dimensional nanoparticle arrays. *J. Phys. Chem. B* **2003,** *107*, 7337-7342.

47 Gunnarsson, L.; Bjerneld, E.J.; Xu, H.; Petronis, S.; Kasemo, B.; Kall, M., Interparticle coupling effects in nanofabricated substrates for surface-enhanced Raman scattering. *Appl. Phys Lett.* **2001,** *78*, 802-804.

48 Tsai, C.-Y.; Lin, J.-W.; Wu, C.-Y.; Lin, P.-T.; Lu, T.-W.; Lee, P.-T., Plasmonic coupling in gold nanoring dimers: Observation of coupled bonding mode. *Nano Lett.* **2012,** *12*, 1648-1654.

49 Rechberger, W.; Hohenau, A.; Leitner, A.; Krenn, J.R.; Lamprecht, B.; Aussenegg, F.R., Optical properties of two interacting gold nanoparticles. *Opt. Communications* **2003**, *220*, 137-141.

50 Johnson, P.B.; Christy, R.W., Optical constants of noble metals. *Phys. Rev. B* **1972**, *6,* 4370-4379.

51 Palik, E.D., Handbook of optical constants in solids, *Academic Press: New York,* **1991**; p.2.

52 Smythe, E.J.; Cubukcu, E.; Capasso, F., Optical properties of surface plasmon resonances of coupled metallic nanorods. *Opt. Expr.* **2007,** *15*, 7439-7447.

53 Lereu, A.L.; Passian, A.; Farahi, R.H.; Abel-Tiberini, L.; Tetard, L.; Thundat, T., Spectroscopy and imaging of arrays of nanorods toward nanopolarimetry. *Nanotechnology* **2012,** *23*, 045701.

54 Gupta, M.K.; König, T.; Near, R.; Nepal, D.; Drummy, L.F.; Biswas, S.; Naik, S.; Vaia, R.A.; El-Sayed, M.A.; Tsukruk, V.V., Surface assembly and plasmonic properties in strongly coupled segmented gold nanorods. *Small* **2013,** *9*, 2979-2990.

55 Smith, R.B., Introduction to hyperspectral imaging. MicroImages, Inc. **2012.**

56 Zhang, S.P.; Bao, k.; Halas, N.J.; Xu, H.X.; Nordlander, P., Substrate-induced Fano resonances of a plasmonic nanocube: A route to increased-sensitivity localized surface plasmon resonance sensors revealed. *Nano Lett.* **2011**, *11*, 1657-1663.

57 König, T.; Tsukruk, V.V.; Santer, S., Controlled topography change of subdiffraction structures based on photosensitive polymer films induced by surface plasmon polaritons. *ACS Appl. Mater. Interfaces* **2013**, *5,* 6009-6016.

58 Wiley, B.J.; Im, S.H.; Li, Z.Y.; McLellan, J.; Siekkinen, A.; Xia, Y.N., Maneuvering the surface plasmon resonance of silver nanostructures through shape-controlled synthesis. *J. Phys. Chem. B* **2006,** *110*, 15666-15675.

59 Combs, Z.A.; Malak, S.T.; König, T.; Mahmoud, M.A.; Chávez, J.L.; El-Sayed, M.A.; Kelley-Loughnane, N.; Tsukruk, V.V., Aptamer-assisted assembly of gold nanoframe dimers. *Particle* **2013,** *30,* 1071-1078.

CHAPTER 5

HIERARCHICAL PLASMONIC SYSTEM: CONTROLLED ASSEMBLY OF SILVER NANOCUBES IN 3D POROUS ALUMINA MEMBRANES

Chapter Based On:
Kodiyath, R.; **Malak, S.T.;** Combs, Z.A.; Koenig, T.; Mahmoud, M.A.; El-Sayed, M.A.; Tsukruk, V.V., Assemblies of silver nanocubes for highly sensitive SERS chemical vapor detection. *J. Mater. Chem. A* **2013,** *1,* 2777-2788.

Chapter Overview

The idea of using the third-dimension in locally-assembled plasmonic structures (via stacking) is now extended to larger-scale three-dimensional arrangements of plasmonic nanostructures. This will be shown to result in the development of a new and novel complex hierarchal system composed of individual and locally-assembled Ag nanocubes (AgNCs) deposited within a microscale three-dimension porous alumina membrane (PAM). In this system, the local assembly of AgNCs was controlled using a polyelectrolyte layering method, allowing for either individual (dispersed) AgNCs or locally-assembled (aggregated) AgNCs. The 3D arrangement of the AgNCs was controlled by the 3D PAM substrate. Furthermore, we suggest that these AgNC-PAM systems can be employed as efficient nanostructures in the fabrication of highly efficient, easily synthesized, robust, tunable surface-enhanced Raman scattering (SERS) substrates for trace level organic vapor detection which is a challenging task in chemical detection.

We demonstrate the ability to tune both the detection limit and the onset of signal saturation of the substrate by switching the adsorption behavior of AgNCs between

highly aggregated to more disperse by varying the number of adsorption-mediating polyelectrolyte bilayers on the pore walls of the membrane (**Figure 5.1**). The different AgNC distributions show large differences in the trace vapor detection limit of the common Raman marker benzenethiol (BT) and a widely used explosive binder n-methyl-4-nitroaniline (MNA), demonstrating the importance of the large electromagnetic field enhancement associated with AgNC coupling. The SERS substrate with highly aggregated AgNCs within the pores of porous alumina membranes allows for the consistent trace detection of mid ppb (~500) for BT, and a record limit of detection of low ppb (~3) for MNA vapors with an estimated limit of detection of approximately 600 ppt, in contrast to the substrate with dispersed AgNC which demonstrates a detection limit of 100 ppb. However, the dispersed AgNC distribution does not saturate at higher ppb concentrations, providing an avenue to distinguish between higher ppb concentrations and increase the effective range of the SERS substrate design. A comparison between the AgNC substrate and an electroless deposition substrate with silver quasi-nanospheres (PAM-AgNS) also demonstrates a higher SERS activity, and better detection limit by the AgNC aggregates. This is supported by FDTD electromagnetic simulations that suggest that the higher integrated electromagnetic field intensity of the hot spots and large specific interfacial areas impart greatly improved SERS activity.

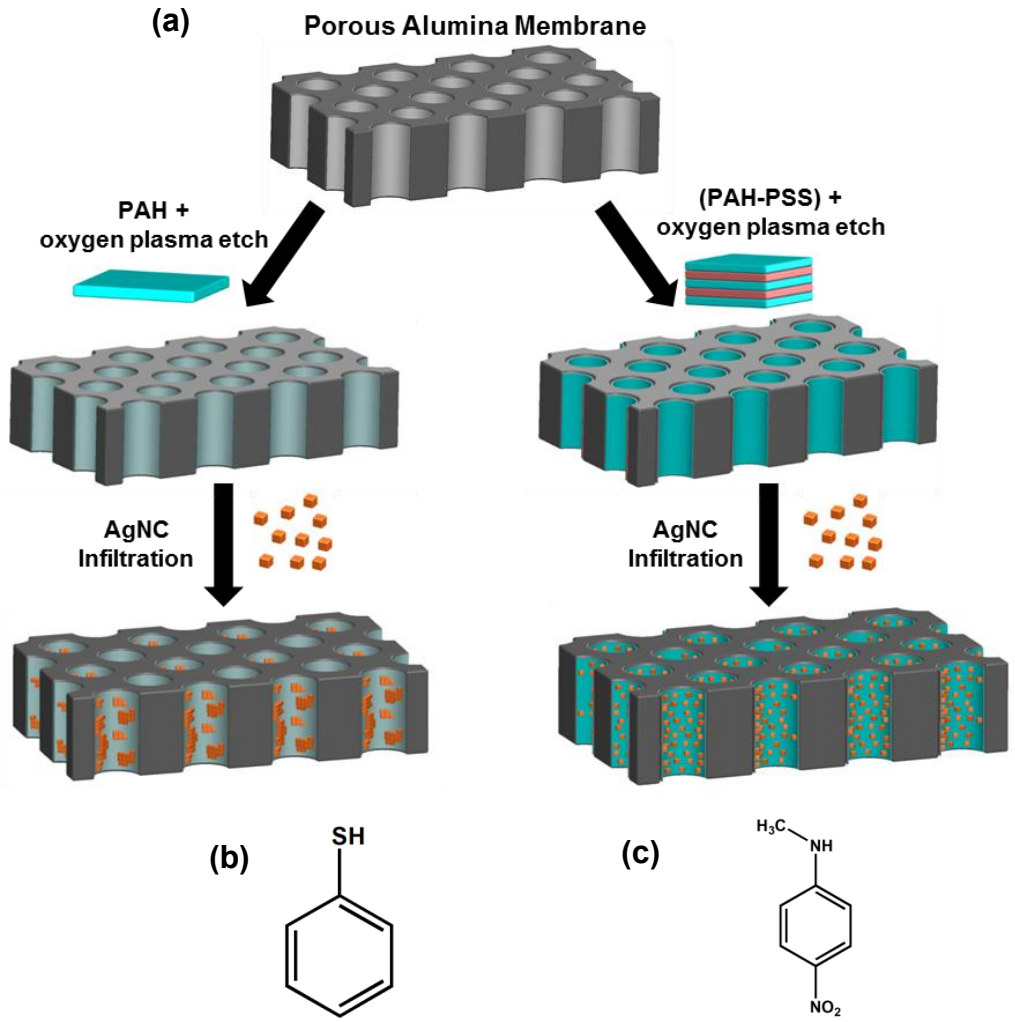

Figure 5.1: (a) Schematic of the AgNC infiltration method showing the porous alumina membrane coated with a positively charged polyelectrolyte (PAH or the PAH-PSS bilayers) that is subsequently decorated with silver nanocubes by infiltration. Molecular structures of the two target molecules (b) the common Raman marker Benzenethiol (BT) and (c) the widely used explosive binder n-methyl-4-nitroaniline (MNA).

5.1 Introduction

5.1.1 Surface-enhanced Raman scattering (SERS)

The surface-enhanced Raman scattering (SERS) technique is highly sensitive, non-destructive, exhibits high-specificity and recognition for trace-level detection of hazardous chemicals and biomolecules,[1] has levels of detection down to a single molecule,[2,3,4,5,6] and works at typical environmental temperatures and pressures. Raman enhancement is largely due to the huge electromagnetic field that exists in the small gaps between plasmonic metal nanostructures, termed hot spots.[7] The electromagnetic (EM) plasmon field increase in the gap between nanoparticles as a result of plasmon field coupling leads to the enhancement of the Raman signals from molecules present in the plasmon field domain.[8] The electromagnetic field intensity depends on nanoparticle size, shape, curvature of the corners and edges, and inter particle spacing.[9,10] The EM enhancement factor has been estimated in the hot spot formed between dimers of spherical nanoparticles as well as nanostructures with sharp edges.[11,12,13,14] It has been reported that nanostructures with sharp edges show higher SERS activity than that of spherical nanoparticles due to the presence of greater electric fields at the edges caused by charge concentration.[15,16,17]

5.1.2 SERS considerations and systems

The most critical aspect for a sensitive and reliable SERS-based detection probe is therefore the design and assembly of well defined nanostructures with a dense and widespread distribution of particle aggregates (hot spots).[18] Nanocubes (NC) are used for the fabrication of SERS substrates because they have sharp edges with high electromagnetic fields and because they can be synthesized in large quantities with high

monodispersity.[13,15] Moreover, adsorption of analyte molecules on the surface is favored due to the presence of exposed (001) uniform crystal planes.[16] A number of studies have reported on the SERS activity of silver nanostructures (nanospheres and nanocubes) and their dimers in two-dimensional (2D) substrates and the dependence of their SERS response on the polarization of the excitation light.[11,13,19,20,21] Although some of these studies demonstrate impressive limits of detection for AgNC, most of them have concentrate on the detection of analytes in/deposited from the solution phase[22,23] or require patterned substrates,[24] while the few that performed trace detection over a variety of concentrations concentrated on aqueous phase exposure.[25] However, the utilization AgNC in a more complex, fabricated substrate that can be used in a realistic environment is largely absent and trace level detection over a wide concentration range, and for the vapor phase, has not been performed. SERS substrates based upon open porous alumina membranes (PAM) offer a route to investigate these avenues because they show high SERS activity since the PAM provides a large nanostructure loading capacity, an increased surface area (number of binding sites) for probing molecules, alumina's optical wave guiding property and good transparency.[26,27] PAM-based 3D SERS substrates decorated with spherical metal nanospheres have demonstrated effective label-free detection of plastic explosive materials and other small molecules in the liquid phase.[28,29,30,34,35]

5.1.3 SERS based vapor phase detection

SERS detection in the vapor phase is still challenging, as demonstrated by the limited number of reports on SERS based vapor phase detection due to the extremely low concentration of non-volatile analytes.[31,32] Various design strategies have been developed to fabricate SERS substrates with high SERS activity for liquid phase

detection.[33,34,35,36] The few reports demonstrating vapor-phase detection of explosive molecules generally concentrate on planar substrates with a limited number of 'hot spots' in the excitation volume. These can require high laser power (100–115 mW) and long detection time (30 seconds) for collecting spectra thus leading to potential burning of organic analytes.[37,38] Due to the absence of flow channels in 2D substrates a stream of flowing vapor must be used which is cumbersome and time consuming.

Although detection studies have investigated nitroaniline molecules,[39,40,41] none of these were for vapor phase detection, used AgNC, implemented 3D substrates, or specifically examined MNA. Typically most vapor detection studies have focused on the recognition of the explosive component, such 2,4,6-trinitrotoluene (TNT) or its byproduct 2,4-dinitrotoulene (DNT),[42,43,44] but have not considered common components of munitions such as stabilizing agents like n-methyl-4-nitraniline (MNA). As known, over the past 20 years the military has moved toward developing insensitive munitions (IM) i.e. munitions that are less likely to accidently explode because they are more resistant to heat and mechanical shock,[45,46] and in some cases has replaced traditional compounds like TNT because of its shock instability.[47,48] Therefore, developing sensing platforms that identify stabilizing agents like MNA that are commonly incorporated into the IM compound[49,50] provides a promising avenue to detect a myriad current and future explosive materials. MNA has been investigated because it is a common binder in insensitive munitions[49,50,51] and an important ingredient in Amatol 40 which is included in the warhead of the V-1 rocket.[52,53] It is also used as a common additive in explosive materials to depress the melting point in the typical melt-cast process.[54] However, detection of MNA in the vapor phase is hampered by its low vapor pressure (3×10^{-8} atm).[55] Therefore, highly sensitive and reliable trace level detection of MNA in the

vapor phase requires a SERS substrate that incorporates a large number of SERS hot spots that are densely and consistently distributed throughout the system and accessible to probing molecules.

Herein, we demonstrate that AgNC can be exploited as efficient nanostructures for SERS-based trace-level vapor detection, allowing for the detection of a common Raman marker benzenethiol (BT) and MNA in the vapor phase down to un-precedential low ppb-ppt level. In addition, it is shown that AgNC can be assembled differently within a porous membrane (large aggregates or more dispersed smaller aggregates) depending on the number of polyelectrolyte bilayers that are incorporated onto the pore walls. This difference in particle adsorption behavior not only leads to noticeable differences in limits of vapor detection but also saturation onset. The ability to tune the onset of SERS intensity saturation is shown to be an important consideration when designing a SERS substrate because it allows for the proper selection of AgNC adsorption behavior according to the expected concentration range of the analyte that is being detected, providing a potential means for quantitative determination of vapor concentration in real-life situations for specific concentration ranges. The silver quasi-spherical nanoparticles are included in this study as a reference to a well know 3D substrate to investigate the effect of nanostructure shape on SERS activity.[34,56] The SERS activity of the PAM-AgNC was found to be much higher than that exhibited by PAM-AgNS, showing very low observed detection limits (LoD) of mid ppb-level (~500) for BT, and low ppb-level (~3) for MNA vapor concentrations with an estimated ultimate limit of detection of about 600 ppt. The substrate's ability to maintain its detection effectiveness after multiple cleaning and reloading cycles has been also demonstrated and compared to the AgNS substrate, demonstrating an additional consideration for designing robust substrates.

5.2 Experimental details

PAM-AgNC SERS substrate. The inner surface of the porous membranes was modified with poly(allylamine hydrochloride) (PAH) (M_w = 55,000), polyethylenimine (PEI) (*M*W = 70,000, Polysciences), or poly(sodium 4-styrenesulfonate) (PSS) (M_W = 70,000) by spin-coating (3,000 rpm, ~45 s) 0.2% aqueous solution followed by rinsing with Nanopure water (18.2 MΩ cm). For the AgNC-PAH and AgNC-PEI substrates 1 layer of the positively-charged polyelectrolyte (PAH) and (PEI), respectively, were spin coated onto each side of the PAM (with washing steps before and after polymer deposition) For the AgNC-(PAH-PSS) substrate, 2.5 (PAH-PSS) bilayers were spin coated onto each side of the PAM with washing steps before and after each polymer deposition. This procedure results in nanometer (2-5 nm) thick polymer coatings depending on the number of bilayers deposited that have been determined by AFM measurements discussed previously.[57] The surface-modified PAM was then oxygen plasma etched for approximately 5 minutes to remove polymer adsorbed on the PAM surface. This treatment minimized adsorption of AgNCs on the PAM surface (and clogging of its pores) during the vacuum infiltration process, allowing for high loading of AgNCs within the pores. The pressure was maintained at 600-700 mmHg during the vacuum infiltration process to ensure widespread, dense deposition of AgNCs onto the pore walls. Substrates were sonicated and washed after vacuum infiltration to remove excess polymer and AgNCs adsorbed on the PAM surface.

PAM-AgNS SERS substrate. AgNS were grown on the pore walls following a two-step electroless deposition process.[29,56] In the first step, the PAMs were immersed in an aqueous solution of $SnCl_2$ (0.02 M) and HCl (0.02 M) for 2 minutes to deposit Sn^{2+} on the pore walls. The PAMs were then rinsed with Nanopure water and subsequently with

acetone and then dried. Growth of silver seeds on the pore walls was carried out in the second step by immersing the PAMs in a 0.02 M aqueous solution of $AgNO_3$ for 2 minutes followed by a second washing step. The deposition of AgNS seeds was carried out three times to obtain uniform and dense particle coverage on the pore walls. The PAMs with silver seeds were then immersed in 0.5 ml of 10 mM $AgNO_3$ and 1 ml of 100 mM ascorbic acid for 28 minutes with shaking at 200 rpm. Afterward, the PAMs were removed from the solution, rinsed thoroughly with Nanopure water in order to remove particles adhered on the top surface of the PAMs, and then dried using nitrogen gas. A detailed growth mechanism and time dependence of particle size and distribution using this method have been reported elsewhere.[56,58]

SERS vapor detection. The vapor-phase detection setup used a suspended substrate ~3 cm above the bottom of the vial. The concentration of BT in the vapor phase was controlled and varied by evaporating known amounts of BT from solution (in ethanol) at 45^{o}C for 4 hours. MNA vapor was produced by heating approximately 15 mg of solid MNA (melting point = 150°C).[59] The whole setup was then heated at different temperatures for 2 hours to ensure saturated MNA vapor conditions. A water bath was used to heat the vial to minimize radial and axial temperature gradients throughout the vial volume. The temperature was monitored and automatically adjusted by a thermocouple and maintained to within 0.5°C of the specified temperature. The experimental setup restricted complete submersion of the glass vial in the water bath so a thermocouple was used to determine the relationship between the water bath temperature and the vial's internal gas temperature. The vapor concentration of MNA in the vial was controlled by changing the vapor pressure of MNA by adjusting the internal temperature of the vial. A more detailed discussion of the calculation of MNA vapor

concentration is provided in **Appendix B**. The experimental setup adopted in this study was chosen because it mimics simple gas diffusion behavior which more closely resembles potential real-world environments (warfield arena, cargo holds, etc.) than other flow-base setups that utilize a targeted puff of analyte vapor or constant pumped vapor flow through the substrate to mimic analyte presence.[60]

To demonstrate the recyclability of our substrates, we have adopted a solvent washing method to remove the adsorbed MNA molecules from the nanoparticle surfaces. The PAM-AgNC and PAM-AgNS substrate was loaded with MNA and then submerged in ethanol for 2 min followed by rinsing in excess of ethanol. After the solvent washing, the substrate was air dried and then subjected to another reloading.

Density functional theory (DFT) simulation of the SERS spectra of MNA. MNA molecule was optimized at the B3LYP/6-31++G** level of theory using the quantum chemistry package Gaussian 03.[61] The geometries of the complex systems, i.e. MNA bound to 2 atom silver cluster (**Appendix B Figure B1**) was optimized at the B3LYP/LANL2DZ level of theory for the Ag atoms and at the B3LYP/6-31++G**level for the atoms of MNA, without the use of vibrational frequency correction factors. We stress that our main goal here is to better understand the different vibrational modes associated with MNA molecule.

Finite-difference time-domain (FDTD) simulations. The FDTD method was used to calculate the extinction spectra and the plasmon field enhancement of AgNC and AgNS (using the commercial software from Lumerical Solutions Inc. FDTD Solutions, Version 7.5.7).[62,63,64] Nanocubes coated with a PVP-layer and different

edge rounding values were used to explain the extinction observed experimentally. Edge rounding is defined as (R/L) where L is the nanocube edge length and R is either the radius of a cylinder fitted to a rounded edge or of a sphere fitting to a rounded corner, as established in the literature.[65] The PVP-layer and the nanocube were defined by the same edge rounding factor.

The PVP-layer was specified with a permittivity of 2.25 while silver was specified with a wavelength dependent permittivity from CRC.[66] Fit analysis at the CRC source showed an RMS error of 0.045 by 6th order polynomial. Permittivity of water was taken from Palik (first order fit with an RMS error of 0.029).[67] The simulation mesh size was chosen to be 0.5 nm for the best possible rendering of edge rounding and second conformal variant for mesh refinement. The mesh size was stretched above the whole field source of 140 nm and the simulation time was chosen to be 75 fs. Anti-symmetric and symmetric boundary conditions were used to reduce the simulation time.

5.3 Results and discussion

5.3.1 Physical characteristics of AgNC and AgNS

Figure 5.2a displays TEM images of the AgNCs used in this study with a narrow size distribution, an edge length of 40±3 nm (See **Appendix B Figure B3** for particle distribution), and an inter particle face-face spacing of 1.8±0.8 nm. The quasi-spherical silver nanoparticles have an average diameter of 30±10 nm (**Figure 5.2b**).

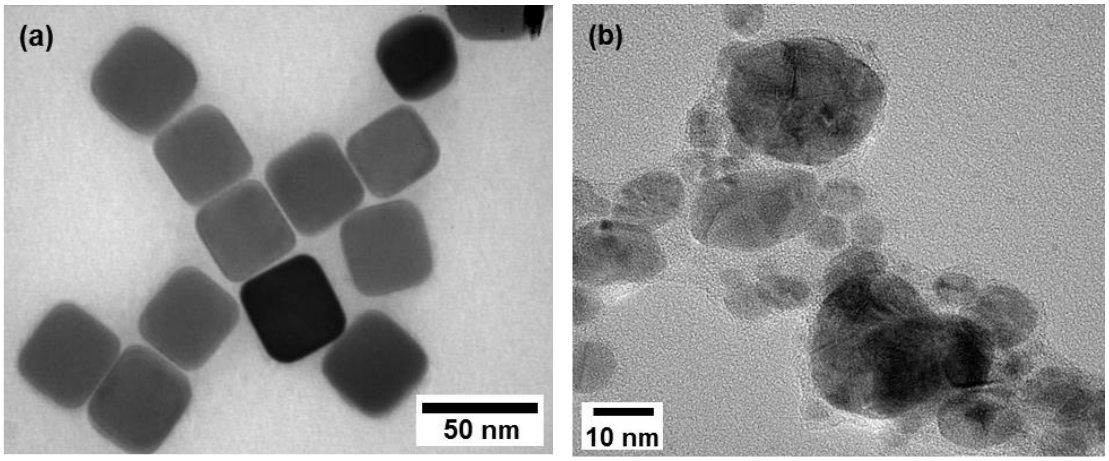

Figure 5.2: TEM micrographs of (a) Ag silver nanocubes capped with a PVP stabilizing layer that were synthesized using the polyol method and (b) silver quasi-nanospheres grown on a PAM using an electroless deposition method that were subsequently released by dissolution of the PAM by NaOH.

Zeta potential measurements of the AgNC solution show that PVP-capped AgNCs possess a strong negative surface charge (-40 mV, pH 5.0), which should provide a strong attraction to the pore walls that are coated with positively-charged PAH and PEI.[34,35,28]

5.3.2 Nanoparticle-porous alumina membrane substrates

PAMs were decorated with AgNCs by infiltrating AgNCs suspended in water (AgNC solution) through surface-modified PAMs. The immobilization of nanocubes on porous alumina membranes was done using a modified literature procedure, where the inner surface of the pore walls was modified with a polyelectrolyte to electrostatically assemble the AgNCs onto the pore walls. [68,69],[70] The type of polyelectrolyte and its layering determine how well the PAM surface is covered, which can lead to unique AgNC adsorption behavior (well-dispersed or aggregated) (**Figure 5.1**).

Analysis of the SEM images of the PAH, PEI, and (PAH-PSS)-coated substrates shows a dense distribution of AgNCs over several microns depth from the top surface of the PAM (**Figure 5.3a,b,c** respectively). **Figure 5.3d** is an SEM image of the PAM-AgNS fabricated by the electroless deposition method, showing a uniform deposition of quasi-spherical nanoparticles over the entire PAM.[29,30]

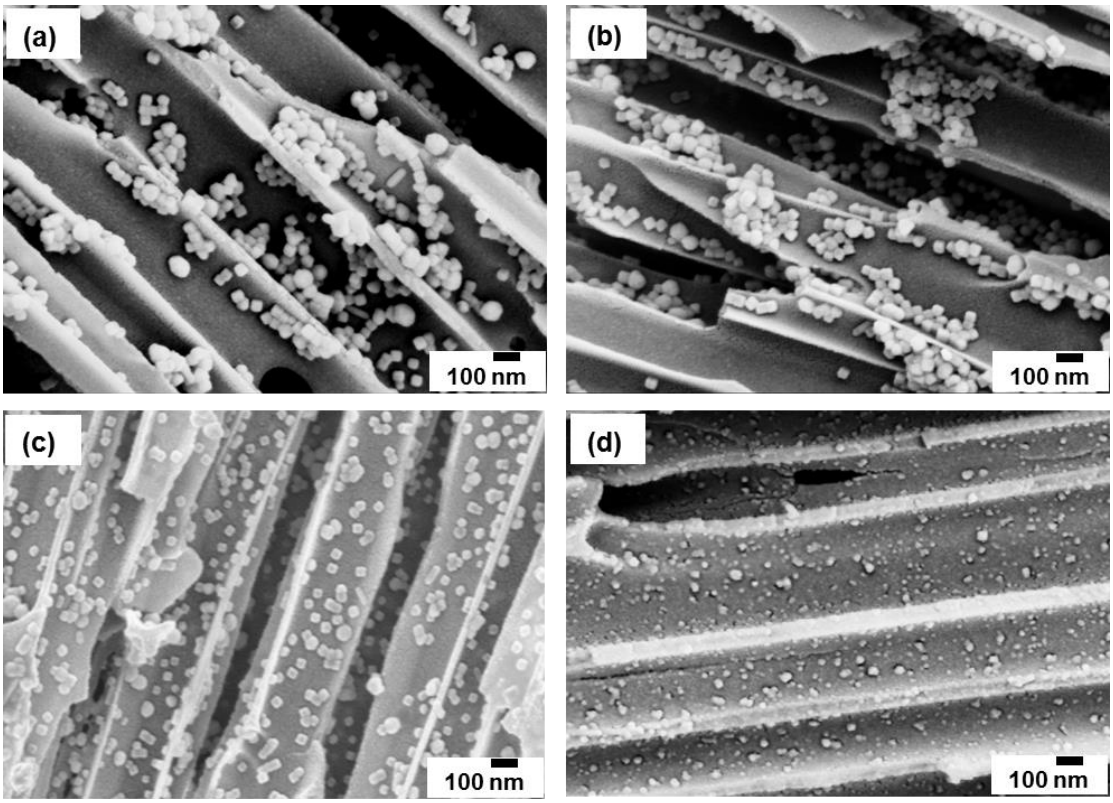

Figure 5.3: SEM micrographs of the cross section of the infiltrated substrates (a) PAM-AgNC (PAH), (b) PAM-AgNC (PEI), and (c) PAM-AgNC (PAH-PSS) demonstrating a very high particle adsorption density. (d) SEM image of the cross section of the PAM-AgNS substrate produced via the electroless deposition method. The PAM-AgNS substrate demonstrates more evenly dispersed AgNS.

The high adsorption of particle density of AgNC on the pore walls is due to the strong electrostatic attraction between the positively-charged polyelectrolyte layer and the negatively-charged PVP-coated AgNCs. The majority of AgNCs in the PAH and PEI

substrates are assembled in many-particle densely-packed aggregates (See **Appendix B Figure B4**), which leads to enhancements in the SERS response through the presence of SERS hot spots between closely adjacent nanocubes. The AgNC-(PAH-PSS) substrate on the average demonstrates single and smaller AgNC aggregates that are more dispersed than the PAH and PEI substrates (See **Appendix B Figure B5** for more images). This difference in adsorption behavior is likely due to the PAH and PEI substrates not having as uniform a polymer layer over the pore surface area after the oxygen plasma etching process, while the (PAH-PSS) substrate has multiple bilayers that are electrostatically bound which are more resistant to oxygen plasma etching. The presence of aggregates in the (PAH-PSS) substrate can be explained by shielding of the repulsive electrostatic interaction between PVP-capped AgNC by the highly positive terminating cationic polymer layer (PAH) on the PAM pore walls which minimizes the repulsive electrostatic interaction between adjacent PVP coated AgNCs,[71,72] potentially allowing for AgNC to adsorb close to each other via Van der Waals interactions. In addition, it is evident from **Figure 5.3a,b,c** that the majority of the AgNC aggregates assemble with a face-to-face orientation which is due to Van der Waals attractions having a stronger influence over assembly orientation than steric hindrance between PVP chains of adjacent AgNCs, an expected result for particles stabilized with short-chain polymers.[73]

5.3.3 Optical extinction characteristics

The face-face orientation can red shift the surface plasmon resonance (SPR) absorption of the AgNCs which has been in fact observed (**Figure 5.4**).[65] The SPR absorption at 450 nm is due to dipolar resonance while the higher energy peaks at 390 and 350 nm are attributed to multipolar excitations.[74] To confirm this, we have simulated the SPR

absorption spectrum of a 40 nm AgNC coated with PVP in water using the FDTD method (**Figure 5.4**).

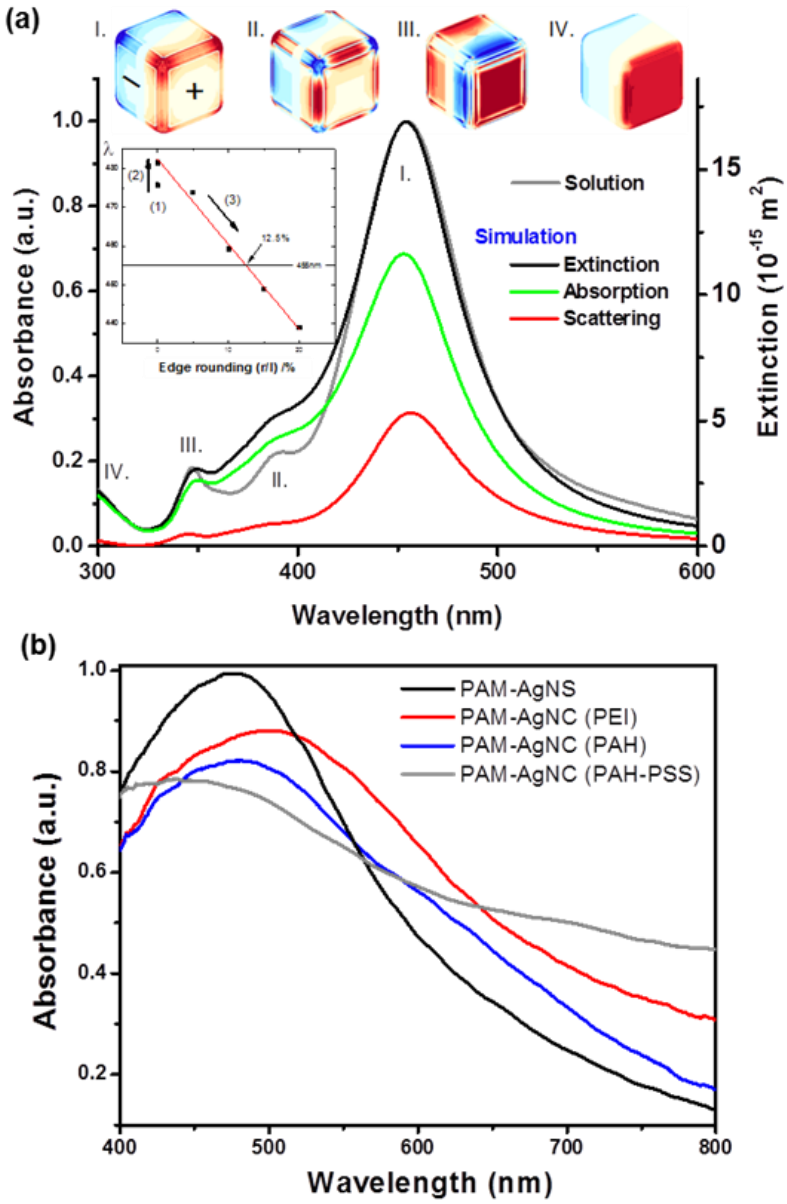

Figure 5.4: (a) Simulated and experimental spectra of 40 nm AgNC in water (the different modes of oscillation associated with the AgNC are also shown in top inset). (b) UV-vis absorption spectra of the PAM-AgNC and PAM-AgNS substrates, which all show high absorption at the laser wavelength (514 nm).

As is clear from simulated spectra, the extinction spectrum is clearly dominated by absorption, which is expected for a cube with 40 nm dimensions.[65] Surface charge distributions show resonances due to the excitation of dipole (I) and higher cube modes (II-IV). The FDTD simulation included a PVP-layer and edge rounding of the AgNC to match the FDTD predictions to the experimental results. The edge rounding induces an increase of symmetry of the charge distribution that reduces the number of resonances.[75] Consequently, only four excitation modes are observed for the rounded cube as compared to the six excitation modes exhibited by a perfect cube.[65] The inset in **Figure 5.4** shows the presence of the higher refractive index PVP layer (estimated to be 1-2 nm) which red shifts the dipole-peak position about 6 nm compared to a perfect cube (indicated as 1-to-2 in the inset) whereas the AgNC's SPR absorption blue shifts as the edge rounding increases (indicated as 2-to-3 in the inset). An exact match between the FDTD simulation and the experimental results occurs for an edge rounding factor of 12.5%, which is a reasonable value considering the multiple treatment steps involved in the substrate preparation. The lack of an absorption peak in the lower energy region indicates that there is minimal particle aggregation occurring in solution,[20] suggesting that aggregation occurs primarily during particle adsorption onto the substrate.

PAM-AgNC (PAH) and (PEI) SERS substrates show a clear peak at 479 nm and 502 nm, respectively, and broad absorption between 600-800 nm (**Figure 5.4b**). The red shift of the dipole resonance absorption from 450 nm in the solution to 479 nm and 502 nm in the AgNC substrates (PAH and PEI, respectively) can be attributed to dipole plasmonic coupling of aggregates in the substrate.[74] The broad absorption in the 600-800 nm range could be due to the presence of aggregates with different orientations, sizes, and inter particle distances, which is observed in the substrate SEM images

(**Figures 3a,b,c**).[20,73] **Figure 5.4b** also shows the absorption spectrum of PAM-AgNS. The optical absorption for PAM-AgNS substrate is centered at around 475 nm due to the silver nanoparticle aggregation. In addition, the refractive index of the alumina membrane (1.6) may also contribute to the observed red shift.[76,77] The increased absorbance of the AgNC substrates (with respect to the AgNS substrate) in the 600-800 nm region indicates a broader distribution in the aggregate resonance frequency. This difference is reasonable since NCs have more orientation parameters that can affect dipole plasmonic coupling of aggregates due to their shape.

5.3.4 SERS activity from PAM-based SERS substrates

The SERS activity of the AgNC-PAM substrates was investigated using a vapor-phase detection setup (**Figure 5.5)**.

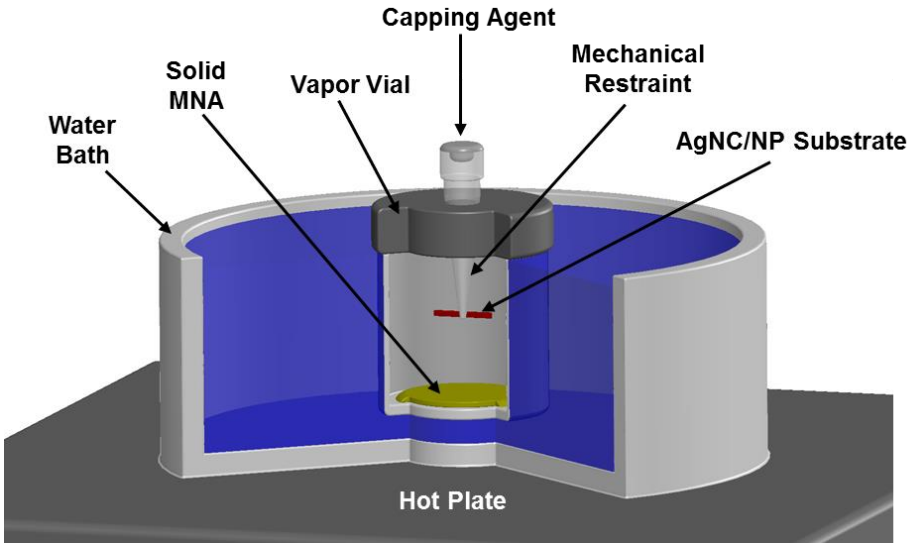

Figure 5.5: Schematic of the experimental setup used for the vapor-phase detection measurement. The substrate is suspended above the solid form of the target substance. The containment vial is heated at various temperatures to produce different vapor concentrations of the target substance. A water bath is used to control the temperature of the vial.

Fabricated substrates are expected to show a high SERS response since they have considerable absorption at the 514 nm excitation wavelength.[78] **Figure 5.6a** shows SERS spectra of BT detected in the vapor phase using PAM-AgNC (PAH) substrate. The characteristic peaks of BT at 1584 cm^{-1} (C=C) stretching), 1077 cm^{-1} (C-C bending) and 999 cm^{-1} (ring breathing) are observed at different vapor concentrations.[79] However, there is an overlap between the peak due to amorphous carbon and the peak from BT (1584 cm^{-1}) while the other two characteristic peaks form BT (999 cm^{-1} and 1077 cm^{-1}) are clearly visible for 500 ppb. From **Figure 5.6a** it can be concluded that BT vapor concentration of 500 ppb can easily be detected with our SERS substrates. The LoD we achieved with our SERS substrate is one order of magnitude lower than that reported for BT.[80] The low LoD for BT demonstrates the high SERS activity of our substrates and suggests that they will be an effective detection platform for MNA.

The SERS substrates were exposed to six different MNA vapor concentrations that were established using specific temperatures: 3 ppb (5°C), 10 ppb (15°C), 29 ppb (25°C), 99 ppb (35°C), 297 ppb (45°C) and 790 ppb (55°C),[55] a procedure similar to previous studies.[59] The ppb vapor concentration of MNA was calculated using theoretical calculations of the MNA vapor pressure at different temperatures and by assuming ideal gas conditions (applicable given the low pressure and temperatures involved) as is standard practice for parts per vapor concentration estimations (a more detailed discussion is provided in **Appendix B**).[55] The SERS substrates were exposed to the MNA vapor (in the vial) for 2 hours, as mentioned above.

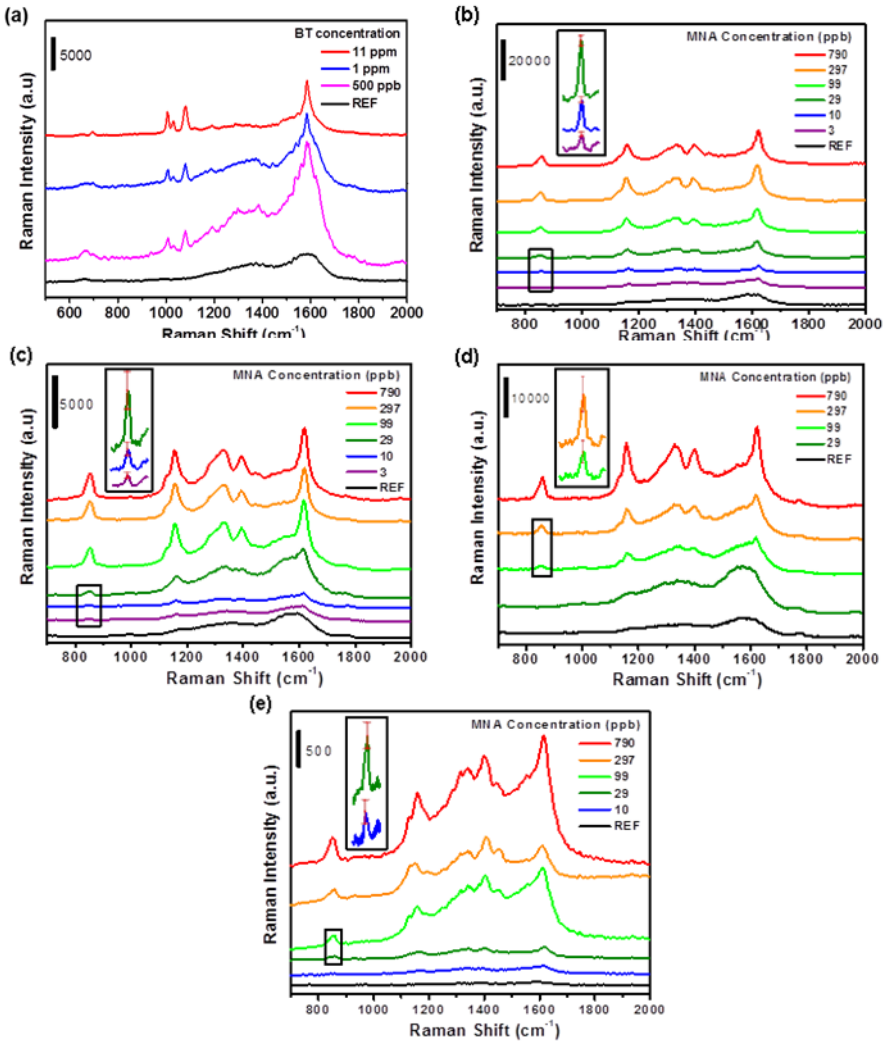

Figure 5.6: SERS spectra of (a) BT vapor by PAM-AgNC (PAH), and MNA vapor by (b) PAM-AgNC (PAH), (c) PAM-AgNC (PEI), (d) PAM-AgNC (PAH-PSS), and (e) PAM-AgNS substrates at various vapor concentrations. The REF for each plot is the bare substrate (i.e. no exposure to MNA). The SERS spectra were vertically translated for clarity. The insets display the 857 cm^{-1} peak at the lower concentrations for clarity, where the error bars represent the standard deviation of the peak height (the scale bars do not apply to the insets).

To gain insight into the different vibrational modes present in the SERS spectrum of the MNA molecules, the Raman spectrum of MNA was modeled using DFT (**Appendix B Figure B1**). The simulated spectrum shows a strong peak at 1363 cm^{-1} and several other peaks at 865, 1133, and 1655 cm^{-1}. Modeling suggests that the peaks at 1363 cm^{-1} and 865 cm^{-1}, although shifted, may be due to symmetrical stretching and out-of-plane bending of the $–NO_2$ group, repectively.[35] The peaks at 1133 and 1655 cm^{-1} arise from C-H in-plane bending and stretching of the aromatic ring, respectively.[81] To understand the effect of binding of the analyte molecule to silver, we simulated the SERS spectrum of MNA using a two-atom silver cluster which shows selective peak enhancement (**Appendix B Figure B1**).[30]

The SERS spectra of MNA from the vapor phase with two different substrates, PAM-AgNC and PAM-AgNS, are shown in **Figure 5.6**. Note that the clean, unexposed substrates (denoted REF in each plot) show no coherent peaks at the 857 or 1157 cm^{-1} position. During spectra acquisition the laser power is attenuated to 50 μW (nearly three orders of magnitude lower than that usually reported) to minimize undesirable phenomena such as photobleaching and photodesorption.[82]

The characteristic Raman peaks of MNA at 857, 1157, 1300, and 1620 cm^{-1} are clearly observed for different concentrations of MNA vapor. The spectral positions of the characteristic vibrational modes are shifted slightly in the SERS spectra with respect to the Raman spectra of pure MNA (**Appendix B Figure B2**) and the simulated MNA SERS spectra. This minor spectral shift could be due to metal-analyte interactions at the nanoparticle surface and due to the presence of PVP on the nanoparticle surface which may induce steric hindrance to the adsorbed MNA molecules. It is important to note that

the Raman band at ~1620 cm^{-1} is enhanced greatly compared to the bulk MNA spectrum which suggests that the MNA molecule adopts a 'face-on' conformation to the metal nanoparticles.[81] **Figure 5.6** shows that the SERS activity of PAM-AgNC (PAH) was found to be more than an order of magnitude higher than that observed for traditional PAM-AgNS substrates for the 857 and 1157 cm^{-1} peaks for all concentrations. The PAM-AgNC (PAH-PSS) and PAM-AgNC (PEI) substrates showed a response similar to the PAH-substrate, although reduced slightly at most concentrations. The inset of each plot in **Figure 5.6** shows the 857 cm^{-1} peak at lower concentrations, where the error bar represents the standard deviation of the peak height. The insets show that a clear peak is present down to 3 ppb and 30 ppb for the AgNC and AgNS substrates, respectively, if a signal to noise ratio of >3 is considered.

Variation of the Raman intensity of the 857 and 1157 cm^{-1} peaks with MNA vapor concentration is shown in **Figure 5.7**. This figure shows that the Raman intensity of the peaks (fitted using a Lorentz function) increases with MNA concentration until they saturate at 300 ppb and 100 ppb for the PAM-AgNC (PAH) and PAM-AgNC (PEI) substrates, respectively. Neither the AgNS nor the AgNC-(PAH-PSS) substrate demonstrates saturation for the concentration range studied. This is likely due to the more dispersed adsorption pattern of the nanostructures which leads to a larger effective surface area. Therefore, the AgNC (PAH) and (PEI) substrates are very effective for low ppb detection but are unable to distinguish between higher vapor concentrations, while the AgNC-(PAH-PSS) and AgNS substrates demonstrate the ability to distinguish between higher ppb concentrations. The ability to change the adsorption behavior of AgNC can therefore offer a means to tailor the substrate's effective concentration response which is an important, but commonly overlooked, substrate parameter.

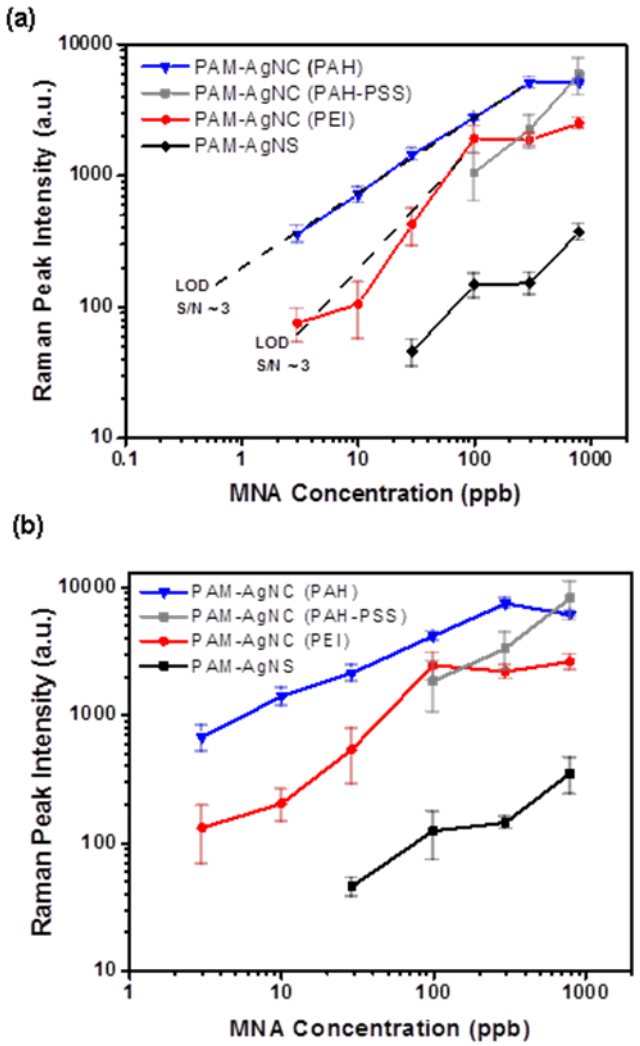

Figure 5.7: Variation of the SERS intensity versus concentration between the PAM-AgNC (PAH), PAM-AgNC (PAH-PSS), PAM-AgNC (PEI), and PAM-AgNS substrates for the (a) 857 cm^{-1} (linear fit to the data for PAM-AgNC (PAH) and (PEI) is shown in Figure 5.7a) and (b) 1157 cm^{-1} peaks. The linear fits weighted data points according to their standard deviation, as noted in the text.

Figure 5.7a,b show that MNA vapor concentrations of approximately 3 ppb can easily be detected by the AgNC-(PAH) and (PEI) substrates by identifying either the 857 cm^{-1} or 1157 cm^{-1} peak, where a signal-to-noise ratio of at least 3 was used to identify peaks. This is a record level of detection for MNA in the vapor phase. The PAM-AgNS does show the 857 and 1157 cm^{-1} peaks at 10 ppb, however, they were not included because the coefficient of variation was 0.43 and 0.85, respectively, making them statistically unreliable. Therefore, the PAM-AgNS is able to reliably detect a concentration of 30 ppb, demonstrating that the detection limit of the PAM-AgNC is one order of magnitude better than that observed for PAM-AgNS. The AgNC-(PAH-PSS) substrate demonstrates detection down to 100 ppb but shows no reliable peak intensity at lower concentrations. However, as mentioned previously it demonstrates a linear response at higher concentrations that may be useful for quantitative determine of vapor concentration in this region (**Appendix B Figure B6**).

The ultimate theoretical LoD for MNA vapor by the PAM-AgNC (PAH) substrate was determined by applying an instrumental error-weighted linear fit to the 857 cm^{-1} peak intensity data shown in **Figure 5.7a** and extrapolating to a signal-to-noise ratio of 3 (**Appendix B Figure B7, B8**). The instrumental error-weighted linear fit weights each data point according to the inverse square of its standard deviation ($w_i = 1/(\sigma_i)^2$), and the noise was determined by calculating the standard deviation from a linear fit to a linear region of the reference spectra. The R-squared value was significantly improved when the saturated data points were excluded from the fitting (**Appendix B Figure B7, B8**). This analysis shows a limit of detection of approximately 600 ppt and 3 ppb for the AgNC-PAH and AgNC-PEI substrates, respectively, demonstrating a LoD more than an order of magnitude better than the AgNS substrate. The LoD of the PAM-AgNS

substrate was not calculated since the standard deviation of the 857 cm^{-1} peak at 30 ppb already puts it at or below the reliable signal-to-noise ratio of 3. The AuNC-(PAH-PSS) substrate demonstrates a LoD of approximately 100 ppb. This decrease in sensitivity compared to the AgNC-PAH and AgNC-PEI substrates is likely due to a decrease in the number of SERS hot spots due to the more dispersed arrangement of AgNC.

5.3.5 Electromagnetic simulations (nanoparticles)

Electromagnetic simulation on AgNC (edge length 40 nm with PVP layer of 1.5 nm thickness) and AgNS (diameter 40 nm with no PVP layer) dimers separated by various inter particle distances clearly shows that the AgNC dimers have a higher integrated electric field intensity than the AgNS dimers for all inter particle distance (**Figure 5.8**). The dimers were excited with a wavelength of 514 nm with a polarization along the long axis of the dimer (labeled in **Figure 5.8** as the E-arrow, where the k-arrow indicates the propagation direction). The electric filed intensity was integrated over a planar profile located at the half height (labeled as the monitor in the top panel of **Figure 5.8**) at the hot-spot area. The integrated electric field intensity in the hot spot as a function of inter particle distance is shown in **Figure 5.8c**. The field intensity was found to be enhanced 50 times for AgNC dimers than that present between AgNS for all inter particle separations.

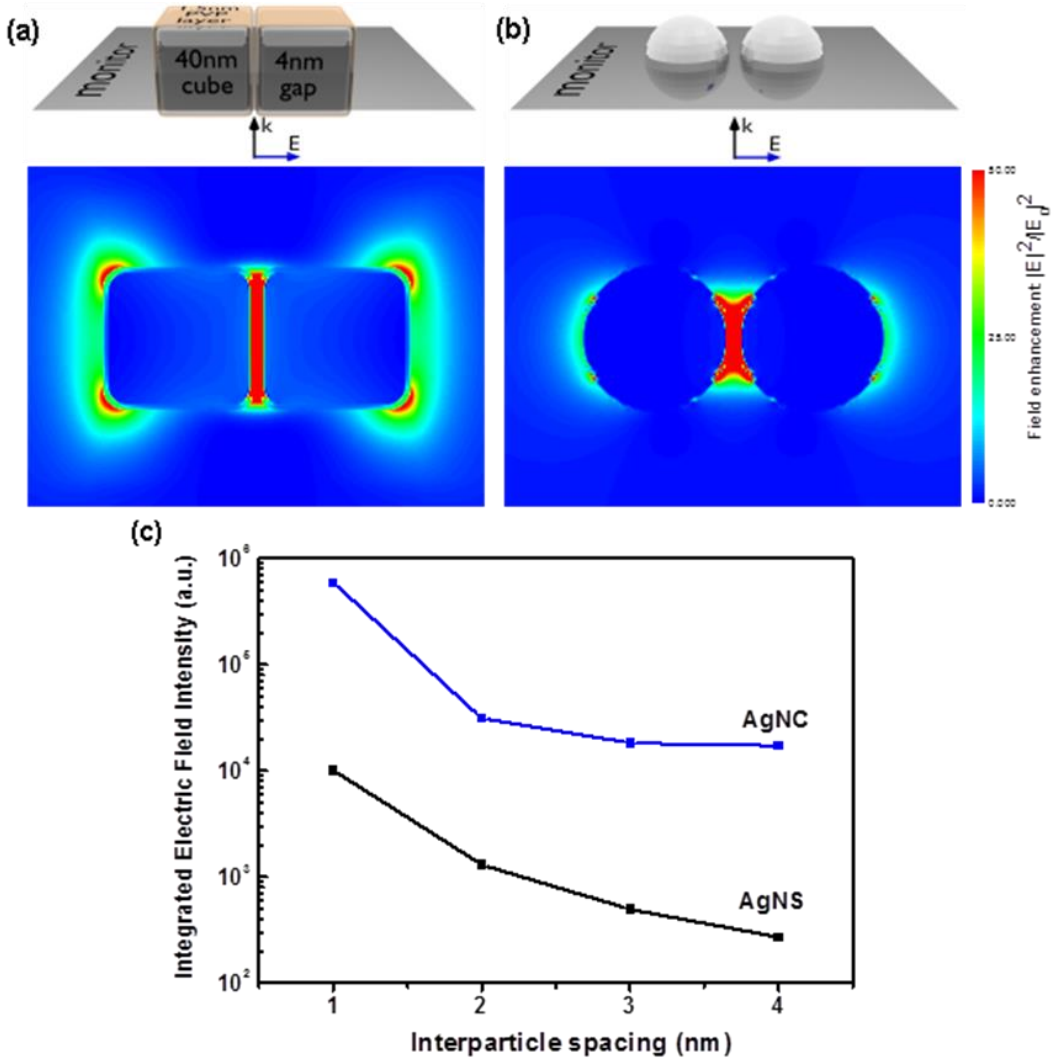

Figure 5.8: FDTD simulation of the electric field intensity at the gap between (a) AgNC (with 40nm edge length) and (b) AgNS (40 nm diameter) dimers. The gap between the nanoparticles is 4 nm. (c) Variation of electric field intensity at the hot-spot as a function of inter-particle separation.

The intensity of the cube dimer is always higher compared to the particle dimer because the cube shape leads to more efficient separation of charges and the high curvature corners allow for larger concentration of charges.[15,16,17] In addition, the presence of aggregates in the PAM-AgNC is higher than that in the PAM-AgNS which suggests more hot spots available for SERS enhancement. Moreover, the AgNC has the (001) plane

exposed at the surface while the nanoparticle surface is dominated by the (111) plane. It has been reported that the surface energy of the (001) plane is higher than that of the (111) plane so molecular adsorption is more favorable for the AgNC and hence SERS activity should increase.[16,30]

5.3.6 Lateral and vertical (depth) SERS mapping

In order to characterize the SERS activity of the 3D PAM-AgNC, Raman mapping of the characteristic MNA peaks in both the (x,y)-plane (substrate surface) and the z-direction (pore depth) of the PAM-AgNC substrate were conducted for the 297 ppb vapor concentration (**Figure 5.9a,b**). The mapping was conducted by monitoring the intensity of the 857 cm^{-1} peak at different z-positions of (x,y) scans. The representative 20 μm by 20 μm 2D Raman map shows that there is a relatively uniform SERS response over the entire region, with a coefficient of variation of 11% of the SERS intensity found by averaging the 3600 data points over the surface area (approximately 300 nm step sizes). This variation is likely a combination of differences in nanoparticle adsorption due to the macroscopic vacuum infiltration process and the inherent difference in nanoparticle adsorption density between the substrate surface and within the pores.

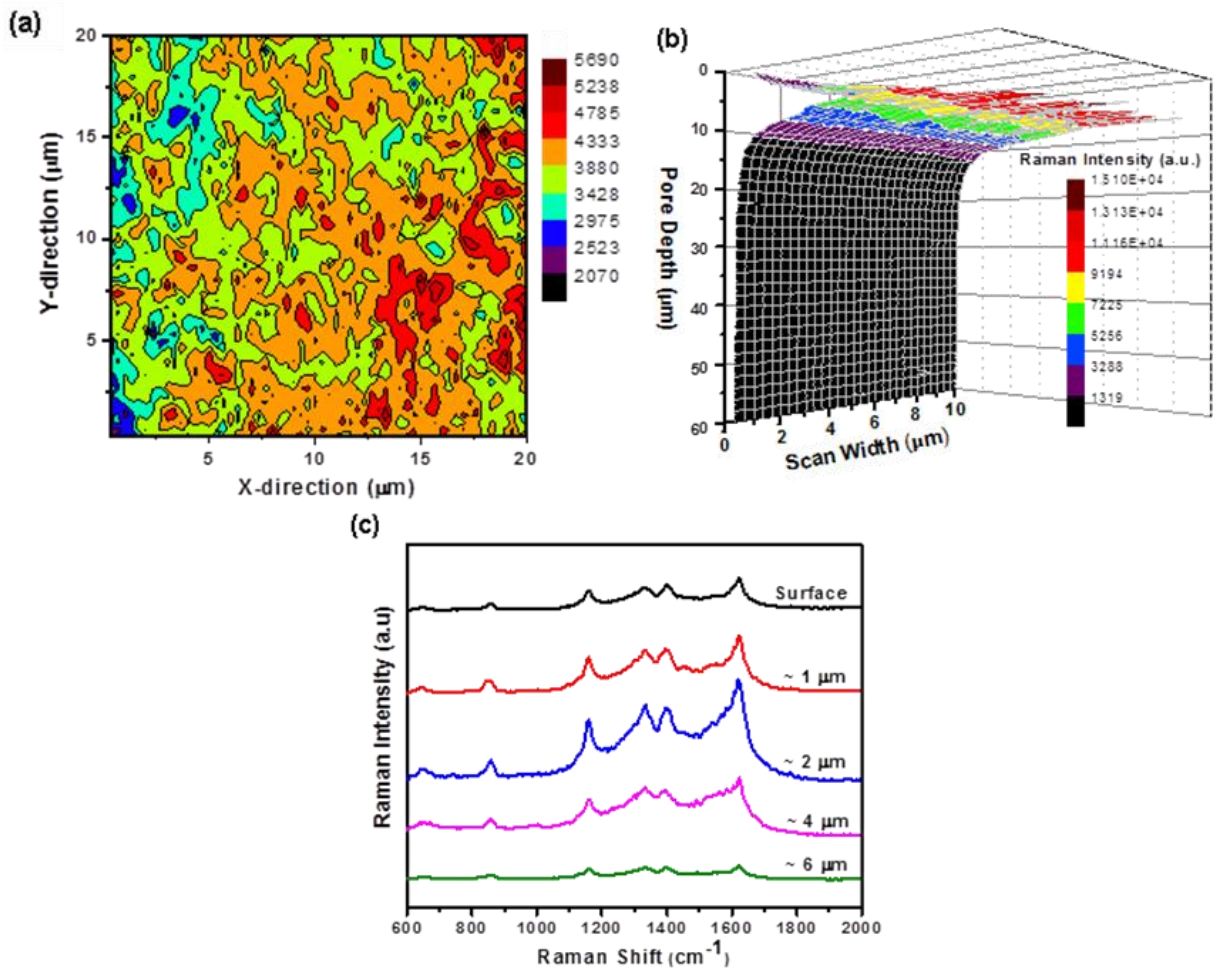

Figure 5.9: (a) Raman surface mapping (20 µm by 20 µm) of the 857 cm^{-1} peak of MNA with PAM-AgNC SERS substrates (the range of Raman signal intensity, Z = 2000-5700 (a.u.). (b) Confocal SERS mapping of the 857 cm^{-1} peak of MNA through the depth of the porous alumina membranes (the range of Raman signal intensity, Z = <1300-15000 (a.u). (c) SERS spectra of MNA extracted at different depths of the PAM-AgNC SERS substrates.

For z-mapping, the SERS activity was mapped by again monitoring the 857 cm^{-1} peak through the depth of the nanopores and it shows that the largest SERS enhancement occurs within the first 3-6 µm depth beneath the PAM surface region similar to previous reports (**Figure 5.9b**).[29,30] SERS spectra of MNA obtained at different depths from the top surface of the PAM show the characteristic MNA spectrum (**Figure 5.9c**). The reduction in intensity of the identifying peaks with depth is likely due to the reduced particle density with pore depth (as mentioned previously). However, the intensity of the 857 cm^{-1} peak is present throughout the whole region of observed high AgNC density which suggests that the large porous nature of the PAM allows MNA molecules to diffuse at least 6 µm into the pores. We suggest that the analyte molecules can access the AgNC surface and get adsorbed. Indeed, the catalytic activity of nanostructures protected with PVP layer suggests that the surface is not fully covered with the polymer,[83] and that the analyte molecules can access the AgNC surface. The total SERS activity reported here may be also a cumulative effect obtained from SERS contributions from multiple depths, which is an added advantage for our PAM-based 3D substrates.

5.3.7 SERS nanoparticle-PAM reusability

The reusability of the substrates was also investigated by exposing the substrates to multiple MNA exposure-ethanol wash cycles. The AgNC substrates were found to be robust against solvent washing and could be readily reloaded for repeated tests. **Figure 5.10** shows the SERS response of the substrate which was exposed to MNA at 45°C after repeated MNA exposure-ethanol washing cycles. The SERS activity of the substrate was monitored by tracking the peak intensity of the 857 cm^{-1} peak (**Figure 5.10b**).

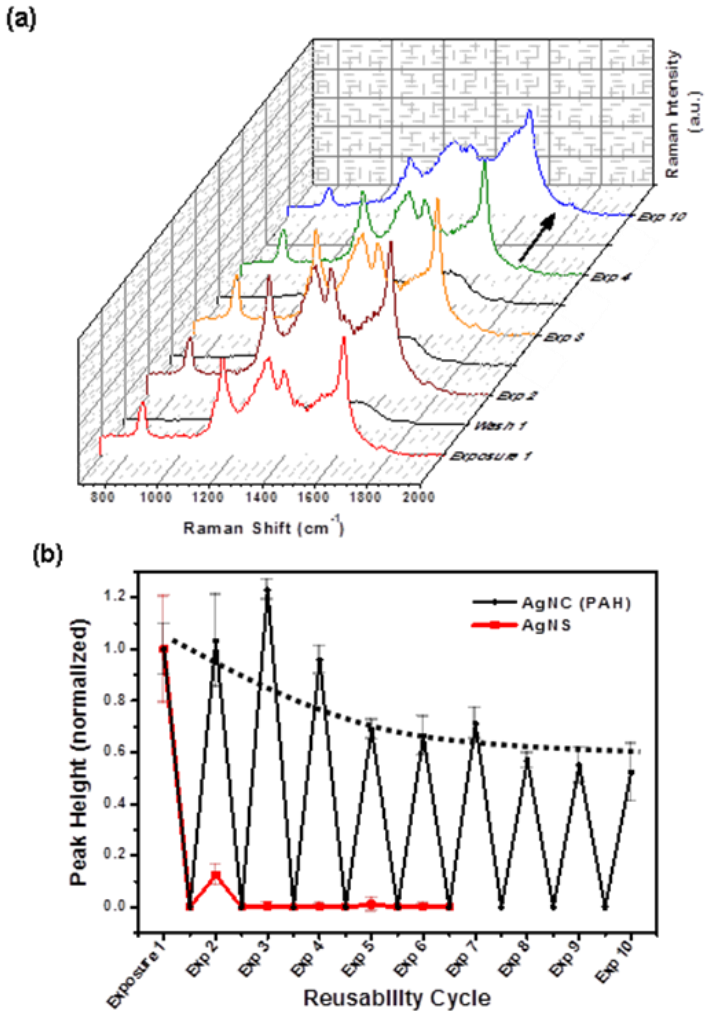

Figure 5.10:(a) SERS responses of PAM-AgNC during repeated MNA exposure-ethanol washing cycles (the sample was exposed to MNA vapor created at 45^{o}C). (b) The normalized SERS response of the 857 cm^{-1} peak through multiple exposure-wash cycles (the dotted line is a visual aid, not a fit). The AgNC (PAH) and AgNS SERS response were normalized according to the intensity of the 857 cm^{-1} peak during the first MNA exposure for each substrate.

The SERS activity remained consistent in the first four repeated measurement-washing cycles and was then found to decrease and finally stabilize in the subsequent cycles. The reduction in intensity is likely due to the removal of lightly bound, physically

adsorbed AgNC during the washing steps. This is further supported by the apparent leveling of the SERS intensity (at later washing steps), which likely occurs as the loose AgNC are removed and the total number of AgNC approaches a constant value. A baseline intensity of <2 % was observed after each washing step (**Figure 5.10b**). The AgNS substrate was not nearly as robust against ethanol washing, showing approximately an 85% decrease from its initial intensity after only one ethanol washing with subsequent cycles showing a decrease in the intensity to nearly zero. This decrease is likely due to oxidation of the AgNS which has been shown to drastically reduce the SERS activity of AgNS.[84] The difference between the AgNC and AgNS substrates in response to washing is likely due to the presence of the PVP capping layer on the AgNC which minimizes degradation of the AgNC by ethanol, whereas the AgNS have no protective polymer capping layer.

5.4 Conclusions

In conclusion, we have demonstrated that AgNC aggregates act as efficient nanostructures for trace level vapor detection of the common Raman marker BT and the explosive binder MNA. The high electric field, higher surface area, and the large hot-spot volume associated with the nanocube-nanocube contacts are efficiently utilized in combination with the enhancement effects provided by PAMs to develop highly active, robust, and reproducible SERS substrates for trace level detection with record sensitivities. A method for varying the adsorption dispersion of AgNC on the PAM pore walls from large aggregates to dispersed AgNC demonstrated the importance of aggregates on SERS effectiveness (by hot spot formation) and also a method to increase the effective range of AgNC substrates by changing the onset of saturation. FDTD simulations support the suggestion that the higher SERS activity of the AgNC

substrates, compared to the AgNS substrate, is due to a combination of higher electric field intensity in gaps and nanocube dimer coupling. The exploration of silver nanocube aggregates on porous substrates show high SERS activity in the vapor phase with a record detection level for BT and MNA (500 ppb and 3 ppb respectively). To the best of our knowledge, this is the first report on the detection of MNA in the vapor phase.

In addition, the AgNC substrates were found to be reusable, demonstrating a consistent SERS activity after multiple exposure-wash cycles. Reusability has therefore become an important design parameter for evaluating the usefulness of SERS detection systems[85,86] and will likely promote the acceptance of SERS as an in-field analytical tool in the areas of life sciences, medical evaluation, and defense. Our results indicate that SERS has the potential to be employed as an effective, consistent detection platform for common explosive stabilizers in the vapor phase over a wide concentration range.

5.5 Chapter acknowledgements

Dr. M.A. Mahmoud (Prof. Mostafa El-Sayed's research lab, Georgia Institute of Technology): synthesizing the colloidal AgNC. Dr. Tobias Koenig (Prof. V.V. Tsukruk's research group, Georgia Institute of Technology): FDTD simulations and analysis.

5.6 References (Chapter 5)

1 Combs, Z.A.; Chang, S.; Clark, T.; Singamaneni, S.; Anderson, K.D.; Tsukruk, V.V., Label-free Raman mapping of surface distribution of protein A and IgG biomolecules. *Langmuir* **2011**, *27,* 3198-3205.

2 Nie, S.M.; Emery, S.R., Probing single molecules and single nanoparticles by surface-enhanced Raman scattering. *Science* **1997**, *275,* 1102-1106.

3 Kneipp, K; Wang, Y.; Kneipp, H.; Perelman, L.T.; Itskan, I.; Dasari, R.; Feld, M.S., Single molecule detection using surface-enhanced Raman scattering (SERS). *Phys. Rev. Lett.* **1997**, *78,* 1667-1670.

4 Camden, J.P.; Dieringer, J.A.; Wang, Y.M.; Masiello, D.J.; Marks, L.D.; Schatz, G.C.; Van Duyne, R.P., Probing the structure of single-molecule surface-enhanced Raman scattering hot spots. *J. Amer. Chem. Soc*. **2008**, *130,* 12616-12617.

5 Kneipp, K.; Kneipp, H.; Deinum, G.; Itzkan, I.; Dasari, R.R.; Feld, M.S., Single-molecule detection of cyanine dye in silver colloidal solution using near-infrared surface-enhanced Raman scattering. *Appl. Spec.* **1998**, *52,* 175-178.

6 Kleinman, S.L.; Ringe, E.; Valley, N.; Wustholz, K.L.; Phillips, E.; Scheidt, K.A.; Schatz, G.C.; Van Duyne, R.P., Single-molecule surface-enhanced Raman spectroscopy of crystal violet isotopologues: Theory and experiment. *J. Amer. Chem. Soc.* **2011**, *133,* 4115-4122.

7 Thaxton, C.S.; Elghanian R.; Thomas, A.D.; Stoeva, S.I.; Lee, J.-S.; Smith, N.D.; Schaeffer, A.J.; Klocker, H.; Horninger, W.; Bartsch, G.; Mirkin, C.A., Nanoparticle-based bio-barcode assay redefines “undetectable” PSA and biochemical recurrence after radical prostatectomy. *Proc. Natl. Acad. Sci. U.S.A.* **2009**, *106,* 18437-18442.

8 Dieringer, J.A., Lettan, R.B., II, Scheidt, K.A., and Van Duyne, R.P. A frequency domain existence proof of single-molecule surface-enhanced Raman spectroscopy. *J. Amer. Chem. Soc*. **2007**, *129*, 16249-16256.

9 Gunnarsson, L.; Bjerneld, E.J.; Xu, H.; Petronis, S.; Kasemo, B.; Kall, M., Inter particle coupling effects in nanofabricated substrates for surface-enhanced Raman scattering. *Appl. Phys. Lett.* **2001**, *78,* 802-804.

10 Mulvihill, M.; Tao, A.; Benjauthrit, K.; Arnold, J.; Yang, P., Surface-enhanced Raman spectroscopy for trace arsenic detection in contaminated water. *Angew. Chem., Int. Ed*. **2008**, *47,* 6456-6460.

11 Li, W.; Camargo, P.H.C.; Au, L.; Zhang, Q.; Rycenga, M.; Xia, Y., Etching and dimerization: A simple and versatile route to dimers of silver nanospheres with a range of sizes. *Angew. Chem., Int. Ed.* **2010**, *49,* 164-168.

12 Talley, C.E.; Jackson, J.B.; Oubre, C.; Grady, N.K.; Hollars, C.W.; Lane, S.M.; Huser, T.R.; Nordlander, P.; Halas, N.J., Surface-enhanced Raman scattering from individual Au nanoparticles and nanoparticle dimer substrates. *Nano Lett*. **2005**, *5,* 1569-1574.

13 Camargo, P.H.C.; Rycenga, M.; Au, L.; Xia, Y., Isolating and probing the hot spot formed between two silver nanocubes. *Angew. Chem., Int. Ed*. **2009**, *48,* 2180-2184.

14 Yang, S.-C.; Kobori, H.; He, C.-L.; Lin, M.-H.; Chen, H.-Y.; Li, C.C.; Kanehara, M.; Teranishi, T.; Gwo, S., Plasmon hybridization in individual gold nanocrystal dimers: Direct observation of bright and dark modes. *Nano Lett*. **2010**, *10,* 632-637.

15 McLellan, J.M.; Seikkinen, A.; Chen, J.; Xia, Y., Comparison of the surface-enhanced Raman scattering on sharp and truncated silver nanocubes. *Chem. Phys. Lett*. **2006**, *427,* 122-126.

16 Yang, Y.; Matsubara, S.; Xiong, L.; Hayakawa, T.; Nogami, M., Solvothermal synthesis of multiple shapes of silver nanoparticles and their SERS properties. *J. Phys. Chem. C* **2007**, *111,* 9095-9104.

17 Rycenga, M.; Kim, M.H.; Camargo, P.H.C.; Cobley, C.; Li, Z.-Y.; Xia, Y., Surface-enhanced Raman scattering: Comparison of three different molecules on single-crystal nanocubes and nanospheres of silver. *J. Phys. Chem. A* **2009**, *113,* 3932-3939.

18 Lu, Y.; Liu, G.L.; Lee, L.P., High-density silver nanoparticle film with temperature-controllable interparticle spacing for a tunable surface enhanced Raman scattering substrate. *Nano Lett* **2005**, *5*, 5-9.

19 McLellan, J.M.; Li, Z.-Y.; Siekkinen, A.R.; Xia, Y., The SERS activity of a supported Ag nanocube strongly depends on its orientation relative to laser polarization. *Nano Lett.* **2007,** *7,* 1013-1017.

20 Mahmoud, M.A.; Tabor, C.E.; El-Sayed, M.A., Surface-enhanced Raman scattering enhancement by aggregated silver nanocube monolayers assembled by the Langmuir-Blodgett technique at different surface pressures. *J. Phys. Chem. C* **2009,** *113,* 5493-5501.

21 Lee, S.Y.; Hung, L.; Lang, G.S.; Cornett, J.E.; Mayergoyz, I.D.; Rabin, O., Dispersion in the SERS enhancement with silver nanocube dimers. *ACS Nano* **2010,** *4,* 5763-5772.

22 Rycenga, M.; Xia, X.; Moran, C.; Zhou, F.; Qin, D.; Li, Z.-Y.; Xia, Y., Generation of hot spots with silver nanocubes for single-molecule detection by surface-enhanced Raman scattering. *Angew. Chem., Int. Ed*. **2011**, *50*, 5473-5477.

23 Wu, H.L.; Tsai, H.R.; Hung, Y.T.; Lao, K.U.; Liao, C.W.; Chung, P.J.; Huang, J.S.; Chen, I.C.; Huang, M.H., A comparative study of gold nanocubes, octahedra, and rhombic dodecahedra as highly sensitive SERS substrates. *Inorganic Chem.* **2011,** *50*, 8106-8111.

24 Lee, S.Y.; Rabin, O., A unique solid-solid transformation of silver nanoparticles on reactive ion-etching-processed silicon. *Nanotechnology* **2012,** *23*, 065301.

25 Costa, J.C.S.; Ando, R.A.; Sant'Ana, A.C.; Rossi, L.M.; Santos, P.S.; Temperini, M.L.A.; Corio, P., High performance gold nanorods and silver nanocubes in surface-enhanced Raman spectroscopy of pesticides. *Phys. Chem. Chem. Phys.* **2009,** *11*, 7491-7498.

26 Saito, M.; Shibasaki, M.; Nakamura, S.; Miyagi, M., Optical waveguides fabricated in anodic alumina films. *Opt. Lett.* **1994,** *19*, 710-712.

27 Lau, K.H.A.; Tan, L.-S.; Tamada, K.; Sander, M.S.; Knoll, W., Highly sensitive detection of processes occurring inside nanoporous anodic alumina templates: A waveguide optical study. *J. Phys. Chem. B* **2004,** *108*, 10812-10818.

28 Chang, S.; Ko, H.; Singamaneni, S.; Gunawidjaja, R.; Tsukruk, V.V., Nanoporous membranes with mixed nanoclusters for Raman-based label-free monitoring of peroxide compounds. *Anal. Chem.* **2009,** *81,* 5740-5748.

29 Kodiyath. R.; Wang. J.; Combs, Z.A.; Chang, S.; Gupta, M.K.; Anderson, K.D.; Brown, R.J.C.; Tsukruk, V.V., SERS effects in silver-decorated cylindrical nanopores. *Small* **2011,** *7,* 3452-3457.

30 Kodiyath. R.; Papadopoulos. T.A.; Wang. J.; Combs, Z.A.; Li, H.; Brown, R.J. C.; Bredas, J.-L.; Tsukruk, V.V., Silver-decorated cylindrical nanopores: combining the third dimension with chemical enhancement for efficient trace chemical detection with SERS. *J. Phys. Chem. C* **2012,** *116,* 13917-13927.

31 Dobrokhotov, V.; Oakes, L.; Sowell, D.; Larin, A.; Hall, J.; Kengne, A.; Bakharev, P.; Corti, G.; Cantrell, T.; Prakash, T.; Williams, J.; McIlroy, D.N., Toward the nanospring-based artificial olfactory system for trace-detection of flammable and explosive vapors. *Sens. Actuators B* **2012***,168,* 138-148.

32 Zhang, W.; Qiu, L.-G.; Yuan, Y.-P.; Xie, A.-J.; Shen, Y.-H.; Zhu, J.-F., Microwave-assisted synthesis of highly fluorescent nanoparticles of a melamine-based porous covalent organic framework for trace-level detection of nitroaromatic explosives. *J. Hazard. Mater*. **2012**, *221,* 147-154.

33 Yang, L.; Ma, L.; Chen, G.; Liu, J.; Tian, Z.Q., Ultrasensitive SERS detection of TNT by imprinting molecular recognition using a new type of stable substrate. *Chem. Eur. J*. **2010**, *16,* 12683-12693.

34 Ko, H.; Tsukruk, V.V., Nanoparticle-decorated nanocanals for surface-enhanced Raman scattering. *Small* **2008**, *4,* 1980-1984.

35 Ko, H.; Chang, S.; Tsukruk, V.V., Porous substrates for label-free molecular level detection of nonresonant organic molecules. *ACS Nano* **2009**, 3*,* 181-188.

36 Dasary, S.S.R.; Singh, A.K.; Senapati, D.; Yu, H.; Ray, P.C., Gold nanoparticle based label-free SERS probe for ultrasensitive and selective detection of trinitrotoluene. *J. Amer. Chem. Soc*. **2009**, *131,* 13806-13812.

37 Schmidt M.S.; Boisen, A., *Advanced Environmental, Chemical, and Biological Sensing Technologies VII*, Orlando, Florida, USA, **2010.**

38 Sylvia, J.M.; Janni, J.A.; Klein, J.D.; Spencer, K.M., Surface-enhanced Raman detection of 2,4-dinitrotoluene impurity vapor as a marker to locate landmines. *Anal. Chem.* **2000,** *72,* 5834-5840.

39 Li, Y.S.; Vo-Dinh, T.; Stokes, D.L.; Yu, W., Surface-enhanced Raman analysis of p-nitroaniline on vacuum evaporation and chemically deposited silver-coated alumina substrates. *Appl. Spec.* **1992,** *46*, 1354-1357.

40 Holze, R., The adsorption of para-niotroaniline on silver and gold electrodes as studied with surface enhanced Raman-spectroscopy (SERS). *Electrochimica Acta* **1990,** *35*, 1037-1044.

41 Ma, W.Q.; Fang, Y., Experimental (SERS) and theoretical (DFT) studies on the adsorption of p-, m-, and o-nitroaniline on gold nanoparticles. *J. Colloid and Interface Sci.* **2006,** *303*, 1-8.

42 Bakken, G.A.; Kauffman, G.W.; Jurs, P.C.; Albert, K.J.; Stitzel, S.S., Pattern recognition analysis of optical sensor array data to detect nitroaromatic compound vapors. *Sens. Actuators B* **2001,** *79,* 1-10.

43 Snels, M.; Venezia, T.; Belfiore, L., Detection and identification of TNT, 2,4-DNT and 2,6-DNT by near-infrared cavity ringdown spectroscopy. *Chem. Phys. Lett.* **2010,** *489,* 134-140.

44 Aguilar, A.D.; Forzani, E.S.; Leright, M.; Tsow, F.; Cagan, A.; Iglesias, R.A.; Nagahara, L.A.; Amlani, I.; Tsui, R.; Tao, N.J.A., Hybrid nanosensor for TNT vapor detection. *Nano Lett.* **2009,** *10,* 380-384.

45 Office of Naval Research. Combat Safe Insensitive Munitions Program. http://www.onr.navy.mil/Science-Technology/Departments/Code-35/All-Programs/aerospace-research-351/combat-safe-insensitive-munitions.aspx (accessed **July 23, 2012**).

46 U.S. Army. Modernizing and equipping the force (Part 1). http://www.army.mil/article/49954/ (accessed **July 23, 2012**), **December 30, 2010**.

47 Global security. insensitive munitions. http://www.globalsecurity.org/military/systems/munitions/im.htm (accessed J**uly 23, 2012**).

48 Joint Requirements Oversight Council. Insensitive Munitions Certification Policy. http://www.insensitivemunitions.org/wp-content/uploads/2011/06/annex3.jpg (accessed **July 23, 2012**), The Joint Staff, Washington, D.C. **July 2, 2004**.

49 Doll, D.W.; Rasmussen, N., Impact resistant explosive compositions. *U.S. Patent 7,744,710,* **June 29, 2010**.

50 Viecelli, J.A.; Wood, L.L.; Ishikawa, M.Y.; Nuckolls, J.H.; Pagoria, P.F., Explosively driven low-density foams and powders. *U.S. Patent 7,707,819,* **May 4, 2010**.

51 Fleming, W.C.; McSpadden, H.J.; Olander, D.E., Ammonium nitrate propellants and methods for preparing the same. *U.S. Patent 6,913,661* **July 5, 2005**.

52 Beanard, P.W.: Fouche, F.C.; Bezuidenhout, H.C., *Australian Explosive Ordance Symposium (Parari' 1997)*, **1997,** *12.*

53 Agrawal, J.P.; Hodgson, R.D., Organic chemistry of explosives, *John Wiley & Sons, Chichester,* **2007**.

54 Nicolish, S.; Niles, J.; Ferlazzo, P.; Doll, D.; Braithwaite, P.; Rausmussen, N.; Ray, M.; Gunger, M.; Spencer, A., Recent developments in reduced sensitivity melt pour explosives, *34th Int. Ann. Conf. of ICT, Karlsruhe, Germany*, **2003**, *135,* 1-21.

55 Toghiani, R.K.; Toghiani, H.; Maloney, S.W.; Boddu, V.M., Prediction of physicochemical properties of energetic materials. In energetic materials: thermophysical properties, predictions, and experimental measurements. *Boddy, V.; Redner, P. Taylor and Francis Group LLC.,* **2011,** pp 171-195.

56 Chang, S.; Combs, Z.A.; Gupta, M.K.; Davis, R.; Tsukruk, V.V., In situ growth of silver nanoparticles in porous membranes for surface-enhanced Raman scattering. *ACS Appl. Mater. & Interfaces* **2010,** *2,* 3333-3339.

57 Tsukruk, V.V., Assembly of supramolecular polymers in ultrathin films. *Prog. Polym. Sci*. **1997** *22,* 247-311.

58 Lee, W.; Scholz, R.; Nielsch, K.; Gosele, U.A., Template-based electrochemical method for the synthesis of multisegmented metallic nanotubes. *Angew. Chem. Int. Ed*. **2005**, *44*, 6050-6054.

59 Fang, X.; Ahmad, S.R., Detection of explosive vapour using surface-enhanced Raman spectroscopy. *Appl. Phys. B*. **2009**, *97*, 723-726.

60 Oo, M.K.K.; Guo, Y.; Reddy, K.; Liu, J.; Fan, X., Ultrasensitive vapor detection with surface-enhanced Raman scattering-active gold nanoparticle immobilized flow-through multihole capillaries. *Anal. Chem*. **2012**, *84*, 3376-3381.

61 Gaussian 03, revision C.06. Frisch, M.J.; Trucks, G.W.; Schlegel, H.B.; Scuseria, G.E.; Robb, M.A.; Cheeseman, J.R.; Montgomery, Jr., J.A.; Vreven, T.; Kudin, K.N.; Burant, J.C et.al *Gaussian Inc., Wallingford CT,* **2004.**

62 Taflove, A., Computational electrodynamics - The finite difference time-domain method, *Artech House,* **1995**.

63 Yee, K.S., IEEE trans. on Antennas and propagation ap-14, **1966,** *302*.

64 Mahmoud, M.A.; Chamanza, M.; Adibi, A.; El-Sayed, M.A., Effect of the dielectric constant of the surrounding medium and the substrate on the surface plasmon resonance spectrum and sensitivity factors of highly symmetric systems: silver nanocubes, *J. Amer. Chem. Soc.* **2012**, *134*, 6434-6442.

65 Grillet, N.; Manchon, D.; Bertorelle, F.; Bonnet, C.; Broyer, M.; Cottancin, E.; Lerme´ J.; Hillenkamp, M.; Pellarin, M., Plasmon coupling in silver nanocube dimers: Resonance splitting induced by edge rounding. *ACS Nano*, **2011**, *12*, 9450-9462.

66 Haynes. W.M., CRC Handbook of chemistry and physics. *CRC PRESS*, *81 edition*, **2000**.

67 Palik. E.D., Handbook of optical constants of solids. *Academic Press, New York,* **1985**.

68 Lahav, M.; Sehayek, T.; Vaskevich, A.; Rubinstein, I., Nanoparticle nanotubes. *Angew. Chem., Int. Ed.* **2003** *42,* 5575-5579.

69 Bruening, M.L.; Dotzauer, D.M.; Jain, P.; Baker, G.L., Creation of functional membranes using polyelectrolyte multilayers and polymer brushes. *Langmuir* **2008**, *24,* 7663-7673.

70 Jiang, C.; Tsukruk, V.V., Free standing nanostructures via layer-by-layer assembly. *Adv. Mater*. **2006**, *18,* 829-840.

71 Aizenberg, J.; Braun, P.V.; Wiltzius, P., Patterned colloidal deposition controlled by electrostatic and capillary forces. *Phys. Rev. Lett.* **2000,** *84,* 2997-3000.

72 Bell, G.M.; Levine, S.; McCartney, L.N., Approximate methods of determining the double-layer free energy of interaction between two charged colloidal spheres. *J. Colloid Interface Sci.* **1970,** *33,* 335-359.

73 Gao, B.; Arya, G.; Tao, A.R., Self-orienting nanocubes for the assembly of plasmonic nanojunctions. *Nat. Nanotech* **2012,** *7*, 433-437.

74 Mahmoud, M.A.; El-Sayed, M.A., Comparative study of the assemblies and the resulting plasmon fields of Langmuir−Blodgett assembled monolayers of silver nanocubes and gold nanocages. *J. Phys. Chem. C* **2008**, *112*, 14618-14625.

75 Cobley, C.M.; Rycenga, M; Zhou, F; Li Z. Y.; Xia, Y., Controlled etching as a route to high quality silver nanospheres for optical studies. *J. Phys. Chem. C*, **2009**, *113* 16975-16982.

76 Hohlbein, J.; Rehn, U.; Wehrspohn, R.B., In-situ optical characterisation of porous alumina. *Phys. Stat. Sol*. *A* **2004**, *201*, 806-810.

77 Mock, J.J.; Smith, D.R.; Schultz, S., Local refractive index dependence of plasmon resonance spectra from individual nanoparticles. *Nano Lett*. **2003**, *3*, 485-491.

78 Haynes, C.L.; Van Duyne, R.P., Plasmon-sampled surface-enhanced Raman excitation spectroscopy. *J. Phys. Chem. B* **2003**, *107*, 7426-7433.

79 Alvarez-Puebla, R.A.; Santos Jr., D.S.; Aroca, R.F., SERS detection of environmental pollutants in humic acid–gold nanoparticle composite materials. *Analyst* **2007**, *132*, 1210-1214.

80 Biggs, K.B.; Camden, J.P.; Anker, J.N.; Van Duyne, R.P., Surface-enhanced Raman spectroscopy of benzenethiol adsorbed from the gas phase onto silver film over nanosphere surfaces: Determination of the sticking probability and detection limit time. *J. Phys. Chem. A* **2009**, *113,* 4581-4586.

81 Ma, W.; Fang, Y., Experimental (SERS) and theoretical (DFT) studies on the adsorption of p-, m-, and o-nitroaniline on gold nanoparticles. *J. Colloid Interface Sci.* **2006**, *303*, 1-8.

82 Kulkarni, D.D.; Kim, S.; Fedorov, A.G.; Tsukruk, V.V., Light-induced plasmon-assisted phase transformation of carbon on metal nanoparticles. *Adv. Func. Mater.* **2012**, *22*, 2129-2139.

83 Mahmoud, M.A.; Saira, F.; El-Sayed, M.A., Experimental evidence for the nanocage effect in catalysis with hollow nanoparticles. *Nano Lett*. **2010**, *10*, 3764-3769.

84 Han, Y.; Lupitskyy, R.; Chou, T.M.; Stafford, C.M.; Du, H.; Sukhishvili, S., Effect of oxidation on surface-enhanced Raman scattering activity of silver nanoparticles: A quantitative correlation. *Anal. Chem.* **2011,** *83*, 5873-5880.

85 Lin, Yi.; Bunker, C.E.; Fernando, K.A.; Connel, J.W., Aqueously dispersed silver nanoparticle-decorated boron nitride nanosheets for reusable, thermal oxidation-resistant surface enhanced Raman spectroscopy (SERS) devices. *ACS Appl. Mater. & Interfaces* **2012,** *4,* 1110-1117.

86 Aldeanueva-Potel, P.; Faoucher, E.; Alvarez-Puebla, R.A.; Liz-Marzan, L.M.; Brust, M., Recyclable molecular trapping and SERS detection in silver-loaded agarose gels with dynamic hot spots. *Anal. Chem.* **2009,** *81,* 9233-9238.

CHAPTER 6

HOW QUANTUM DOT ARCHITECTURE AFFECTS THE EVOLUTION OF EMISSION: DECAY, RECOVERY, AND DECAY-TO-RECOVERY BEHAVIOR

Chapter Based On:
Malak, S.T.; Yoon, Y.J.; Smith, M.J.; Lin, C.H.; Jung, J.; Lin, Z.; Tsukruk, V.V., Decay-to-recovery behavior and controllable on-off recovery of emission: The importance of the quantum dot composition profile, *in preparation.*

Chapter Overview

Quantum dots (QDs) are an ideal nanostructure for studying confinement mechanisms in light emitting systems since they experience quantum confinement of their exciton (electron-hole pair), a fascinating phenomenon that allows their photoluminescence (light emission) to be tuned across the visible spectrum. However, a survey of the literature showed a general lack of confirmation of how quantum confinement of the exciton (and its relaxation pathways) can evolve when the QDs are encapsulated into polymer matrices in films. Therefore, an in-depth examination of the evolution of photoluminescence from CdSe core, CdSe/ZnS core/shell, and CdSe/$Cd_{1-x}Zn_xSe_{1-y}S_y$ core/graded shell QDs is presented.

It is shown that the composition profile of the quantum dot significantly affects how the optical characteristics evolve in darkness and under light exposure, with distinct shifts of emission occurring. For example, decreases and increases of intensity and spectral position are all observed, which can be reversible or irreversible depending on QD architecture and exposure conditions (**Figure 6.1**). Furthermore, it is revealed that competition between the reversible and irreversible mechanisms underlying these optical changes can lead to: unique decay-to-recovery behavior for intensity, meta-stable bright states that can be activated and deactivated numerous times, and decoupled optical changes (reversible intensity changes versus

irreversible spectral shifts). Furthermore, there is a large difference of rate between the decay and recovery mechanisms (seconds versus many minutes), which means fast mechanisms (like immediate decay upon light exposure) have likely been entirely overlooked in previous QD stability studies. The distinct response of each QD architecture arises from how the core and shell material interact with each other (crystal lattice mismatches) and the environment (oxygen, H_2O, and light). The results clearly demonstrate that the QD composition profile is a critical factor to consider when evaluating QDs for use in photonic systems. This work can act as a general framework for evaluating quantum dots in future studies where stable emission is required to obtain meaningful results (like the variable strip length method or fluorescence lifetime imaging), and in situations where long device lifetimes are desired (LEDs and lasers).

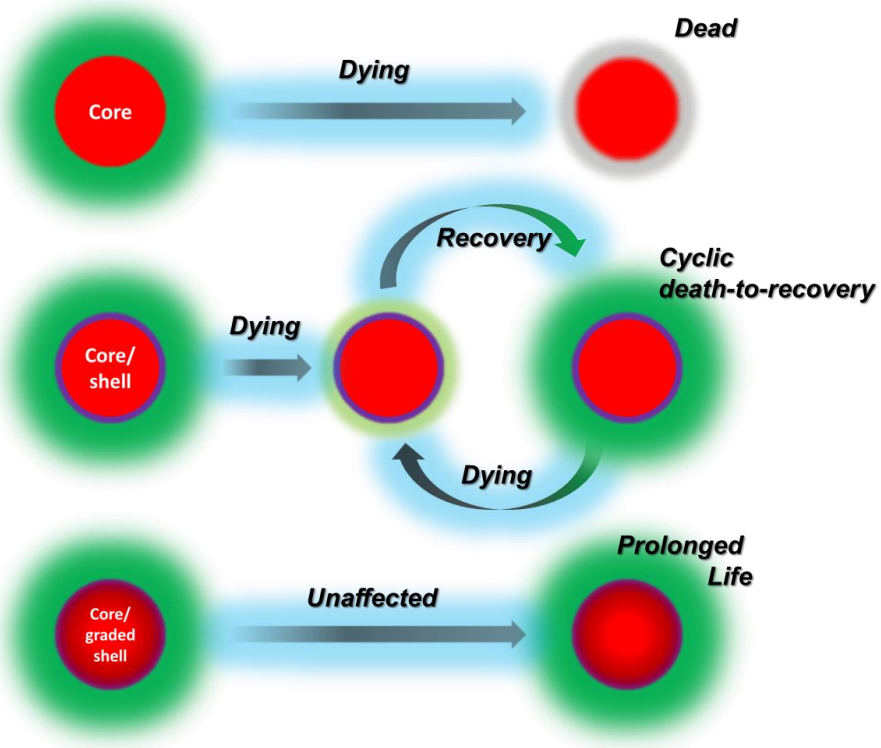

Figure 6.1: General schematic outlining the general PL intensity trends that occur when the QDs are exposed to light. The design of a quantum dot (core, core/shell, or core/graded shell) strongly influences how the emission evolves, with intensity decay, cyclic decay-to-recovery, and stable emission all possible.

6.1 Introduction

6.1.1 Quantum dot optical characteristics

Quantum dots have gained significant interest in the area of photonics due to their tunable emission across the visible spectrum, narrow emission bands, and high quantum yields.[1] In addition, these small semiconductor nanoparticles are compatible with many surface functionalization schemes,[1] deposition approaches,[2,3] and patterning techniques,[4,5] making them ideal candidates for a variety of technologies including LEDs,[6,7] solar cells,[8] lasing media,[2,3] and cell tracking.[9]

The wide range of applications for quantum dots (QDs) have therefore resulted in a large amount of research examining how to the compositional profile (core, core/shell, and core/graded shell) can be used to tune the optical properties in a controllable manner.[10,11,12,13,14] Typically, the introduction of a protective inorganic shell around a QD core improves properties, with graded or alloyed core/shell interfaces providing the greatest improvements.[13,14] QDs are commonly evaluated by considering steady-state characteristics like quantum yield, emission FWHM, photoluminescence (PL) lifetime, and Auger relaxation dynamics, with significant improvements occurring since initial QD discovery.[10-15] The formation and dynamics of single excitons and multiexcitons have also been shown to depend on the presence (and type) of inorganic shell.[16,17] However, one of the most critically important metrics of evaluation, emission stability, and how its dependence on the QD composition profile has not been thoroughly investigated.

6.1.2 Quantum dot emission stability

The issue of QD emission stability (in terms of spectral position, FWHM, and intensity) are very important to consider for characterization techniques like the variable strip length method (for

optical gain) or fluorescence lifetime imaging (for cellular and nanoparticle imaging/tracking) where stable emission is required to obtain meaningful results.[9,18,19] Additionally, QD stability is critically important in photonic systems that need to have a long lifetime but which experience a variety of environmental conditions (QD LEDs, displays, and lasers).[6,20,21] Deviations from perfect emission stability can therefore introduce unreliable results or non-ideal system properties. On the other hand, in some instances like in photopatterning, unstable QD emission behavior is actually necessary.[22] These issues make it critical to understand the mechanisms present in QDs that can lead to an evolution of emission.

Various studies have examined how the emission of quantum dots evolve in response to chemicals, gaseous environments, polyelectrolyte matrices, substrates, and light exposure.[23,24,25,26,27] Spectral blue shifting is a very common phenomenon and is caused by an increase of quantum confinement of the exciton due to a reduction of QD size. Typically size reduction is attributed to chemical or photochemical oxidation and corrosion of the QD surface,[28],[29,30,31] since it can be significantly reduced placing QDs in a nitrogen environment or vacuum.[31,32,33] Spectral blue shifting of PL can vary from a few nanometers in dark environments (simple oxidation),[32] to 15-20 nm under light exposure (photooxidation).[28,31,32]
Changes of QD emission intensity (decreases and increases) have also been observed. In general, intensity is altered by modifying non-radiative trap states, which includes bypassing (via a more efficient recombination pathway), saturating (by ligand, H_2O, or charge carriers), or removing these pathways (shelling, photo-restructuring/annealing of the QD surface). The variety of mechanisms that affect emission makes the evaluating and understanding the situation complex. In general, increases of PL intensity are much more common in the literature than decreases. For example, increasing intensity upon light exposure have been attributed to photoactivation (in vacuum),[32] photo- induced H_2O defect passivation,[28] increased coordination of ligands with the QD surface via pH changes or light,[34,35] and photo-induced surface

annealing/restructuring.[31] On the other hand, decreases (photobleaching) of PL intensity have been credited to the formation of surface quenching states during photooxidation.[32,33] Interestingly, photobleaching has been shown to still occur in a nitrogen environment, so it has been suggested that the formation of lattice defects in the CdSe/ZnS QD likely leads to nonradiative recombination pathways.[36]

Additional complexity is added by the fact that some of these changes are reversible and some irreversible. For example, reversible changes to intensity were demonstrated by heat cycling (due to photoinduced surface transformation),[37] pressure cycling (due to adsorption/desorption of H_2O),[28] and light exposure cycling (due to light-activated rearrangement of surfactant molecules).[35] Additional complications include the variety of rates over which these changes can occur (seconds versus minutes versus hours). For example, studies that utilized PL integration times on the order of 20 seconds to 2 minutes might have missed changes occurring within the first seconds of light exposure.[38,39]

Studies have presented routes for mediating these changes to emission, typically involving the introduction of an inorganic protective shell around the QD core where the exciton is located.[31,32,35] For example, previous studies have compared CdSe core QDs to CdSe/ZnS core/shell QDs in a variety of environments.[32] However, these measurements were performed either under continuous darkness or continuous light exposure without checking for reversibility and therefore did not observe the unique light-mediated on-off (reversible) PL intensity recovery outlined in this work.

In this work, we examine how the emission from QD-polymer films with different QD architectures (core, core/shell, core/graded shell) evolve when in darkness, when exposed to light, and when put through light-dark-light cycles. In short, responsive behavior can be

engineered into a QD by ensuring that the CdSe core (where the exciton is located) is exposed to the environment, either upon synthesis or through chemical/physical modification/degradation of the protective inorganic shell by light, oxygen, and water. Furthermore, the competition between reversible and irreversible mechanisms can lead to unique decay-to-recovery behavior for intensity, meta-stable bright states that can be turned on and off many times, and decoupled optical changes (reversible intensity changes versus irreversible spectral shifts). Furthermore, there is a large difference of rate between the decay and recovery mechanisms (seconds versus many minutes), which means fast mechanisms (like immediate decay upon light exposure) have likely been overlooked in previous QD stability studies. The distinct response of each QD architecture arises from how the core and shell material interact with each other (crystal lattice mismatches) and the environment. This work can act as a general framework for evaluating quantum dots in future studies where stable emission is required to obtain meaningful results and in situations where long device lifetimes are desired.

6.2 Experimental details

Sample preparation. QD-polymer films had a QD-loading of approximately 1% (volume fraction) and thickness of 270 nm (±50 nm). They were fabricated by spin-casting a QD-polymer mixture at 2500 rpm for 1 min, as outlined previously.[22] The QD-polymer mixture was made by mixing equal volumes of QD (toluene) solution with a 10-12% PMMA (toluene) solution, which was then vortexed. Films were deposited on silicon with a ≈290 nm surface layer of SiO_2.

Characterization. Photoluminescence evolution studies of QDs in solution were performed using UV–vis extinction spectra of quantum dots in solution using a quartz cuvette. A spectral range of 400–750 nm (1 nm intervals) was used. Data was collected using a Shimadzu UV–vis-

2450 spectrometer with D2 and tungsten lamps provided a wavelength range of 300-1100 nm. Extinction spectra were corrected against the solvent background using the same quartz cuvette. Photoluminescence of QDs in solution were collected using a Shimadzu RF-5301PC spectrofluorophotometer.

The photoluminescence evolution studies of QD-polymer films were carried out by examining spectra of the QD-polymer films from hyperspectral datacubes that were collected using a CytoViva Hyperspectral scanning system with a diffraction grating spectrophotometer (spectral range: 400-1000 nm). The evolution of photoluminescence (PL) intensity the various QD types was examined under continuous light exposure (450-490 nm) over a period of 45 minutes. A 10x objective (NA: 0.30) was used during scanning. All power values are the power measured at 470 nm (center wavelength of the 450-490 nm blue filter bandwidth). The photoluminescence filter cube had optical excitation from a blue bandpass filter (450-490 nm) with a dichroic mirror that reflects optical wavelengths below 495 nm and with a longpass emission filter that passes optical wavelengths above 500 nm. A 0.25 second exposure time (per line) was used for most scans, with the early dynamics collected by treating a line of a hyperspectral data cube as a point in time (approximately 650 points per line were averaged). Hyperspectral scanning was performed using the same blue excitation bandpass filter (450-490 nm) used for light exposure. The light source was a 120 W Hg vapor short arc lamp with controllable power output (X-cite series, 120Q, Lumen Dynamics). Note, a Savitzky-Golay filter was applied in some instances to reduce high frequency noise.

For the PL evolution studies of QD-polymer films in darkness, each data point (at each time step) were collected from a region of the film that had not yet been exposed to light. This approach helped minimize “contaminating” the darkness study by previous light exposure. The continuous light exposure evolution study of QD-polymer films focused on a single region of the

film throughout the entire exposure period (typically 45 minutes). Each hyperspectral scan composed approximately (650 points) which were averaged together. Three evolution trials of 45 minutes were then averaged together. The light exposure-darkness-light exposure experiment was performed by also examining a specific region of the QD-polymer film throughout the trial. The darkness step was performed by closing the shutter on the microscope, which allowed the sample to remain in the same spot after the measurement resumed. All evolution studies were performed under ambient temperature, pressure, and atmosphere unless otherwise specified.

6.3 Results and discussion

6.3.1 QD optical characteristics

Core, core/shell, and core/graded shell QDs were used to examine how the compositional profile affects the general optical characteristics in the solution state (**Table 6.1**). Each QD type displays a broadband absorbance down to the UV and narrowband emission in the green region (**Appendix C Figure C.1**).

Table 6.1: Optical characteristics of the CdSe core, CdSe/ZnS core/shell, and CdSe/$Cd_{1-x}Zn_xSe_{1-y}S_y$ core/graded shell QDs in the solution state.

Quantum Dot	Composition	Absorption Peak (nm)	PL Peak (nm)	Stokes Shift (nm)	FWHM (nm)	Quantum Yield (%)
Core	CdSe	553	560	7	26	3
Core/shell	CdSe/ZnS	546	554	8	28	16
Core/graded shell	$CdSe/Cd_{1-x}Zn_xSe_{1-y}S_y$	492	508	16	33	73

In addition, the full-width half-maximum (FWHM) of all the QD types is under 35 nm, indicating a relatively homogeneous size distribution. However, the quantum yield (QY) shows a strong

dependence on QD composition profile, with the core CdSe QDs having the lowest QY and the core/graded shell CdSe/$Cd_{1-x}Zn_xSe_{1-y}S_y$ QDs having the highest QY. The significant increase of QY for the core/shell and core/graded shell QDs can be attributed to the passivation of the CdSe core surface states.[14,15,40,41] In addition, core/shell alloying provides more effective surface passivation via the removal of defect sites that arise from the crystal lattice mismatch (12%) between CdSe and ZnS.[14,41] These trends are consistent with previous studies examining how QD shelling can influence the optical characteristics.[14,41,42]

6.3.2 Emission evolution: darkness

In addition to quantum yield, the QD composition profile should also strongly influence the optical stability (intensity and spectral position) of the QDs since the environment can lead to changes in the QD surface composition (oxidation, corrosion, etc.) which can affect surface passivation and the relaxation pathways available to the exciton (trap states and non-radiative relaxation pathways). The QD composition profile becomes particularly important for type-I QD designs since the exciton can be localized to the QD core and therefore isolated from the environment. Furthermore, QD composition profile is very important when QDs are encapsulated into polymer films since the QDs are in close contact with a variety of additional factors (oxygen, moisture, and surrounding material) that have been shown to cause changes of the spectral position and quantum yield of QDs.[22,32,33]

To examine how QD composition profile affects photoluminescence stability in a dark environment (ambient atmosphere, temperature, pressure, each type of QD (core, core/shell, core/graded shell) was deposited into a film (QD-polymer composition). All QD-polymer films uniformly covered the substrate, exhibiting minimum scattering, and displayed uniform PL emission (**Appendix C Figure C.2**). The photoluminescence (PL) intensity and spectral

position were then monitored over a period of 45 minutes. The composition profile of the QD was found to strongly influence how the intensity and spectral position evolve during this period of darkness (**Figure 6.2**). The core CdSe QDs display a large decrease of intensity (↓95%) and moderate blue shift (5 nm), which we believe result from oxidation and corrosion of the CdSe surface to $CdSeO_2$, and activates non-radiative surface quenching states (**Figure 6.3**).[32,33]

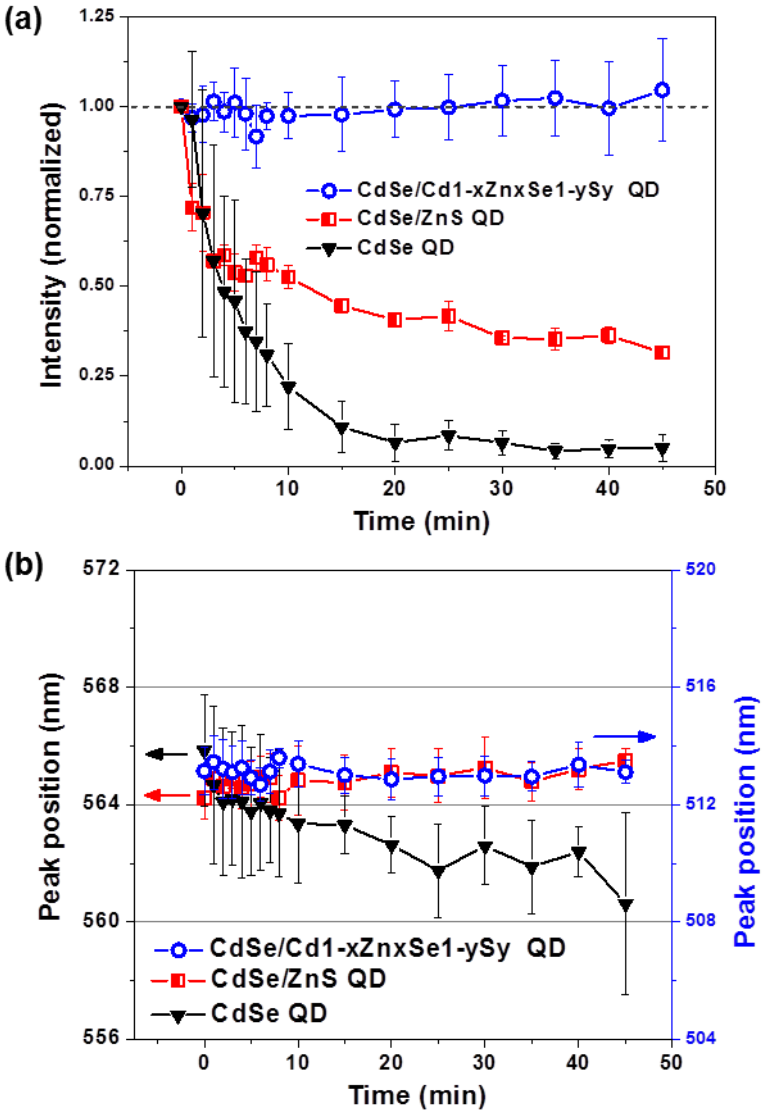

Figure 6.2: Evolution of the PL intensity (a) and spectral position (b) of QD-PMMA films using the CdSe core, CdSe/ZnS core/shell, or CdSe/$Cd_{1-x}Zn_xSe_{1-y}S_y$ core/graded shell QDs under darkness.

The core/shell CdSe/ZnS QD undergoes a less pronounced decrease of intensity (↓60%) and a small red-shift ($\Delta \approx 1$nm) over the same period. The reduction of intensity indicates a decreased passivation of the CdSe core by the ZnS shell. The very small red shift could be due to a slight expansion of the CdSe core due to a removal of the compressive ZnS shell.[43,44,45] However, in general the very weak spectral shift indicates quantum confinement of the exciton is not significantly altered, which means the core undergoes minimal alteration since the CdSe/ZnS QD is type-I with the exciton confined to the CdSe core. In short, we propose that the CdSe/ZnS QD experiences degradation of the ZnS shell by oxidation and corrosion with little modification to the CdSe core (**Figure 6.3**). This scenario is not surprising since the ZnS shell is the material in direct contact with the environment.

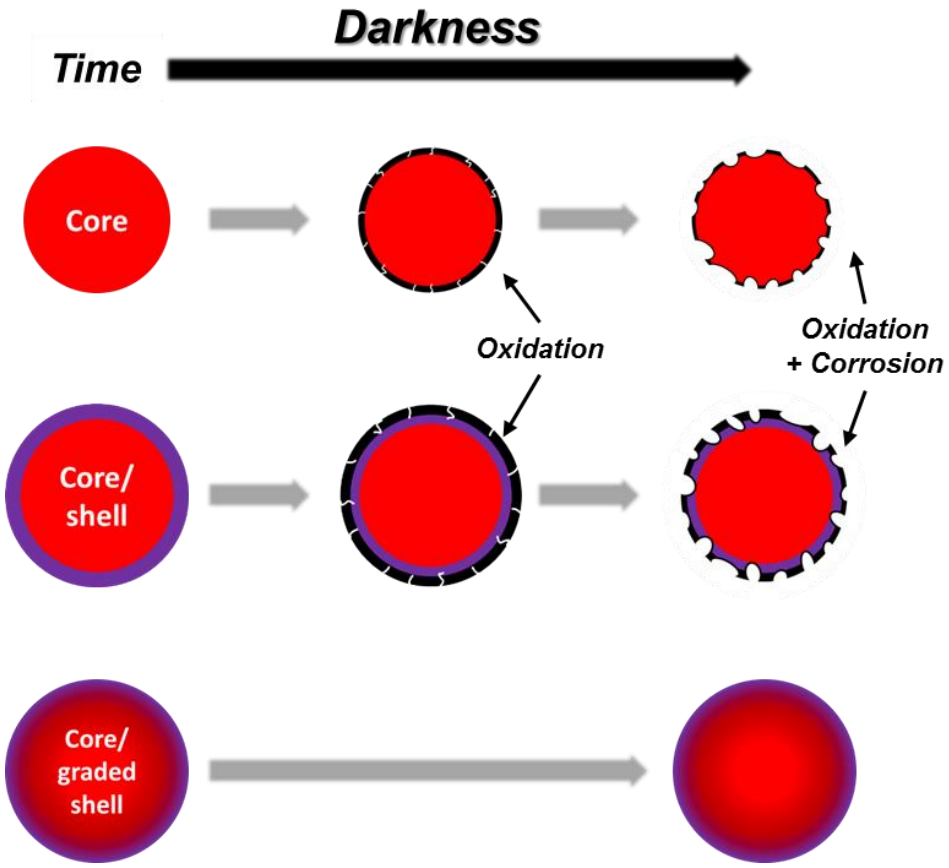

Figure 6.3: Schematic outlining the proposed physical evolution of each type of QD (CdSe core, CdSe/ZnS core/shell, or CdSe/$Cd_{1-x}Zn_xSe_{1-y}S_y$ core/graded shell) in darkness (air) over a period of 45 minutes (organic ligand not shown for clarity).

Finally, the core/graded shell CdSe/$Cd_{1-x}Zn_xSe_{1-y}S_y$ QD shows no clear change of intensity ($\Delta < 5\%$) or spectral position ($\Delta < 1$nm) over the same period. The optical stability of the core/graded shell CdSe/$Cd_{1-x}Zn_xSe_{1-y}S_y$ QDs arises from the smeared composition profile (imparted during synthesis), which reduces the strain energy from the crystal lattice mismatch between CdSe and ZnS and makes the QD more thermodynamically stable.[41,43]

These distinct emission trends clearly show that the composition profile of the QD composition strongly affects how the optical properties evolve in a dark environment under ambient temperature, pressure, and gaseous composition. The consideration of these trends is very

relevant for improving the lifetime and storage of QD devices and systems during storage. The proposed physical mechanisms leading to this distinct behavior are based on the indirect evidence from PL emission. Direct verification of reduced QD size or crystal lattice due to oxidation and corrosion via high-resolution TEM is extremely difficult due to the very small physical changes that are likely occurring (<1 nm change in diameter). Furthermore, high-resolution TEM often requires UV and ozone cleaning which could alter the QDs and make them poor representatives of the QDs from this darkness study.

6.3.3 Emission evolution: continuous light exposure

In the next step, we examined whether continuous light exposure elicits additional mechanisms within the QDs that alter how the emission evolves (compared to darkness), which is particularly important to know when developing QD devices and systems that experience constant harsh light excitation and exposure. In this case the QD-polymer films are continuously exposed to light (450-490 nm) over a period of 45 minutes while their photoluminescence (PL) intensity and spectral position are monitored.

Once again, the QD composition profile profoundly impacts how the intensity and spectral position of the emission evolves. Furthermore, continuous light exposure leads to more pronounced shifts in some instances (compared to when in darkness) (**Figure 6.4**). For example, the core CdSe QDs undergo a much larger blue shift (16 nm) compared to when in darkness (5 nm), indicating an accelerated oxidation and corrosion of the CdSe core that reduces the diameter and increases quantum confinement. The intensity follows a similar decay rate and magnitude presumably due to a saturation of non-radiative surface quenching states. The decay of PL intensity was corroborated with PL imaging (**Appendix C Figure C.5**).

Light exposure for the core/shell CdSe/ZnS QDs leads to more pronounced shifts and new behavior, signifying the emergence of photo-mediated mechanisms. For example, a large continuous spectral blue shift occurs (16 nm) throughout the 45 minutes of light exposure (instead of a red shift). Furthermore, upon exposure to light the intensity decreases more rapidly than in the darkness case, and then undergoes a recovery of intensity. The convolution of the competing decay and recovery mechanisms leads to a decay-to-recovery evolution of intensity (**Figure 6.4a,b**). Interestingly, the decay occurs much more quickly (seconds-to-minutes) than the recovery step (tens of minutes).

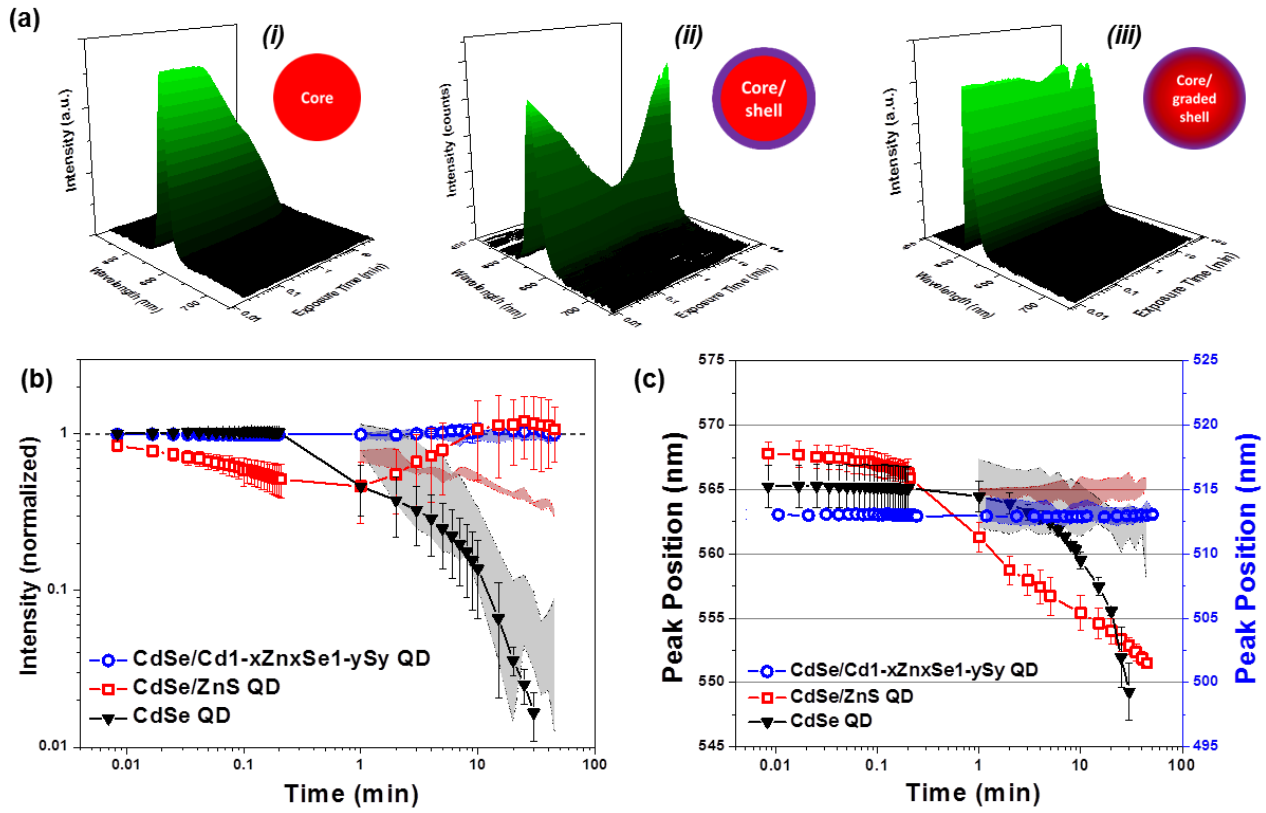

Figure 6.4: Examination of the photoluminescence stability of QD-PMMA films with different types of QD design (CdSe core, CdSe/ZnS core/shell, or CdSe/$Cd_{1-x}Zn_xSe_{1-y}S_y$ core/graded shell). (a) 3D and (b) 2D representation of PL intensity and (c) spectral peak position under continuous light exposure (blue light: 450-490 nm, 24-28 mW). The ribbons represent a standard deviation range for the emission evolution of the QDs in darkness.

As in the darkness case, the intensity and spectral position of the core/graded shell CdSe/$Cd_{1-x}Zn_xSe_{1-y}S_y$ QDs show minimal change under continuous light exposure (verified with PL imaging in **Appendix C Figure C.6**). The FWHM for the core CdSe QD increases by more than 10 nm, the core/shell CdSe/ZnS QDs by less than 2 nm, and the core/graded shell CdSe/$Cd_{1-x}Zn_xSe_{1-y}S_y$ QDs by less than 0.5 nm. Continuous exposure experiments of each QD in solution show no clear shift of intensity, peak position, or FWHM for the core CdSe and core/graded shell CdSe/$Cd_{1-x}Zn_xSe_{1-y}S_y$ QDs (**Appendix C Figure C.2**). The core/shell CdSe/ZnS QDs show similar, but much less pronounced, evolution of the PL compared to the film state (**Appendix C Figure C.3**). This indicates that deposition into a solid film state, which increases the interaction of the QDs with the surrounding gaseous environment, is critical for this type of behavior. The evolution of the UV-vis absorption profile of the unstable core/shell CdSe/ZnS QDs in solution state was also examined (**Appendix C Figure C.4**). A 3.5 nm blue shift of the 1s absorption peak occurred, supporting the claim that increased quantum confinement of the exciton is occurring.

6.3.4 Emission evolution: decay-to-recovery behavior (CdSe/ZnS QD)

As mentioned, the decay-to-recovery evolution of intensity for the CdSe/ZnS QDs arises from a combination of competing decay and recovery mechanisms. However, there are a variety of mechanisms that lead to decay and recovery (reversible or irreversible) in QDs so additional information is required before a conclusive determination can be made.

6.3.4.1 Continuous light exposure of different power

PL intensity recovery only occurs with continuous light exposure so it is likely that the characteristics of recovery depend on the exposure power. However, it is also possible that light exposure also affects the decay mechanism. Therefore, the relative strength of each effect

and its dependence on exposure power needs to be compared. The time-to-recovery is an ideal parameter to consider for this comparison since it represents the time required for the effects of the recovery mechanism to overcome those from the decay mechanism.

A number of observations and conclusions can be drawn from the results. First, the decay-to-recovery behavior is affected by the exposure power, where a higher exposure power reduces the time required for the CdSe/ZnS QDs to enter the recovery stage (**Figure 6.5a,b**). This indicates that the recovery mechanism has a stronger dependence on (and is proportional to) the number of incident photons than the decay mechanism since recovery overcomes decay eventually (for the power range examined).

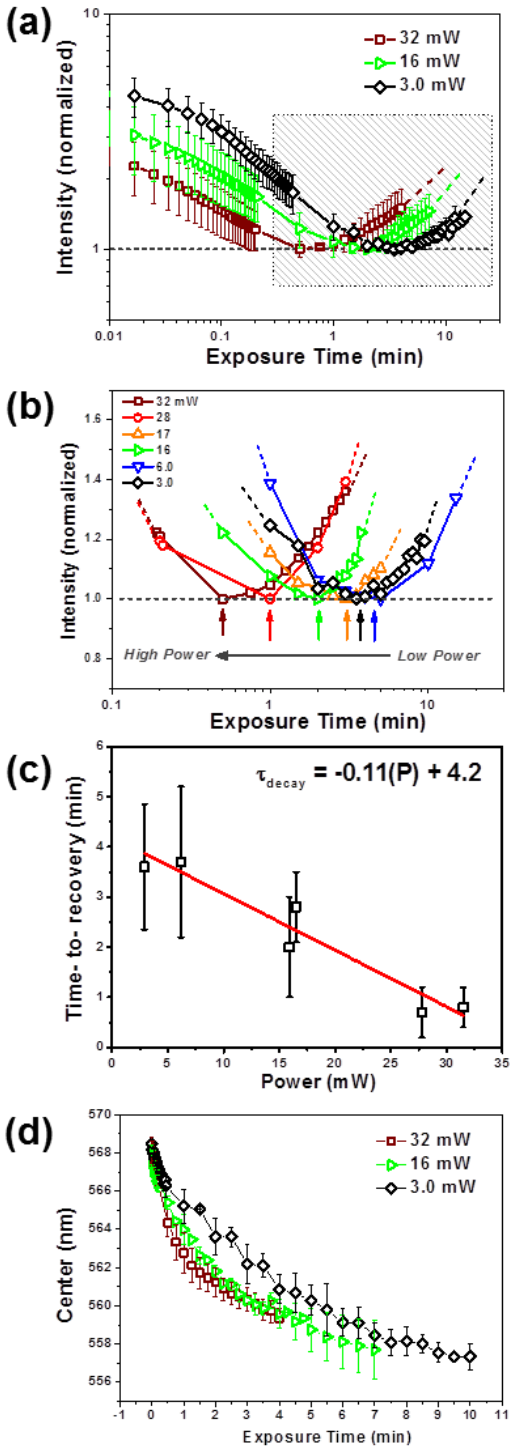

Figure 6.5: Evolution of the (a) PL intensity for core/shell CdSe/ZnS QD-PMMA films at three different exposure powers (continuous exposure), and (b) a narrowed viewing range of the time-to-recovery for additional exposure powers (dashed lines are guides only). (c) The time-to-recovery of PL intensity versus incident exposure power. (d) Spectral peak position of the emission peak at three different exposure powers (continuous exposure).

Second, the time-to-recovery follows a downward linear relationship with exposure power (**Figure 6.5c**). This suggests that the rate of the recovery mechanism is linearly proportional to the number of incident photons, or that the ratio of the rates of the recovery and decay mechanism is linear. Third, the rate of blue shifting increases with higher exposure power (**Figure 6.5d**), which shows that photooxidation and corrosion of the CdSe core scales with the number of incident photons. In order for photooxidation and corrosion to reduce the CdSe core size, the ZnS shell must either be removed or significantly degraded during this period. However, removal and degradation of the ZnS shell should reduce surface passivation (and the intensity). Therefore, we can surmise that the blue shifting is a result of the decay mechanism, which means the decay mechanism also is proportional to the exposure power. No clear relationship between exposure power and full-width half-maximum was observed.

6.3.4.2 Cyclic light exposure (exposure-darkness-exposure)

A variety of mechanisms have been presented in the literature to explain the recovery/enhancement of emission upon light exposure. These include irreversible options like photoinduced surface annealing/restructuring and photoactivation,[31,32] which remain upon removal of light. However, reversible mechanisms have also been presented like photoinduced surface transformation (via heat cycling),[37] adsorption/desorption of H_2O (via pressure cycling),[28] and light-activated rearrangement of surfactant molecules in solution (via light exposure cycling of QDs in solution).[35] However, so far, reversibility has either required the external modification of the surrounding environment or focused on QDs in solution (neither of which applies to this study). The identification of whether the recovery of PL intensity is irreversible of reversible will help identify the underlying mechanisms behind this behavior.

Therefore, the core/shell CdSe/ZnS QD-polymer films (which evolve very differently depending on whether they are in darkness or being exposed to light) were exposed to a cyclic light

exposure regime to determine how the recovered PL state responds to a period of darkness (i.e. the removal of electromagnetic energy). A single cycle involves a period of light exposure, followed by a period of darkness, followed by a resumption of light exposure. This sequence is designated an exposure-darkness-exposure cycle. Exposure-darkness-exposure cycling will determine whether the recovered PL state requires continuous light exposure to be maintained (suggesting a reversible dynamic process that requires continuous input of energy to occur), or is not affected by the removal of light (suggesting it is an irreversible process).

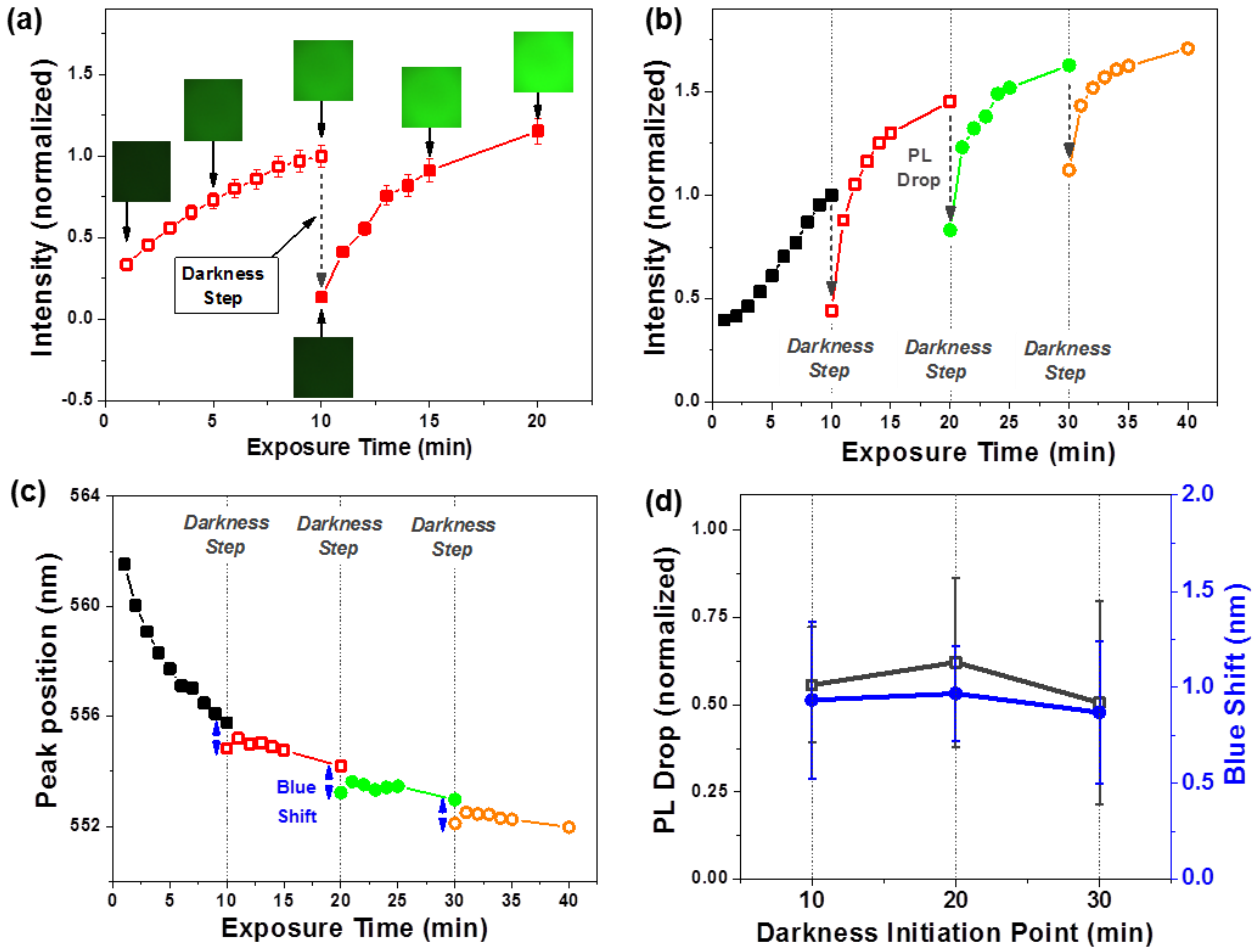

Figure 6.6: Examination of the charge-discharge effect observed upon light exposure and removal for a CdSe/ZnS core/shell QD-PMMA film. (a) The evolution of PL intensity during an exposure-darkness-exposure trial (darkness period: 20 minutes) (exposure: 450-490 nm, ≈19 mW). The (b) PL intensity and (c) PL spectral position during exposure-darkness-exposure cycling (5 min darkness periods). (d) The drop of PL intensity and spectral shift after each darkness period.

The results of a single exposure-darkness-exposure cycle are shown in **Figure 6a**. The QD-polymer film was continuously exposed to light for 10 minutes during which a continuous recovery of emission occurred (as expected). After 10 minutes of continuous light exposure, the light is removed for 20 minutes (20 minute darkness step). Light exposure is then resumed and a measurement is collected immediately to determine whether the period of darkness affected the PL recovery.

It is clear from **Figure 6a** (images and spectral intensity data) that removal of light for 20 minutes leads to a drastic decrease in intensity of the recovered PL state (more than 85% reduction). Subsequent continuous light exposure leads to a gradual increase of PL intensity back to the initial recovered state (larger PL images of the film during this process provided in **Appendix C Figure C.7**). Repeated exposure-darkness-exposure cycles at different times throughout the recovery process leads to a similar response (**Figure 6.6b**) (5 min darkness periods). These results indicate that the PL recovery is a reversible process (or partially reversible). However, the spectral blue shift that occurred during the continuous exposure step does not disappear during a darkness step (it actually continues) (**Figure 6.6c**). This irreversibility indicates that the blue shifting of emission is not directly tied to the PL recovery mechanism, but more likely to the photooxidative decay process. The independence of the decay and recovery mechanisms is also supported by the fact that the intensity drop and blue shift from that occur after a darkness step appear independent of when the darkness step is initiated over the recovery period (**Figure 6.6d**).

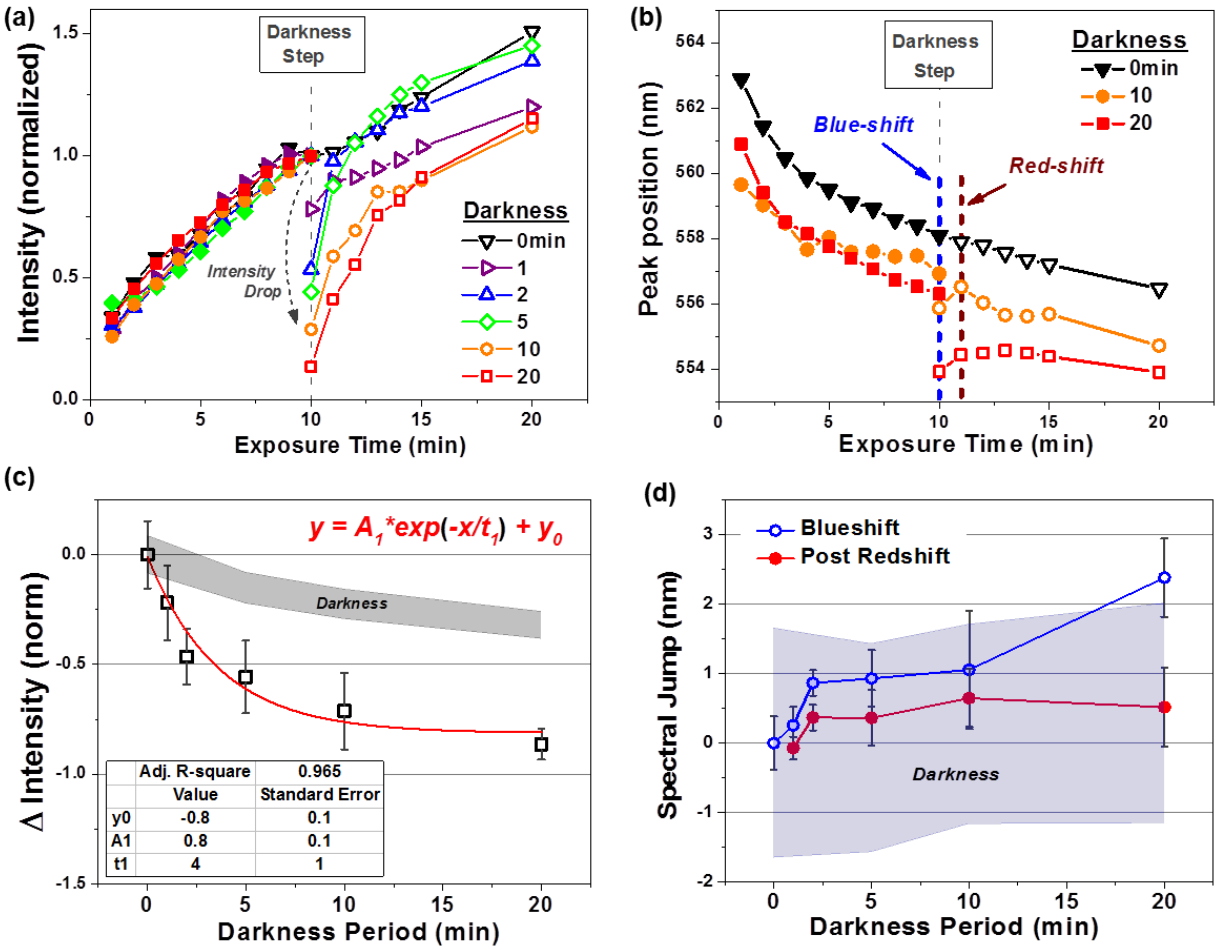

Figure 6.7: Examination of how periods of darkness affect the PL intensity of CdSe/ZnS core/shell QDs (QD-polymer film) exposed to light (exposure: 450-490 nm, ≈18.5 mW)(QD-PMMA films). (a) PL intensity decay dip and (b) spectral shift for different periods of darkness (10 min into light exposure regime). Magnitude of the (c) PL decay dip and (d) spectral shift versus the duration of the darkness step. The shaded regions depict the range (one standard deviation) of change occurring for samples never exposed to light.

The PL intensity drop and blue shift are directly related to the duration of the darkness step, with longer darkness periods leading to greater intensity drops and blue shifts (**Figure 6.7**). The PL intensity drop follows an exponential trend (negative time constant) (**Figure 6.7c**). The blue shift also appears to scale with darkness time, matching closely with the blue shift observed in previous darkness studies (**Figure 6.7d**). It is interesting to note that a slight red-shift occurs within the first minute of resuming light exposure after a darkness step (**Figure 6.7b,d**), which

could be due to an increase in the dielectric constant of the immediate surroundings.[35,46] The origin behind this phenomenon is unclear but could be due to a chemical change to the surrounding material or an adsorption/desorption of molecules.

6.3.4.3 Cyclic darkness (darkness-exposure-darkness)

An opposite cycling approach can be performed as well (darkness-exposure-darkness cycle), which also leads to jumps of intensity and spectral position (**Figure 6.8**). The exponential decay of intensity during a darkness period (**Figure 6.8a,b**) corroborates the trend seen in the previous study (**Figure 6.7c**). The large blue shift observed during the first exposure step is due to the onset of photooxidation (as shown previously) (**Figure 6.6c**).

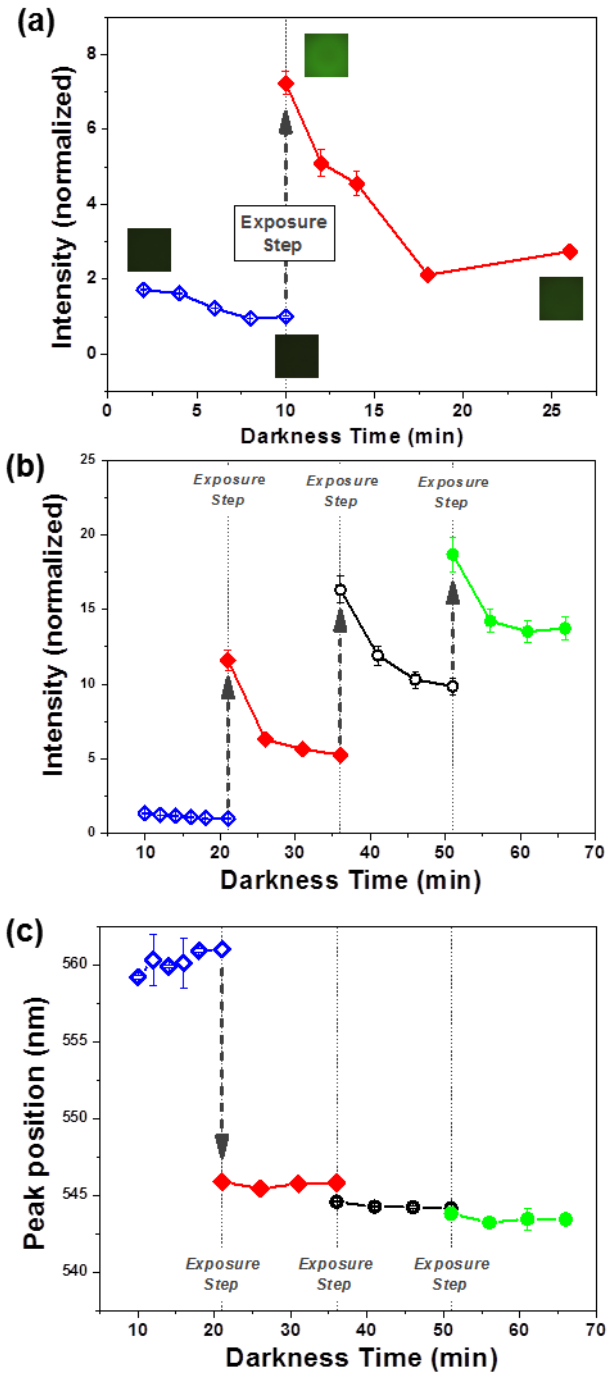

Figure 6.8: Examination of the discharge-charge effect observed upon darkness and light exposure steps for a CdSe/ZnS QD-polymer film. (a) The evolution of PL intensity during a darkness-exposure-darkness trial (exposure period of 10 minutes)(blue light: 450-490 nm, 26.5 mW). The (b) PL intensity and (c) PL spectral position during cycling of darkness-exposure-darkness (11 min exposure periods)(blue light: 450-490 nm 25.3 mW).

The results from the exposure-darkness-exposure experiments indicate a number of things: First, the recovery of PL intensity and spectral blue shift are not coupled, which means at least two mechanisms are present. Second, the process causing recovery of the PL intensity is (at least partially) reversible since it requires a constant input of electromagnetic energy to be maintained. Third, the mechanism underlying PL intensity recovery may be diffusion-based since it dissipates with time after light is removed. Fourth, whatever mechanism underlies the PL intensity recovery process also leads to a small immediate red-shift upon resuming the input of electromagnetic energy (after a darkness period).

6.3.5 Underlying mechanisms

There are a variety of mechanisms that could be present in each of the QD architectures that could account for the corresponding evolution of PL emission.[32,35,47] A summary of the evolutionary trends for the core, core/shell, and core/graded shell QD-polymer films under various external factors is provided in **Table 6.2**.

Table 6.2: Evolution of the optical characteristics of the CdSe core, CdSe/ZnS core/shell, and CdSe/$Cd_{1-x}Zn_xSe_{1-y}S_y$ core/graded shell QD-polymer films in a dark environment (top frame) and under continuous light exposure (middle frame) (blue light: 450-490 nm). PL evolution of CdSe/ZnS QD-polymer film under cyclic light exposure (exposure-darkness-exposure) (bottom frame). The proposed mechanisms causing this behavior are noted as well.

Darkness (Continuous)				
Design	**Composition**	**Intensity**	**Peak Position**	**Proposed Mechanism**
Core	CdSe	Decay (↓*96%*)	Blue shift *(5nm)*	Oxidation
Core/shell	CdSe/ZnS	Decay (↓*68%*)	Red shift *(1nm)*	Oxidation
Core/graded shell	CdSe/Cd1-xZnxSe1-ySy	Stable *(±10%)*	Stable *(±0.5nm)*	NA

Light Exposure (continuous)				
Design	**Composition**	**Intensity**	**Peak Position**	**Proposed Mechanism**
Core	CdSe	Decay (↓*98%*)	Blue shift *(16nm)*	Oxidation, photooxidation
Core/shell	CdSe/ZnS	Decay-to-recovery	Blue shift *(16nm)*	Photooxidation, light-mediated H_2O passivation
Core/graded shell	CdSe/Cd1-xZnxSe1-ySy	Stable *(±8%)*	Stable *(±0.5nm)*	NA

Cyclic Light Exposure (exposure-dark-exposure)				
Design	**Composition**	**Intensity**	**Peak Position**	**Proposed Mechanism**
Core/shell CdSe/ZnS	Initial Light Exposure	Recovery	Blue shift *(Varies)*	Photooxidation, light-mediated H_2O passivation
	Darkness step	Decay & discharge of recovery	Blue shift *(1nm)*	Oxidation & discharge of recovery mechanism
	Subsequent Light Exposure	Recovery	Initial red shift *(1nm)*, Blue shift *(Varies)*	Photooxidation, light-mediated H_2O passivation

As noted previously, direct confirmation of physical (diameter) and material (surface oxidation/corrosion, H_2O passivation) changes to QDs via techniques like high-resolution TEM or NMR are very difficult due to the scale of the physical changes (<1 nm), the complexity in identifying different crystal structures over these small scales, the rate of the changes, and the reversibility of some mechanisms. Therefore, the following discussion of mechanisms is based on indirect evidence from the evolution of optical emission under the various external factors,

since these characteristics exhibit shifts can be observed real time, with high accuracy, and require no cleaning steps that could modify the QD-polymer films.

The core/shell QDs are the initial focus since they exhibit the most complex and interesting shifts of intensity and spectral position. To recap, the following phenomena need to be explained: First, continuous light exposure causes a decay-to-recovery behavior for intensity (**Figure 6.4b**). Second, the decay step is much faster than the recovery step (by an order of magnitude) **(Figure 6.4b)**. Third, the recovery phase occurs earlier for high exposure power **(Figure 6.5c)**. Fourth, there is a continuous blue shift throughout the decay-to-recovery evolution (most pronounced during the recovery step)(**Figure 6.4c)**. Fifth, the recovery of intensity is semi-reversible, requiring continuous light input to be maintained (**Figure 6.6a)**. Sixth, the blue shift is largely irreversible (**Figure 6.6c**). Seventh, the recovery process can be "discharged" and "recharged" multiple times (**Figure 6.6b)**. Eighth, the "discharge" of recovery upon darkness is proportional to the darkness period (**Figure 6.7c**). Finally, a small red-shift occurs immediately after light exposure is resumed during "recharging" (**Figure 6.7b,d**). Therefore, mechanisms need to be identified that alter quantum confinement and quantum yield. Furthermore, one (or more) of the mechanisms needs to be semi-reversible and one (or more) needs to be irreversible.

The core/shell CdSe/ZnS QDs likely have at least two competing mechanisms at play to explain all the phenomena. The continuous irreversible blue shift that occurs during light exposure indicates an increase of quantum confinement of the exciton caused by a reduction in size of the CdSe core. Size reduction is typically attributed to an irreversible photooxidation and corrosion of the QD surface, which is reasonable since the QD-polymer film is exposed to an environment with oxygen.[32] The rate of spectral blue shifting also slightly increases with exposure power which is expected since photons cause the process to occur.

Photooxidation and corrosion of the ZnS shell, which occurs before and concurrently with oxidation of the CdSe core, can explain the fast decay of intensity that occurs immediately upon light exposure. Corrosion of the ZnS shell reduces surface passivation of the CdSe core (where the exciton is located) which decreases quantum yield.[12,14,40] The ZnS shell is in a meta-stable state before illumination due to the large (12%) crystal lattice mismatch between CdSe and ZnS which causes strain to build up at the CdSe/ZnS interface and within the ZnS shell.[14,41] Degradation of the ZnS shell during photooxidation leads to the formation of physical defects as the ZnS shell relaxes that act as nonradiative recombination pathways.[32,33] This conclusion is supported by the fact that aged CdSe/ZnS QDs (6 months) have a significantly less pronounced initial high quantum yield state and blue shifted emission peak compared to newly synthesized QDs (**Appendix C Figure C.8**). The disappearance of the initial meta-stable high QY state is caused by slow oxidation and degradation of the ZnS shell while the QDs are stored in solution (air environment). This is bolstered by the fact that aged QDs (with more surface defects) undergo much more recovery upon light exposure, presumably due to there being more defects on the CdSe surface that are temporarily passivated. Decay of QD PL intensity has also been attributed to heating,[47] which in this case could occur due to the continuous light exposure. However, this is unlikely since the area of the QD-polymer film exposed to light shows no measurable increase of temperature over a period of 45 minutes ($\Delta T < 1°C$) (**see Experimental Section**).

A number of mechanisms have been presented in the literature to explain the recovery of PL intensity (and its reversible behavior). These include photoinduced QD surface transformation (caused by heat cycling),[37] light-activated rearrangement of surfactant molecules (caused by light exposure cycling),[35] and light-mediated adsorption/desorption of H_2O (caused by pressure cycling).[28] Semi-reversible intensity recovery attributed to QD surface transformation

(CdSe/ZnS QD solutions and films) is unlikely because it requires deliberate heating above room temperature, and localized heating of the QD-polymer film was ruled out in this system. Light-activated rearrangement of ligands is also an unlikely mechanism since this effect is observed in core/shell CdSe/ZnS QD solutions where ligand dynamics are not hindered.[35] However, the system here is a solid QD-polymer film, so the solid polymer matrix surrounding the QDs should hamper the rearrangement of ligands on, and their diffusion to/from, the QD surface. Furthermore, if rearrangement of ligands is the underlying reason for the reversible nature of PL recovery, it is reasonable to assume that the matrix would play an important role. However, PL recovery was observed in two different polymers (poly(methyl methacrylate) and polystyrene) which should interact with the QD ligand differently due to the different side groups.

We suggest that ZnS shell oxidation/degradation combined with light-mediated adsorption/desorption of H_2O serves as the mechanism behind PL recovery and its reversible behavior. During QD encapsulation in the polymer matrix (spin-casting), water is likely trapped in the QD-polymer film at the QD surface. When light is incident on the CdSe/ZnS QDs it leads to oxidation/degradation of the ZnS (initial PL decay behavior and blue shifting). However, the degradation of the ZnS shell allows water to interact with the CdSe core, leading to H_2O mediated passivation (PL recovery behavior). Because light and H_2O are required for the PL recovery to occur, the PL recovery dissipates when light is removed. However, the slow dissipation suggests that the PL recovery mechanism is due to a chemical reaction at the QD surface that continues briefly after the light is removed. PL recovery can be reinitiated upon light exposure because the H_2O surrounding the QD is encased by the surrounding polymer matrix. The irreversible spectral blue shift can also be explained by this light-H2O mechanism since the ZnS shell is irreversibly oxidized and corroded, which leads to irreversible oxidation and corrosion of the CdSe QD core.

It is interesting that the core CdSe core QDs do not undergo PL recovery for a number of reasons. First, previous studies have shown that CdSe core QDs can undergo PL recovery upon light exposure. Second, because CdSe core QDs do not have a protective ZnS shell, they should experience the light-H_2O mechanism. It is possible that PL recovery is occurring but that the oxidation and degradation of the CdSe core is so profound that it overwhelms the PL recovery.

The stable optical properties of the core/graded shell CdSe/$Cd_{1-x}Zn_xSe_{1-y}S_y$ QDs supports the outlined mechanisms for the core CdSe and core/shell CdSe/ZnS QDs. The gradient composition of the shell reduces the radial lattice mismatch between the core and shell, making the core/graded shell QDs thermodynamically stable. The physically stability hinders degradation of the inorganic shell which prevents exposure and modification of the CdSe core by oxygen and H_2O. In short, the thorough isolation and passivation of the CdSe core by the gradient shell prevents blue shifting, initial intensity decay, and intensity recovery. A schematic outlining the physical evolution of each type of QD under light exposure is shown in **Figure 6.9**.

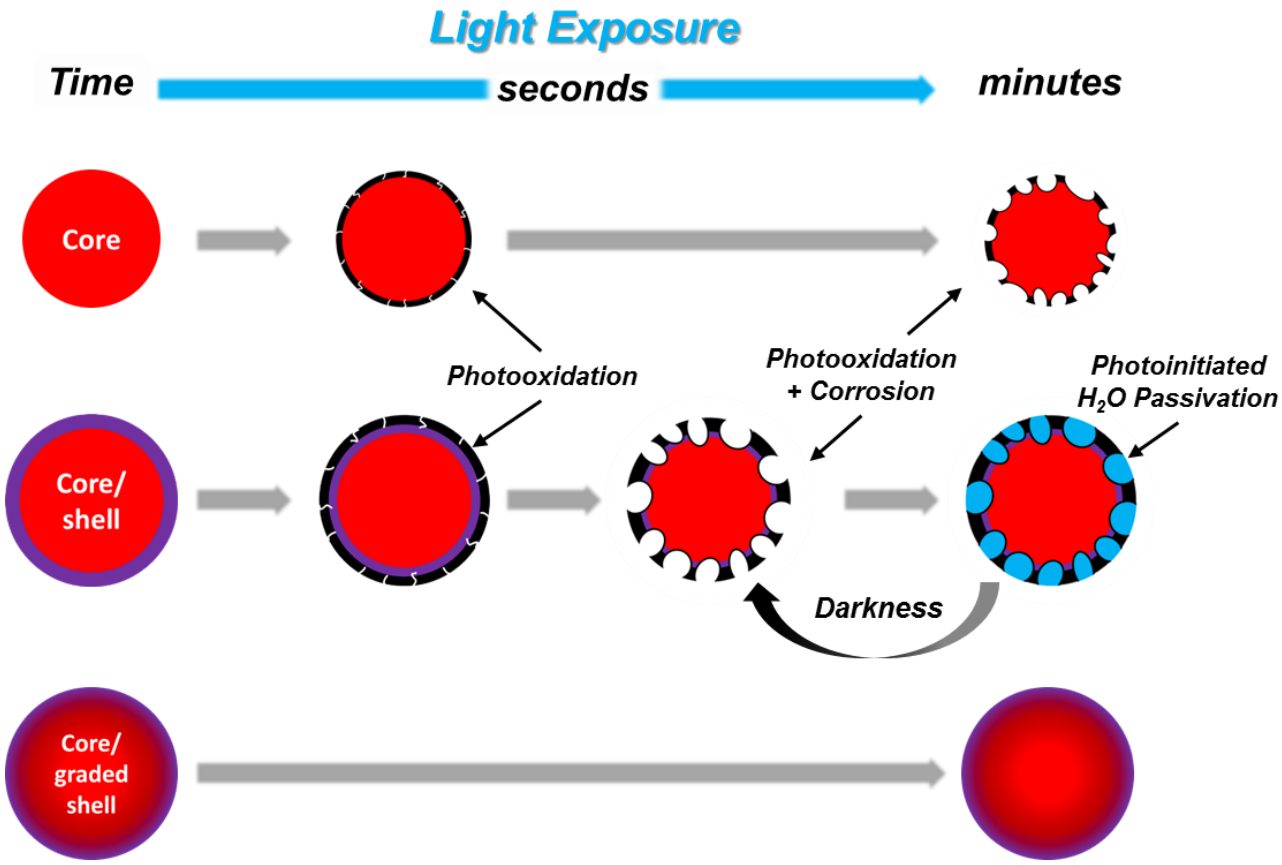

Figure 6.9: Schematic outlining the proposed physical evolution of each type of QD (CdSe core, CdSe/ZnS core/shell, or CdSe/$Cd_{1-x}Zn_xSe_{1-y}S_y$ core/graded shell) under light exposure in air over a period of 45 minutes (organic ligand not shown for clarity).

6.4 Conclusions

The evolution of photoluminescence from core, core/shell, and core/graded shell QDs in QD-polymer films was examined under different light exposure conditions in environments commonly experienced by quantum dot systems. It was shown that the compositional profile of the quantum dot (core, core/shell, core/graded shell) significantly affects how the optical characteristics evolve, with very distinct changes occurring for different QD types. For example, decreasing, increasing, and stable intensity were all observed, which could be reversible or

irreversible (depending on QD type). In addition, spectral blue shifting was observed in some instances and not in others.

The distinct response of each type of QD arises from how the core (and shell) material interacts with oxygen, H_2O, and light. For a core CdSe QD, the material confining the exciton is in immediate contact with its surroundings and thus responds quickly and strongly to external stimuli. However, a core/shell CdSe/ZnS QD has an inorganic barrier that can (initially) isolate the core from the environment but that can eventually degrade leading to competing physical mechanisms and interesting optical behavior. Finally, a graded shell in core/graded shell $Cd_{1-x}Zn_xSe_{1-y}S_y$ QD provides exceptional protection for the CdSe core, due to thermodynamic considerations, which leads to very stable optical properties. These results clearly demonstrate the importance of proper compositional design for the quantum dot depending on the requirements of the photonic system. General QD selection and evaluation guidelines have been developed based on these findings that outline the experimental tests that should be employed to test whether a specific QD architecture meets the requirements or assumptions of the device/process/application/measurement for which the QD is being considered (**Table 6.3**).

Table 6.3: General QD selection and evaluation guidelines to consider when trying to identify a QD architecture that satisfies specific emission evolution behavior in darkness or upon light exposure. Examples of common devices/processes/applications/measurements that utilize QD PL emission and specific QD emission evolution behavior are provided for context.

QD Selection & Evaluation Guidelines					
Requirements/ Assumptions	**Test**	**Data**	**QD Option**	**Example**	**Type**
Darkness + air → ΔI or Δλ	Darkness test in air	ΔI, Δλ, rate ΔI, rate Δλ	(Unstable) core or core/shell	QD air sensor	Device
Light exposure → ΔI or Δλ (irreversible or long-lived)	Cyclic light exposure	irreversibility ΔI or Δλ	(Unstable) core/shell	Photoannealing	Process
				QD photopatterning	Application
Light exposure → ΔI or Δλ (reversible)	Continuous & cyclic light exposure	ΔI, Δλ, rate ΔI, rate Δλ, reversibility	(Unstable) core/shell	QD photodetector	Device
Light exposure → ΔPL = 0	Continuous light exposure	ΔI, Δλ, rate ΔI, rate Δλ	(Stable) core/graded shell	Variable strip length (VSL)	Measurement
				QD imaging and labelling	Application
				Optically pumped QD lasers	Device
Darkness → ΔPL = 0, Light exposure → ΔPL = 0	Darkness test in air, continuous light exposure	ΔI, Δλ, rate ΔI, rate Δλ	(Stable) core/graded shell	QD light-emitting diode	Device
				Color filters in QD displays	Device

Examples of common devices/processes/applications/measurements that utilize QD PL emission and specific QD emission evolution behavior are provided for context. The QD options provided in this table are based on the results in this work.

These experiments compose one of the first comprehensive studies on how QD architecture relates to emission evolution under various external influences, and they provide evidence of the chemical and physical changes underlying this evolution. For example, we are able to dispel the common notion that depositing an inorganic shell on a core QD (to make a core/shell QD) ensures strong isolation from the environment. These results provide significant insight into the various mechanisms at play in QDs of different compositional profile under the conditions often experienced by QD photonic systems. Furthermore, it was demonstrated that both reversible and irreversible mechanisms can be active within a QD at the same time, which can lead to a decoupling of optical properties that might not be anticipated (reversible intensity changes versus irreversible spectral shifts). This work can help act as a general framework for evaluating quantum dots in future studies, as well as help identify the appropriate QD composition profile for a specific application.

We suggest these results (and the strategies to obtain them) are significant because they are relevant to the majority of scientific studies and technological applications that make use of the emission from quantum dots. Furthermore, these results are critical to consider when making assumptions about the stability of QD emission (spectral position, FWHM, and intensity). This includes characterization techniques where stable emission is required to obtain meaningful results (like the variable strip length method or fluorescence lifetime imaging), and photonic systems where long lifetimes are desired (like QD displays, LEDs, and lasers). Finally, scenarios exist where unstable emission is desired (or required) for the device to function (sensors for light, oxygen, water).

6.5 Chapter acknowledgements

Dr. Jaehan Jung and Young Jun Yoon (Prof. Lin group, Georgia Institute of Technology): QD synthesis and ligand exchange.

6.6 References (Chapter 6)

1 Medintz, I.L.; Uyeda, H.T.; Goldman, E.R.; Mattoussi, H., Quantum dot bioconjugates for imaging, labelling and sensing. *Nat. Mater.* **2005,** *4,* 435-446.

2 Adachi, M.M.; Fan, F.; Sellan, D.P.; Hoogland, S.; Voznyy, O.; Houtepen, A.J.; Parrish, K.D.; Kanjanaboos, P.; Malen, J.A.; Sargent, E.H., Microsecond-sustained lasing from colloidal quantum dot solids. *Nat. Communications* **2015,** *6,* 8694-8694.

3 Lin, C.H.; Lafalce, E.; Jung, J.; Smith, M.J.; Malak, S.T.; Aryal, S.; Yoon, Y.J.; Zhai, Y.; Lin, Z.; Vardeny, Z.V.; Tsukruk, V.V., Core/alloyed-shell quantum dot robust solid films with high optical gains. *ACS Photonics* **2016,** *3,* 647-658.

4 Kim, T.-H.; Cho, K.-S.; Lee, E.K.; Lee, S.J.; Chae, J.; Kim, J.W.; Kim, D.H.; Kwon, J.-Y.; Amaratunga, G.; Lee, S.Y.; Choi, B.L.; Kuk, Y.; Kim, J.M.; Kim, K., Full-colour quantum dot displays fabricated by transfer printing. *Nat. Photonics* **2011,** *5,* 176-182.

5 Kim, B.H.; Onses, M.S.; Lim, J.B.; Nam, S.; Oh, N.; Kim, H.; Yu, K.J.; Lee, J.W.; Kim, J.-H.; Kang, S.-K.; Lee, C.H.; Lee, J.; Shin, J.H.; Kim, N.H.; Leal, C.; Shim, M.; Rogers, J.A., High-resolution patterns of quantum dots formed by electrohydrodynamic jet printing for light-emitting diodes. *Nano Lett.* **2015,** *15,* 969-973.

6 Gong, X.; Yang, Z.; Walters, G.; Comin, R.; Ning, Z.; Beauregard, E.; Adinolfi, V.; Voznyy, O.; Sargent, E.H., Highly efficient quantum dot near-infrared light-emitting diodes. *Nat. Photonics* **2016,** *10,* 253-257.

7 Mashford, B.S.; Stevenson, M.; Popovic, Z.; Hamilton, C.; Zhou, Z.Q.; Breen, C.; Steckel, J.; Bulovic, V.; Bawendi, M.; Coe-Sullivan, S.; Kazlas, P.T., High-efficiency quantum-dot light-emitting devices with enhanced charge injection. *Nat. Photonics* **2013,** *7,* 407-412.

8 Carey, G.H.; Abdelhady, A.L.; Ning, Z.J.; Thon, S.M.; Bakr, O.M.; Sargent, E.H., Colloidal quantum dot solar cells. *Chem. Rev.* **2015,** *115,* 12732-12763.

9 Zhang, L.; Chen, C.; Li, W.J.; Gao, G.H.; Gong, P.; Cai, L.T., Living cell multilifetime encoding based on lifetime-tunable lattice strained quantum dots. *ACS Appl. Mater. & Interf.* **2016,** *8,* 13187-13191.

10 Qu, L.H.; Peng, X.G., Control of photoluminescence properties of CdSe nanocrystals in growth. *J. Amer. Chem. Soc.* **2002,** *124,* 2049-2055.

11 Qu, L.H.; Peng, Z.A.; Peng, X.G., Alternative routes toward high quality CdSe nanocrystals. *Nano Lett.* **2001,** *1,* 333-337.

12 Dabbousi, B.O.; RodriguezViejo, J.; Mikulec, F.V.; Heine, J.R.; Mattoussi, H.; Ober, R.; Jensen, K.F.; Bawendi, M.G., (CdSe)ZnS core-shell quantum dots: Synthesis and characterization of a size series of highly luminescent nanocrystallites. *J. Phys. Chem. B* **1997,** *101,* 9463-9475.

13 Beane, G.A.; Gong, K.; Kelley, D.F., Auger and carrier trapping dynamics in core/shell quantum dots having sharp and alloyed interfaces. *ACS Nano* **2016,** *10,* 3755-3765.

14 Jung, J.; Lin, C.H.; Yoon, Y.J.; Malak, S.T.; Zhai, Y.; Thomas, E.L.; Vardeny, V.; Tsukruk, V.V.; Lin, Z., Crafting core/graded shell–shell quantum dots with suppressed re-absorption and tunable Stokes shift as high optical gain materials. *Angewandte Chemie Intern. Ed.* **2016,** *55,* 5071-5075.

15 Bae, W.K.; Park, Y.S.; Lim, J.; Lee, D.; Padilha, L.A.; McDaniel, H.; Robel, I.; Lee, C.; Pietryga, J.M.; Klimov, V.I., Controlling the influence of Auger recombination on the performance of quantum-dot light-emitting diodes. *Nat. Communications* **2013,** *4,* 2661.

16 Walsh, B.R.; Saari, J.I.; Krause, M.M.; Nick, R.; Coe-Sullivan, S.; Kambhampati, P., Controlling the surface of semiconductor nanocrystals for efficient light emission from single excitons to multiexcitons. *J. Phys. Chem. C* **2015,** *119,* 16383-16389.

17 Cooney, R.R.; Sewall, S.L.; Sagar, D.M.; Kambhampati, P., State-resolved manipulations of optical gain in semiconductor quantum dots: Size universality, gain tailoring, and surface effects. *J. Chem. Phys.* **2009,** *131,* 164706.

18 Shaklee, K.L.; Leheny, R.F., Direct determination of optical gain in semiconductor crystals. *Appl. Phys. Lett.* **1971,** *18,* 475.

19 Liang, X.W.; Wang, H.L.; Zhu, Y.; Zhang, R.; Cogger, V.C.; Liu, X.; Xu, Z.P.; Grice, J.E.; Roberts, M.S., Short- and long-term tracking of anionic ultrasmall nanoparticles in kidney. *ACS Nano* **2016,** *10,* 387-395.

20 Rizzo, A.; Mazzeo, M.; Palumbo, M.; Lerario, G.; D'Amone, S.; Cingolani, R.; Gigli, G., Hybrid light-emitting diodes from microcontact-printing double-transfer of colloidal semiconductor CdSe/ZnS quantum dots onto organic layers. *Adv. Mater.* **2008,** *20,* 1886-1891.

21 Dang, C.; Lee, J.; Breen, C.; Steckel, J.S.; Coe-Sullivan, S.; Nurmikko, A., Red, green and blue lasing enabled by single-exciton gain in colloidal quantum dot films. *Nat. Nanotech.* **2012,** *7,* 335-339.

22 Malak, S.T.; Jung, J.; Yoon, Y.J.; Smith, M.J.; Lin, C.H.; Lin, Z.; Tsukruk, V.V., Large-area multicolor emissive patterns of quantum dot–polymer films via targeted recovery of emission signature. *Adv. Opt. Mater.* **2016,** *4,* 608-619.

23 Zucolotto, V.; Gattas-Asfura, K.M.; Tumolo, T.; Perinotto, A.C.; Antunes, P.A.; Constantino, C.J.L.; Baptista, M.S.; Leblanc, R.M.; Oliveira, O.N., Nanoscale manipulation of CdSe quantum dots in layer-by-layer films: influence of the host polyelectrolyte on the luminescent properties. *Appl. Surf. Sci.* **2005,** *246,* 397-402.

24 Zhang, S.C.; Yu, J.H.; Li, X.G.; Tian, W.H., Photoluminescence properties of mercaptocarboxylic acid-stabilized CdSe nanoparticles covered with polyelectrolyte. *Nanotechnology* **2004,** *15,* 1108-1112.

25 Zimnitsky, D.; Jiang, C.; Xu, J.; Lin, Z.; Tsukruk, V.V., Substrate- and time-dependent photoluminescence of quantum dots inside the ultrathin polymer LbL film. *Langmuir* **2007,** *23,* 4509-4515.

26 Komarala, V.K.; Rakovich, Y.P.; Bradley, A.L.; Byrne, S.J.; Corr, S.A.; Gun'ko, Y.K., Emission properties of colloidal quantum dots on polyelectrolyte multilayers. *Nanotechnology* **2006,** *17,* 4117-4122.

27 Zimnitsky, D.; Jiang, C.; Xu, J.; Lin, Z.; Zhang, L.; Tsukruk, V.V., Photoluminescence of a freely suspended monolayer of quantum dots encapsulated into layer-by-layer films. *Langmuir* **2007,** *23,* 10176-10183.

28 Cordero, S.R.; Carson, P.J.; Estabrook, R.A.; Strouse, G.F.; Buratto, S.K., Photo-activated luminescence of CdSe quantum dot monolayers. *J. Phys. Chem. B* **2000,** *104,* 12137-12142.

29 Munro, A.M.; Jen-La Plante, I.; Ng, M.S.; Ginger, D.S., Quantitative study of the effects of surface ligand concentration on CdSe nanocrystal photoluminescence. *J. Phys. Chem. C* **2007**, *111,* 6220-6227.

30 Lee, W.; Kim, H.; Jung, D.-R.; Kim, J.; Nahm, C.; Lee, J.; Kang, S.; Lee, B.; Park, B., An effective oxidation approach for luminescence enhancement in CdS quantum dots by H2O2. *Nanoscale Res. Lett.* **2012,** *7*, 672*.*

31 Wang, Y.; Tang, Z.; Correa-Duarte, M.A.; Pastoriza-Santos, I.; Giersig, M.; Kotov, N.A.; Liz-Marzán, L.M., Mechanism of strong luminescence photoactivation of citrate-stabilized water-soluble nanoparticles with CdSe cores. *J. Phys. Chem. B* **2004,** *108,* 15461-15469.

32 Nazzal, A.Y.; Wang, X.Y.; Qu, L.H.; Yu, W.; Wang, Y.J.; Peng, X.G.; Xiao, M., Environmental effects on photoluminescence of highly luminescent CdSe and CdSe/ZnS core/shell nanocrystals in polymer thin films. *J. Phys Chem. B* **2004,** *108,* 5507-5515.

33 van Sark, W.; Frederix, P.; Van den Heuvel, D.J.; Gerritsen, H.C.; Bol, A.A.; van Lingen, J.N.J.; Donega, C.D.; Meijerink, A., Photooxidation and photobleaching of single CdSe/ZnS quantum dots probed by room-temperature time-resolved spectroscopy. *J. Phys. Chem. B* **2001,** *105,* 8281-8284.

34 Zhang, H.; Zhou, Z.; Yang, B.; Gao, M.Y., The influence of carboxyl groups on the photoluminescence of mercaptocarboxylic acid-stabilized CdTe nanoparticles. *J. Phys. Chem. B* **2003,** *107,* 8-13.

35 Jones, M.; Nedeljkovic, J.; Ellingson, R.J.; Nozik, A.J.; Rumbles, G., Photoenhancement of luminescence in colloidal CdSe quantum dot solutions. *J. Phys. Chem. B* **2003,** *107,* 11346-11352.

36 van Sark, W.; Frederix, P.; Bol, A.A.; Gerritsen, H.C.; Meijerink, A., Blueing, bleaching, and blinking of single CdSe/ZnS quantum dots. *ChemPhysChem* **2002,** *3,* 871-879.

37 Hess, B.C.; Okhrimenko, I.G.; Davis, R.C.; Stevens, B.C.; Schulzke, Q.A.; Wright, K.C.; Bass, C.D.; Evans, C.D.; Summers, S.L., Surface transformation and photoinduced recovery in CdSe nanocrystals. *Phys. Rev. Lett.* **2001,** *86,* 3132-3135.

38 Oda, M.; Shen, M.Y.; Saito, M.; Goto, T., Photobrightening of CuBr nanocrystals in PMMA. *J. Luminescence* **2000,** *87–89,* 469-471.

39 Shinya, M.; Ceco Danov, D.; Soichiro, S.; Yukio, Y., Optical memory media based on excitation-time dependent luminescence from a thin film of semiconductor nanocrystals. *Jap. J. Appl. Phys.* **2000,** *39,* 4006-4012.

40 Qin, H.Y.; Niu, Y.; Meng, R.Y.; Lin, X.; Lai, R.C.; Fang, W.; Peng, X.G., Single-dot spectroscopy of zinc-blende CdSe/CdS core/shell nanocrystals: Nonblinking and correlation with ensemble measurements. *J. Amer. Chem. Soc.* **2014,** *136,* 179-187.

41 Xie, R.; Kolb, U.; Li, J.; Basché, T.; Mews, A., Synthesis and characterization of highly luminescent CdSe−core CdS/Zn0.5Cd0.5S/ZnS multishell nanocrystals. *J. Amer. Chem. Soc.* **2005,** *127,* 7480-7488.

42 Choi, D.; Pyo, J.Y.; Kim, Y.; Jang, D.J., Facile synthesis of composition-gradient Cd(1-x)ZnxS quantum dots by cation exchange for controlled optical properties. *J. Mater. Chem. C* **2015,** *3,* 3286-3293.

43 Smith, A.M.; Nie, S., Semiconductor nanocrystals: Structure, properties, and band gap engineering. *Acc. Chem. Res.* **2010,** *43,* 190-200.

44 Smith, A.M.; Mohs, A.M.; Nie, S., Tuning the optical and electronic properties of colloidal nanocrystals by lattice strain. *Nat. Nanotech.* **2009,** *4,* 56-63.

45 Yu, P.; Cardona, M., Fundamentals of semiconductors, physics and materials properties. *4th Ed. Springer,* **2010.**

46 Franceschetti, A.; Zunger, A., Pseudopotential calculations of electron and hole addition spectra of InAs, InP, and Si quantum dots. *Phys. Rev. B* **2000,** *62,* 2614-2623.

47 Valerini, D.; Creti, A.; Lomascolo, M.; Manna, L.; Cingolani, R.; Anni, M., Temperature dependence of the photoluminescence properties of colloidal CdSe/ZnS core/shell quantum dots embedded in a polystyrene matrix. *Phys. Rev. B* **2005,** *71,* 235409.

CHAPTER 7

ENHANCEMENT OF OPTICAL GAIN CHARACTERISTICS OF QUANTUM DOT FILMS BY OPTIMIZATION OF ORGANIC LIGANDS

Chapter Based On:
Malak, S.T.; Lafalce, E.; Jung, J.; Lin, C.H.; Smith, M.J.; Yoon, Y.J.; Lin, Z.; Vardeny, Z.V.; Tsukruk, V.V., Enhancement of optical gain characteristics of quantum dot films by optimization of organic ligands. *J. Mater. Chem. C* **2016,** *4,* 10069-10081.

Chapter Overview

Following the study on how QD compositional design affects emission evolution for isolated QDs in QD-polymer films, the focus shifts to how QD-QD spacing in thin films of stable CdSe/$Cd_{1-x}Zn_xSe_{1-y}S_y$ QDs impacts the light-matter interactions over larger scales (microns-millimeters). Specific attention is placed on characteristics like light propagation, optical amplification, and optical attenuation.

QD packing density is altered by using organic ligands of different molecular dimension and chemical functionality (**Figure 7.1**). It is shown that the QD-packing density can be tuned by a factor of ~2 by changing the ligand from a traditional long ligand (hexadecylamine) to a shorter ligand (butylamine). The increase of QD packing when using butylamine results in a two-fold increase in optical gain. Overall, the highly packed QD films exhibit very large gain values (~500 cm^{-1}) which greatly exceed typical Cd-based QD films with traditional ligands. In addition, thresholds for amplified-spontaneous emission (ASE) down to 50 μJ/cm^2 were observed, which is exceptionally low for ns-pulse pumped QD systems. These results confirm an additional route for obtaining high optical gain using QDs, and outline a strategy for modifying the optical gain characteristics by ligand exchange without needing to modify the QD synthesis.

Consideration of the ligands along with QD compositional design could make it possible to fabricate photonic systems with exceptionally low lasing thresholds, and offers a route toward achieving high gain using steady state pumping, an extremely difficult feat to achieve in traditional QD systems.

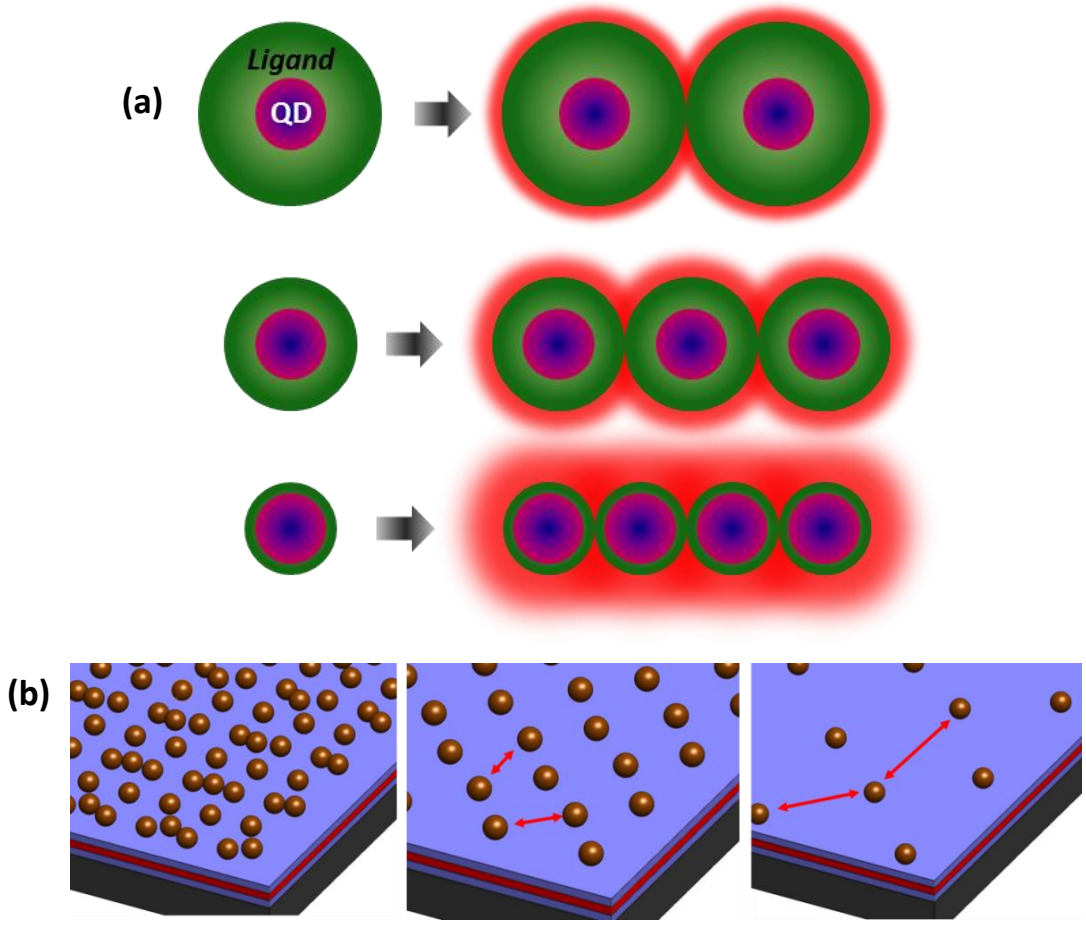

Figure 7.1: (a) Selection of quantum dot ligands of different size alters the local QD packing density, which (b) affects the overall QD arrangement and film properties (which affects the refractive index of the QD film and how light propagates in the film over larger distances).

7.1 Introduction

7.1.1 Nanotechnology

The large variety of nanoparticles, nanoscale deposition approaches, and nanoscale patterning strategies that have been recently introduced open up tremendous possibilities in the area of nanophotonics.[1,2,3,4] A primary advantage of nanoscale particles over conventional bulk materials is their size-and-shape dependent properties.[5,6,7,8,9] The tuning of nanoparticle properties is possible by carefully controlling their molecular dimensions and shape, and allows a single nanomaterial to satisfy multiple system constraints (for example, multiple emission colors), which in a bulk scale system may require multiple materials. This tunability has led to exciting possibilities in the areas of lasers,[10,11] LEDs,[12,13] solar cells,[14,] and imaging.[15]

7.1.2 Quantum dot characteristics

Quantum dots (QDs) are well-known semiconducting nanoparticles with a diameter typically below 10 nm that exhibit size-dependent properties due to quantum confinement of the exciton Bohr radius.[5] QDs have attracted much attention due to their broadband absorption, narrow band emission, high quantum yield, and minimal optical loss (which continues to be an obstacle for plasmonic particles).[16] Since the degree of confinement depends on the size and material of the quantum dot, the absorption and emission can be tuned from blue to NIR,[17] with smaller QDs displaying bluer absorption/emission.[18] QDs exhibit a number of additional characteristics that make them ideal candidates for photonic applications, including: polydispersity below 10%,[19] full-width at half-maximum (FWHM) down to 30 nm,[17] quantum yields up to 90%,[20] and tunable chemical functionality and packing density via ligand exchanges.[21,22] Research into the underlying mechanisms behind the confinement phenomena has been enabled

in large part by the development of reliable synthesis approaches for semiconducting QDs.[23,24] Furthermore, QDs are compatible with many nanoscale deposition techniques (spin-assisted layer-by-layer assembly,[25,26] Langmuir-Blodgett,[27] Langmuir-Schaefer[28]) and patterning techniques (jet printing,[29] μContact printing,[12] transfer printing,[30] photopatterning[31]), allowing for control over the arrangement of QDs and their collective behavior. This universality makes QDs ideal candidates for next generation photonic applications, including imaging and labelling,[15] solar cells,[14] LEDs,[13] and quantum computing.[32]

7.1.3 Optical gain in quantum dot systems

Quantum dots have particular potential in the area of optical gain and lasing systems. For example, gain from the blue to NIR has been demonstrated using many types of QDs, including CdTe,[33] PbS,[34] CdSe,[35,36] CdSe/ZnS,[37] and CdSe/CdS/ZnS.[38] Typical gain values range from 60-200 cm^{-1} depending on the pumping conditions, system design, and type of QD.[33-38] Various feedback mechanisms for lasing have also been demonstrated, including microcapillary resonators,[35,39] microsphere resonators,[40] distributed feedback resonators,[41] and planar microcavities.[42] These studies clearly demonstrate the potential of quantum dots for optical gain and lasing applications.

To date, the majority of studies have tried to maximize optical gain by minimizing the Auger recombination rate via size,[43] type-I design,[11] type-II design,[44,45] and QD composition.[33-38] These studies have been complemented by investigations of the formation and relaxation dynamics of the various exciton, biexciton, and multiexciton states in different types of quantum dots (core, core/shell, core/graded shell) using state-resolve pumping/probing.[46,47,48,49] This has resulted in a steady increase in

understanding of the structural dynamics of multi-excitons, and led to important discoveries like size-independent occupation thresholds and gain tailoring via excitonic state.[48,50]

However, only a few studies have considered how QD packing density and thermodynamic properties of the film affect the optical gain characteristics.[33] This is surprising since QD packing is a particularly important area of investigation in QD photovoltaics where ligand selection has been used to increase QD packing and therefore charge transport.[22] Initial results, however, have shown that small ligand engineering can allow for ultra-high optical gain of 650 cm^{-1} to 1200 cm^{-1}.[10,51] The increase of optical gain stems from the fact that the ligand affects QD packing density (QD-loading), and, in turn QD-loading affects the stimulated emission build-up time and optical gain value (**Eq. 7.1 & 7.2**).[5]

Eq. 7.1: Equation outlining the various factors that influence the optical gain magnitude in QD films.[5]

$$G = \frac{\sigma_g \xi}{V_{dot}}$$

Where,

G = gain value
σ_g = gain cross-section
ξ = packing fraction
V_{dot} = volume of QD

Eq. 7.2: Equation outlining the various factors that influences the stimulated emission lifetime in QD films.[5]

$$\tau_{SE} = \frac{n_r V_{dot}}{c \sigma_g \xi}$$

Where,

τ_{SE} = Stimulated emission build up time
c = speed of light
G = gain value
n_r = effective refractive index
V_{dot} = volume of QD
ξ = packing fraction
σ_g = gain cross-section

In addition, QD-loading affects the effective refractive index of the film which affects the degree of light confinement.[5] Furthermore, tightly packed QD films with short QD ligands exhibit higher thermal transport, which is an important factor to consider for film integrity under opt ical pumping.[10,52] The functional groups of the ligand also control the type of bonding to the QD surface (L-type versus X-type) and how readily reversible adsorption/desorption occurs.[53,54] Finally, the thermodynamic properties of the ligands (melting point, vapor pressure, boiling point) can vary widely between short and long ligands,[55] which can affect the physical and optical stability of the films due to desorption of ligands, film dewetting, or rearrangements of QDs. Understanding how the QD ligand choice affects the optical gain properties is thus critical to optimize system design, and could offer new strategies for tuning the magnitude and stability of optical gain that have not been considered before.

In this work, we demonstrate how the optical gain characteristics (threshold, magnitude, and stability) of QD films depend on the type of ligand used to stabilize the QD. These results are examined from the perspective of how the size and thermodynamic

properties of the QD ligand affect the physical properties of the film, including QD-loading fraction and refractive index. We show that replacing traditional long chain ligands with shorter ligands can increase QD-loading up to 50% and consequently increase the refractive index up to 1.88 (at 650 nm). These changes profoundly influence the emission light confinement within the film, as well as the optical gain magnitude, with more than a two-fold increase observed between the long and short QD-ligand systems. These property changes have led to exceptionally high gain values (~500 cm^{-1}) for a Cd-based QD system, as well as excellent optical stability. This research shows a facile approach for tuning the QD gain characteristics that does not require any modification to the QD synthesis process.

7.2 Experimental details

QD-ligand film preparation. QD films were fabricated via spin-casting (2000 rpm, 1.5 minutes) a QD solution (heptane or toluene). Film thickness ranged from 150-250 nm in order to support only the first waveguide mode. QD films were deposited on a CYTOP film (1400-1600 nm thick) which has a sufficiently low refractive index (n_{650} = 1.34) to cause light confinement and waveguiding within the QD film.[56] The CYTOP was exposed to air or Ar plasma for 5 seconds in order to improve wetting of the CYTOP by the QDs. Silicon with a 290-295 nm thick SiO_2 surface layer was used as a substrate to minimize leakage (and attenuation) of light from the QD film. However, the attenuation of light that does leak from the QD film into the Si substrate helps ensure that the light detected at the edge is the light that has propagated through the QD film (and not the substrate). The substrates were cleaved to obtain sharper, cleaner edges which improve the intensity of the output light and to help ensure that the area of the film exposed to the pump light was uniform over the length of the pump strip length.

Confinement factor modeling. Modeling of the confinement factor was done using Mode Solutions (version 7.7.786) from Lumerical Solutions Inc. The confinement factor (for the E_x component) was determined by integrating the power of the electric field over the thickness of the QD film and normalizing against the total power in the system. A 1 dimension y-direction solver (1DT: Z-propagation model) was used to determine the modes and electric field distributions, where the film cross-section was in the xy-plane and the light propagation in the z-direction. The theoretical layered model corresponded closely to the actual layered systems in terms of thicknesses and refractive index (the refractive index of each QD-ligand combination was obtained from an average of multiple films).

Optical gain and loss measurements and fitting. The third harmonic (355 nm) of a Spectra Physics Quanta-Ray INDI-series Pulsed Nd:YAG laser (pulse width of 5-8 ns, repetition rate of 10 Hz) was used as a seed for a GWU-Lasertechnik basiScan Beta-Barium Borate Optical Parametric Oscillator, producing a pulse of wavelength 440 nm. 440 nm was used for all ASE threshold, gain, and loss measurements.

Variable stripe length (VSL) gain measurements were performed according to standard procedure.[74] The excitation beam was shaped into a stripe of 125 μm width using a cylindrical lens (15 cm focus length), and the stripe length was controlled by a pair of blades mounted on mechanically controlled stages that provided an adjustable slit. Only the central 10% of the beam was used to minimize pump inhomogeneity due the Gaussian intensity profile. The pump beam intensity, I_{pump}, was varied by means of a pair of polarizers or neutral density filters. One end of the stripe excitation was placed on the cleaved edge of the film while the length of the excitation stripe was progressively

increased. The emission from the edge was collected with a 5 mm fiber and recorded using a commercial spectrometer (Ocean Optics USB4000; resolution 2 nm). Gain values were extracted according to the model proposed by Malko et al.,[39] that, in addition to the exponential gain term, incorporates a linear exciton term to account for photoluminescence. This has been a common approach for fitting QD gain.[11,33,35,51]

Loss measurements were conducted in the same experimental geometry. However, in this case, the length of the excitation stripe was held constant, while the distance of the stripe from the edge of the film, d, was varied by simultaneously varying the position of both blades.[57] As the emission propagates towards the collecting fiber, it experiences attenuation by scattering and re-absorption in the unexcited region of the film. The decay of the collected emission signal with increasing distance, d, from the edge was fit to an exponential law: $I(d) = I(0)\,\mathrm{Exp}(-\alpha d)$ to extract the loss coefficient α.

Gain threshold values were obtained by determining the intersection of the linear fits to the low intensity (linear) region and the high intensity (superlinear) region of the pump fluence versus emission plot (on a log-log scale).

7.3 Results and discussion

7.3.1 Quantum dot characteristics

The quantum dots in this study have a core/graded shell type-I composition ($CdSe/Cd_{1-x}Zn_xSe_{1-y}S_y$), diameter near 8 nm, and exhibit typical broadband absorbance below 614 nm and a Stokes-shifted narrow emission peak near 624 nm (**Figure 7.2a**). All QD films use the same type of quantum dot since the presence (and type) of inorganic passivating shell has been shown to affect exciton dynamics and gain

properties.[46,48] The length of the amine-functionalized ligands was varied from 16 (hexadecylamine), 8 (octylamine), to 4 (butylamine) carbon atoms in order to examine how the maximum QD-packing density depends on the ligand length (**Figure 7.2b,c**). Oleic acid was chosen as a standard control primarily because it is a common QD ligand widely used in the literature.[10,24,45,58]

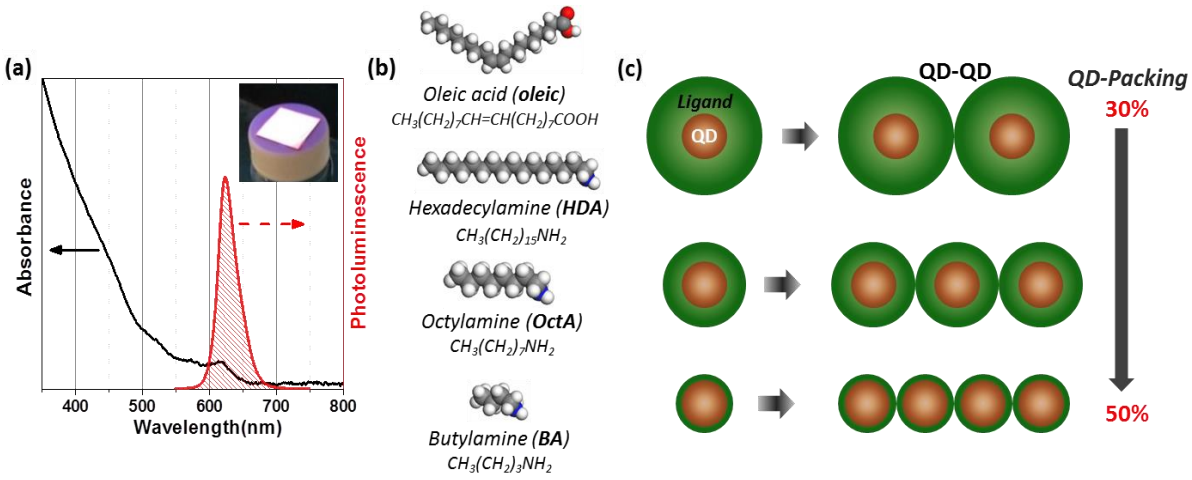

Figure 7.2: The QDs show broadband absorption and narrowband emission (a). Ligands of different size (b) were used to stabilize the QDs in order to control the spacing between adjacent QDs when deposited into film (c). The QD-QD spacing dictates the maximum QD-packing density.

The efficiency of the ligand exchange process is monitored and confirmed via NMR, an example of which is shown in **Figure 7.3**. . The optical properties of the QDs were examined before and after the ligand exchange since the process involves exposure to multiple solvents and washing steps, as well as a change from a carboxylic functional binding group to an amine group.

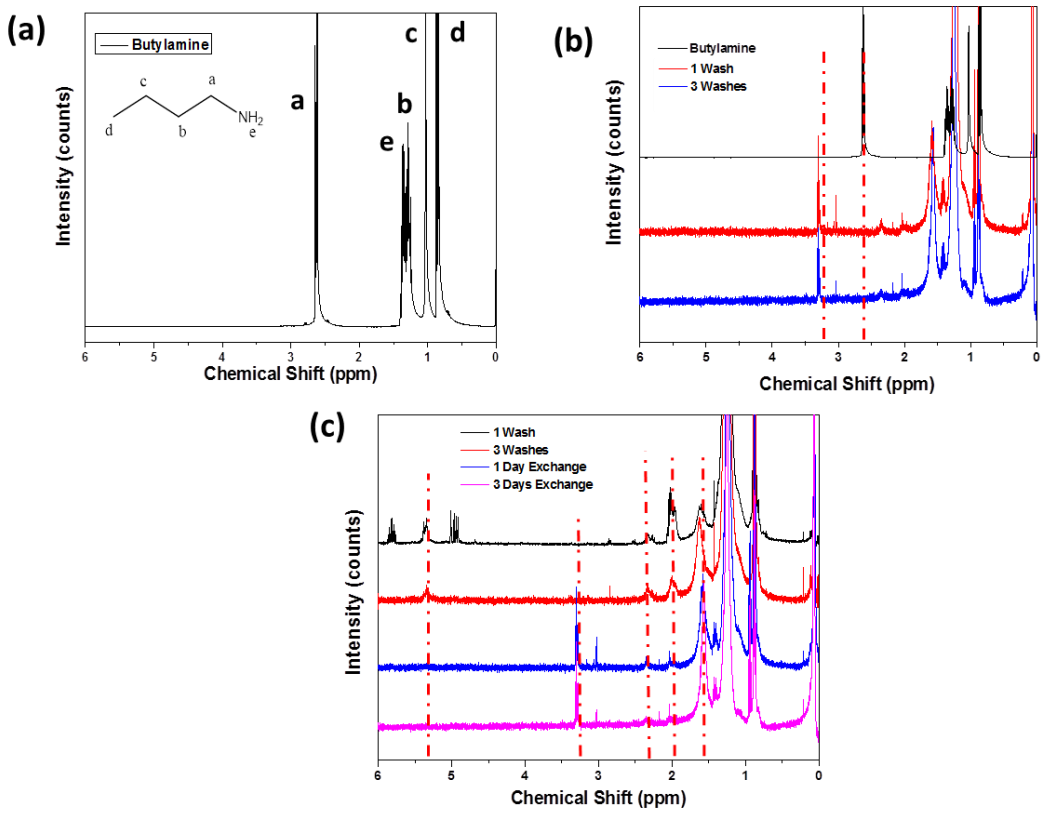

Figure 7.3: NMR was used to evaluate the efficiency of the ligand exchange. (a) NMR of butylamine (the ligand that will be displacing oleic acid on the QD surface). (b) NMR of butylamine and of QDs that underwent a ligand exchange from oleic acid to butylamine. The BA peak at 2.8 ppm (hydrogen peak) shifts to 3.2 ppm which is likely due to interaction with QD surface. (c) Comparison of NMR from different points in the washing process and ligand exchange process.

Quantum yield experienced the most notable change (decrease) after the ligand exchange process, with other optical properties remaining nearly unaffected (**Table 7.1)**. Decreases in quantum yield are typically attributed to less effective passivation of the QD surface which opens up nonradiative relaxation pathways for exciton recombination.[53,59,60] The absorbance and emission profiles are similar before and after the ligand exchange procedure.

Table 7.1: Optical properties of the QDs before and after the ligand exchange process.

	Oleic-acid	Hexadecylamine	Octylamine	Butylamine
QY (%)	50	50	20	29
ABS_{1s} (nm)	614	614	617	617
Emission Position (nm)	624	624	624	623
FWHM (nm)	32	34	31	30

However, in this case the variation in QY should not be a critical factor since the stimulated emission lifetime of these QD films (less than 0.1 ns as predicated by **Eq. 7.2**) (**Table 7.2**) is much shorter than typical alloyed QD spontaneous recombination lifetimes (<4 ns).[59,60]

Table 7.2: Table of the predicted stimulated emission lifetime of the ligand-QD films based on the measured refractive index and optical gain values of the QD films.

QD-ligand	Predicted Stimulated Build-Up Time (ps)
Oleic acid	94
Hexadecylamine	26
Octadecylamine	12
Butylamine	12

7.3.2 QD film uniformity & morphology

QD films were fabricated via spin-casting, covering the substrates uniformly and having uniform PL emission, as evidenced by bright field, dark field, and photoluminescence imaging (**Figure 7.4**).

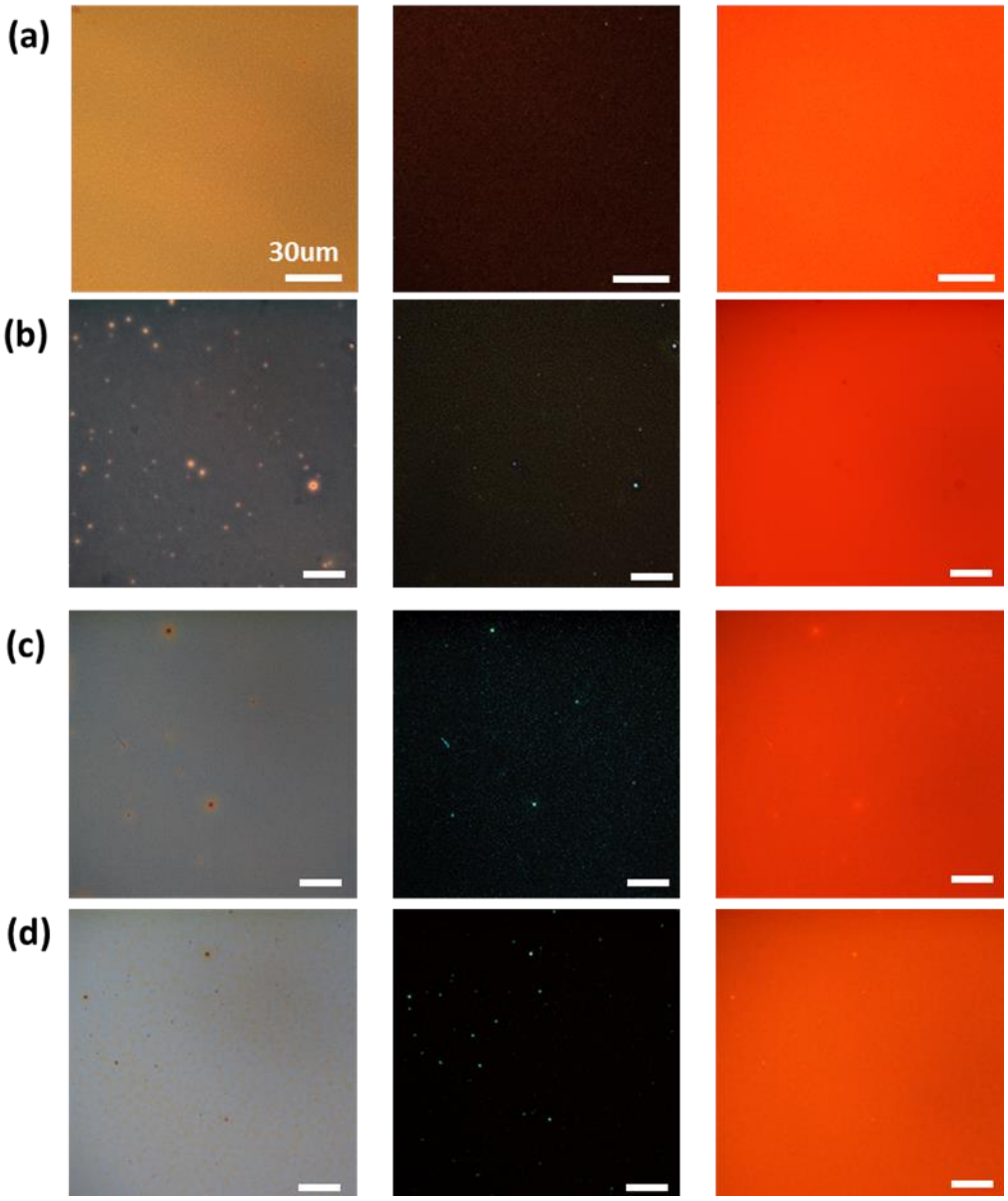

Figure 7.4: Bright field (column 1), dark field (column 2), and fluorescence (column 3) images of (a) oleic acid, (b) hexadecylamine, (c) octylamine, and (d) butylamine capped QD films. Imaging shows that the films exhibit similar uniform morphology and fluorescence emission as well as some scattering due to surface defects. All scale bars are 30 um.

The QD films were deposited on a fluorinated polymer layer (CYTOP) with a low refractive index to improve light confinement (waveguiding) within the QD film.[51,56] The CYTOP film was briefly exposed to plasma in order to promote wide-spread wetting by the QD film. AFM topographical and phase images show that the morphology of the QD films depends on the ligand coating the QDs. Films of oleic acid capped QDs (oleic-QD) show the presence of domains with a lattice-like arrangement of QDs (**Figure 7.5a**). The phase image indicates that the QD domains are separated from adjacent QD domains by regions of a different phase which is likely excess oleic acid that was not removed during washing as well as a thick coating of oleic acid from submerged QDs.

The QD films of hexadecylamine-capped QDs (HDA-QD), octylamine-capped QDs (OctA-QD), and butylamine-capped QDs (BA-QD) have larger particle-like domains (likely aggregated QDs) that appear to cover the entire surface area (**Figure 7.5b,c,d**). The formation of localized lattice-like regions has been observed previously in oleic acid-QDs films, as well as the transformation to a more chaotic pattern upon replacement with a shorter ligand like butylamine.[22] We attribute the presence of a lattice arrangement in the oleic-QD film and the tighter aggregate arrangement in the BA-QD, OctA-QD, and HDA-QD films to two factors.

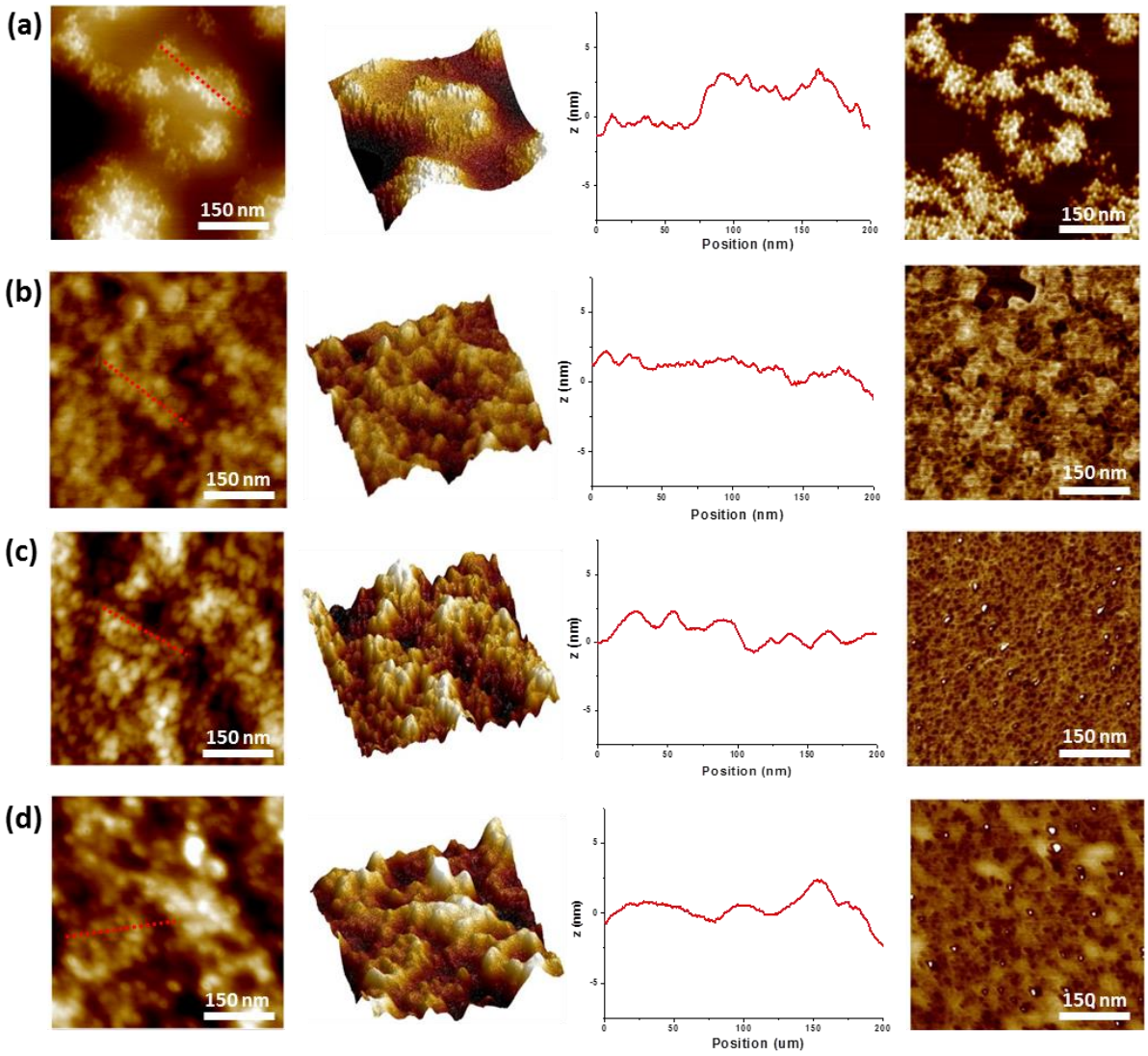

Figure 7.5: AFM surface morphology (column 1), 3D topography projection (column 2), topographical cross-section (column 3), and phase (column 4) for (a) oleic acid, (b) hexadecylamine, (c) octylamine, and (d) butylamine capped QD films. Z-scale is 20 nm for the oleic-QD film scan and 10 nm for all others. Phase scale is 20° for the oleic-QD film scan and 10° for all others.

First, oleic acid provides exceptional colloidal stability due to its covalent bond with the QD surface and large size, which reduces aggregation of QDs in solution and allows for deposition of individual QDs that can form uniform QD lattice domains during spin-casting. On the other hand, the QD colloidal stability provided by the amine-based ligands (BA, OctA, HDA) is not as effective, which can lead to minor QD aggregation in solution that leads to larger domains in the film state. Second, the volume of oleic acid is greater than all the amine functionalized ligands (discussed later), which leads to greater spacing between QDs in the film state than that provided by the smaller amine-ligands. Greater QD spacing makes it easier for lattice-like QD arrangements to be observed.

Cross-sections of the height scans show a surface with sub-nanometer high bumps, indicating that the QDs are tightly packed with the free ligand filling the areas between adjacent QDs. The R_q roughness spans from approximately 4 nm (500 nm scan area) to 8 nm (10 um scan area) for all samples. In some instances, BA-QD films will appear smooth with no clear indication of QDs if examined very soon after film deposition, which is likely due to the fluid-like nature of butylamine at room temperature (melting point of -49°C in free state) and its volatility (vapor pressure of 82 mmHg).[55] This fluid nature can compromise the AFM scanning to track surface features.

7.3.3 Ligand characteristics & QD-loading (volume fraction)

The four ligands used in this study each have a different molecular volume in the free-state (oleic acid: 0.320 nm^3, HDA: 0.295 nm^3, OctA: 0.159 nm^3, BA: 0.091 nm^3).[55] Therefore, changing the ligand may change the maximum allowable QD-packing density

(volume loading) in QD films, which could impact the magnitude and threshold of optical gain.

The QD-packing density was monitored using a variety of approaches. High-resolution TEM (HR-TEM) of drop-cast QD films shows that the space between QDs decreases as the size of the ligand is decreased, with oleic-QDs having the largest QD spacing and BA-QDs having the smallest (**Figure 7.6a**). In addition, QD content was estimated using ellipsometry (**see Experimental section**).[51] Examination of multiple films for each type of ligand-QD film agrees with the trend observed in HR-TEM, with QD-loading (volume percent) ranging from approximately 30% for oleic-QD films to 50% for the BA-QD films (**Figure 7.6b**).

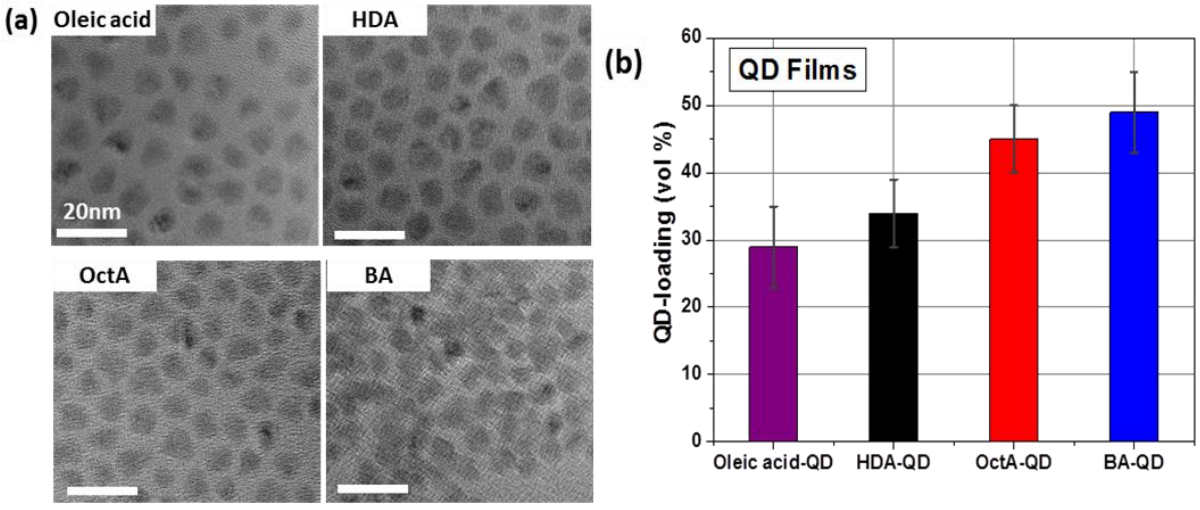

Figure 7.6: Four ligands of different size were used in order to examine how QD-packing is affected by ligand size. (a) HR-TEM micrographs of drop-cast QD solutions and (b) ellipsometry characterization of spin-cast QD films show that reducing the size of the ligand increases the QD-loading (packing density) of QDs in films. Scale bar is 20 nm for all TEM micrographs.

A similar increase in density of QD films has been observed previously upon exchanging oleic acid for butylamine (before film deposition).[22] The observed trend between ligand size and QD-loading follows the theoretical relationship between QD-loading and ligand size, which predicts 40% face-centered-cubic (FCC) loading for oleic-QD and 50% for BA-QD (no unbound ligand is present in the film) (**Appendix D Figure D.1**). Finally, TGA of drop-cast QD films shows that the amount of organic material (excess ligand and bound ligand) present in the QD solutions generally decreases for shorter ligands **(Figure 7.7a)**, which corroborates the trend seen in HR-TEM and ellipsometry.

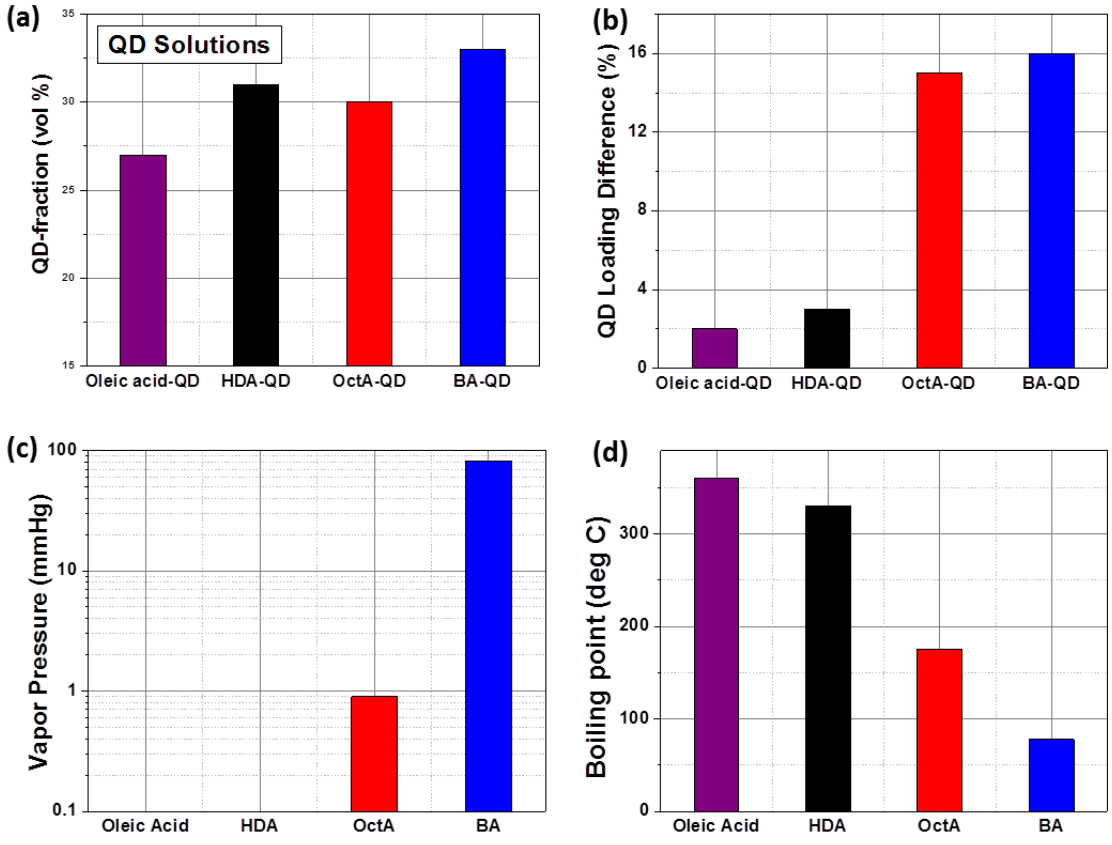

Figure 7.7: Examination of the QD fraction in solutions and how it compares to QD films. (a) Thermogravimetric analysis (TGA) of QD solutions. (b) The difference in QD volume fraction between QD films and the QD solutions. The (c) vapor pressure and (d) boiling point of each ligand. Note, the vapor pressure of oleic acid and hexadecylamine area very low at room temperature (< 1 mmHg) and therefore were approximated to have a zero value.

Differences in the specific QD volume fraction between the spin-cast QD films and drop-cast QD films can be attributed to the difference in deposition methods, as well as the volatility of the ligands (**Figure 7.7**).[55,61,62] There appears to be a difference of QD volume fraction between the QD films and QD solutions. The magnitude of this difference correlates with the volatility of the specific ligand. For example, butylamine-QDs, which display the largest difference between the film state (49 ±6%) and solution state (33%) also is the most volatile ligand (highest vapor pressure, lowest boiling point). Note, value ranges are one standard deviation in the film state (29 ±6%) and solution state (27%) is the least volatile (lowest vapor pressure (V_p), highest boiling point). This trend occurs for all ligands examined (**Table 7.3)**.

Table 7.3: Table of the QD-loading (%) of the QD films, the QD volume fraction (%) of the QD solutions (determined by ellipsometry and TGA, respectively), and the thermodynamic properties of each ligand.[55]

QD-ligand	Film QD-loading (%)	Solution QD-loading (%)	Solution-Film Difference (%)	Vapor Pressure, 25C (mmHg)	Boiling Point (°C)
Oleic acid	29	27	2	0	360
HDA	34	31	3	0	330
OctA	45	30	15	0.9	175
BA	49	33	16	82	78

The volatility of the ligand is an important factor affecting the formation of the film during spin-casting and storage. The volatility of the QD ligand has been shown to strongly impact ligand desorption, with a highly volatile ligand (pyridine, V_p = 20 mmHg at 25°C) showing large desorption (≈70%) under ambient conditions while a low volatility ligand (trioctylphosphine oxide, $V_p \approx 0$ mmHg at 25°C) shows nearly no desorption.[55,61,62] Therefore, the high volatility of butylamine and octylamine leads to some degree of desorption from the film during storage. Even more importantly, the volatile ligands will

experience strong desorption from the film surface during spin-casting (unbound ligands in particular) due to the highly turbulent atmosphere above the film. These two factors thus increase the QD volume fraction and lead to a large difference between the QD volume fraction measured in the film state and solution state.

QD packing is a critical characteristic since optical gain is proportional to QD volume fraction.[5] For example, an increase of QD packing from 30% to 45% (factor increase of 1.5) is expected to cause a similar 1.5 factor increase in the magnitude of optical gain (**Eq. 7.1**). In addition, QD packing affects the film refractive index, which affects the degree of light confinement within the QD film, the number of waveguide modes, and the optical loss due to leakage of light during propagation.[63] A higher film refractive index increases the index contrast with the underlying material (CYTOP) and increases light confinement within the film, a necessary condition for achieving high optical gain.

7.3.4 Optical gain threshold, magnitude, & stability

The existence of ASE is supported by a number of emission characteristics such as the presence of clear threshold behavior in emission intensity versus excitation intensity plots.[11,45,64] At threshold, the emission dependence on the pump excitation intensity transitions from approximately linear at low intensity to super-linear at successively higher pump fluence, as was clearly observed for all QD samples **(Figure 7.8)** (note both axes are log scale). ASE threshold values were obtained by determining at what fluence this transition occurs (**Appendix D Figure D.2**).

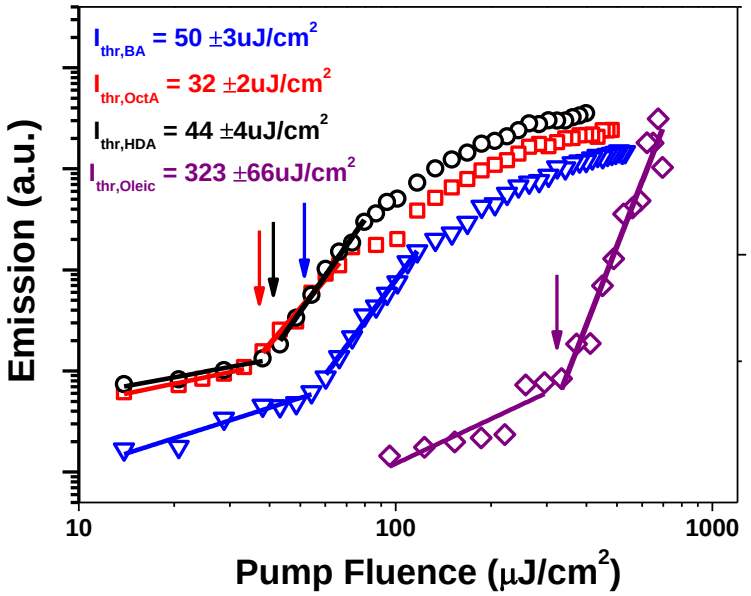

Figure 7.8: ASE in the QD films is identified by multiple characteristics of QD emission as the QD film is pumped with different excitation powers. Emission intensity (log-log, scaled for clarity) showing threshold behavior.

The light-light curves were quite consistent over multiple spots (**Appendix D Figure D.3**). The BA-QD, OctA-QD, and HDA-QD films exhibited thresholds of approximately 30-50 uJ/cm^2 which matches many of the lowest QD film thresholds to date,[10,11] and is 5-10 times lower than the threshold of typical drop-cast QD films using traditional ligands.[45,64]

The exceptionally low thresholds are attributed to the uniformity of the QD films and the high QD-packing density, which allow for efficient light generation and propagation. Furthermore, the core/graded shell composition of the QD also plays an important role, with previous studies showing that a graded shell imparts very effective surface passivation of the core. This passivation decouples the core exciton states from surface trap states, effectively deactivating the non-radiative surface trap relaxation pathway.[46,65]

ASE threshold indicates the point where optical gain and loss are equal, and can depend on a number of factors.[66] In this case, the large differences in threshold are attributed primarily to the nature of the physical and thermal properties of the ligand. All ligands with the alkane structure and amine functionalization (butylamine, octylamine, and hexadecylamine) have similar thresholds, which are also much lower than that shown by the film with the oleic acid ligand (which has an internal double bond and a carboxylic acid terminal group). The internal double bond makes oleic acid waxy at room temperature and therefore highly fluid under optical pumping. This fluidity allows for more QD diffusion, which can lead to QD aggregation that increases optical scattering (optical loss) and modifies the localized refractive index (disrupts light propagation), both of which would delay the onset of ASE (increase the threshold). Furthermore, the waxy nature makes oleic acid QD films highly susceptible to physical damage.

The functional group of the ligand could play a role as well by imparting different degrees of surface passivation to the QD, which has been shown to have an impact on exciton trapping rates and the required average exciton gain threshold.[46,67] Auger recombination (an important obstacle for achieving QD optical gain) has also been shown to depend on factors like charged exciton states that could be influenced by the ligand functional group.[68,69] In addition, non-radiative hole relaxation has been shown to occur through a non-adiabatic ligand-mediated mechanism, which means different ligands could increase or decrease this non-radiative pathway.[70] However, this phenomenon is hindered by the presence of an inorganic shell so it is not likely to be an important factor for the core/graded shell QDs in this study. Likewise, it has also been shown that the Auger recombination rate can, in certain instances, be relatively independent of surface passivation.[71] So, at this point in time it is unclear how intrinsic exciton dynamics are affected by the ligand choice and its influence on ASE threshold.

Spectral narrowing of the emission peak occurs simultaneously with threshold behavior and is an additional critical indication of the ASE phenomenon.[11,64] The FWHM of PL of all samples was approximately 30-40 nm, but narrowed to around 10 nm once ASE emerged (**Figure 7.9**), which is common for QD ASE.[11,64]

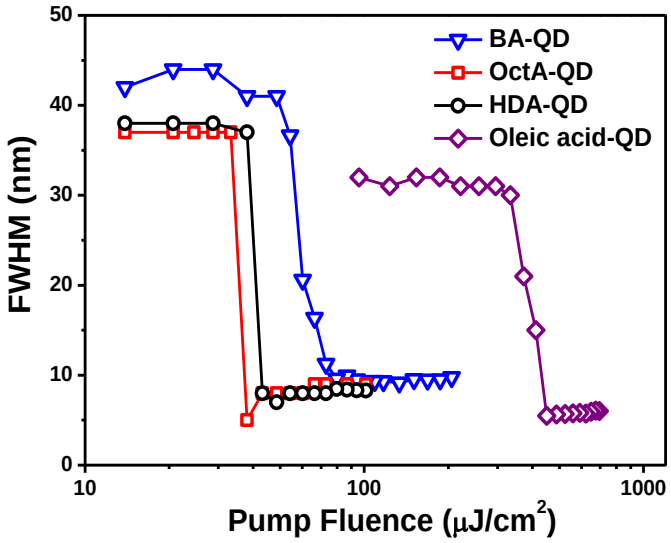

Figure 7.9: The full-width at half-maximum (FWHM) of the QD emission peak for various QD-ligand combinations showing spectral narrowing upon the onset of ASE.

All films show similar spectral narrowing (78 ±3% reduction) compared to their initial PL FWHM. However, the QD film with the oleic acid ligand (carboxylic acid functionality) displayed the narrowest ASE FWHM (6 nm) since it began with the narrowest PL FWHM (32 nm). The QD films with amine functionalized ligands all show similar spectral narrowing to a FWHM of 11 nm (from ≈40 nm). The difference in PL FWHM appears to be correlated with how well the QDs are physically arranged and the chemical functionality of the ligand. As shown previously, the oleic acid-QD film has domains of well-ordered QDs while the amine-QD films (BA-QD, OctA-QD, and HDA-QD) have a less ordered arrangement (**Figure 7.5**). These differences could affect the degree of

optical scattering during light propagation (and therefore the broadening of PL FWHM). In addition, the chemical functionality of the ligand can affect QD surface passivation which affects the emission position, quantum yield, and electronic structure of the QD surface.[72] Additional confirmation of ASE is provided by the 10-15 nm red-shift of the ASE peak compared to the PL peak (**Appendix D Figure D.4)**. This is a common trait of ASE often attributed to interparticle electronic energy transfer and optical re-absorption.[64,73]

The direct quantitative measurement of optical gain for each film was obtained using the variable stripe length (VSL) pumping approach, which involves optical excitation of the film using an excitation strip of variable length.[74] If positive net gain is achieved, the spectrally narrowed ASE peak will emerge as the pump length is increased and the emission will exhibit an exponential increase of intensity as the optical pump strip is lengthened (**Figure 7.10a,b**).[33-35]

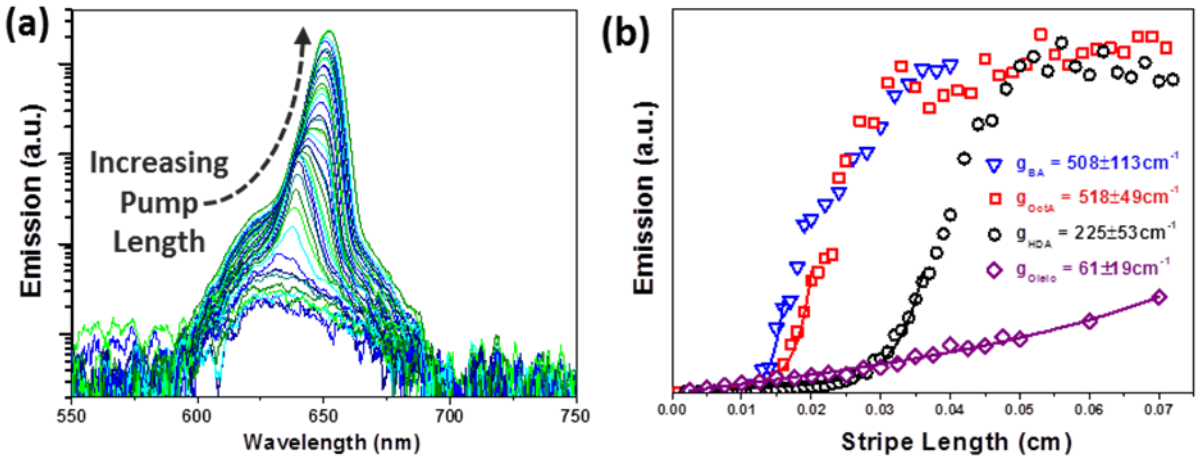

Figure 7.10: The optical characteristics of the QD films were determined using the variable strip length (VSL) method. (a) Emission of an OctA-QD film (log-intensity) at various pump strip lengths. The emergence of ASE is indicated by narrowing of the emission peak. (b) Emission intensity versus pump length for various QD-ligands (curves were off-set for clarity) (I_{pump} = 200 uJ/cm^2).

Optical gain appears to scale with QD-packing (for the same ligand functional group), with the HDA-QD film displaying modest gain (225 ±53 cm^{-1}) similar to that reported in the literature for Cd-based QD films.[33,64] In contrast, the OctA-QD and BA-QD films exhibit the highest gain (518 ±49 cm^{-1} and 508 ±113 cm^{-1}, respectively) (**Figure 7.11**).

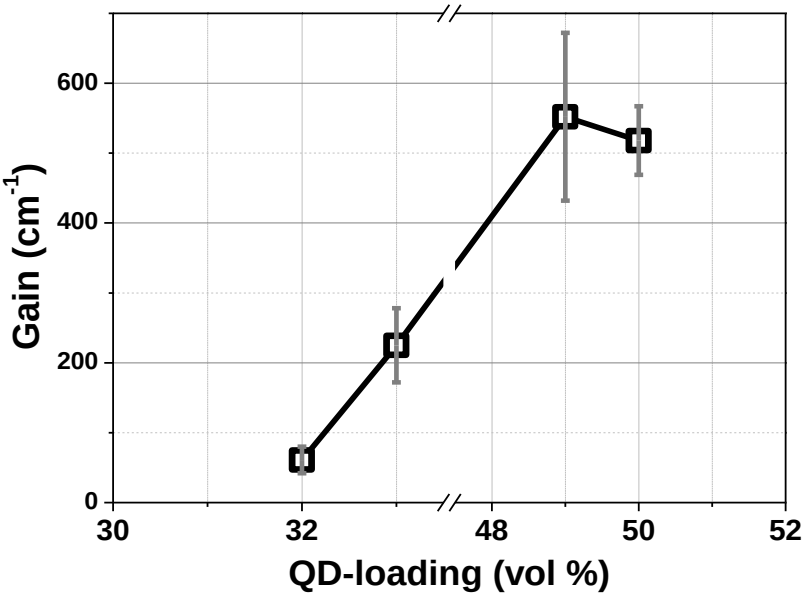

Figure 7.11: Optical gain versus QD-packing density. QD films with higher QD-packing exhibit higher optical gains.

The OctA-QD and BA-QD films have similar gain values because in this case the films had similar QD-loading (50% and 49%, respectively), indicating that QD-loading is affected by both ligand length and the washing process. Gain values were averaged from multiple spots over a sample (**Appendix D Figure D.5)**.

These gain values exceed typical QD gain values (60-200 cm^{-1}) due to the exceptionally high QD-loading,[33-35,37,38] approaching some of the highest values reported.[36] Although, as we suggest, the high optical gain is primarily a result of QD-loading, a number of additional system characteristics play a role. These factors include reduced surface

trapping and Auger recombination due to the core/graded shell QD interface,[24,46] strong light confinement due to the incorporation of a sub-cladding layer with a very low refractive index, and increased absorption of the pump beam caused by the use of a reflective substrate.[51] An oleic acid QD film displayed a low optical gain (61 ±19 cm^{-1}) that was difficult to reliably measure due to its fluctuating ASE but was included as a reference sample since oleic acid is a commonly used QD ligand (discussed below).

The difference in optical gain magnitude between the films with different ligand-QD combinations can be attributed to a number of factors. First, as mentioned above, the material gain value is expected to depend on the QD packing density (**Eq.7.1**)[5] due to an increase in the density of optically excited QDs that participate in the ASE process as well as an increase in the optical density of the film. An increase of optical gain due to higher QD packing density has been observed experimentally in layer-by-layer systems.[33] For example, the increase of QD packing from the HDA-capped QD film (34%) to the BA-capped QD film (49%) can explain a factor increase of 1.44 for the gain, which accounts for a portion of the differences between these films (factor of 2.3).

Second, gain depends on the degree of light confinement exhibited by the film since efficient light confinement leads to more stimulated emission within the film, as well as lower propagation losses from light leakage into adjacent layers. Light confinement depends primarily on film thickness and refractive index (RI) contrast between the QD film and the surrounding layers, with higher refractive index contrast leading to more efficient light confinement. Refractive index contrast was dictated by the RI of the QD film since the underlying material was always CYTOP (n = 1.34) and the top layer always air. Reducing the molecular dimensions of the ligands increases QD-loading

which increases the RI of the film (since QDs have a higher refractive index than the ligand).

For example, the OctA-QD and BA-QD films had the highest refractive index of all the films (1.86±0.05 and 1.88±0.06, respectively) near the propagation wavelength (630-650 nm). On the other hand, the oleic-QD and HDA-QD films had the lowest refractive index (1.72±0.04 and 1.76±0.05, respectively). The resulting degree of light confinement can be quantified by the confinement factor (Γ), which is a measure of the power of the E-field confined to the QD film versus the power of the E-field present within the entire system.[10] Higher confinement factors indicate greater localization of light within the QD film and an increase of modal gain ($g_{modal} = \Gamma \times g_{material}$).[10] Modeling of the confinement factor for each of the ligand systems for various thicknesses shows that the BA-QD film can exhibit a confinement factor up to 1.7 times that shown by the oleic-QD films and 1.4 times that exhibited by the HDA-QD films for relevant thicknesses (**Figure 7.12**).

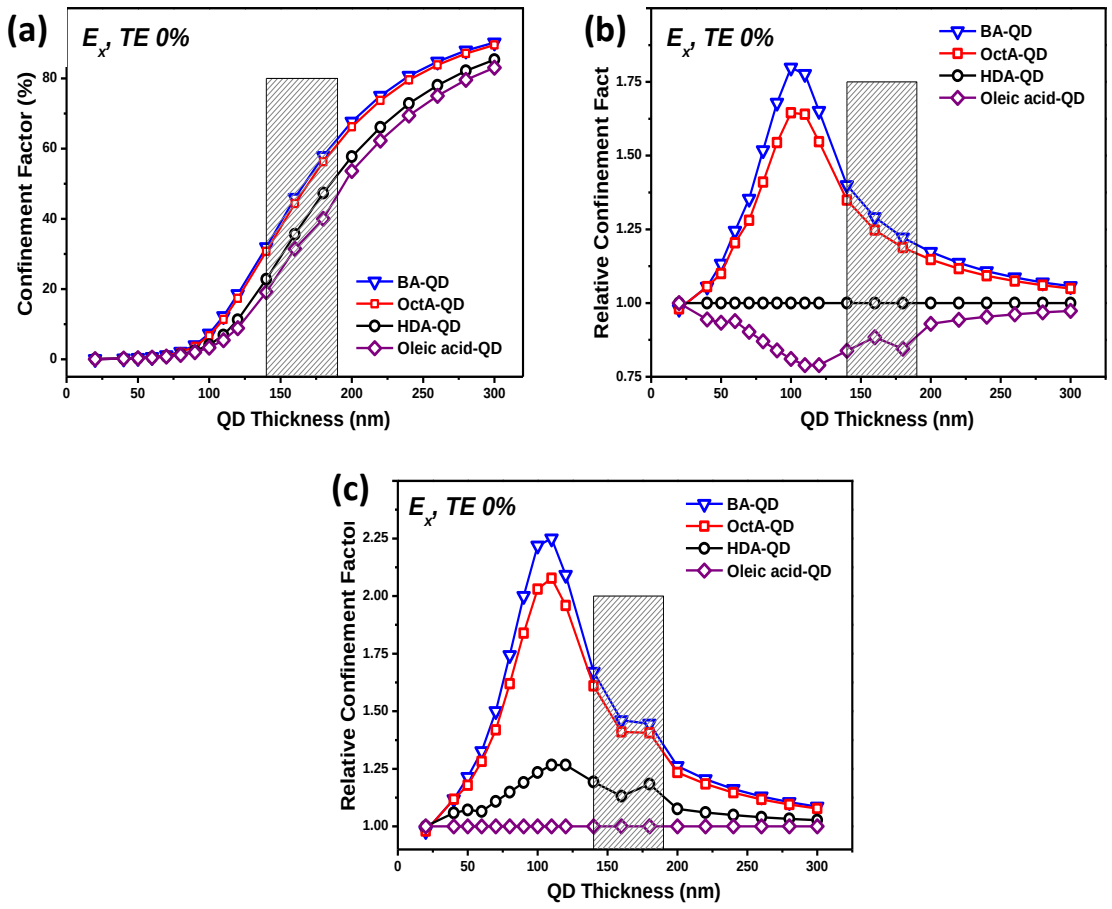

Figure 7.12: (a) Plot of the confinement factor (Ex, TE 0% mode) at 635 nm for films of different thickness and different refractive index. The relative confinement factor of each film compared to (b) the HDA-QD film and compared to (c) the oleic-QD film. The confinement factor is higher (for a given film thickness) for films with a higher refractive index. The grey shaded areas represent typical QD film thicknesses in this study.

In addition, the refractive index and thickness of the QD film determines the number and type of waveguiding modes, which affects propagation losses and might increase waveguiding efficiency. Therefore, all samples were designed to support only one waveguide mode by ensuring that the film thickness was above the first critical waveguiding thickness ($t_{c,1}$) but below the next highest critical waveguiding thickness ($t_{c,2}$) (**Figure 7.13**).[63]

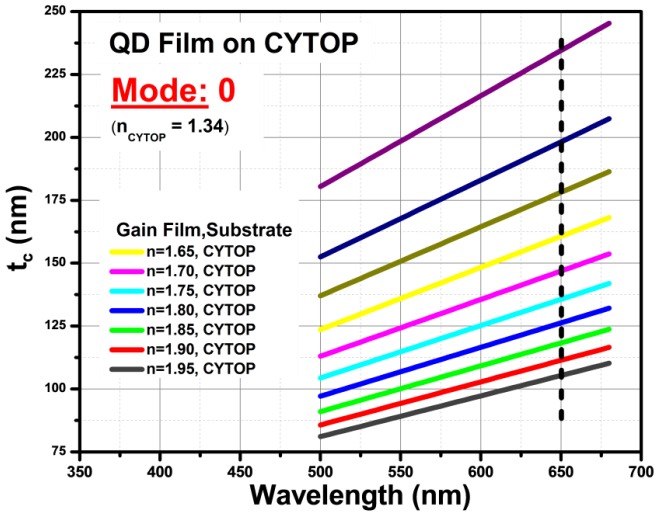

Figure 7.13: Plot of the critical thickness for the primary waveguiding mode for QD films with different refractive index on a CYTOP film (refractive index of 1.34). The function used to calculate the critical film thickness (t_c) assumes that the top layer is air.

Third, the arrangement of QDs within the film (lattice-like, aggregated, or intermittently spaced) can affect how light propagates through the film, either through the introduction of scattering sites, QD-QD coupling,[73] or transverse localization effects.[75] Optical losses associated with scattering (and re-absorption) are examined later. Fourth, thermal transport (and dissipation) depends on the length of the QD ligand and has been shown to be an important factor in QD gain systems due to thermal mediated Auger recombination.[10,52,76] Finally, the difference in gain value between the oleic-QD and HDA-QD film could be due in part to the chemical functionality of the ligands since these films have similar QD-loading and refractive index. The chemical functionality of the ligand has been shown to affect QD surface passivation, which in turn affects the quantum yield and electronic structure of the QD surface and trapping rates.[67,72] The Auger recombination rate could also play a role, although previous studies have shown the Auger recombination rate is more strongly dependent on other factors like the QD core-shell interface and volume than surface passivation.[70,77] The combination of these

factors likely contributes to the difference in optical gain values that can be obtained from QD films and indicates that the type of ligand on the QD surface can strongly impact optical gain a number of ways.

7.3.5 Photostability of the QD films

The stability of ASE was examined over a period of 30 minutes for each type of QD film (**Figure 7.14**). The QD films with amine functionalized ligands (HDA-QD, OctA-QD, BA-QD) display very stable ASE, which is an indication of the stable physical and thermal characteristics of the films under pumping.

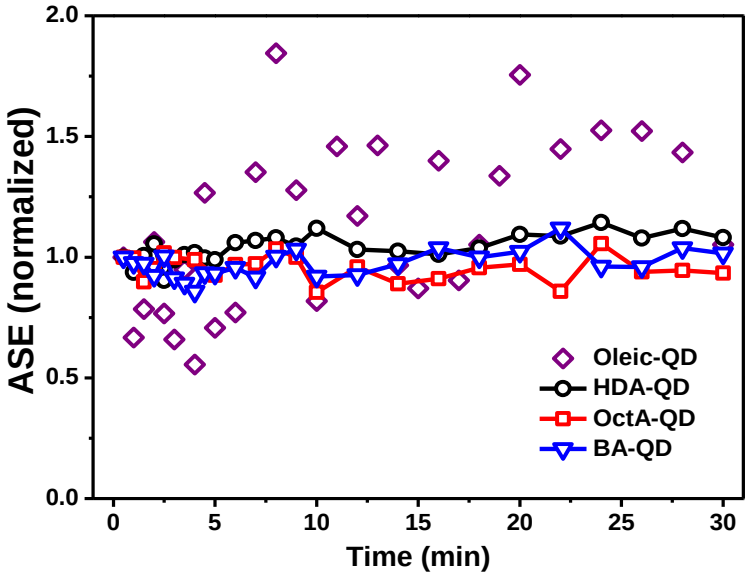

Figure 7.14: The magnitude and stability of optical gain depends on the type of QD-ligand pairing. (a) Optical gain versus QD-packing density. QD films with higher QD-packing exhibit higher optical gains. (b) Stability of ASE over a 30 minute period.

The stability of each ligand-QD combination can be explained by considering the interplay between QD-loading, the thermodynamic properties of the ligands, and the thermal transport/dissipation of the film. In general, stable ASE will arise if QD mobility

is minimized since mobility/rearrangement of QDs during optical pumping can lead to the formation of scattering sites (which increase optical loss) in the film, as well as alter the effective refractive index (which can affect light propagation). In addition, ASE will be more stable if heat dissipation is efficient since localized heating of the film can lead to dissociation of the ligands from the QD surface (which results in loss of QD surface passivation), and to more efficient Auger recombination (which also increases intrinsic optical loss).[76]

It is worth noting that the HDA ligand is relatively long so it yields films with relatively low QD-loading (34%) and only moderate thermal conductivity (near 0.25 W/m*k).[52] However, the HDA-QD films show stable ASE, which suggests the solid state of HDA (melting point of 45°C) and its low vapor pressure (≈0 mmHG at 25°C) are the strongest factors.[55] On the other hand, butylamine seems to derive its ASE stability from its high QD packing (49%) and higher thermal conductivity (1.5x higher than oleic-QD),[52] rather than its low melting point (-49°C) or high vapor pressure (8 mmHG at 25°C).[55] In fact, it is somewhat surprising that BA-QD films exhibit such stable ASE given the volatile nature of butylamine. It is likely that desorption of weakly bound BA occurs very quickly during spin-casting and storage so that by the time gain measurements are conducted there is minimal loosely bound BA to desorb during the optical pumping process. On the other hand, apart from its low vapor pressure (≈0 mmHG at 25°C) oleic acid is a poor choice for imparting optical stability due to the low QD-loading (29%), moderate thermal conductivity (near 0.25 W/m*k),[52] and its relatively low melting point (14°C) due to the double bond in its structure. These characteristics could allow for significant QD mobility and thermal modification of the ligands when the QD films are optically pumped, which manifest in the widely fluctuating ASE. These results show that consideration of the QD ligand is an important factor to consider in terms of optical gain magnitude and stability.

7.3.6 Optical loss

The intrinsic optical loss of the films was also measured to determine whether loss can account for differences in the gain values. Optical loss is determined by measuring the attenuation of ASE over different propagation distances.[57] Greater attenuation of ASE occurs as the distance travelled by the light to the edge of the sample increases. Attenuation of ASE is clearly evident in the spectra for all films and is shown for the HDA-capped QD film (**Figure 7.15a**). All amine films exhibit an exponential decrease in emission as the collective distance is increased (**Figure 7.15b**), as expected for films that exhibit optical loss. Loss values are averaged from multiple spots (**Appendix D Figure D.6)**.

The optical loss is observed to be proportional to the QD-loading of the film, with the HDA-QD film (lowest QD-loading) exhibiting the lowest loss (60±19 cm^{-1}) and the BA-QD and OctA-QD films (highest QD-loading) exhibiting the highest loss (82 cm^{-1}) (**Figure 15c**). It is difficult to judge the magnitude of these QD loss values since optical loss is often overlooked in gain studies on QD films.

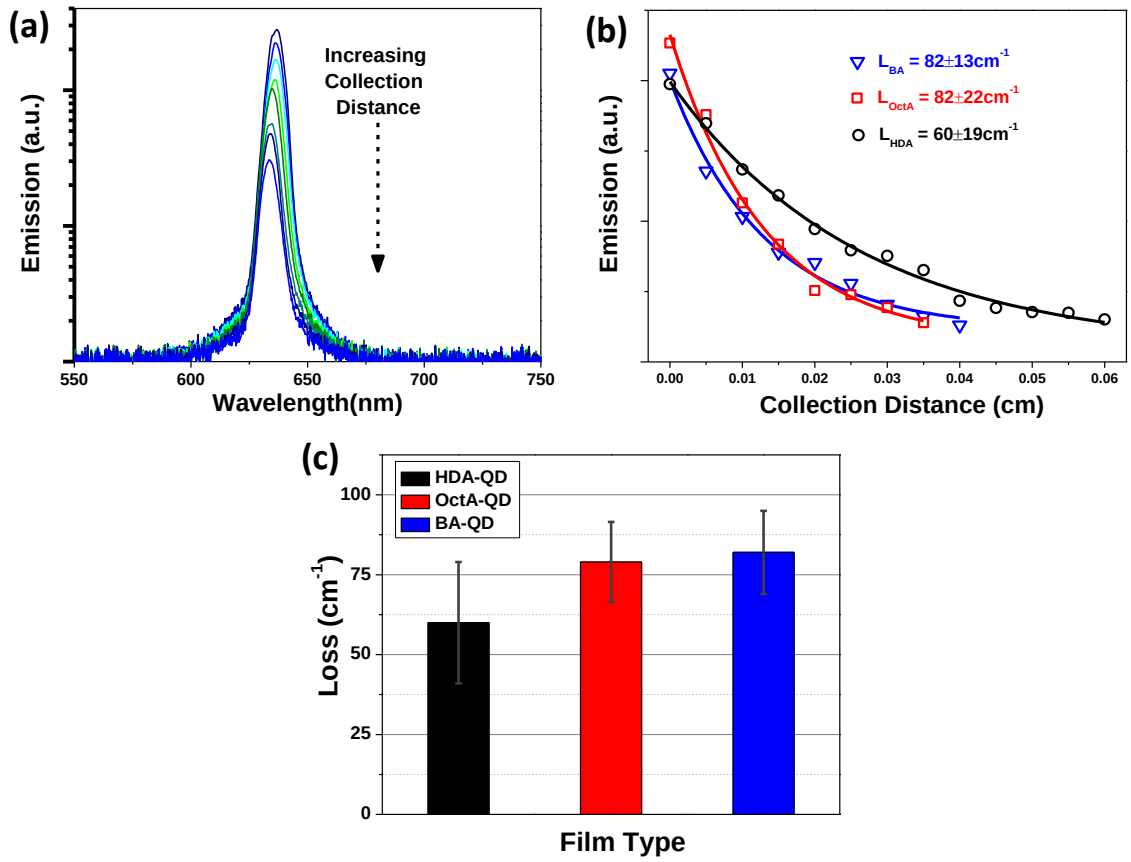

Figure 7.15: (a) Typical emission spectra from the variable attenuation length method for a HDA-QD film (log intensity). (b) Optical loss fitting for the HDA-QD, OctA-QD, and BA-QD films shows an exponential decrease with collection length. (c) Optical loss for different QD-ligand films.

However, these optical loss values are similar (within a factor of 2) to those exhibited by conjugated polymers films.[57] The scaling of loss with QD-loading is not surprising since optical re-absorption (an important component of optical loss) is proportional to QD-loading since the emitted light encounters more QDs (for a given distance) as it propagates through the film. In fact, the predicted loss for the BA-QD and OctA-QD films (scaled against the HDA-QD loss) falls within ±5% of the measured values, well within the measured standard deviations. The unstable nature of ASE for the oleic-QD film made measuring loss unreliable (**Figure 7.14**). These results suggest that optical loss is not the primary factor underlying the observed trends in gain versus QD-loading since the films with highest optical loss still displayed the highest net optical gain.

7.3.7 Ligand selection

The ideal ligand depends on the relative importance of gain threshold, FWHM, magnitude, and stability, as well as optical loss. A set of general ligand selection guidelines are provided in **Table 7.4**:

Table 7.4: General ligand selection rules for thin QD films for optical gain (or loss) systems.

QD Ligand Selection Guidelines			
Requirements	**Ligand Characteristic**	**Reason**	**Ligand Option**
Higher QD-QD packing	Smaller volume	Reduces fill between QDs	Butylamine, octylamine
Higher refractive index	Smaller volume	Reduces fill between QDs (which tend to have a high refractive index)	Butylamine, octylamine
Higher optical gain	Smaller volume	Higher QD-loading, higher confinement factor	Butylamine
Lower gain threshold	Aliphatic structure, no internal double bond	Minimum QD mobility under optical pumping	Butylamine, octylamine, hexadecylamine
Narrower PL & ASE FWHM	Carboxylic acid functionality	Better QD surface passivation	Oleic acid
Lower optical losses	Longer ligand	Lower optical density and less optical reabsorption	Hexadecylamine
Higher ASE stability	High T_m, low V_p, high B_p, ligand provides high QD-loading	These characteristics minimize QD-mobility when heated during optical pumping	Butylamine, octylamine, hexadecylamine
Lower volatility film	Longer ligand	Longer ligands tend to have higher vapor pressure	Hexadecylamine, oleic acid
Higher melting point film	Longer ligand (avoid internal double bond)	Longer ligands have higher melting points (in general)	Hexadecylamine
Higher colloidal stability	Longer ligand, covalent bonding functional group	Provides better steric hinderence, less desorption from QD	Hexadecylamine, oleic acid
Higher colloidal quantum yield	Carboxylic acid functionality	Better QD surface passivation	Oleic acid

Aliphatic amine functionalized ligands (butylamine, octylamine, hexadecylamine) were shown to provide lower gain threshold than that provided by oleic acid (internal double bond and carboxylic acid functionalization), while the narrowest FWHM of ASE was obtained using oleic acid (presumably due to the well-ordered physical domains). On

the other hand, shorter ligands can result in higher QD-loading (which increases the number of optically stimulated QDs) and higher refractive index (which increases the confinement factor), both of which result in proportional increases to optical gain.

Obtaining stable ASE is slightly more complex, but generally requires very tight QD packing, good thermal stability (high melting and boiling points, low vapor pressure), and high thermal transport/dissipation. Unfortunately, these characteristics are not always independent, as seen with short organic ligands that offer high QD packing and large thermal dissipation,[52] but which typically exhibit low melting and boiling points and high volatility (and vice versa).[55] Predicting the relative impact of these factors is difficult. Finally, optical loss scales closely to QD-loading (neglecting losses associated with the presence of physical defects, surface roughness, and waveguiding losses).

Additional considerations when choosing a ligand include the colloidal stability imparted to the QDs in solution. Oleic acid typically provides very good colloidal stability due to its strong covalent bonding to the QD surface (X-type ligand).[53,54] However, amine functionalized ligands (butylamine, octylamine, hexadecylamine) form a coordinate bond to the QD surface (L-type ligand) that leads to reversible adsorption/desorption from the QD surface.[53,54] The desorption of ligands can lead to colloidal instability (aggregation of QDs) which causes scattering sites to form in the QD film during deposition and a lower than expected optical gain. QD instability was observed to be more pronounced for shorter ligands like butylamine than for longer ligands like octylamine or hexadecylamine. Therefore, the length of time before the colloidal QDs are deposited into films should factor into the choice of ligand.

7.4 Conclusions

This work demonstrates how the molecular dimensions and functionality of the ligand capping the QD affects film morphology, QD-packing density, refractive index, and the resulting optical gain characteristics. Specifically, this work shows that changing the ligand greatly affects the factors that control light propagation in the film (refractive index and refractive index contrast). Furthermore, the ligand affects QD-packing density, which has a direct effect on optical gain. Finally, evidence was provided that the chemical structure and physical and thermal properties of the ligand affect ASE threshold. The combination of these factors resulted in a 2.25 fold increase in optical gain between the lowest and highest QD-packed films (with the same functional group), with the highest QD-packed films exhibiting exceptionally high gain values (≈500 cm^{-1}). Reductions in ASE threshold and stability were also observed when switching from the commonly used waxy, large ligand oleic acid to the amine-functionalized ligands.

These findings outline a simple but significant strategy for altering optical gain that does not require modification to the synthesis approach or composition of the QDs. This approach allows for significant improvements in optical gain characteristics (5x reduced threshold, 2.25x increased magnitude, improved stability) via simple post-synthesis modification of the QD ligand. Furthermore, this approach should be compatible with any type of QD, representing a significant departure from previous studies on increasing QD gain through a sole focus on QD composition.

7.5 Chapter acknowledgements

Dr. Jaehan Jung and Young Jun Yoon (Prof. Lin group, Georgia Institute of Technology): QD synthesis, performing the QD ligand exchange, TEM micrographs, and NMR

characterization. Marcus Smith (Prof. Tsukruk group, Georgia Institute of Technology): TGA measurements and data analysis. Dr. Evan Lafalce (Prof. Vardeny group, University of Utah): gain (variable strip length) and loss (variable attenuation length) measurements.

7.6 References (Chapter 7)

1 Talapin, D.V.; Lee, J.S.; Kovalenko, M.V.; Shevchenko, E.V., Prospects of colloidal nanocrystals for electronic and optoelectronic applications. *Chem. Rev.* **2010,** *110,* 389-458.

2 Tame, M.S.; McEnery, K.R.; Oezdemir, S.K.; Lee, J.; Maier, S. A.; Kim, M.S., Quantum plasmonics. *Nat. Phys.* **2013,** *9,* 329-340.

3 Gates, B.D.; Xu, Q.B.; Stewart, M.; Ryan, D.; Willson, C.G.; Whitesides, G.M., New approaches to nanofabrication: Molding, printing, and other techniques. *Chem. Rev.* **2005,** *105,* 1171-1196.

4 Biswas, A.; Bayer, I.S.; Biris, A.S.; Wang, T.; Dervishi, E.; Faupel, F., Advances in top-down and bottom-up surface nanofabrication: Techniques, applications & future prospects. *Adv. Coll. Interf. Sci.* **2012,** *170,* 2-27.

5 Hoogland, S., Optical gain and lasing in colloidal quantum dots, Colloidal quantum dot optoelectronics and photovoltaics. *Cambridge University Press:* **2013.**

6 Ko, H.; Singamaneni, S.; Tsukruk, V.V., Nanostructured surfaces and assemblies as SERS media. *Small* **2008,** *4,* 1576-1599.

7 Xia, Y.N.; Yang, P.D.; Sun, Y.G.; Wu, Y.Y.; Mayers, B.; Gates, B.; Yin, Y. D.; Kim, F.; Yan, Y.Q., One-dimensional nanostructures: Synthesis, characterization, and applications. *Adv. Mater.* **2003,** *15,* 353-389.

8 Huang, X.H.; El-Sayed, I.H.; Qian, W.; El-Sayed, M.A., Cancer cell imaging and photothermal therapy in the near-infrared region by using gold nanorods. *J. Amer. Chem. Soc.* **2006,** *128,* 2115-2120.

9 Hanske, C.; Tebbe, M.; Kuttner, C.; Bieber, V.; Tsukruk, V V.; Chanana, M.; Koenig, T.A.F.; Fery, A., Strongly coupled plasmonic modes on macroscopic areas via template-assisted colloidal self-assembly. *Nano Lett.* **2014,** *14,* 6863-6871.

10 Adachi, M.M.; Fan, F.; Sellan, D.P.; Hoogland, S.; Voznyy, O.; Houtepen, A.J.; Parrish, K.D.; Kanjanaboos, P.; Malen, J.A.; Sargent, E.H., Microsecond-sustained lasing from colloidal quantum dot solids. *Nat. Comm.* **2015,** *6,* 8694-8694.

11 Dang, C.; Lee, J.; Breen, C.; Steckel, J.S.; Coe-Sullivan, S.; Nurmikko, A., Red, green and blue lasing enabled by single-exciton gain in colloidal quantum dot films. *Nat. Nanotech.* **2012,** *7,* 335-339.

12 Rizzo, A.; Mazzeo, M.; Palumbo, M.; Lerario, G.; D'Amone, S.; Cingolani, R.; Gigli, G., Hybrid light-emitting diodes from microcontact-printing double-transfer of colloidal semiconductor CdSe/ZnS quantum dots onto organic layers. *Adv. Mater.* **2008,** *20,* 1886-1891.

13 Mashford, B.S.; Stevenson, M.; Popovic, Z.; Hamilton, C.; Zhou, Z.Q.; Breen, C.; Steckel, J.; Bulovic, V.; Bawendi, M.; Coe-Sullivan, S.; Kazlas, P.T., High-efficiency quantum-dot light-emitting devices with enhanced charge injection. *Nat. Photonics* **2013,** *7,* 407-412.

14 Xin, X.; Li, B.; Jung, J.; Yoon, Y.J.; Biswas, R.; Lin, Z., Ab initio simulation of charge transfer at the semiconductor quantum dot/TiO2 interface in quantum dot-sensitized solar cells. *Par. & Par. Sys. Charact.* **2015,** *32,* 80-90.

15 Medintz, I.L.; Uyeda, H.T.; Goldman, E.R.; Mattoussi, H., Quantum dot bioconjugates for imaging, labelling and sensing. *Nat. Mater.* **2005,** *4,* 435-446.

16 Khurgin, J.B., How to deal with the loss in plasmonics and metamaterials. *Nat. Nanotech.* **2015,** *10,* 2-6.

17 Gaponik, N.; Hickey, S.G.; Dorfs, D.; Rogach, A.L.; Eychmüller, A., Progress in the light emission of colloidal semiconductor nanocrystals. *Small* **2010,** *6,* 1364-1378.

18 Klimov, V.I., Spectral and dynamical properties of multilexcitons in semiconductor nanocrystals. *Ann. Rev. Phys. Chem.*, Annual Reviews: Palo Alto, **2007;** *58,* 635-673.

19 Talapin, D.V.; Rogach, A.L.; Kornowski, A.; Haase, M.; Weller, H., Highly luminescent monodisperse CdSe and CdSe/ZnS nanocrystals synthesized in a hexadecylamine-trioctylphosphine oxide-trioctylphospine mixture. *Nano Lett.* **2001,** *1,* 207-211.

20 Greytak, A.B.; Allen, P.M.; Liu, W.; Zhao, J.; Young, E.R.; Popovic, Z.; Walker, B.J.; Nocera, D.G.; Bawendi, M.G., Alternating layer addition approach to CdSe/CdS core/shell quantum dots with near-unity quantum yield and high on-time fractions. *Chem. Sci.* **2012,** *3,* 2028-2034.

21 Bailey, R.E.; Smith, A.M.; Nie, S.M., Quantum dots in biology and medicine. *Physica E-Low-Dimensional Systems & Nanostructures* **2004,** *25,* 1-12.

22 Kuo, C.Y.; Su, M.S.; Ku, C.S.; Wang, S.M.; Lee, H.Y.; Wei, K.H., Ligands affect the crystal structure and photovoltaic performance of thin films of PbSe quantum dots. *J. Mater. Chem.* **2011,** *21*, 11605-11612.

23 Murray, C.B.; Norris, D.J.; Bawendi, M.G., Synthesis and characterization of nearly monodisperse CdE (E = S, Se, Te) Semiconductor nanocrystallites. *J. Amer. Chem. Soc.* **1993,** *115,* 8706-8715.

24 Jung, J.; Lin, C.H.; Yoon, Y.J.; Malak, S.T.; Zhai, Y.; Thomas, E.L.; Vardeny, V.; Tsukruk, V.V.; Lin, Z., Crafting core/graded shell–shell quantum dots with suppressed re-absorption and tunable Stokes shift as high optical gain materials. *Angewandte Chemie Intern. Ed.* **2016**, *55,* 5071-5075.

25 Zimnitsky, D.; Jiang, C.Y.; Xu, J.; Lin, Z.Q.; Zhang, L.; Tsukruk, V.V. Photoluminescence of a freely suspended monolayer of quantum dots encapsulated into layer-by-layer films. *Langmuir* **2007,** *23*, 10176-10183.

26 Zimnitsky, D.; Jiang, C.; Xu, J.; Lin, Z.; Tsukruk, V.V., Substrate- and time-dependent photoluminescence of quantum dots inside the ultrathin polymer LbL film. *Langmuir* **2007,** *23,* 4509-4515.

27 Gole, A.; Jana, N.R.; Selvan, S.T.; Ying, J.Y., Langmuir−Blodgett thin films of quantum dots: Synthesis, surface modification, and fluorescence resonance energy transfer (FRET) studies. *Langmuir* **2008,** *24,* 8181-8186.

28 Bourvon, H.; Le Calvez, S.; Kanaan, H.; Meunier-Della-Gatta, S.; Philippot, C.; Reiss, P., Langmuir-Schaeffer monolayers of colloidal nanocrystals for cost-efficient quantum dot light-emitting diodes. *Adv. Mater.* **2012,** *24,* 4414-4418.

29 Kim, B.H.; Onses, M.S.; Lim, J.B.; Nam, S.; Oh, N.; Kim, H.; Yu, K.J.; Lee, J.W.; Kim, J.-H.; Kang, S.-K.; Lee, C.H.; Lee, J.; Shin, J.H.; Kim, N.H.; Leal, C.; Shim, M.; Rogers, J.A., High-resolution patterns of quantum dots formed by electrohydrodynamic jet printing for light-emitting diodes. *Nano Lett.* **2015,** *15,* 969-973.

30 Kim, T.-H.; Cho, K.-S.; Lee, E.K.; Lee, S.J.; Chae, J.; Kim, J.W.; Kim, D.H.; Kwon, J.-Y.; Amaratunga, G.; Lee, S.Y.; Choi, B.L.; Kuk, Y.; Kim, J.M.; Kim, K., Full-colour quantum dot displays fabricated by transfer printing. *Nat. Photonics* **2011,** *5,* 176-182.

31 Malak, S.T.; Jung, J.; Yoon, Y.J.; Smith, M.J.; Lin, C.H.; Lin, Z.; Tsukruk, V.V., Large-area multicolor emissive patterns of quantum dot–polymer films via targeted recovery of emission signature. *Adv. Opt. Mater.* **2016**, *4,* 608-619.

32 Engel, H.-A.; Loss, D., Fermionic bell-state analyzer for spin qubits. *Science* **2005,** *309*, 586-588.

33 Roither, J.; Pichler, S.; Kovalenko, M.V.; Heiss, W.; Feychuk, P.; Panchuk, O.; Allam, J.; Murdin, B.N., Two- and one-dimensional light propagations and gain in layer-by-layer-deposited colloidal nanocrystal waveguides. *Appl. Phys. Lett.* **2006,** *89,* 111120.

34 Sukhovatkin, V.; Musikhin, S.; Gorelikov, I.; Cauchi, S.; Bakueva, L.; Kumacheva, E.; Sargent, E.H., Room-temperature amplified spontaneous emission at 1300 nm in solution-processed PbS quantum-dot films. *Opt. Lett.* **2005,** *30,* 171-173.

35 Petruska, M.A.; Malko, A.V.; Voyles, P.M.; Klimov, V.I., High-performance, quantum dot nanocomposites for nonlinear optical and optical gain applications. *Adv. Mater.* **2003,** *15,* 610-613.

36 Klimov, V.I.; Mikhailovsky, A.A.; Xu, S.; Malko, A.; Hollingsworth, J.A.; Leatherdale, C.A.; Eisler, H.J.; Bawendi, M.G., Optical gain and stimulated emission in nanocrystal quantum dots. *Science* **2000,** *290,* 314-317.

37 Chan, Y.; Steckel, J.S.; Snee, P.T.; Caruge, J.M.; Hodgkiss, J.M.; Nocera, D.G.; Bawendi, M.G., Blue semiconductor nanocrystal laser. *Appl. Phys. Lett.* **2005,** *86,* 073102.

38 Jasieniak, J; Fortunati, I.; Gardin, S.; Signori, R.; Bozio, R.; Martucci, A.; Mulvaney, P., Highly efficient amplified stimulated emission from CdSe-CdS-ZnS quantum dot doped wavequides with two-photon infrared optical pumping. *Adv. Mater.* **2008,** *20,* 69-73.

39 Malko, A.V.; Mikhailovsky, A.A.; Petruska, M.A.; Hollingsworth, J.A.; Htoon, H.; Bawendi, M.G.; Klimov, V.I., From amplified spontaneous emission to microring lasing using nanocrystal quantum dot solids. *Appl. Phys. Lett.* **2002,** *81,* 1303-1305.

40 Hare, J.; Steiner, S.; Orucevic, F.; Lefevre-Seguin, V., Silica microspheres as high-Q microcavities for semiconductor quantum-dot lasers. In *Optoelectronic Integrated Circuits VII*, Eldada, L. A.; Lee, E. H., Eds. **2005;** *5729,* 94-103.

41 Sundar, V.C.; Eisler, H.J.; Deng, T.; Chan, Y.T.; Thomas, E.L.; Bawendi, M.G., Soft-lithographically embossed, multilayered distributed-feedback nanocrystal lasers. *Adv. Mater.* **2004,** *16,* 2137-2141.

42 Finlayson, C.E.; Ginger, D.S.; Greenham, N.C., Optical microcavities using highly luminescent films of semiconductor nanocrystals. *Appl. Phys. Lett.* **2000,** *77,* 2500-2502.

43 Garcia-Santamaria, F.; Chen, Y.F.; Vela, J.; Schaller, R.D.; Hollingsworth, J.A.; Klimov, V.I., Suppressed Auger recombination in "giant" nanocrystals boosts optical gain performance. *Nano Lett.* **2009,** *9,* 3482-3488.

44 Nanda, J.; Ivanov, S.A.; Achermann, M.; Bezel, I.; Piryatinski, A.; Klimov, V.I., Light amplification in the single-exciton regime using exciton-exciton repulsion in type-II nanocrystal quantum dots. *J. Phys. Chem. C* **2007,** *111,* 15382-15390.

45 Klimov, V.I.; Ivanov, S.A.; Nanda, J.; Achermann, M.; Bezel, I.; McGuire, J.A.; Piryatinski, A., Single-exciton optical gain in semiconductor nanocrystals. *Nature* **2007,** *447,* 441-446.

46 Walsh, B.R.; Saari, J.I.; Krause, M.M.; Nick, R.; Coe-Sullivan, S.; Kambhampati, P., Controlling the surface of semiconductor nanocrystals for efficient light emission from single excitons to multiexcitons. *J. Phys. Chem. C* **2015,** *119*, 16383-16389.

47 Kambhampati, P., Unraveling the structure and dynamics of excitons in semiconductor quantum dots. *Acc. Chem. Res.* **2011,** *44*, 1-13.

48 Cooney, R.R.; Sewall, S.L.; Sagar, D.M.; Kambhampati, P., State-resolved manipulations of optical gain in semiconductor quantum dots: Size universality, gain tailoring, and surface effects. *J. Chem. Phys.* **2009,** *131*, 164706.

49 Kambhampati, P., Multiexcitons in semiconductor nanocrystals: A platform for optoelectronics at high carrier concentration. *J. Phys. Chem. Lett.* **2012,** *3*, 1182-1190.

50 Cooney, R.R.; Sewall, S.L.; Sagar, D.M.; Kambhampati, P., Gain control in semiconductor quantum dots via state-resolved optical pumping. *Phys. Rev. Lett.* **2009,** *102*, 127404.

51 Lin, C.H.; Lafalce, E.; Jung, J.; Smith, M.J.; Malak, S.T.; Aryal, S.; Yoon, Y.J.; Zhai, Y.; Lin, Z.; Vardeny, Z.V.; Tsukruk, V.V., Core/alloyed-shell quantum dot robust solid films with high optical gains. *ACS Photonics* **2016,** *3,* 647-658.

52 Liu, M.; Ma, Y.; Wang, R.Y., Modifying thermal transport in colloidal nanocrystal solids with surface chemistry. *ACS Nano* **2015,** *9*, 12079-12087.

53 Anderson, N.C.; Hendricks, M.P.; Choi, J.J.; Owen, J.S., Ligand exchange and the stoichiometry of metal chalcogenide nanocrystals: Spectroscopic observation of facile metal-carboxylate displacement and binding. *J. Amer. Chem. Soc.* **2013,** *135,* 18536-18548.

54 Krause, M.M.; Jethi, L.; Mack, T.G.; Kambhampati, P., Ligand surface chemistry dictates light emission from nanocrystals. *J. Phys. Chem. Lett.* **2015,** *6,* 4292-4296.

55 Sigma-Aldrich, ChemSpider, and Chemicalize for measured and theoretical thermodynamic data and geometry data for butylamine, octylamine, hexadecylamine, oleic acid, trioctylphosphane oxide, and pyridine.

56 Bellex International Coportation, Wilmington DE, USA. CYTOP chemical and physical properties. http://www.bellexinternational.com/products/cytop/

57 McGehee, M.D.; Gupta, R.; Veenstra, S.; Miller, E.K.; Diaz-Garcia, M.A.; Heeger, A.J., Amplified spontaneous emission from photopumped films of a conjugated polymer. *Phys. Rev. B* **1998,** *58,* 7035-7039.

58 Guyot-Sionnest, P.; Wehrenberg, B.; Yu, D., Intraband relaxation in CdSe nanocrystals and the strong influence of the surface ligands. *J. Chem. Phys.* **2005,** *123,* 074709.

59 Choi, D.; Pyo, J.Y.; Kim, Y.; Jang, D.J., Facile synthesis of composition-gradient Cd(1-x)ZnxS quantum dots by cation exchange for controlled optical properties. *J. Mater. Chem. C* **2015,** *3,* 3286-3293.

60 Maity, P.; Debnath, T.; Ghosh, H.N., Slow electron cooling dynamics mediated by electron hole decoupling in highly luminescent CdSxSe1-x alloy quantum dots. *J. Phys. Chem. C* **2015,** *119,* 10785-10792.

61 Kim, B.S.; Avila, L.; Brus, L.E.; Herman, I.P., Organic ligand and solvent kinetics during the assembly of CdSe nanocrystal arrays using infrared attenuated total reflection. *Appl. Phys. Lett.* **2000,** *76,* 3715-3717.

62 Kim, D.I.; Islam, M.A.; Avila, L.; Herman, I.P., Contribution of the loss of nanocrystal ligands to interdot coupling in films of small CdSe/1-thioglycerol nanocrystals. *J. Phys. Chem. B* **2003,** *107,* 6318-6323.

63 Hunsperger, R.G., Integrated optics, theory and technology, Ch.2: Optical waveguide modes. *Springer Science and Business Media*, **2009.**

64 Todescato, F.; Fortunati, I.; Gardin, S.; Garbin, E.; Collini, E.; Bozio, R.; Jasieniak, J.J.; Della Giustina, G.; Brusatin, G.; Toffanin, S.; Signorini, R., Soft-lithographed up-converted distributed feedback visible lasers based on CdSe-CdZnS-ZnS quantum dots. *Adv. Func. Mater.* **2012,** *22,* 337-344.

65 Sewall, S.L.; Cooney, R.R.; Anderson, K.E.H.; Dias, E.A.; Sagar, D.M.; Kambhampati, P., State-resolved studies of biexcitons and surface trapping dynamics in semiconductor quantum dots. *J. Chem. Phys.* **2008,** *129*, 084701.

66 Yang, S.; Wang, Y.; Sun, H., Advances and prospects for whispering gallery mode microcavities. *Adv. Opt. Mater.* **2015,** *3,* 1136-1162.

67 Califano, M., Origins of photoluminescence decay kinetics in CdTe colloidal quantum dots. *ACS Nano* **2015,** *9,* 2960-2967.

68 Park, Y.-S.; Bae, W.K.; Pietryga, J.M.; Klimov, V.I., Auger recombination of biexcitons and negative and positive trions in individual quantum dots. *ACS Nano* **2014,** *8*, 7288-7296.

69 Bae, W. K.; Park, Y.-S.; Lim, J.; Lee, D.; Padilha, L.A.; McDaniel, H.; Robel, I.; Lee, C.; Pietryga, J.M.; Klimov, V.I., Controlling the influence of Auger recombination on the performance of quantum-dot light-emitting diodes. *Nat. Communications* **2013,** *4*, 2661.

70 Cooney, R.R.; Sewall, S.L.; Anderson, K.E.H.; Dias, E.A.; Kambhampati, P., Breaking the phonon bottleneck for holes in semiconductor quantum dots. *Phys. Rev. Lett.* **2007,** *98*, 177403.

71 Klimov, V.I.; Mikhailovsky, A.A.; McBranch, D.W.; Leatherdale, C.A.; Bawendi, M.G., Quantization of multiparticle Auger rates in semiconductor quantum dots. *Science* **2000,** *287,* 1011-1013.

72 Green, M., The nature of quantum dot capping ligands. *J. Mater. Chem.* **2010,** *20*, 5797-5809.

73 Kagan, C.R.; Murray, C.B.; Bawendi, M.G., Long-range resonance transfer of electronic excitations in close-packed CdSe quantum-dot solids. *Phys. Rev. B* **1996,** *54*, 8633-8643.

74 Shaklee, K.L.; Leheny, R.F., Direct determination of optical gain in semiconductor crystals. *Appl. Phys. Lett.* **1971,** *18,* 475-477.

75 Segev, M.; Silberberg, Y.; Christodoulides, D.N., Anderson localization of light. *Nat. Photonics* **2013,** *7,* 197-204.

76 Javaux, C.; Mahler, B.; Dubertret, B.; Shabaev, A.; Rodina, A.V.; Efros, Al.L.; Yakovlev, D.R.; Liu, F.; Bayer, M.; Camps, G.; Biadala, L.; Buil, S.; Quelin, X.; Hermier, J.P., Thermal activation of non-radiative Auger recombination in charged colloidal nanocrystals. *Nat. Nano* **2013,** *8,* 206-212.

77 Cragg, G.E.; Efros, A.L., Suppression of Auger processes in confined structures. *Nano Lett.* **2010,** *10,* 313-317.

CHAPTER 8

PHOTOPATTERNING APPROACHES: NEGATIVE-TO-POSITIVE PATTERNING USING THE DECAY-TO-RECOVERY BEHAVIOR OF QUANTUM DOTS

Chapter Based On:
Malak, S.T.; Smith, M.J.; Yoon, Y.J.; Lin, C.H.; Jung, J.; Lin, Z.; Tsukruk, V.V., Programmed emission transformations: Negative-to-positive patterning using the decay-to-recovery behavior of quantum dots. *Adv. Opt. Mater.* **2016,** *in print.*

Chapter Overview

Following the examination of how large-scale light-matter interactions like waveguiding and optical gain can be controlled via QD-QD proximity, we now identify and develop photopatterning techniques to control the large-scale spatial modulation of PL emission from QD films. Photopatterns are photoluminescent patterns written into a film which arise from intrinsic modification of unstable CdSe/ZnS quantum dot (QD) emission upon exposure to light. In this case, unstable green CdSe/ZnS QDs are used as the active optical nanostructure.

This chapter outlines approaches for fabricating photoluminescent photopatterns that have positive and negative intensity contrasts (**Figure 8.1**). The ability to fabricate positive or negative photopatterns (using a single type of quantum dot) is due to the two-step decay-to-recovery evolution exhibited by the CdSe/ZnS QDs upon light exposure (as discussed in Chapter 6). It is shown that high-contrast photopatterns spanning mm^2 areas can be fabricated within seconds with a facile one-step process, representing a drastic reduction in the time required to develop an emissive pattern in a QD-polymer film (from hours to seconds). Furthermore, the controlled light exposure allows for a

programmed transformation of the emissive pattern contrast, with a reversal of the bright/dark regions of the QD-polymer photopattern demonstrated. Finally, it is shown that the photopatterns can be stored over a period of time and then "recharged" using simple light exposure to partially recovery the intensity and contrast of aged photopatterns. The outlined patterning strategies open up new pathways for facile, one-step parallel fabrication of anti-counterfeiting emitting labels and light sensors, as well as for gain-loss parity-time systems where an emission contrast is required but where physical patterning may not be appropriate.

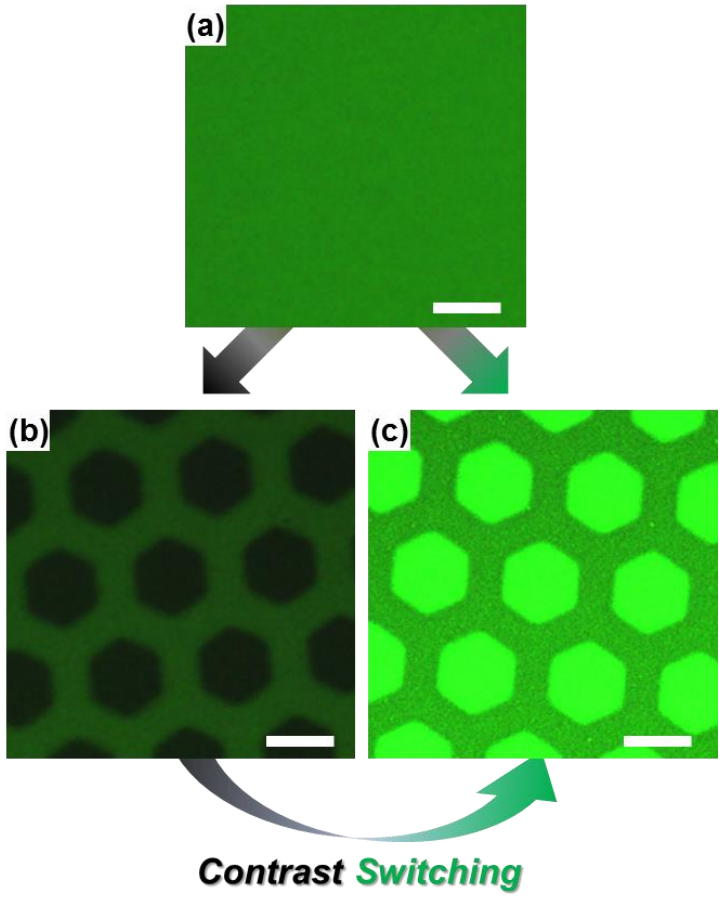

Figure 8.1: General concept of photopatterning, where a QD-polymer film of uniform emission is modified to have a spatially modulated emission pattern. PL images of (a) a green PL CdSe/ZnS QD-polymer film, (b) a negative photopattern, and (c) a positive photopattern of hexagonal features. Contrast switching from a negative photopattern to a positive photopattern is also possible. Scale bar is 40 μm for all images.

8.1 Introduction

8.1.1 Nanoparticles and quantum dots

The area of photonic materials and systems has benefited greatly from the development of nanoparticles that display highly controlled light emission, scattering, and absorption properties.[1,2,3,4] The great versatility of nanoparticles is due in large part to the tunable nature of their properties, with changes in size, shape, coupling, and orientation leading to large controllable changes in the optical properties.[5,6,7,8] Quantum dots (QDs) are a particularly interesting nanostructure for applications that require optical emission in the visible or near-infrared spectrum. These small (D < 10 nm) semiconducting nanoparticles exhibit size-dependent broadband absorption and narrowband photoluminescence (full-width half-maximum below 40 nm) due to quantum confinement of the exciton.[9,10,11] Many synthesis approaches have been developed for different quantum dot architectures, including core,[12] core-shell,[13,14] alloyed core-shell,[15] and even core-shell-shell QDs,[16] which offer a range of optical characteristics. Not surprisingly, the intrinsic properties of QDs and the wide variety of QDs available have led to their implementation in a number of applications, including: imaging/labelling/sensing in biological investigations,[17] LEDs,[18] solar cells,[19,20] quantum computing,[21] and, more recently, lasers and optical gain media.[22,23,24]

8.1.2 Micro- and nanoscale patterning

In addition, the application of nanotechnology for controlled light-matter interactions has been augmented by the variety of micro- and nanoscale patterning approaches that have been developed, including techniques like electron- and photolithography,[25] soft lithographies,[26,27] inkjet printing,[28] and molding and printing.[29] One of the unifying

principles of these approaches is that patterns are created by adding, removing, or rearranging material during a multi-step fabrication procedure.

8.1.3 Photopatterning

Less investigation has been done on “non-physical” patterning approaches like spectral photopatterning, which creates patterns by modifying the emission efficiency of quantum dots in specific areas of the film without physically modifying the film.[30,31,32,33] The modification of QD emission efficiency is due to intrinsic modification of the exciton relaxation pathways within the QD, so no physical deposition or removal of material is required to impart an emission pattern in a spectral photopattern. The non-physical aspect of spectral photopatterning is in sharp contrast to the traditional micro- and nanoscale physical patterning techniques. For this reason, spectral photopatterning could be very useful in areas such as photonic parity-time systems that require periodic modulation of optical gain and loss with no corresponding change in the real refractive index (which can limit the applicability of more traditional physical patterning approaches).[34,35] In addition, spectral photopatterning has potential in overcoming the obstacles associated with the scaling-up of nano/microscale patterned systems because pattern contrast can be imparted and controlled via simple remote light exposure.

The spectral photopatterning approach requires optically emitting nanostructures that exhibit a change in emission (an increase or decrease of intensity or a spectral shift) when exposed to light.[30,31,32,33] Although quantum dots are typically used in photopatterning, other materials like conjugated polymers, dyes, and nanostructures can also be used if their emission changes in response to light. Photopatterning requires the deliberate introduction of optical nanostructures with unstable photoluminescence (PL)

into a system, which is generally considered detrimental in optical systems since the emission intensity, position, and full-width half-maximum (FWHM) can be intimately tied to the functioning of the device. Quantum dots can be synthesized to have unstable emission (while maintaining a narrow emission band and strong photoluminescence in the visible spectrum),[30-33] making them promising candidates for photopatterning. Previous QD photopatterning studies have almost exclusively exploited QDs that undergo an increase in emission when exposed to light, and have required up to 24-72 hours to develop a photopattern.[30,31,36] However, QDs can show complex changes in their PL emission when exposed to light, including an increase, decrease, or spectral shift depending on their synthesis, surrounding environment, and exposure conditions.[37,38] The underlying mechanisms behind these changes in QD emission intensity include degradation of emission quenchers,[30] photoactivation,[31,39] photoelectrification,[40,41] photoionization,[42] as well as the underlying substrate.[43,44] All of these changes and mechanisms can be taken advantage of to develop new strategies for photopatterning.

In this work, we introduce novel approaches for developing pre-determined formations of positive and negative contrast emissive patterns in QD-polymer films. The resulting photopatterns have strong emission contrast, microscale resolution, and can span macroscopic lateral areas. Furthermore, the contrast of a negative pattern can be transformed to a positive pattern, a feat not possible using traditional lithographic approaches. The outlined strategies rely on the intrinsic modification of QD emission that occurs when exposed to light, with multiple patterns strategies possible due to the unique decay-to-recovery evolution of the emission over intermediate time-scales (seconds-minutes). However, the outlined strategies are not limited to quantum dot systems, instead being compatible with any material (dye, conjugated polymer,

nanoparticle) that undergoes a change of emission (intensity or color) when exposed to light. These novel approaches offer a complementary microscale patterning option to traditional lithographies that require the addition or removal of material and chemical treatments to provide pattern contrast.

8.2 Experimental details

Synthesis of unstable green CdSe/ZnS QDs. Performed according to the methods outlined in "Chapter 3: Experimental Techniques and Materials"

Film preparation. QD-polymer films of thickness 350 nm (±90 nm) (as evaluated by ellipsometry) were prepared by spin-casting a QD-polymer mixture at 2000-2500 rpm for 1-1.5 min. Films typically films had a QD-loading of approximately 1% volume fraction, which was estimated via fitting of refractive indices derived from ellipsometry data with the Bruggeman model.[45] The QD-polymer mixture was made by mixing equal parts of a QD toluene solution with a 10-12% PMMA toluene solution, and then vortexing. Films were deposited on silicon with a 290-295 nm surface layer of SiO_2.

Photomask & photopattern development. The photomask was a hexagonal mesh (G400H-Cu grid) TEM grid from Electron Microscopy Sciences. The TEM grid was designed to have a pitch of 62 um, holes of 37 um, and bars of 25 um. Photopatterning development was performed using a 10x objective (NA: 0.30) with excitation light of 450-490 nm light over a range of powers. The light source was a 120 W Hg vapor short arc lamp (X-cite series, 120Q, Lumen Dynamics) with controllable power output.

8.3 Results and discussion

8.3.1 QD properties and PL emission evolution

The photoluminescence of the CdSe/ZnS QDs is in the green region and has a full-width half-maximum near 40 nm (**Figure 8.2**). The evolution of PL intensity for the QD-polymer film when exposed to light has two distinct steps: a fast and large decay on the order of seconds followed by a slower partial recovery on the order of many minutes (**Figure 8.2a,b**, log scales). A large decrease of intensity occurs within the first seconds of light exposure while the spectral center and FWHM remain nearly constant (**Appendix E Figure E.1**).

This decay-to-recovery behavior occurs over a range of exposure powers with higher exposure power reducing the time required for the PL intensity to reach its minimum value (**Figure 8.2b**). Note, it appears that lower exposure power leads to a greater decrease of intensity within the first seconds of light exposure. However, this trend is likely due to the higher exposure power decaying the PL so quickly that it cannot be measured by the instrument in the first moments of exposure (while low power exposure causes a slower PL decay rate that can be tracked easily). For these reasons, the PL intensity data was normalized against the lowest emission value, which occurs over longer time scales (minutes) and can be accurately measured.

The time-to-minimum intensity (or the time required to enter the recovery stage) shows a clear dependence on exposure power for the power range examined, with higher exposure power reducing the amount of time required to enter the recovery stage. This trend suggests that the physical mechanisms causing the decay-to-recovery behavior is controlled by the number of incident photons. In contrast, the spectral center of the PL peak undergoes a blue-shift over the entire exposure period (**Figure 8.2c**), indicating an

increase in quantum confinement of the exciton throughout the process. The FWHM of the emission shows no clear trend with exposure power (**Appendix E Figure E.2**).

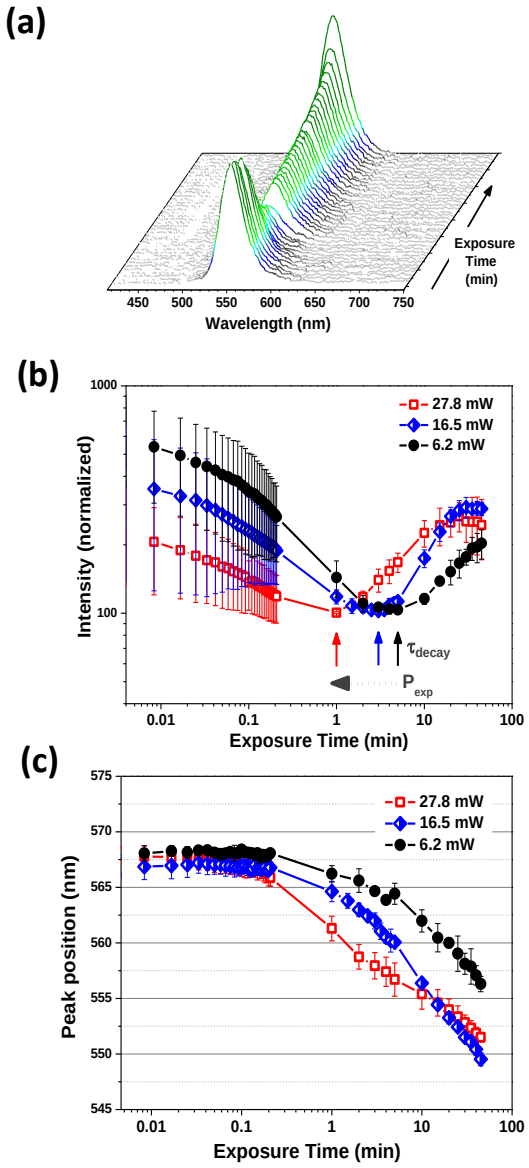

Figure 8.2: The photoluminescence intensity and spectral position of QD-polymer films changes when exposed to light. (a) Waterfall plot of the photoluminescence spectrum when exposed to light (470 nm) over a period of 45 min. Peak fitting of the photoluminescence spectra show that the (b) intensity (normalized to minimum value) and (c) spectral center shift under continuous light exposure of different incident power.

Multiple mechanisms might control the decay-to-recovery behavior of emission intensity, with all likely involving changes to surface passivation of the quantum dot since surface passivation is often cited as strongly affecting quantum yield.[14,46] In this case, a decay of photoluminescence can be attributed to a reduction of surface passivation of the QD core by the shell. Most specifically, the sharp core-shell interface of the QDs and lattice mismatch between CdSe and ZnS (12%) cause voids and defects to form due to lattice strain.[15,47,48] Before exposure to light, the sharp core-shell CdSe/ZnS interface is in a metastable state. Upon light exposure, the interface is disrupted by the formation of surface oxides and the potential rearrangement of ZnS atoms which reduces surface passivation (at least initially).[14] In addition, photooxidation/corrosion of the ZnS shell has been shown to form surface quenching states that reduce quantum yield and cause a spectral blue shift.[38,49] On the other hand, previous reports have attributed a recovery of intensity (upon light exposure) to a variety of mechanisms including photoinduced surface annealing/restructuring,[50] interfacial alloying of the core-shell interface,[15,51] or light induced H_2O passivation of surface defects.[38] In this case, it is likely a combination of photoinduced surface annealing/restructuring of the QD surface (irreversible) and light induced H_2O defect passivation (reversible) because the PL recovery is partially reversible (discussed later).

It is important to recognize the importance of the very fast decay of emission (within seconds) after light exposure for materials patterning. The high rate of this decay can be difficult to observe due to it being in an intermediate time scale (seconds) that is much slower than intrinsic exciton dynamic lifetimes (picosecond to nanosecond) but much faster than typical steady state PL measurements (minutes). Therefore, this behavior has likely been not accounted for in QD stability studies that measured emission using much longer time-steps (on the order of minutes).

8.3.2 General photopatterning approach

The general approach for spectral photopatterning involves the selective exposure of specific regions of a film composed of light emitting structures that undergo a change of emission intensity or spectral position when exposed to light (**Figure 8.3**). In this study, a simple copper TEM grid serves as the photomask to provide selective exposure of specific regions of the QD-polymer film. However, the only constraint of the mask is that it be opaque to the light wavelength used to develop the photopattern. The resulting emissive pattern is due to the intrinsic modification of QD emission (intensity) due to light exposure; the pattern is not due to the addition or removal of material as in conventional photolithography and electron beam lithography. This is indeed confirmed by atomic force microscopy (AFM) and bright field imaging of photopatterned regions that show no physical modification of the film that could account for the PL pattern **(Appendix E Figure E.3, E.4**).

Nearly all previous demonstrations of spectral photopatterning were of positive photopatterns, meaning the regions of the film exposed to light undergo an increase in their emission and therefore are the highest intensity regions. However, the photopatterning approach can be extended beyond positive photopatterns by using QDs that undergo the complex decay-to-recovery intensity behavior of the CdSe/ZnS QDs mentioned in this study (**Figure 8.2b**).

‘

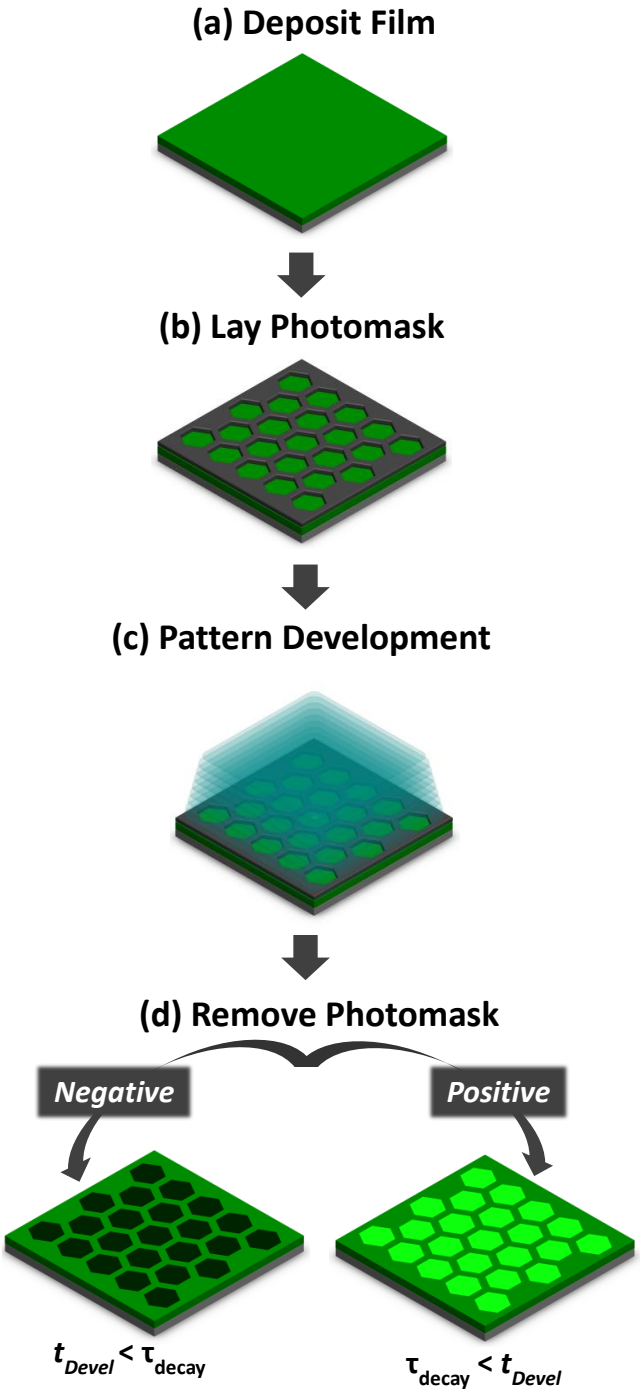

Figure 8.3: Schematic of the two most basic photopatterning approaches in this study: a QD-polymer film is deposited on a substrate (a) and a photomask is laid on top (b). The system is exposed to light to develop the photopattern (c) and then the mask is removed to reveal the photopattern (d). The type of photopattern (negative or positive) depends on whether the development time (t_{Devel}) was less than or greater than the time-to-minimum (τ_{decay}).

In this situation, both positive and negative contrast patterns can be fabricated by controlling the amount of light exposure time. Specifically, negative contrast patterns can be fabricated by developing for an amount of time less than the time-to-minimum period (τ_{decay}), while positive patterns can be fabricated for development times longer than τ_{decay} without changing the overall setup (**Figure 8.3d**). Overall, the τ_{decay} defines the transition between negative and positive photopattern development, and τ_{decay} can be controlled explicitly by the exposure power (**Figure 8.2b**). The following section outlines these points in detail.

8.3.2.1 Negative photopatterning (NP)

Approach & Requirements

The negative photopatterning approach yields a photopattern where the regions of the QD-polymer film exposed to the development light have a lower PL intensity than the regions protected by the photomask (**Figure 8.3**). A negative photopattern is fabricated by developing the film for a time (t_{devel}) shorter than the QD time-to-minimum period (i.e. $t_{devel} < \tau_{decay}$) since the exposed QDs are still within the decay phase of their PL evolution (**Figure 8.2a,b**).

Outcome

The negative photopatterns are shown to display a clear intensity contrast between the exposed and protected regions of the film, which increases in magnitude as the development time approaches the τ_{decay} (**Figure 8.4a)**. The photopattern corresponds closely to the photomask (**Appendix E Figure E.5**) and is very uniform in terms of shape, size, and intensity over mm^2 lateral areas (**Figure 8.4b**).

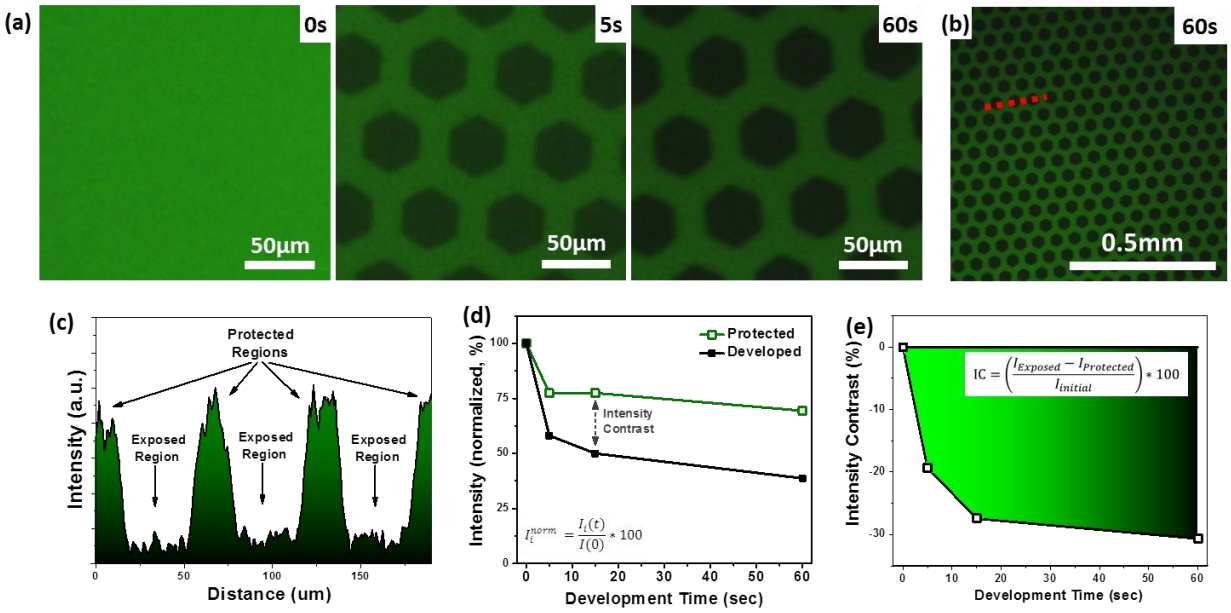

Figure 8.4: Negative photopatterning (NP) occurs if the QD-polymer film is developed for a time period less than the characteristic PL time-to-minimum (i.e. $t_{devel} < \tau_{decay}$). (a) PL images of a negative photopattern at different stages of pattern development (developed using light of 470 nm, 5.7 mW). (b) Photoluminescence image of a negative photopattern spanning a large area (mm^2). (c) PL intensity cross-section of a negative photopattern PL image (60 s development pattern). (d) Intensity of the protected and developed regions of the photopattern and (e) the corresponding intensity contrast IC for different development times.

The intensity contrast (IC) between the exposed (dark) and protected (bright) regions of the negative photopattern is clearly visible from the PL cross-sections (**Figure 8.4c**). Comparison of the intensity from the exposed ($I_{exposed}$) and protected ($I_{protected}$) regions, normalized against the intensity of the film before pattern development ($I_{Initial}$), shows that the developed region experiences twice as much decay as the protected region (50% versus 25%) (**Figure 8.4d**). The intensity contrast of a photopattern, which indicates how distinct a pattern appears, is a critical parameter for evaluation and therefore should be quantified. Intensity contrast is therefore defined as **Eq. 8.1**:

Equation 8.1: Intensity contrast (IC) for QD photopatterns, where $I_{Exposed}$, $I_{Protected}$, and $I_{initial}$ are obtained from intensity cross-sections of PL images.

$$\mathrm{IC} = \left(\frac{I_{Exposed} - I_{Protected}}{I_{initial}} \right) * 100$$

According to this definition of intensity contrast, negative photopatterns have a negative intensity contrast since the developed regions of the photopattern have a lower intensity (they are darker) than the protected regions. Positive photopatterns have a positive IC which indicates the opposite scenario. Overall, we can conclude that the magnitude of intensity contrast is largest when there is a large difference of intensity between the developed regions of the pattern and the protected regions of the pattern. In this demonstration of negative patterning, it is clear that the magnitude of IC increases as $t_{devel} \rightarrow \tau_{decay}$ (as expected), increasing from an IC of 0% at 0 sec to -30% at 60 sec of development (**Figure 8.4e**).

An attractive advantage of the negative photopatterning approach is that photopatterns with high contrast can be developed very quickly (<5 seconds) because of the rapid decay that occurs upon light exposure. In addition, because the τ_{decay} displays a negative trend with development power, the rate of pattern development can be controlled by exposure power. These patterns were developed significantly faster (more than 10000 times) than some previous literature demonstrations (which often required 24-72 hours) while maintaining spatial resolution (≈25 μm).[30,31] Spatial resolution in this case is dictated by the mask dimensions since the distances are much larger than the diffraction-limit for 470 nm (< 1 μm). In fact, demonstrations of higher resolution photopatterns using high resolution TEM grids have been demonstrated,[33] but were not the focus of this investigation. The substantial reduction in the time required to develop

a high contrast photopattern stems from the fact that the fast PL decay mechanism provides the pattern contrast, whereas previous literature demonstrations used the degradation of quenchers or photoactivation to develop the pattern contrast (which are slower processes).[30,31]

8.3.2.2 Positive photopatterning (PP)

Approach & Requirements

The positive photopatterning approach yields a photopattern where the regions of the film exposed to the development light have a higher PL intensity than the regions protected by the photomask (**Figure 8.3**). A positive photopattern results if the pattern development time is longer than the decay period (i.e. $\tau_{decay} < t_{devel}$) since the exposed regions enter the recovery phase of their PL evolution (**Figure 8.2b**). Positive photopatterns require more time to develop ($t_{devel} \approx$ minutes) than negative photopatterns because the rate of PL recovery is slower than the rate of PL decay, but positive patterns tend to be very bright.

Outcome

A demonstration of positive patterning is shown in **Figure 8.5a**. The areas exposed to light during the pattern development step are very bright while the protected regions are darker (positive intensity contrast). The photopattern is very uniform in terms of shape, size, and intensity over areas approaching mm^2 with a similar spatial resolution to negative photopatterning (**Figure 8.5b**). Cross-sections of the PL image show a clear increase of PL intensity for the regions of the film exposed to light compared to the regions protected by the mask during the pattern development stage (**Figure 8.5c,d**). Tracking of PL intensity from the different regions of the pattern shows a positive

intensity contrast that increases with development time and eventually reaches a value of 30% at the longest development time (10 min) (**Figure 8.5e**).

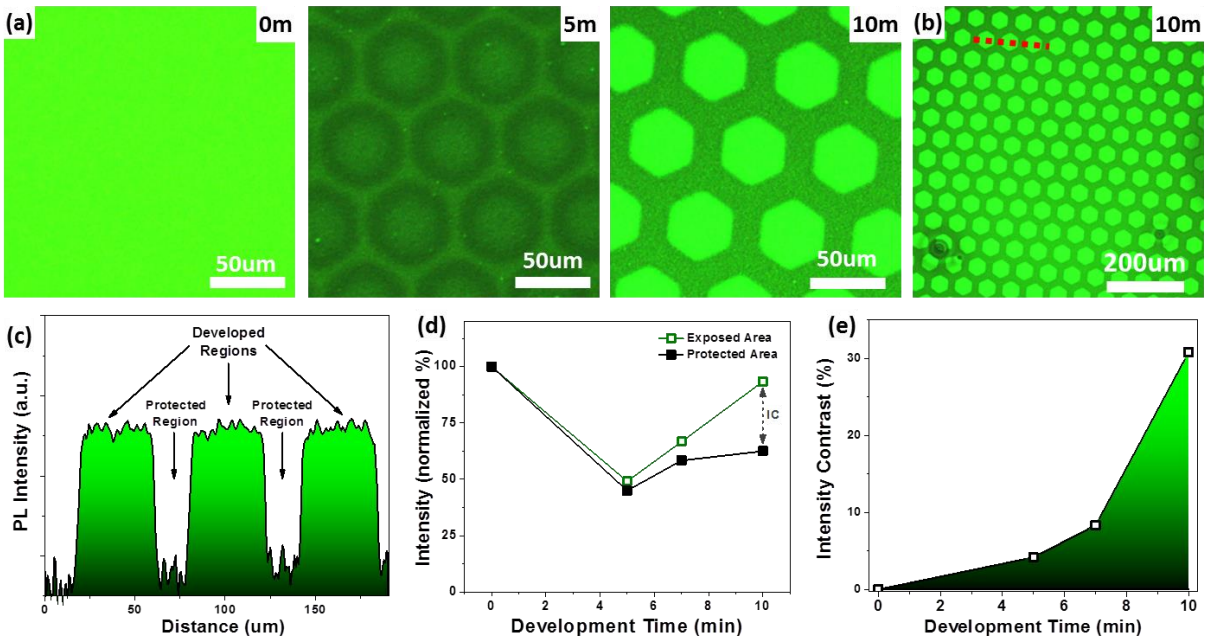

Figure 8.5: Positive contrast patterning (PP) occurs if the QD-polymer film is developed for a time period longer than the characteristic PL time-to-minimum (i.e. $\tau_{decay} < t_{devel}$). (a) PL images of a positive photopattern at different stages of pattern development (developed using light of 470 nm, 34 mW). (b) Photoluminescence image of a positive photopattern spanning a large area (mm^2). (c) PL intensity cross-section of a positive photopattern PL image (10 min development pattern). (d) Intensity of the protected and developed regions of the photopattern and (e) the corresponding intensity contrast for different development times.

It is interesting to note that at intermediate development times (5 min) a coronal pattern is formed with a high intensity central region surrounded by a lower intensity corona. This effect arises due to low intensity light bleeding (proximity effect) into the region surrounding the exposed hexagon region. The low intensity leads to decay of intensity but is not sufficiently strong to cause intensity recovery in the allotted time (**Figure 8.5a & Appendix E Figure E.6**).

In this instance of positive photopatterning, dark field imaging does show some indication of the photopattern (**Appendix E Figure E.7**). The exposed areas of the QD-polymer films scatter less light, which could be due to a reduction in the size of the QDs from oxidation that reduces their scattering cross-section. The time required to fabricate these positive photopatterns is more than 100 times faster than previous demonstrations (from hours to minutes). This reduction results from the unstable core-shell composition.[30,31]

Overall, positive photopatterns exhibit higher PL intensity and better pattern stability than negative photopatterns because the pattern contrast is provided by the slower recovery step. When the positive photopattern is exposed to light, the protected regions undergo a rapid decay (as in the case of negative patterns). The rapid decay of the protected regions actually increases the pattern contrast since the difference of intensity between the high and low intensity regions is now greater. Nevertheless, continued exposure eventually causes the protected regions to enter their recovery phase which does lead to a decrease in pattern contrast (shown later).

8.3.2.3 Preliminary decay-positive patterning (preD-PP)

Approach & Requirements

More stable positive photopatterns can be fabricated by decaying the film to near its minimum intensity before performing the steps for positive patterning (**Figure 8.6)**. The introduction of a preliminary decay step can improve pattern stability because all regions of the film have already experienced the fast decay step, essentially deactivating it. This means stray light exposure of the protected regions, which tends to reduce pattern stability, is less significant. Although this preD-PP approach incorporates an additional

pre-decay step ($t_{devel} < \tau_{decay}$) before the positive patterning step, the resulting photopattern appears similar to the positive patterns shown previously.

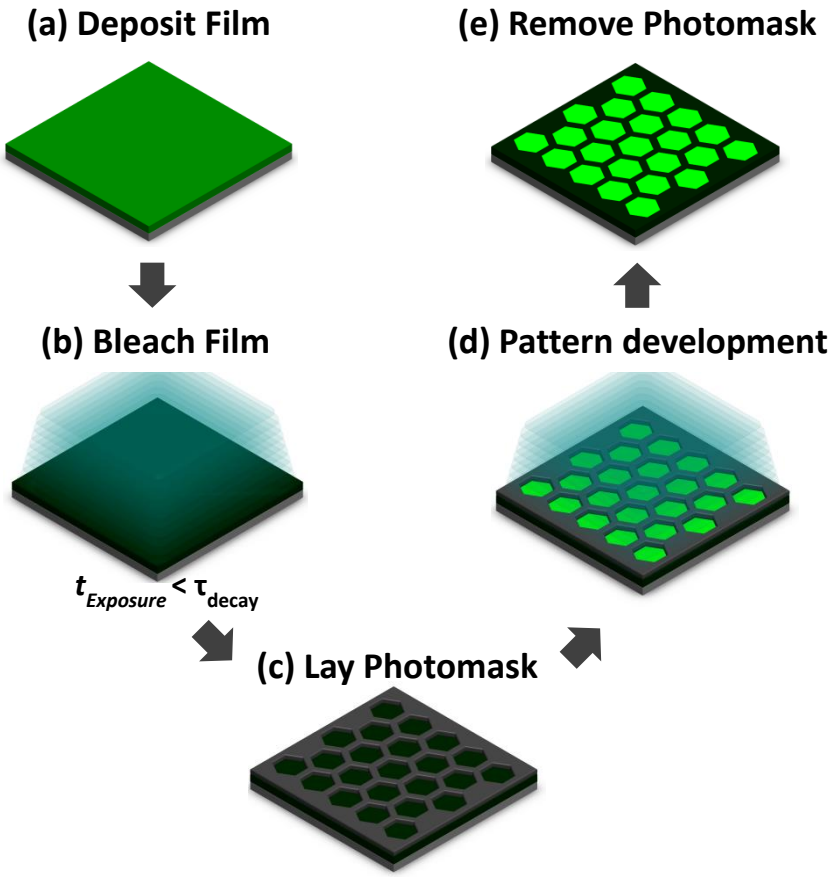

Figure 8.6: A positive photopatterning approach that can yield more stable photopatterns. This approach (preliminary decay-positive patterning, preD-PP) involves reducing the PL of the QD-polymer film before developing a positive photopattern. A QD-polymer film (a) is exposed to light to reduce its PL to a near-minimum value (b). A photomask is laid on top (c) and the system is exposed to light to develop the pattern (d). After removing the photomask, a positive photopattern is present (e).

Outcome

These preD-PP patterns display a positive intensity contrast that corresponds closely to the mask and shows a similar development rate of intensity contrast to positive photopatterning **(Figure 8.7a)**.

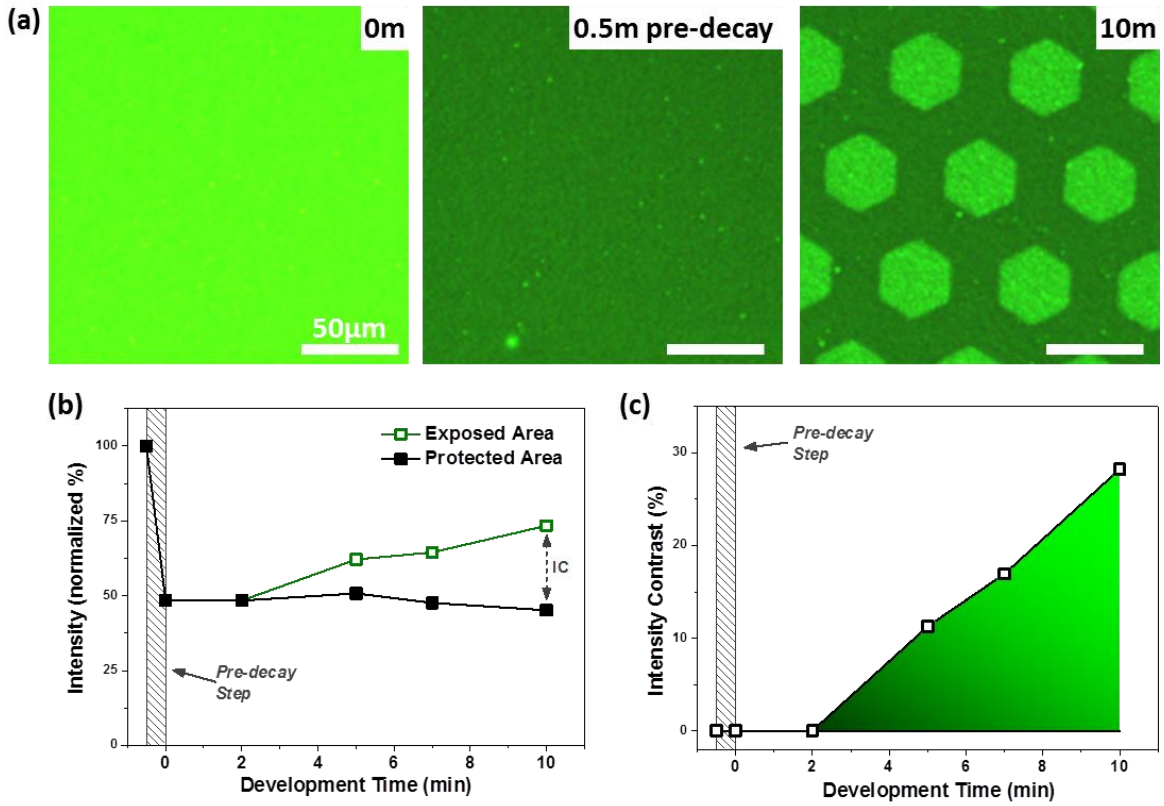

Figure 8.7 The preliminary decay-positive patterning (preD-PP) approach yields a stable positive photopattern. (a) PL images of a preD-PP positive photopattern at different stages of development (developed using light of 470 nm, 34 mW). All scale bars are 50 um. (b) Intensity of the protected and developed regions of the photopattern and (c) the corresponding intensity contrast for different development times.

PL cross-sections and intensity tracking show a clear positive intensity contrast between the developed and protected regions of the photopattern (**Figure 8.7b,c**). A maximum IC of 30% occurs at the longest development time (10 min). PL imaging using smaller time steps provides a more clear indication of how the pattern develops over a period of 10 minutes (**Appendix E Figure E.8**). As mentioned, this preD-PP approach yields a positive photopattern similar to that obtained from the PP approach outlined previously, but exhibits better stability upon subsequent light exposure because all regions of the film have had their decay-step deactivated.

8.3.2.4 Negative-to-positive contrast switching (N-P-CS)

Approach & Requirements

The most intriguing discovery was that the approach explored here makes it possible to switch a negative photopattern to a positive photopattern (**Figure 8.8**).

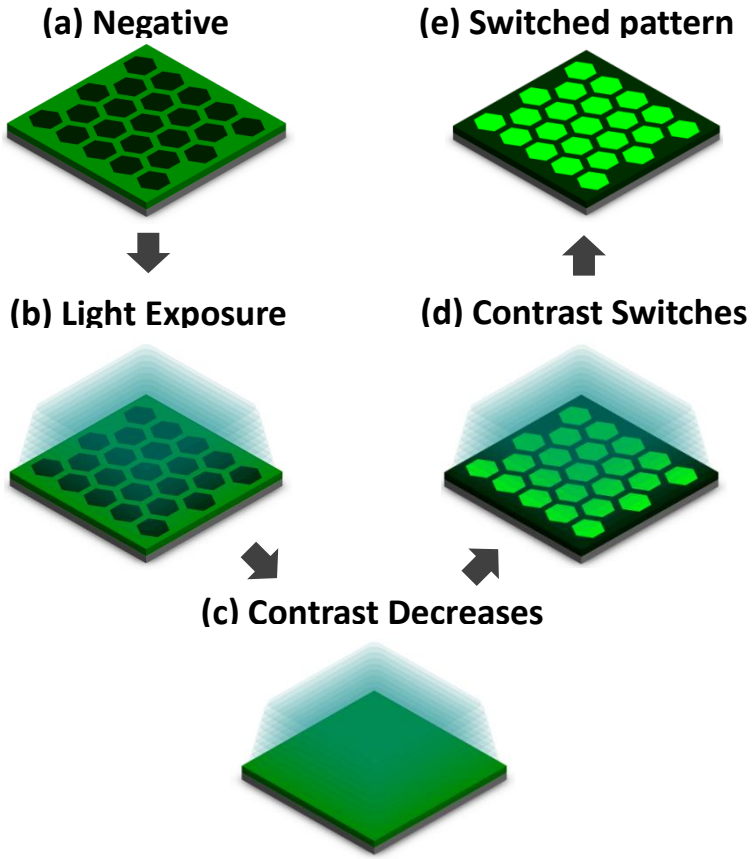

Figure 8.8: A photopatterning approach that can switch the contrast of the photopattern from negative-to-positive. This approach (negative-to-positive contrast switching, N-P-CS) involves exposing a negative photopattern (a) to light for extended periods of time (b). The intensity contrast of the pattern decreases to a near-neutral contrast state (c) and then emerges with a switched contrast (dark-to-bright and bright-to-dark) with continued light exposure (d). In the end, the photopattern has an intensity contrast that is opposite to the original contrast (e).

This strategy, called negative-to-positive contrast switching (N-P-CS), involves exposing an entire negative photopattern to light (no mask present) after the pattern has already been developed. Contrast switching from negative to positive occurs because the low intensity and high intensity regions of the QD-polymer film are at different stages of the decay-to-recovery evolution. For instance, the low intensity regions of the negative photopattern have already undergone decay so further exposure to light causes these regions to enter the PL recovery step. On the other hand, the high intensity regions of the negative photopattern have not undergone their decay step (since they were protected from the exposure light by the mask) so light exposure causes these regions to enter the rapid PL decay step.

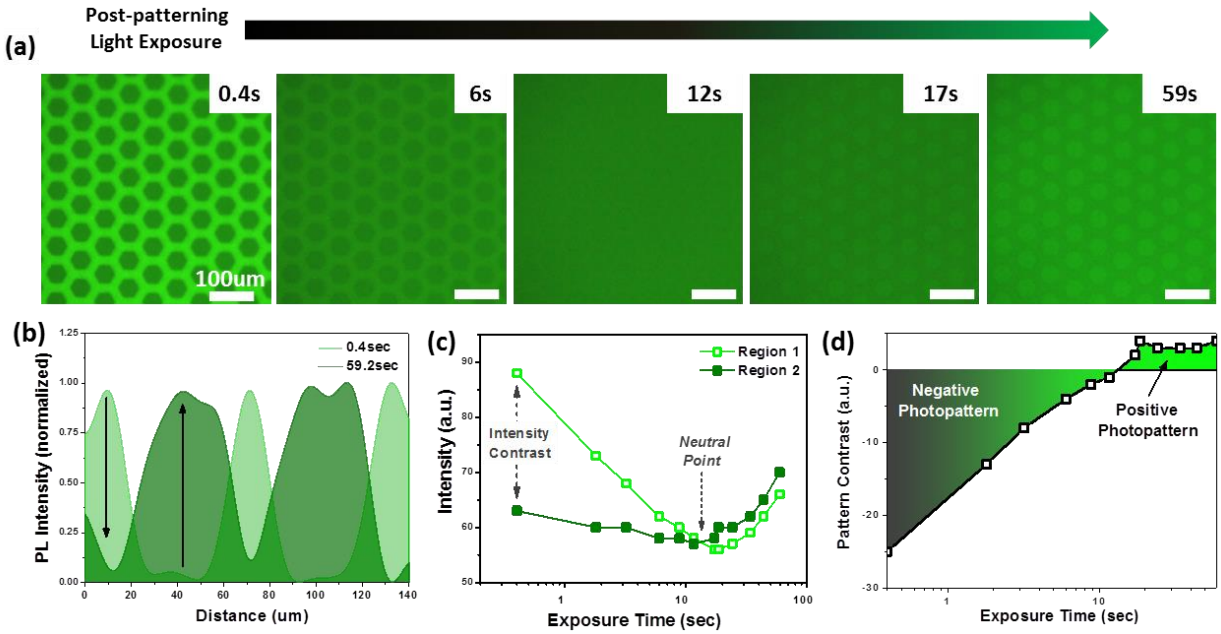

Figure 8.9: Negative-to-positive contrast switching (N-P-CS) occurs by exposing a negative photopattern to light for extended periods of time (470 nm, 23 mW). (a) PL imaging of the photopattern during different stages of the post exposure. (b) Cross-section of the photopattern at the beginning (0.4 s) and toward the end (59 s) of post exposure, demonstrating the switch of photopattern contrast (negative-to-positive). (c) Intensity of the different regions of the photopattern and (d) the corresponding intensity contrast. All scale bars are 100 µm.

Outcome

A demonstration of this negative-to-positive contrast switching (N-P-CS) approach is shown in **Figure 8.9a**. A negative photopattern was first fabricated. Following this, the entire negative photopattern was exposed to light (470 nm, 23 mW) for one minute or greater. Initially the negative photopattern displays a large negative intensity contrast (0.4 s panel). However, upon continued light exposure the intensity contrast decreases in magnitude since the negative regions of the pattern enter their PL recovery stage while the positive regions of the pattern enter their PL decay stage (6 s panel). Eventually these shifts cause the intensity contrast to reach a zero value (12 s panel) which makes the photopattern difficult to observe. Continued light exposure after this point switches leads to emergence of a positive contrast (17 s panel). The pattern contrast stabilizes once all regions of the pattern enter the linear portion of their PL recovery stage since there is a near constant difference of intensity (59 s panel).

PL cross-sections, intensity tracking, and intensity contrast determination at different stages of the post-exposure period show a clear switch from a negative IC to a positive IC after 59 sec of post exposure (**Figure 8.9b,c,d**). It is worth noting that the magnitude of intensity contrast is greater for the negative photopattern than for the positive photopattern. This asymmetry of pattern contrast stems from the large difference of rate between the decay step (seconds) and the recovery step (minutes), as made clear by the logarithmic time scale (**Figure 8.2b**). When the negative photopattern is exposed to light, the high intensity regions undergo a rapid decay while the low intensity regions undergo a slow recovery. In other words, the high intensity regions (which are decaying) “catch up” to the low intensity regions (which are recovering). Because this contrast asymmetry is intrinsically linked to the relative magnitude of the decay and recovery rates, it could be minimized if the decay and recovery rates were equalized (potentially

through QD composition engineering). The ability to switch from negative to positive intensity contrast without changing experimental setup is unprecedented and could have interesting applications in light sensing and switching.

8.3.3 Photopatterning stability (fading and recharging)

The unstable nature of the QD emission (which allows for the photopatterns to be fabricated) raises questions about the stability of these photopatterns after fabrication. PL imaging of a positive photopattern placed in darkness over a period of 1 day shows that the intensity and contrast of the pattern decreases continuously, leading to a faded pattern (**Figure 8.10a,c**).

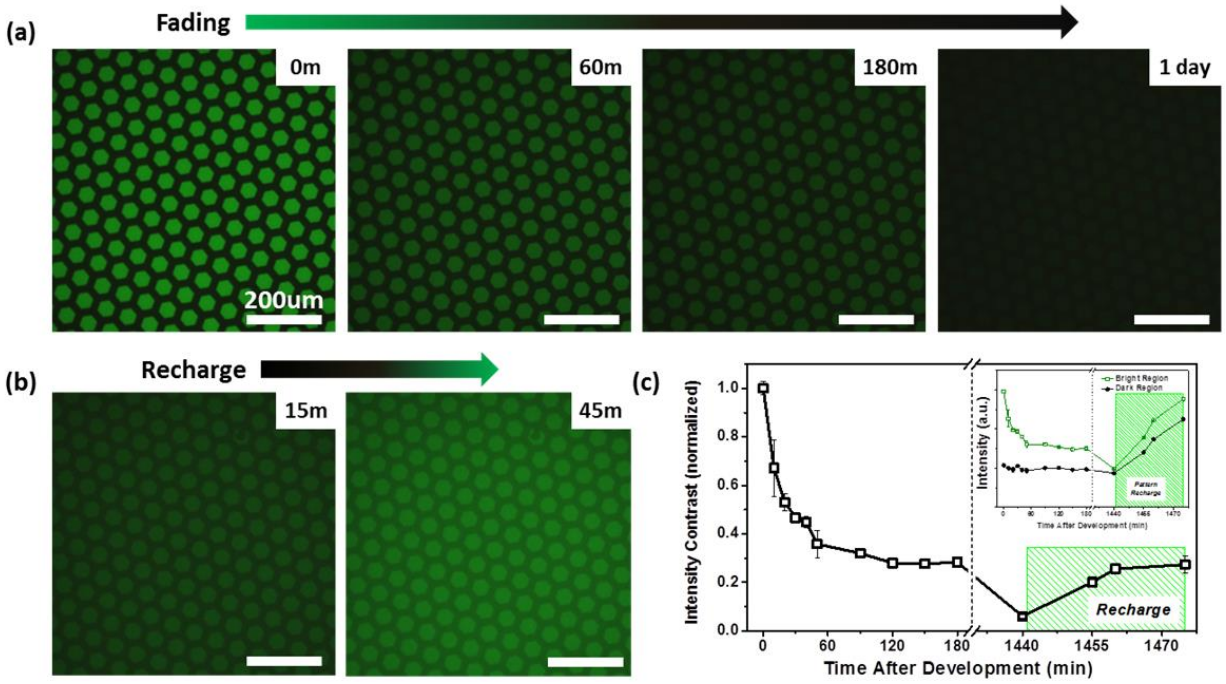

Figure 8.10: The unstable nature of the QD emission (which allows for photopatterns to be fabricated) also causes the pattern contrast to fade over time. (a) PL imaging of a positive photopattern over a period of 1 day (in darkness) demonstrating the fading behavior. (b) PL imaging of the same (1 day old) photopattern after being recharged by light exposure for 15 min and 45 min (470 nm). (c) Evolution of the intensity contrast of the positive pattern. (Inset) The intensity of the bright and dark regions of the pattern over the same period of time. All scale bars are 200 µm.

However, the intensity and contrast of the faded photopattern can be "recharged" by continuous light exposure (**Figure 8.10b,c**). Recharging can effectively recover the intensity to near the initial value, while the pattern contrast is only partially recovered since recharging increases the intensity of both the dark and bright regions of the photopattern (**Figure 8.10c, inset**). Nearly identical fading and recharging of intensity and contrast are observed for a photopattern placed in an ambient light environment (instead of darkness) (**Appendix E Figure E.9**). These results show that mechanism leading to the PL intensity recovery, which is used to create the positive photopatterns, is partially reversible and requires constant input of light to be maintained. This suggests that the recovery of PL intensity is due to a reversible dynamic process, possibly light-mediated H_2O surface passivation of the QD,[38] or photo-initiated ligand rearrangement.[52]

8.3.4 Comparison of approaches

The advantages and disadvantages of the four outlined photopatterning approaches in terms of the required development times, pattern contrast, complexity, and pattern stability are outlined in **Table 8.1**.

Table 8.1: Overview of the four photopatterning techniques outlined and the advantages and disadvantages associated with each technique.

Approach	Int. Contr.	Advantages	Disadvantages
Negative (NP)	Negative	Fast development (sec) High contrast	Poor pattern stability
Positive (PP)	Positive	Moderate pattern stability High contrast	Longer development (min)
Pre-decay positive (preD-PP)	Positive	Good pattern stability High contrast	Longer development (min) Requires two-steps
Neg-to-pos contrast switching (N-P-CS)	Negative-to-positive	Switchable intensity contrast High negative contrast	Requires post-exposure Low positive contrast

8.4 Conclusions

In conclusion, we demonstrated that traditional core-shell CdSe/ZnS QDs exhibit a two-step decay-to-recovery behavior of PL emission under continuous light exposure, with a two orders of magnitude difference in the rate of these steps (seconds versus minutes) that can be efficiently exploited for facile PL patterning. The two-step decay-to-recovery behavior of the unstable CdSe/ZnS QDs makes possible novel photopatterning strategies for creating a variety of photopatterns (negative, positive, preliminary-decay positive, and negative-to-positive contrast switching) significantly extending the capability to spatially manipulate the emissive properties of PL materials. These photopatterning strategies are analogous to traditional positive and negative patterning in electron/photolithography, a first in the area of photopatterning, and represent a noteworthy development in the area of photonics. Furthermore, the four different photopatterning approaches considerably extend the field of PL photopatterning by reducing pattern development time by a factor of 100-10000 (from hours to seconds) while maintaining spatial resolution. Finally, the most striking feature is the ability to continuously convert from a negative to a positive pattern using simple light exposure.

The variety of approaches and the range of advantages and disadvantages of each approach provide a great degree of flexibility in terms of pattern development, vastly increasing the potential applications. For example, microscale optical sensors could be developed where the response time of the system is controlled by utilizing either the decay step (responds in seconds) or the recovery step (responds over many minutes). Furthermore, these approaches can be combined by successively developing the same areas of a film using different photopatterning approaches to create complex spatial and spectral patterns that may not be possible using other traditional lithographic patterning

approaches. In addition, the outlined approaches are quite general, being compatible with other materials like conjugated polymers and dyes as long as their emission changes in response to light. Finally, these results have important implications in the development of nano/microscale photonic patterns over macroscopic lateral areas, a significant obstacle in microscale technologies.

8.5 Chapter acknowledgements

Dr. Jaehan Jung and Young Jun Yoon (Prof. Lin group, Georgia Institute of Technology): QD synthesis and ligand exchange.

8.6 References (Chapter 8)

1 Talapin, D.V.; Lee, J.S.; Kovalenko, M.V.; Shevchenko, E.V., Prospects of colloidal nanocrystals for electronic and optoelectronic applications. *Chem. Rev.* **2010,** *110,* 389-458.

2 Rosi, N.L.; Mirkin, C.A., Nanostructures in biodiagnostics. *Chem. Rev.* **2005,** *105*, 1547-1562.

3 Ko, H.; Singamaneni, S.; Tsukruk, V.V., Nanostructured surfaces and assemblies as SERS media. *Small* **2008,** *4*, 1576-1599.

4 Xia, Y.N.; Yang, P.D.; Sun, Y.G.; Wu, Y.Y.; Mayers, B.; Gates, B.; Yin, Y.D.; Kim, F.; Yan, Y.Q., One-dimensional nanostructures: Synthesis, characterization, and applications. *Adv. Mater.* **2003,** *15*, 353-389.

5 Hanske, C.; Tebbe, M.; Kuttner, C.; Bieber, V.; Tsukruk, V.V.; Chanana, M.; Konig, T.A.F.; Fery, A., Strongly coupled plasmonic modes on macroscopic areas via template-assisted colloidal self-assembly. *Nano Lett.* **2014,** *14*, 6863-6871.

6 Huang, X.H.; El-Sayed, I.H.; Qian, W.; El-Sayed, M.A., Cancer cell imaging and photothermal therapy in the near-infrared region by using gold nanorods. *J. Amer. Chem. Soc.* **2006,** *128*, 2115-2120.

7 Gandra, N.; Abbas, A.; Tian, L.M.; Singamaneni, S., Plasmonic planet-satellite analogues: Hierarchical self-assembly of gold nanostructures. *Nano Lett.* **2012,** *12*, 2645-2651.

8 Geryak, R.; Geldmeier, J.; Wallace, K.; Tsukruk, V.V., Remote giant multispectral plasmonic shifts of labile hinged nanorod array via magnetic field. *Nano Lett.* **2015,** *15*, 2679-2684.

9 Kapitonov, A.M.; Stupak, A.P.; Gaponenko, S.V.; Petrov, E.P.; Rogach, A.L.; Eychmuller, A., Luminescence properties of thiol-stabilized CdTe nanocrystals. *J. Phys. Chem. B* **1999,** *103,* 10109-10113.

10 Lin, K.F.; Cheng, H.M.; Hsu, H.C.; Lin, L.J.; Hsieh, W.F., Band gap variation of size-controlled ZnO quantum dots synthesized by sol-gel method. *Chem. Phys. Lett.* **2005,** *409,* 208-211.

11 Gaponik, N.; Hickey, S.G.; Dorfs, D.; Rogach, A.L.; Eychmüller, A., Progress in the light emission of colloidal semiconductor nanocrystals. *Small* **2010,** *6,* 1364-1378.

12 Peng, Z.A.; Peng, X.G., Formation of high-quality CdTe, CdSe, and CdS nanocrystals using CdO as precursor. *J. Amer. Chem. Soc.* **2001,** *123,* 183-184.

13 Qin, H.Y.; Niu, Y.; Meng, R.Y.; Lin, X.; Lai, R.C.; Fang, W.; Peng, X.G., Single-dot spectroscopy of zinc-blende CdSe/CdS core/shell nanocrystals: Nonblinking and correlation with ensemble measurements. *J. Amer. Chem. Soc.* **2014,** *136,* 179-187.

14 Dabbousi, B.O.; RodriguezViejo, J.; Mikulec, F.V.; Heine, J.R.; Mattoussi, H.; Ober, R.; Jensen, K.F.; Bawendi, M.G., (CdSe)ZnS core-shell quantum dots: Synthesis and characterization of a size series of highly luminescent nanocrystallites. *J. Phys. Chem. B* **1997,** *101,* 9463-9475.

15 Jung, J.; Lin, C.H.; Yoon, Y.J.; Malak, S.T.; Zhai, Y.; Thomas, E.L.; Vardeny, V.; Tsukruk, V.V.; Lin, Z., Crafting core/graded shell–shell quantum dots with suppressed re-absorption and tunable Stokes shift as high optical gain materials. *Angewandte Chemie Intern. Ed.* **2016,** *55,* 5071-5075.

16 Talapin, D.V.; Mekis, I.; Götzinger, S.; Kornowski, A.; Benson, O.; Weller, H., CdSe/CdS/ZnS and CdSe/ZnSe/ZnS core−shell−shell nanocrystals. *J. Phys. Chem. B* **2004,** *108,* 18826-18831.

17 Medintz, I.L.; Uyeda, H.T.; Goldman, E.R.; Mattoussi, H., Quantum dot bioconjugates for imaging, labelling and sensing. *Nat. Mater.* **2005,** *4,* 435-446.

18 Mashford, B.S.; Stevenson, M.; Popovic, Z.; Hamilton, C.; Zhou, Z.Q.; Breen, C.; Steckel, J.; Bulovic, V.; Bawendi, M.; Coe-Sullivan, S.; Kazlas, P.T., High-efficiency quantum-dot light-emitting devices with enhanced charge injection. *Nat. Photonics* **2013,** *7,* 407-412.

19 Gratzel, M., Solar energy conversion by dye-sensitized photovoltaic cells. *Inorganic Chem.* **2005,** *44,* 6841-6851.

20 Kamat, P.V., Quantum dot solar cells. Semiconductor nanocrystals as light harvesters. *J. Phys. Chem. C* **2008,** *112,* 18737-18753.

21 Engel, H.-A.; Loss, D., Fermionic bell-state analyzer for spin qubits. *Science* **2005,** *309*, 586-588.

22 Dang, C.; Lee, J.; Breen, C.; Steckel, J.S.; Coe-Sullivan, S.; Nurmikko, A., Red, green and blue lasing enabled by single-exciton gain in colloidal quantum dot films. *Nat. Nanotechnology* **2012,** *7,* 335-339.

23 Klimov, V.I.; Ivanov, S.A.; Nanda, J.; Achermann, M.; Bezel, I.; McGuire, J.A.; Piryatinski, A., Single-exciton optical gain in semiconductor nanocrystals. *Nature* **2007,** *447,* 441-446.

24 Lin, C.H.; Lafalce, E.; Jung, J.; Smith, M.J.; Malak, S.T.; Aryal, S.; Yoon, Y.J.; Zhai, Y.; Lin, Z.; Vardeny, Z.V.; Tsukruk, V.V., Core/alloyed-shell quantum dot robust solid films with high optical gains. *ACS Photonics* **2016,** *3,* 647-658.

25 Biswas, A.; Bayer, I.S.; Biris, A.S.; Wang, T.; Dervishi, E.; Faupel, F., Advances in top-down and bottom-up surface nanofabrication: Techniques, applications & future prospects. *Adv. Colloid and Inter. Sci.* **2012,** *170,* 2-27.

26 Qin, D.; Xia, Y.N.; Whitesides, G.M., Soft lithography for micro- and nanoscale patterning. *Nat. Protocols* **2010,** *5,* 491-502.

27 Young, S.L.; Gupta, M.; Hanske, C.; Fery, A.; Scheibel, T.; Tsukruk, V.V., Utilizing conformational changes for patterning thin films of recombinant spider silk proteins. *Biomacromolecules* **2012,** *13,* 3189-3199.

28 Kuang, M.; Wang, J.; Bao, B.; Li, F.; Wang, L.; Jiang, L.; Song, Y., Inkjet printing patterned photonic crystal domes for wide viewing-angle displays by controlling the sliding three phase contact line. *Adv. Opt. Mater.* **2014,** *2,* 34-38.

29 Gates, B.D.; Xu, Q.B.; Stewart, M.; Ryan, D.; Willson, C.G.; Whitesides, G.M., New approaches to nanofabrication: Molding, printing, and other techniques. *Chem. Rev.* **2005,** *105,* 1171-1196.

30 Tagliazucchi, M.; Amin, V.A.; Schneebeli, S.T.; Stoddart, J.F.; Weiss, E.A., High-contrast photopatterning of photoluminescence within quantum dot films through degradation of a charge-transfer quencher. *Adv. Mater.* **2012,** *24,* 3617-3621.

31 Wang, Y.; Tang, Z.Y.; Correa-Duarte, M.A.; Liz-Marzan, L.M.; Kotov, N.A., Multicolor luminescence patterning by photoactivation of semiconductor nanoparticle films. *J. Amer. Chem. Soc.* **2003,** *125,* 2830-2831.

32 Chen, J.; Chan, Y.-H.; Yang, T.; Wark, S.E.; Son, D.H.; Batteas, J.D., Spatially selective optical tuning of quantum dot thin film luminescence. *J. Amer. Chem. Soc.* **2009,** *131,* 18204-18205.

33 Malak, S.T.; Jung, J.; Yoon, Y.J.; Smith, M.J.; Lin, C.H.; Lin, Z.; Tsukruk, V.V., Large-area multicolor emissive patterns of quantum dot–polymer films via targeted recovery of emission signature. *Adv. Opt. Mater.* **2016,** *4,* 608-619.

34 Miri, M.A.; Regensburger, A.; Peschel, U.; Christodoulides, D.N., Optical mesh lattices with PT symmetry. *Phys. Rev. A* **2012,** *86,* 023807.

35 Regensburger, A.; Bersch, C.; Miri, M.A.; Onishchukov, G.; Christodoulides, D.N.; Peschel, U., Parity-time synthetic photonic lattices. *Nature* **2012,** *488,* 167-171.

36 Uematsu, T.; Kimura, J.; Yamaguchi, Y., The reversible photoluminescence enhancement of a CdSe/ZnS nanocrystal thin film. *Nanotechnology* **2004,** *15,* 822-827.

37 Pechstedt, K.; Whittle, T.; Baumberg, J.; Melvin, T., Photoluminescence of colloidal CdSe/ZnS quantum dots: The critical effect of water molecules. *J. Phys. Chem. C* **2010,** *114,* 12069-12077.

38 Nazzal, A.Y.; Wang, X.Y.; Qu, L.H.; Yu, W.; Wang, Y.J.; Peng, X.G.; Xiao, M., Environmental effects on photoluminescence of highly luminescent CdSe and CdSe/ZnS core/shell nanocrystals in polymer thin films. *J. Phys. Chem. B* **2004,** *108,* 5507-5515.

39 Cordero, S.R.; Carson, P.J.; Estabrook, R.A.; Strouse, G.F.; Buratto, S.K., Photo-activated luminescence of CdSe quantum dot monolayers. *J. Phys. Chem. B* **2000,** *104,* 12137-12142.

40 Kimura, J.; Uematsu, T.; Maenosono, S.; Yamaguchi, Y., Photoinduced fluorescence enhancement in CdSe/ZnS quantum dot submonolayers sandwiched between insulating layers: Influence of dot proximity. *J. Phys. Chem. B* **2004,** *108,* 13258-13264.

41 Shinya, M.; Ceco Danov, D.; Soichiro, S.; Yukio, Y., Optical memory media based on excitation-time dependent luminescence from a thin film of semiconductor nanocrystals. *Japanese J. Appl. Phys.* **2000,** *39,* 4006-4012.

42 Maenosono, S., Modeling photoinduced fluorescence enhancement in semiconductor nanocrystal arrays. *Chem. Phys. Lett.* **2003,** *376,* 666-670.

43 Zimnitsky, D.; Jiang, C.Y.; Xu, J.; Lin, Z.Q.; Tsukruk, V.V., Substrate- and time-dependent photoluminescence of quantum dots inside the ultrathin polymer LbL film. *Langmuir* **2007,** *23*, 4509-4515.

44 Zimnitsky, D.; Jiang, C.Y.; Xu, J.; Lin, Z.Q.; Zhang, L.; Tsukruk, V.V., Photoluminescence of a freely suspended monolayer of quantum dots encapsulated into layer-by-layer films. *Langmuir* **2007,** *23*, 10176-10183.

45 J.A. Woollam Co. Inc. “Guide to using WVase32.” Ch.2, A short course in ellipsometry. **2010.**

46 Greytak, A.B.; Allen, P.M.; Liu, W.; Zhao, J.; Young, E.R.; Popovic, Z.; Walker, B.J.; Nocera, D.G.; Bawendi, M.G., Alternating layer addition approach to CdSe/CdS core/shell quantum dots with near-unity quantum yield and high on-time fractions. *Chem. Sci.* **2012,** *3,* 2028-2034.

47 Gong, K.; Kelley, D.F., Lattice strain limit for uniform shell deposition in zincblende CdSe/CdS quantum dots. *J. Phys. Chem. Lett.* **2015,** *6,* 1559-1562.

48 Smith, A.M.; Mohs, A.M.; Nie, S., Tuning the optical and electronic properties of colloidal nanocrystals by lattice strain. *Nat. Nanotech.* **2009,** *4,* 56-63.

49 van Sark, W.; Frederix, P.; Van den Heuvel, D.J.; Gerritsen, H.C.; Bol, A.A.; van Lingen, J.N.J.; Donega, C.D.; Meijerink, A., Photooxidation and photobleaching of single CdSe/ZnS quantum dots probed by room-temperature time-resolved spectroscopy. *J. Phys. Chem. B* **2001,** *105*, 8281-8284.

50 Wang, Y.; Tang, Z.Y.; Correa-Duarte, M.A.; Pastoriza-Santos, I.; Giersig, M.; Kotov, N.A.; Liz-Marzan, L.M., Mechanism of strong luminescence photoactivation of citrate-stabilized water-soluble nanoparticles with CdSe cores. *J. Phys. Chem. B* **2004,** *108*, 15461-15469.

51 Beane, G.A.; Gong, K.; Kelley, D.F., Auger and carrier trapping dynamics in core/shell quantum dots having sharp and alloyed interfaces. *ACS Nano* **2016,** *10,* 3755-3765.

52 Jones, M.; Nedeljkovic, J.; Ellingson, R.J.; Nozik, A.J.; Rumbles, G., Photoenhancement of luminescence in colloidal CdSe quantum dot solutions. *J. Phys. Chem. B* **2003,** *107*, 11346-11352.

CHAPTER 9

LARGE-AREA, HIGH-RESOLUTION, HIGH-THROUGHPUT EDGE-PROFILE AND FACE-PROFILE QD PHOTOPATTERNING

Chapter Based On:
Malak, S.T.; Ramathasan, T.; Liang, G.; Yoon, Y.J.; Smith, M.J.; Lin, C.H.; Lin, Z.; Thomas, E.L.; Tsukruk, V.V., Large-area high-resolution high-throughput quantum dot edge-profile and face-profile photopatterning approaches, *in preparation.*

Chapter Overview

Following the examination on how the duration of light exposure affects photopattern contrast, our attention shifts to how the spatial arrangement of light exposure can be tuned and utilized to control photopattern development. New photopatterning approaches based on near-field and far-field interference phenomena are presented that yield highly-uniform high-resolution large-area face-profile and novel edge-profile photopatterns (**Figure 9.1a,b**). These techniques replace the traditional opaque photomask with interference-based masks (or maskless exposure), representing a significant paradigm shift in the area of photopatterning. Photopatterns fabricated using these interference-based techniques can reach minimum feature sizes of ~550-1800 nm which matches the current high resolution offered by direct-write single-laser exposure (~575 nm). Furthermore, these near-field and far-field interference techniques also drastically increase the patternable area (cm^2) and throughput (increases of up to six orders of magnitude) while maintaining pattern uniformity.

These advances address the major constraints associated with resolution and throughput that have plagued traditional photopatterning. Moreover, these strategies use easy-to-handle reusable photomasks (or no mask at all) which is a significant

improvement over the easily deformable TEM grids typically used in photopatterning. Finally, all three interference-based approaches can be applied multiple times on the same film area to yield ultra-dense multi-level intensity contrast photopatterns that are very difficult (if not impossible) to obtain using traditional strategies (**Figure 9.1c,d**). These high throughput strategies will be valuable for systems that require very uniform large-area high-resolution photopatterns, such as light sensors, anti-counterfeiting labels, and display technology.

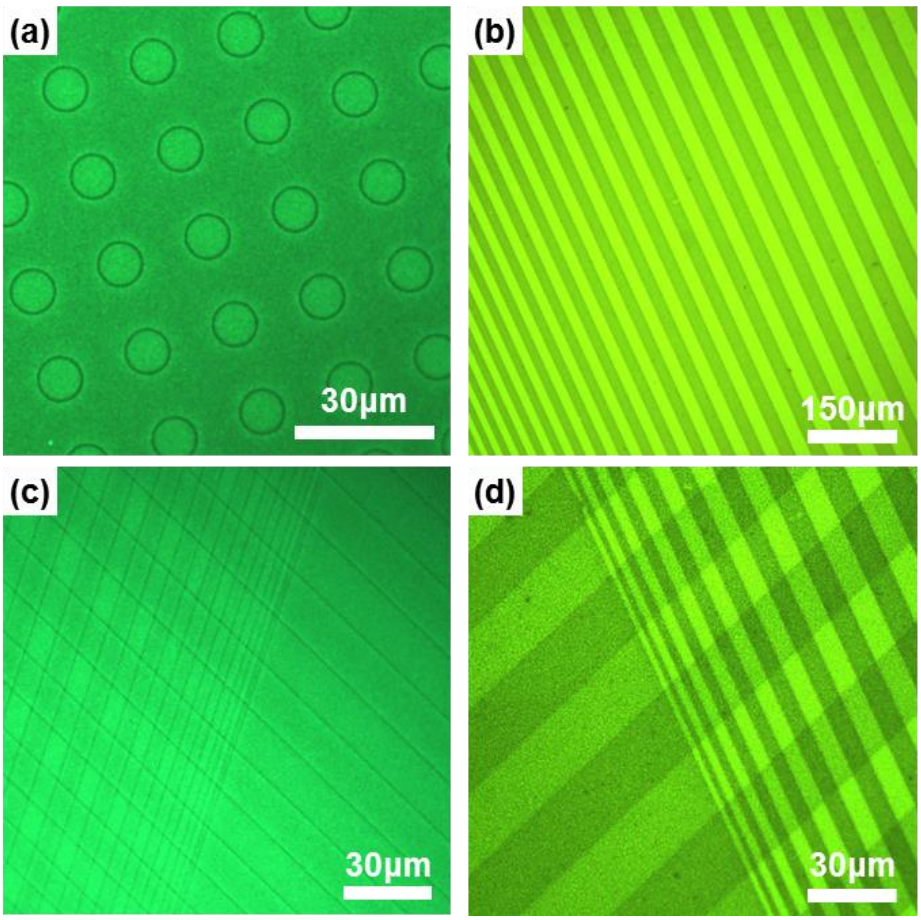

Figure 9.1: PL images of high-resolution photopatterns of edge-profile (a,c) circles and lines and (b,d) face-profile lines fabricated using interference-based light exposure strategies.

9.1 Introduction

9.1.1 Nano/microscale patterning

The field of photonics has experienced a variety of impressive recent developments including broader spectral range lasers, more efficient LEDs, and improved light harvesting energy systems.[1,2,3,4] Many of the developments have been driven by advances in the field of photonic nanotechnology, particularly in the area of microscale and nanoscale patterning techniques.[5,6,7] There is a wide variety of micro/nanoscale patterning techniques and designations. One of the most important distinctions is whether the patterning technique is a serial or parallel process.[8,9] Serial processes sequentially fabricate one structure at a time via a direct-write approach, and include techniques like electron beam lithography (EBL) or focused ion beam milling (FIB). These techniques often have high resolution (below 50 nm) but poor throughput.[8,9] A parallel process fabricates multiple structures simultaneously, and includes processes like photolithography, colloidal lithography, and soft-lithography.[10,11] The throughput of these techniques is typically high but can sometimes have a trade-off in resolution.[10,12]

Another important, but more recent, patterning classification is whether the technique yields physical or non-physical patterns. Physical patterning involves the addition, removal, or rearrangement of material to create a pattern, and includes most of the techniques listed above.[8,9] Non-physical patterns are those which involve the intrinsic modification of the material (often via light exposure) to provide chemical, ion doped, stiffness, or photonic patterns that do not have a clear corresponding physical pattern.[13,14,15,16]

Photopatterning is an emerging technique in the area of non-physical patterning that involves the fabrication of a photoluminescence emission pattern via selective light exposure of a light-sensitive film.[13,14,15,16] Typically, unstable quantum dots are utilized as the light-sensitive component since they can undergo increases or decreases in intensity or undergo spectral shifts when exposed to light.[13,14,16] In addition, these semiconducting nanoparticles exhibit size-dependent emission across the visible spectrum, high quantum yield, narrowband emission, and are compatible with surface functionalization techniques.[17,18,19,20,21,22] The combination of characteristics exhibited by photopatterns and quantum dots allows for potential applications in anti-counterfeiting, light sensing, and display technologies.[14,15]

9.1.2 Photopatterning limitations (resolution and throughput)

A variety of studies have outlined photopatterning strategies that yield photopatterns with high intensity contrast and single (or multiple) colors.[14,15,23] These developments have been driven in part by inexpensive and widely available photomasks (often Cu TEM grids).[13,14,15,24] Although initial results are promising, a number of important limitations remain in terms of poor resolution (features are generally tens of microns or more) and low throughput (small areas and long development times). Photopatterning using TEM grid photomasks is a parallel process so it yields moderate throughput (mm^2/minute) but compromises on resolution and has limited pattern options. Some studies have attempted to bridge the resolution gap by employing TEM grids with smaller feature sizes (~7 μm).[15] However, this does not overcome the fundamental limitations associated with TEM grid photomasks. Furthermore, common handling of TEM grids can deform them, which makes sequential multi-exposure photopatterning difficult when using the same mask. Photopatterning via a scanning laser based exposure setup

significantly improves resolution (feature size of ~575 nm) but has very low throughput due to the serial process nature.[23] Clearly new photomasks and exposure strategies need to be identified that can address the obstacles associated with photopattern resolution and throughput.

9.1.3 Near-field and far-field interference exposure

A number of patterning approaches exist that could simultaneously address the issue of resolution and throughput currently plaguing the field of photopatterning. These techniques use either near-field or far-field light interference to obtain very small feature sizes but work via a parallel process that allows for high throughput. Near-field phase-shift lithography is a particularly promising near-field interference technique because it is a parallel process that can pattern features down to 90 nm.[25] This approach uses a robust patterned PDMS stamp to obtain specific pre-determined regions of destructive interference.[25,26,27] Furthermore, patterned PDMS stamps can be fabricated with arbitrary shapes.[10] Far-field interference patterning via laser interference lithography (LIL) can also create high-resolution patterns over large areas.[28,29] LIL uses two or more light beams to create an interference pattern, and has been shown to be an efficient method for fabricating micron to sub-micron scale microstructures for photonic, phononic, and mechanical applications.[28,29] A variety of patterns can be generated by LIL depending on the number of interfering beams and exposure steps. For example, 1D gratings with very uniform periodicity can be fabricated by utilizing the traditional multi-beam one-step exposure approach.[28] Higher dimensional patterns (cross-hatched, diamond symmetry structures, etc.) can also be developed using dual-beam multiple-step exposures or an elliptical polarization triple beam setup.[30,31,32] Traditionally, both

the near-field and far-field interference approaches are used to initiate cross-linking (or chain scission) reactions in polymer films to create physical patterns.[25,26,27,29,30]

In this work, we outline new interference-based photopatterning strategies that simultaneously address both the issue of limited resolution and throughput (two parameters that are often mutually exclusive) in conventional photopatterning. The capabilities of these three approaches stem from them being based on near-field and far-field interference phenomena, representing one of the first demonstrations in the field of photopatterning. The two near-field interference approaches employ patterned PDMS stamps (like those typically employed in soft lithography) and specific exposure conditions to create unique edge-profile or face-profile photopatterns. The far-field interference approach utilizes a two-beam laser interference lithography setup to produce a photopattern with sinusoidal intensity modulation. All three approaches yield high-throughput large-scale highly-uniform photopatterns with pre-determined designs, overcoming many of the issues associated with photopatterning using traditional TEM grid photomasks and serial laser scanning exposure.

9.2 Experimental details

Sample preparation. QD-polymer films have a QD-loading near or below 1% (volume fraction) and thickness ranging from 260±50 nm to 560±60 nm depending upon spin conditions and polymer solution concentration. The QD-polymer mixture was composed of equal parts of a QD toluene solution and a 10-12% PMMA toluene solution, and vortexed to ensure complete mixing. Films were deposited on silicon with a 290-295 nm surface layer of SiO_2.

Photomask fabrication & photopattern development. The patterned polydimethylsiloxane (PDMS) photomasks (used for near-field photopatterning) were fabricated using a common fabrication procedure for PDMS soft-lithography stamps.[10,27] Patterns of various size, shape, and spacing were dictated by a chrome master pattern on a quartz substrate. The height of the patterned features on the PDMS photomask were 1.1-1.2 μm. Photopatterning using the near-field patterned PDMS stamp used a 10x objective (NA: 0.30) with excitation light of either UV (325-375 nm) or blue (450-490 nm) (over a range of powers), as outlined in previous work.[14,15] The light source was a 120 W Hg vapor short arc lamp (X-cite series, 120Q, Lumen Dynamics) with controllable power output.

Far-field photopatterning via laser interference lithography was conducted by creating an interference pattern using two (interfering) laser beams.[28,30,31] Specifically, a 532 nm laser beam was output from a Coherent Verdi 5 system and then passed through a beam splitter cube to create two laser beams. The two beams traveled the same optical path length after the beam-splitting point. Each beam was expanded to have a diameter of approximately 18 mm. The power density of each beam was measured to be near 955 mW/cm^2. The two beams were symmetrically incident on the same side of the polymer film at an incident angle "θ" with respect to the normal of the film. An angle of 3.05° was used to obtain a sinusoidal periodicity "a" of approximately 5 μm (predicted via $a = \lambda/2\sin\theta$). A high interference contrast of the two beams was obtained by utilizing parallel linear polarization.

The interference pattern manifested itself as a 1D grating on the polymer-quantum dot film. The cross-hatched array was fabricated by a two-step exposure of the 1D grating.

More specifically, QD-polymer film was mounted on a rotational stage and rotated 90° after the first exposure for the consequent exposure. Short light exposure times during pattern development were used to minimize the effects of spatial drift on the photopattern contrast.

9.3 Results and discussion

9.3.1 Photopatterning via on-beam incidence (PDMS mask)

High-resolution photopatterns were fabricated by selective light exposure to a light sensitive film, as outlined in previous works.[14,15] In this case, the light-sensitive film is a CdSe/ZnS QD-polymer composite that exhibits an increase in its QD PL intensity when exposed to light over many minutes (**Appendix F Figure F.1a**). The QDs have photoluminescence emission in the green (~528 nm) and yellow (~592 nm) wavelength regions (**Appendix F Figure F.1b**). Briefly, a QD-polymer film is deposited onto a substrate (**Figure 9.2, step 1**) and then a polydimethylsiloxane (PDMS) stamp with a patterned surface is brought into conformal contact with the film (**Figure 9.2, step 2**). The system is then exposed to light of a wavelength the QDs can absorb (**Figure 9.2, step 3**). It is critical to mention that the exposure light is directly incident on the patterned region of the PDMS mask at a direction normal to the pattern (termed "on-beam" incidence).

On-beam exposure → light beam directly incident on patterned mask region

Edge-profile pattern → photopattern mimics edges of mask pattern

(ex. circular mask structure → ring photopattern)

The PDMS photomask then modulates the exposure light in certain regions while leaving the light intensity in other regions unchanged. The spatially modulated light intensity is incident on the underlying light-responsive QD-polymer film, leading to a contrast in the amount of PL recovery that occurs in different regions (high exposure regions undergo significant PL recovery while low exposure regions do not). After the PDMS mask is removed a photopattern can be observed (**Figure 9.2, step 4**). A unique characteristic of on-beam PDMS photopatterning is that the resulting photopatterns are defined primarily by the edges of the PDMS pattern (discussed in detail later). For example, a circular hole and a circular pillar in the PDMS mask will both yield a dark circular ring photopattern (**Figure 9.2, step 4**).

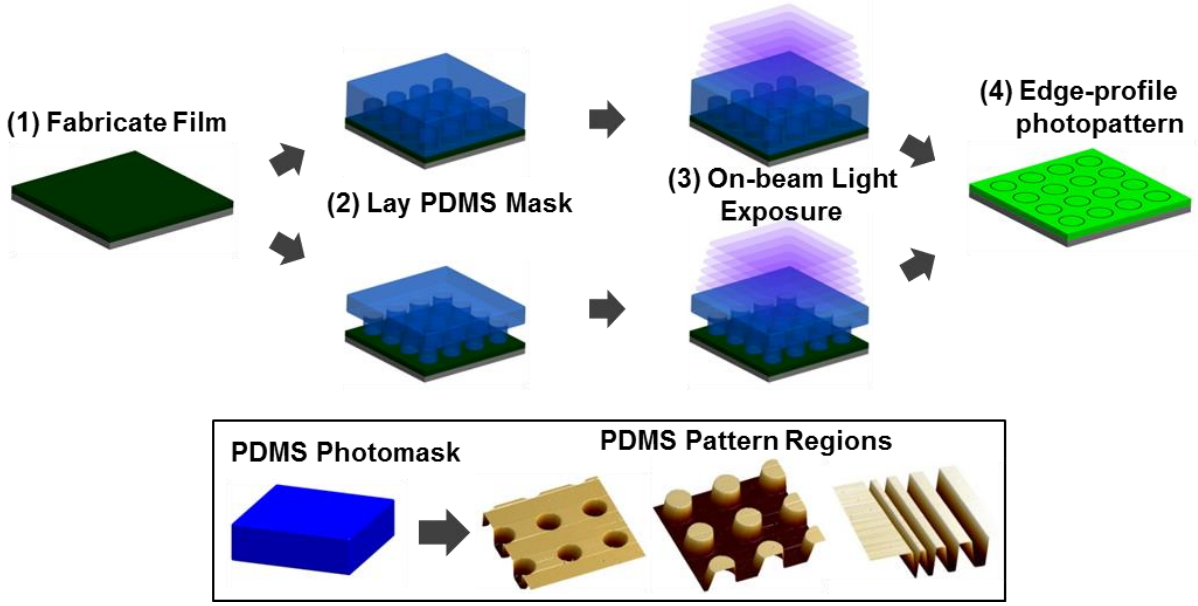

Figure 9.2: Schematic outlining the "on-beam" photopatterning process using a PDMS stamp. (1) A QD-polymer film is deposited and (2) a PDMS stamp is placed on its surface. (3) Light is incident on the patterned region of the PDMS stamp (on-beam incidence). (4) When the PDMS stamp is removed a photopattern is present corresponding to the edge-profile of the PDMS pattern. PDMS patterns that have the same edge-profiles (for example circular pillars and circular holes) will lead to the same photopattern. (Bottom panel) 3D AFM height projections of the patterned region of the PDMS photomasks used in this study.

The unique "edge-profile" photopattern results from the distinct near-field phase-shift interference phenomenon that occurs within the PDMS pattern.[25,26,27] It is important to

note that this phase-shift approach is in stark contrast to nearly all demonstrations of photopatterning that use a photomask composed of opaque materials like Cu (TEM grid) or Cr (photolithograph mask).[13,14,15,24,33] Metal masks provide light exposure contrast to the underlying light responsive film by blocking the passage of light through the photomask in certain regions via reflection or absorption. Therefore, areas of the light-responsive film protected by the photomask remain unchanged while areas of the film exposed to the development light undergo a change of their PL (increase/decrease of intensity or spectral shift).[13,14]

However, a PDMS photomask is nearly transparent to the development light and therefore modulates light intensity using a fundamentally different mechanism than the opaque photomasks.[25,26,27] In this case, modulation of light intensity arises from destructive interference at certain regions of the patterned interface of the PDMS photomask. This near-field phase-shift phenomenon (NfPs) has been described in detail previously.[25,26,27] Briefly, light that enters the PDMS and propagates to the patterned PDMS surface will encounter either recessed (hole) or raised (pillar) PDMS structures and a second medium (typically air). In this scenario, the vertical edges of the PDMS structures have a PDMS-air interface. The difference in refractive index between PDMS (≈1.41) and air (1.00) at the exposure wavelength leads to a difference in the effective propagation distance in each medium due to wavelength shortening in the PDMS. Therefore, a phase difference can emerge between light traveling in the PDMS and air at this vertical interface (**Appendix F Equation F.1**). If the phase difference is an odd multiple of π, then destructive interference occurs and the light intensity will be zero, which means no PL recovery occurs in this region of the light-responsive QD-polymer film. Furthermore, this is a highly localized near-field phenomenon, since it is the evanescent waves at the PDMS-air interface that undergo destructive interference, thus

sub-wavelength features can be patterned.[25,26,27] Finally, since the near-field phase-shift destructive interference phenomenon underlying on-beam photopatterning occurs primarily at the PDMS pattern edges, the resulting photopattern should not be sensitive to whether the PDMS pattern is composed of raised (pillars) or recessed (holes) structures (**Figure 9.3**).

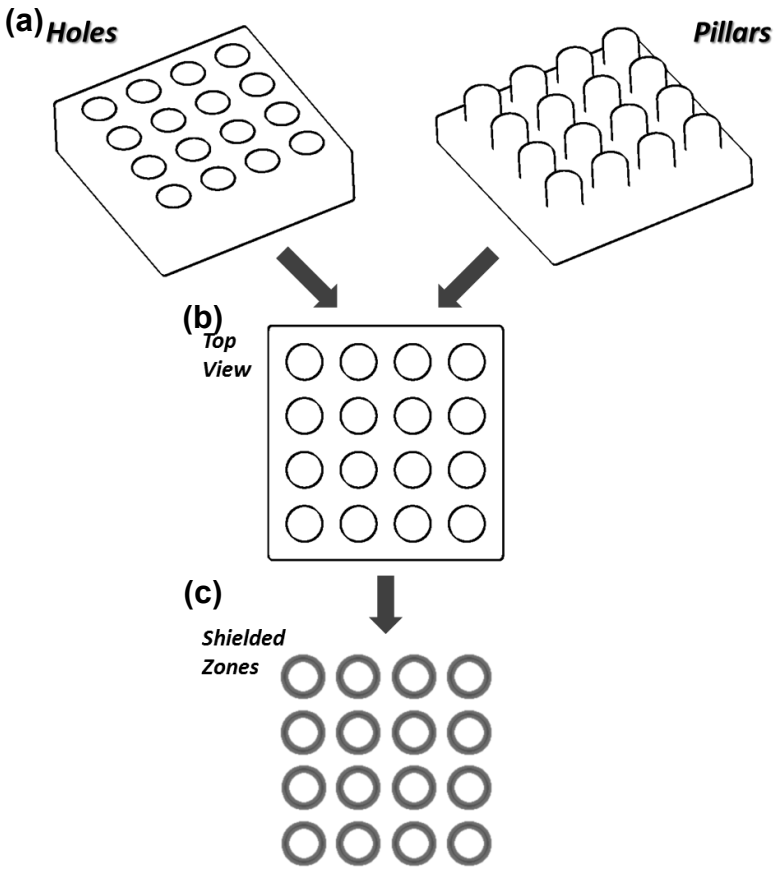

Figure 9.3: Schematic detailing "on-beam" edge-profile photopatterning and its insensitivity to the z-profile of the PDMS stamp (pillar versus hole). The edge-profile and insensitivity stem from: (1) the fact that the exposure light is normal to the direction of the PDMS stamp and (2) it is the vertical sides of the holes and pillars that shield the underlying QD-polymer film from the exposure light (providing the photopattern intensity contrast). Since the hole and pillar pattern (a) have the same lateral cross-section (b), the shielded zones will be the same (and therefore the photopattern will be the same) (c).

To confirm these predictions, on-beam photopatterning was conducted using patterned PDMS photomasks of either circular holes or circular pillar arrays that have the same dimensions and arrangement (**Appendix F Figure F.2,3**). Photoluminescence images of a photopattern of circular rings, which was created using a patterned PDMS photomask of circular holes, proves that the photopattern is indeed of the edge-profile type (**Figure 9.4a-d)**. The PL images also show that longer development times increase both the PL intensity and contrast of the photopattern (**Figure 9.4a**). PL cross-sections of the PL images quantifiably confirm the increase of PL intensity with exposure time and make it possible to measure the PL intensity of the dark and bright regions of the pattern (**Figure 9.4b,c**). The intensity contrast, which is a measure of the difference of PL between dark and bright regions of a pattern, clearly increases with development time (**Figure 9.4d**). This approach and behavior is consistent with the PL recovery mentioned earlier and previous studies (**Appendix F Figure F.1**).[14,15] As mentioned before, photopatterns result from intrinsic modification of the QDs within the QD-polymer film, and not due to physical addition or removal of material from the film.[13,14,15,24,33] The featureless topography is confirmed by atomic force microscopy (AFM) scanning of the film in regions that have been photopatterned (**Appendix F Figure F.4**).

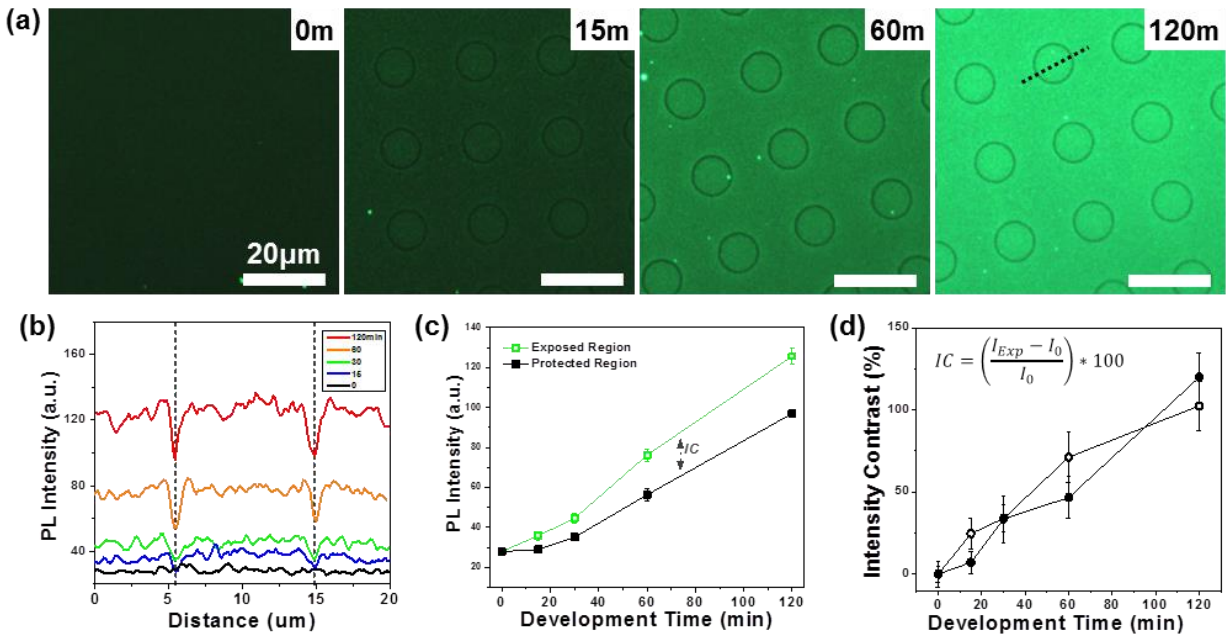

Figure 9.4: Demonstration of the "on-beam" photopatterning process using a PDMS stamp with a hole array pattern. (a) PL images of a circular edge-profile photopattern at different stages of pattern development (developed using UV light (325-375 nm), 19.8 mW/cm^2). (b) PL intensity cross-section across edge-profile rings. (c) PL intensity of the protected and exposed regions of the photopattern, and (d) the intensity contrast at different stages of pattern development using a hole or pillar PDMS photomask. Scale bar is 20 μm for all images.

The insensitivity of on-beam photopatterning to the recessed/raised nature of the PDMS photomask was confirmed by fabricating a photopattern with a patterned PDMS photomask of raised circular pillars. PL imaging shows a photopattern that is practically identical to the photopattern created using a hole PDMS photomask (**Appendix F Figure F.5**), with the majority of the photopattern contrast occurring at the edges of the pattern of the PDMS photomask (in this case the circumference of each pillar or hole). In addition, the patterned hole and pillar PDMS photomasks yield photopatterns with similar intensity contrast (**Figure 9.4d**).

An important characteristic of the edge-profile photopattern is that it has feature sizes extending down to the sub-micron region (fitting of PL cross-section shows a FWHM

~550 nm), which is an impressive feat and previously required a scanning laser based exposure setup (**Figure 9.5a,b**).[23] The sub-wavelength feature size can be obtained using either UV (325-375 nm) or blue (450-490 nm) development light (**Figure 9.5a-d**). However, the intensity contrast obtained from blue exposure is lower than that provided by UV exposure since blue wavelengths do not adhere as closely to the requirements for complete destructive interference (π-shift) as the UV wavelengths (**Figure 9.5e)(Appendix F Figure F.6, Equation F.1**).[25] Note, further reductions in feature size will approach the diffraction limit of the optical system (~300 nm in this case) and likely require the use of confocal scanning systems.

Finally, to the best of the authors' knowledge, this represents the first demonstration of edge-profile photopatterning. Previous photopatterns (made using photomasks) are of the face-profile type, where the photopattern mimics the "face" of the mask's pattern (a photomask with a square hole yields a photopatterned square).[13,14,15,24,33] As mentioned, the primary intensity contrast of the edge-profile photopatterns stems from their edges. However, the edge-profile patterns do have some face-profile intensity contrast (increase of PL intensity in the internal regions) but this is only clearly evident at lower viewing magnifications (**Appendix F Figure F.7**).

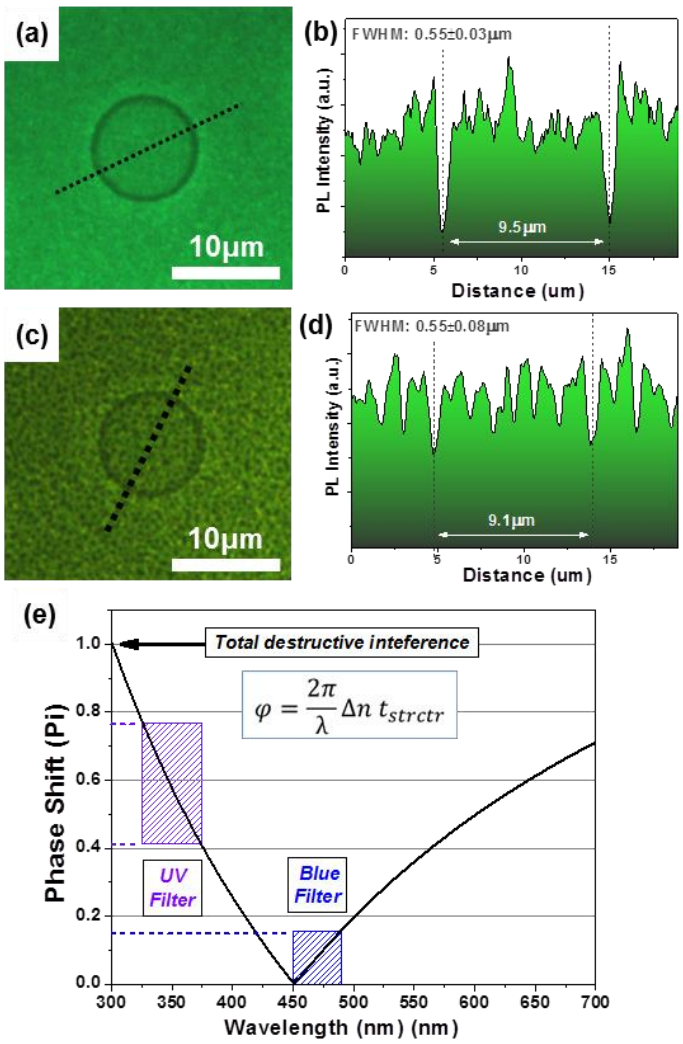

Figure 9.5: PL image and intensity cross-section of photopatterned rings made using the "on-beam" approach with (a,b) UV (325-375 nm) and (c,d) blue (450-490 nm) development light (10 μm hole photomask). Plot of the relationship between the phase shift (between light in the PDMS and in the air gaps of the PDMS pattern) and the wavelength of exposure light. The relationship follows the equation (inset) and the actual system parameters ($\Delta n = 0.41$, $t_{strctr} = 1.1$ um). Phase shift values closer to 1 indicate a stronger adherence to the destructive interference requirement (odd integer of π phase difference).

9.3.2 Photopatterning via off-beam incidence (PDMS mask)

Patterned PDMS stamps have a number of advantages over the traditional metal photomasks typically used in photopatterning (like Cu TEM grids). These advantages include PDMS being more robust than TEM grids (allowing them to be reused), easier to

handle (making patterning more simple and reliable), and having higher resolution and more pattern choices (permitting more applications). However, PDMS also has a very different complex refractive index than metals which enables it to waveguide light with minimal optical attenuation losses. Optical waveguiding and scattering, in turn, makes possible a unique indirect exposure approach that is not possible using traditional metal photomasks.

The specific steps of the "off-beam" indirect exposure approach are outlined in **Figure 9.6**. Overall this approach is similar to the on-beam approach outlined earlier except that indirect light incidence is used to develop the photopattern. In this scenario, the development light is incident on a region of the PDMS photomask that is not patterned (**Figure 9.6, step 3**). When light enters the PDMS material much of it propagates to the underlying QD-polymer film. However, some light also diffuses/scatters throughout the PDMS material in the lateral directions and propagates to the patterned area of the PDMS mask to create a photopattern in the underlying light-sensitive film.

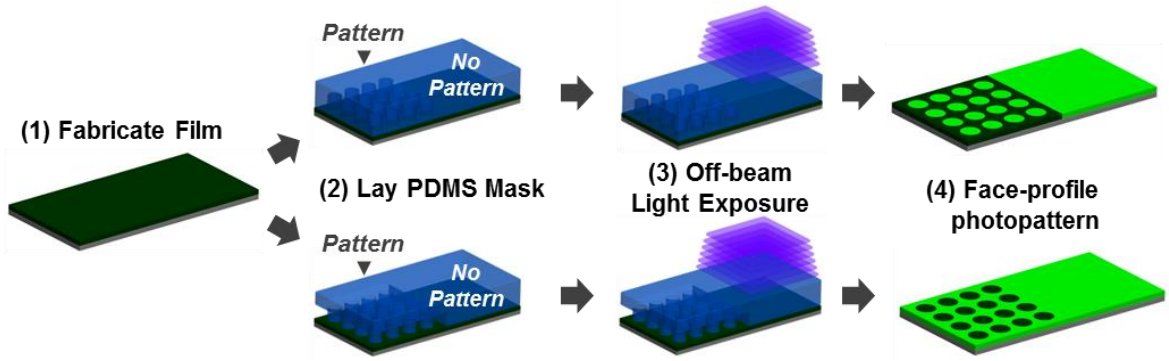

Figure 9.6: Schematic outlining the "off-beam" photopatterning process using a PDMS stamp. (1) A QD-polymer film is deposited and (2) a PDMS stamp is placed on its surface. (3) Light is incident on the PDMS stamp on a region where there is no underlying physical pattern (off-beam light incidence). (4) When the PDMS stamp is removed a positive photopattern is present corresponding to the face-profile of the regions of the PDMS patterns (so the pillar and hole patterns will yield different patterns). In this case the photopattern is due to indirect scattered and waveguided light that travels through the PDMS stamp to the patterned (hole and pillar) regions.

There are a number of important differences between the off-beam indirect exposure approach and the on-beam exposure approach. First, off-beam patterning is based on waveguiding and localized scattering (not on destructive interference) and therefore does not require adherence to a strict relationship between the mask dimensions and exposure wavelength (as outlined by **Appendix F Equation F.1**). Second, off-beam exposure yields more traditional "face-profile" photopatterns (i.e. a circular PDMS pillar will yield a photopatterned circle) (**Figure 9.6, step 4**). Finally, the resulting photopattern depends on whether the PDMS pattern is recessed or raised (because waveguiding and localized scattering develop the photopattern)(**Figure 9.6, step 4**).

Off-beam exposure → light beam <u>indirectly</u> incident on patterned mask region

Face-profile pattern → photopattern mimics <u>face</u> of mask pattern

(ex. circular mask structure → solid circle photopattern)

The off-beam patterning approach is demonstrated using a PDMS stamp with either recessed circular holes or raised circular pillars (**Figure 9.7a,b and 9.7c,d, respectively)**. PL imaging of these photopatterns reveals a number of important observations.

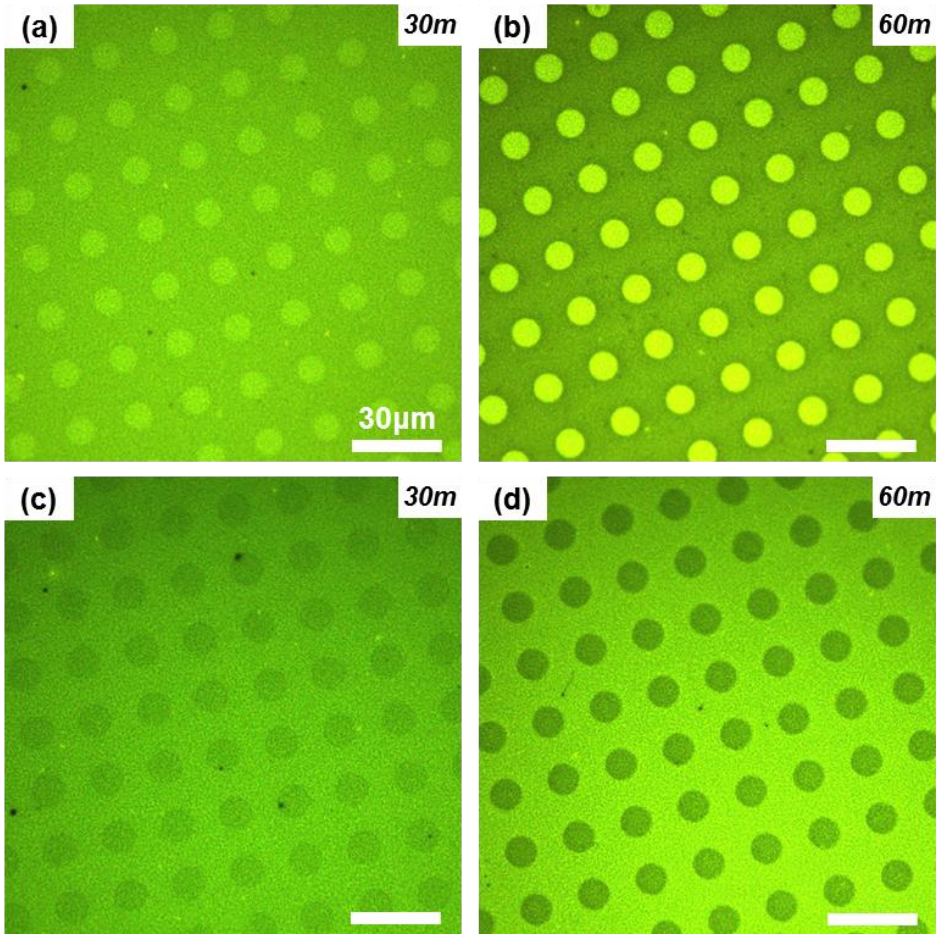

Figure 9.7: PL images of photopatterns developed using the off-beam exposure approach. (a,b) PL image of a photopattern fabricated using a PDMS mask of 10 μm holes. (c,d) PL image of a photopattern fabricated using a PDMS mask of 10 μm pillars. Patterns were developed using UV light (325-375 nm) (15 mW/cm^2). Scale bar is 30 μm for all images.

First, the off-beam approach yields face-profile photopatterns (as opposed to the edge-profile photopatterns shown earlier using the on-beam approach). Second, the contrast of the photopattern increases with longer development time. And finally, the resulting

photopattern depends on whether the PDMS pattern was recessed or raised. A PDMS stamp with recessed circular holes yields high intensity circles while a PDMS stamp with raised circular pillars yields low intensity circles (or a surrounding area of high intensity). The exact mechanisms underlying this trend are not clear because light (from the PDMS photomask) can enter the light-sensitive QD-polymer film via both optical scattering and waveguide bleeding. However, it is clear that the recessed holes cause light to enter the underlying QD-polymer film more efficiently than the raised pillars since PDMS holes lead to bright circular disks (and QDs undergo an increase in PL intensity when exposed to light (**Appendix F Figure F.1a**)). The positive and negative face-profile photopatterns (resulting from PDMS hole and pillar photomasks, respectively) are present over larger lateral areas as well (mm^2) (**Appendix F Figure F.8**) These demonstrations clearly show that very different types of photopatterns can be obtained by simply changing how the exposure light is incident on the patterned PDMS photomask (on-beam versus off-beam).

9.3.3 Large-area photopatterning (PDMS mask)

The parallel nature of the on-beam and off-beam photopatterning strategies suggests that large film areas could be photopatterned quickly. In fact, we show that very large photopatterns (spanning areas of ~0.9 cm x 1.0 cm) can be fabricated using large patterned PDMS photomasks (**Appendix F Figure F.9,10**). Considered in terms of throughput (patterned area/time) on-beam patterning offers ~50000 μm^2/sec and off-beam ~6250 μm^2/sec (or ~125 structures/sec and ~16 structures/sec, respectively). Although we consider these values to be notable, it is difficult to quantitatively compare these values to other studies because throughput is not often quantified in the photopatterning literature. Furthermore, the throughput could be increased by

increasing the intensity of light exposure so these values serve as a general indication of the capabilities offered by these strategies. These photopatterns also have very consistent spatial characteristics over the patterned area (standard deviation ≈ 5%) (**Appendix F Figure F.11**). One current drawback of the large-scale on-beam photopatterning is that edge-profile patterns are difficult to obtain because the light spot is very large and diffuse (**Appendix F Figure F.10**). However, we believe this is a technical challenge not a fundamental limitation of the technique.

9.3.4 High-resolution/high-throughput photopatterning (PDMS mask)

One of the most important advantages of using a patterned PDMS photomask (as opposed to an opaque metal grid) is the potential increase in photopattern resolution. To examine this possibility, a PDMS mask with parallel lines of different width was used to create photopatterns. In this case, both the on-beam and off-beam exposure approach were implemented (**Figure 9.8a and 9.8b, respectively**).

PL imaging and cross-sections of PL images reveal a number of observations. First, on-beam patterning can create edge-profile lines with an average FWHM of 0.63±0.08 μm (periodicity down to 1.86±0.03 μm). Clearly, this sub-micron resolution represents a significant development in the area of photopatterning because sub-micron resolution has previously only been possible using a laser exposure source.[23] Additionally, off-beam patterning yields high-contrast lines of width down to 1.8±0.2 μm. This width is believed to be limited by the width of the physical line on the patterned PDMS stamp and not an intrinsic limitation of the technique. Although the off-beam width of 1.8 μm does not fall within the sub-micron range, it still signifies a significant improvement of pattern

resolution (~5-10x smaller) over other non-laser based photopatterning demonstrations.[13,24,33]

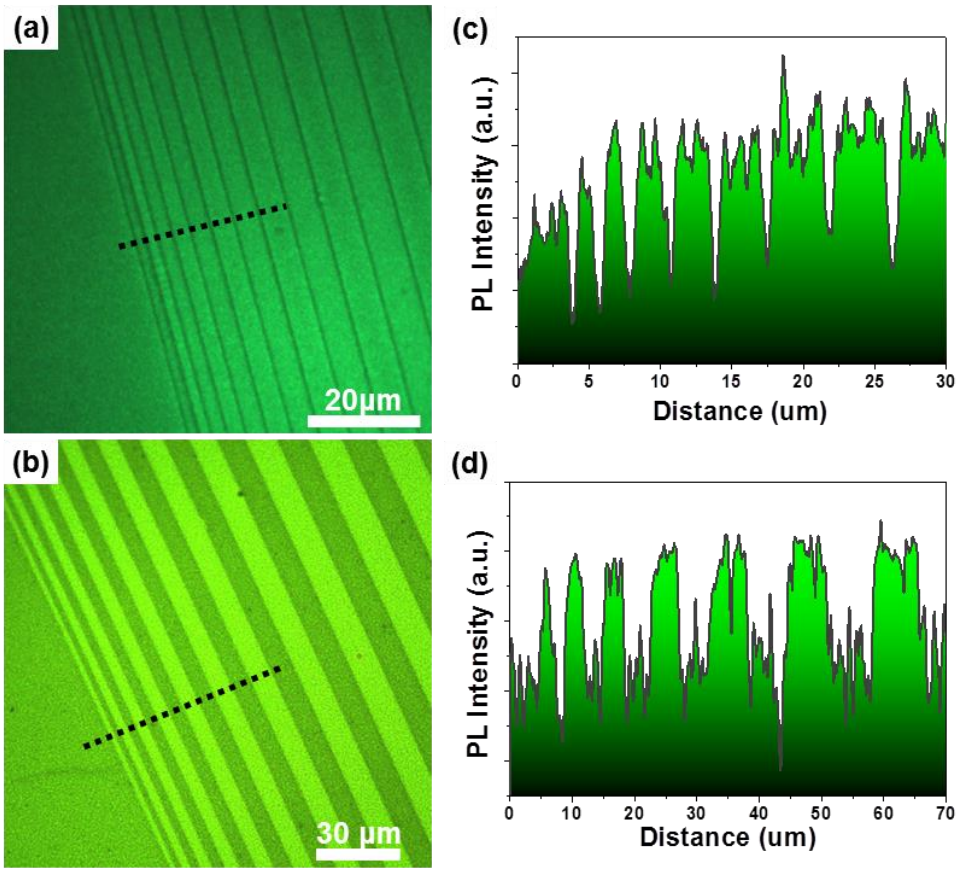

Figure 9.8: PL images of (a) on-beam (of negative edge-profile) and (b) off-beam (positive face-profile) photopatterns of lines of different width. PL cross-sections for the (c) on-beam and (d) off-beam photopatterned lines shown in (a) and (b), respectively. Both the on-beam and off-beam photopatterned lines in (a) and (b) were fabricated using the same PDMS mask.

Second, both on-beam edge-profile lines and off-beam face-profile lines can be patterned with very good resolution without compromising the intensity contrast of the photopattern. Third, these photopatterns correspond closely in size and arrangements to the patterned PDMS photomask used to develop the photopatterns (**Appendix F Figure F.2,12,13**). Finally, the high resolution afforded by both strategies (sub-micron for on-beam and low-micron for off-beam) is also accompanied by high-

throughput due to the parallel nature of the PDMS patterning mechanism. The high-resolution high-throughput nature of these two strategies is particularly significant when considering that previous high-resolution photopatterning was performed using a direct laser writing approach, which has low throughput due its serial patterning nature.[23]

9.3.5 Multi-exposure photopatterning (PDMS mask)

Finally, the simplicity of the photopatterning approach and robust nature of the PDMS photomask make multi-exposure photopatterning possible. In this case, a photopattern can be created using either of the outlined approaches and then additional photopatterns can be fabricated in the same region. A number of examples of multi-exposure on-beam and off-beam photopatterns are shown in **Figure 9.9**. These examples represent only a small fraction of the complex pattern possibilities that can be achieved using this multi-exposure approach (**Appendix F Figure F.14,15**). However, it is clear from the examples that very complex and unique photopatterns can be developed that might be difficult (or impossible) to create using other more traditional patterning approaches. Furthermore, multi-exposure photopatterning allows for ultra-dense patterns that can overcome limitations in resolution encountered when using only a single exposure (**Figure 9.9a-c**). Finally, multi-level intensity contrast photopatterns are possible in the overlap regions of the photopattern (this is particularly evident for multi-exposure off-beam patterning). For example, **Figure 9.9d** clearly shows a four-level contrast system in the cross-hatched region where the photopatterned lines from each exposure step overlap (low, medium, high, very high intensity regions are present (**Figure 9.9d inset)(Appendix F Figure F.15**). This is a particularly important advancement given that nearly all previous demonstrations of photopatterning display simple dual-level intensity contrast (low intensity and high intensity regions).

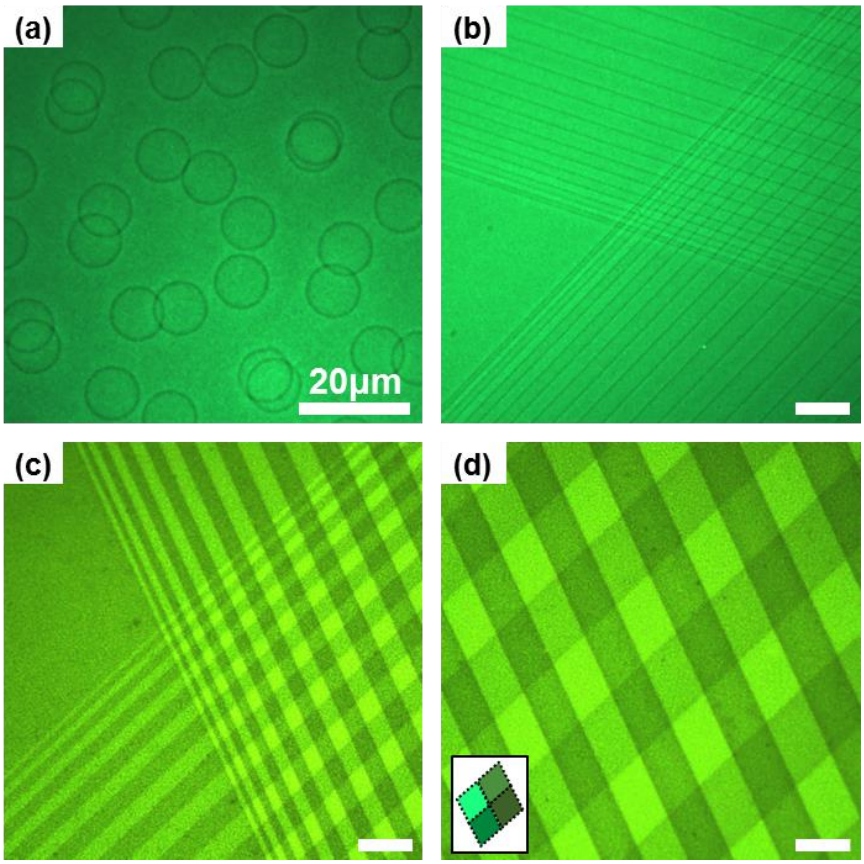

Figure 9.9: PL images of high-density photopatterns created using multi-exposures. Photopattern of multiple exposure “on-beam” holes (a), multiple exposure “on-beam” lines (b), and multi-exposure “off-beam” lines (c,d). (Inset) Simple schematic of the multi-level intensity contrast present in the cross-hatched patterns (low, medium, high, and very high intensity regions). Scale bar is 20 μm for all images.

9.3.6 Photopatterning via laser interference lithography

Nearly all demonstrations of photopatterning have used some type of photomask to spatially modulate the exposure light in order to create a photopattern. However, an additional possibility exists where the spatial modulation of light intensity could be provided by the light exposure setup, thereby removing the necessity of having a mask at all. Laser interference lithography (LIL) is an ideal candidate for maskless photopatterning because it provides high-resolution and the potential for high throughput.

Photopatterning via LIL involves exposing a light-sensitive film (QD-polymer in this case) to an interference pattern to create the photopattern. An example of photopatterned parallel lines is shown in **Figure 9.10** and **Appendix F Figure F.16**. PL imaging shows highly uniform parallel lines with FWHM of ~3 μm and periodicity of ~4.5 μm (**Figure 9.10a**). A fast Fourier transform (FFT) confirms the highly uniform periodicity of the photopattern (**Figure 9.10a inset** and **Appendix F Figure F.16 row 2**). Furthermore, lines of sub-micron FWHM (520±130 nm) and periodicity (800±100 nm) can be created using this technique (**Figure 9.10b**)(**Appendix F Figure F.17**). Although the sinusoidal intensity contrast and sub-micron width make the photopatterned lines more difficult to observe, a FFT of the PL image clearly confirms their presence (**Figure 9.10b, inset**). **Figure 9.10c** shows a cross-section of the PL intensity for the lines of ~3 μm FWHM, which follows a near-sinusoidal spatial modulation. A sinusoidal modulation is in accordance with expectations for an interference pattern from two lasers.[28] As with the photopatterns created using the near-field PDMS photomasks, AFM scanning shows no physical patterning of the QD-polymer film that could account for this PL photopattern, confirming the non-physical nature of the photopattern (**Appendix F Figure F.18**).

The LIL patterning approach is also compatible with a multiple-exposure strategy, which can yield a more complex photopattern than that available via a single exposure. **Figure 9.10d** shows a PL image of an ultra-dense cross-hatched photopattern created by patterning two sets of lines orthogonal to each other. A FFT of the PL image confirms the cross-hatched periodicity of the photopattern (**Figure 9.10d inset**).

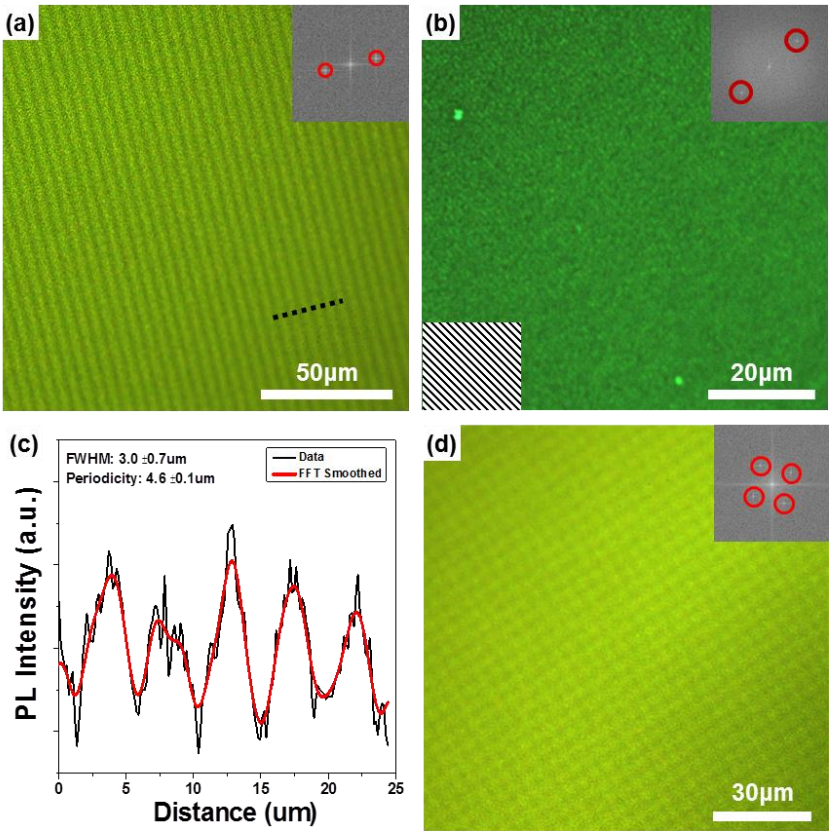

Figure 9.10: Highly uniform photoluminescence photopatterns created using interference lithography. PL images of photopatterned parallel lines of FWHM (a) ~3.0 µm and (b) ~0.5 µm (Bottom left inset is a schematic of the line direction). (c) PL cross-section of the photopatterned lines (~3 µm FWHM). (d) Photopattern of cross-hatched lines created by multi-step patterning. Insets (top right) are fast Fourier transforms (FFT) of the PL images.

Maskless photopatterning using laser interference lithography is also able to create photopatterns over large areas (1.3 cm x 1.3 cm) in a short time with exceptional spatial uniformity (FWHM and periodicity)(**Figure 9.11a**)(**Appendix F Figure F.19**). In fact, examination of the four corners and center of a 1.3 cm x 1.3 cm photopattern shows an average periodicity of 5.5±0.5 µm, with the lines in the corners and central region having periodicity falling well within the 5.5±0.5 µm range (**Figure 9.11b,c**). It is worth noting that the variation (standard deviation) in periodicity of the entire substrate (and the corners and central region) is approximately 10% or less, which is exceptional given the lateral areas being considered.

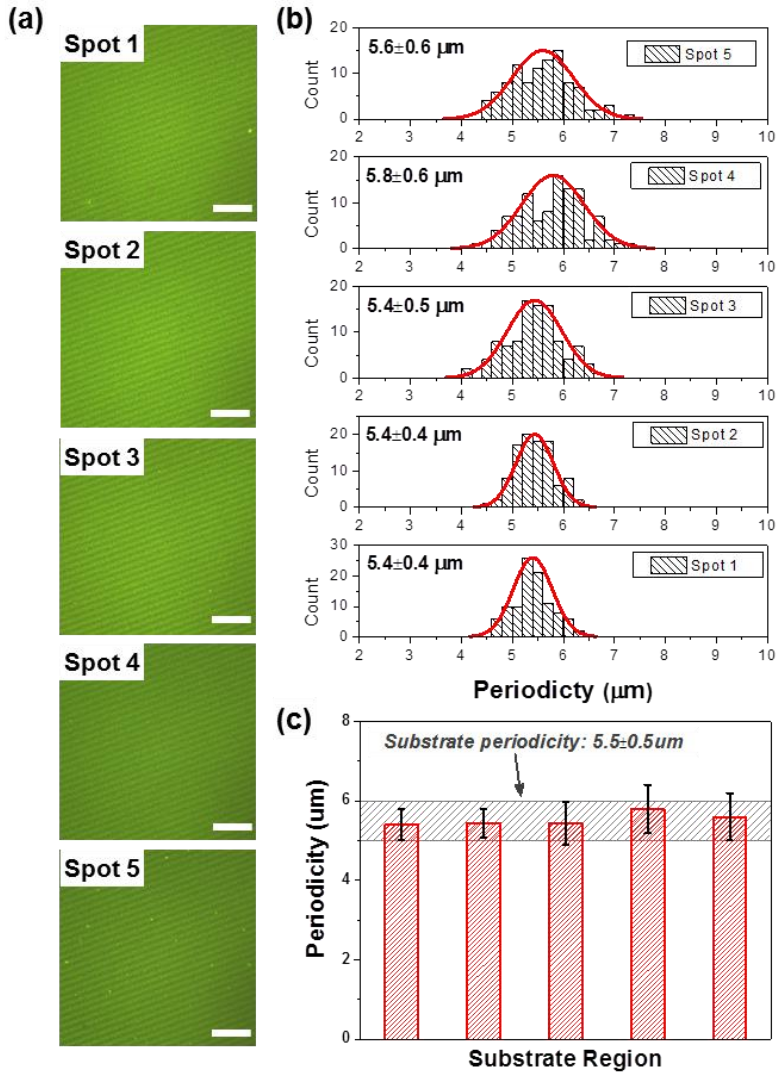

Figure 9.11: (a) PL images of the LIL photopatterned lines from the corners and center of the substrate. (b) Histograms and (c) average periodicity of the line periodicity from the five regions of a substrate with a size of ≈1.3 cm x 1.3 cm. The photopattern was developed using laser interference lithography with an exposure of 532 nm light for 15 min. The film is an unstable yellow CdSe/ZnS QD-polymer film. Scale bar is 30 µm for all PL images.

In addition to uniformity, this signifies a notable achievement in terms of throughput (~0.19 mm^2/sec or ~34,000 µm/sec) given that this pattern was developed in 15 minutes. More specifically, it indicates a factor increase of $8x10^3$ – $1x10^6$ compared to previous photopatterning demonstrations using TEM grids.[16,23]

9.3.7 Comparison of approaches

A number of photopatterning approaches were outlined that yield either edge-profile or face-profile photopatterns with high-resolution over large-areas. A summary of the photopatterning approaches is shown in **Table 9.1**.

Table 9.1: Overview of the three outlined interference-based photopatterning approaches, and their corresponding advantages and disadvantages. Note, the resolution values correspond to the full-width half-maximum of photopatterned lines.

Approach	Mask	Photopattern	Advantages	Disadvantages
On-beam *(near-field)*	Patterned PDMS *(recessed or raised structures)*	Edge-profile	High resolution (550nm), high intensity contrast, very uniform, fast development	Requires π-shift *(constraints on photomask and λ_{exp})*
Off-beam *(near-field)*	Patterned PDMS *(recessed or raised structures)*	Face-profile	Moderate resolution (1.8um), high intensity contrast, large-area, very uniform	Requires longer development time
Laser Interference Lithography *(Far-field)*	None *(2-beam interference)*	Sinusoidal periodicity	High resolution (520nm), large-area, very uniform, fast development	Requires multiple beams for complex patterns, limited intensity contrast for 2-beam interference

9.4 Conclusions

We demonstrate new photopatterning approaches based on near-field and far-field interference phenomena that yield very high resolution quantum dot photopatterns over exceptionally large areas at exceptionally high throughput. These strategies replace the traditional opaque photomask with either near-field or far-field interference phenomena to create the photopattern. The shift from an opaque photomask to interference-based exposure strategies represents a significant paradigm shift in the field of photopatterning. Notably, photopatterns fabricated using these interference-based techniques can reach minimum feature sizes of ~550-1800 nm, which matches the current high resolution offered by direct-write scanning-laser exposure (~575 nm). In

addition, these techniques drastically increase the patternable area (cm^2) and throughput (increases of up to six orders of magnitude) while maintaining pattern uniformity. These advances address the major constraints associated with resolution and throughput that have traditionally plagued photopatterning.

Furthermore, for the first time a single type of photomask is able to pattern both (novel) edge-profile and (common) face-profile photopatterns by simple changes to the light exposure conditions. Finally, all three interference-based approaches can be applied multiple times on the same film area to fabricate ultra-dense multi-level contrast photopatterns that are difficult (if not impossible) to obtain using traditional single-exposure strategies. These results highlight an important advance in the area of photopatterning by connecting nano/microscale features to the macroscale sizes relevant to many technologies. The simultaneous increase of resolution and throughput offered by these strategies, coupled with their simple and reliable nature, will be critically important for systems that require highly-uniform large-area high-resolution photopatterns (e.g. anti-counterfeiting labels and display technologies).

9.5 Chapter acknowledgements

Professor Dong Qin (Georgia Institute of Technology): assisting in the fabrication of the patterned PDMS photomasks and providing the master Cr-on-quartz master pattern.

9.6 References (Chapter 9)

1 Dang, C.; Lee, J.; Breen, C.; Steckel, J.S.; Coe-Sullivan, S.; Nurmikko, A., Red, green and blue lasing enabled by single-exciton gain in colloidal quantum dot films. *Nat. Nanotechnology* **2012,** *7,* 335-339.

2 Gong, X.; Yang, Z.; Walters, G.; Comin, R.; Ning, Z.; Beauregard, E.; Adinolfi, V.; Voznyy, O.; Sargent, E.H., Highly efficient quantum dot near-infrared light-emitting diodes. *Nat. Photonics* **2016,** *10,* 253-257.

3 Mashford, B.S.; Stevenson, M.; Popovic, Z.; Hamilton, C.; Zhou, Z.Q.; Breen, C.; Steckel, J.; Bulovic, V.; Bawendi, M.; Coe-Sullivan, S.; Kazlas, P.T., High-efficiency quantum-dot light-emitting devices with enhanced charge injection. *Nat. Photonics* **2013,** *7,* 407-412.

4 Chuang, C.-H. M.; Brown, P.R.; Bulovic, V.; Bawendi, M.G., Improved performance and stability in quantum dot solar cells through band alignment engineering. *Nat. Materials* **2014,** *13,* 796-801.

5 Todescato, F.; Fortunati, I.; Gardin, S.; Garbin, E.; Collini, E.; Bozio, R.; Jasieniak, J.J.; Della Giustina, G.; Brusatin, G.; Toffanin, S.; Signorini, R., Soft-lithographed up-converted distributed feedback visible lasers based on CdSe-CdZnS-ZnS quantum dots. *Adv. Func. Mater.* **2012,** *22,* 337-344.

6 Hodaei, H.; Miri, M.-A.; Heinrich, M.; Christodoulides, D.N.; Khajavikhan, M., Parity-time-symmetric microring lasers. *Science* **2014,** *346,* 975-978.

7 Bozhevolnyi, S.I.; Volkov, V.S.; Devaux, E.; Laluet, J.Y.; Ebbesen, T.W., Channel plasmon subwavelength waveguide components including interferometers and ring resonators. *Nature* **2006,** *440,* 508-511.

8 Biswas, A.; Bayer, I.S.; Biris, A.S.; Wang, T.; Dervishi, E.; Faupel, F., Advances in top-down and bottom-up surface nanofabrication: Techniques, applications & future prospects. *Adv. Colloid and Interface Sci.* **2012,** *170,* 2-27.

9 Gates, B.D.; Xu, Q.B.; Stewart, M.; Ryan, D.; Willson, C.G.; Whitesides, G.M., New approaches to nanofabrication: Molding, printing, and other techniques. *Chem. Rev.* **2005,** *105,* 1171-1196.

10 Qin, D.; Xia, Y.N.; Whitesides, G.M., Soft lithography for micro- and nanoscale patterning. *Nat. Protocols* **2010,** *5,* 491-502.

11 Young, S.L.; Gupta, M.; Hanske, C.; Fery, A.; Scheibel, T.; Tsukruk, V.V., Utilizing conformational changes for patterning thin films of recombinant spider silk proteins. *Biomacromolecules* **2012,** *13,* 3189-3199.

12 Whitesides, G.M.; Ostuni, E.; Takayama, S.; Jiang, X.Y.; Ingber, D.E., Soft lithography in biology and biochemistry. *Ann. Rev. Biomedical Eng.* **2001,** *3,* 335-373.

13 Wang, Y.; Tang, Z.Y.; Correa-Duarte, M.A.; Liz-Marzan, L.M.; Kotov, N.A., Multicolor luminescence patterning by photoactivation of semiconductor nanoparticle films. *J. Amer. Chem. Soc.* **2003,** *125,* 2830-2831.

14 Malak, S.T.; Smith, M.J.; Yoon, Y.J.; Lin, C.H.; Jung, J.; Lin, Z.; Tsukruk, V.V., Programmed emission transformations: Negative-to-positive patterning using the decay-to-recovery behavior of quantum dots. *Adv. Opt. Mater.* **2016,** *in print.*

15 Malak, S.T.; Jung, J.; Yoon, Y.J.; Smith, M.J.; Lin, C.H.; Lin, Z.; Tsukruk, V.V., Large-area multicolor emissive patterns of quantum dot–polymer films via targeted recovery of emission signature. *Adv. Opt. Mater.* **2016,** *4,* 608-619.

16 Chen, J.; Chan, Y.-H.; Yang, T.; Wark, S.E.; Son, D.H.; Batteas, J.D., Spatially selective optical tuning of quantum dot thin film luminescence. *J. Amer. Chem. Soc.* **2009,** *131,* 18204-18205.

17 Gaponik, N.; Hickey, S.G.; Dorfs, D.; Rogach, A.L.; Eychmüller, A., Progress in the light emission of colloidal semiconductor nanocrystals. *Small* **2010,** *6,* 1364-1378.

18 Kapitonov, A.M.; Stupak, A.P.; Gaponenko, S.V.; Petrov, E.P.; Rogach, A.L.; Eychmuller, A., Luminescence properties of thiol-stabilized CdTe nanocrystals. *J. Phys. Chem. B* **1999,** *103,* 10109-10113.

19 Carey, G.H.; Abdelhady, A.L.; Ning, Z.J.; Thon, S.M.; Bakr, O.M.; Sargent, E.H., Colloidal quantum dot solar cells. *Chem. Rev.* **2015,** *115,* 12732-12763.

20 Lin, K.F.; Cheng, H.M.; Hsu, H.C.; Lin, L.J.; Hsieh, W.F., Band gap variation of size-controlled ZnO quantum dots synthesized by sol-gel method. *Chem. Phys. Lett.* **2005,** *409,* 208-211.

21 Lin, C.H.; Lafalce, E.; Jung, J.; Smith, M.J.; Malak, S.T.; Aryal, S.; Yoon, Y.J.; Zhai, Y.; Lin, Z.; Vardeny, Z.V.; Tsukruk, V.V., Core/alloyed-shell quantum dot robust solid films with high optical gains. *ACS Photonics* **2016,** *3,* 647-658.

22 Jung, J.; Lin, C.H.; Yoon, Y.J.; Malak, S.T.; Zhai, Y.; Thomas, E.L.; Vardeny, V.; Tsukruk, V.V.; Lin, Z., Crafting core/graded shell–shell quantum dots with suppressed re-absorption and tunable Stokes shift as high optical gain materials. *Angewandte Chemie Intern. Ed.* **2016,** *55,* 5071-5075.

23 Tagliazucchi, M.; Amin, V.A.; Schneebeli, S.T.; Stoddart, J.F.; Weiss, E.A., High-contrast photopatterning of photoluminescence within quantum dot films through degradation of a charge-transfer quencher. *Adv. Mater.* **2012,** *24,* 3617-3621.

24 Park, Y.; Felipe, M.J.; Advincula, R.C., Facile patterning of hybrid CdSe nanoparticle films by photoinduced surface defects. *ACS Appl. Mater. & Interfaces* **2011,** *3,* 4363-4369.

25 Rogers, J.A.; Paul, K.E.; Jackman, R.J.; Whitesides, G.M., Generating similar to 90 nanometer features using near-field contact-mode photolithography with an elastomeric phase mask. *J. Vac. Sci. & Tech. B* **1998,** *16,* 59-68.

26 Hesjedal, T.; Seidel, W.; Kostial, H., Near-field phase shift photolithography for high-frequency SAW transducers. In *2002 Ieee Ultrasonics Symposium Proceedings, Vol.1-2*, Yuhas, D. E.; Schneider, S. C., Eds. **2002;** pp 247-250.

27 Rogers, J.A.; Paul, K.E.; Jackman, R.J.; Whitesides, G.M., Using an elastomeric phase mask for sub-100 nm photolithography in the optical near field. *Appl. Phys. Lett.* **1997,** *70,* 2658-2660.

28 Maldovan, M.; Thomas, E.L., Periodic materials and interference lithography: for photonics, phononics, and mechanics. *Wiley-VCH* **November 2008.**

29 Pu, Y.-Y.; Liang, G.-Q.; Mao, W.-D.; Dong, J.-W.; Wang, H.-Z., Fabrication of two-dimensional photonic crystals with triangular rods by single-exposure holographic lithography. *Chinese Phys. Let.* **2007,** *24,* 983-985.

30 Jia, L.; Bita, I.; Thomas, E.L., Level set photonic quasicrystals with phase parameters. *Adv. Func. Mater.* **2012,** *22,* 1150-1157.

31 Liang, G.Q.; Zhu, X.L.; Xu, Y.G.; Li, J.; Yang, S., Holographic design and fabrication of diamond symmetry photonic crystals via dual-beam quadruple exposure. *Adv. Mater.* **2010,** *22,* 4524-4529.

32 Mao, W.D.; Zhong, Y.C.; Dong, J.W.; Wang, H.Z., Crystallography of two-dimensional photonic lattices formed by holography of three noncoplanar beams. *J. Opt. Soc. America B Opt. Phys.* **2005,** *22,* 1085-1091.

33 Chen, X.; Rogach, A.L.; Talapin, D.V.; Fuchs, H.; Chi, L., Hierarchical luminescence patterning based on multiscaled self-assembly. *J. Amer. Chem. Soc.* **2006,** *128,* 9592-9593.

CHAPTER 10

MULTICOLOR QD PHOTOPATTERNING APPROACHES

Chapter Based On:
Malak, S.T.; Jung, J.; Yoon, Y.J.; Smith, M.J.; Lin, C.H.; Lin, Z.; Tsukruk, V.V., Large-area multicolor emissive patterns of quantum dot–polymer films via targeted recovery of emission signature. *Adv. Opt. Mater.* **2016,** *4,* 608-619.

Chapter Overview

This final photopatterning investigation concentrates on how the unique spectral absorption profile of different color QDs can be utilized to create multicolor photopatterns. A facile one-step fabrication approach for creating large-area multicolored emissive photopatterns in mixed quantum dot-polymer films is outlined. This is in sharp contrast to the current photopatterning approaches that utilize only a single quantum dot (QD) component for single-color patterns.

Strategies are presented that allow for either selective or collective modification of specific pre-determined photoluminescent peaks of green and red QDs during photopattern development. These strategies allow novel single or multicolor patterns to be developed and allow for unprecedented control over how the color contrast of the photopattern evolves with continuous light illumination (**Figure 10.1**). These results clearly show that the evolution of the emission spectra of a multicolor mixed QD-polymer film can be readily tailored during pattern development, either by careful selection of the excitation wavelength or through combinations of controllably unstable and stable QDs with different recovery rates. Notably, these strategies are simple, fast, and robust, yielding high-resolution microscopic patterns over large areas (mm^2). Furthermore, the flexibility and capability of these strategies greatly expand the potential capabilities of

multicolor emissive photopatterns, particularly in the areas of sensing, imaging, and lasing systems where it is important to exert delicate control over the intensity of selected colors within specific spatial regions.

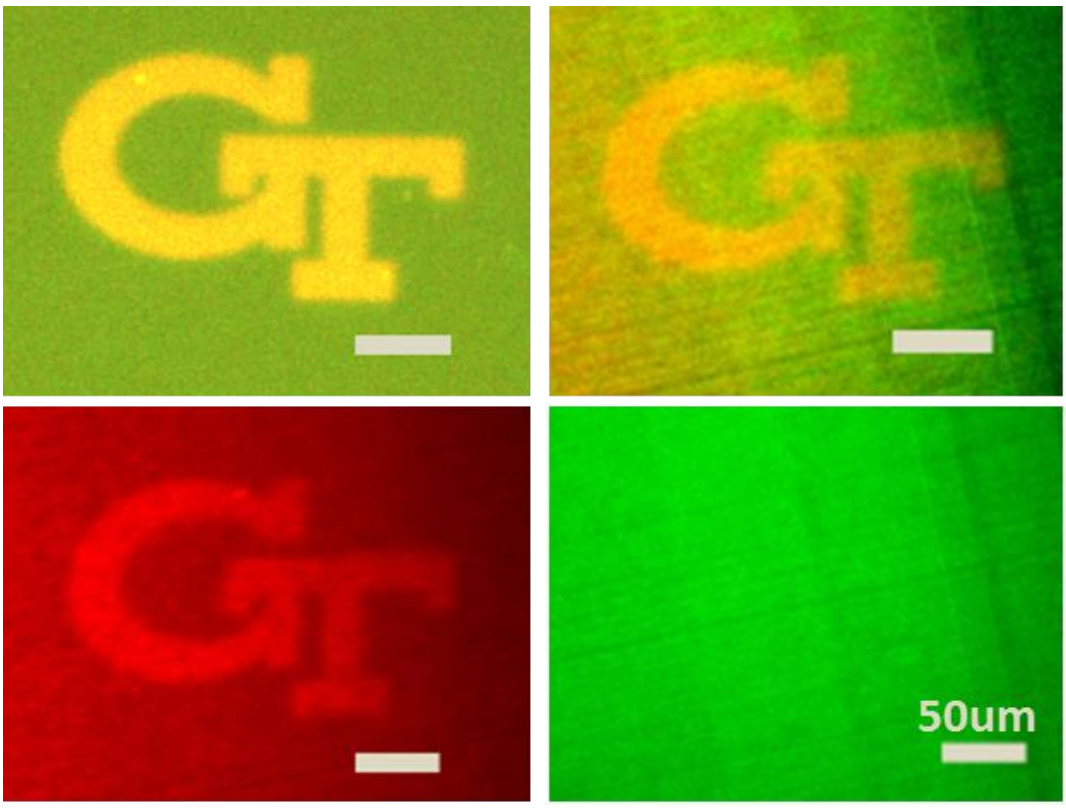

Figure 10.1: (a) Photoluminescence image of a multicolor photopattern composed of red and green quantum dots created using a selective patterning approach. (b) Hyperspectral images tracking (b) both the red and green emission peaks, (c) only the red emission peak, and (d) only the green emission peak. Scale bars are 50 um for all images.

10.1.Introduction

10.1.1. Current physical nanoscale patterning techniques

Patterning optical materials is often utilized to develop photonic systems for lasers,[1,2,3] diffraction gratings,[4] waveguides,[5] and LEDs.[6,7] Typically, nanoscale and microscale patterning are achieved via physical or chemical modification of materials using a variety of techniques[8] including optical and electron beam lithographies,[9] capillary transfer lithography,[10] inkjet printing,[11] self-assembly,[12] transfer printing,[13] and template-based infiltration,[14] with some like inkjet printing have the potential for large-scale patterning of nanostructures.[15,16] However, typically material and manufacturing restrictions often limit or prohibit large-scale physical patterning of nanoparticles and nanostructures. In contrast, techniques such as spectral photopatterning use light to intrinsically modify the emission of photoluminescent components. This produces a photoluminescence (PL) pattern without adding or removing material, substantially reducing the complexity of the patterning procedure.

10.1.2. Single component single color photopatterning

QD nanostructures are good candidates for such emissive photopatterning because they exhibit size-dependent absorption and emission that can be readily tuned over much of the visible spectrum due to the quantum confinement effect.[17,18] This tunability makes it possible to develop photopatterns in the visible range with colors ranging from blue to red. Single-color photopatterning has been demonstrated using single-type quantum dots (QDs), with approaches including degradation of a photoluminescence quenching agent,[19] photoactivation of QDs,[20] photooxidation of QDs,[21] and photoenhancement through the passivation of surface traps or photoionization.[22] Recently, multicolor photopatterning was demonstrated using the blue-shift in emission that accompanies the

photoactivation of QDs, but the color contrast required weeks to develop.[20] These initial demonstrations hint at the potential of photopatterning by showing that high-contrast photoluminescence patterns can be developed.

However, using only a single material component severely limits its spectral signature and practical utilities. Furthermore, restricting the photopattern system to one PL component prohibits the use of variations in QD emission dynamics (exhibited by QDs of different size and stability) to develop photopatterns that evolve in unique ways and display more complex multi-peak emission profiles. These restrictions severely hinder the potential of emissive photopatterning in the areas of sensing, LED lighting,[23] displays,[24] and labeling and imaging,[25] where the presence and control of multi-peak emission are highly advantageous.

10.1.3. Multi-component multi-color photopatterning

The limitations encountered by single PL component photopattern systems can be overcome by using a mixture of emission components, opening up possibilities to create next-generation photopatterns that exhibit complex spectral profiles. To date, limited multicolor photopatterning has been demonstrated using a combination of QD and dye, with photobleaching of the dye providing the contrast.[26] However, pure QD-mixtures are a more versatile alternative than the QD-dye mixture for a number of reasons. First, QDs exhibit size-dependent optical absorption and emission over the optical wavelength region.[17,18] This feature provides flexibility in terms of color output. Second, the size-dependent absorption provides a route for selective or collective modification of specific QDs within the mixture via excitation wavelength since the recovery of emission is proportional to the absorbance at the excitation wavelength. For example, the difference

of absorbance between red and green QDs at a specific wavelength leads to different recovery rates which can be used to tune color contrast. Finally, QDs can be synthesized to exhibit stable emission intensity or synthesized to display an increase, decrease, or shift in emission when exposed to light (dynamic emission behavior is often attributed to photoactivation,[27] photoelectrification,[28] or photoneutralization[29]). The capability to engineer photoluminescence stability or instability into the QD provides a promising route for selective modification of the unstable QD color while the stable QD color remains unchanged.

Herein, we report how the dynamics of QD emission recovery can be exploited to control the development of multi-peak photoluminescence patterns in mixed QD-polymer films. These emissive patterns can span large areas (up to fractions of a cm^2) and develop over relatively short time scales (often less than 1 hour). Specifically, two general and robust strategies for fabricating photoluminescent photopatterns in mixed color QD films are demonstrated. These strategies stem from judicious consideration of factors such as development wavelength and the stability/instability of QD emission, which have been largely overlooked in previous photopatterning studies. The first strategy allows for the modification of multiple emissive bands concurrently (collective recovery), while the second strategy involves the modification of an individual emissive band (selective recovery) during the development process. Since the spectral signature controls the color appearance, these strategies allow for the fabrication of single or multicolor photopatterns depending upon the employed development strategy.

10.2.Experimental details

Film preparation. QD-polymer films of thickness 840 nm (±120 nm) were prepared by spin-casting a QD-polymer mixture at 2000 rpm for 1.5 mins. Films typically films had a QD-loading (volume fraction) of approximately 3% (±1%), which was estimated via fitting of refractive indices derived from ellipsometry data with the Bruggeman model.[30] The QD-polymer mixture was made by mixing a QD toluene solution with a 10-12% PMMA toluene solution, and then vortexing. Equal parts QD solution and polymer solution were used. The concentration of the stock unstable CdSe/ZnS QD solutions was approximately 50 uM, while the concentration of the stock stable CdSe/$Cd_{1-x}Zn_xSe_{1-y}S_y$ QD solution was approximately 1uM. The ratio of red-to-green QDs for the unstable red-green QD-polymer films was generally close 1:3 as estimated from initial solution concentrations. The unstable red-stable green QD-polymer films had a red-green ratio closer to 200:1 since the emission of the stable green QDs is much higher than the unstable red QDs. Films were deposited on silicon with a 292 nm surface layer of SiO_2.

Photomasks. The GT photomask (Photo Sciences Inc.) was made of an opaque chrome pattern on a quartz substrate. The hexagonal circular mesh photomask was a G2000HA circular mesh (G2000HA-Cu) TEM grid from Electron Microscopy Sciences. The TEM grid was designed to have a pitch of 12.5 um, holes with a diameter of 6.5 um, and bars of 6 um.

Photopattern development. Photopatterning development involved two exposure steps, each utilizing a 10x objective (NA: 0.30). For the first step, the film (without the mask) was exposed to 450-490 nm light with a power ranging from 30.5 mW to 39.5 mW, or 325-375 nm light with a power of 2.5 mW to bleach the film to near its

minimum value (approximately 2 min of exposure). For the second exposure step, the film with the mask was exposed to either UV light (325-375 nm), a blue bandpass filter (450-490 nm), or a yellow bandpass filter (568-593nm) depending on the type of photopattern development. The light source was a 120 W Hg vapor short arc lamp (X-cite series, 120Q, Lumen Dynamics).

Photoluminescence imaging and scanning. Photoluminescence spectra from the QD-polymer films were collected from hyperspectral datacubes. Hyperspectral datacubes which were collected using a CytoViva Hyperspectral imaging system using a 10x objective (NA: 0.30). A 0.3-1.0 second exposure time (per line) was used. Hyperspectral scans were performed using either the blue bandpass filter (450-490 nm) excitation setup or UV light (325-375 nm) excitation setup already mentioned. The light source was the 120 W Hg vapor short arc lamp, X-cite series, 120Q, Lumen Dynamics. 120-250 spectra were collected and averaged from the exposed and protected regions of the photopatterns from the hyperspectral maps to provide data on the development of the photopattern under the various development conditions over the period of development. Hyperspectral images were constructed from the data cube by the tracking three wavelength bands (red, green, and blue). The red and green emission bands were centered at the position of the red and green emission peaks, while the blue emission was centered at a default position with 400-460 nm. Hyperspectral images were smoothed with a Savitzky-Golay filter to reduce noise. Noise from the blue region was also reduced during filtering.

10.3.Results and discussion

10.3.1. Multicolor photopatterning: general strategy

Figure 10.2 depicts the general procedure for photopatterning the QD-polymer films. In this strategy, both decay and recovery of photoluminescence are utilized to fabricate the photopatterns. In the first step the QD-polymer film is deposited onto a wafer (step 1). The film is then exposed to light for approximately two minutes to reduce the QD emission to approximately its minimum value (step 2). A photomask that is opaque to the development light is then placed on the film to protect specific areas of the film from direct exposure to the development light (step 3). The sample is then exposed to light that causes the emission in the unprotected areas of the film to recover (step 4) (**Figure 10.2**). The color appearance of the photopattern depends on the stability type of QDs and the wavelength of development light (discussed in detail in later section).

This work focuses on how the photopattern process can be altered to control how the spectral properties of the photopattern evolves during the development process (**Figure 10.2, step 4**). Specifically, we examine how to selectively recover a single color or collectively recover multiple colors in the photopattern. Since the ratio of emission bands controls the overall color, selective recovery and collective recovery can cause the color of the photopattern to evolve differently during the development process (**Figure 10.2, step 5**). For example, for a mixture of red and green QDs, collective recovery will increase the intensity but not change the color of the photopattern since the relative intensity between green and red emission remains nearly equal during the development. On the other hand, selective recovery of red QDs in a mixed red-green QD film produces a photopattern that becomes redder when developed.

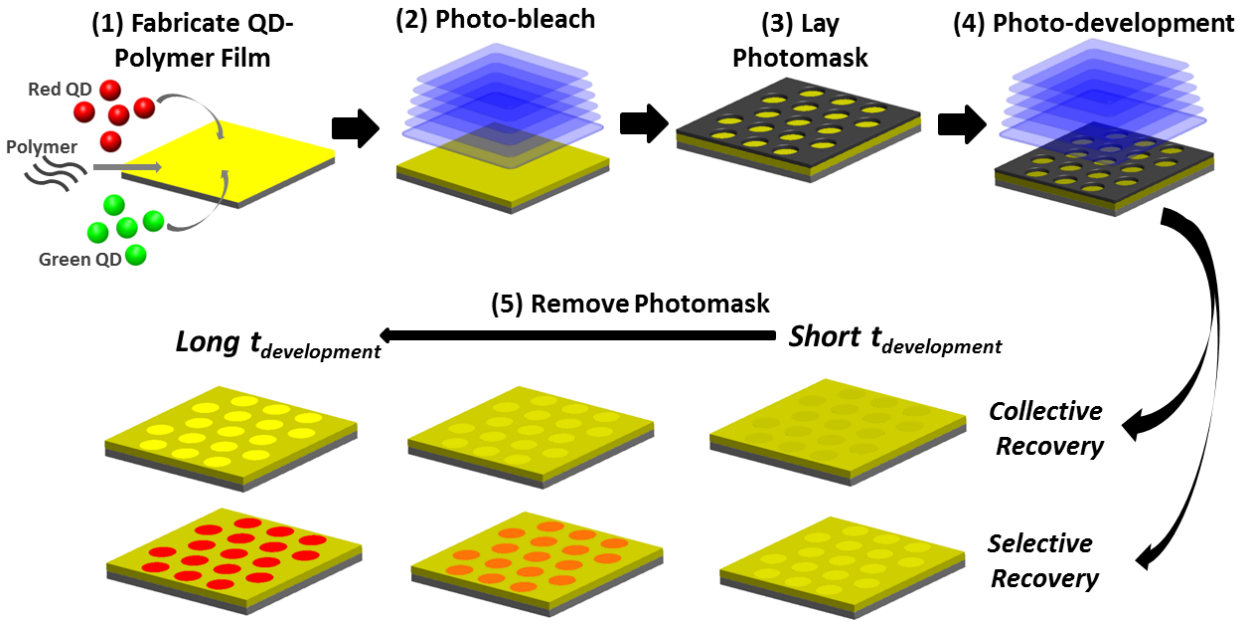

Figure 10.2: Schematic outlining the utilization of both decay and recovery of emission to create photopatterns. (1) A mixture of polymer, red QD, and green QD are deposited onto a wafer. (2) The film is exposed to light to reduce the QD emission to approximately its minimum value. (3) A photomask that is opaque to the exposure light is then placed on the film to protect specific areas of the film from direct exposure to the development light. (4) The sample is then exposed to light causing the emission of the exposed areas of the film to recover. (5) The photomask is removed, yielding a non-physical photoluminescence photopattern. The color of the photopattern depends on the color of QDs and the approach (selective or collective recovery) used to develop the pattern.

10.3.2. Film characteristics: physical and optical

Two general types of core-shell Cd-based QDs were used to fabricate photopatterns: one type that maintains the emission intensity when exposed to light (stable QDs) and another type that exhibits a change in the emission intensity (reduction or increase) when exposed to light (unstable QDs). Stable emission was imparted to the stable QDs using a synthesis approach that yields an alloyed core-shell interface (i.e. $CdSe/Cd_{1-x}Zn_xSe_{1-y}S_y$ QD composition, see Experimental Section), which has been shown to render improved photostability.[31] The improvement in photostability is attributed to a reduction in crystallographic lattice mismatch at the interface which reduces the lattice

strain and in turn the number of defect sites.[32] Furthermore, a smeared potential over the entire QD can suppress the Auger recombination processes, a common obstacle for stable, high quantum yield QDs.[33,34] Unstable emission was engineered into the unstable QDs using a synthesis approach that imparts a sharp core-shell interface (i.e. CdSe/ZnS QD composition, see Experimental Section), which can yield a metastable energetic interface state that is susceptible to external factors such as temperature and light exposure.[32]

The QD-polymer films studied here are composed of a mixture of red QDs (614 nm emission) and green QDs (512 nm or 541 nm emission) (**Figure 10.3a & inset**). The difference in emission positions are due to the degree of quantum confinement of the exciton, which is controlled by the size and composition of the QDs.[17]

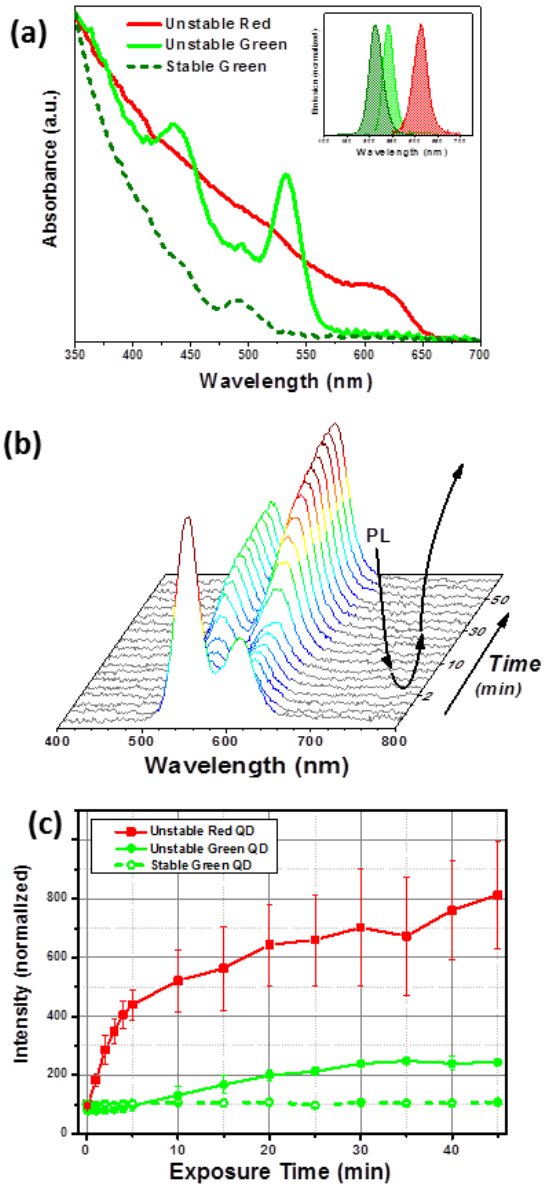

Figure 10.3: Photopatterning is performed on QD-polymer films with a mixture of green and red QDs which have different absorbance profiles (a) and emission positions (inset). A waterfall plot of the PL (b) shows the changes in intensity of unstable red and green QD PL that occurs over a period of 45 mins of light exposure. (c) Gaussian fitting of the PL peaks provides information on as to how emission intensity evolves during light exposure (normalized to intensity at 0 min).

Films with minimized agglomeration of the QDs in PMMA matrix were fabricated by utilizing hexadecylamine or butylamine as the primary ligand (small amounts of oleic acid still present), which interact favorably with PMMA and share a common solvent (i.e. toluene) with PMMA. Films typically had a thickness near 800 nm with a QD-loading (volume fraction) of approximately 3%. The ratio of red-to-green QDs for the unstable red-green QD-polymer films was approximately 1:3. The QD-polymer films with the mixture of unstable red and stable green QDs had a red-to-green ratio closer to (200:1) since the emission of the stable green QDs is much higher than the unstable red QDs. The films typically were smooth and uniform with minor surface depletions below 10 nm and occasional deeper (>100 nm) holes caused by solvent evaporation during drying (**Appendix G Figure G.1**). The overall R_q surface microroughness was near 6±2 nm over a 50 um^2 area, which confirms a smooth and uniform surface morphology.[35] The films also exhibited uniform bright photoluminescence indicating the uniform distribution of QDs throughout the entire film (**Appendix G Figure G.2**).

10.3.3. Emission dynamics: decay-to-recovery process

The QDs exhibit an emission that can fluctuate in response to light exposure, where the rate and magnitude of emission fluctuation depends on the wavelength of exposure light and whether the QD was synthesized to be stable or unstable under the excitation light. By carefully considering these parameters, it is possible to fabricate photopatterns with multiple emission peaks and to control the relative intensities of emission bands during the photopattern development process. Controlling the emission peaks can occur either through selective recovery of a specific band within the pattern (red emission increases, green emission does not) or through collective recovery of multiple bands within the pattern (red and green emission both increase). In order to effectively control the

intensity of each emission band during photopattern development, it is necessary to understand how the emission changes in response to the wavelength of development light.

Examination of the emission spectra of the unstable red and unstable green QDs upon light exposure shows that the PL intensity exhibits large changes in intensity over a period of 45 mins (**Figure 10.3b)**. Fitting of the photoluminescence peaks for the three types of QDs used in this study (stable green alloyed CdSe/$Cd_{1-x}Zn_xSe_{1-y}S_y$, and unstable green and red CdSe/ZnS) shows that the dynamic behavior of emission involves two steps, where the first step is a quick decay within the first seconds/minutes and the second step is a slower recovery of emission over a period of 45 mins or more (**Figure 10.3c & Appendix G Figure G.3**). This behavior has been observed in QD systems exposed to low-humidity oxygen environments.[36] The initial fast decay could be caused by the photooxidation of the diethylzinc precursor which is sensitive to oxygen. The recovery of emission for the unstable QDs is likely due to further photooxidation of the QD surface since the emission exhibits a blue-shift during the recovery period (11 nm for unstable green CdSe/ZnS QD and 3 nm for unstable red CdSe/ZnS QD) (**Appendix G Figure G.4**).[27,37] The stable green QDs display a small red-shift of emission (1-2 nm), which could result from the annealing of the core-shell interface which reduces the quantum confinement by smearing the exciton wavefunction.[31,33,38]

The rate of decay and recovery and the plateau recovery value depends on the type of QD (stable alloyed interface QD or unstable sharp interface QD). For example, when unstable green QDs are exposed to 470 nm 28 mW light they exhibit a rapid decay of approximately 25% followed by a recovery plateau value of approximately 250%,

whereas the unstable red QDs show values of 10% and 800%, respectively. The stable green QDs show modest fluctuations of intensity (10 %) over the 45 mins of exposure.

The difference in decay rates and recovery plateaus between red and green QDs is attributed to the differences in the number of defects in the QD, the amount of absorbance at the pumping wavelength, and the optical absorbance cross-sections. The unstable red QDs exhibit a larger recovery of PL than their green counterpart likely because they have higher absorbance than green QDs at any particular wavelength, which is due to their higher optical absorbance cross-section arising from their larger physical size.[39] These effects cause the red QDs to absorb more photons than the green QDs, leading to an increased probability for PL recovery to occur.

10.3.4. Multicolor photopatterning characterization

The multicolor photopatterning process is exemplified by fabricating a GT photopattern on an unstable red-stable green QD-polymer film (**Figure 10.4**). The light used to develop the pattern ("development" light) was selected to fall within the absorbance range of both the red and green QDs (470 nm, 30.5 mW). Photoluminescence imaging shows a yellow emission pattern (exposed region) surrounded by a green region (protected region) (**Figure 10.4a**). The yellow color results from the recovery of red QD emission mixing with the stable green QD emission. The pattern corresponds closely in shape and size to the original photomask.

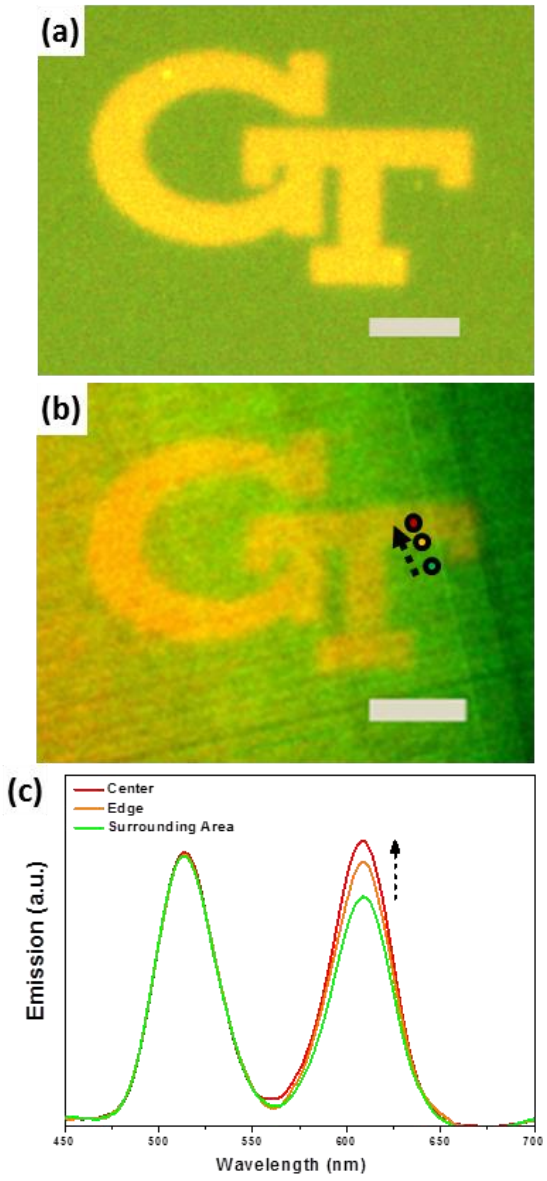

Figure 10.4: The development of a photopattern in QD-polymer film (20 min, 470 nm and 30.5 mW) is monitored via PL imaging and hyperspectral mapping. (a) PL imaging and (b) hyperspectral scanning clearly show the presence of a photopattern made on a stable green-unstable red QD-polymer film, which corresponds closely in shape and size to the photomask. Areas of the film exposed to development light exhibit higher emission than areas of the pattern not exposed to development light. (c) PL spectra were collected from three regions (green, yellow, and green circles from (b) to quantitatively evaluate the emission from different areas of the pattern. The results confirm the recovery of only red emission. All scale bars are 50 um.

Quantitative spectral evaluation of emission from different regions of the photopattern is provided by hyperspectral imaging, which tracks the intensity of specific red, green, and blue wavelengths over the sample, as noted by the circles in **Figure 10.4b**.[40,41] The hyperspectral map shows a pattern with similar shape, size, and pattern to that observed via photoluminescence imaging. PL spectra collected from points inside and outside the photopatterned area confirms the increase in red emission due to the light exposure (**Figure 10.4c**).

Bright field imaging, dark field imaging, and AFM scanning of photopatterned films show no indication of changes in film surface characteristics that could account for the observed PL patterns, which shows that these patterns are induced by intrinsic modification of the emission pathways in the QDs without changes in the physical morphology of the film (**Appendix G Figure G.5,6,7)**.

10.3.5. Collective recovery (C)

Approach & requirements

The first and most simple photopatterning method for QD-polymer films with a mixture of QDs is collective recovery. This strategy uses a mixture of unstable red and unstable green QDs (both QDs exhibit recovery of their emission) and a development wavelength that falls within the absorbance of each QD ($\lambda_{devel} < \lambda_{1s,QD1,QD2}$) where λ_{1s} represents the lowest energy transition. This strategy is useful when trying to develop a photopattern where the exposed region of the photopattern has a higher intensity but similar spectral signature (color) to the protected region of the film. In other words, the exposed and protected regions maintain the same relative intensity between emission peaks (i.e. green versus red) but both increase for the duration of pattern development.

Outcome

Collective recovery was demonstrated by developing the photopattern with 350 nm light at 2.5 mW, which significantly exceeds the bandgap energy of both the green and red QDs, and provides near-equal recovery of the red and green emission intensity during early development **(Figure 10.5a)**.

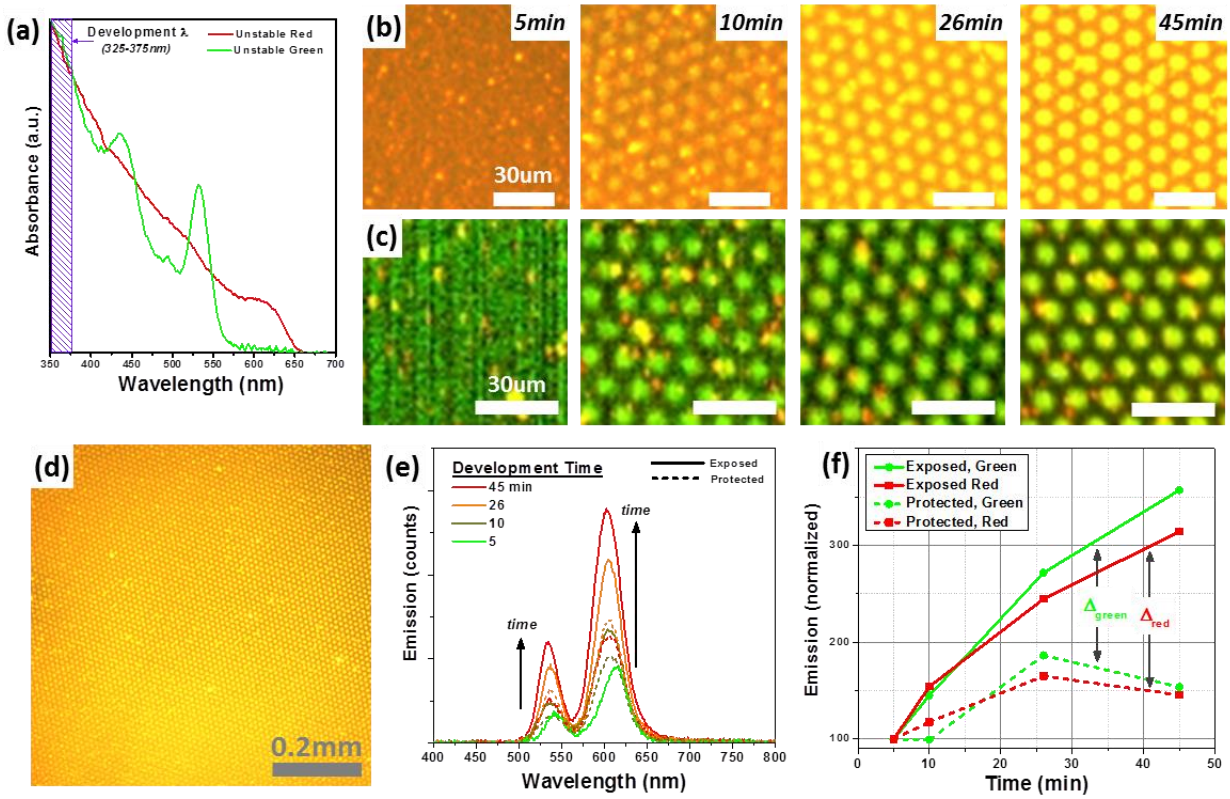

Figure 10.5: Collective recovery via near-equal recovery rates method (C): Unstable red and unstable green QDs are used to develop a photopattern where both emission peaks recover at a similar rate (i.e. green versus red) for the duration of pattern development. (a) Near-equal recovery was achieved by developing the pattern with high energy light of 360 nm and 2.5 mW ($\lambda_{development} << \lambda_{1s,green}$ & $\lambda_{1s,red}$) (absorbance normalized at 350 nm for clarity). (b) PL imaging and (c) hyperspectral scanning show that longer exposure times lead to more recovery, yielding photopatterns with greater intensity contrast (all scale bars are 30 µm). PL imaging of the pattern (d) demonstrating the large-area uniformity of the pattern. PL spectra from the (e) exposed and protected regions of the film show that the exposed regions have higher intensity than the protected regions. (f) Peak fitting (normalized) shows a near equal increase in emission for the red and green emission peaks.

The similar recovery rate for the red and green QDs is likely due to the generation of hot excitons (a result of the high energy development light). Hot excitons have a higher probability of entering a surface trap state than a lower energy exciton,[42] and therefore potentially initiate the recovery mechanism. Additional factors that determine the relative rate of recovery between the red and green QDs include the amount of light absorbed by each QD, which depends on the absorbance profile of each QD and the relative concentration of each QDs in the film. The photopattern closely corresponds in shape and size to the photomask after development and covers an area of 100 microns (**Appendix G Figures G.8-G.9**). In addition, this photopattern is 5-10 times smaller than those from previous studies that use a non-laser exposure source.[27]

As the photopattern develops, both the unstable red and unstable green QDs experience a recovery of emission in the regions exposed to light. Photoluminescence imaging and hyperspectral scanning show that longer exposure times lead to more recovery, yielding photopatterns with greater intensity contrast (**Figures 10.5b-c)**. PL imaging over a large area suggests uniformity of the photopattern over areas approaching mm^2 (**Figure 10.5d**). Spectra from the exposed and protected regions of the photopattern are selected from the hyperspectral scan during the course of development, revealing that the exposed regions exhibit more intense emission than the protected regions, and that the emission increases with longer development times (**Figure 10.5e**). Gaussian peak fitting (and normalization) of the red and green emission peaks from the exposed and protected regions of the pattern confirms these observations and shows that the photoluminescence recovery is similar for both colors (**Figure 10.5f**). It is worth mentioning that the protected regions also exhibit PL recovery, which is due to proximity effects during the pattern development (i.e. the development light enters the protected

regions). The proximity effect reduces pattern contrast and is an ongoing challenge in photopatterning.

Collective or selective recovery can be verified by tracking the intensity of red emission and green emission separately using a hyperspectral scan. For example, hyperspectral scanning of both the red and green peaks shows a clear photopattern which appears yellow due to the combination of red and green intensity **(Figure 10.6a)**. However, a pattern is also present when tracking either the red PL peak only or the green PL peak only **(Figures 10.6b-c)**. The presence of a pattern for both the red and green emission peaks indicates that the photopattern is a result of collective recovery (i.e. recovery of both colors).

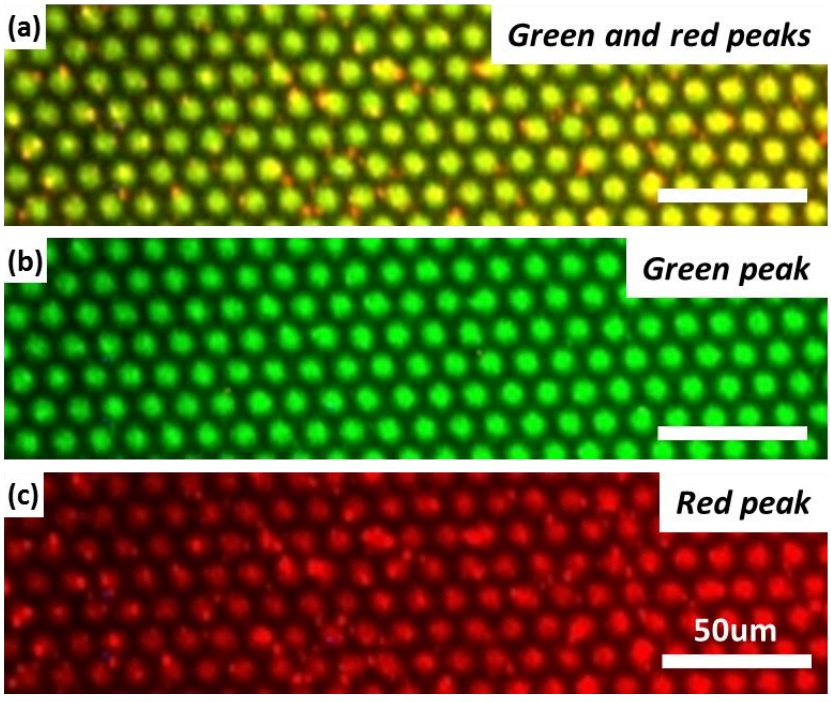

Figure 10.6: A multicolor photopattern fabricated using collective recovery. The unstable red and unstable green QDs are used to develop a photopattern where both emission peaks recover for the duration of pattern development. Collective recovery is confirmed using hyperspectral scans by tracking the intensity of (a) both the red and green PL peaks, (b) only the red PL peak, and (c) only the green PL peak intensity. All scans show a clear photopattern of the QD-polymer film, indicating that the overall photopattern is due to collective recovery of both the red and green QDs. All scale bars are 50 µm.

Differences in color between the exposed regions and protected regions of the photopattern can be evaluated by examining the color contrast (CC), where color contrast at a specific time (t) is defined as follows (**Eq.10.1**):

Equation 10.1: Definition of color contrast for multicolored QD photopatterns.

$$\mathbf{Eq.10.1}\text{: } \mathrm{CC(t)} = |\Delta_{\mathrm{green}} - \Delta_{\mathrm{red}}|$$

$$(\Delta_{color} = I_{norm}^{exposed} - I_{norm}^{protected}$$

Small color contrast values indicate that the red and green QDs in the exposed region of the film underwent a similar amount of recovery, which means that the exposed region will have a similar color to the protected region of the film (since the ratio between red and green intensity does not change). In contrast, large CC values imply that the red and green QDs experienced a different amount of recovery in the exposed region of the film, suggesting that the exposed region will have a different color than the protected region of the film due to the change in the ratio between red and green intensity. These statements are summarized below, assuming equal red and green intensity initially:

$$\text{Small CC} \rightarrow \mathrm{Color}_{\mathrm{exposed}} \sim \mathrm{Color}_{\mathrm{protected}} \rightarrow \textit{single color pattern}$$

$$\text{Large CC} \rightarrow \mathrm{Color}_{\mathrm{exposed}} \neq \mathrm{Color}_{\mathrm{protected}} \rightarrow \textit{multicolor pattern}$$

For the present example of collective patterning, the average CC during the course of pattern development is 16% (zero min values not included). The maximum color contrast is 34% at 45 mins of development (**Appendix G Figure G.10)**. Photopatterning

was also performed using the 470 nm development light at 28 mW, and showed similar results in terms of collective recovery and the pattern contrast (**Appendix G Figures G.11-G.12)**.

10.3.6. Selective recovery via development wavelength (S1)

Approach & requirements

Selective recovery is useful when trying to develop a photopattern with different colors in exposed and protected regions (high color contrast). The first method for selective recovery (i.e. selective recovery via development wavelength) uses a mixture of QDs that are both unstable and development light that only the low energy bandgap QD can absorb ($\lambda_{1s,high\ energy} < \lambda_{development} < \lambda_{1s,low\ energy}$). The low energy bandgap component in this example is the unstable red-emitting QD, so the wavelength of the development light is selected to satisfy $\lambda_{1s,green} < \lambda_{development} < \lambda_{1s,red}$. This type of development causes the emission of only the low energy bandgap QD to recover while the PL of the high energy bandgap QD remains constant.

Outcome

To demonstrate this selective recovery method, unstable green and unstable red QDs were deposited into a film and developed using 580 nm light at 17 mW, which satisfies the condition $\lambda_{1s,green} < \lambda_{development} < \lambda_{1s,red}$ so that only the red QDs absorb the light and exhibit PL recovery (**Figure 10.7a**). Photoluminescence imaging and hyperspectral characterization show that the contrast of the film increases and the color of the exposed regions become more orange over 153 min of development (**Appendix G Figure G.13**).

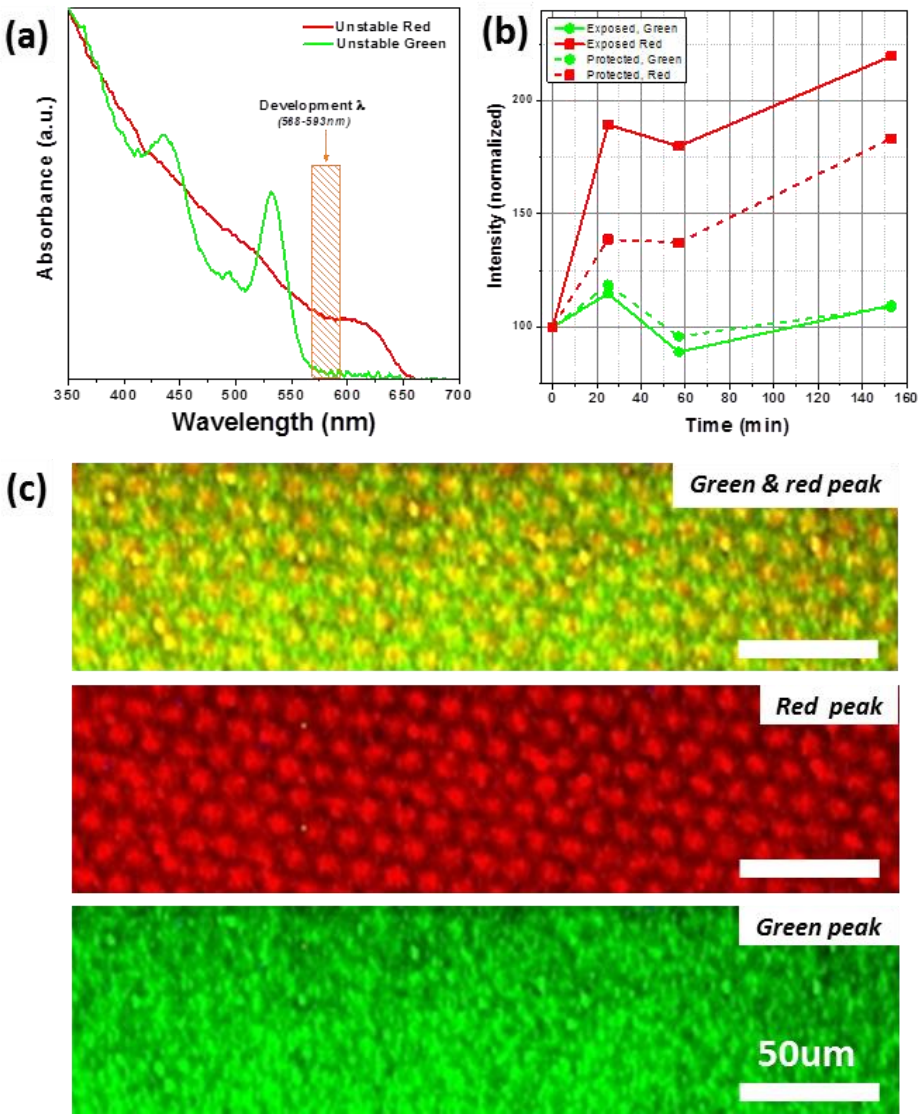

Figure 10.7: Selective recovery via development wavelength method (S2): Unstable red and unstable green QDs are used to develop a photopattern where a specific emission peak is recovered while the other remains constant for the duration of pattern development. (a) Unequal emission recovery was achieved by developing the pattern with light that only the red QDs can absorb strongly, in this case 580 nm and 17 mW ($\lambda_{1s,green} < \lambda_{development} < \lambda_{1s,red}$) (absorbance normalized at 350 nm for clarity). (b) Peak fitting of emission from the exposed and protected regions of the film show that the red emission increases while the green emission remains nearly constant. Hyperspectral scans of (c) both red and green, only red, and only green emission shows selective recovery of only the red QDs. All scale bars are 50 μm.

Hyperspectral characterization of the photopattern shows that the selective recovery of red QD emission occurs with very little recovery of green emission (**Figure 10.7b**). In this phase of patterning, the average color contrast between red and green recovery is 46% (not including the zero minute mark), with the maximum color contrast of 54% occurring after 25 min of development (**Appendix G Figure G.13e**). Selective recovery is confirmed by hyperspectral maps which clearly show that the red QDs are patterned while the green QDs are not patterned, proving that the photopattern is due only to the recovery of red emission (**Figure 10.7c**).

The efficiency of this strategy depends largely on the difference in absorbance positions between the unstable components. Using optical components that have similar λ_{1s} positions (for example, orange QDs with red QDs) could lead to a non-zero amount of absorption by the high energy QD, which will result in collective recovery instead of selective recovery. Collective recovery can be avoided by increasing the difference in λ_{1s} position between the two components (for example, using red QDs with blue QDs), which minimizes absorbance by the high energy QD and provides a larger region of appropriate development wavelengths to achieve selective recovery. Taking these steps can improve color contrast and the ability to develop a multicolored photopattern. However, developing the pattern with redder wavelengths tends to slow the PL recovery, and thus more time is required for recovery to occur. The increase in the required development time can lead to more pronounced proximity effects of the development light into the protected regions of the film due to small variations in mask position, which reduces intensity contrast. These competing effects need to be considered when utilizing this technique.

10.3.7. Selective recovery via stable-unstable mixtures (S2)

Approach & requirements

The second method for selective recovery photopatterning (i.e. selective recovery via a stable-unstable mixture) utilizes a mixture of an unstable QD and a stable QD. The only requirement for $\lambda_{development}$ is that it falls within the absorbance region of the unstable QDs ($\lambda_{development} < \lambda_{1s,unstable}$). In this process, only the emission from the unstable QD recovers when exposed to light, resulting in an increase in the intensity difference between the emission of the stable and unstable QDs. This approach is useful when trying to develop a photopattern with very high color contrast. The advantage of this selective recovery strategy over the previous selective recovery strategy (S1) is that there is less restriction on the wavelength that can be used to develop the pattern. In this case, higher energy light can be used for pattern development, which increases the PL recovery rate, and reduces proximity effects caused by small fluctuations in the mask position.

Outcome

To verify this method, stable green QDs and unstable red QDs were deposited into a film and developed with 350 nm light at 2.5 mW, which satisfies the condition of $\lambda_{development} < \lambda_{1s,unstable}$ (**Figure 10.8a**). Photoluminescence imaging and hyperspectral characterization reveal that the contrast of the film increases and the color of the exposed regions become more orange over 86 min of development **(Appendix G Figure G.14)**. The orange color is due to the recovery of red emission (with no corresponding recovery of green emission observed) (**Figure 10.8b**).

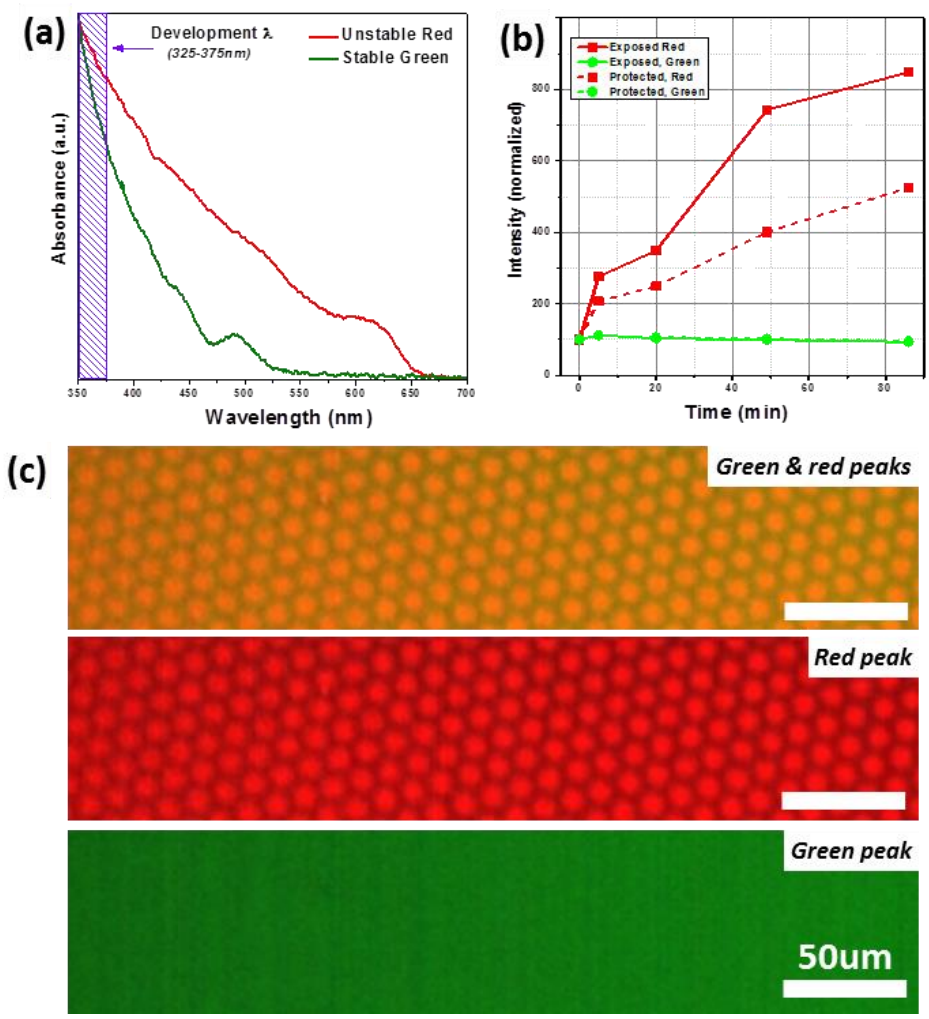

Figure 10.8: Selective recovery via stable-unstable mixtures method (S2): Stable green and unstable red and stable green QDs are used to perform selective recovery photopatterning where only the emission of the unstable red QDs recovers. $\lambda_{development}$ is selected so that it can be absorbed by the unstable QDs ($\lambda_{development} < \lambda_{1s,unstable}$). In this case, (a) this requirement is satisfied by using light of 350 nm (2.5 mW) which falls within the absorbance of the unstable red QDs (absorbance normalized at 350 nm for clarity). (b) Peak fitting of emission from the exposed and protected regions of the film show that the red emission increases while the green emission remains nearly constant. Hyperspectral scans of (c) both red and green, only red, and only green emission shows selective recovery of only the red QDs. All scale bars are 50 µm.

Hyperspectral scanning of specific peaks clearly shows that the photopattern results from the recovery of only red emission, a clear indication of selective recovery (**Figure 10.8c**). In this patterning process, the average color contrast is 211% (not including the zero minute mark) with a maximum color contrast of 346% emerging after 49 min of development (**Appendix G Figure G.14e**). Obviously, the CC provided by this patterning method is significantly higher than the collective recovery method. The effectiveness and flexibility of this method depends on the degree of PL stability of the stable QD, and can be compromised at high excitation intensities.

10.3.8. Comparison of photopatterning strategies

Two general strategies were introduced for developing photopatterns (selective recovery and collective recovery) which provide the platform to develop single-color or multi-color photopatterns. These strategies offer flexibility during pattern development depending on the type of system being patterned. Each method has advantages and disadvantages in terms of the required exposure wavelength and the required types of QDs (stable or unstable). The requirements and characteristics of each method for a mixture of red and green QDs are summarized in **Table 10.1**.

Table 10.1: Summary of the requirements and characteristics of the collective and selective photopatterning strategies.

Method	Recovery	QD Stability Type	Development λ	Color Contrast
C	Collective *(↑ green & red PL)*	Unstable QDs *Near-equal recovery rates*	$\lambda_{devel} < \lambda_{1s,red}$ & $\lambda_{1s,green}$	Low *(single color)*
S1	Selective *(↑ red PL)*	Unstable QDs	$\lambda_{1s,green} < \lambda_{devel} < \lambda_{1s,red}$	Medium *(multicolor)*
S2	Selective *(↑ red PL)*	Unstable QD + stable QD	$\lambda_{devel} < \lambda_{1s,unstable\ red}$	High *(multicolor)*

It is notable that previous photopatterning studies demonstrated significant limits of resolution and photoluminescence pattern contrast, which were important steps in the early development of photopatterning. In sharp contrast, our work offers an important advancement in the photopatterning process by examining how mixtures of QDs of different emission with various development approaches can be implemented to provide unprecedented control over the development of single-color or multicolor photopatterns. The potential of the strategies and methods explored in this work is much broader than the few examples shown here. Simple extensions include using QDs with emission other than red and green, increasing the number of QD colors in the mixture, and capitalizing on more complex combinations of stable and unstable QDs. In addition, these photopatterning strategies can be employed with any optical nanostructures or chemicals that exhibit changes in their PL when exposed to light. Furthermore, there exist many combinations of selective recovery and collective recovery that could potentially lead to photopatterns that are more complex than any presented in this work.

Future challenges for photopatterning include imparting optical stability to the photopatterns since exposure to light can reduce pattern contrast and alter the color (due to the unstable optical nature of the QDs). Weak photopatterns were found to be present two to four months after fabrication; however, they experienced exhibited significantly reduced emission intensity and contrast, as well as a shift in color.

10.4.Conclusions

In summary, we report simple yet robust photopatterning strategies that use mixtures of different QDs and judicious implementation of the development wavelength to produce high-resolution multicolor photopatterns with tunable color appearance. The collective and selective recovery strategies are easy to implement, applicable to a large variety of QD systems, and yield complex multipeak emission profiles, representing a significant departure from previous single-component photopatterning studies. Finally, these patterns have periodic shapes pre-programmed by the photomask, extend over large areas, and exhibit high-resolution features smaller than those previously reported which used a traditional non-coherence excitation source.

10.5.Chapter acknowledgements

Dr. Jaehan Jung and Young Jun Yoon (Prof. Lin group, Georgia Institute of Technology): QD synthesis and ligand exchange. Ruilong Ma: designing the GT photomask.

10.6.References (Chapter 10)

1 Todescato, F.; Fortunati, I.; Gardin, S.; Garbin, E.; Collini, E.; Bozio, R.; Jasieniak, J.J.; Della Giustina, G.; Brusatin, G.; Toffanin, S.; Signorini, R., Soft-lithographed up-converted distributed feedback visible lasers based on CdSe-CdZnS-ZnS quantum dots. *Adv. Func. Mater.* **2012,** *22,* 337-344.

2 Hodaei, H.; Miri, M.-A.; Heinrich, M.; Christodoulides, D.N.; Khajavikhan, M., Parity-time-symmetric microring lasers. *Science* **2014,** *346,* 975-978.

3 Tulek, A.; Vardeny, Z.V., Unidirectional laser emission from pi-conjugated polymer microcavities with broken symmetry. *Appl. Phys. Lett.* **2007,** *90*, 161106.

4 Hampton, M.J.; Templeton, J.L.; DeSimone, J.M., Direct patterning of CdSe quantum dots into sub-100 nm structures. *Langmuir* **2010,** *26,* 3012-3015.

5 Bozhevolnyi, S.I.; Volkov, V.S.; Devaux, E.; Laluet, J.Y.; Ebbesen, T.W., Channel plasmon subwavelength waveguide components including interferometers and ring resonators. *Nature* **2006,** *440,* 508-511.

6 Rizzo, A.; Mazzeo, M.; Palumbo, M.; Lerario, G.; D'Amone, S.; Cingolani, R.; Gigli, G., Hybrid light-emitting diodes from microcontact-printing double-transfer of colloidal semiconductor CdSe/ZnS quantum dots onto organic layers. *Adv. Mater.* **2008,** *20,* 1886.

7 Kim, L.; Anikeeva, P.O.; Coe-Sullivan, S.A.; Steckel, J.S.; Bawendi, M.G.; Bulovic, V., Contact printing of quantum dot light-emitting devices. *Nano Lett.* **2008,** *8,* 4513-4517.

8 Gates, B.D.; Xu, Q.B.; Stewart, M.; Ryan, D.; Willson, C.G.; Whitesides, G.M., New approaches to nanofabrication: Molding, printing, and other techniques. *Chem. Rev.* **2005,** *105,* 1171-1196.

9 Biswas, A.; Bayer, I.S.; Biris, A.S.; Wang, T.; Dervishi, E.; Faupel, F., Advances in top-down and bottom-up surface nanofabrication: Techniques, applications & future prospects. *Adv. Colloid and Interface Sci.* **2012,** *170*, 2-27.

10 Young, S.L.; Gupta, M.; Hanske, C.; Fery, A.; Scheibel, T.; Tsukruk, V.V., Utilizing conformational changes for patterning thin films of recombinant spider silk proteins. *Biomacromolecules* **2012,** *13,* 3189-3199.

11 Bao, B.; Jiang, J.K.; Li, F.Y.; Zhang, P.C.; Chen, S.R.; Yang, Q.; Wang, S.T.; Su, B.; Jiang, L.; Song, Y.L., Fabrication of patterned concave microstructures by inkjet imprinting. *Adv. Func. Mater.* **2015,** *25,* 3286-3294.

12 Xu, J.; Xia, J.F.; Lin, Z.Q., Evaporation-induced self-assembly of nanoparticles from a sphere-on-flat geometry. *Angewandte Chemie-Intern. Ed.* **2007,** *46,* 1860-1863.

13 Kim, T.-H.; Cho, K.-S.; Lee, E.K.; Lee, S.J.; Chae, J.; Kim, J.W.; Kim, D.H.; Kwon, J.-Y.; Amaratunga, G.; Lee, S.Y.; Choi, B.L.; Kuk, Y.; Kim, J.M.; Kim, K., Full-colour quantum dot displays fabricated by transfer printing. *Nat. Photonics* **2011,** *5,* 176-182.

14 Xu, J.; Xia, J.F.; Wang, J.; Shinar, J.; Lin, Z.Q., Quantum dots confined in nanoporous alumina membranes. *Appl. Phys. Lett.* **2006,** *89*, 133110.

15 Bao, B.; Li, M.Z.; Li, Y.; Jiang, J.K.; Gu, Z.K.; Zhang, X.Y.; Jiang, L.; Song, Y.L., Patterning fluorescent quantum dot nanocomposites by reactive inkjet printing. *Small* **2015,** *11*, 1649-1654.

16 Kuang, M.X.; Wang, J.X.; Bao, B.; Li, F.Y.; Wang, L.B.; Jiang, L.; Song, Y.L., Inkjet printing patterned photonic crystal domes for wide viewing-angle displays by controlling the sliding three phase contact line. *Adv. Opt. Mater.* **2014,** *2*, 34-38.

17 Kapitonov, A.M.; Stupak, A.P.; Gaponenko, S.V.; Petrov, E.P.; Rogach, A.L.; Eychmuller, A., Luminescence properties of thiol-stabilized CdTe nanocrystals. *J. Phys. Chem. B* **1999,** *103,* 10109-10113.

18 Lin, K.F.; Cheng, H.M.; Hsu, H.C.; Lin, L.J.; Hsieh, W.F., Band gap variation of size-controlled ZnO quantum dots synthesized by sol-gel method. *Chem. Phys. Lett.* **2005,** *409,* 208-211.

19 Tagliazucchi, M.; Amin, V.A.; Schneebeli, S.T.; Stoddart, J.F.; Weiss, E.A., High-contrast photopatterning of photoluminescence within quantum dot films through degradation of a charge-transfer quencher. *Adv. Mater.* **2012,** *24,* 3617-3621.

20 Wang, Y.; Tang, Z.Y.; Correa-Duarte, M.A.; Liz-Marzan, L.M.; Kotov, N.A., Multicolor luminescence patterning by photoactivation of semiconductor nanoparticle films. *J. Amer. Chem. Soc.* **2003,** *125,* 2830-2831.

21 Chen, J.X.; Chan, Y.H.; Son, D.H.; Cremer, P.S.; Batteas, J.D., Spatially selective tuning of quantum dot thin film optical properties by photopatterning. *Abstr. Pap. Amer. Chem. Soc.* **2009,** *237.*

22 Uematsu, T.; Kimura, J.; Yamaguchi, Y., The reversible photoluminescence enhancement of a CdSe/ZnS nanocrystal thin film. *Nanotech.* **2004,** *15,* 822-827.

23 Anikeeva, P.O.; Halpert, J.E.; Bawendi, M.G.; Bulović, V., Electroluminescence from a mixed red−green−blue colloidal quantum dot monolayer. *Nano Lett.* **2007,** *7,* 2196-2200.

24 Jang, E.; Jun, S.; Jang, H.; Lim, J.; Kim, B.; Kim, Y., White-light-emitting diodes with quantum dot color converters for display backlights. *Adv. Mater.* **2010,** *22,* 3076-3080.

25 Wu, X.Y.; Liu, H.J.; Liu, J.Q.; Haley, K.N.; Treadway, J.A.; Larson, J.P.; Ge, N.F.; Peale, F.; Bruchez, M.P., Immunofluorescent labeling of cancer marker Her2 and other cellular targets with semiconductor quantum dots. *Nat. Biotech.* **2003,** *21,* 41-46.

26 Chen, X.; Rogach, A.L.; Talapin, D.V.; Fuchs, H.; Chi, L., Hierarchical luminescence patterning based on multiscaled self-assembly. *J. Amer. Chem. Soc.* **2006,** *128,* 9592-9593.

27 Wang, Y.; Tang, Z.; Correa-Duarte, M.A.; Pastoriza-Santos, I.; Giersig, M.; Kotov, N.A.; Liz-Marzán, L.M., Mechanism of strong luminescence photoactivation of citrate-stabilized water-soluble nanoparticles with CdSe cores. *J. Phys. Chem. B* **2004,** *108,* 15461-15469.

28 Maenosono, S., Modeling photoinduced fluorescence enhancement in semiconductor nanocrystal arrays. *Chem. Phys. Lett.* **2003,** *376,* 666-670.

29 Oda, M.; Shen, M.Y.; Saito, M.; Goto, T., Photobrightening of CuBr nanocrystals in PMMA. *J. Luminescence* **2000,** *87–89,* 469-471.

30 J.A. Woollam Co. Inc. “Guide to using WVase32.” Ch.2, A short course in ellipsometry. **2010.**

31 Grumbach, N.; Capek, R.K.; Tilchin, E.; Rubin-Brusilovski, A.; Yang, J.F.; Ein-Eli, Y.; Lifshitz, E., Comprehensive route to the formation of alloy interface in core/shell colloidal quantum dots. *J. Phys. Chem. C* **2015,** *119*, 12749-12756.

32 Gong, K.; Kelley, D.F., Lattice strain limit for uniform shell deposition in zincblende CdSe/CdS quantum dots. *J. Phys. Chem. Lett.* **2015,** *6*, 1559-1562.

33 Cragg, G.E.; Efros, A.L., Suppression of Auger processes in confined structures. *Nano Lett.* **2010,** *10*, 313-317.

34 Garcia-Santamaria, F.; Brovelli, S.; Viswanatha, R.; Hollingsworth, J.A.; Htoon, H.; Crooker, S.A.; Klimov, V.I., Breakdown of volume scaling in Auger recombination in CdSe/CdS heteronanocrystals: The role of the core-shell interface. *Nano Lett.* **2011,** *11*, 687-693.

35 Tsukruk, V.V. & Singamaneni, S., “Scanning probe microscopy of soft matter: fundamentals and practices.” *Wiley-VCH,* **2012.**

36 Pechstedt, K.; Whittle, T.; Baumberg, J.; Melvin, T., Photoluminescence of colloidal CdSe/ZnS quantum dots: The critical effect of water molecules. *J. Phys. Chem. C* **2010,** *114,* 12069-12077.

37 Nirmal, M.; Dabbousi, B.O.; Bawendi, M.G.; Macklin, J.J.; Trautman, J.K.; Harris, T.D.; Brus, L.E., Fluorescence intermittency in single cadmium selenide nanocrystals. *Nature* **1996,** *383,* 802-804.

38 Garcia-Santamaria, F.; Chen, Y.F.; Vela, J.; Schaller, R.D.; Hollingsworth, J.A.; Klimov, V.I., Suppressed Auger recombination in "giant" nanocrystals boosts optical gain performance. *Nano Lett.* **2009,** *9*, 3482-3488.

39 Hoogland, S., “Colloidal quantum dot optoelectronics and photovoltaics” Ch.8, Optical gain and lasing in colloidal quantum dots. *Cambridge University Press,* **2013.**

40 Konig, T.A.F.; Ledin, P.A.; Russell, M.; Geldmeier, J.A.; Mahmoud, M.A.; El-Sayed, M.A.; Tsukruk, V.V., Silver nanocube aggregation gradient materials in search for total internal reflection with high phase sensitivity. *Nanoscale* **2015,** *7*, 5230-5239.

41 Malak, S.T.; Konig, T.; Near, R.; Combs, Z.A.; El-Sayed, M.A.; Tsukruk, V.V., Stacked gold nanorectangles with higher order plasmonic modes and top-down plasmonic coupling. *J. Phys. Chem. C* **2014,** *118*, 5453-5462.

42 Klar, T.A.; Franzl, T.; Rogach, A.L.; Feldmann, J., Super-efficient exciton funneling in layer-by-layer semiconductor nanocrystal structures. *Adv. Mater.* **2005,** *17,* 769-773.

CHAPTER 11

GENERAL CONCLUSIONS AND BROADER IMPACT

11.1 General conclusions and discussion

Generally this work focused on developing an understanding how the three levels of system design (individual nanostructure, nanostructure-nanostructure local-assembly, and large-scale nanostructure arrangement) affect the confinement mechanisms and light propagation/emission in nanoscale-microscale photonic and plasmonic systems. The surface confinement of plasmons (collective electron oscillations) and quantum confinement of excitons (electron-hole pair quasiparticles) were specifically considered.

We suggest that this work provides a scientific and engineering framework that can be referenced when designing and fabricating photonic systems that require specific optical characteristics. The major themes included:

1. Measure, examine, and understand the mechanisms affecting the confinement phenomena of plasmons and excitons in individual photonic nanostructures and their local-assemblies, with an aim to expand upon the versatility/tunability offered by these nanostructures;

2. Examine how the large-scale arrangement (of individual and coupled nanostructures) affects the overall light propagation, absorption, and emission resulting from the confined photonic nanostructures, and show how it can be utilized to develop novel photonic systems;

3. Develop approaches to control/modulate the three spatial levels of system design to control light-matter interactions in localized (nanoscale) regions and over delocalized large (microscale) areas to discover new scientific/engineering frameworks for creating novel photonic systems.

Specific issues and challenges addressed in this study:

(1) Identify structure-photonic correlations (specifically the optical scattering profile) for specific individual plasmonic nanostructures and their local-assemblies via direct SEM-AFM-hyperspectral comparisons;
(2) Develop and implement non-traditional local-assemblies (particle stacking) and large-scale arrangements (3D substrates) of plasmonic nanostructures to provide new ways to tailor plasmonic coupling and overall electromagnetic enhancement;
(3) Advance the fundamental understanding of how the properties of individual plasmonic nanostructures, their local-assembly, and their large-scale arrangement affect the attenuation/enhancement and propagation of the light interacting with the system;
(4) Examine how quantum confinement and relaxation pathways of the exciton of widely-spaced isolated QDs evolve over different time-scales (seconds-minutes-hours) upon light exposure (via examination of photoluminescence characteristics), and how this evolution relates to the compositional design of the quantum dot (core, core/shell, core/graded shell);
(5) Outline the experimental tests and procedures that should be employed when examining the emission stability of isolated quantum dots of specific compositional design, and when trying to determine the applicability of QDs to specific scientific experiments and engineering applications;
(6) Examine how the large-scale arrangement of quantum dots in films can be controlled and how it affects the refractive index, light propagation, optical amplification, and optical attenuation;
(7) Finally, utilize knowledge of QD compositional design to develop new and unique photopatterning strategies that vastly expand the ability to spatially modulate QD emission via non-physical photopatterning (unique pattern contrasts, spectral color variations, unprecedented resolution, large-scale uniformity, and increased throughput).

A large amount of research in the field of plasmonics has focused on the optical characteristics of individual particles and their coupling behavior. However, a number of important limitations in this body of work were identified. **First, most studies develop structure-photonic relationships by averaging physical/optical data over hundreds**

of nanostructures. Although this approach does provide useful information on general trends, it cannot easily identify how specific physical variations/defects (and unique coupling schemes) specifically affect optical scattering (since this data tends to get washed out in the statistics). This limitation stems primarily from the experimental difficulty associated with collecting optical spectra from individual nanoparticles (and their local-assemblies) and from the additional complexity associated with correlating physical and optical data obtained from different instruments (AFM/SEM and optical spectroscopies).

Second, the majority of studies on coupled plasmonic structures have almost exclusively examined planar local-assemblies, with few considering how the third (vertical) dimension can be utilized in the assembly design. The sole focus on planar assemblies is a significant limitation since vertical stacking can minimize the lateral footprint of the local assembly (which could be important in applications requiring high-density arrangements), and since new and unique resonances could emerge in a vertically stacked assembly because the underlying substrate is only directly influencing the base nanostructure.

These two limitations were addressed by examining stacked local-assemblies of plasmonic nanostructures that were fabricated in well-ordered arrays so that direct correlation could be made between AFM, SEM, and hyperspectral scanning. Using this approach, we correlated the structural characteristics of specific plasmonic structures (and their stacked assemblies) with their unique optical scattering spectrum. This work revealed that the presence of stacked Au caps on hollow rectangular Au nanostructures can dramatically redshift the primary plasmon resonances and increase the local electrical field within open “hotspots.” Electromagnetic modeling of the plasmonic

modes in these assemblies (compared to the conventional solid nanorectangles) indicated that the electric field from the higher energy dipole and quadrupolar modes is increased manifold through the interaction of the cap with the underlying hollow nanostructure.

The idea of using the third-dimension in locally-assembled plasmonic structures (via stacking) was extended to larger-scale three-dimensional arrangements of plasmonic nanostructures. This resulted in the development of a new and novel complex hierarchal system composed of individual and locally-assembled Ag nanocubes (AgNCs) deposited within a microscale three-dimension porous alumina membrane (PAM). In this system, the local assembly of AgNCs was controlled using a polyelectrolyte layering method, allowing for either individual (dispersed) AgNCs or locally-assembled (aggregated) AgNCs. The 3D arrangement of the AgNCs was controlled by the 3D PAM substrate. The electric fields and electric hot-spot volume of the plasmons associated with the local nanocube-nanocube contacts were examined with FDTD modeling. FDTD modeling showed greatly enhanced electric fields were present in the nanocube-nanocube local-assembly (compared to individual nanocubes) due to the presence of electromagnetic coupling. Furthermore, FDTD modeling showed that the coupled AgNCs exhibited larger electric field strengths than nanosphere-nanosphere contacts. The 3D PAM substrate increased the light-matter interactions (compared to a 2D planar substrate) by acting as an adsorption scaffold to hold a high density of nanostructures, as well as acting as an optical waveguide to guide the incident light to the dense distribution of AgNCs throughput the PAM membrane.

The FDTD modeling predictions of electric field magnitude were tested and confirmed by comparing the limits of chemical detection from each substrate via the SERS technique.

The PAM-AgNC substrates with AgNC aggregates were shown to exhibit much better limits-of-detection than the substrates with individual (dispersed) AgNCs. In addition, both types of PAM-AgNC substrates were shown to exhibit better limits-of-detection than PAMs with Ag nanospheres (AgNS). The performance differences were attributed to the unique plasmonic resonances and enhanced electric fields associated with the plasmons of individual AgNCs and their local-assemblies (compared to AgNS). Finally, the PAM-AgNC substrates with AgNC aggregates displayed exceptional limits-of-detection for vapor phase benzene thiol and n-methyl-4-nitroaniline (500 ppb and 3 ppb respectively).

The highly-localized and intense electric fields of localized plasmons (of plasmonic structures) allows for greatly enhanced light-matter interactions. Strong light-matter interactions in turn make it possible to leverage the tunable properties of these nanostructures to create photonic systems with enhanced optical scattering and absorption. For example, strong optical scattering and absorption could be particularly useful when trying to develop very thin film optical filters and light absorbers that require specific spectral profiles (i.e. targeted low-pass, high-pass, or band-pass filtering). However, a drawback of plasmonic nanostructures is that they do not emit light and thus have limited application in emission-based systems like lasers and display technologies. Therefore, we shifted attention to a different confinement-based photonic nanostructure that can emit light when excited.

Quantum dots are an ideal nanostructure for studying confinement mechanisms in light emitting systems since they experience quantum confinement of their exciton (electron-hole pair), a fascinating phenomenon that allows their photoluminescence (light emission) to be tuned across the visible spectrum. The electronic energy transitions of quantum confined excitons in a QD depend on the individual characteristics of the QD

(size, shape, surface, and surrounding environment of the QD). Furthermore, isolated QDs can be examined via QDs in solution or in QD-polymer films with low QD-loading (both systems have large separation between adjacent QDs). These options provide for a wide-range of fundamental scientific inquiries into the confined exciton of a QD. A significant amount of research has been conducted on quantum dots and their applications. Much of this work has concentrated on increasing optical characteristics like quantum yield and narrowing emission FWHM, as well as on surface-functionalization techniques and physical patterning compatibilities. Great advancements in these areas have led to the incorporation of quantum dots in many photonic technologies.

In addition, it is known that the compositional profile of a QD (core, core/shell, core/graded shell) dictates the localization of its exciton and therefore how exposed the exciton is to the surrounding conditions/environment. The relationships between exciton localization (and its relaxation pathways) and QD composition profile are typically examined via photoluminescence properties like quantum yield, full-width half-maximum, spectral position, and emission lifetimes of QDs in solution. **However, a survey of the literature showed a general lack of understanding/confirmation of how quantum confinement of the exciton (and its relaxation pathways) can evolve when the QDs are encapsulated into polymer matrices in films.** This is an issue because many QD scientific studies and engineering applications utilize QDs encapsulated in a polymer film (to form a QD-polymer composite film). Therefore, we wanted to examine changes to the photoluminescence emission of quantum dots (which reflect changes to the confined exciton) upon light exposure. **Major assumptions have been made in claiming that a stable exciton of QDs in solution (as observed via stable emission intensity and spectral position) remains after QDs are deposited into films.** However, in films a

variety of new factors are present that can interact with the QD and consequently affect the QD exciton (including H_2O, oxygen, and the matrix material). Furthermore, many variety QD architectures have been proposed and demonstrated (core/shell, core/shell/shell, and core/graded shell) that are assumed to effectively isolate the QD core exciton from the environment, which should render the emission of the QD stable. However, these assumptions are rarely thoroughly tested.

Therefore, we performed an in-depth examination of how the compositional design of a QD (CdSe core, CdSe/ZnS core/shell, and CdSe/CdSe/$Cd_{1-x}Zn_xSe_{1-y}S_y$ core/graded shell) encapsulated in a polymer film affects how the QD photoluminescence evolves under various light exposure conditions. **Contrary to major assumptions, we found that the stable emission of QDs in solution does not necessarily remain once the QDs are encapsulated in polymer films.** Results show that QDs with a protective shell can exhibit minimal changes in their emission (intensity and spectral position) while in solution, but display significant changes when they are encapsulated into a polymer film.

Furthermore, we demonstrated that the composition profile of a quantum dot significantly affects the evolution of its optical characteristics while in darkness and under light exposure in a thin film, with distinct shifts occurring for different shell designs. For example, changes of emission intensity (decreasing and increasing) and spectral position (blue shifting and red shifting) are all observed, which can be reversible or irreversible (depending on QD architecture and exposure conditions). Additionally, it is revealed that competition between the reversible and irreversible mechanisms underlying these optical changes can lead to unique and important behavior, including: **decay-to-recovery intensity trends, meta-stable bright states**

that can be activated/deactivated numerous times, and decoupled optical changes (reversible intensity changes versus irreversible spectral shifts). Furthermore, there is a large difference of rate between the decay and recovery mechanisms (seconds versus many minutes), which means fast mechanisms (like immediate decay upon light exposure) have likely been entirely overlooked in previous QD stability studies focusing on slower mechanisms (like slow recovery of emission).

Once the relationships between QD compositional design and emission evolution were examined for isolated QDs in QD-polymer films, **the focus was shifted to how QD-QD spacing in films affects light-matter interactions over larger scales (microns-millimeters). Specific attention was placed on characteristics like light propagation, light amplification, and light attenuation.** Optical amplification (in the form of amplified spontaneous emission (ASE)) is a particularly interesting light-matter interaction since the propagating light interacts with the QDs to form additional photons via stimulated electron relaxation. A strategy involving QD ligand selection was developed to control the average QD-QD packing. It was shown that the molecular dimensions and functionality of the QD ligand affects important physical properties (film morphology, QD-packing density) and optical characteristics of the QD films (optical density, refractive index, refractive index contrast). These changes directly influence the light-matter interactions over larger scales, specifically waveguiding efficiency/losses and optical amplification/attenuation within the film. More specifically, we proved that increasing QD-packing density can increase both optical gain (via increased stimulated emission and improved waveguiding) and optical attenuation (via increased optical density and reabsorption). However, a preferential increase in gain (over loss) was observed. Finally, evidence was provided that the chemical structure and physical and thermal properties of the ligand affect gain threshold and ASE stability.

Once we examined how large-scale light-matter interactions like waveguiding and optical gain can be controlled via QD-QD proximity, we **shifted attention to identifying and developing techniques to control the large-scale spatial modulation of PL emission from QD films. Regions of spatially modulated PL emission are known as non-physical QD emissive photopatterns.** We utilized knowledge obtained from the QD exciton evolution study (emission of core-shell CdSe/ZnS QDs exhibits a two-step decay-to-recovery behavior under continuous light exposure) to conceive of novel and facile strategies for creating a variety of photopatterns. It was shown that careful control of the duration of light exposure allowed for photopatterns of either negative or positive intensity contrast. **These non-physical photopatterns are analogous to traditional positive and negative physical patterns in electron/photolithography but have no topographical variation.** In addition, negative-to-positive contrast switching was successfully demonstrated using an understanding of the overall exciton evolution curve under continuous light exposure.

Following the examination on how the duration of light exposure affects photopattern contrast, **our attention shifted to how the spatial arrangement of light exposure can be tuned and utilized to control photopattern development**. Exposure strategies based on near-field PDMS photomasks and far-field (maskless) laser interference lithography were identified and implemented. These interference based techniques yielded improvements in minimum feature size (550 nm to 1800 nm) which match the feature sizes offered by direct-write single-laser exposure (~575 nm). Furthermore, these near-field and far-field interference techniques can pattern large areas (cm^2), have high throughput (~0.19 mm^2/sec), and very good pattern uniformity (over areas of mm^2 to cm^2). **Finally, for the first time in the field of photopatterning, both face-profile**

and (novel) edge-profile photopatterns were be fabricated, in this case by properly controlling the location of the exposure beam with respect to the PDMS photomask. These techniques made it possible to fabricate localized nanoscale patterned features over macroscopic lateral areas (i.e. combining knowledge of individual QD properties with localized modification techniques to create photonic systems with predetermined large-scale emission modulation).

The final photopatterning investigation concentrated on how the unique spectral absorption profile of different color QDs can be utilized to create multicolor photopatterns. QD-polymer films composed of two or more quantum dots with different color emission were fabricated and exposed to specific light wavelengths. Specific QD colors within the film could be selectively or collectively modified through judicious consideration and implementation of the development wavelength and knowledge of the unique spectral absorption profile exhibited by different color QDs. These selective and collective PL recovery strategies made is possible to fabricate multicolor photopatterns with unprecedented control.

11.2 Significance and broader impact

11.2.1 Scientific significance and impact

The scientific significance of these studies spans both theoretical and practical considerations pertaining to confinement-based photonic nanostructures. In general, these data established clear relationships between the confinement phenomenon (plasmon or exciton) and the characteristics of individual structures and their local-assembly, as well as how to leverage this localized control over macroscale dimensions by controlling their large-scale arrangement.

The study of various stacked plasmonic nanostructures using direct structure-photonic correlation (across multiple techniques) was a **clear departure from the majority of current plasmonic investigations, which establish structure-photonic relationships based on data averaged across hundreds of nanostructures.** However, aggregated data washes out deviations from the average, which means a large amount of data is lost pertaining to unique structure-property relationships. For example, we identified unique resonances across specific stacked plasmonic structures (offset-capped) but not others (central-capped). Even within the same subgroup of offset-capped local-assemblies, significant differences in red-shifting of the primary plasmonic resonance were observed, indicating subtle differences in stacking architecture are critically important. From this study, we were able to determine that local-assemblies extending into the third dimension (z-direction) can yield higher order complex plasmonic resonances depending upon the design of the local-assembly. **Overall, this serves as an important initial demonstration of how critical targeted characterization can be when trying to identify how specific physical defects and local-assemblies manifest themselves optically.**

The work on hierarchical AgNC-PAMs and AgNS-PAMs 3D substrates outlined an interesting approach for tailoring light-matter interactions using all three levels of system design (individual structure, structure-structure local-assembly, and large-scale arrangement). **Consideration of all three-levels of plasmonic system design is a highly unique approach in the field of plasmonics and SERS detection. Utilizing all three-levels made it possible to control the concentration range over which a SERS substrate was effective and to reach unprecedented limits of chemical vapor detection.** An examination of the nanoparticle shape (cube versus sphere) demonstrated that the presence of rounded or sharp edges drastically affects the

plasmon resonance and corresponding local electric fields. The presence of sharp and rounded edges also affects how the EM fields of adjacent particles coupled together and the strength of the coupling fields.

Additionally, the volume of the EM coupling region was larger in the case of the nanocubes (compared to the nanospheres), which means more analytes can be present within the enhanced SERS region. **These differences resulted in noticeably different detection ranges between coupled nanocubes and nanospheres.** Finally, the reusability of these substrates was examined and shown to be an important design parameter for evaluating the usefulness of SERS detection systems. **This consideration is particularly significant because reusability will likely promote the acceptance of SERS as an in-field analytical tool in the fields of life science, medical sensing/evaluation, and defense technologies.**

The work examining the evolution of the QD emission (exciton) upon light exposure yielded some very interesting and unexpected discoveries which overturn common assumptions found in the literature. First, we proved that the stability of the exciton (PL emission) for QDs in solution is not necessarily the same when QDs are in the film state. **This discovery clearly shows that exciton stability in one environment (fluid state) cannot be assumed to be present in another state (solid film state).** When QDs are deposited into a solid film they interact with a number of new environmental factors (water, oxygen, matrix material) which can alter the size, surface states, and surface composition of the QD. These changes can alter the confinement of the QD exciton, which manifests as shifts in the photoluminescence intensity and spectral position.

Second, we showed that the QD architecture (core, core/shell, core/graded shell) imparts distinct emission behavior in darkness and upon light exposure. **These experiments compose one of the first comprehensive studies on how QD architecture relates to emission evolution under various external influences, and they provide evidence of the chemical and physical changes underlying this evolution.** The distinct evolutionary behavior of PL results from the specific physical and chemical processes that can occur on the surface and within the QD as it interacts with the environment, and how these processes affect the confinement of the exciton and its relaxation pathways (radiative versus non-radiative). **For example, we are able to dispel the common notion that depositing an inorganic shell on a core QD (to make a core/shell QD) ensures strong isolation from the environment.** In fact, the degree of core isolation (and its stability) depends on the type of shell (graded or sharp composition transition) since the crystalline thermodynamics can be very different.

Third, the data shows that a variety of processes are occurring concurrently within a QD when exposed to light, which lead to decay, recovery, and spectral shifting of the emission. **This provides clear evidence that QDs can experience a series of physical and chemical changes that manifest as complex convoluted optical behavior.** These mechanisms operate at different rates (seconds versus minutes) which can make them difficult to observe and experimentally measure with proactive consideration. For example, shell oxidation and corrosion appears to initiate within seconds of light exposure and continues rapidly for a few minutes and then tapers off. However, light-induced PL recovery (which appears tied to H_2O mediated QD surface reactions) occurs more slowly over a period of many minutes. The combination of these changes can lead to interesting (and previously unobserved) decay-to-recovery intensity behavior.

Finally, our data challenges the notion that changes to QD emission are irreversible, an assumption commonly made in the literature and therefore not often tested. We showed that certain phenomena are indeed irreversible (spectral blue shifting and intensity decay), while others are reversible and can be activated and deactivated repeatedly (the recovery of PL intensity upon light exposure). The presence of reversible mechanisms is particularly important to consider (and check for) when utilizing new QD architectures in emitting applications (like lasing and display technologies). For example, it has been suggested that the QD emission can reach stable property plateau-regions (stabilized) by the implementation of photo-annealing steps. However, our results show that the stabilization of optical properties may not be permanent (dissipate after removal of light), and therefore the effectiveness of the photo-annealing processes need to be verified before and after initiation of the light exposure process over different time-scales.

We suggest these results (and the strategies to obtain them) are significant because they are relevant to the majority of scientific studies and technological applications that make use of the emission from quantum dots. Almost all scientific studies and engineering applications using QDs make assumptions regarding the stability of QD emission. This work **outlines strategies to test those assumptions.** In addition, a general set of guidelines for determining the applicability of a specific type of quantum dot architecture for an application were presented.

For example, QDs are increasingly being employed in optical gain systems. Typically optical gain is determined using the variable strip length (VSL) measurement. However, the VSL measurement assumes that the QDs have stable emission under the light

exposure. Therefore, core/graded shells QDs are the appropriate choice for this type of system. However, many studies routinely use core or core/shell QDs whose emission can (often) change upon light exposure. This violates the assumptions of most VSL fitting models and can potentially lead to an overestimation of the gain value.

As mentioned, quantum dots are increasingly being employed in optical gain systems because they can be tuned across the visible spectrum and exhibit strong optical gain and stability (under pulsed optical pumping). Most studies examine how to modify the synthesis, material composition, and architecture of the QD to tune optical gain. However, we show that the ligand can affect QD gain significantly by altering average QD-QD spacing (>2 fold factor difference between the lowest and highest QD-packed films). **This post-synthesis modification approach represents a clear departure from previous studies. Most importantly, it can be implemented with any QD architecture and therefore has wide-spread relevance to all QD gain systems.** Furthermore, implementation of this approach with very short ligands **yields some of the highest QD gain values reported in current literature (~500 cm^{-1}).** Finally, we examined how the interplay between QD-QD packing and thermodynamics properties of the ligand (melting point, boiling point, vapor pressure) affect ASE stability. In fact, we showed that the commonly used waxy, large ligand oleic acid yields poor ASE stability compared to amine-functionalized ligands. **Overall, we provided the first comprehensive examination on how the ligand affects QD optical gain, loss, and stability via various physical, thermal, and optical characteristics.**

The final contribution of this research work was to the area of patterned photonic systems. Examination of the literature showed some impressive work had been done to physically pattern optical cavities (disks and rings), waveguides, and diffraction gratings.

However, much less research has examined how to fabricate non-physical photopatterns, which are emissive patterns written into films. Photopatterns are fundamentally different from physical patterns fabricated using lithographic approaches because emissive photopatterns result from targeted intrinsic modification of the QD emission (**doping QDs with light**), not from the addition, removal, or rearrangement of material. Therefore, emissive photopatterns have no modulated physical topography. The limited amount of research that had been done on photopatterning has focused almost exclusively on rudimentary approaches that yield simple patterns with poor characteristics (low resolution, poor contrast, and low throughput). Therefore, we focused our work on QD evolution to invent multiple photopatterning approaches for QD-polymer films. **These new approaches not only expand the number and type of photopatterns that can be created on QD-polymer films, they significantly improve characteristics like resolution, feature density, throughput, uniformity, contrast, and color complexity.**

First, we demonstrated that QDs that exhibit decay-to-recovery of their PL intensity can be utilized to fabricate either positive or negative non-physical photopatterns depending on the duration of light exposure. ***This is the first time a single type of quantum dot has been used to fabricate photopatterns of opposite contrast.*** Negative-to-positive contrast switching was also successfully performed using an understanding of the overall exciton evolution curve under continuous light exposure. ***The concept of contrast switching is entirely new to the field of photopatterning and could have broad applications in light sensing and photopattern lifetime studies.***

Furthermore, the different photopatterning approaches utilize PL intensity decay and recovery mechanisms with significantly higher rate constants than previous studies. **The**

utilization of these faster mechanisms reduces the time required to develop a photopattern by a factor of 100-10000 (from hours to seconds) while maintaining spatial resolution. Finally, lifetime studies show that the degradation of a photopattern can be partially reversed by recharging with light exposure. **Not only is this the first time photopattern lifetime has been clearly examined, but a simple strategy was also presented that partially reverses this degradation behavior.**

We then identified near-field and far-field interference-based light exposure strategies to develop photopatterns. **This change represents a significant paradigm shift in the area of photopatterning (moving away from simple transmission-based photomasks) and it allowed us to simultaneously increase resolution to the sub-micron regime and obtain exceptionally high throughput.** In fact, photopatterns fabricated using these interference based techniques can reach minimum feature sizes of ~500-1800 nm, which matches the current high resolution offered by direct-write scanning-laser exposure (~575 nm). In addition, these techniques drastically increase the patternable area (cm^2) and throughput (increases of up to six orders of magnitude) while maintaining pattern uniformity. **These advances address the major constraints associated with resolution and throughput that have traditionally plagued photopatterning.**

It is common in photopatterning studies to utilize brittle TEM grids as the photomask since they are cheap and widely available. Although high contrast photopatterns have been developed using TEM grid photomasks, they have limited resolution (typically above 10 um), limited pattern options, and cannot be easily reused. On the other hand, the interference-based exposure strategies have the advantage of using easy-to-handle robust reusable photomasks (PDMS in the case of near-field patterning) or no mask at

all (in the case of far-field laser interface patterning). **These characteristics make it easy to pattern the same region multiple times to create ultra-dense, multi-level contrast photopatterns that are very difficult (if not impossible) to obtain using single exposure strategies.**

Finally, QD-polymer films composed of a mixture of quantum dots with different color emission were fabricated and exposed to specific light wavelengths to develop multicolor photopatterns. By judicious consideration and implementation of the development wavelength, we were able to selectively or collectively modify specific QD colors within the film. **The resulting multicolor photopatterns were a first in the field of QD photopatterns, and the strategies made it possible to fabricate multicolor photopatterns with highly predictable (and unprecedented) control.** These collective and selective exposure strategies are easy to implement, applicable to a large variety of QD systems, yield complex multipeak emission profiles, and **represent a significant departure from previous single-component photopatterning studies.** In addition, these spectral tuning strategies are compatible with the previously outlined photopatterning approaches and therefore do not compromise on pattern resolution, uniformity, or throughput.

Overall, these photopatterning studies utilize the characteristics of individual quantum dots (the evolution of their confined exciton) to create large-scale arrangements of emissive regions, a significant achievement in nanoscale and microscale technologies. In addition, the variety of approaches and the range of advantages and disadvantages of each approach provide a great degree of flexibility in terms of pattern development, vastly increasing the scientific and technological applications.

11.2.2 Potential applications and future prospects

Many of the most promising potential applications and future prospects of this work pertain to the optical gain of QDs and the ability to manipulate the spatial arrangement of their emission via photopatterning.

Parity-time photonic systems are a notable example of how the combination of photopatterning and optical gain will be critical. Parity-time (PT) systems exhibit interesting properties like unidirectional invisibility, loss-induced rival of lasing, and optical isolation.[1,2,3,4] However, PT systems require periodic modulation of optical gain and loss with minimal variation in real refractive index.[5] Satisfying both criteria using traditional lithographic patterning approaches is difficult because physically patterned systems have a modulated refractive index (resulting from the addition, removal, or rearrangement of material during physical patterning). However, the combination of photopatterning and optical gain can overcome this challenge because photopatterning produces emissive contrast by intrinsically modifying the optical efficiency of the QD film in specific regions. In order words, photopatterning imparts an emissive intensity contrast (gain/loss modulation) without physically patterning the film surface (minimal modulation of the real refractive index). Thus photopatterning combined with optical gain satisfies both criteria required in PT systems. For example, a photopattern of dark and bright periodic lines could act as the pump source for an adjacent gain layer.

More complex PT systems involve a combination of photopatterning with physical patterning. Generally this type of PT system is composed of a physically patterned photonic cavity (disk or ring) that has periodic gain/loss regions. These optical gain/loss Janus structures could be composed of light sensitive core/shell QDs and fabricated

using one of the common microscale patterning techniques (EBL, photolithography, soft-lithography). Once the physical disk or ring cavity was present, the periodic gain/loss regions could be produced by photopatterning the structure (selectively activating or deactivating the PL of targeted areas within the structure). A similar process could be implemented to fabricate waveguides with periodic gain/loss regions.

Some of the most interesting types of PT systems involve coupling interactions between physical gain/loss structures. A common example is two closely spaced optical cavities (disk-disk dimer) where one disk exhibits optical gain while the other exhibits optical loss. If the PT requirements are met, then asymmetric energy transfer can occur or enhanced single-mode lasing.[6,7] However, meeting the PT requirement is difficult because it depends on the coupling strength between structures (spacing, refractive index) and their gain/loss contrast.[6,7] In addition, disks with defects/notches can focus emission in a specific direction which can promote or hinder coupling.[8]

Clearly, there is a rich set of technical challenges and scientific investigations that can be explored. Briefly, one of the primary technical obstacles facing the integration of physical patterning with photopatterning is the alignment of the photomask with the physical structures since the photopatterned gain/loss regions need to adhere to strict spatial modulation within the physical structure. This could be approached using techniques developed in the semiconductor industry to pattern integrated circuits using multiple exposure cycles.

Other applications for photopatterning include systems for light sensors, lighting, and display technologies where precise control over emission strength for specific colors is important. For example, multicolor photopatterning could be used to pattern the red,

green, and blue pixels in QD displays, circumventing the current fabrication approaches that require the deposition of each individual color. In addition, multi-exposure multicolor photopatterning could be used to develop exceptionally complex “multi-layered photopatterns” for applications as anti-counterfeiting labels. In this case, each layer of the photopattern would be a pattern composed of a specific color (or colors). The ability to tune the QD color during synthesis makes possible very unique color profiles. Furthermore, each layer could be activated using a specific excitation, adding in additional complexity. The combination of multiple photopattern “layers” that have a unique color and require a specific excitation wavelength all would be very difficult to replicate.

11.3 General acknowledgements

Financial support for this work was provided by a number of sources and was gratefully appreciated. Financial support for the research involving plasmonic nanoscale systems is acknowledged from the DARPA/US Army W31P4Q10C0027 grant through EngeniusMicro, and from the U.S. Department of Energy, Office of Basic Energy Sciences, Division of Materials Sciences and Engineering, under Award DE-FG02-09ER46604. Financial support for the research on quantum dots is acknowledged from the Air Force Office of Scientific Research FA9550-14-1-0037 (Synthetic Photonics Multidisciplinary University Research Initiative).

Much of the work outlined in this thesis was done in collaboration with other research groups at the Georgia Institute of Technology and universities around the United States.

Professor El-Sayed's research group (Georgia Institute of Technology): Plasmonic colloidal AgNC synthesis (Dr. M.A. Mahmoud) and the fabricated of stacked AuNR via EBL (Dr. R. Near).

Professor Z. Lin's research group (Georgia Institute of Technology): QD synthesis, ligand exchange, and TEM (Dr. J. Jung and Y.J. Yoon).

Professor Vardeny's research group (University of Utah): Pulsed laser optical gain (VSL) and loss measurements (Dr. E. Lafalce).

Professor Thomas' group (Rice University): Laser interference lithography photopatterning (Dr. T. Ramathasan and Dr. G. Liang).

Professor Dong Qin (Georgia Institute of Technology): assisting in the fabrication of the patterned PDMS photomasks and providing the master Cr-on-quartz master pattern.

11.4 Dissemination of work

This work has resulted in 14 scientific publications (2 in progress, 1 recently submitted), 3 oral presentations, 7 poster presentations (3 poster awards), and one provisional patent.

11.4.1 Publications

First author

1. **Malak, S.T.**; Smith, M.J.; Yoon, Y.J.; Lin, C.H.; Jung, J.; Lin, Z.; Tsukruk, V.V., Programmed Emission Transformations: Negative-to-Positive Patterning Using the Decay-to-Recovery Behavior of Quantum Dots. *Adv. Opt. Mater.* **2016,** *in print.*

2. **Malak, S.T.**; Jung, J.; Yoon, Y.J.; Smith, M.J.; Lin, C.H.; Lin, Z.; Tsukruk, V.V., Large-Area Multicolor Emissive Patterns of Quantum Dot–Polymer Films via Targeted Recovery of Emission Signature. *Adv. Opt. Mater.* **2016,** *4,* 608-619.

3. **Malak, S.T.**; Lafalce, E.; Jung, J.; Lin, C.H.; Smith, M.J.; Yoon, Y.J.; Lin, Z.; Vardeny, Z.V.; Tsukruk, V.V., Enhancement of optical gain characteristics of quantum dot films by optimization of organic ligands. *J. Mater. Chem. C* **2016,** *4,* 10069-10081.

4. **Malak, S.T.**; König, T.; Near, R.; Combs, Z.A.; El-Sayed, M.A.; Tsukruk, V.V., Stacked Gold Nanorectangles with Higher Order Plasmonic Modes and Top-Down Plasmonic Coupling. *J. Phys. Chem.* C **2014,** *118,* 5453-5462.

5. **Malak, S.T.**; Yoon, Y.J.; Smith, M.J.; Lin, C.H.; Jung, J.; Lin, Z.; Tsukruk, V.V., Decay-to-recovery behavior and controllable on-off recovery of emission: the importance of the quantum dot composition profile, *in preparation.*

6. **Malak, S.T.**; Ramathasan, T.; Liang, G.; Yoon, Y.J.; Smith, M.J.; Lin, C.H.; Lin, Z.; Thomas, E.L.; Tsukruk, V.V., Large-area high-resolution high-throughput quantum dot edge-profile and face-profile photopatterning approaches, *in preparation.*

Co-first author

7. Kodiyath, R.; **Malak, S.T.**; Combs, Z.A.; Koenig, T.; Mahmoud, M. A.; El-Sayed, M.A.; Tsukruk, V.V., Assemblies of silver nanocubes for highly sensitive SERS chemical vapor detection. *J. Mater. Chem. A* **2013,** *1,* 2777-2788. *(Front Cover Article)*

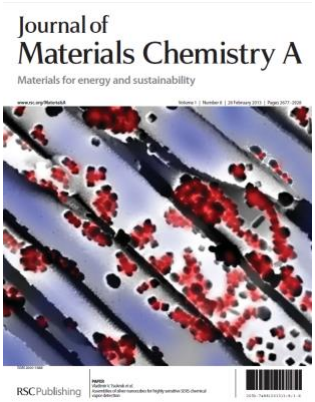

Co-author

8. Lin, C.H.; Zeng, Q.; Lafalce, E.; Smith, M.J.; **Malak, S.T.;** Jung, J.; Yoon, Y.J.; Lin, Z.; Vardeny, Z.V.; Tsukruk, V.V., Large-Scale Robust Quantum Dot Microdisk Lasers with Controlled High Quality Cavity Modes for Parity-Time Arrays. *Nano Lett.,* **submitted.**

9. Jung, J.; Lin, C.H.; Yoon, Y.J.; **Malak, S.T.**; Zhai, Y.; Thomas, E.L.; Vardeny, V.; Tsukruk, V.V.; Lin, Z., Crafting Core/Graded Shell–Shell Quantum Dots with Suppressed Re-absorption and Tunable Stokes Shift as High Optical Gain Materials. *Angewandte Chemie International Ed.* **2016,** *55,* 5071-5075. (*Designated very important paper)*

10. Lin, C.H.; Lafalce, E.; Jung, J.; Smith, M.J.; **Malak, S.T.**; Aryal, S.; Yoon, Y.J.; Zhai, Y.; Lin, Z.; Vardeny, Z. V.; Tsukruk, V. V., Core/Alloyed-Shell Quantum Dot Robust Solid Films with High Optical Gains. *ACS Photonics* **2016,** *3,* 647-658.

11. Ye, C.; **Malak, S.T.**; Hu, K.; Wu, W.; Tsukruk, V.V., Cellulose Nanocrystal Microcapsules as Tunable Cages for Nano- and Microparticles. *ACS Nano* **2015,** *9,* 10887-10895.

12. Combs, Z.A.; **Malak, S.T.**; König, T.; Mahmoud, M.A.; Chávez, J.L.; El-Sayed, M.A.; Kelley-Loughnane, N.; Tsukruk, V.V., Aptamer-Assisted Assembly of Gold Nanoframe Dimers. *Particle & Particle Sys. Characterization* **2013,** *30,* 1071-1078.

13. Choi, I.; **Malak, S.T.**; Xu, W.; Heller, W.T.; Tsitsilianis, C.; Tsukruk, V.V., Multicompartmental Microcapsules from Star Copolymer Micelles. *Macromolecules* **2013,** *46,* 1425-1436.

14. Wallet, B.; Kharlampieva, E.; Campbell-Proszowska, K.; Kozlovskaya, V.; **Malak, S.**; Ankner, J.F.; Kaplan, D.L.; Tsukruk, V.V., Silk Layering As Studied with Neutron Reflectivity. *Langmuir* **2012,** *28,* 11481-11489.

11.4.2 Presentations

Oral

1. **Malak, S.;** Lin, C.H.; Ledin, P.; Ye, C.; Tsukruk, V., MURI Meeting 2: GT-Tsukruk. *Multidisciplinary University Research Initiative (MURI) Summer Meeting* **2014**.

2. **Malak, S.**; Tsukuk, V.V., Engineered SERS substrates and nanostructures. *Flexible SERS Substrates Workshop (Washington University in St. Louis, St. Louis)* **2014**.

3. **Malak, S.T.**; Kodiyath, R.; Combs, Z.A.; Koenig, T.; Mahmoud, M.A.; El-Sayed, M.A.; Tsukruk, V.V., Trace level vapor detection of an explosive-related organic molecule by a SERS-active 3D nanoporous membrane decorated with silver nanostructures. *Materials Research Society Conference* **Fall 2012***.*

Poster

1. **Malak, S.T.**; Jung, J.; Yoon, Y.J.; Smith, M.J.; Lin, C.H.; Lin, Z.; Tsukruk, V.V., Fabricating large-area multicolored photopatterns via targeted recovery of selected QD emission peaks in mixed QD films. *Materials Research Society Conference* **Spring 2016***.*

2. **Malak, S.T.**; Smith, M.; Yoon, Y.J.; Lin, Z.; Tsukruk, V.V., Positive/negative photopatterning: Utilizing the decay-to-recovery of quantum dot emission to control the development process. *Materials Research Society Conference* **Spring 2016***.*

3. **Malak, S.T.**; Jung, J.; Yoon, Y.J.; Lin, C.H.; Lin, Z.; Tsukruk, V.V., Tuning chromaticity via emission decay in quantum dot films: A route toward white light emission. *Georgia Tech, Materials Science & Engineering Competition* **2015***.*

4. **Malak, S.T.**; König, T.; Near, R.; Combs, Z.A.; El-Sayed, M.A.; Tsukruk, V.V., Route toward stacked nanostructures, higher order plasmonic resonances, and localized SERS detection sites. *Georgia Tech, Materials Science & Engineering Competition* **2014***.*

5. **Malak, S.T.**; König, T.; Near, R.; Combs, Z.A.; El-Sayed, M.A.; Tsukruk, V.V., Route toward stacked nanostructures, higher order plasmonic resonances, and localized SERS detection sites. *Materials Research Society Conference* **Fall 2013***.*

6. Ye, C.; Wallet, B.; **Malak, S.T.**; Ankner, J.F.; Kaplan, D.L.; Tsukruk, V.V., Investigation of the layered structure of ultrathin silk films and modified silk microcapsules using neutrons. *Materials Research Society Conference* **Fall 2012**.

7. Kodiyath, R.; **Malak, S.**; Combs, Z.; Koenig, T.; Mahmoud, M.A.; El-Sayed, M.A.; Tsukruk, V.V., Silver Nanocube Aggregates for Extremely Sensitive SERS Vapor Detection. *Georgia Tech, Materials Science & Engineering Competition* **2012***.*

11.4.3 Intellectual property

Provisional patent application

1. **Malak, S.T.**; Tsukruk, V.V., High-resolution color displays via selective photopatterning of mixed quantum dot films. *United States Patent Office* **2016,** *serial # 62412312.*

11.4.4 Fellowships and awards

1. Grover Mohan Fellowship *(Georgia Tech),* **2016 & 2014.**
2. Best in show & first place poster *(Georgia Tech MSE poster session, nanotechnology section),* **2016.**

3. Third place poster *(Georgia Tech MSE poster session, nanotechnology section),* **2015.**

11.5 References (Chapter 11)

1 Regensburger, A.; Bersch, C.; Miri, M.A.; Onishchukov, G.; Christodoulides, D.N.; Peschel, U., Parity-time synthetic photonic lattices. *Nature* **2012,** *488,* 167-171.

2 Lin, Z.; Ramezani, H.; Eichelkraut, T.; Kottos, T.; Cao, H.; Christodoulides, D.N., Unidirectional invisibility induced by PT-symmetric periodic structures. *Phys. Rev. Lett.* **2011,** *106,* 213901.

3 Ramezani, H.; Kottos, T.; El-Ganainy, R.; Christodoulides, D.N., Unidirectional nonlinear PT-symmetric optical structures. *Phys. Rev. A* **2010,** *82,* 043803.

4 Peng, B.; Ozdemir, S.K.; Rotter, S.; Yilmaz, H.; Liertzer, M.; Monifi, F.; Bender, C.M.; Nori, F.; Yang, L., Loss-induced suppression and revival of lasing. *Science* **2014,** *346,* 328-332.

5 Makris, K.G.; El-Ganainy, R.; Christodoulides, D.N.; Musslimani, Z.H., Beam dynamics in PT symmetric optical lattices. *Phys. Rev. Lett.* **2008,** *100,* 103904.

6 Chang, L.; Jiang, X.S.; Hua, S.Y.; Yang, C.; Wen, J.M.; Jiang, L.; Li, G.Y.; Wang, G.Z.; Xiao, M., Parity-time symmetry and variable optical isolation in active-passive-coupled microresonators. *Nat. Photonics* **2014,** *8,* 524-529.

7 Hodaei, H.; Miri, M.A.; Heinrich, M.; Christodoulides, D.N.; Khajavikhan, M., Parity-time-symmetric microring lasers. *Science* **2014,** *346,* 975-978.

8 Tulek, A.; Vardeny, Z.V., Unidirectional laser emission from pi-conjugated polymer microcavities with broken symmetry. *Appl. Phys. Lett.* **2007,** *90,* 161106.

Appendix A

Chapter 4 supporting data

(STACKED GOLD NANORECTANGLES WITH HIGHER ORDER PLASMONIC MODES AND TOP-DOWN PLASMONIC COUPLING)

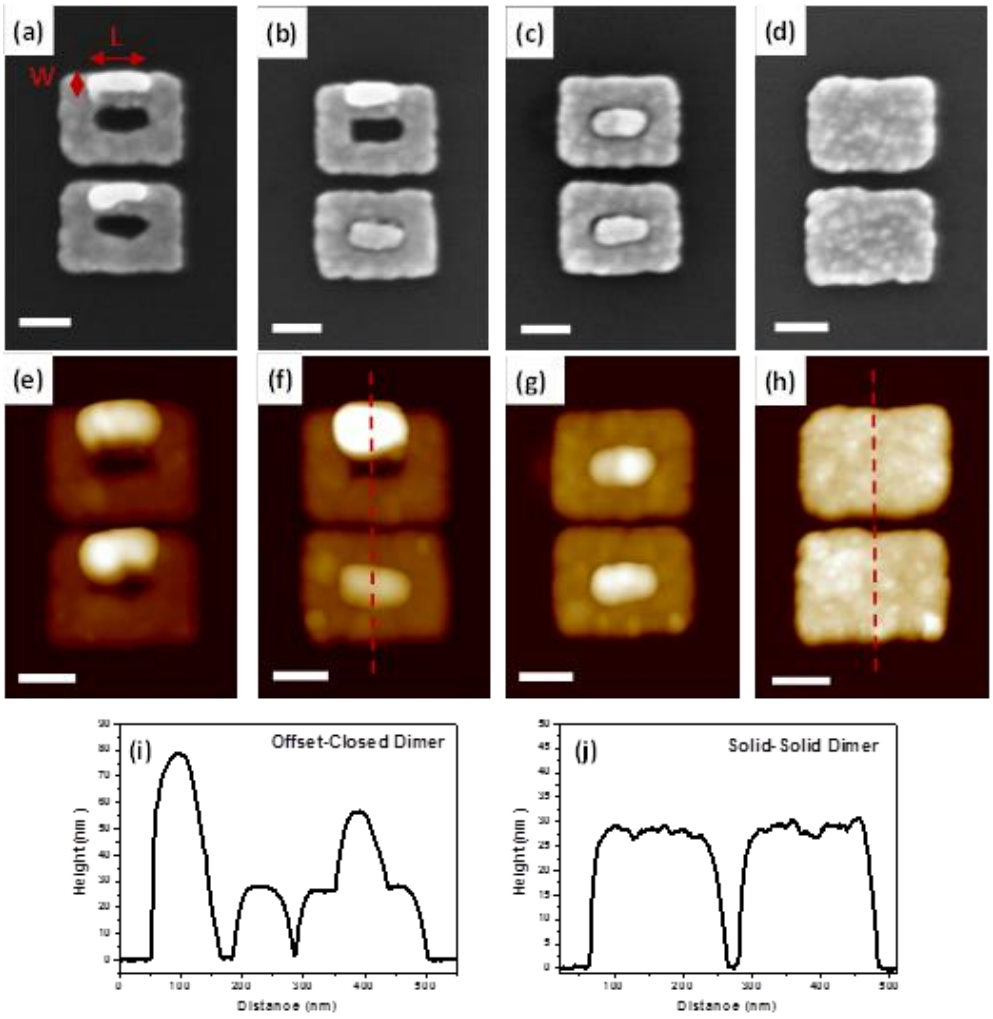

Figure A.1: SEM and AFM of the different nanostructures observed in the wide orientation EBL system demonstrating that these structures can be fabricated with small separation distances (30 ±3nm). (a,e) offset-offset (height scale, 105 nm), (b,f) offset-closed (height scale, 80 nm), (c,g) closed-closed (height scale, 70 nm), and (d,h) solid-solid (height scale 40 nm) nanorectangle dimers (scale bar = 100 nm for all images). AFM x-sections along the dimer axis for the (i) offset-open and (j) solid-solid dimers show the clear difference in height due to the residual cap and hollow core region compared to the flat top of the solid nanorectangles.

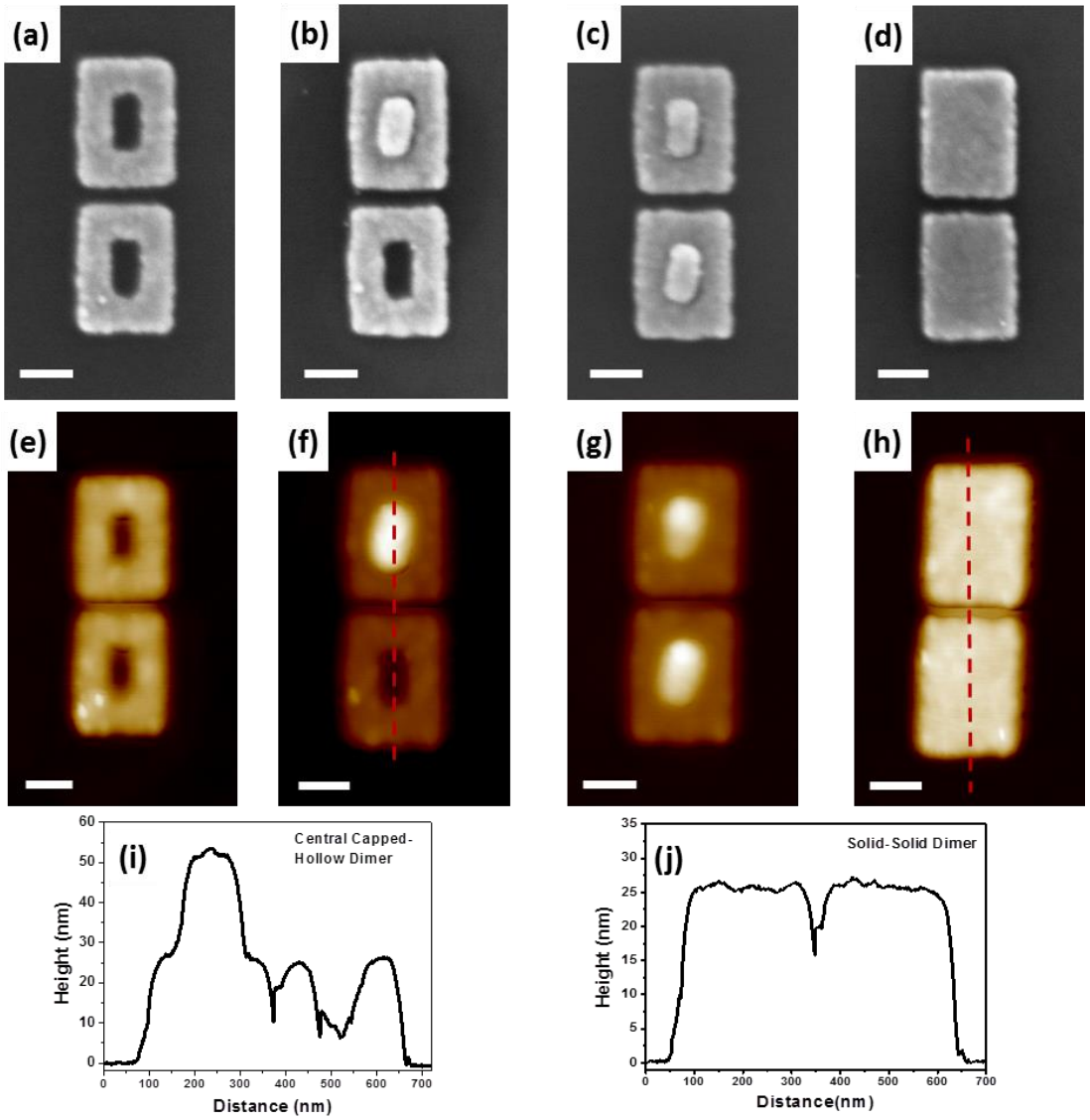

Figure A.2: SEM and AFM of the different nanostructures observed in the long orientation EBL system demonstrating that these structures can also be fabricated with small separation distances (23 ±4nm). (a,e) open-open (height scale, 40 nm), (b,f) closed-open (height scale, 60 nm), (c,g) closed-closed (height scale, 65 nm), and (d,h) solid-solid (height scale 35 nm) nanorectangle dimers (scale bar = 100 nm for all images). AFM x-sections along the dimer axis for the (i) closed-open and (j) solid-solid dimers show the clear difference in height due to the residual cap and hollow core region compared to the flat top of the solid nanorectangles.

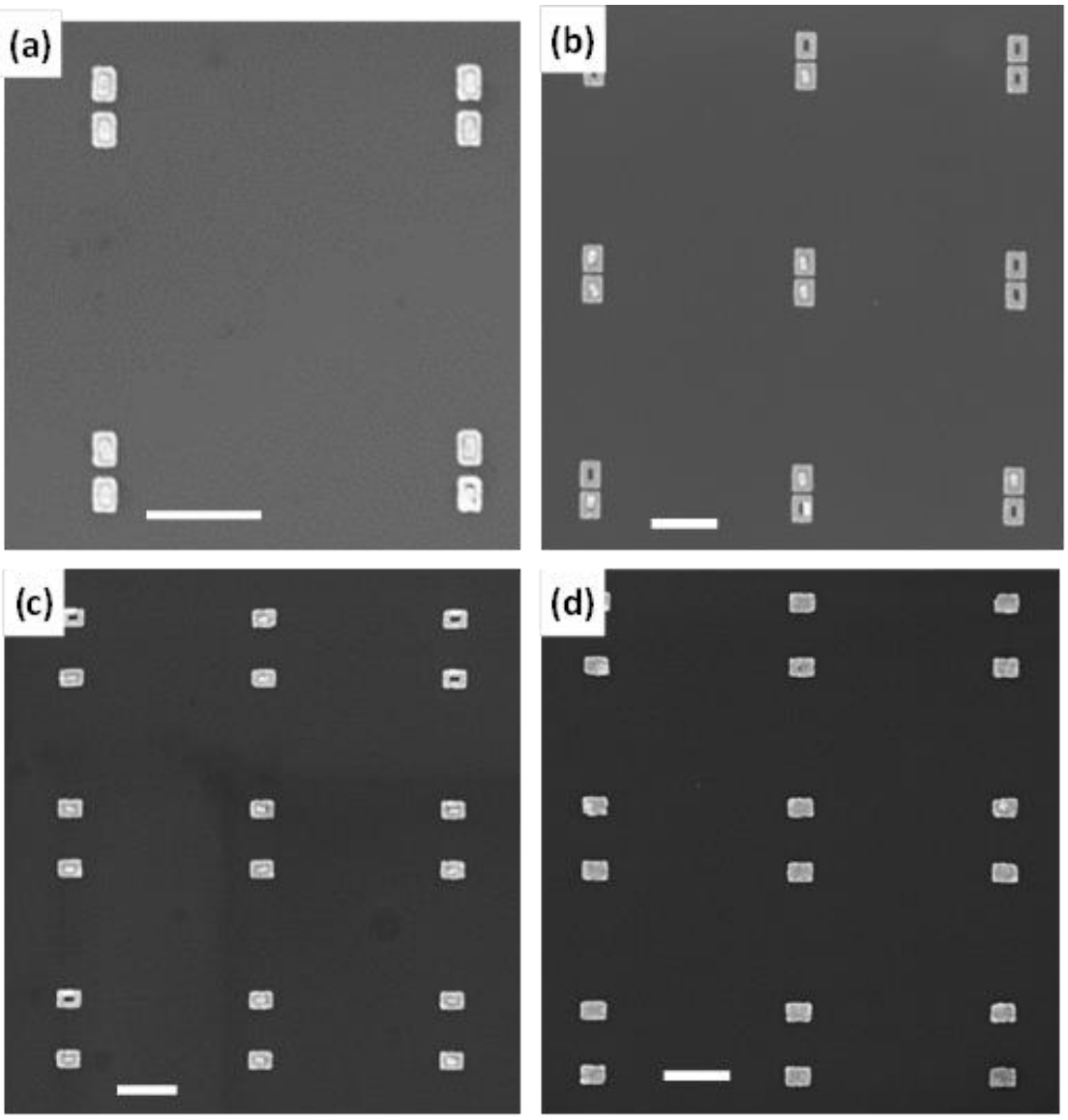

Figure A.3: HR-SEM images of various EBL arrays demonstrating the variety of nanostructures available, including: (a) large-core nanorectangles that are predominantly closed (separation distance of 47 ±3nm), (b) small-core nanorectangles (separation of 23 ±4nm) that display a larger percentage of open structures, (c) wide orientation structures (separation of 433 ±7nm), and (d) solid nanorectangles (separation of 439 ±6nm). All scale bars are 600 nm.

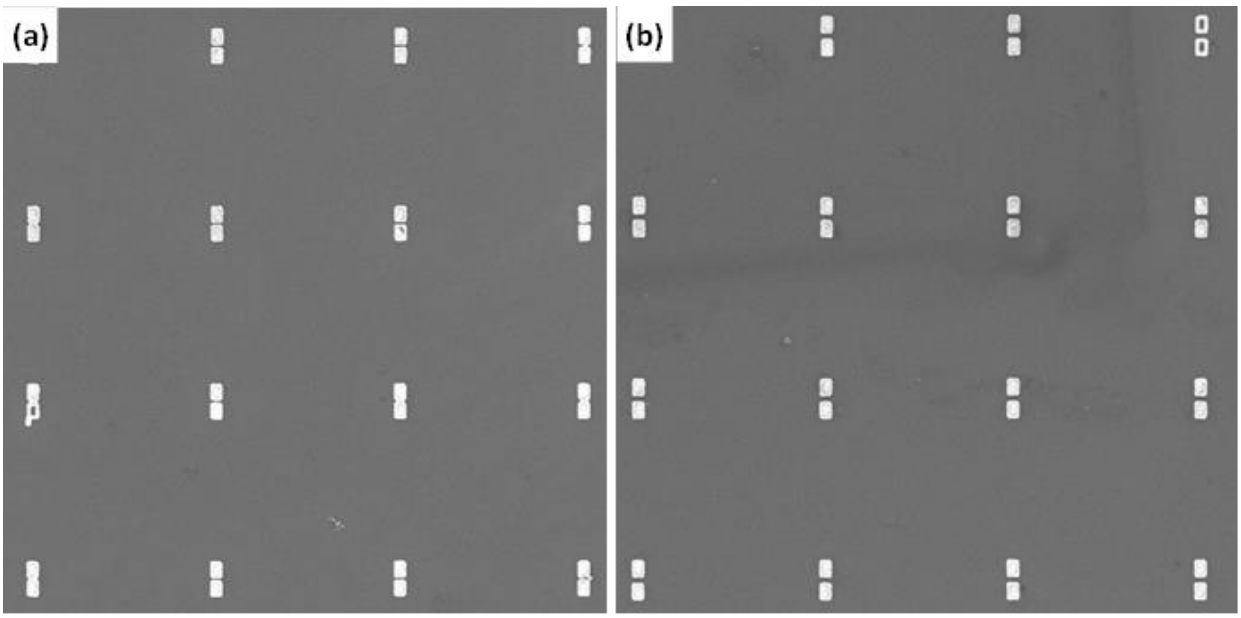

Figure A.4: (a,b) SEM of smaller nanorectangles (length 197 nm x 141 nm) and larger cores (124 nm x 71 nm) compared to those discussed in the main text. A smaller overall size and larger core tend to yield a larger percentage of closed structures than larger nanorectangles with smaller cores.

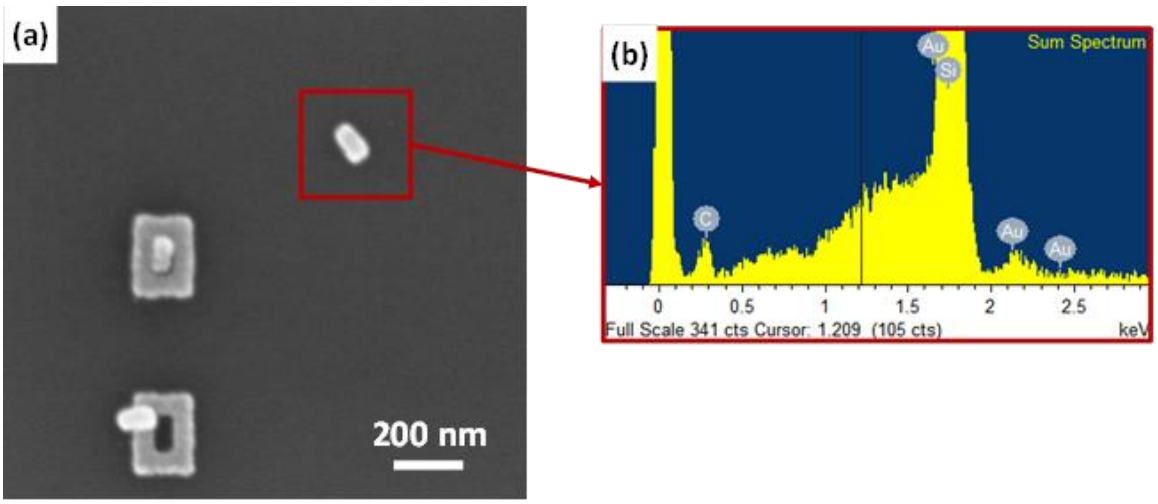

Figure A.5: (a) SEM of residual core that has been separated from its nanorectangle (not shown) with the red-box denoting the area examined with EDX. (b) The EDX results show that both carbon and Au (and Si) were identified in the region examined, suggesting that the residual core regions are composed of both polymer resist (PMMA) and Au.

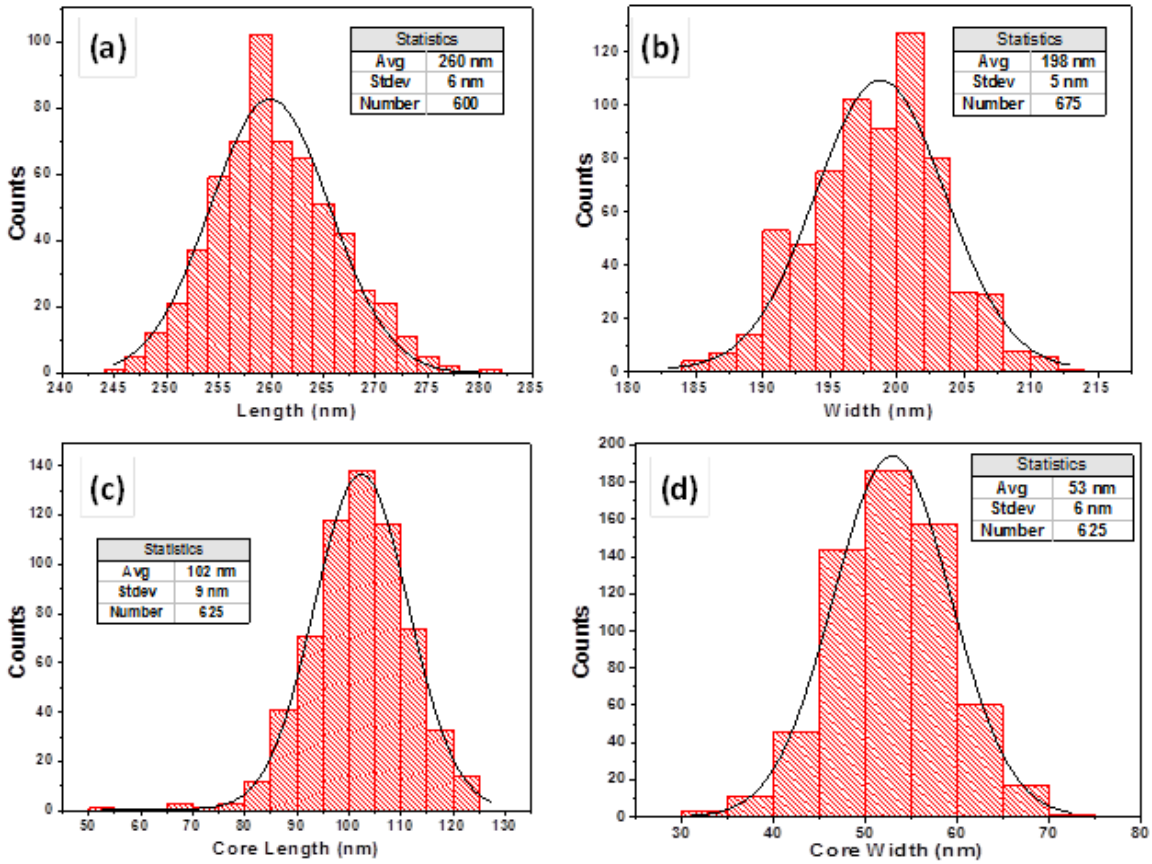

Figure A.6: Distribution of the outside (a) length and (b) width of the hollow nanorectangles and the (c) length and (d) width of their core region.

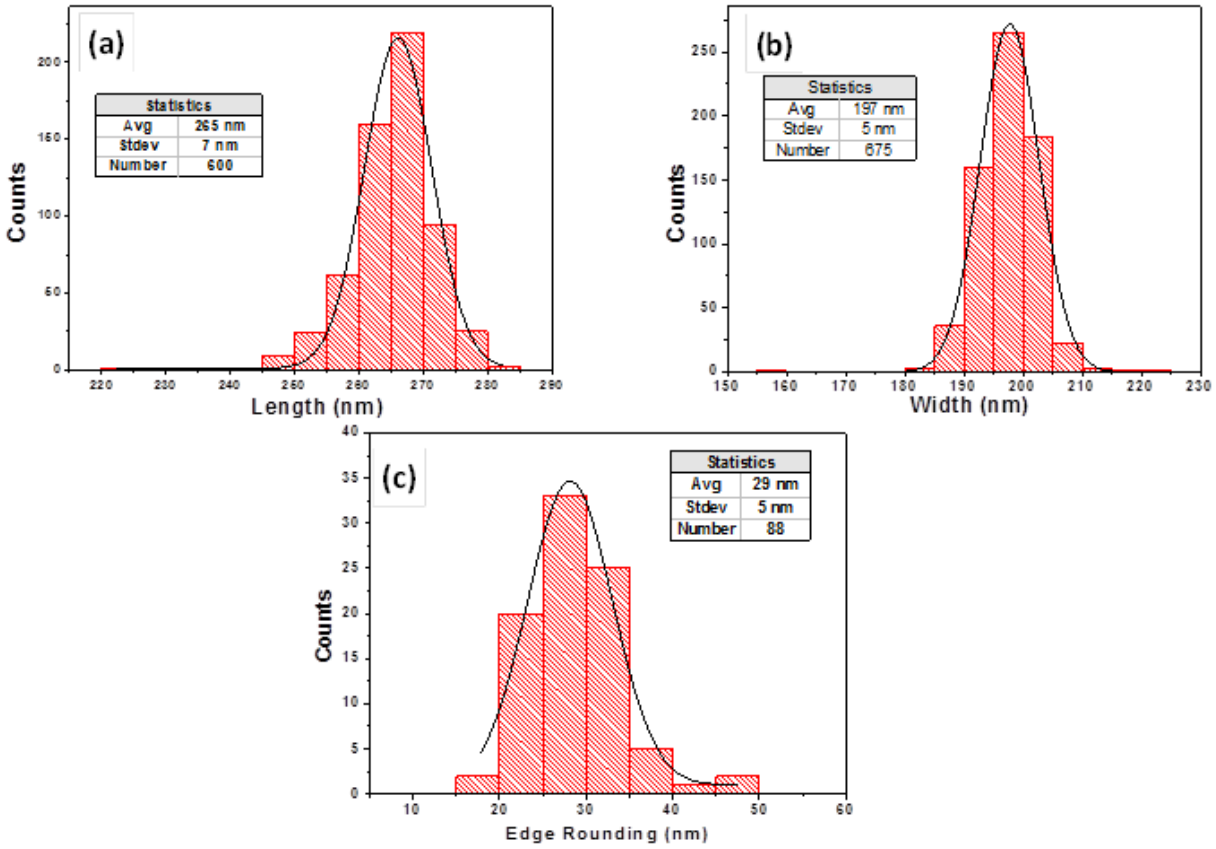

Figure A.7: Distribution of the (a) length, (b) width, and (c) edge rounding of the nanorectangles.

SERS Mapping Capabilities

The nanostructures were exposed to 10^{-5} M R6G and the characteristic peaks of R6G at 1374 cm^{-1} and 1658 cm^{-1}, which correspond to aromatic C-C stretching, were monitored across the array (**Figure A.9 and A.10**).[1,2.3] Surface maps detailing the SERS response were obtained by plotting at each position the magnitude of the area under the characteristic peaks. **Figure A.9,10** show Raman maps of an array of nanorectangles with central caps. There is a clear correspondence of the areas of higher Raman enhancement for characteristic peaks of R6G at the positions of the nanostructures in the array (**Figure A.9,10a,b**). The 520 cm^{-1} of Si was mapped to provide additional evidence that the positions with the SERS response correspond to the positions of the individual nanostructures and their pairs.

Figure A.9,10d shows average Raman spectrum ($N \geq 50$) from the position of the capped nanorectangles and of the Si wafer surface. Five additional peaks at 619, 778, 1195, 1515, and 1583 cm^{-1} can be identified that are characteristic peaks for R6G.[1] The peak near 970 cm^{-1} is attributed to an overtone of a transverse mode of Si.[4] There is a clear Raman signature of R6G at the position of the nanostructures and no response at positions away from the nanostructures, in agreement with the Raman maps.

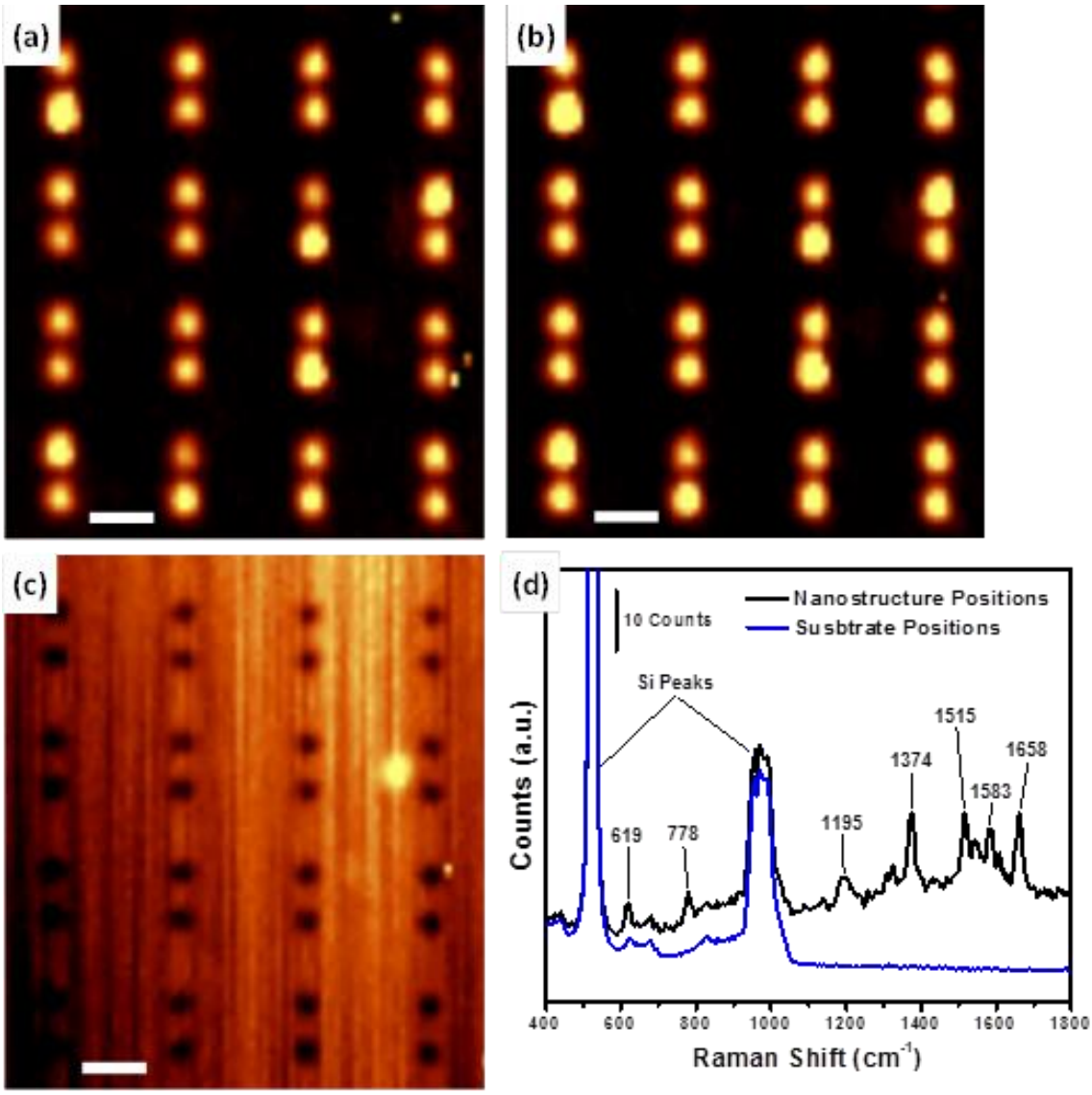

Figure A.8: Raman mapping of an array of capped nanorectangles exposed to R6G. The The (a) 1374 cm^{-1} and (b) 1658 cm^{-1} peaks of R6G and the (c) 520 cm^{-1} peak of Si were monitored. A brighter color indicates an area of stronger Raman response for the respective peak. (d) The Raman response from the positions of the nanostructures (black (black curve) and the Si substrate regions (blue curve), showing a clear presence of R6G only at the nanostructure positions. The nanostructures have a length 239 ±8nm, width 169 ±6nm, and edge-edge interparticle spacing 550 ±9nm. The color scale for (a) and (b) is 150 counts and for (c) is 500. All spatial scale bars are 1.0 μm.

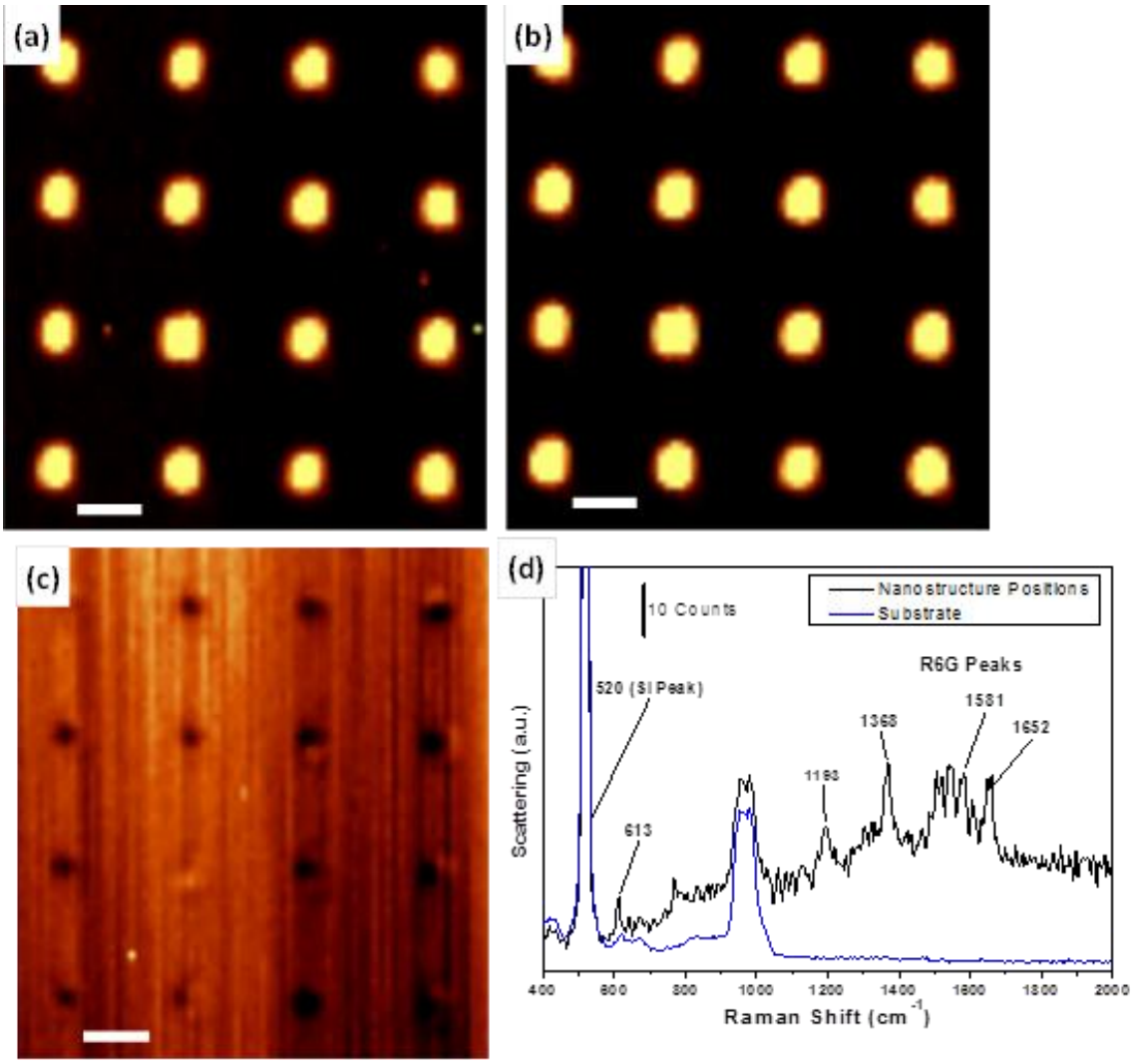

Figure A.9: Raman mapping of an array of capped nanorectangles exposed to 10^{-5} M R6G. The (a) 1374 cm^{-1} and (b) 1658 cm^{-1} peaks of R6G and the (c) 520 cm^{-1} peak of Si were monitored. A more yellow color indicates an area of stronger Raman response for the respective peak. (d) The Raman response from the positions of the nanostructures (blue curve) and the Si substrate regions (black curve), showing a clear presence of R6G only at the nanostructure positions. The nanostructures have a length of 192 ±6nm, width of 133 ±5nm, and edge-edge interparticle spacing of 19 ±2nm. The color scale for (a) and (b) is 250 counts and for (c) is 600. All spatial scale bars 1.0 µm.

References

1 Hildebrandt, P.; Stockburger, M., Surface-enhanced resonance Raman-spectroscopy of rhodamine-6G adsorbed on colloidal silver. *J. Phys. Chem.* **1984,** *88*, 5935-5944.

2 Dieringer, J.A.; Wustholz, K.L.; Masiello, D.J.; Camden, J.P.; Kleinman, S.L.; Schatz, G.C.; Van Duyne, R.P., Surface-enhanced Raman excitation spectroscopy of a single Rhodamine 6G molecule. *J. Amer. Chem. Soc.* **2009,** *131*, 849-854.

3 Michaels, A.M.; Jiang, J.; Brus, L., Ag nanocrystal junctions as the site for surface-enhanced Raman scattering of single Rhodamine 6G molecules. *J. Phys. Chem. B* **2000,** *104*, 11965-11971.

4 Brodsky, M.H.; Cardona, M.; Cuomo, J.J., Infrared and Raman spectra of the silicon-hydrogen bonds in amorphous silicon prepared by glow discharge and sputtering. *Phys. Rev. B* **1977,** *16,* 3556-3571.

Appendix B

Chapter 5 supporting data

(HIERARCHICAL PLASMONIC SYSTEM: CONTROLLED ASSEMBLY OF SILVER NANOCUBES IN 3D POROUS ALUMINA MEMBRANES)

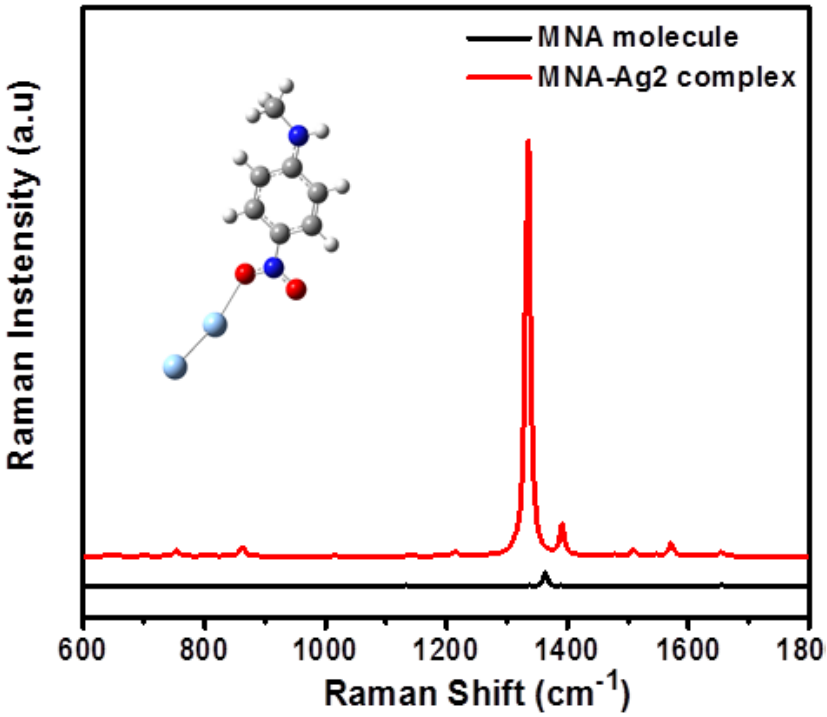

Figure B1. DFT simulation of the (black curve) MNA molecule using the quantum chemistry package Gaussian 03 by optimization at the B3LYP/6-31++G** level of theory, and (red curve) from MNA with a two atom Ag cluster (optimized at the B3LYP/LANL2DZ level of theory for the Ag atoms). The presence of Ag atoms leads to enhancement of the 865 and 1365 cm^{-1} modes. The inset represents the MNA-Ag atom cluster used to determine the SERS response of MNA.

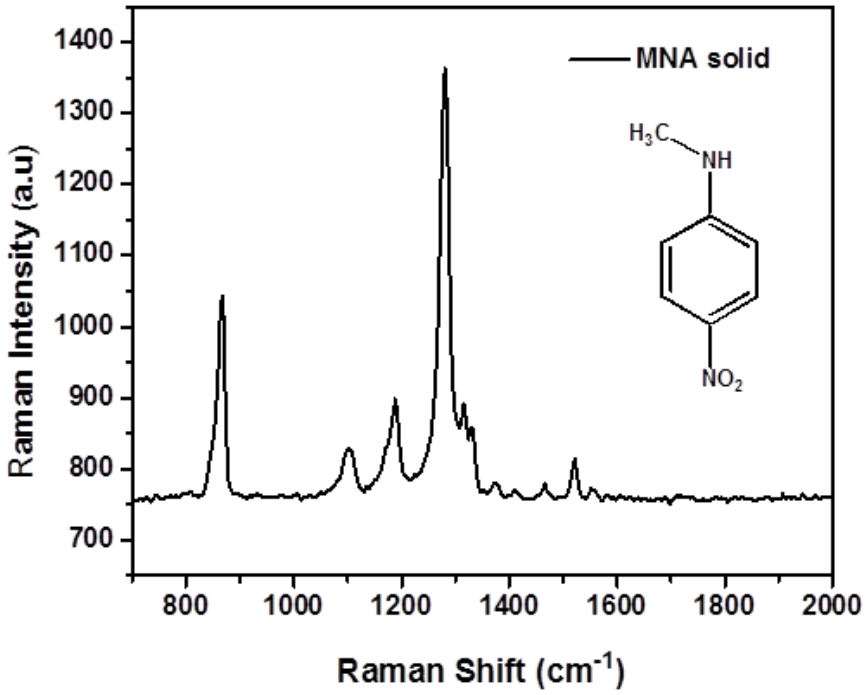

Figure B2. Raman spectrum of solid n-methyl-4-nitroaniline (MNA) and (inset) chemical structure of MNA.

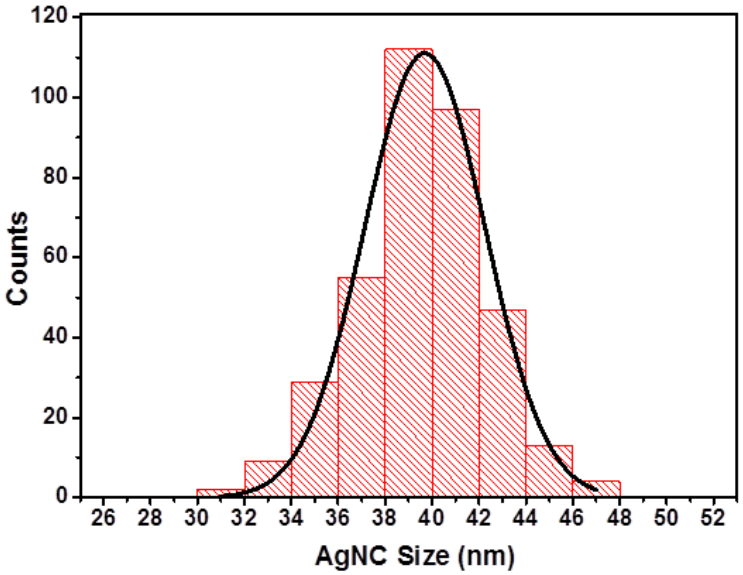

Figure B3. Size distribution of 40 nm AgNC, synthesized using the polyol method, determined by TEM (more than 350 AgNC were measured). A Gaussian fit was applied in order to determine the average value and the standard deviation.

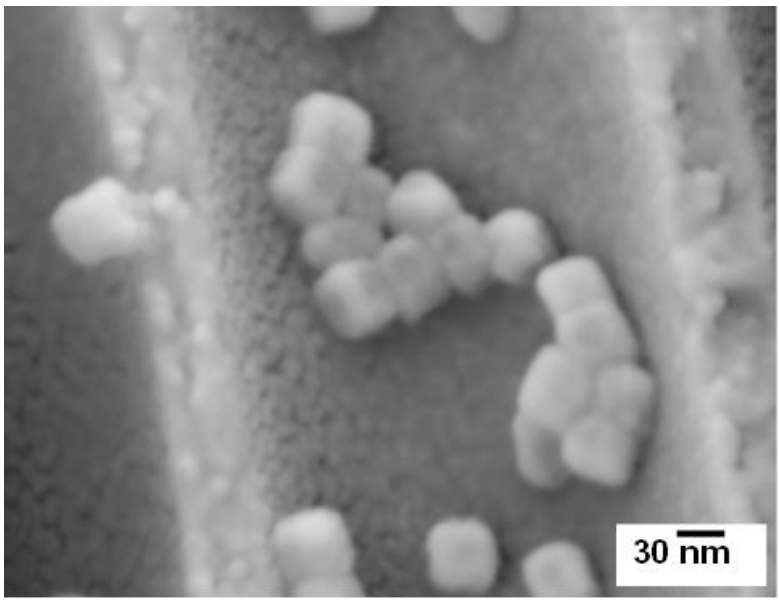

Figure B4. Magnified SEM micrograph of AgNC aggregate in an AgNC-PAH substrate, showing that the majority of AgNC in the aggregate take a face-face orientation to adjacent cubes.

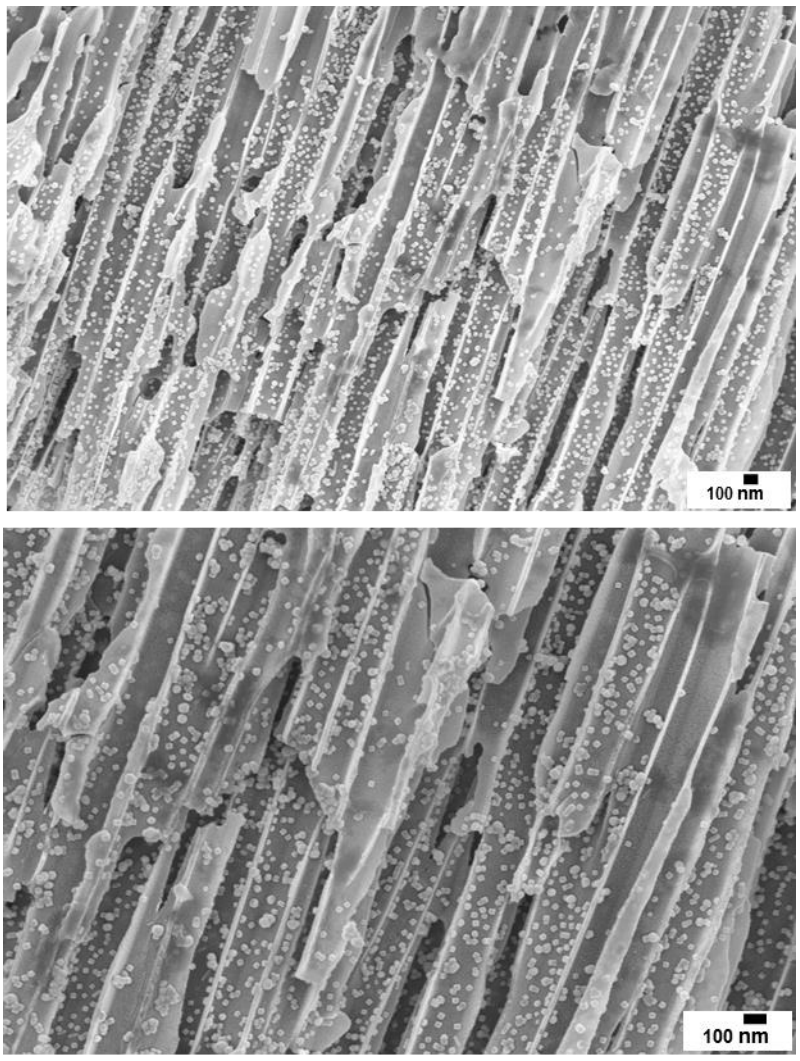

Figure B5. The more dispersed AgNC adsorption behavior that occurs when 2.5 (PAH-PSS) bilayers are spin-coated onto the PAM (instead of the single PAH or PEI used in the other AgNC substrates). There are a large number of AgNC present within the pores, primarily present as individual or small aggregates (on the average). The majority of the particles are located within 5-6 microns from the PAM surface.

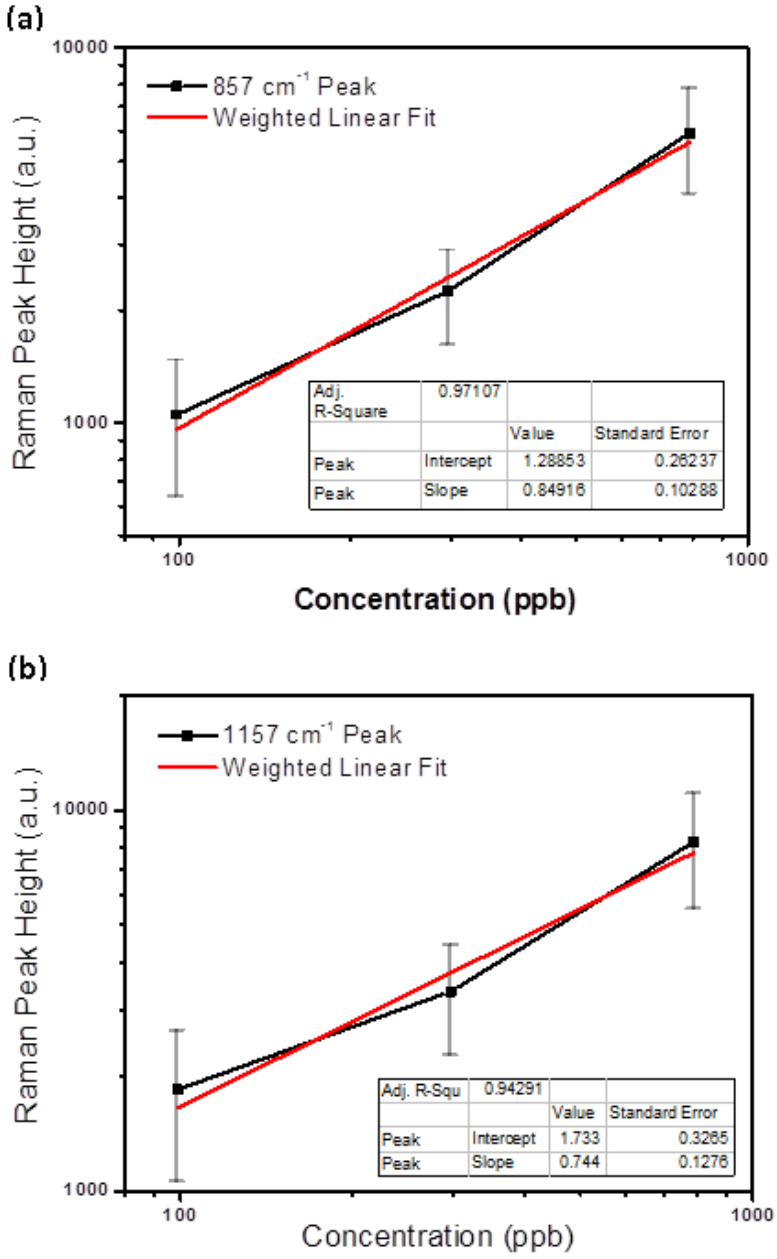

Figure B6. The instrumental error weighted linear fit for the (a) 857 cm^{-1} and (b) 1157 cm^{-1} MNA peak using the AgNC-(PAH-PSS) substrate, demonstrating the linear response of the substrate at higher ppb concentrations. The weighting (w_i) is inversely proportional to the standard deviation (σ_i) of the data point ($w_i = 1/(\sigma_i)^2$).

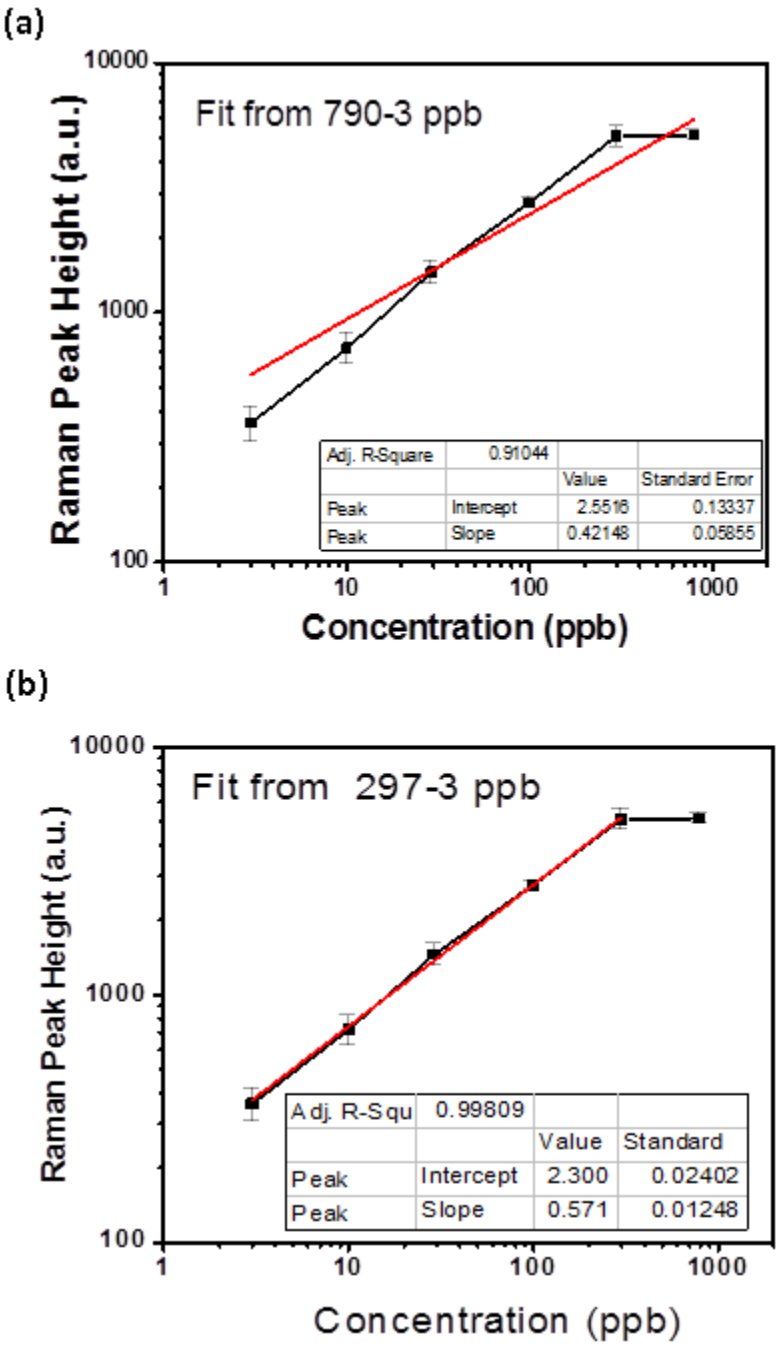

Figure B7. The instrumental error weighted linear fit for the 857 cm^{-1} MNA peak using the AgNC-PAH substrate, where the weighting (w_i) is inversely proportional to the standard deviation (σ_i) of the data point ($w_i = 1/(\sigma_i)^2$). The R-squared value improves significantly when the fit is applied to the (a) 297-3 ppb range compared to the fit (b) from 790-3 ppb.

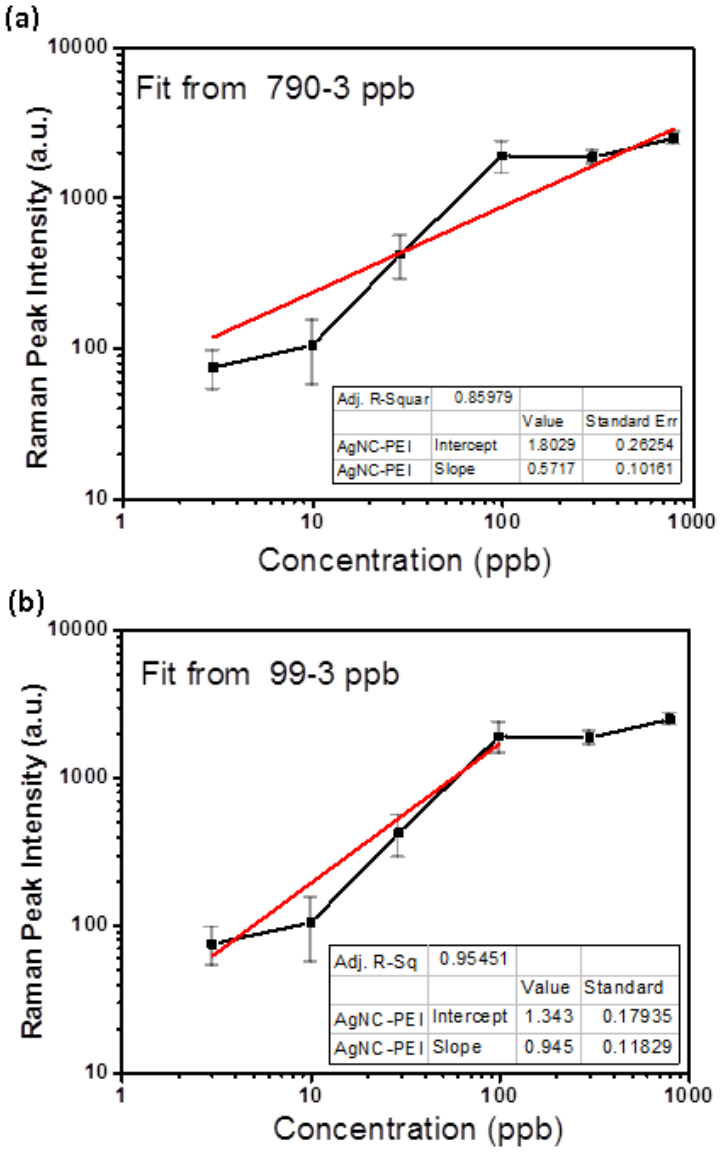

Figure B8. The instrumental error weighted linear fit for the 857 cm^{-1} MNA peak using the AgNC-PEI substrate, where the weighting (w_i) is inversely proportional to the standard deviation (σ_i) of the data point ($w_i = 1/(\sigma_i)^2$). The R-squared value improves significantly when the fit is applied to the (a) 99-3 ppb range compared to the fit (b) from 790-3 ppb.

Calculation of MNA vapor concentration:

The vapor concentration of MNA (in ppb) was calculated using theoretical estimations of the vapor pressure of MNA over a temperature range of 270K to 400K (or -3°C to 127°C). The vapor pressure of MNA at various temperatures is approximately[i]:

5.0°C (278 K): P ~ 0.0003

15 °C (288 K): P ~ 0.001 Pa

25 °C (298 K): P ~ 0.003 Pa

35 °C (308 K): P ~ 0.01 Pa

45 °C (318 K): P ~ 0.03 Pa

55 °C (328 K): P ~ 0.08 Pa

The vapor concentration (in ppb) was determined using the typical method found in the literature, shown below:

$$C\ (ppb) = \frac{p_{MNA}}{P_{Tot}} * 10^9$$

Where C (ppb) is the concentration in parts per billion, P_{MNA} is the partial pressure of MNA at a specific temperature, and P_{Tot} is the total pressure of the system. This calculation assumes ideal gas conditions so that a ratio between pressures can be related to a ratio between molar values

$$(\frac{P_i}{P_{Tot}} = \frac{n_i}{n_{Tot}}).$$

In reality the vapor pressures we are reporting are likely higher than those actually present because the theoretical estimations for vapor pressure have been found to be consistently higher than experimental values, so the MNA values reported are likely overestimating the vapor pressure of MNA (and hence its concentration). In some instances this can be found to overestimate the vapor pressure by two to three orders of magnitude.[i]

The molar concentration can be obtained from the vapor pressure through the ideal gas law (appropriate given the low pressures and temperatures involved).

$$C = \frac{n_i}{V} = \frac{P_i}{R\,T} \quad \text{(R = 8.31 J/K*mol)}$$

5.0°C (278 K), P ~ 0.0003 → C = $1.38*10^{-7}$ moles/m^3 = $1.38*10^{-10}$ moles/L

15 °C (288 K), P ~ 0.001 Pa → C = $4.28*10^{-7}$ moles/m^3 = $4.28*10^{-10}$ moles/L

25 °C (298 K), P ~ 0.003 Pa → C = $1.21*10^{-6}$ moles/m^3 = $1.21*10^{-9}$ moles/L

35 °C (308 K), P ~ 0.01 Pa → C = $3.91*10^{-6}$ moles/m^3 = $3.91*10^{-9}$ moles/L

45 °C (318 K), P ~ 0.03 Pa → C = $1.14*10^{-5}$ moles/m^3 = $1.14*10^{-8}$ moles/L

55 °C (328 K), P ~ 0.08 Pa → C = $2.94*10^{-5}$ moles/m^3 = $2.94*10^{-8}$ moles/L

References

1 Toghiani, R.K.; Toghiani, H.; Maloney, S.W.; Boddu, V.M., Energetic materials: Thermophysical properties, predictions, and experimental measurements. Research and development. *Taylor and Francis Group LLC.* **2011***. Pages 171-195.*

Appendix C

Chapter 6 supporting data

(HOW QUANTUM DOT ARCHITECTURE AFFECTS THE EVOLUTION OF EMISSION: DECAY, RECOVERY, AND DECAY-TO-RECOVERY BEHAVIOR)

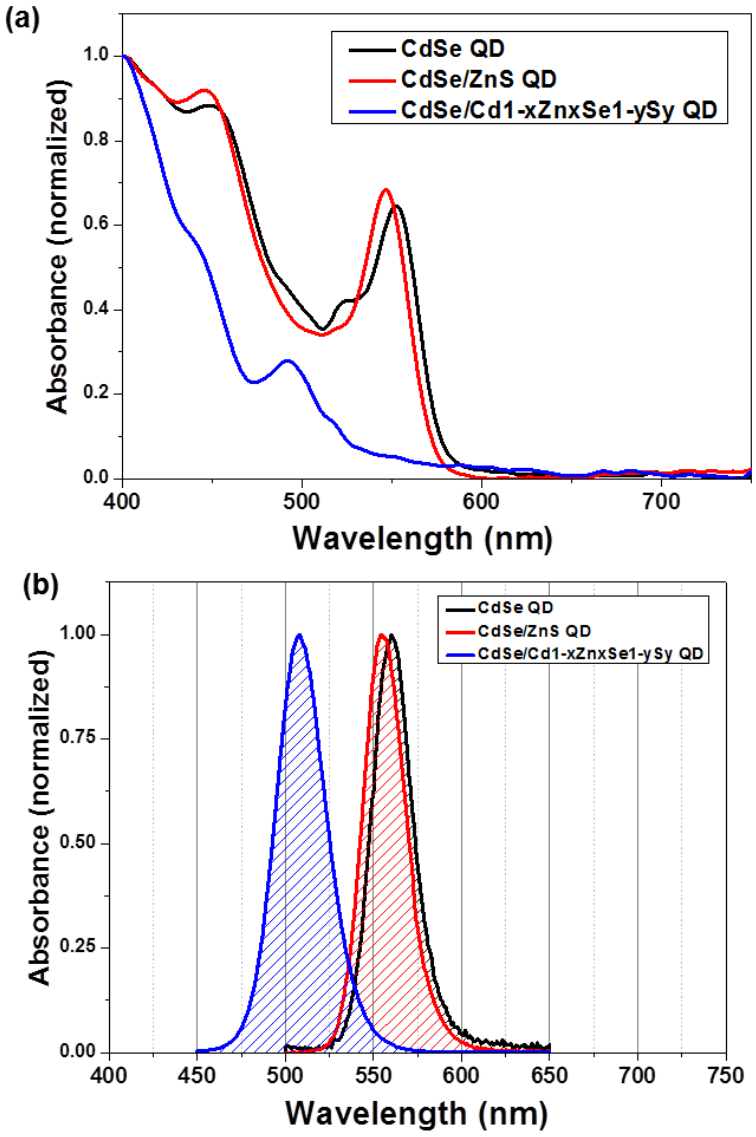

Figure C.1: UV-vis absorbance and photoluminescence of each type of QD design (core CdSe QD, core/shell CdSe/ZnS QD, and core/graded shell CdSe/$Cd_{1-x}Zn_xSe_{1-y}S_y$ QD).

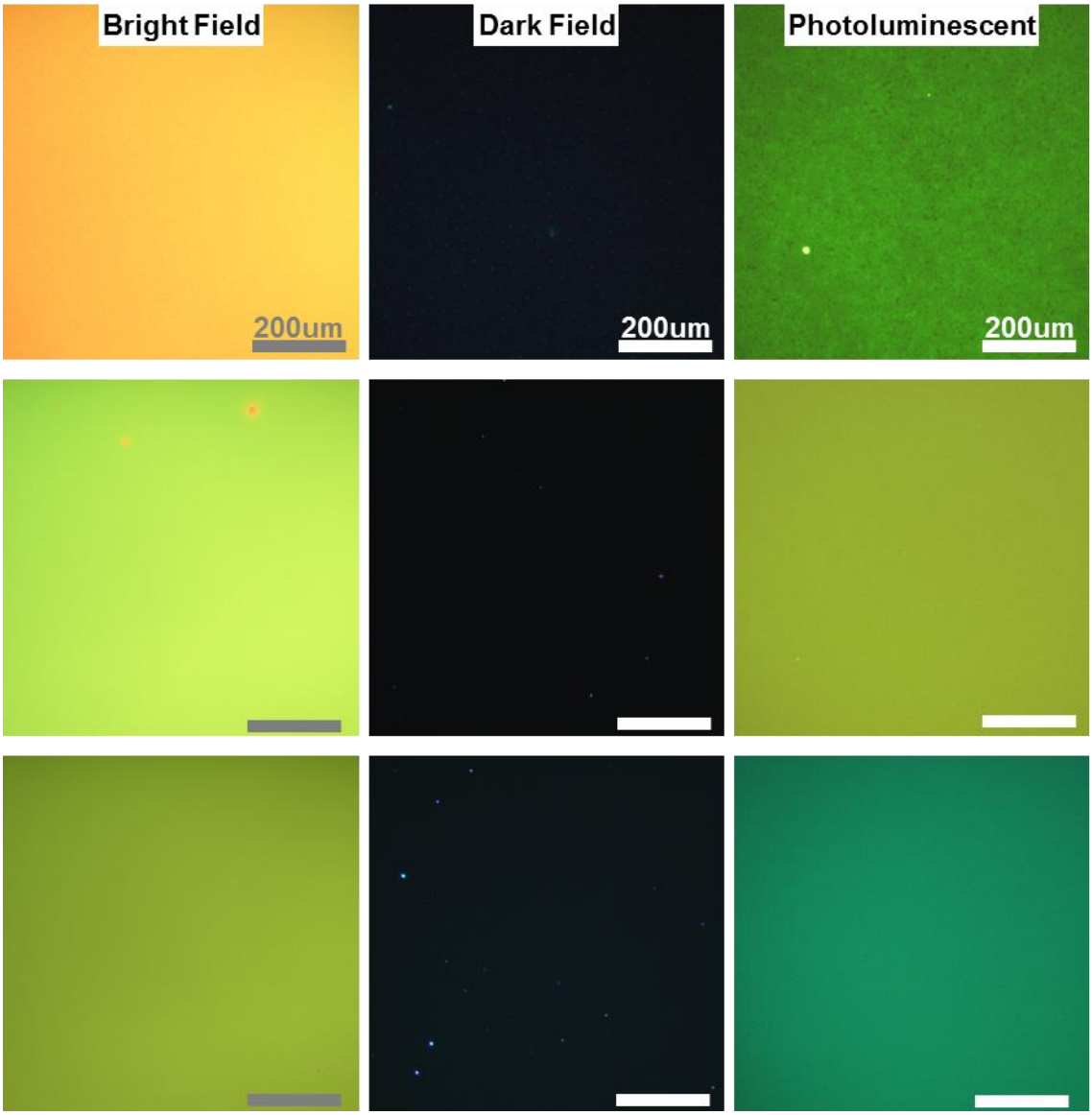

Figure C.2: Bright field (column 1), dark field (column 2), and photoluminescence (column 3) imaging of QD-PMMA films with each type of QD design (core CdSe QD, row 1)(core/shell CdSe/ZnS QD, row 2) (core/graded shell CdSe/$Cd_{1-x}Zn_xSe_{1-y}S_y$ QD, row 3). All scale bars are 200 um.

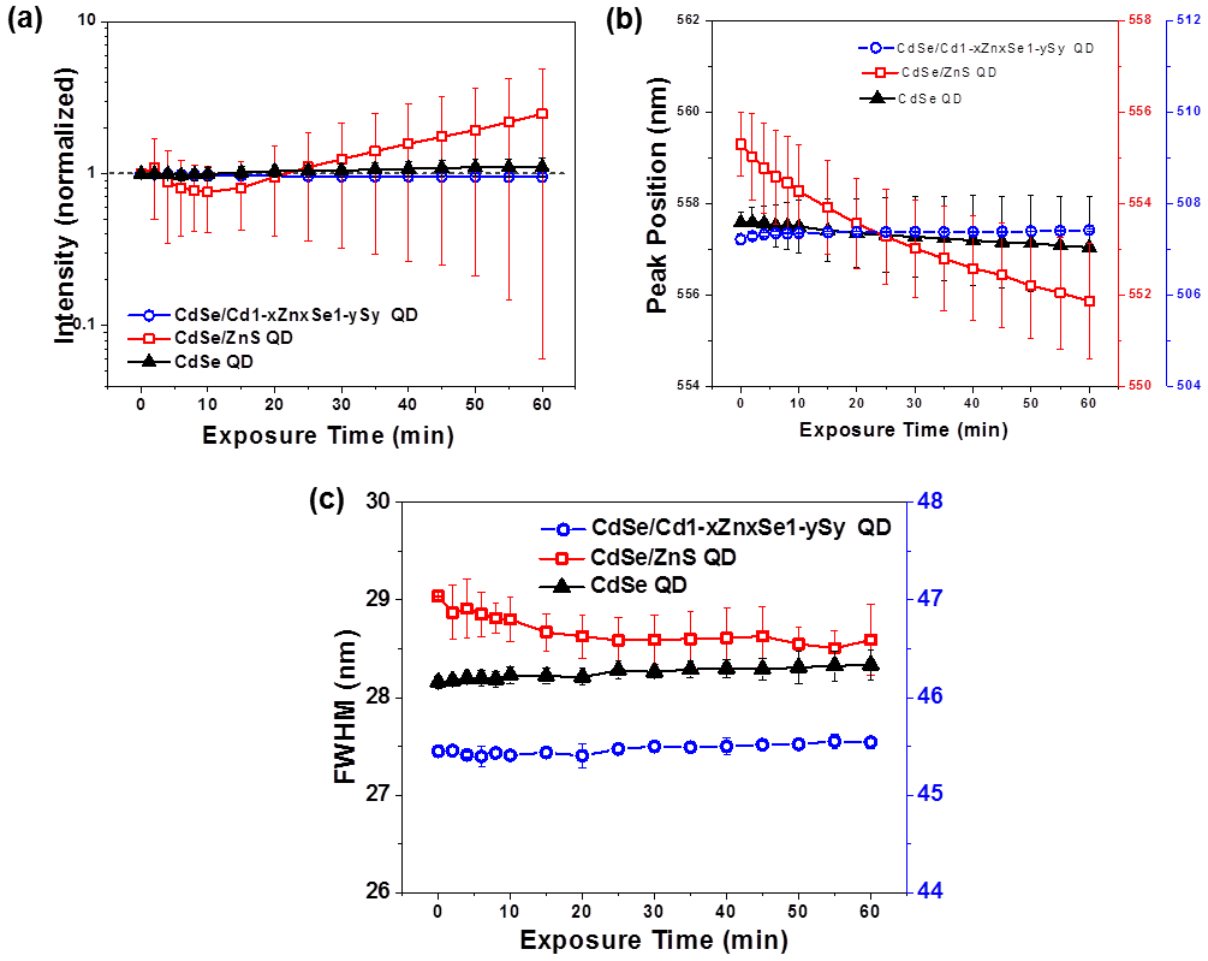

Figure C.3: Evolution of the (a) PL intensity, (b) spectral position, (c) and FWHM of each QD solution (core CdSe, core/shell CdSe/ZnS, or core/graded shell CdSe/$Cd_{1-x}Zn_xSe_{1-y}S_y$ QDs) under continuous light exposure (blue: 450-490 nm, 1.9 mW).

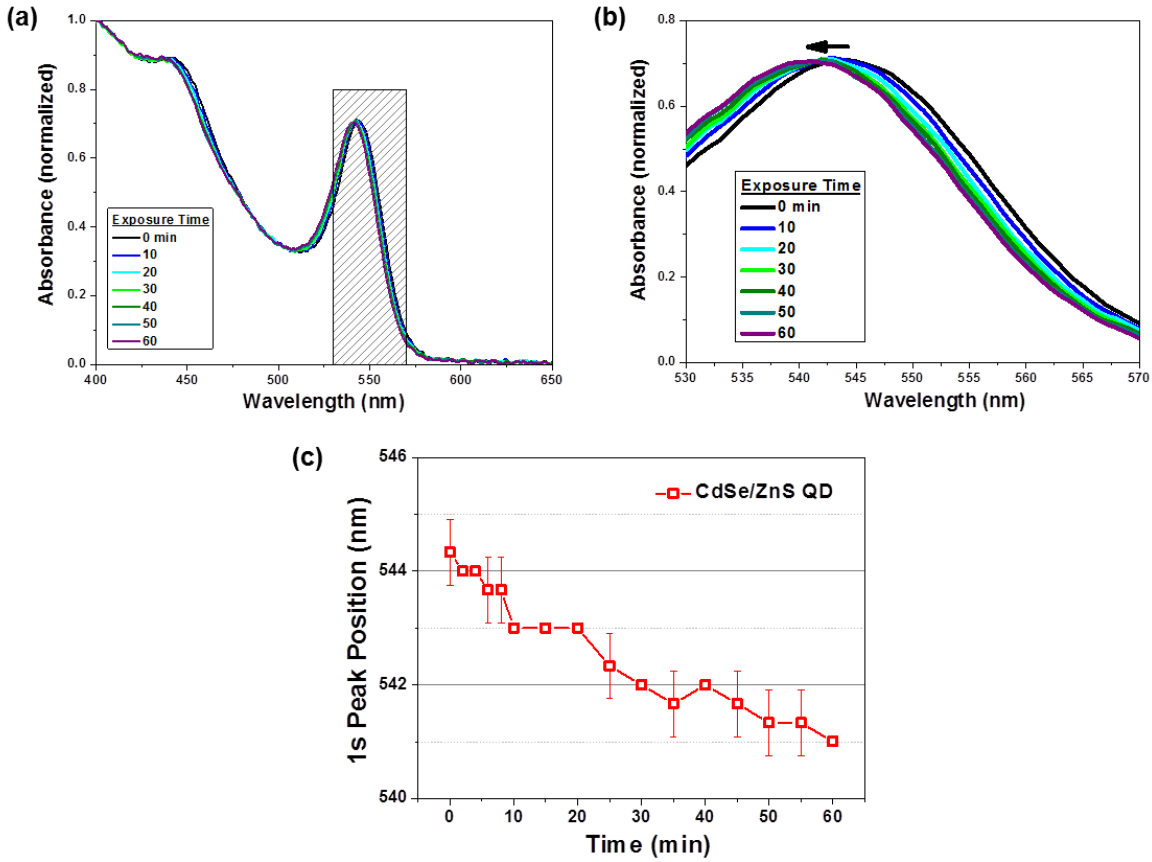

Figure C.4: Evolution of the (a,b) UV-vis absorption of the CdSe/ZnS QDs in solution at different times during light exposure (blue: 450-490 nm, 0.7 mW). (c) Evolution of 1s peak position during light exposure.

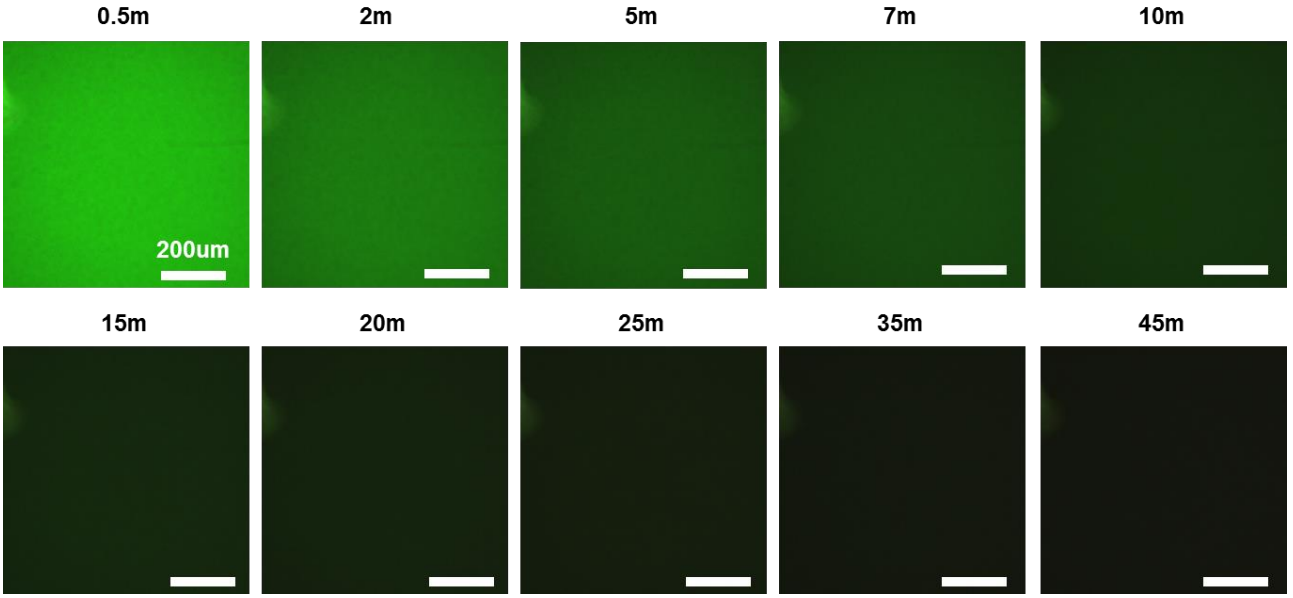

Figure C.5: PL imaging of an unstable core CdSe QD-PMMA film under continuous light exposure for 45 minutes (blue: 450-490 nm, 22.5 mW). All scale bars are 200 um.

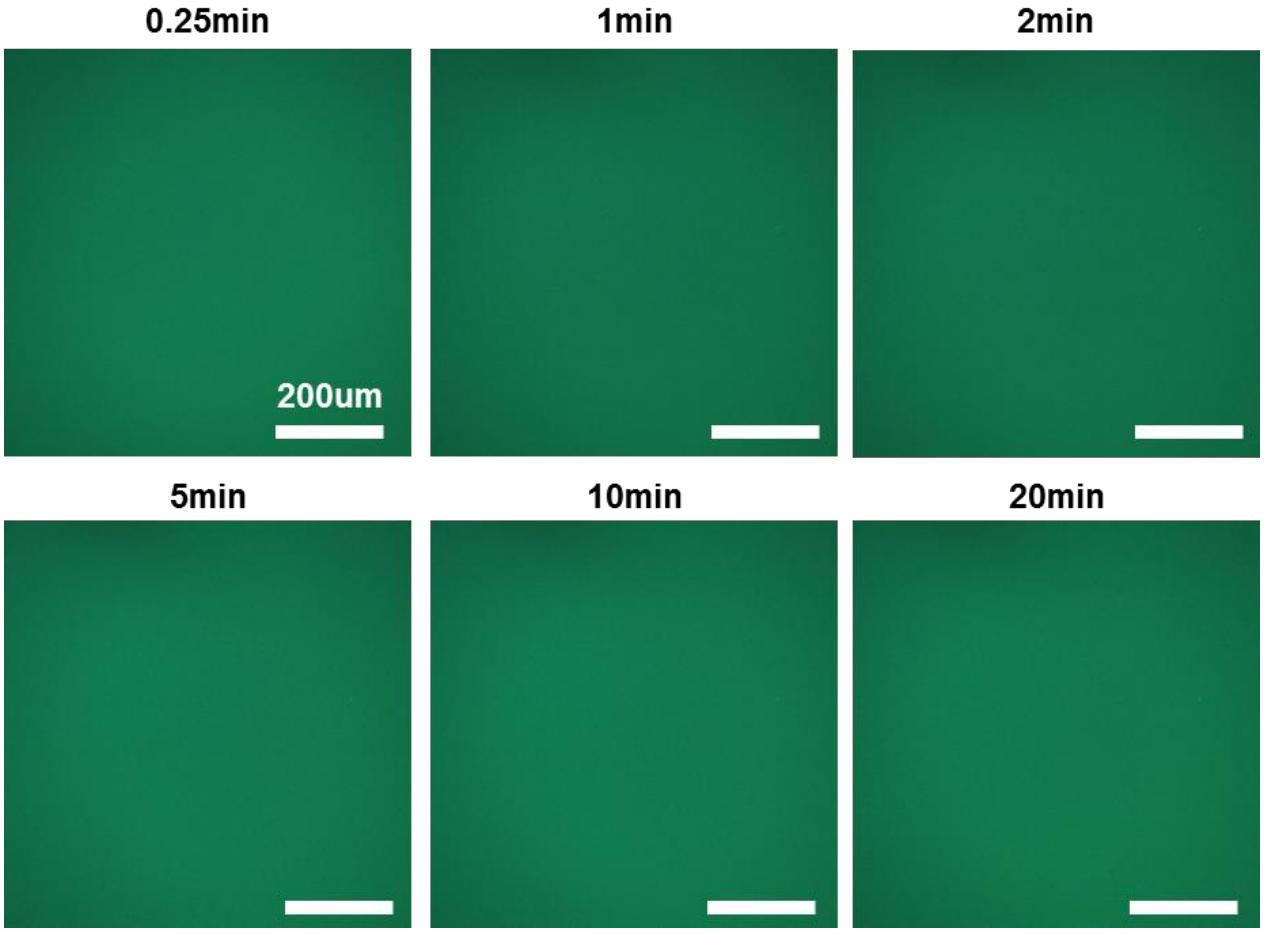

Figure C.6: PL imaging of a stable core/graded shell CdSe/$Cd_{1-x}Zn_xSe_{1-y}S_y$ QD-PMMA film under continuous light exposure for 20 minutes (blue: 450-490 nm, 25 mW). All scale bars are 200 um.

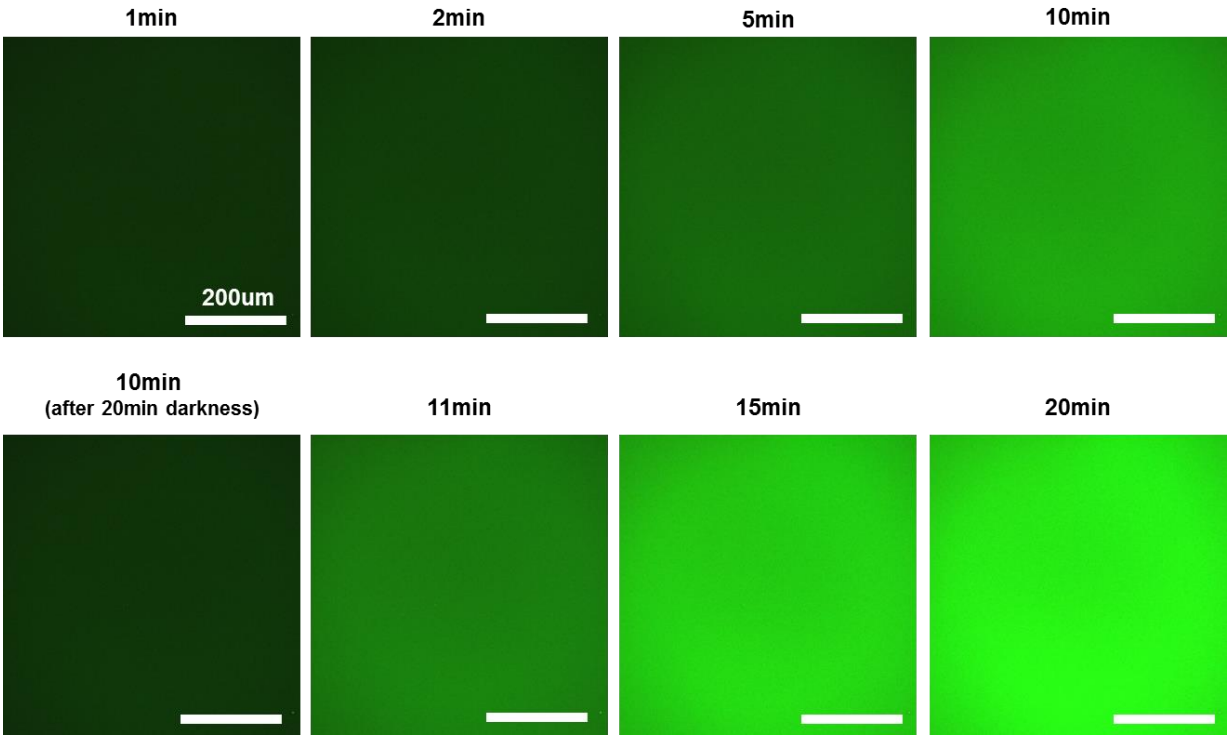

Figure C.7: PL imaging of an unstable core/shell CdSe/ZnS QD-PMMA film under an exposure-darkness-exposure light cycle (blue: 450-490 nm, 19.9 mW). All scale bars are 200 um.

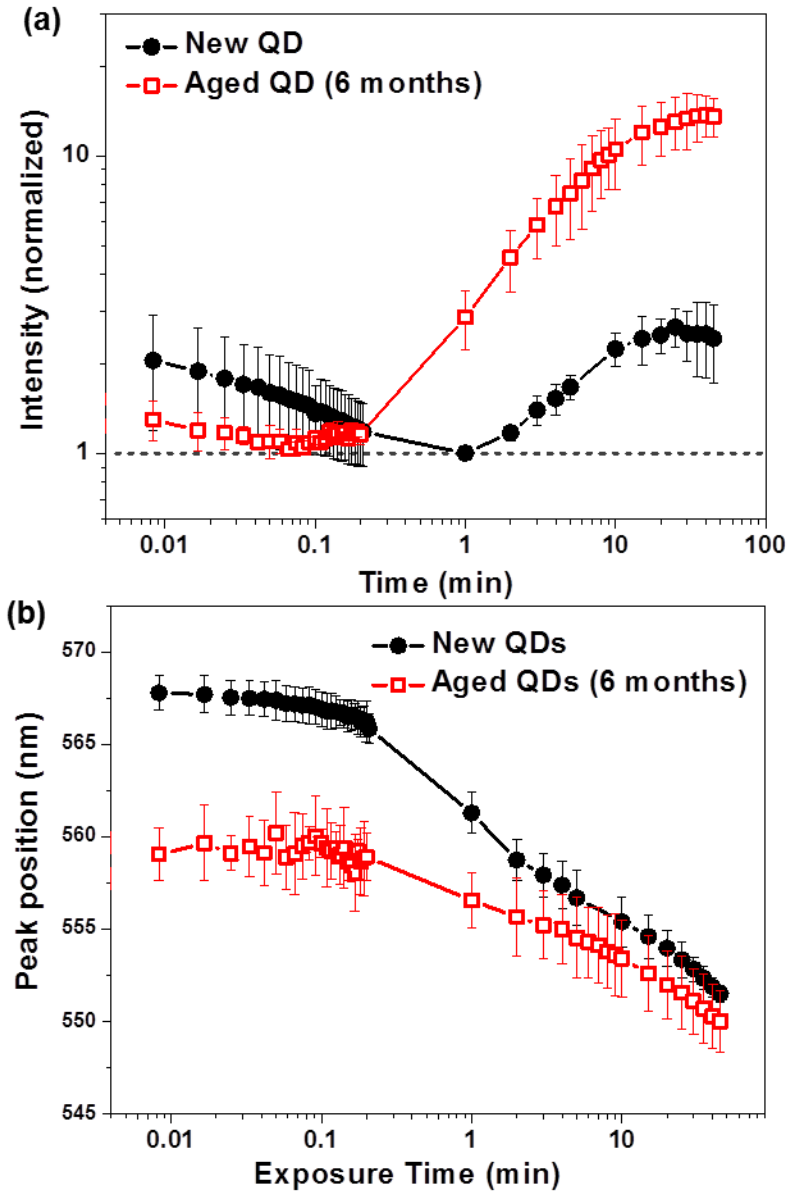

Figure C.8: Evolution of the (a) PL intensity and (b) spectral position of QD-polymer films under continuous exposure (blue: 450-490 nm, 24-28 m) with either recently synthesized or aged (6 months) unstable core/shell CdSe/ZnS QDs.

Appendix D

Chapter 7 supporting data

(ENHANCEMENT OF OPTICAL GAIN CHARACTERISTICS OF QUANTUM DOT FILMS BY OPTIMIZATION OF ORGANIC LIGANDS)

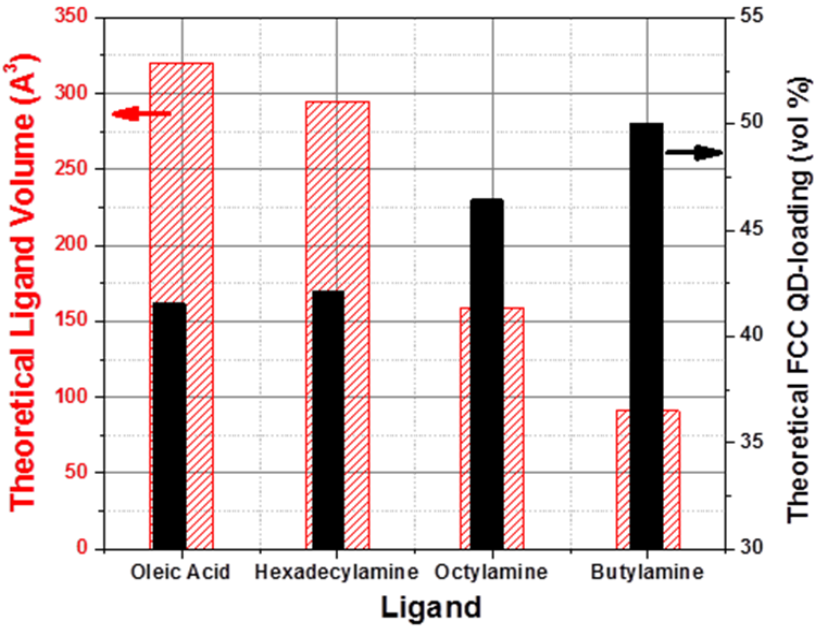

Figure D.1: Plot of the predicted free volume of each QD ligand and the corresponding maximum theoretical FCC QD-packing density (assuming diameter of 8 nm). Reducing the size of the ligand leads to a larger maximum FCC packing for the QDs in the film (and vice versa).

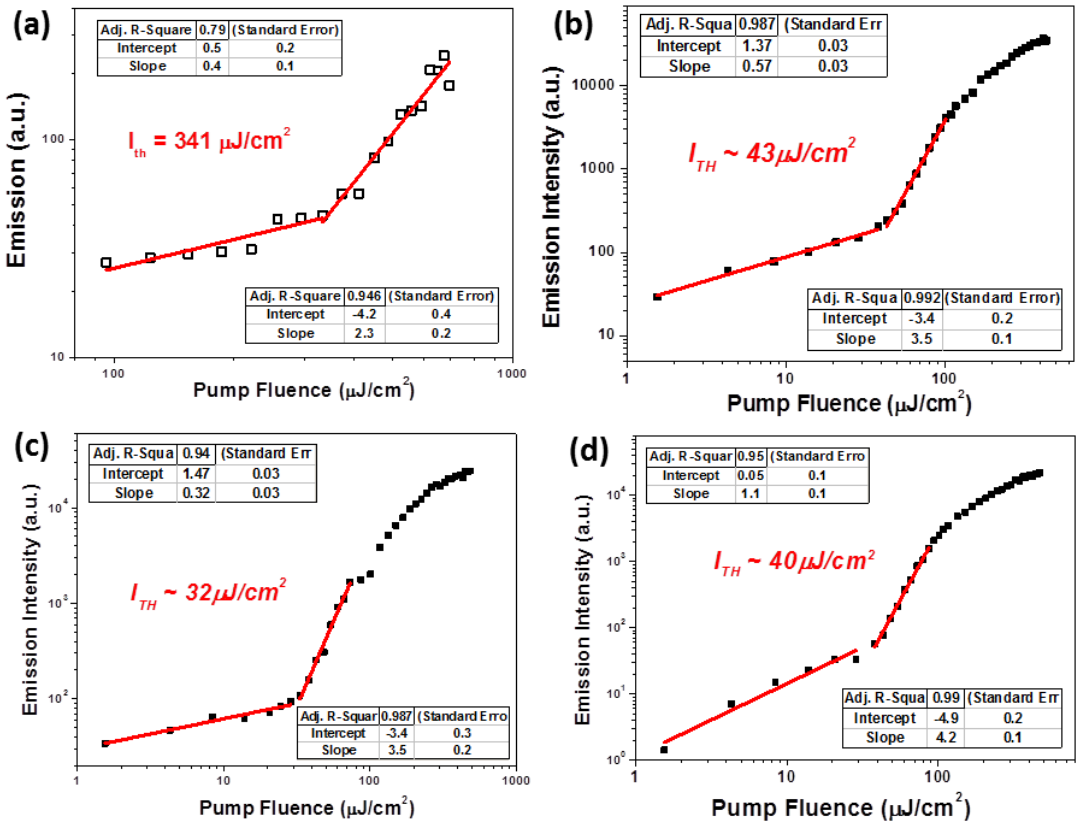

Figure D.2: ASE threshold plots and fitting for different QD-ligand combinations. The threshold value of the QD film is determined by linear fitting of the shallow and steep pump fluence versus emission curve. The pump fluence value at the intersection of the linear fit from the two regions is the threshold fluence. Examples of threshold determination are shown for (a) oleic acid-QD, (b) HDA-QD, (c) OctA-QD, and (d) BA-QD films.

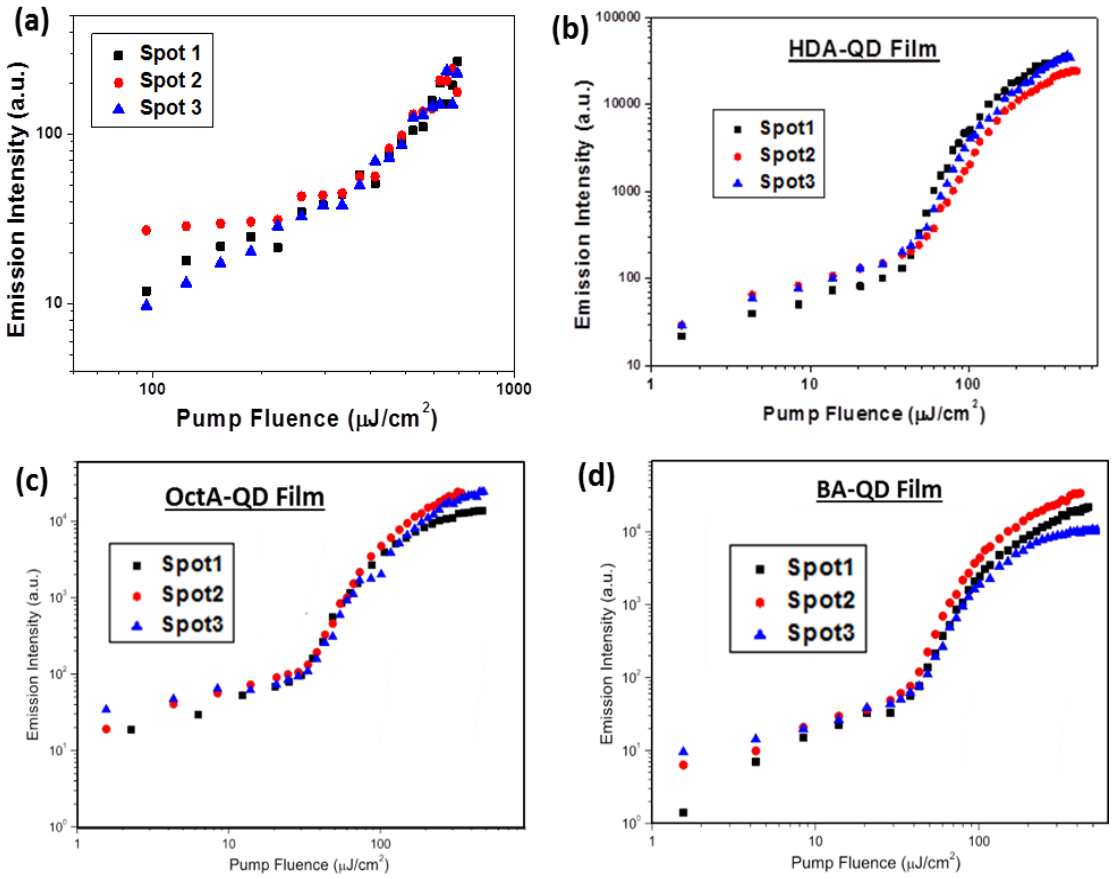

Figure D.3: ASE threshold plots for different QD-ligand combinations from multiple spots. The threshold behavior of the QD films was determined by examining how the pump fluence affects the emission intensity. A transition from a shallow slope to a steep slope indicates an ASE threshold. The threshold behavior for each type of QD film was verified over multiple trials. Examples of threshold examination are shown for (a) oleic acid-QD, (b) HDA-QD, (c) OctA-QD, and (d) BA-QD films.

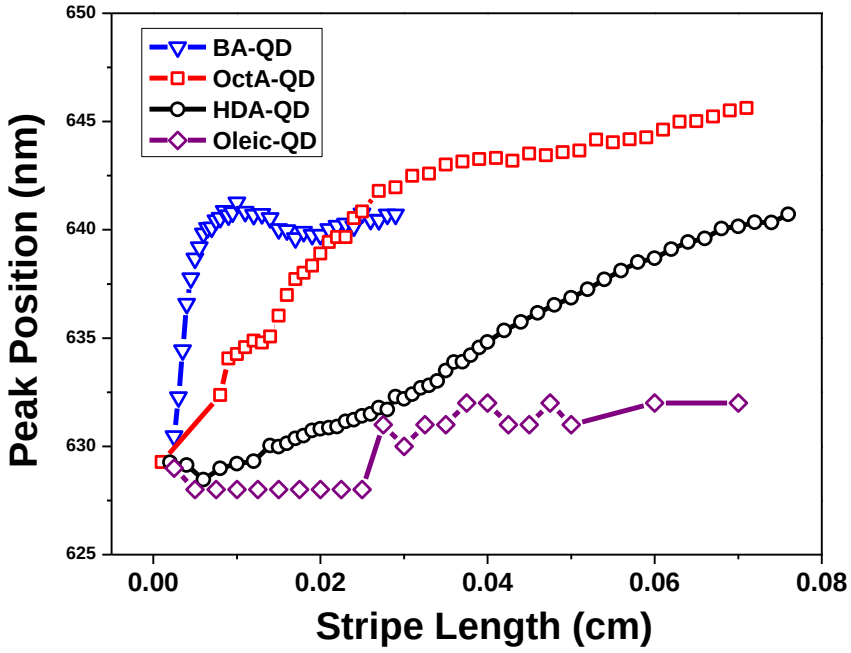

Figure D.4: Peak position of the maximum emission peak versus pump strip length. All the QD films with amine functionalization in this study exhibited a red-shift of approximately 10-15 nm compared to the PL peak, while the oleic-QD film show a red-shift of only 4 nm, indicating a smaller amount of reabsorption during light propagation.

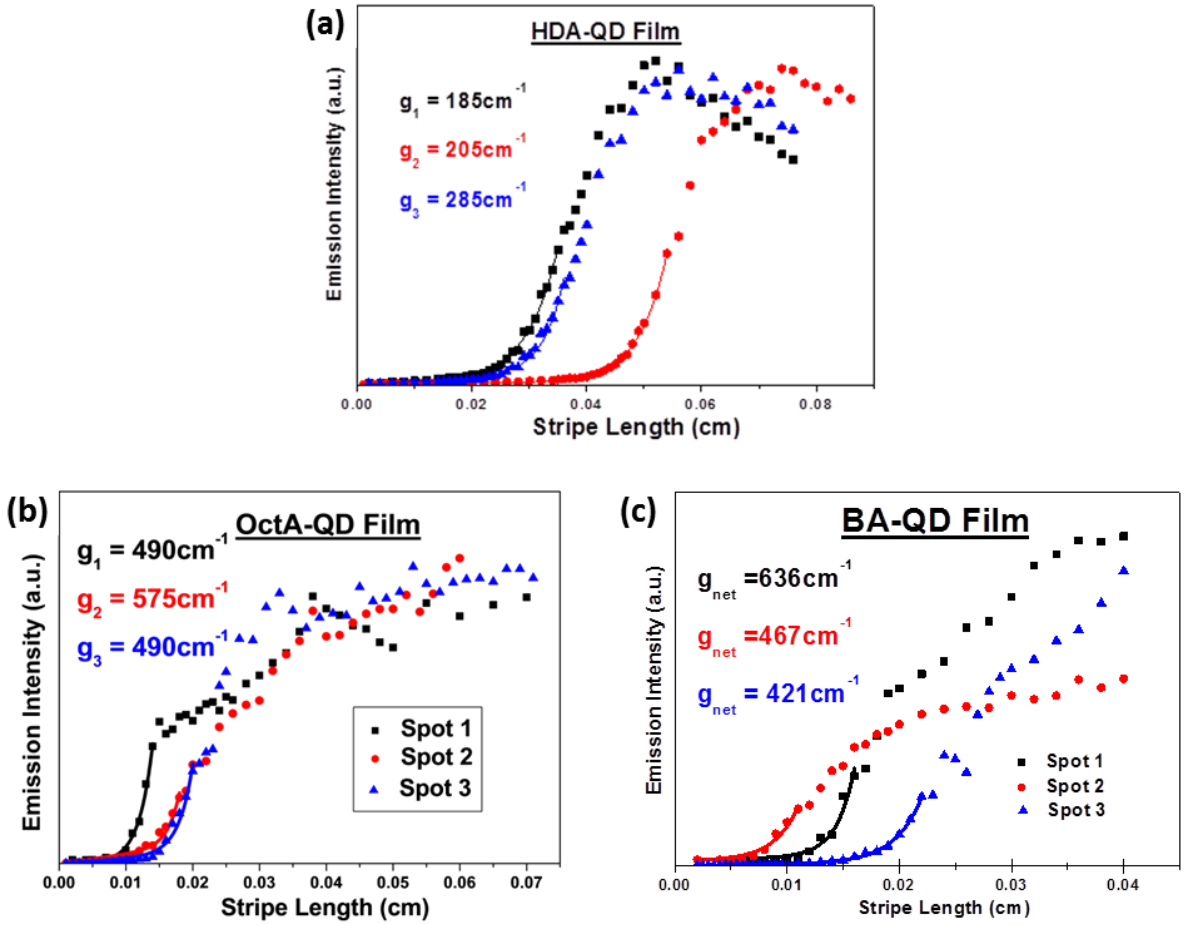

Figure D.5: Data of the emission intensity versus pump strip length from the variable stripe length (VSL) method for various QD-ligand combinations. The optical gain of the QD films was determined by fitting data from the VSL method with an exponential function. The gain value for each type of QD film was determined by averaging over multiple trials. Examples of VSL data and fitting are shown for (a) HDA-QD, (b) OctA-QD, and (c) BA-QD films.

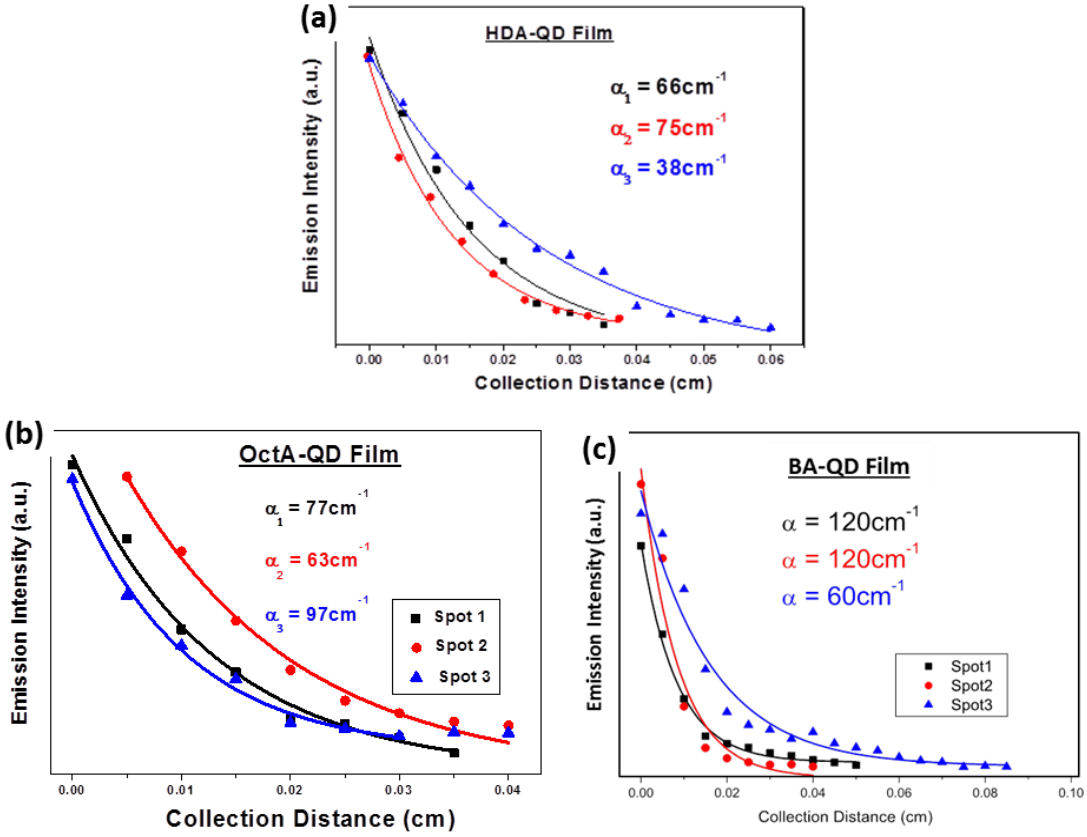

Figure D.6: Plots of optical loss data and fitting for various QD-ligand combinations. The optical loss of the QD films was examined by altering the distance the emission travels through the QD film before reaching the edge of the film. The optical loss value is determined by fitting the data with an exponential decay function. The loss value for each type of QD film was determined by averaging over multiple trials. Examples of loss data and fitting are shown for (a) oleic acid-QD, (b) HDA-QD, (c) OctA-QD, and (d) BA-QD films.

Appendix E

Chapter 8 supporting data

(PHOTOPATTERNING APPROACHES: NEGATIVE-TO-POSITIVE PATTERNING USING THE DECAY-TO-RECOVERY BEHAVIOR OF QUANTUM DOTS)

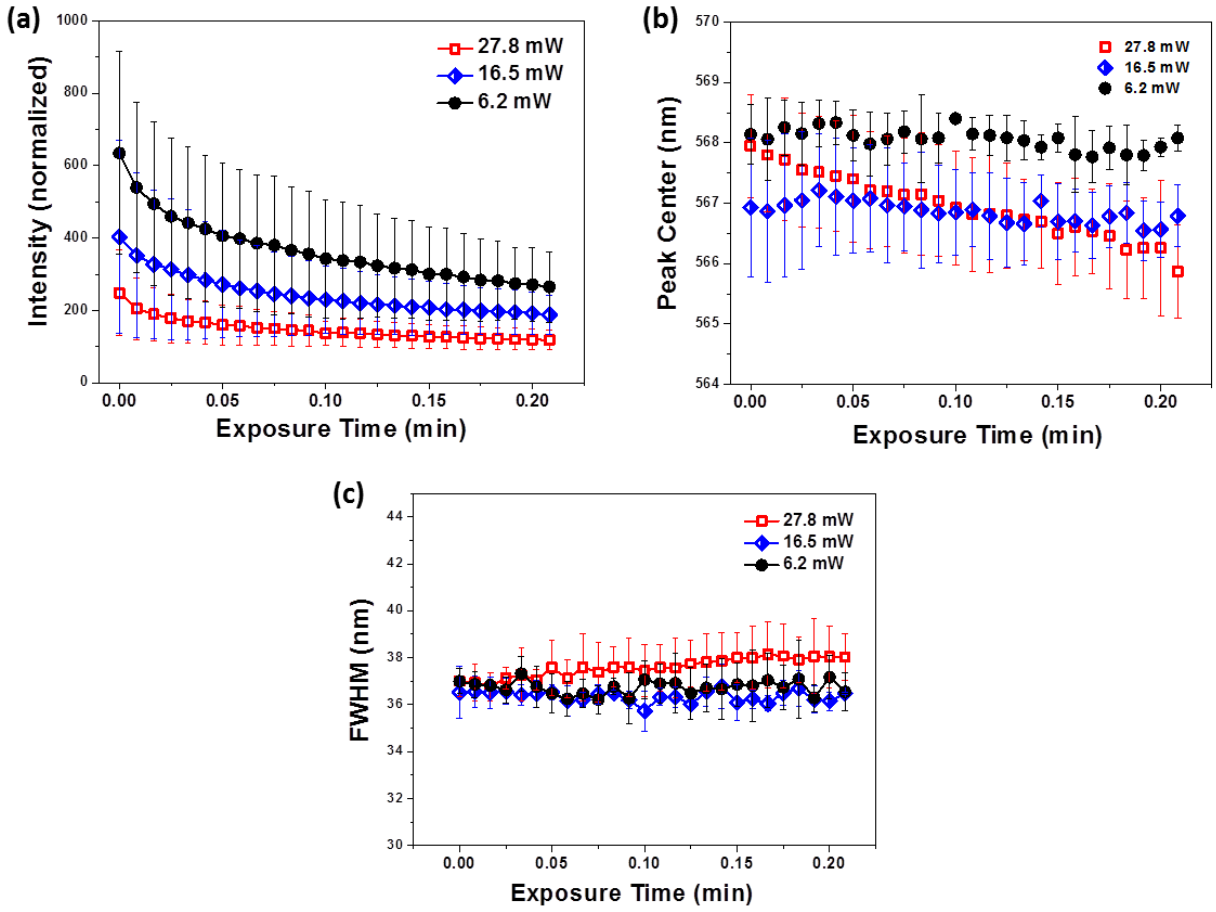

Figure E.1: The emission characteristics of unstable CdSe/ZnS QDs in a QD-polymer film during the first moments after exposure to light (470 nm) of different power. (a) PL intensity, (b) spectral peak center, and (c) FWHM.

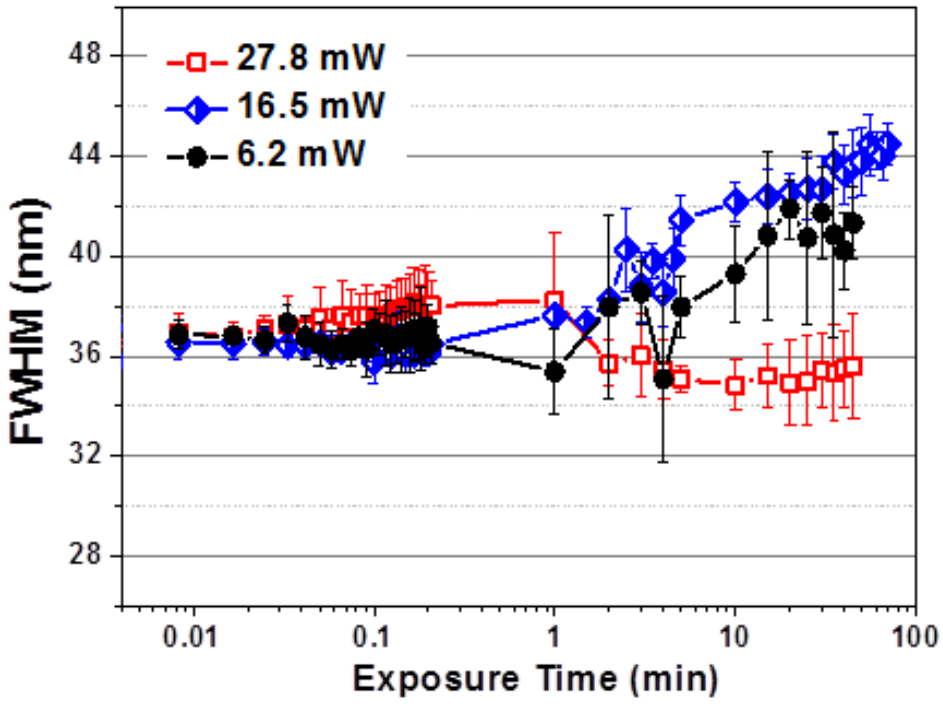

Figure E.2: The FWHM of unstable CdSe/ZnS QDs in a QD-polymer film during exposure to light (470 nm) at different power.

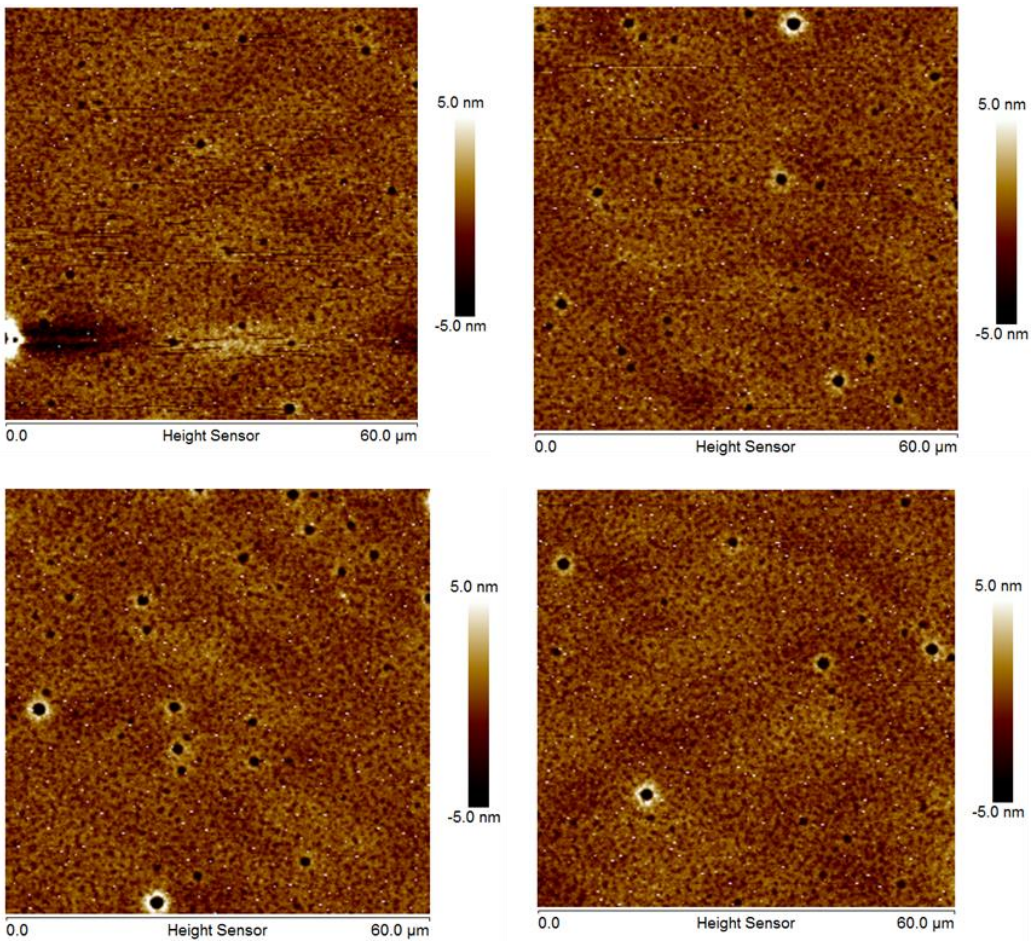

Figure E.3: AFM topographical images of photopatterned areas (preliminary decay-positive patterning, 470 nm, 34 mW). No indication of physical patterning of the QD-polymer film that could account for the PL pattern.

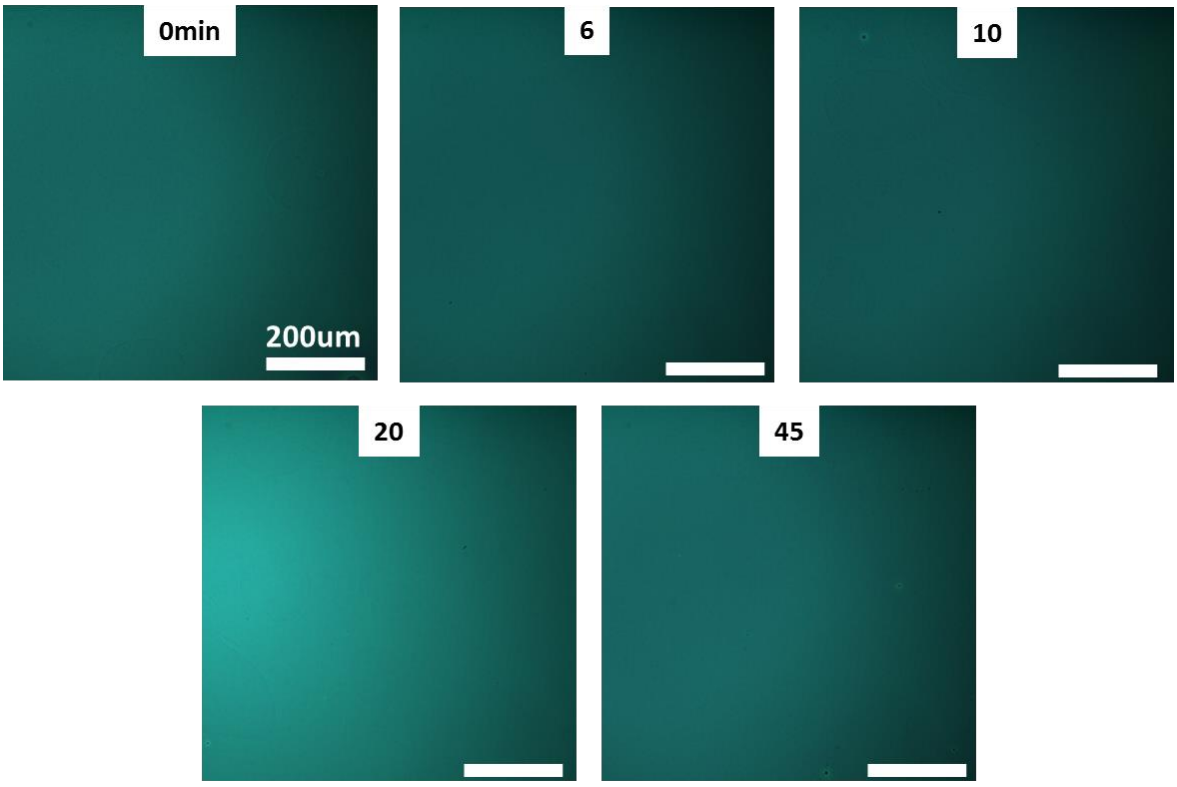

Figure E.4: Bright field microscopy images of photopatterned areas (positive patterning, 470 nm, 26 mW) at different stages of pattern development. No indication of physical patterning of the QD-polymer film that could account for the PL pattern.

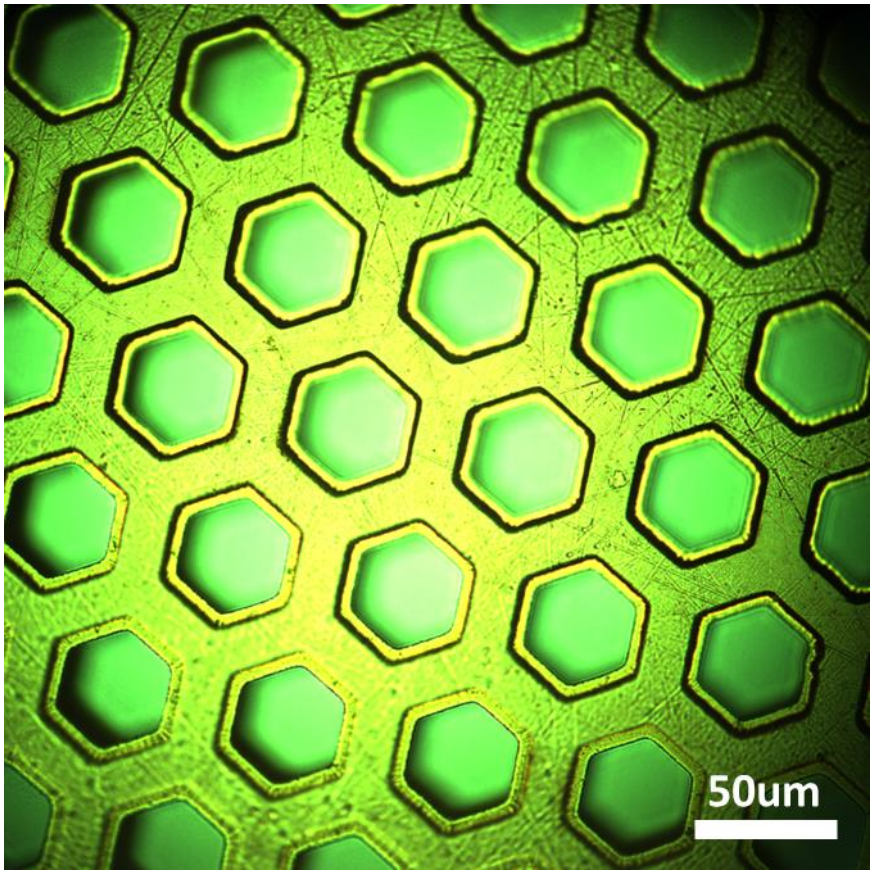

Figure E.5: Bright field image of the TEM grid (Electron Microscopy Sciences, G400H-Cu grid) used as the photomask in this study. The pitch is 62 um, the hexagonal hole is 37 um, and the bar is 25 um.

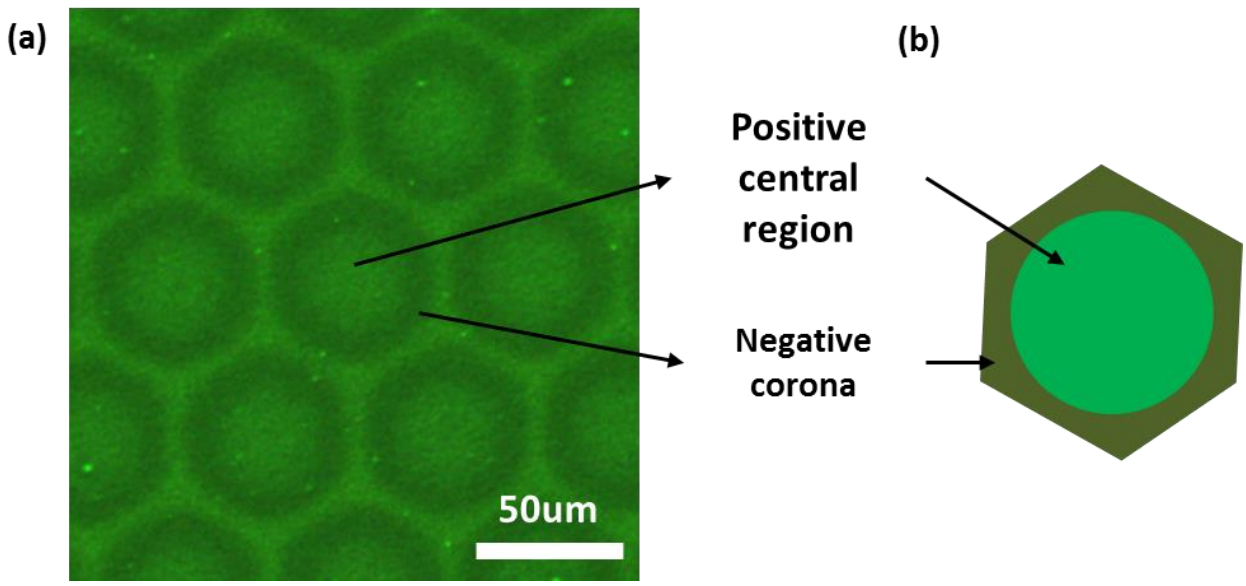

Figure E.6: (a) Fluorescence imaging and (b) schematic of the coronal pattern that can occur at intermediate exposure periods during positive photopatterning (5 min, 470 nm, 34 mW).

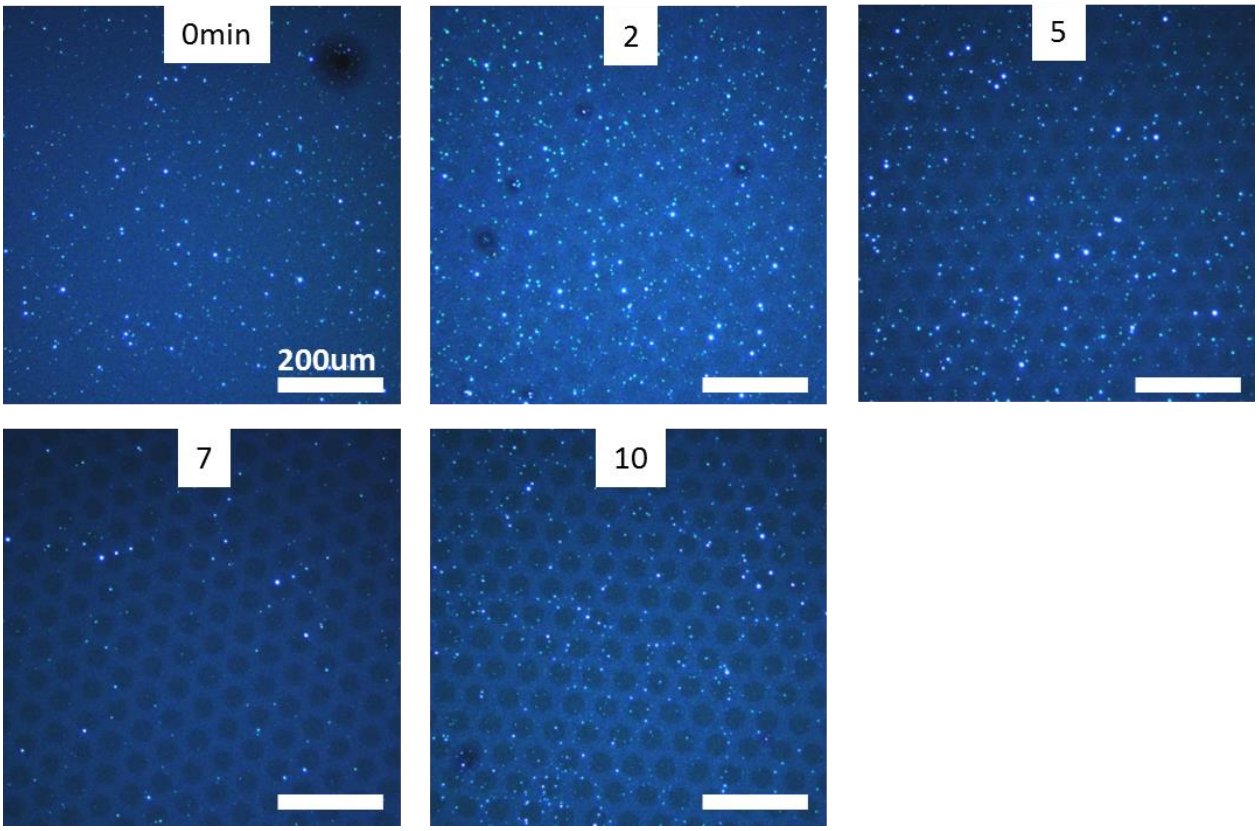

Figure E.7: Dark field microscopy images of a positive photopattern at different stages of development (470 nm, 34 mW). Faint outline of pattern visible in dark field possibly indicates modification of QD size. All scale bars are 200 µm.

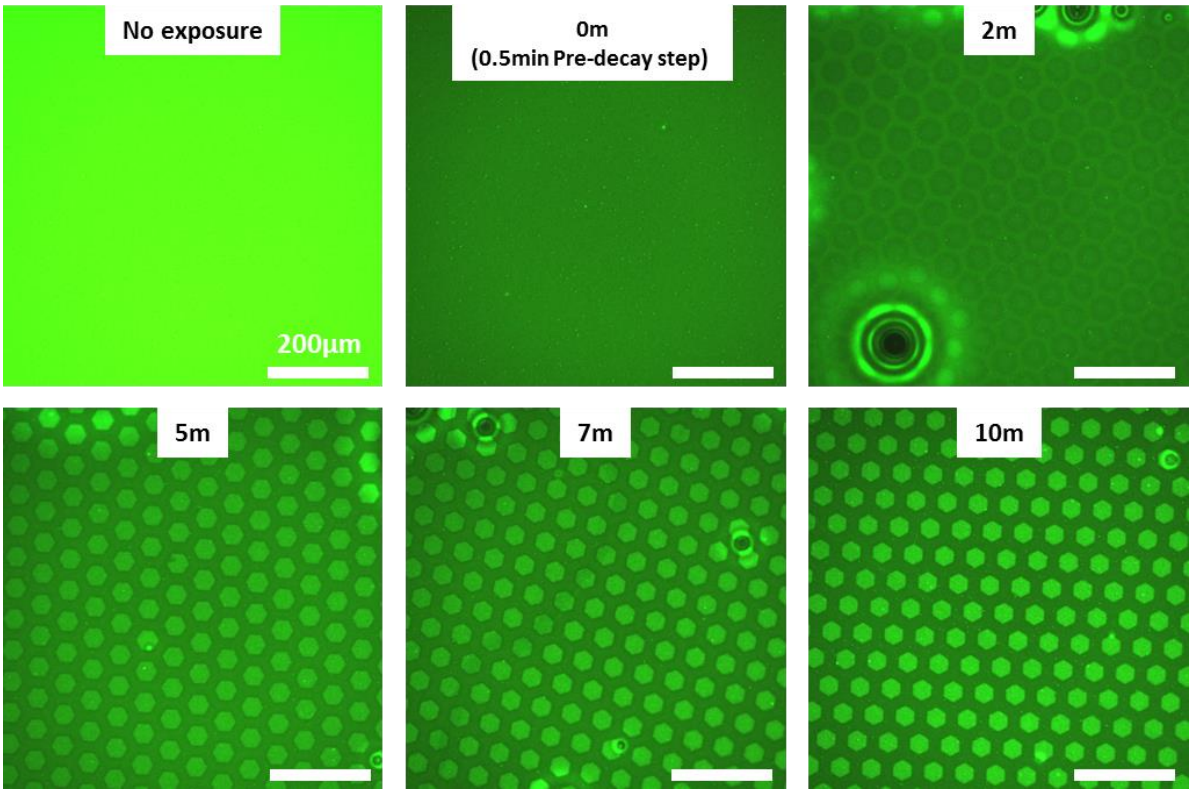

Figure E.8: Fluorescence images of a preliminary decay-positive pattern at different stages of development (470 nm, 34 mW). All scale bars are 200 µm.

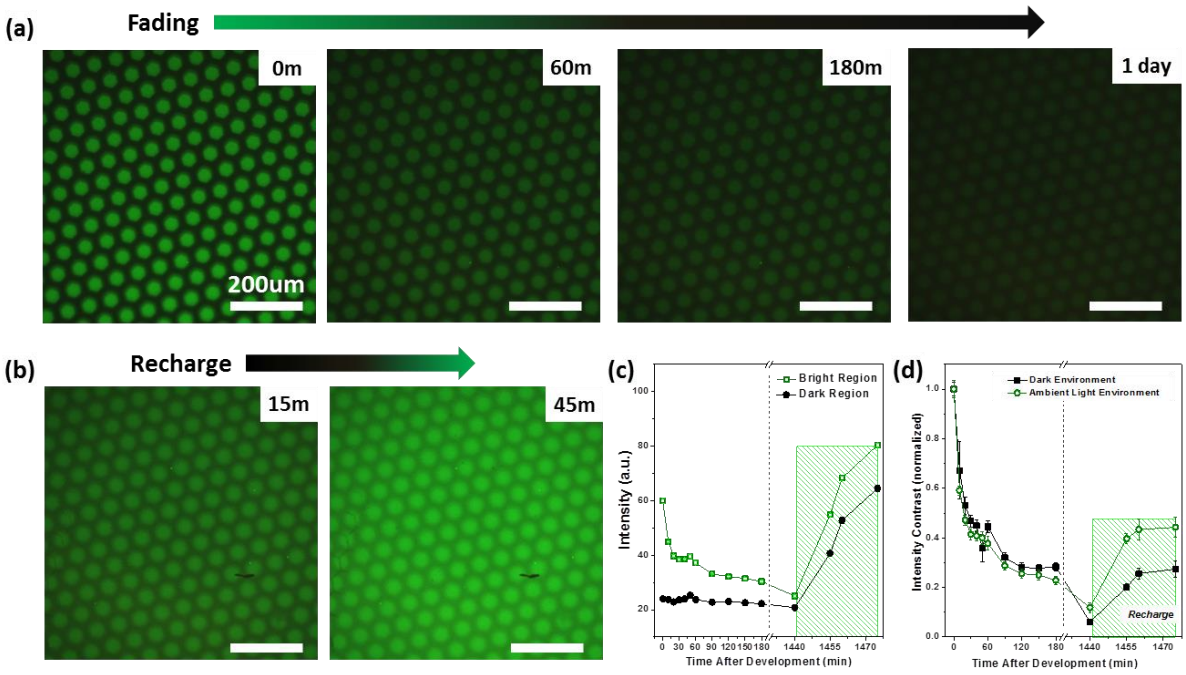

Figure E.9: Evolution of a positive photopattern in an ambient light environment. (a) PL imaging of a positive photopattern over a period of 1 day demonstrating the fading phenomenon. (b) PL imaging of the same (1 day old) photopattern after being recharged by light exposure for 15 min and 45 min (470 nm). (c) The intensity of the bright and dark regions of the pattern over the same period of time. (d) Evolution of the intensity contrast of a positive pattern in a dark environment and an ambient light environment. All scale bars are 200 µm.

Appendix F

Chapter 9 supporting data

(LARGE-AREA, HIGH-RESOLUTION, HIGH-THROUGHPUT EDGE-PROFILE AND FACE-PROFILE QD PHOTOPATTERNING)

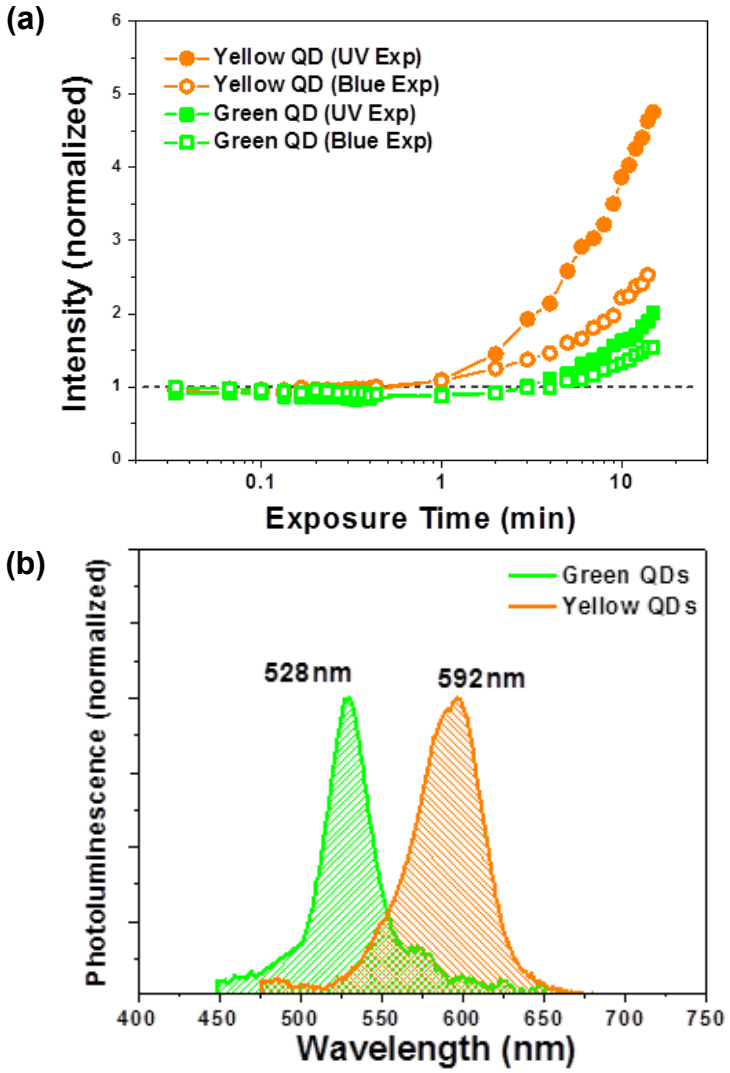

Figure F.1: (a) Evolution of the photoluminescence intensity of the unstable green and unstable yellow CdSe/ZnS QD-polymer films under continuous UV (325-375 nm) or blue (450-490 nm) light exposure. (b) Photoluminescence spectra of the unstable green and yellow CdSe/ZnS QDs.

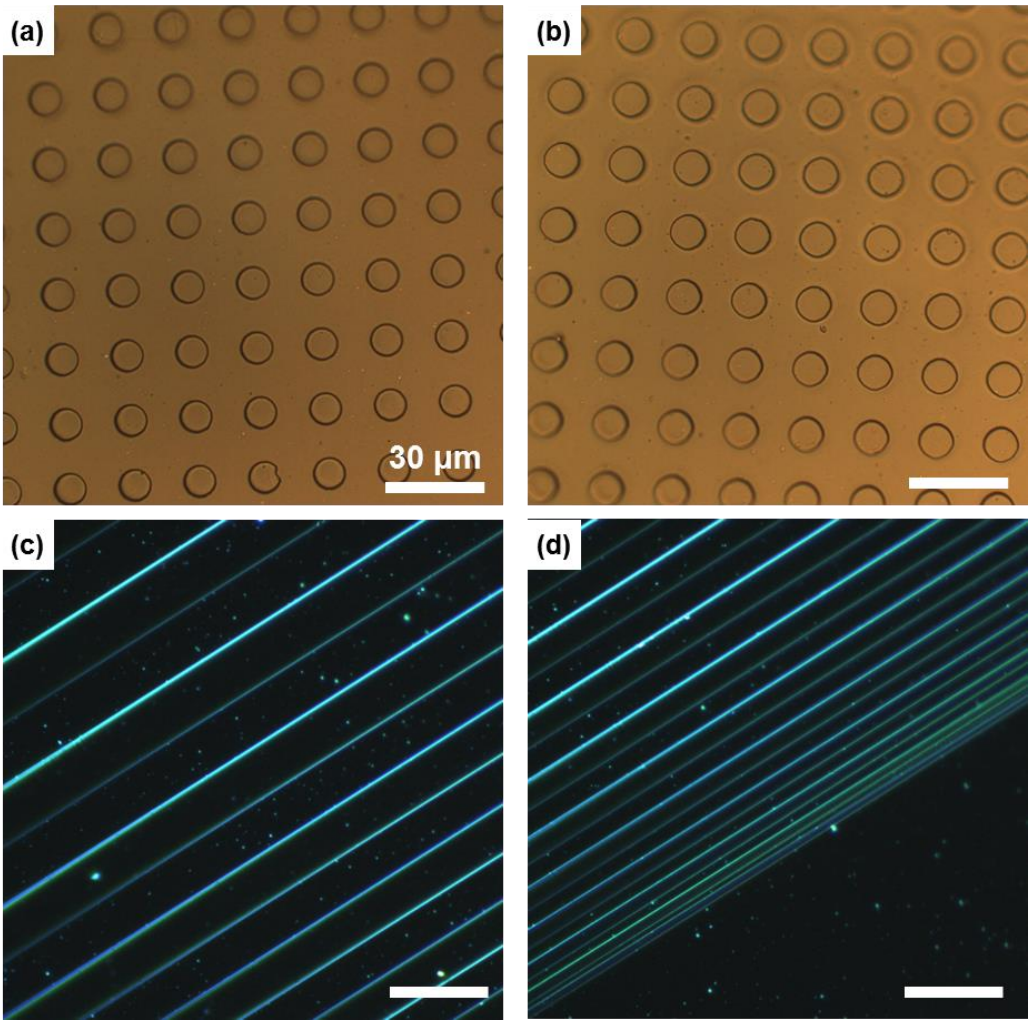

Figure F.2: Microscopy imaging of the various patterned PDMS stamps used as photomasks in this study. Bright field imaging of the array of circular (a) holes and (b) pillars. Dark field imaging of the (c,d) varied width strip pattern. All scale bars are 30 µm.

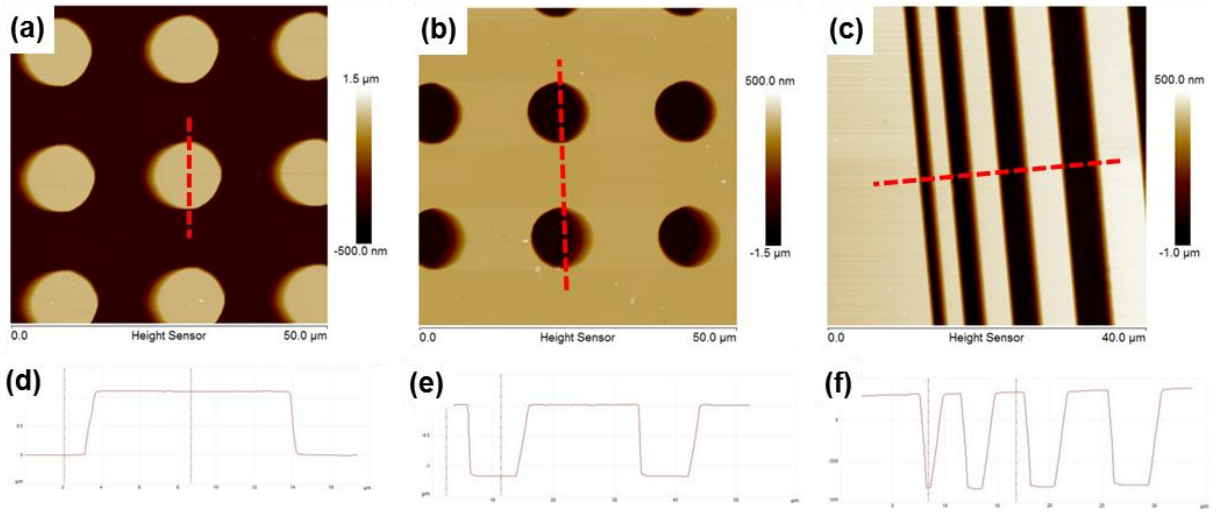

Figure F.3: AFM height scans of the (a) hole, (b) pillar, and (c) varied strip patterned PDMS stamps used in this study as photomasks. Height profile of the (d) hole, (e), pillar, and (f) varied strip patterns. All features have a height/depth of 1.1 - 1.2 µm.

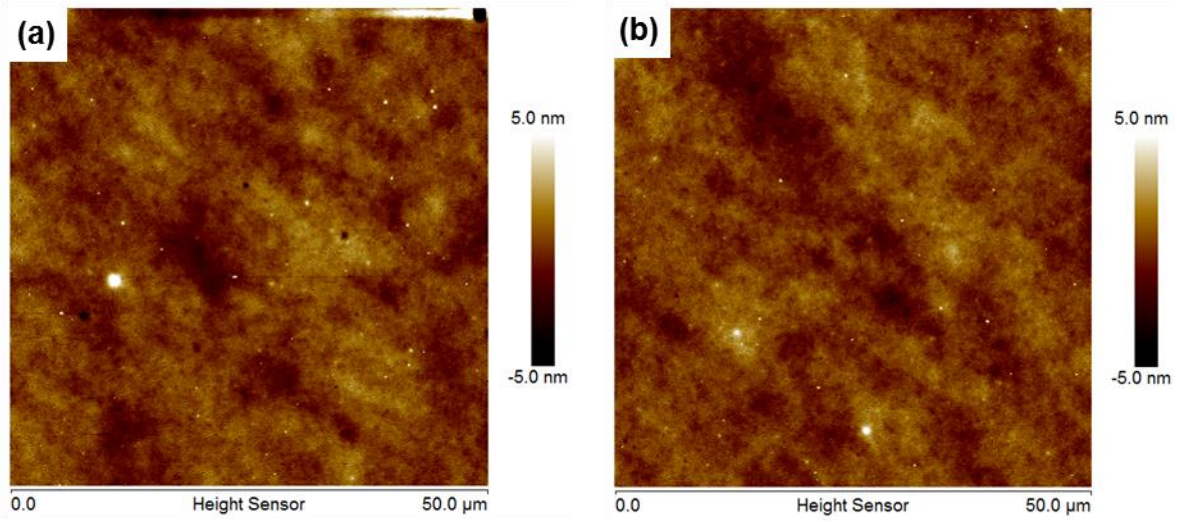

Figure F.4: AFM scans of QD-PMMA films that underwent photopatterning using a PDMS photomask (pillar array, UV exposure). (a,b) Height scans show no indication of physical height changes that could account for the PL photopattern.

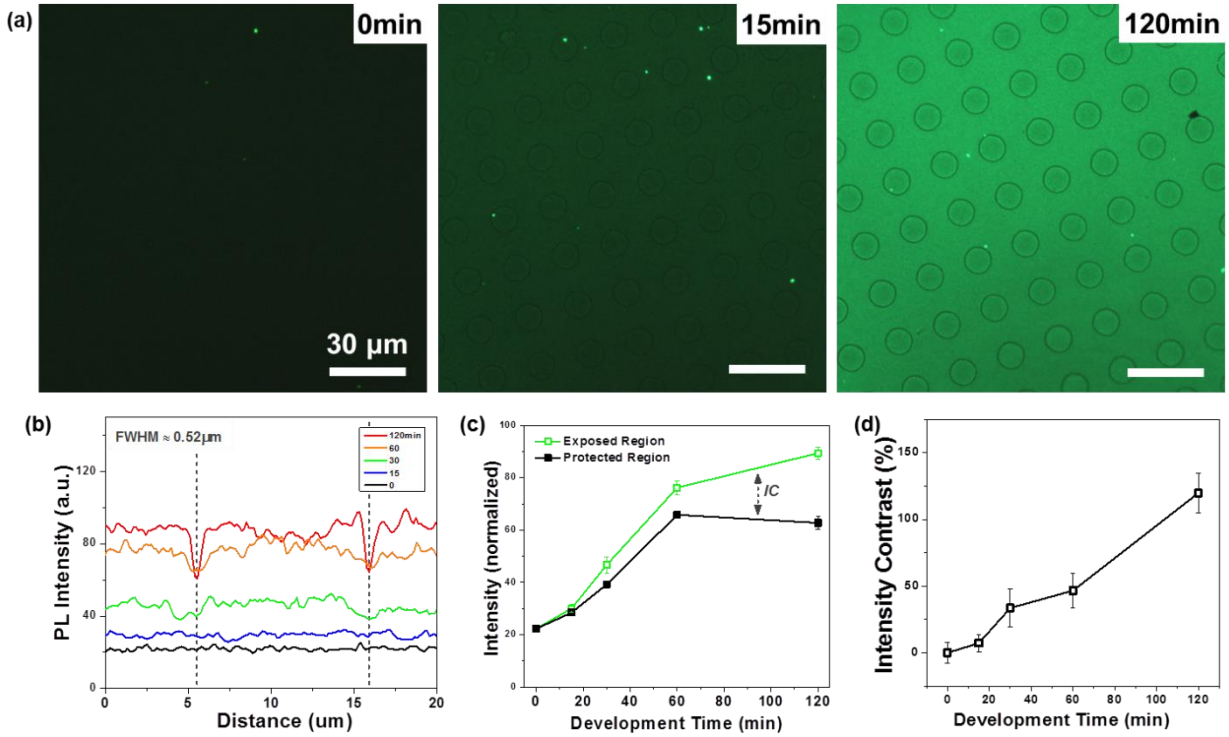

Figure F.5: Demonstration of the "on-beam" photopatterning process using a PDMS stamp with a pillar array pattern. (a) PL images of a circular edge-profile photopattern at different stages of pattern development (developed using UV light, 21.7 mW/cm^2). (b) PL intensity cross-section, (c) PL intensity of the protected and exposed regions of the photopattern, and (d) the intensity contrast at different stages of pattern development. Scale bar is 30 μm for all images.

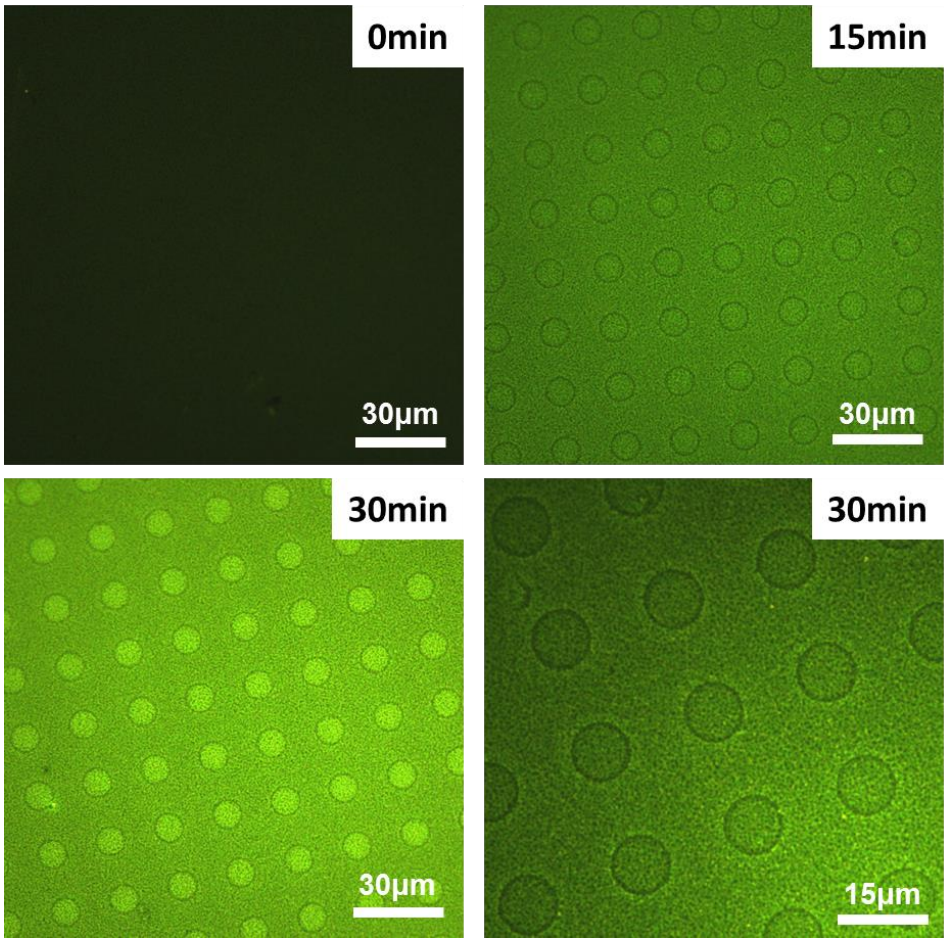

Figure F.6: PL of an edge-profile on-beam photopattern created using blue exposure light (450-490 nm) on an unstable yellow CdSe/ZnS QD-polymer film. The PDMS photomask had a pattern of 10 um circular holes. The time stamp represents how long the photopattern was developed.

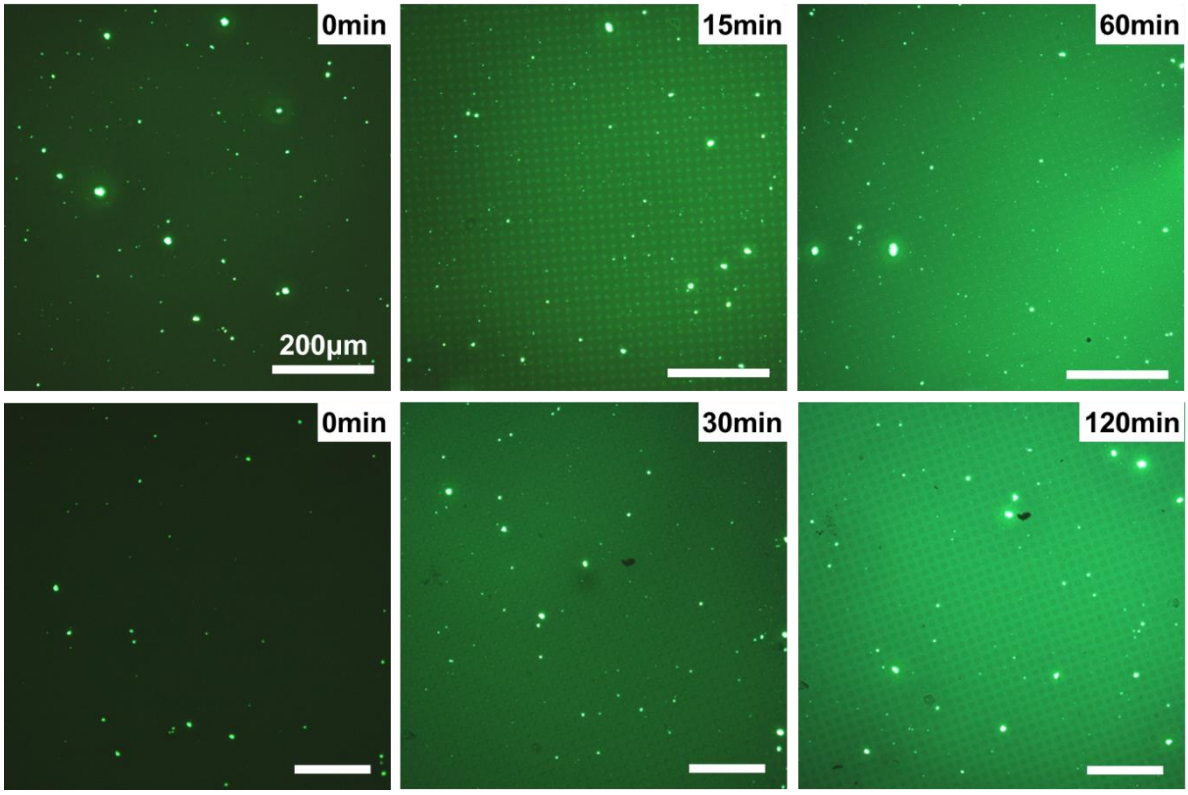

Figure F.7: Low-magnification PL images of photopatterns fabricated via the on-beam approach using a patterned PDMS photomask with (row 1) a hole array or (row 2) a pillar array. Low-magnification PL imaging does show some indication of a face-profile photopattern. Scale bar is 200 μm for all images.

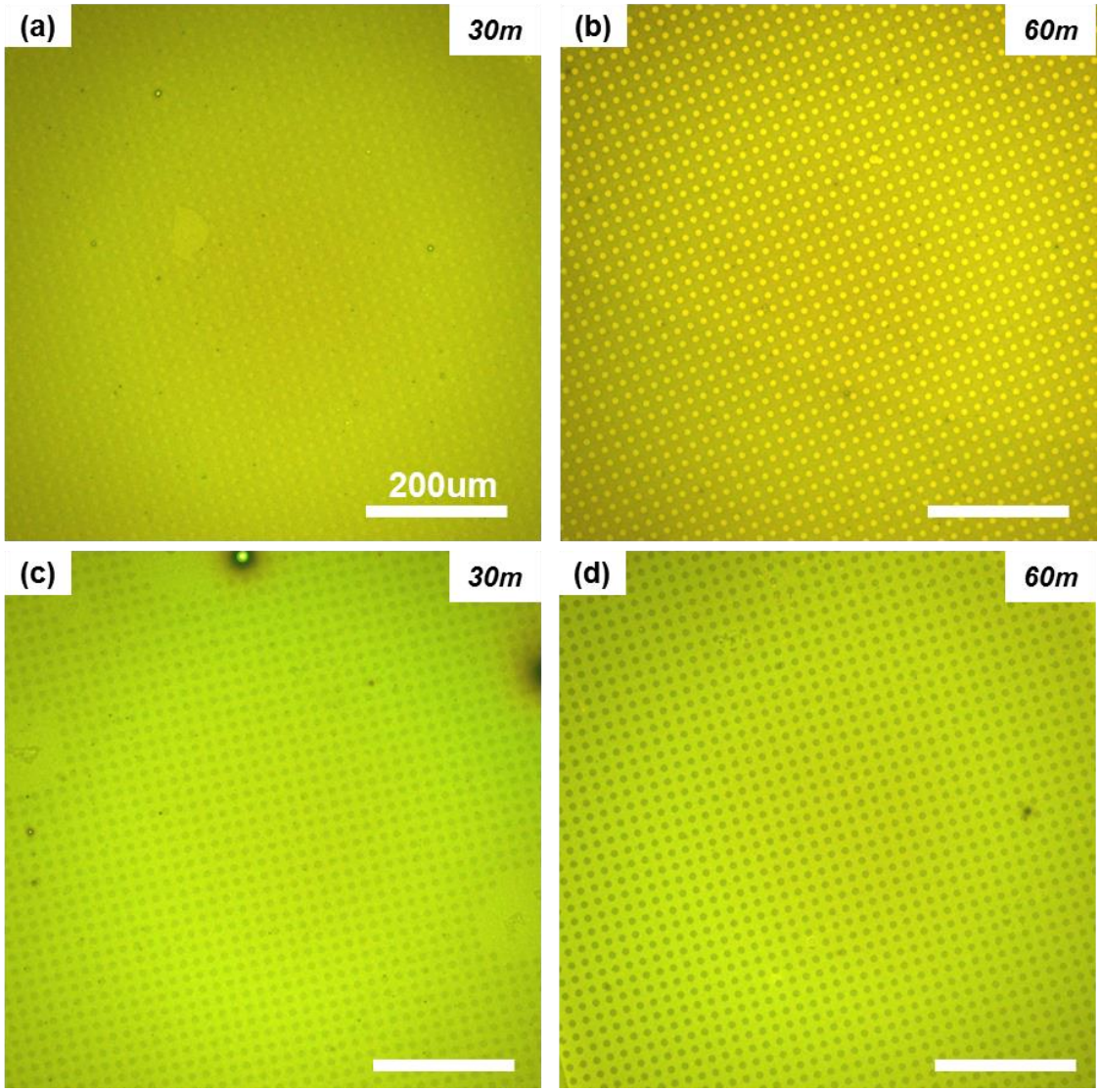

Figure F.8: Large-view PL images of photopatterns developed using the off-beam exposure approach. (a,b) PL image of a photopattern fabricated using a PDMS mask of 10 μm holes. (c,d) PL image of a photopattern fabricated using a PDMS mask of 10 μm pillars. Patterns were developed using UV light (325-375 nm) (15 mW/cm^2). Scale bar is 200 μm for all images.

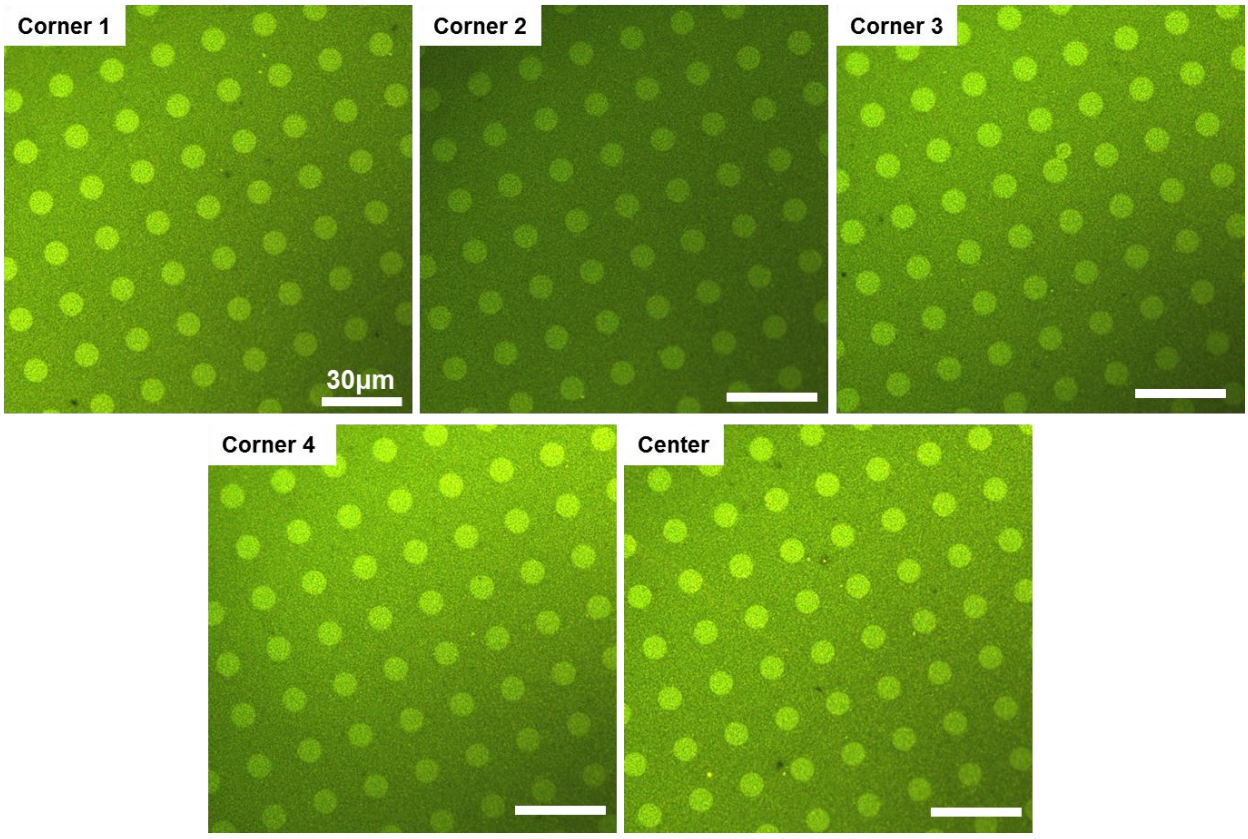

Figure F.9: PL images from different regions of an unstable yellow QD-polymer film photopatterned over a large lateral area (≈0.9 x 1.0 cm^2) using a diffuse on-beam exposure. The photopatterned circles have an average diameter of 8.9±0.1 um. The photopattern was developed using UV light (21 mW/cm^2) for 30 minutes. A PDMS stamp with 10 um diameter holes was used as the photomask. Scale bar is 30 µm for all images.

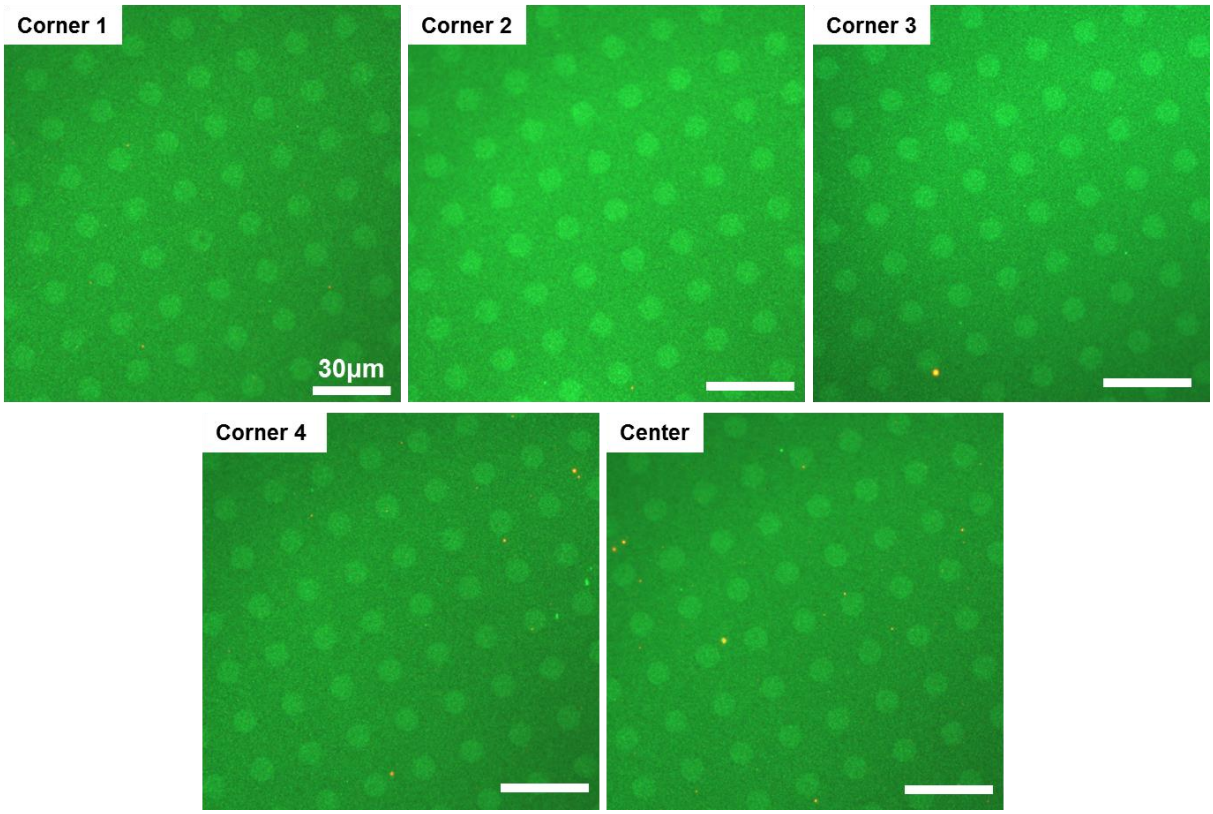

Figure F.10: PL images from different regions of an unstable green QD-polymer film photopatterned over a large lateral area (≈0.9 x 1.0 cm^2) using an off-beam exposure. The photopatterned circles have an average diameter of 9.3±0.2 um. The photopattern was developed using UV light (10 mW/cm^2) for 240 minutes. A PDMS stamp with 10 um diameter holes was used as the photomask. Scale bar is 30 µm for all images.

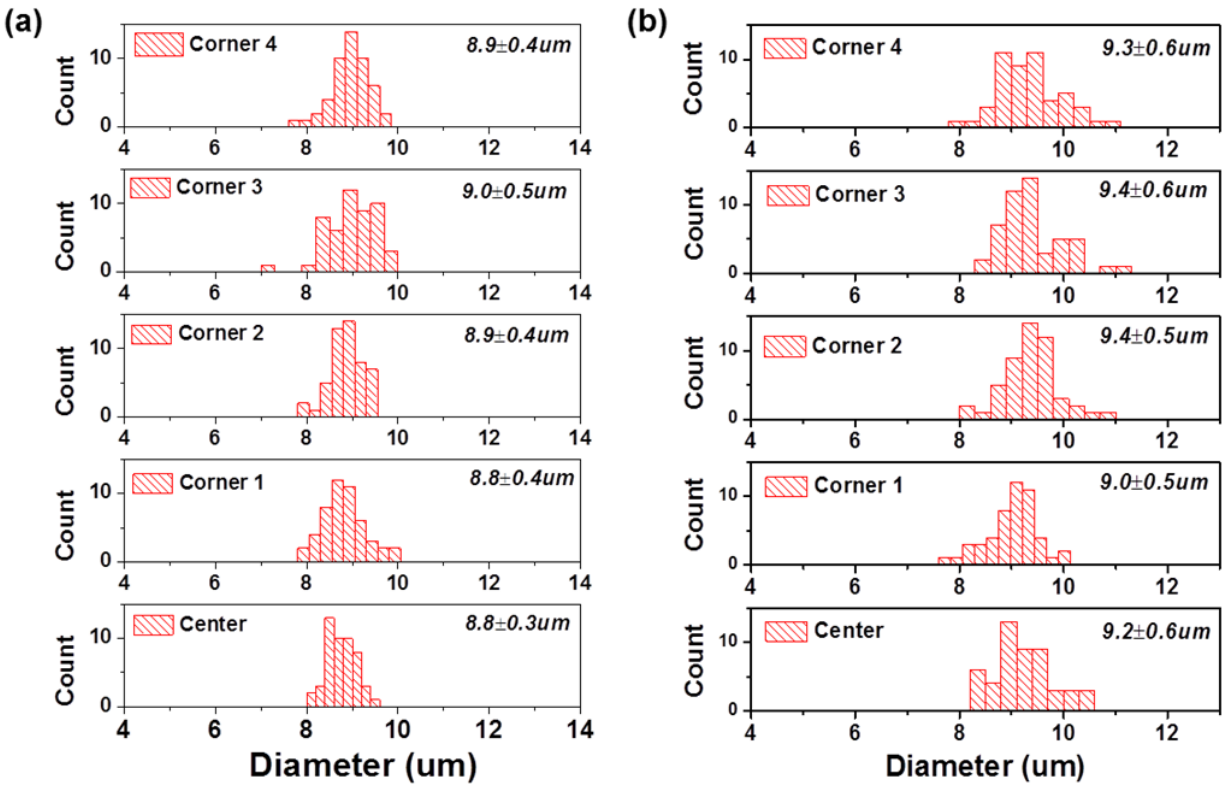

Figure F.11: Histograms of the diameter of the large-area circle photopatterns fabricated using the (a) diffuse on-beam patterning approach (photopatterned circles have average diameter of 8.9±0.1 μm) and (b) the off-beam patterning approach (photopatterned circles have average diameter of 9.3±0.2 μm).

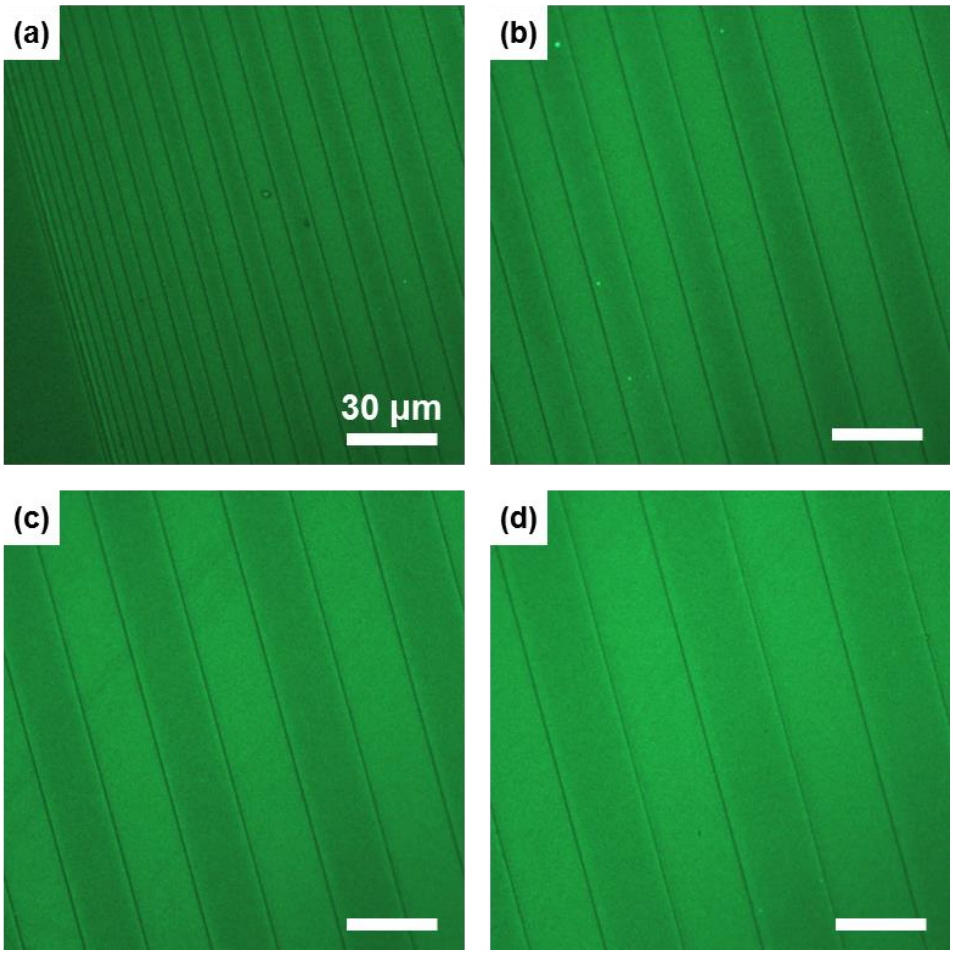

Figure F.12: PL images of an “on-beam” photopattern of negative edge-profile lines with different periodicity (using a varied width strip PDMS mask). (a) Small, (b) medium, (c) large, and (d) very large periodicity lines. All scale bars are 30 μm.

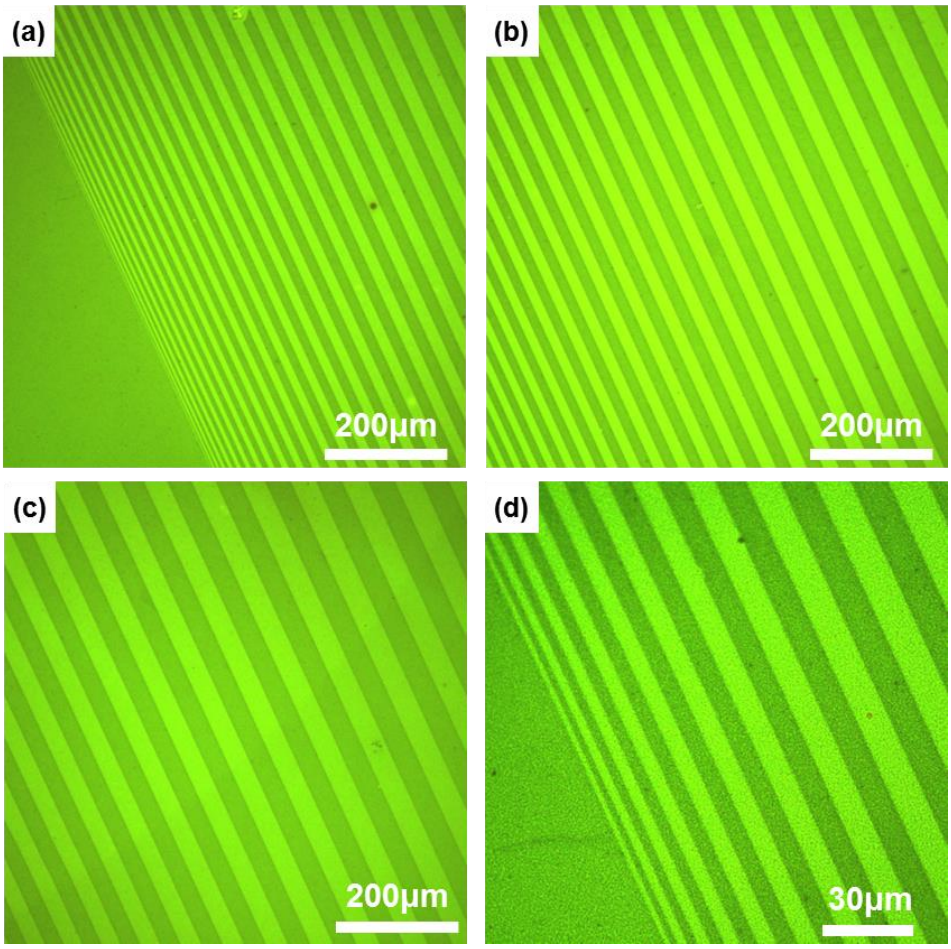

Figure F.13: PL images of an "off-beam" photopattern of positive face-profile lines with different width (using a varied width strip PDMS mask). (a) Small, (b) medium, (c) large, and (d) very large width lines. All scale bars are 200 µm. The photopattern was developed on an unstable yellow QD-PMMA film using UV light (21 mW/cm^2) for 60 minutes.

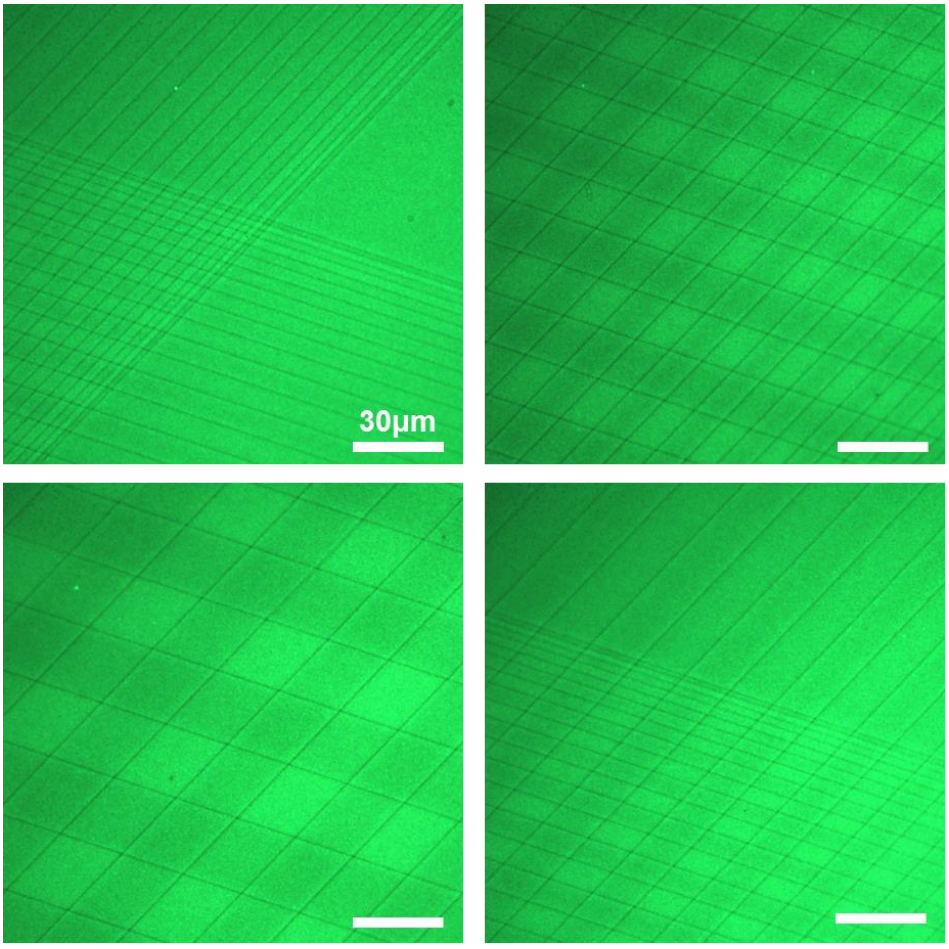

Figure F.14: PL images of a QD-polymer film (unstable green CdSe/ZnS QDs) photopatterned twice (on-beam patterning approach) using a PDMS mask of strips of varied width. The PDMS mask of each layer was angle off-set from each other to yield the cross-hatched photopattern. Each layer of the photopattern was developed for 20 minutes using UV light (21 mW/cm^2). Scale bar is 30 µm for all images.

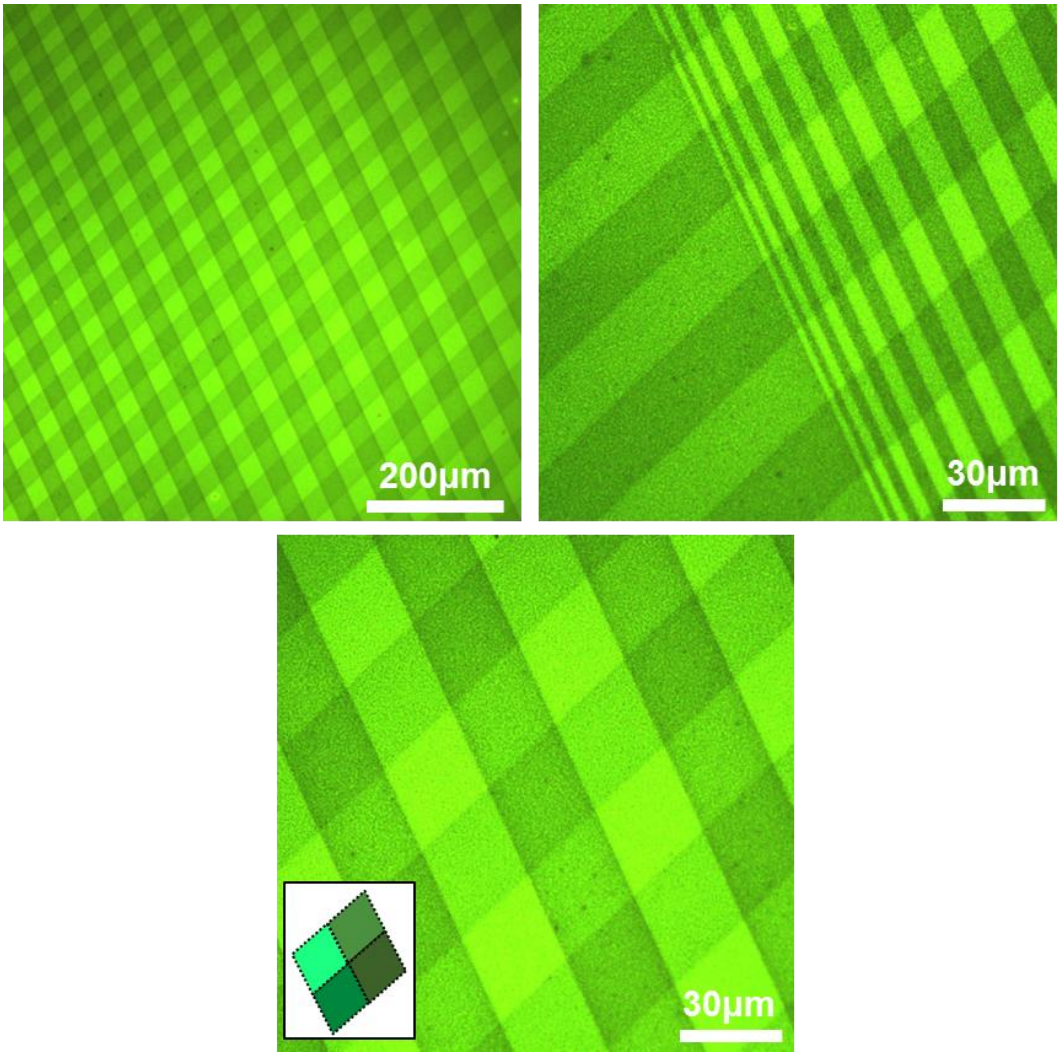

Figure F.15: PL images of a QD-polymer film (unstable yellow CdSe/ZnS QDs) photopatterned twice (off-beam patterning approach) using a PDMS mask of strips of varied width. The PDMS mask of each layer was angle off-set from each other to yield the cross-hatched photopattern. Each layer of the photopattern was developed for 60 minutes using UV light (21 mW/cm^2). (Inset) Simple schematic of the multi-level intensity contrast present in the cross-hatched patterns (low, medium, high, and very high intensity regions).

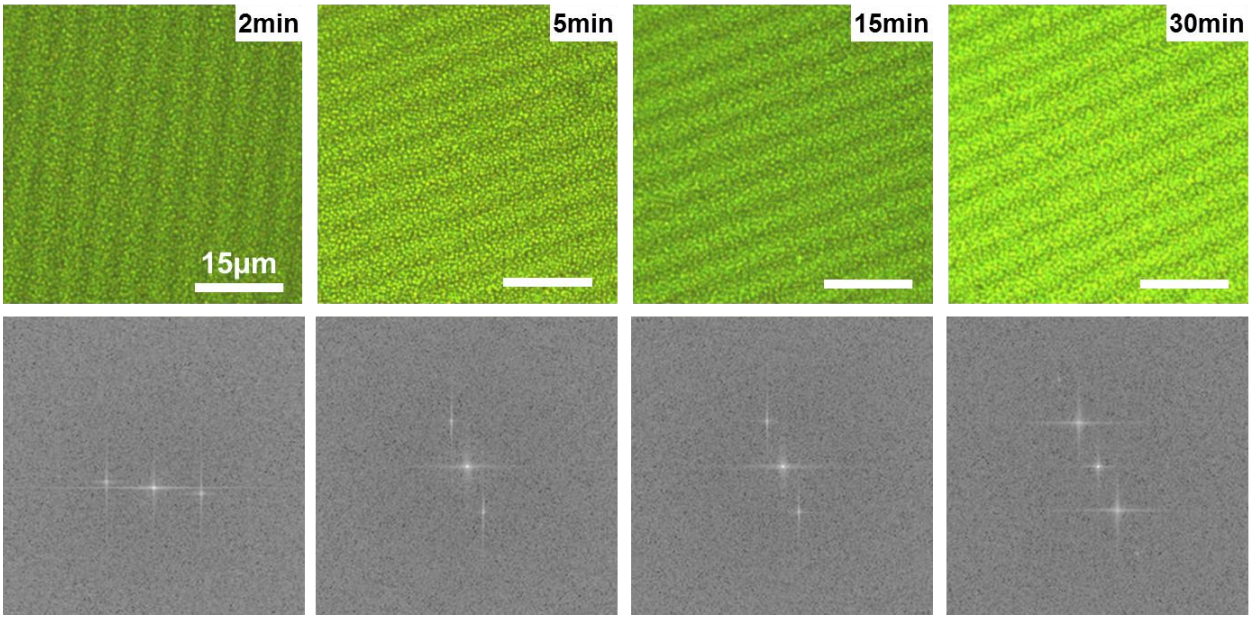

Figure F.16: (Top row) PL images of photopatterned parallel lines created using interference lithography for different development times. (Bottom row) Fast Fourier transforms of the PL images shown in the top row. The photopattern was developed on an unstable yellow QD-PMMA film using 532 nm light. Scale bar is 15 µm for all images.

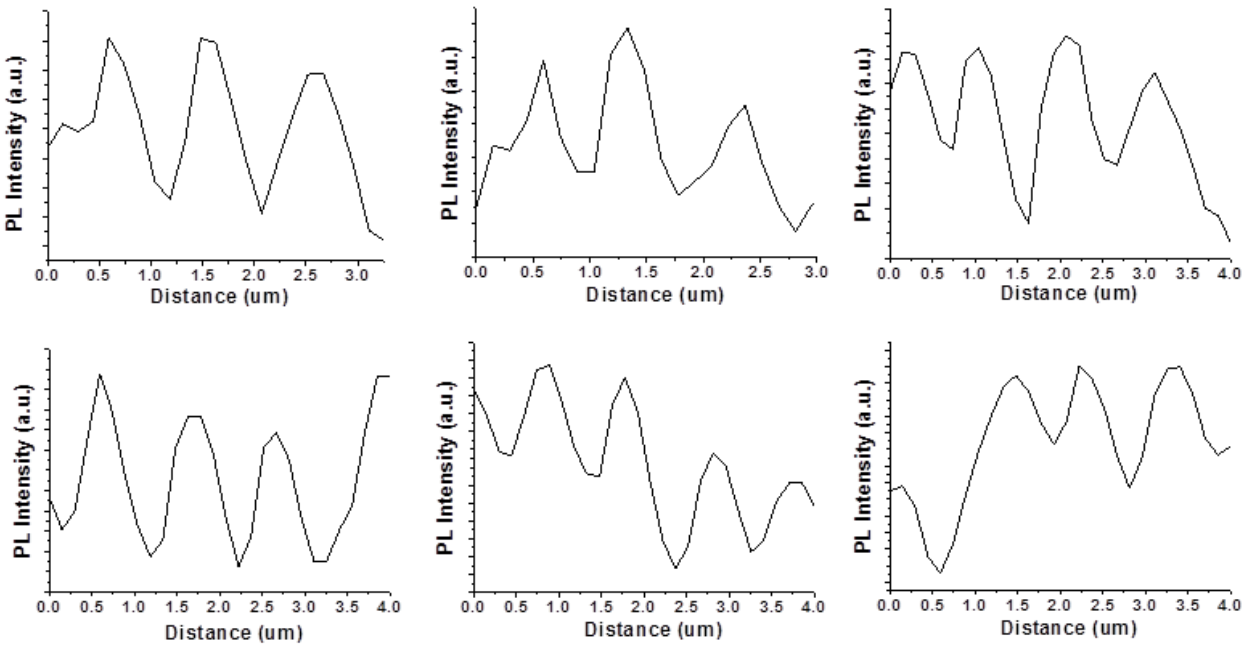

Figure F.17: Cross-sections of PL intensity of photopatterned sub-micron width periodic parallel lines (FWHM of 520±130 nm (N: 100), periodicity of 800±100 nm (N: 24). The photopattern was developed using laser interference lithography (Exposure: 532 nm light, 15 min).

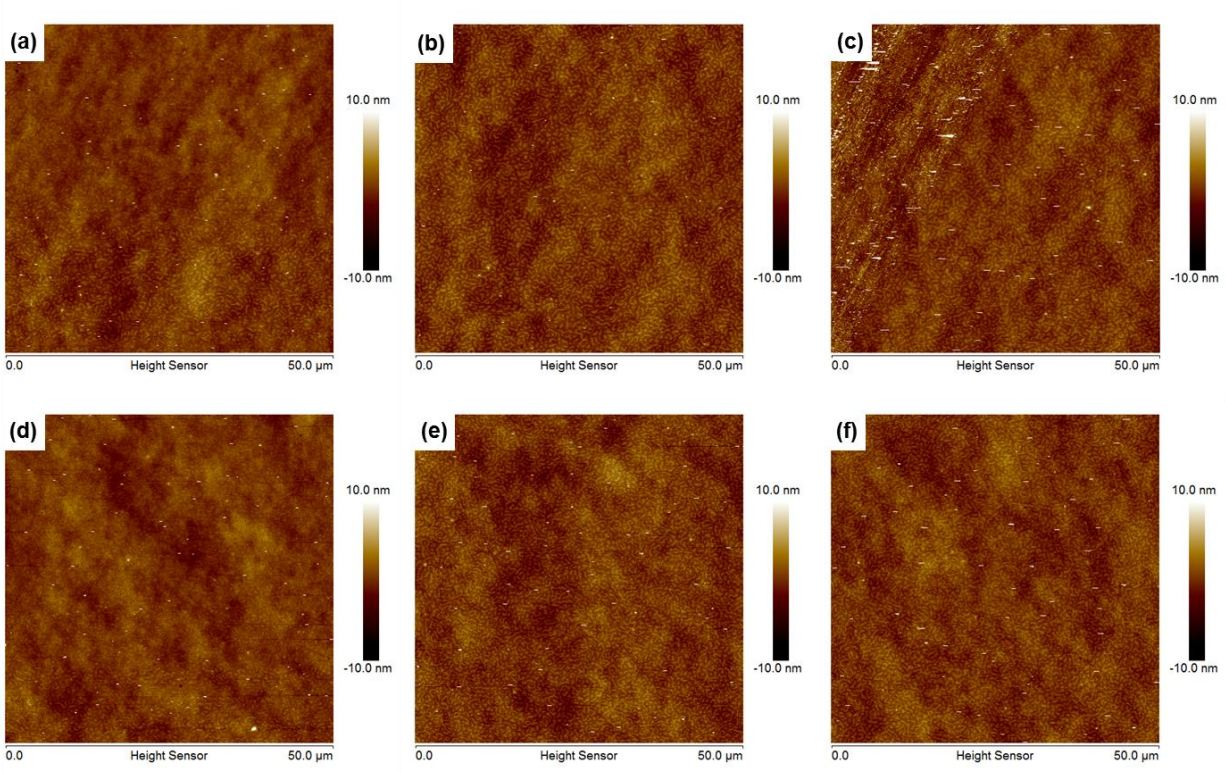

Figure F.18: AFM height scans of QD-PMMA films that were photopatterned using interference lithography for (a,b,c) a 30 min exposure period and (d,e,f) a 10 min exposure period.

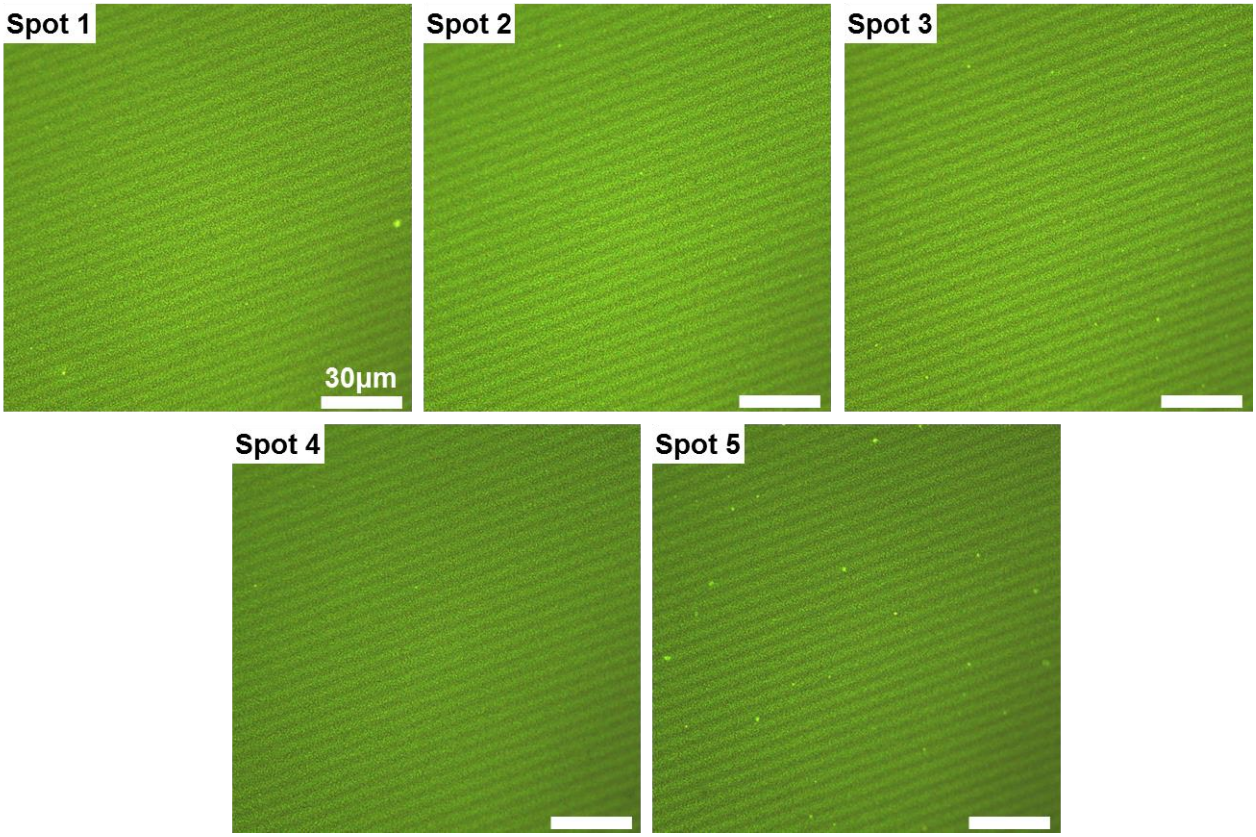

Figure F.19: PL images of photopatterned parallel lines of 5.5±0.5 um periodicity (created using interference lithography) from the four corners and center of a ≈1.3 cm x 1.3 cm substrate (larger size PL images of those shown in **Figure 9.10a**). The photopattern was developed using 532 nm light over 15 min. The film is an unstable yellow CdSe/ZnS QD-polymer film. Scale bar is 30 µm for all images.

Equation F.1: Equation outlining the relationship between the phase-shift (between light propagating in two adjacent materials) and the various system parameters (physical and optical).[1]

$$\textbf{\textit{Equation F.1}}: \qquad \varphi = \frac{2\pi}{\lambda} \Delta n \, t_{strctr}$$

Where:

φ = phase shift
λ = wavelength of light (in vacuum)
Δn = difference in refractive index between two materials
t_{strctr} = thickness of structure

References

1 Rogers, J.A.; Paul, K.E.; Jackman, R.J.; Whitesides, G.M., Generating similar to 90 nanometer features using near-field contact-mode photolithography with an elastomeric phase mask. *J. Vacuum Sci. & Tech. B* **1998,** *16,* 59-68.

Appendix G

Chapter 10 supporting data

(MULTICOLOR QD PHOTOPATTERNING APPROACHES)

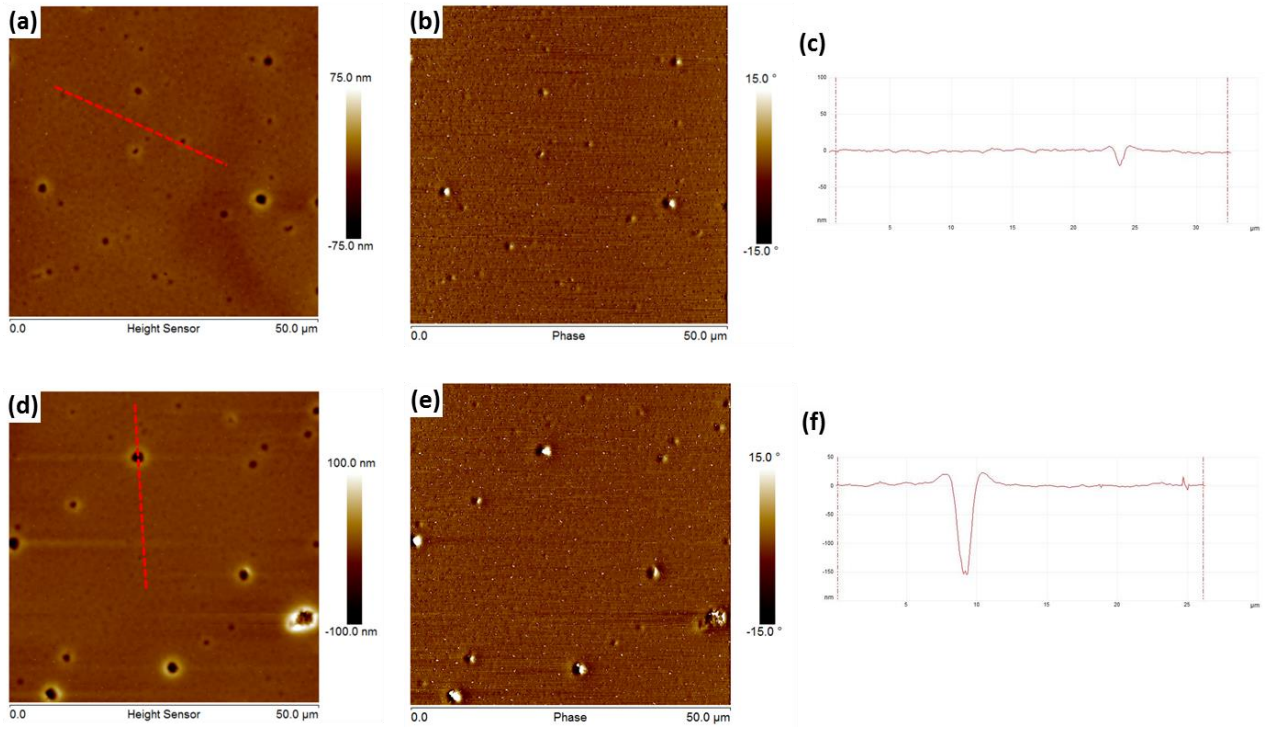

Figure G.1: AFM scans of height (a,d), phase (b,e), and height cross-sections (c,f) of different spots on the QD-polymer film show some defects but generally a surface with physical features less than 10 nm deep. A smooth phase image indicates minimal phase separation between the QD and PMMA.

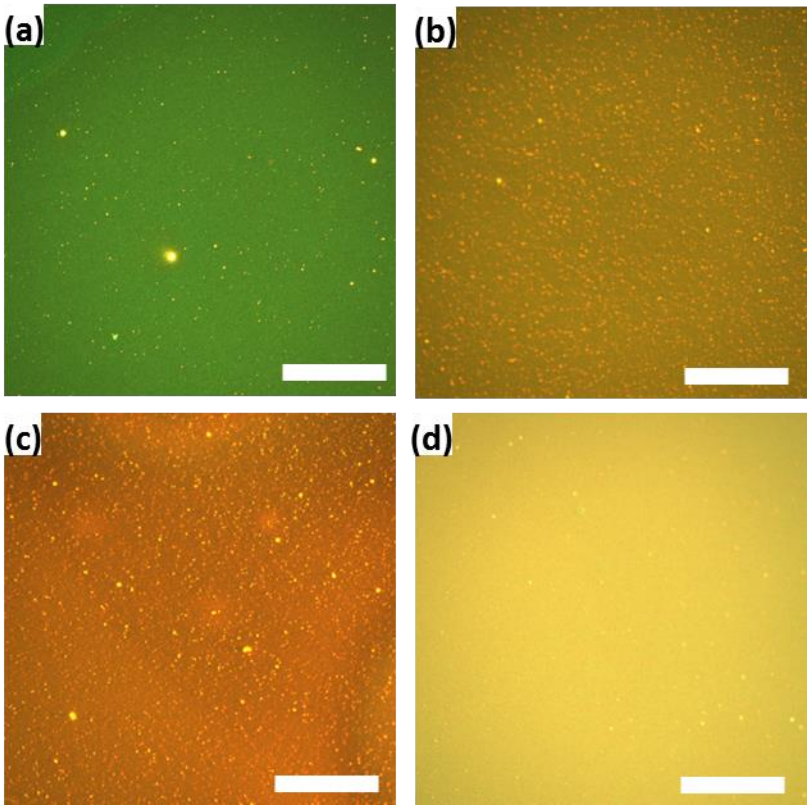

Figure G.2: Fluorescence imaging of the QD-polymer films before photopatterning with various red-green QD ratios and stability combinations. (a,b,c) Unstable green-red QD-polymer films and (d) Stable green-unstable red QD-polymer film. All scale bars are 200 um.

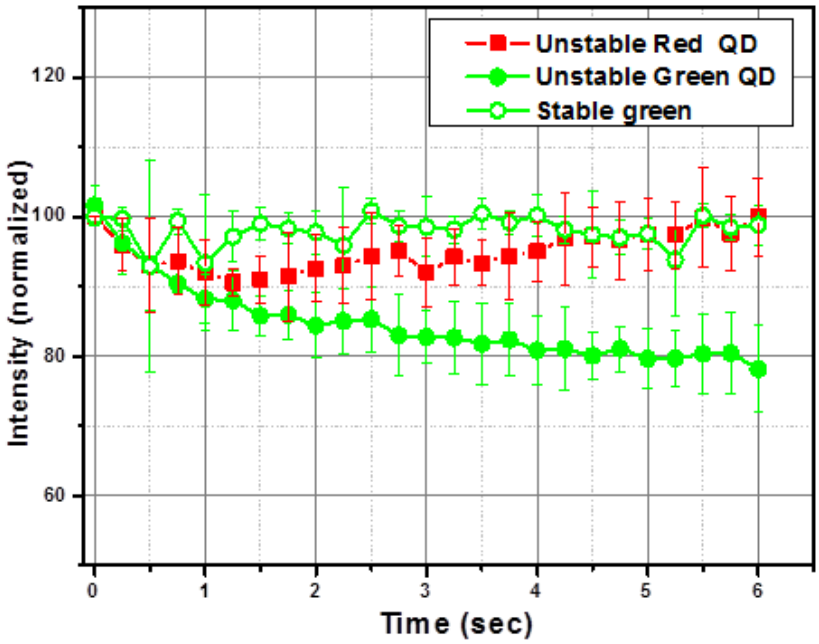

Figure G.3: The unstable QDs can exhibit both rapid and slower decay routes when exposed to light of 470 nm (28 mW). The initial rapid decay (first seconds of exposure) can reduce emission intensity by 10% for the unstable red QD and by 20% for the unstable green QDs. Decay quickly subsides for the unstable red QDs but continues to occur over minute time scales for the unstable green QDs (typically plateaus after 2 minutes). After the plateau period, recovery occurs over a period of 60 minutes or more. Stable alloyed green QDs show small fluctuations in intensity (±5%) but no significant change.

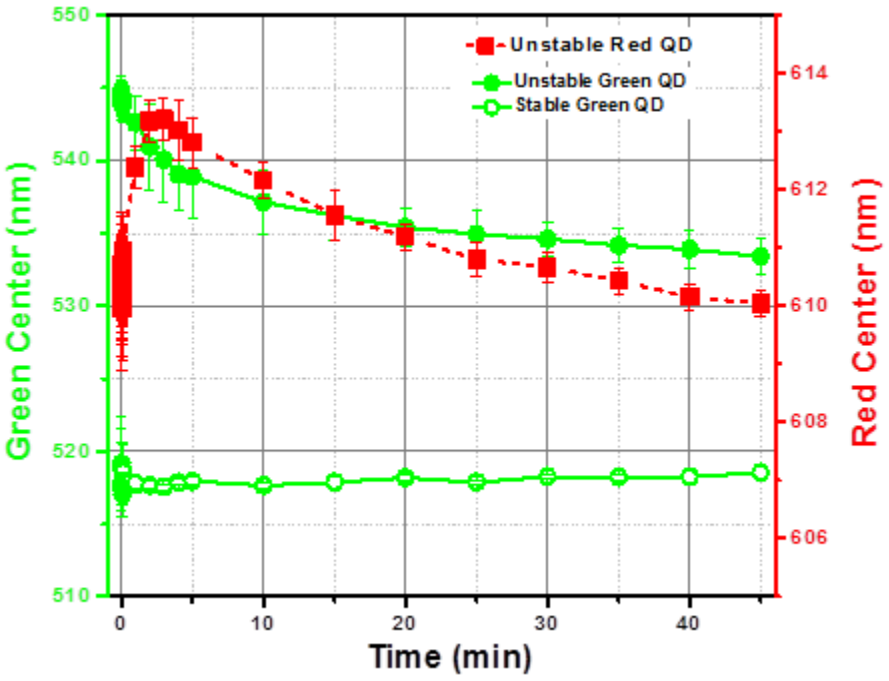

Figure G.4: The emission position can also shift when exposed to light (470 nm, 28 mW) due to changes in the size of the QDs and internal annealing of the core-shell interface. The emission position of the stable green QDs shows a small (1 nm) initial red-shift. Both the unstable red and green QDs exhibit a long-term blue shift in emission over an exposure period of 45 minutes (3 nm and 11 nm, respectively), which could be due to size reduction caused by photoannealing of the QD shell.

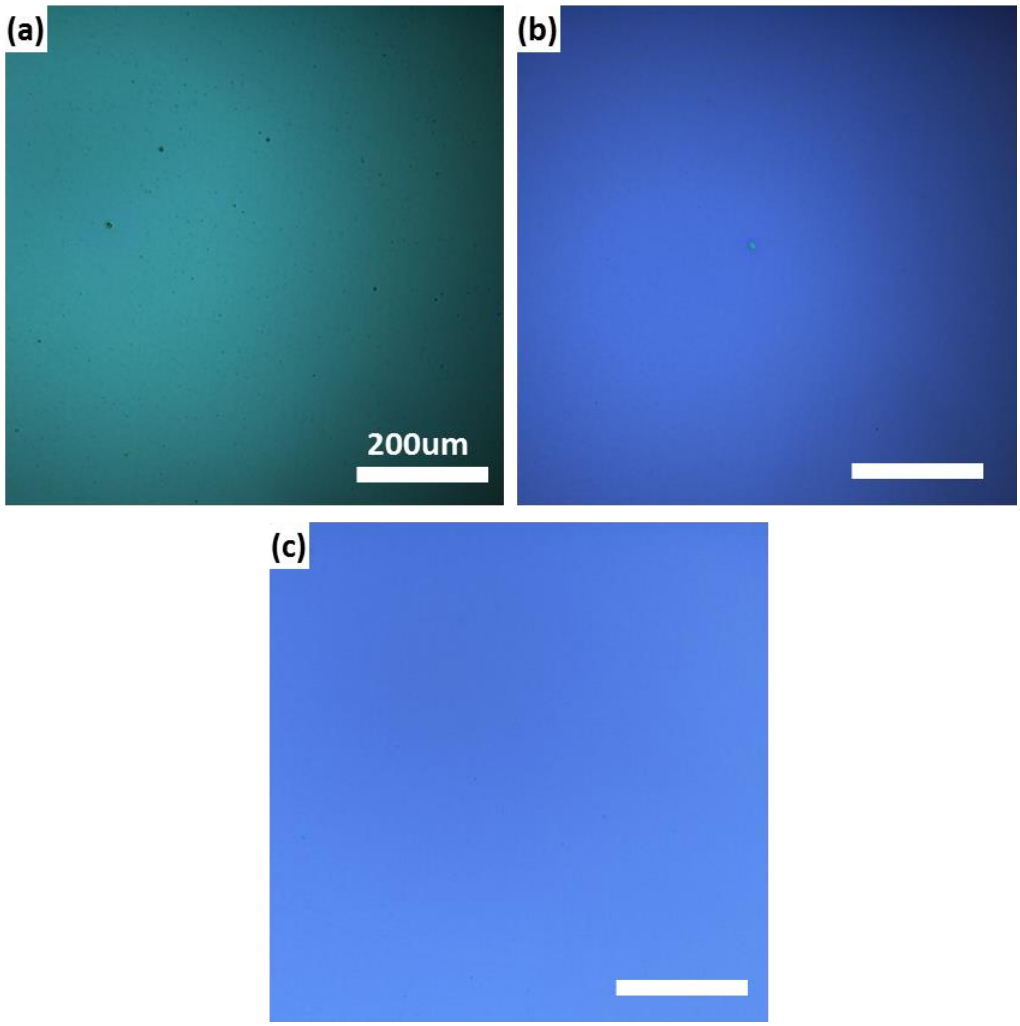

Figure G.5: Bright filed imaging of photopatterned regions developed using an (a) unstable red-green QD-polymer film (470 nm, 39.5 mW)and (b,c) stable green-unstable red QD-polymer film (350 nm, 2.5 mW) light. The blue color is due to the light source. There is no indication of any physical features that could account for the PL photopatterns. All scale bars are 200 um.

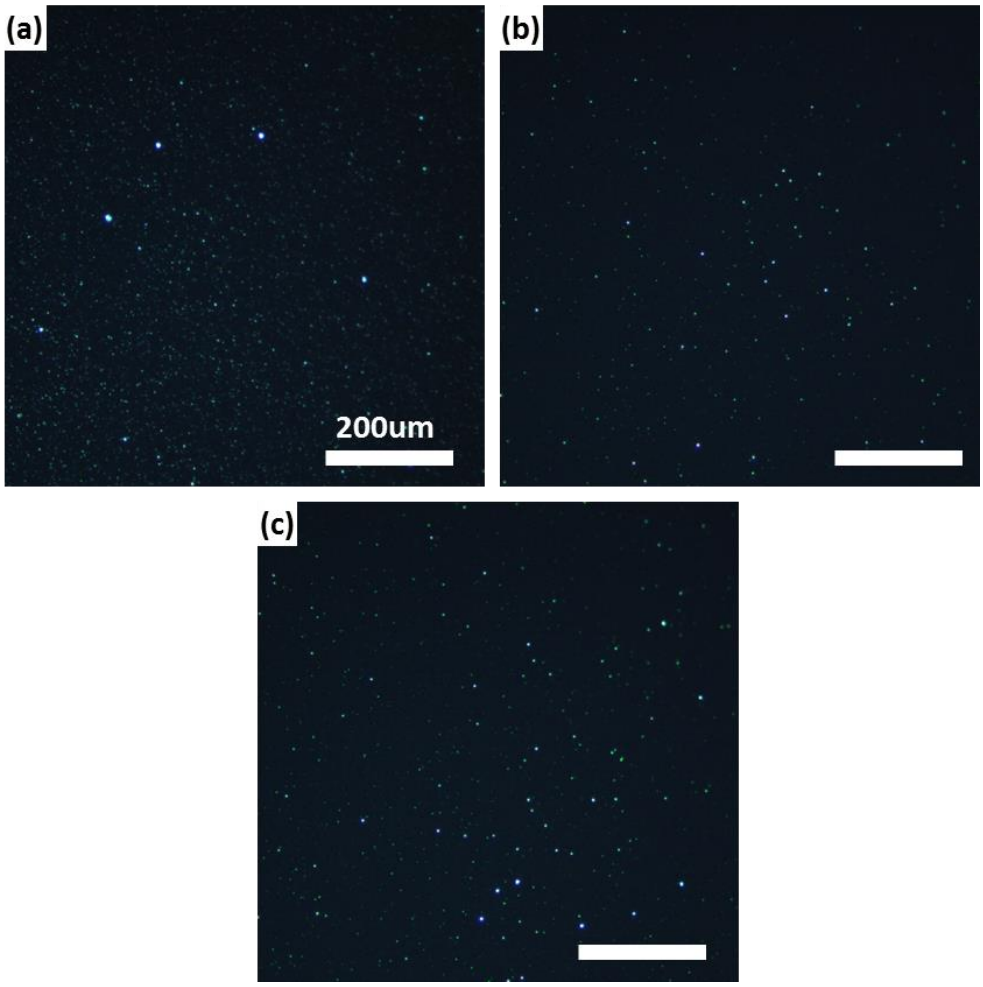

Figure G.6: Dark filed imaging of photopatterned regions developed using an (a) unstable red-green QD-polymer film (470 nm, 39.5 mW)and (b,c) stable green-unstable red QD-polymer film (350 nm, 2.5 mW) light. There is no indication of any physical features that could account for the PL photopatterns. All scale bars are 200 um.

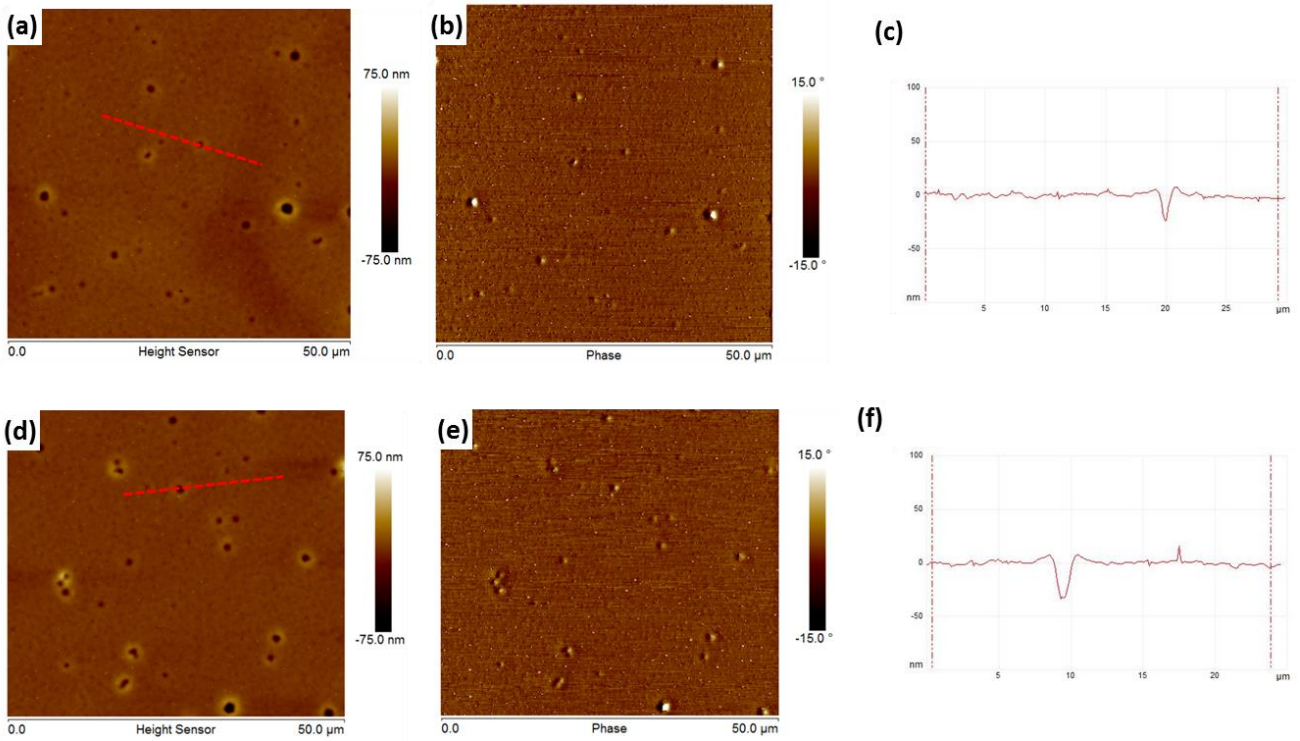

Figure G.7: AFM scans of height (a,d), phase (b,e), and height cross-sections (c,f) of different spots on the QD-PMMA film where photopatterns are present show no indication of physical patterning of the film. The lack of physical patterning indicates that the FL photopattern is due to intrinsic modification of the QD emission from exposure to the development light and not due to removal or deposition of material on the QD-PMMA film due to the deposition, presence, or removal of the TEM mask.

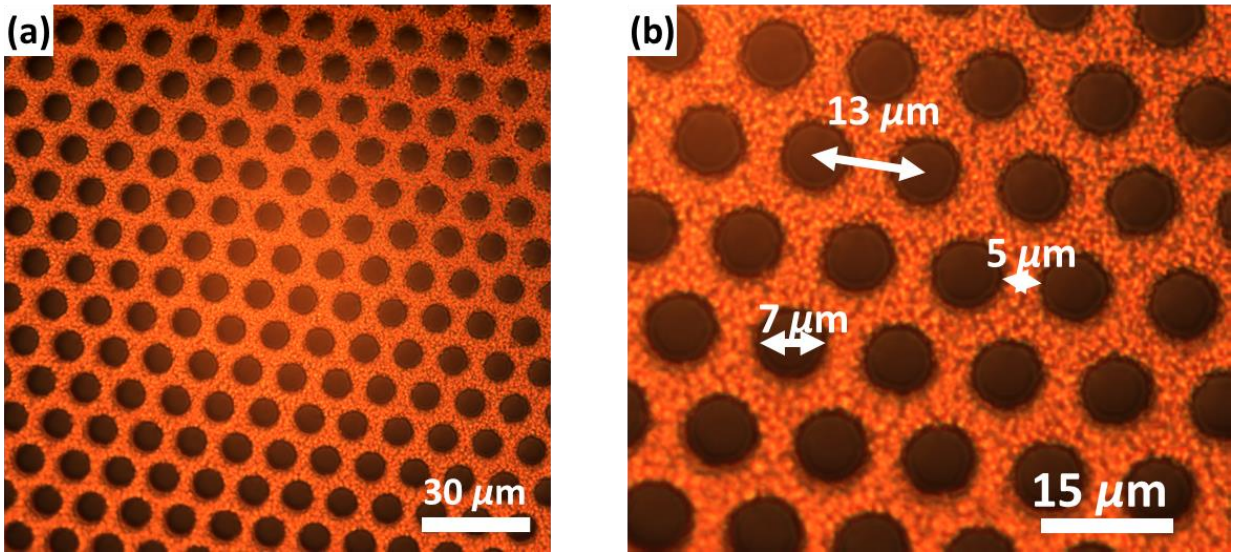

Figure G.8: The photomask used to fabricate the photopatterns is a G2000HA circular mesh (G2000HA-Cu) TEM grid (Electron Microscopy Sciences). The TEM grid was designed to have a pitch of 12.5 um, holes with a diameter of 6.5 um, and bars of 6 um. (a,b) Bright field imaging shows that the TEM grid is uniform over hundreds of microns and has dimensions closely matching those specified by the manufacturer.

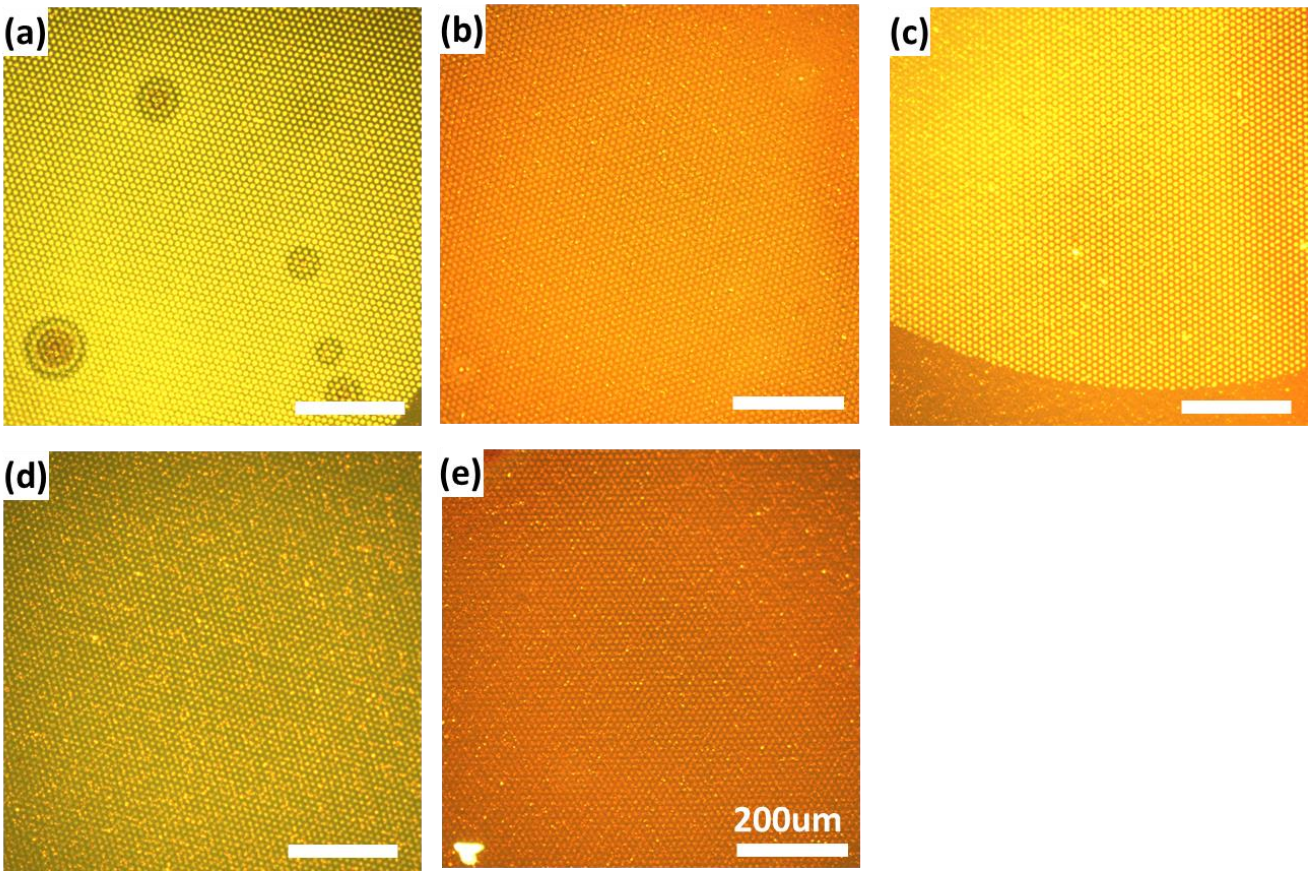

Figure G.9: Fluorescence imaging using light of (a,d) 470 nm (39.5 mW), (b,e) 580 nm (18.8 mW), and (c) 350 nm (2.5 mW), shows that the photopatterns cover areas of many 100 microns. All scale bars are 200 um.

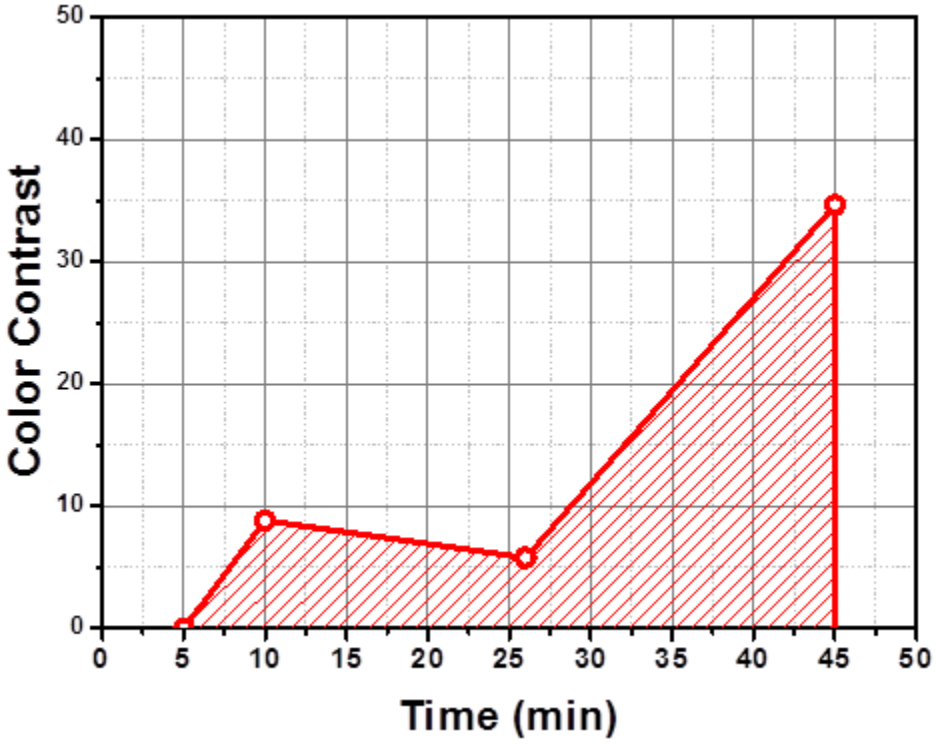

Figure G.10: The color contrast of the unstable red-green QD-polymer film patterned using the collective recovery method C1 is low early in development, increasing as development continues.

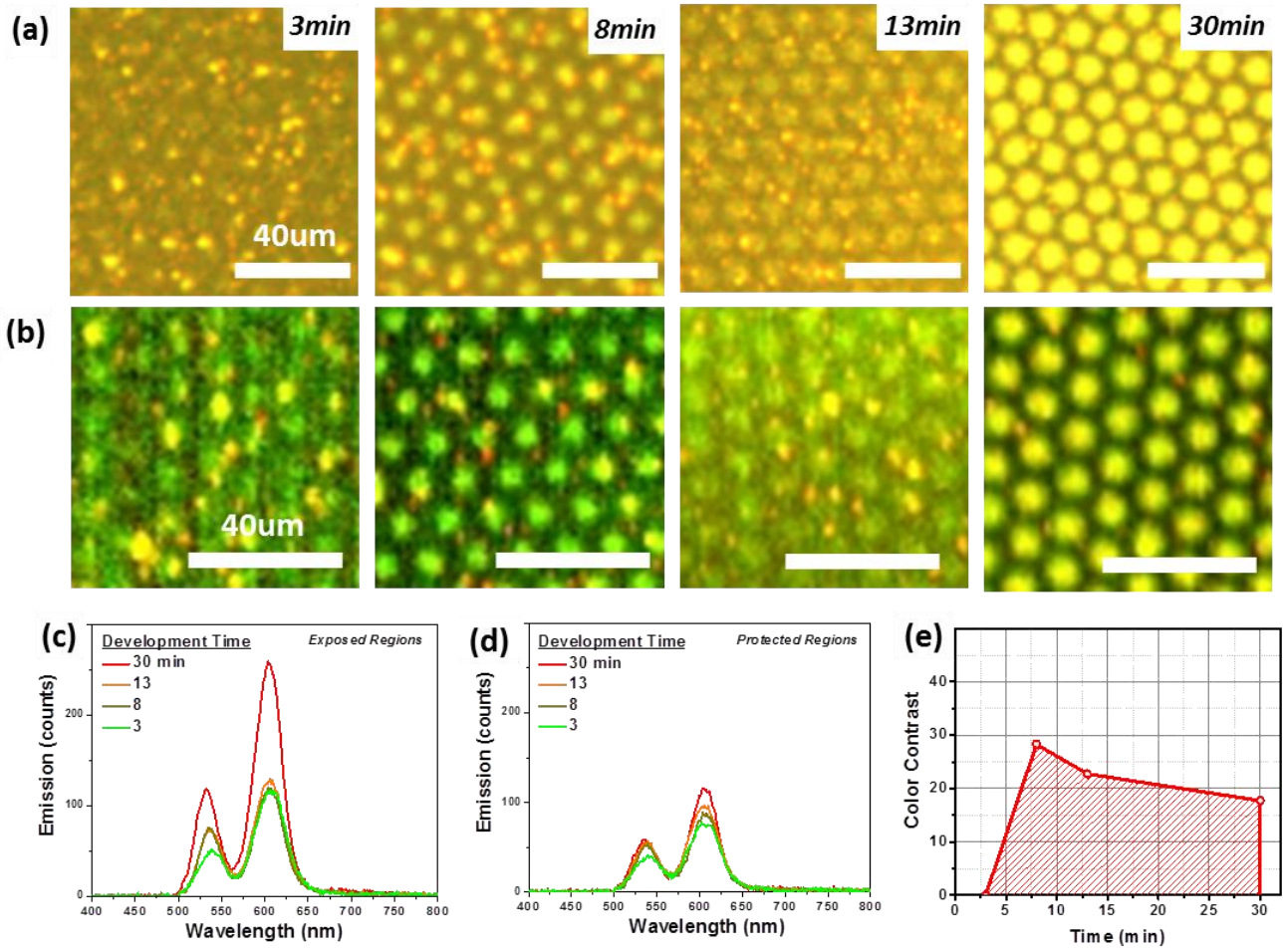

Figure G.11: Collective recovery: Unstable red and unstable green QDs are used to develop a photopattern using 470 nm and 39.5 mW ($\lambda_{development} < \lambda_{1s,green}$ & $\lambda_{1s,red}$). PL imaging (a) and hyperspectral scanning (b) show that longer exposure times lead to more recovery, yielding photopatterns with greater intensity contrast. PL spectra from the (c) exposed and (d) protected regions of the film show increases in emission intensity for both the red and green peaks. (e) The color contrast during the course of pattern development. All scale bars are 40 µm.

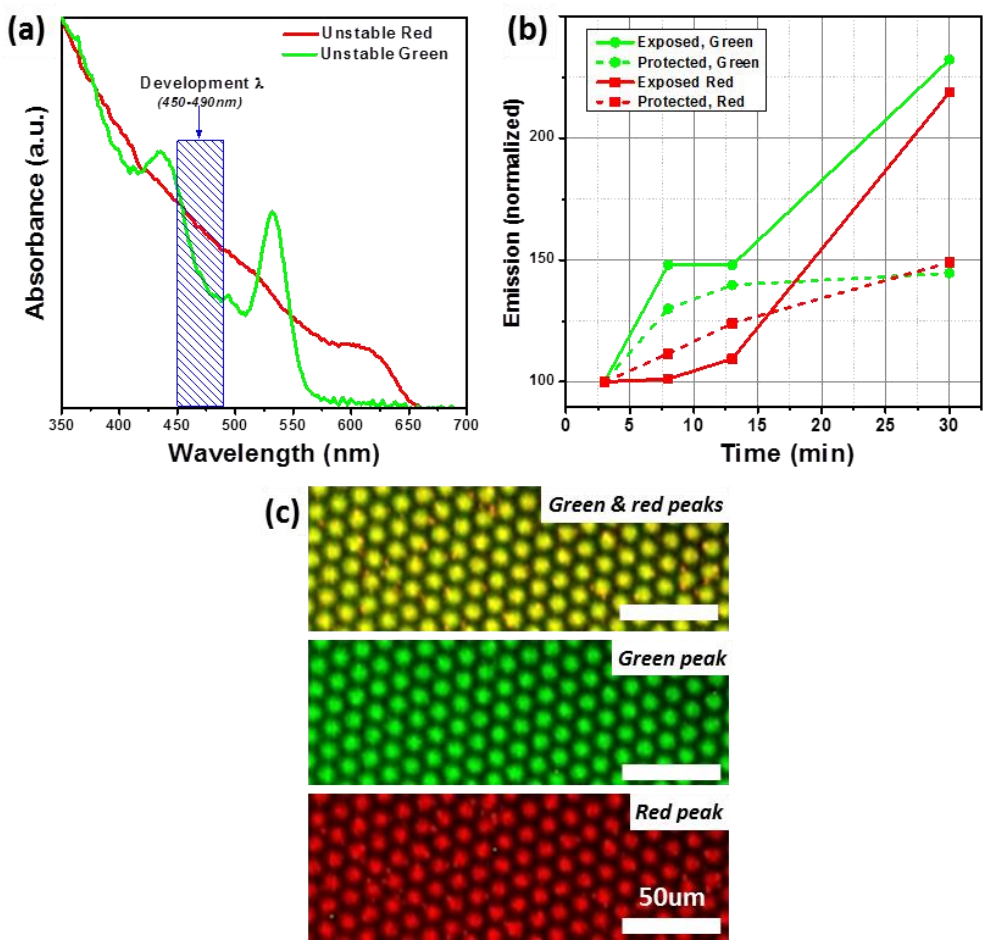

Figure G.12: Collective recovery: Unstable red and unstable green QDs are used to develop a photopattern using 470 nm (39.5 mW) light. (a) Collective recovery was achieved by developing the pattern with a wavelength that falls within the absorbance range of both QDs ($\lambda_{development} < \lambda_{1s,green}$ & $\lambda_{1s,red}$)(absorbance normalized at 350 nm for clarity). (b) Peak fitting of the PL spectra from the exposed and protected regions of the film show that the emission of both colors increases during the development period. Collective recovery patterning is confirmed via (c) hyperspectral scanning of the red & green, green, and red peaks shows a photopattern (30 minutes development) with high intensity contrast.

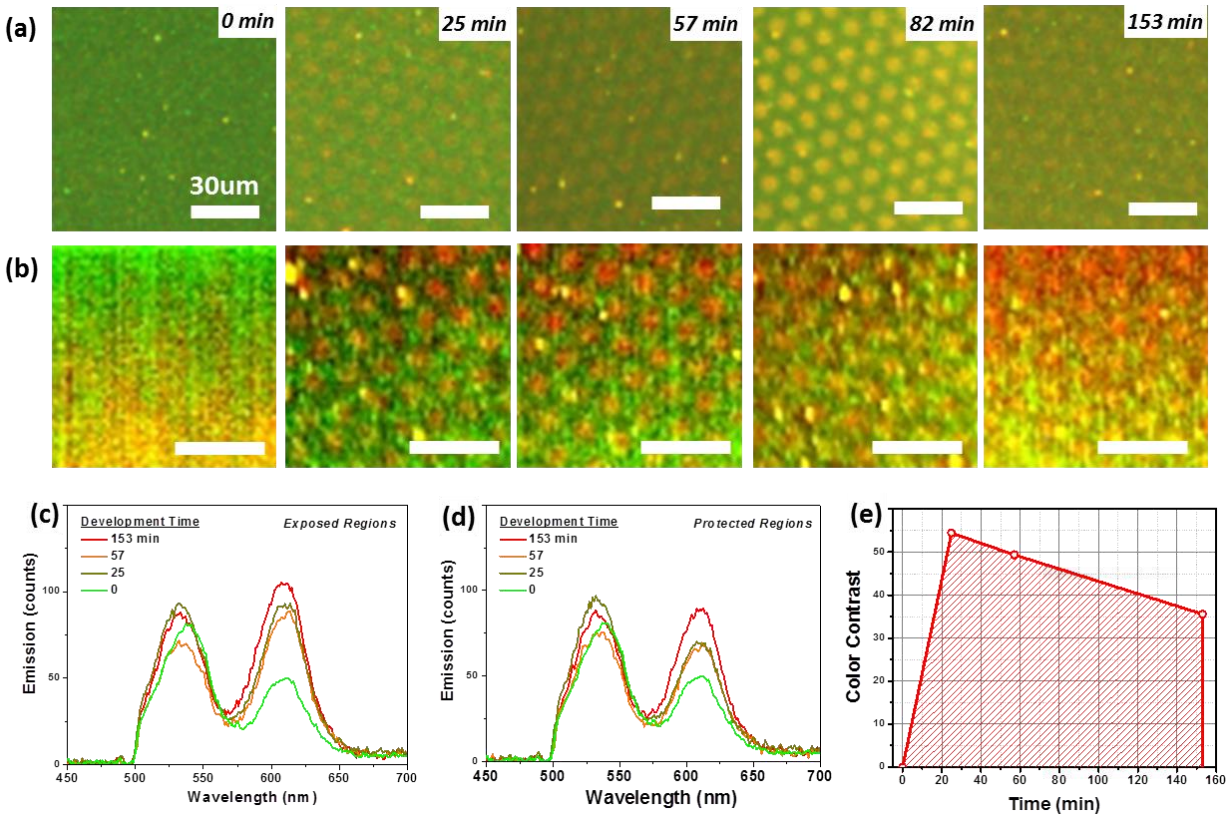

Figure G.13: Selective recovery via development wavelength (S1): Unstable red and unstable green QDs are used to develop a photopattern where a specific emission peak is recovered while the other remains constant for the duration of pattern development. (a) Unequal emission recovery was achieved by developing the pattern with light that only the red QDs can absorb strongly, in this case 580 nm and 17 mW ($\lambda_{1s,green} < \lambda_{development} < \lambda_{1s,red}$)(absorbance normalized at 350 nm for clarity). PL imaging (b) and hyperspectral scanning (c) show that longer exposure times lead to more recovery, yielding photopatterns with greater intensity contrast. PL spectra from the (c) exposed and (d) protected regions of the film show that the red emission increases while the green emission remains nearly constant during pattern development period. (e) The color contrast during the course of pattern development. All scale bars are 30 μm.

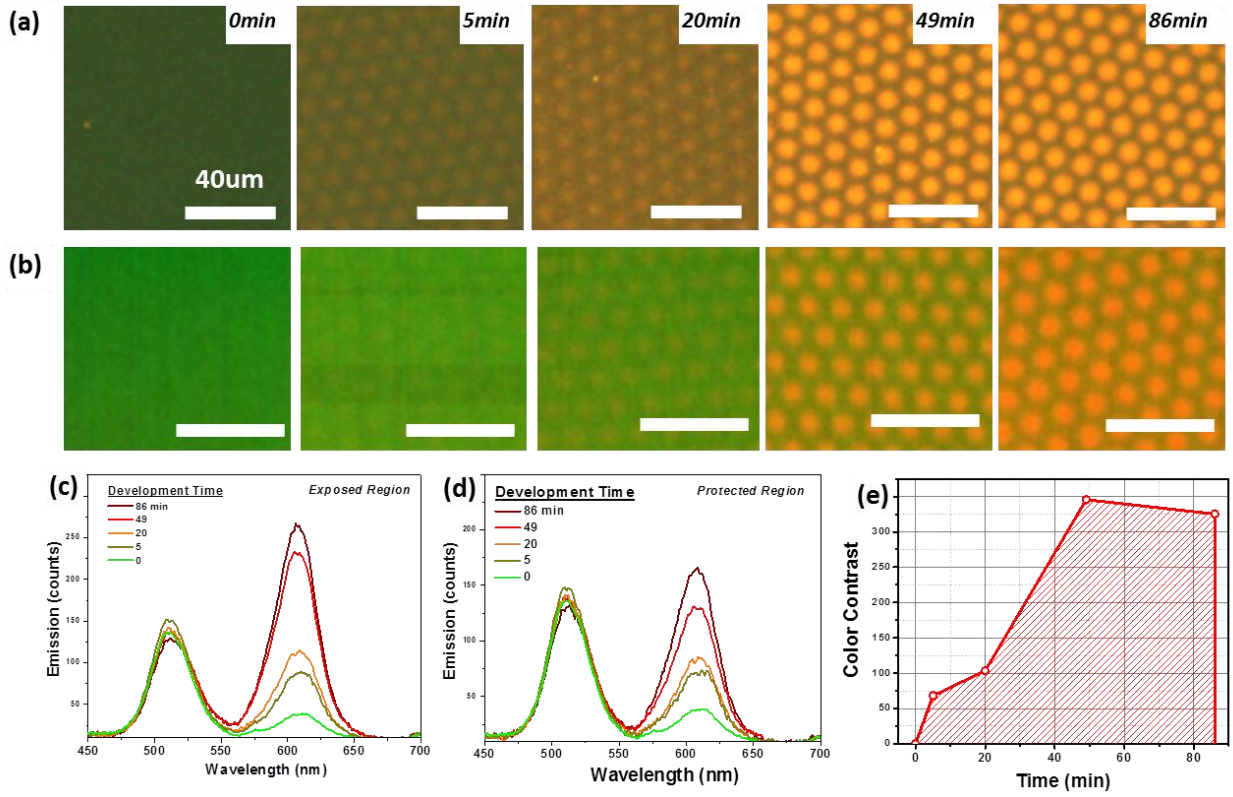

Figure G.14: Selective recovery via stable-unstable mixtures method (S2): Stable green and unstable red QDs are used to obtain a photopattern where only the emission of the unstable red QDs recovers. The only requirement for $\lambda_{development}$ is that it can be absorbed by the unstable QDs ($\lambda_{development} < \lambda_{1s,unstable}$). In this case, (a) this requirement is satisfied by using light of 350 nm (2.5 mW) which falls within the absorbance of the unstable red QDs (the absorbance is normalized at 350 nm for clarity). PL imaging (b) and hyperspectral scanning (c) show that longer exposure times lead to more recovery, yielding photopatterns with greater intensity contrast. PL spectra from the (c) exposed and (d) protected regions of the film show that the red emission increases while the green emission remains nearly constant during pattern development period. (e) The color contrast during the course of pattern development. All scale bars are 40 μm.

VITA

SIDNEY T. MALAK

Sidney T. Malak was born in Milwaukee, Wisconsin in May 1987 to Lea and Stephen Malak. He later moved with his family to Tulsa, Oklahoma where he attended elementary school. After finishing elementary school he and his family moved to Syracuse, New York where he attended Eagle Hill Middle School and Fayetteville-Manlius High School. He earned his BS in Physics (*cum laude*) and BS in Mechanical Engineering (*cum laude*) from Binghamton University (State University of New York, SUNY) in 2011. Following this he pursued his PhD in Materials Science and Engineering at the Georgia Institute of Technology where he was advised and mentored by Professor Vladimir V. Tsukruk. After finishing his PhD in late 2016/early 2017 he plans to pursue a career in industry pertaining to technology development.